The Effects of Hypoxia on the Anti-tumour Immune Response



Philip Macklin

Lincoln College

Nuffield Department of Medicine

University of Oxford

A thesis submitted for the degree of

Doctor of Philosophy

November 2020

For Catherine, Sebbie and Dad

Abstract – The Effects of Hypoxia on the Anti-tumour Immune Response

Philip Macklin, Lincoln College *DPhil in Clinical Medicine, Michaelmas Term 2020*

Hypoxia is an adverse prognostic feature in cancer, conferring resistance to treatments including immunotherapy. In this thesis, image analysis of human tumour histology samples and murine models is utilised to evaluate some aspects of the interactions between tumour oxygenation, cellular oxygen sensing and immunity.

In Chapter 1, a novel image analysis pipeline is validated and utilised to analyse the distribution, relative to hypoxia, of tumour infiltrating leukocytes in pimonidazole-treated head and neck squamous cell carcinomas before comparing the observed distributions to those in clear cell renal cell carcinoma, a tumour characterised by perturbed oxygen sensing. Leukocyte-specific distribution patterns were shared by both tumour types, with lymphoid cells largely restricted to better oxygenated perivascular regions and myeloid cells being more diffusely distributed including within profoundly hypoxic necrotic regions.

In Chapter 2, this pipeline is used to evaluate immunohistochemically labelled hypoxia, vascular and immunological markers in lung cancer samples from participants in a clinical study evaluating whether atovaquone, an oxidative phosphorylation inhibitor, reduces tumour hypoxia. Although scoring of all markers was equivalent between groups, given that atovaquone-treated tumours were more hypoxic at baseline, this may represent a meaningful finding.

Abstract

Chapter 3 concerns histological phenotyping of transgenic mice in which hypoxia-inducible factor (HIF) was up-regulated through reversible prolyl hydroxylase domain-containing protein 2 (*Phd2*) gene silencing, leading to regulatory T lymphocyte dysfunction and autoimmunity.

Given that regulatory T lymphocytes suppress anti-tumour immunity, in Chapter 4, the effects of host *Phd2* silencing are assessed in murine tumour models. Disappointingly, this intervention affected neither tumour growth nor immune contexture.

Declaration of Authorship

I declare that the work presented in this thesis is wholly my own work, with the exception of the following components:

Chapter 1

- Image analysis scripts (also used in Chapters 2 and 4) developed by Dr Joshua Bull and Professor Helen Byrne (The Wolfson Centre for Mathematical Biology, University of Oxford)
- Image analysis classifiers trained by Dr Síle Johnson (The University of Oxford Medical School) and Dr Atsushi Yamamoto (Nuffield Department of Medicine, University of Oxford)
- Immune cell counts performed by Dr Robert Pell (Department of Oncology, University of Oxford) and Dr Kalani Kuruppu (Department of Cellular Pathology, Oxford University Hospitals NHS Foundation Trust)
- Kidney cancer samples for semaphorin 3A histological analysis provided by Dr Mike Barnkob and Professor Vincenzo Cerundolo (Weatherall Institute of Molecular Medicine, University of Oxford)

Chapter 2

- Lung cancer samples for histological analysis provided by Dr Michael Skwarski, Mr Marcus Green and Professor Geoff Higgins (Department of Oncology, University of Oxford)

- Pimonidazole, carbonic anhydrase 9, CD31 and CD146 immunohistochemical staining performed by Ms Leticia Campo and Ms Tasneem Hassanali (Department of Oncology, University of Oxford)
- PD-L1 immunohistochemical staining performed by Ms Victoria Barnwell (Department of Cellular Pathology, Oxford University Hospitals NHS Foundation Trust)
- Image analysis classifier validation performed by Dr Alistair Easton (Department of Oncology, University of Oxford)
- PD-L1 immunohistochemistry manual scoring performed by Dr Mark McCole (Department of Cellular Pathology, Oxford University Hospitals NHS Foundation Trust)

Chapter 3

- Phenotypic data and murine tissue samples for histological analysis provided by Dr Atsushi Yamamoto
- Some histological processing performed by Ms Hiromi Kudo and Professor Robert Goldin (Centre for Pathology, Imperial College London)
- Anti-nuclear antibody analysis (as for Chapter 4) performed by Ms Tanya Crockford (Nuffield Department of Medicine, University of Oxford)
- Bone marrow transplantation experiments performed by various members of the Transplant Research and Immunology Group under the supervision of Dr Fadi Issa and Dr Joanna Hester (Nuffield Department of Surgery, University of Oxford)

Chapter 4

- Some histological sectioning performed by Dr Indrika Ratnayaka (Ludwig Institute for Cancer Research, University of Oxford) and Dr Ida Parisi (Kennedy Institute of Rheumatology, University of Oxford)

- Flow cytometry conducted jointly with Dr James McAuliffe and Ms Laurine Noblecourt (Ludwig Institute for Cancer Research, University of Oxford)

Appendix 1

- Systematic literature search conducted jointly with Dr Tessa Greenhalgh (Department of Oncology, University of Oxford) with advice from Ms Eli Harriss (Bodleian Health Care Libraries, University of Oxford)

Acknowledgements

I acknowledge the contribution to this study made by the Oxford Centre for Histopathology Research (OCHRe) and the Oxford Radcliffe Biobank, which are supported by the National Institute for Health Research (NIHR) Oxford Biomedical Research Centre. In addition, I would like to thank Dr Russell Leek (Medical Sciences Division, University of Oxford) and Professor Adrian Harris (Department of Oncology, University of Oxford) for facilitating access to pimonidazole-treated head and neck tumour samples, Dr Michael Skwarski, Mr Marcus Green and Professor Geoff Higgins (Department of Oncology, University of Oxford) for providing pimonidazole-treated lung tumour samples from the ATOM (Atovaquone as Tumour HypOxia Modifier) study and Dr Tessa Greenhalgh and Professor Tim Maughan (Department of Oncology, University of Oxford) for providing pimonidazole-treated rectal tumour samples from the RHYTHM-I: Investigating Hypoxia in Rectal Tumours study. Dr Mike Barnkob and Professor Vincenzo Cerundolo (Weatherall Institute for Molecular Medicine, University of Oxford) provided kidney tumour samples for analysis of semaphorin 3A expression whilst Dr Ketan Shah and Dr Lisa Browning (Department of Cellular Pathology, Oxford University Hospitals NHS Foundation Trust) provided useful assistance in selecting appropriate human tumour blocks for histological analysis.

All automated immunohistochemical staining of human tumour samples was performed in the Translational Histopathology Laboratory in the Department of Oncology, University of Oxford, with assistance and training provided by Ms Leticia Campo and Ms Tasneem Hassanali. Slide scanning was performed in the Ludwig Institute of Cancer Research, University of Oxford, with assistance from Mr Richard Lisle. I am extremely grateful to Dr Joshua Bull and Professor Helen Byrne (Wolfson Centre for Mathematical Biology, University

of Oxford) for access to image analysis scripts and for our ongoing collaboration developing novel approaches to describing the spatial distribution of tumour infiltrating leukocytes. I would like to acknowledge the contributions of Dr Robert Pell (Department of Oncology, University of Oxford), Dr Kalani Kuruppu (Department of Cellular Pathology, Oxford University Hospitals NHS Foundation Trust) and Dr Síle Johnson (The University of Oxford Medical School) in developing and validating image analysis classifiers. Mr Mark Shipman (Ludwig Institute of Cancer Research, University of Oxford), Dr Nasullah Khalid Alham (Department of Engineering Science, University of Oxford) and Dr Alistair Easton (Department of Oncology, University of Oxford) all provided help in benchmarking our image analysis algorithms against scoring undertaken by a human pathologist and other available image analysis software. Dr Mark McCole (Department of Cellular Pathology, Oxford University Hospitals NHS Foundation Trust) performed manual scoring of PD-L1 immunohistochemistry slides from the ATOM study.

I am grateful to all members of the Wellcome Centre for Human Genetics Functional Genetics Facility, University of Oxford, for their assistance with animal care and the *in vivo* experiments that I conducted. In particular, Mr Douglas Dos Santos Passos, Mr Luke Harris, Ms Claudia Cifrodelli, Ms Heather Chandler and Ms Viv Clark were of great help. Dr Indrika Ratnayaka (Ludwig Institute for Cancer Research, University of Oxford), Dr Ida Parisi (Kennedy Institute of Rheumatology, University of Oxford) and Ms Hiromi Kudo (Centre for Pathology, Imperial College London) assisted in histological preparation of some murine tissue samples. Dr Cheryl Scudamore (Veterinary Pathology, Medical Research Council [MRC] Harwell Institute), Dr Elizabeth Soilleux, Dr Daniel Royston and Professor Ian Roberts (Department of Cellular Pathology, Oxford University Hospitals NHS Trust), Professor Robert Goldin and Professor Gordon Stamp (Centre for Pathology, Imperial College London) all contributed helpful

opinions on the murine histopathology presented in this thesis. I am grateful to Dr Fadi Issa and Dr Joanna Hester (Nuffield Department of Surgery, University of Oxford) for sharing flow cytometry reagents and to Dr James McAuliffe and Ms Laurine Noblecourt (Ludwig Institute for Cancer Research, University of Oxford) for assistance in undertaking flow cytometry and analysing the results. Ms Tanya Crockford (Nuffield Department of Medicine, University of Oxford) kindly screened murine serum samples for the presence of anti-nuclear antibodies. Dr Tessa Greenhalgh (Department of Oncology, University of Oxford) and Ms Eli Harriss (Bodleian Health Care Libraries, University of Oxford) kindly assisted with the systematic literature search presented in Appendix 1.

I am indebted to the Jean Shanks Foundation and The Pathological Society of Great Britain and Ireland who supported my research through provision of a Clinical Research Training Fellowship. I would like to acknowledge Professor Bass Hassan, my college advisor, and all of the Fellows and staff of Lincoln College, University of Oxford, for their support. I would also like to thank all members of the Oxygen Sensing Group at the University of Oxford for helpful discussions relating to my data, and oxygen biology in general, and for their ongoing encouragement. In particular, I am grateful to Professor Peter Ratcliffe for hosting me in his laboratory and to his personal assistant, Ms Catherine King, for administrative support. I am particularly thankful to Dr Atsushi Yamamoto for assistance with undertaking animal experiments and general training in laboratory techniques and to the examiners who assessed me during my doctoral studies, particularly Professor Gareth Thomas (University of Southampton), Professor Jane McKeating (Nuffield Department of Medicine, University of Oxford) and Dr Gareth Turner (Department of Cellular Pathology, Oxford University Hospitals NHS Foundation Trust).

Acknowledgements

I would like to thank my supervisors Professor Vincenzo Cerundolo and Professor Chris Pugh. Sadly, Enzo died during my doctorate but I am grateful for the encouragement and support that he provided during its early stages. Chris's intellectual input, academic supervision and broader mentorship were critical to completion of this thesis. His generosity, patience and humour were a source of inspiration during the more challenging times. Finally, but most importantly, I would like to thank my friends and family for their understanding and support throughout my doctoral studies.

Contents

Introduction **1**

Scientific background 1

Thesis aims and structure 34

Materials and Methods **35**

Chapters 1 and 2 35

Chapters 3 and 4 45

Statistical analyses 64

Chapter 1 **65**

Chapter aim 65

Introduction 65

Results 68

Discussion 99

Chapter 2 **126**

Chapter aim 126

Introduction 126

Results 137

Discussion 167

Chapter 3 **174**

Chapter aim 174

Introduction 174

Results 176

Discussion 194

Chapter 4 **203**

Chapter aim 203

Introduction 203

Results 208

Discussion 226

Discussion and Future Directions **236**

Appendix 1 – A systematic review of immunohistochemical studies comparing the expression of endogenous hypoxia markers to exogenous hypoxia marker labelling in malignant human tumours **241**

Appendix 2 – Head and neck squamous cell carcinoma cohort **287**

Appendix 3 – Clear cell renal cell carcinoma with necrosis cohort **292**

Appendix 4 – Semaphorin 3A clear cell renal cell carcinoma cohort **305**

Appendix 5 – ATOM (Atovaquone as Tumour HypOxia Modifier) study cohort **308**

Appendix 6 – Human immunohistochemistry optimisation/validation **312**

Appendix 7 – Semi-automated ImaGe analysis for HisTology data (SIGHT) pipeline **319**

Appendix 8 – Inducible knockdown transgenic mice **323**

Appendix 9 – Murine immunohistochemistry optimisation/validation **326**

Appendix 10 – Flow cytometry gating strategies **328**

Publications **333**

References **337**

List of Figures

Figure I.1 – Overview of glycolysis and oxidative phosphorylation 2

Figure I.2 – Regulation of the hypoxia-inducible factor (HIF) system by oxygen availability 5

Figure I.3 – Overview of acute and chronic tumour hypoxia 11

Figure I.4 – Overview of the tumour microenvironment 13

Figure I.5 – Overview of the innate and adaptive immune systems 14

Figure I.6 – Overview of the cancer-immunity cycle 16

Figure I.7 – Overview of helper T lymphocyte differentiation 21

Figure I.8 – Overview of macrophage polarisation 23

Figure I.9 – Overview of immune checkpoint blockade in cancer immunotherapy 26

Figure I.10 – Overview of opportunities for immunotherapeutic intervention in cancer 28

Figure 1.1 – Optimisation of pimonidazole immunohistochemistry 69

Figure 1.2 – Validation of Semi-automated ImaGe analysis for HisTology data (SIGHT) image analysis pipeline 72

Figure 1.3 – Correlation of markers of hypoxia in head and neck squamous cell carcinoma cohort 79

Figure 1.4 – Correlation between tumour hypoxia and immune cell infiltration in head and neck squamous cell carcinoma cohort 81

Figure 1.5 – Analysis of immune cell spatial distribution with respect to regions of tumour hypoxia in head and neck squamous cell carcinoma cohort 83

Figure 1.6 – Qualitative analysis of $CD68^+$ cell distribution with respect to regions of tumour hypoxia in head and neck squamous cell carcinoma cohort 85

Figure 1.7 – Analysis of T lymphocyte to macrophage ratios with respect to regions of tumour hypoxia in head and neck squamous cell carcinoma cohort 87

List of Figures

Figure 1.8 – Qualitative analysis of $CD4^+$ and $CD19^+$ cell distributions in head and neck squamous cell carcinoma cohort 88

Figure 1.9 – Comparison of carbonic anhydrase 9 expression in clear cell renal cell carcinoma and chromophobe renal cell carcinoma 89

Figure 1.10 – Analysis of the spatial distribution of tumour infiltrating lymphocytes along oxygen gradients in clear cell renal cell carcinoma 91

Figure 1.11 – Analysis of the spatial distribution of tumour infiltrating macrophages along oxygen gradients in clear cell renal cell carcinoma 93

Figure 1.12 – Comparison of the spatial distribution of tumour infiltrating macrophages and neutrophils along oxygen gradients in clear cell renal cell carcinoma 95

Figure 1.13 – Analysis of the spatial distribution of tumour infiltrating dendritic cells along oxygen gradients in clear cell renal cell carcinoma 96

Figure 1.14 – Analysis of the spatial distribution of $CD8^+$ T lymphocytes and semaphorin 3A expression relative to tumour vasculature in clear cell renal cell carcinoma 98

Figure 1.15 – Development of novel mathematical descriptors of immune cell distribution within tumours 123

Figure 2.1 – ATOM (Atovaquone as Tumour HypOxia Modifier) study protocol 135

Figure 2.2 – Macroscopic image of a sliced lung resection specimen 136

Figure 2.3 – Validation of pimonidazole, carbonic anhydrase 9, CD31 and CD146 classifiers 139

Figure 2.4 – Comparison of hypoxia marker labelling between cohorts and treatment groups 146

Figure 2.5 – Analysis of inter- and intratumoural heterogeneity of lung cancer hypoxia 148

Figure 2.6 – Correlation between pimonidazole labelling and carbonic anhydrase 9 expression 150

Figure 2.7 – Comparison of vascular marker expression between cohorts and treatment groups 157

Figure 2.8 – Comparison of immune cell infiltration between cohorts and treatment groups 159

Figure 2.9 – Correlation between tumour hypoxia and immune cell infiltration 161

Figure 2.10 – Qualitative analysis of $CD8^+$, $FOXP3^+$ and $CD68^+$ cell distributions with respect to regions of tumour hypoxia 162

Figure 2.11 – Comparison of programmed death-ligand 1 expression between cohorts and treatment groups 164

Figure 2.12 – Correlation between programmed death-ligand 1 expression and tumour hypoxia and immune cell infiltration 166

Figure 3.1 – Macroscopic and haematological phenotyping of *Phd2* knockdown mice 177

Figure 3.2 – Histological phenotyping of *Phd2* knockdown mice 181

Figure 3.3 – Histological phenotyping of mice bearing a different short hairpin RNA (shRNA) sequence targeting *Phd2* for knockdown 186

Figure 3.4 – Reduction of *Hif2a* expression reverses the phenotype in *Phd2* knockdown mice 188

Figure 3.5 – Phenotypic reversal following withdrawal of doxycycline 190

Figure 3.6 – Transfer of the *Phd2* knockdown phenotype by bone marrow transplantation 193

Figure 4.1 – Development of a murine tumour model 211

Figure 4.2 – Effects of systemic *Phd2* knockdown after subcutaneous inoculation of LL/2 tumour cells 215

Figure 4.3 – Effects of systemic *Phd2* knockdown after subcutaneous inoculation of E0771 tumour cells 217

Figure 4.4 – Effects of systemic *Phd2* knockdown before subcutaneous inoculation of LL/2 tumour cells 219

Figure 4.5 – Confirmation of transactivation of knockdown system and comparison of phenotypes between groups 225

List of Tables

Table I.1 – Major cell types involved in anti-tumour immune responses 18

Table M.1 – Leica BOND-MAX single staining protocol 39

Table M.2 – Leica BOND-MAX double staining protocol 40

Table M.3 – Primary antibodies used in immunohistochemical staining of human specimens 41

Table M.4 – Routine overnight tissue processing programme 49

Table M.5 – Primary antibodies used in immunohistochemical staining of murine specimens 53

Table M.6 – T lymphocyte panel for flow cytometric analysis of spleen and tumour samples 59

Table M.7 – Regulatory T lymphocyte panel for flow cytometric analysis of spleen and tumour samples 60

Table M.8 – Myeloid cell panel for flow cytometric analysis of spleen and tumour samples 61

Table M.9 – Lymphocyte and myeloid cell panel for flow cytometric analysis of peripheral blood 62

Table M.10 – Lymphocyte differentiation panel for flow cytometric analysis of peripheral blood 63

Table 1.1 – Quantification of hypoxia markers in head and neck squamous cell carcinoma cohort 77

Table 1.2 – Summary of human histological studies evaluating the relationship between T lymphocyte infiltration and tumour hypoxia 102

Table 1.3 – Summary of human histological studies evaluating the relationship between $FOXP3^+$ regulatory T lymphocyte infiltration and tumour hypoxia 106

List of Tables

Table 1.4 – Summary of human histological studies evaluating the relationship between $CD68^+$ macrophage infiltration and tumour hypoxia 110

Table 1.5 – Summary of human histological studies evaluating the relationship between M1 and M2 macrophage infiltration and tumour hypoxia 116

Table 2.1 – ATOM (Atovaquone as Tumour HypOxia Modifier) study patient eligibility criteria 133

Table 2.2 – Quantification of hypoxia markers in the ATOM (Atovaquone as Tumour HypOxia Modifier) study 143

Table 2.3 – Quantification of vascular markers in the ATOM (Atovaquone as Tumour HypOxia Modifier) study 153

List of Abbreviations

2-OG	2-oxoglutarate
A2AR	adenosine A2A receptor
aHIF	antisense HIF1α
AHR	aryl hydrocarbon receptor
AKT	protein kinase B
ANA	anti-nuclear antibody
ANOVA	analysis of variance
APC	antigen-presenting cell(s)
ARCON	Accelerated Radiotherapy plus CarbOgen and Nicotinamide
ARG1	arginase 1
ARNT	aryl hydrocarbon nuclear translocator
ATOM	Atovaquone as Tumour HypOxia Modifier
ATP	adenosine triphosphate
AUC	area under the curve
BCG	Bacillus Calmette-Guérin
CA IX	carbonic anhydrase 9
CAR	chimeric antigen receptor
CA XII	carbonic anhydrase 12
CCRCC	clear cell renal cell carcinoma
CPS	Combined Positive Score
CSF1	colony stimulating factor 1
CTL	cytotoxic T lymphocyte(s)
CTLA-4	cytotoxic T lymphocyte-associated protein 4
DAB	diaminobenzidine

List of Abbreviations

DAMP	damage-associated molecular pattern
DC	dendritic cell(s)
DMOG	dimethyloxalylglycine
DNA	deoxyribonucleic acid
EF5	pentafluorinated etanidazole
EPO	erythropoietin
ETC	electron transport chain
FACS	fluorescence-activated cell sorting
$FADH_2$	reduced flavin adenine dinucleotide
FAZA	[^{18}F]fluoroazomycinarabinofuranoside
FBS	fetal bovine serum
FIH	factor inhibiting HIF
FMISO	[^{18}F]fluoromisonidazole
FOXP3	forkhead box protein 3
GFP	enhanced green fluorescent protein
GITR	glucocorticoid-induced tumour necrosis factor receptor
GLUT1	glucose transporter 1
H&E	haematoxylin and eosin
HBOT	hyperbaric oxygen therapy
HER2	human epidermal growth factor receptor 2
HIF	hypoxia-inducible factor
HMGB1	high-mobility group box 1 protein
HNSCC	head and neck squamous cell carcinoma
HRE	hypoxia response element(s)
HSC	haematopoietic stem cells

List of Abbreviations

ICB	immune checkpoint blockade
IDO	indoleamine 2,3-dioxygenase
IFN	interferon
IL	interleukin
IPAS	inhibitory Per-ARNT-Sim domain protein
KDM	histone lysine demethylases
LAG3	lymphocyte activation gene 3
M1 macrophage	classically activated (pro-inflammatory) macrophage
M2 macrophage	alternatively activated (anti-inflammatory) macrophage
MCAM	melanoma cell adhesion molecule
MCP1	monocyte chemoattractant protein 1
M-CSF	macrophage colony stimulating factor
MDSC	myeloid-derived suppressor cell(s)
MHC	major histocompatibility complex
MRC1	mannose receptor C-type 1
MSR1	macrophage scavenger receptor 1
mTOR	mechanistic target of rapamycin
NADH	reduced nicotinamide adenine dinucleotide
NBF	neutral buffered formalin
NEPAS	neonatal and embryonic Per-ARNT-Sim domain protein
NF-κB	nuclear factor kappa-light-chain-enhancer of activated B cells
NK cell	natural killer cell
NSCLC	non-small cell lung cancer
PAX5	paired box protein Pax-5
PBS	phosphate buffered saline

List of Abbreviations

PD-1	programmed cell death protein 1
PD-L1	programmed death-ligand 1
PD-L2	programmed death-ligand 2
PECAM-1	platelet endothelial cell adhesion molecule
PET-CT	positron emission tomography-computed tomography
PHD	prolyl hydroxylase domain-containing protein(s)
PI3K	phosphoinositide 3-kinase
PPL	Procedure Project Licence
RCC	renal cell carcinoma
RNA	ribonucleic acid
RNAi	RNA interference
ROC	receiver operating characteristic
ROI	region(s) of interest
RORγt	retinoic acid receptor-related orphan receptor gamma t
SCC	squamous cell carcinoma
SDF1	stromal cell-derived factor 1
SEMA3A	semaphorin 3A
shRNA	short hairpin RNA
SIGHT	Semi-automated ImaGe analysis for HisTology data
TAM	tumour-associated macrophage(s)
TAN	tumour-associated neutrophil(s)
T-bet	T-box expressed in T cells
TCA	tricarboxylic acid
TCR	T cell receptor
TEM	TIE2-expressing monocyte(s)

List of Abbreviations

TET	ten-eleven translocation
TGF	transforming growth factor
T_H1 lymphocyte	T helper 1 lymphocyte
T_H2 lymphocyte	T helper 2 lymphocyte
T_H9 lymphocyte	T helper 9 lymphocyte
T_H17 lymphocyte	T helper 17 lymphocyte
TLR	toll-like receptor
TME	tumour microenvironment
TNBC	triple negative breast cancer
TNF	tumour necrosis factor
TPS	Tumour Proportion Score
T_{Reg}	regulatory T lymphocyte(s)
VEGF	vascular endothelial growth factor
VEGFR	vascular endothelial growth factor receptor
VHL	von Hippel–Lindau

Introduction

Scientific background

Oxygen and its importance to multicellular life

2.5 billion years ago, the evolution of photosynthesis in cyanobacteria first liberated oxygen into the Earth's atmosphere [1]. Under standard temperature and pressure, two atoms of oxygen bind to form molecular oxygen ('dioxygen'/O_2), which is a colourless and odourless gas; when assessed by mass, oxygen is now the third most abundant element in the universe (after hydrogen and helium) [2]. This increase in atmospheric oxygen coincided with the evolutionary development of multicellular animals (Metazoa) [3], which depend upon oxygen for a range of physiological processes, most notably cellular energy production. Cellular respiration describes a set of metabolic reactions that convert macronutrients (carbohydrates, proteins and fats) into adenosine triphosphate (ATP), a complex organic chemical that acts as an energy source for activities such as biosynthesis and cell division. Cells have two major pathways for producing ATP (**Figure I.1**):

1. Glycolysis – this process takes place within the cytosol and can occur without oxygen (i.e. under anaerobic conditions); during glycolysis, glucose is converted to pyruvate and ATP (however, this is an inefficient process, generating only net 2 ATP molecules per glucose molecule);
2. Oxidative phosphorylation – this process takes place within the mitochondrion and requires oxygen (i.e. it is an aerobic process); it is much more efficient at generating ATP (net ~31 ATP molecules per glucose molecule). Mitochondrial metabolism proceeds in two distinct phases. Firstly, within the mitochondrial matrix, the tricarboxylic acid (TCA) cycle converts acetyl coenzyme A (generated from pyruvate) into ATP and the electron carriers NADH (reduced nicotinamide adenine dinucleotide) and $FADH_2$ (reduced flavin adenine

dinucleotide). Subsequently, NADH and $FADH_2$ act as electron donors to the electron transport chain (ETC), four protein complexes (complex I-IV) anchored to the inner mitochondrial membrane that carry out oxidative phosphorylation through a series of redox reactions to drive ATP production.

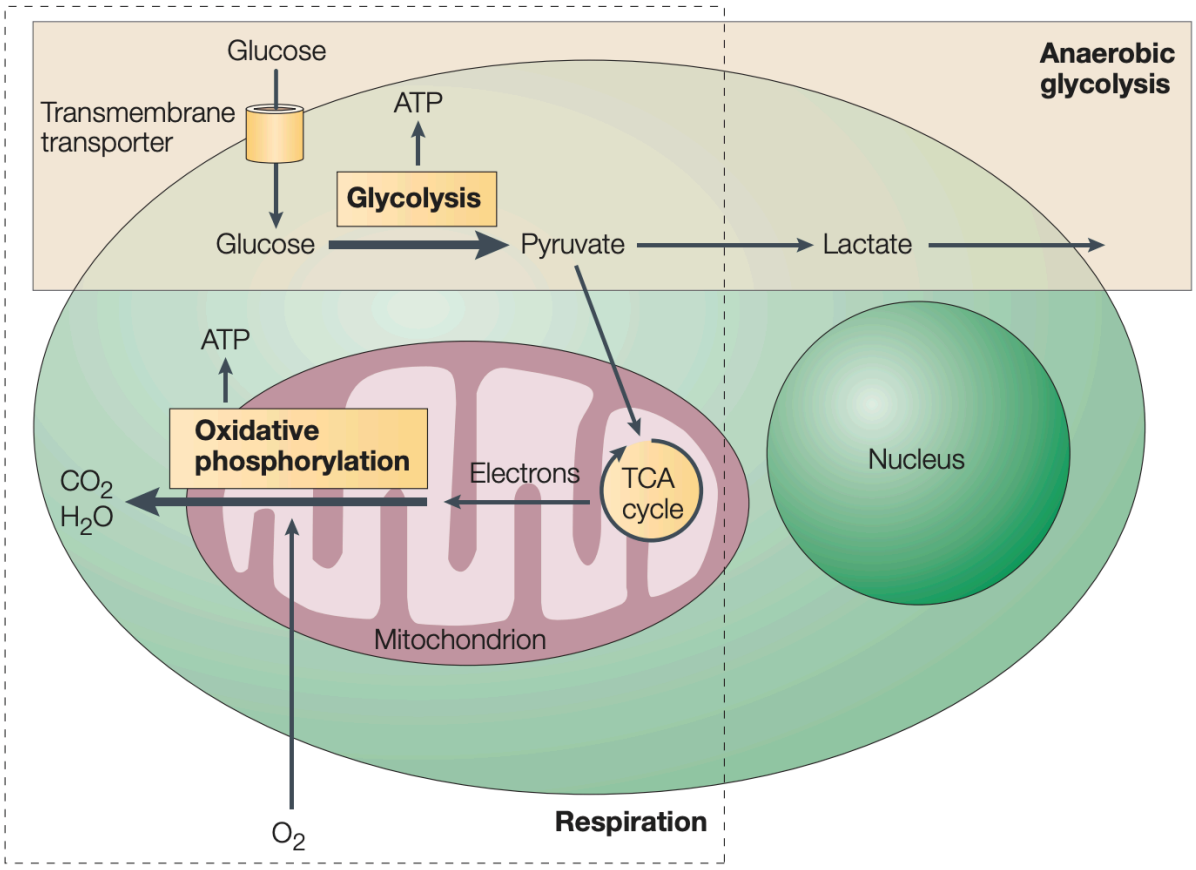


Figure I.1 – Overview of glycolysis and oxidative phosphorylation

During cytoplasmic glycolysis, glucose is converted to pyruvate with concomitant production of adenosine triphosphate (ATP). In the presence of oxygen (O_2), pyruvate is converted to acetyl coenzyme A which then enters the mitochondrial tricarboxylic acid (TCA) cycle, a series of enzymatic reactions that generate electrons and carbon dioxide (CO_2). These electrons then enter the electron transport chain located at the inner mitochondrial membrane. As electrons pass along this chain of four multiprotein complexes (complex I-IV), energy is released and protons are pumped from the mitochondrial matrix to the intermembrane space, producing an electrochemical gradient. ATP is generated as these protons flow back into the mitochondrial

matrix. At the end of the electron transport chain, oxygen is reduced to form water (H_2O). In the absence of oxygen, anaerobic glycolysis proceeds with the reduction of pyruvate to lactate, which is then released from the cell.

Image from [4]; reprinted by permission from Nature Publishing Group, copyright 2005.

Oxygen sensing and the hypoxia-inducible factor (HIF) system

Whilst oxygen provides energy to support essential homeostatic functions, given that it is toxic at high concentrations (as reviewed in [5]), it is critical that its supply is carefully matched to the exact requirements of each cell. In higher animals, the main organ systems responsible for transport of oxygen from atmospheric air to individual cells are generally well understood and comprise the respiratory, cardiovascular and haematopoietic systems and peripheral chemoreceptors, such as the carotid bodies, which are clusters of chemosensitive cells that sense and respond to low levels of arterial oxygen by stimulating an acute increase in respiratory rate. Together, these systems regulate an oxygen gradient between:

- Inspired air – ~160 mm Hg/21 kPa* at sea level;
- Distal airways – ~100 mmHg/13 kPa;
- Arterial blood – ~90 mmHg/12 kPa;
- Peripheral tissues – variable, but often ~40 mmHg/5 kPa (as reviewed in [6]).

**Oxygen level can be reported either as its percentage composition in air or as a partial pressure in mmHg or kPa (partial pressure is defined as the pressure that would be exerted by one of the gases in a mixture, if it alone occupied the entire volume of the original mixture at the same temperature; i.e. the oxygen percentage within a mixture of gases multiplied by the overall pressure). Thus, at sea level, where atmospheric pressure is 760 mmHg (or 101.3 kPa) and oxygen percentage is ~21%, the partial pressure of oxygen is 760 x 0.21 = 159.6 mmHg (or 101.3 x 0.21 = 21.2 kPa).*

However, the main molecular mechanisms that underpin cellular oxygen sensing have only been defined relatively recently (with the seminal scientific discoveries being recognised by the award of the 2019 Nobel Prize in Physiology or Medicine [7]). All metazoans share an evolutionarily conserved molecular oxygen sensing mechanism that permits fine-tuning of cellular physiology in response to varying oxygen availability. Under hypoxia (broadly defined as inadequate oxygenation at the tissue level; given the wide range of oxygen tensions encountered across different tissues under physiological conditions, it is difficult to provide a quantitative definition of hypoxia, as reviewed in [8]), cells up-regulate hypoxia-inducible factor (HIF), a highly-conserved transcription factor that co-ordinates appropriate adaptive responses. HIF functions as a heterodimer of a labile α subunit (HIF1α, HIF2α or HIF3α) and a stable β subunit (HIFβ; also known as aryl hydrocarbon nuclear translocator [ARNT] as it is capable of dimerising with aryl hydrocarbon receptor [AHR] as part of the xenobiotic response), the latter being widely expressed in an oxygen-independent manner. Regulation of this system is described in **Figure I.2**.

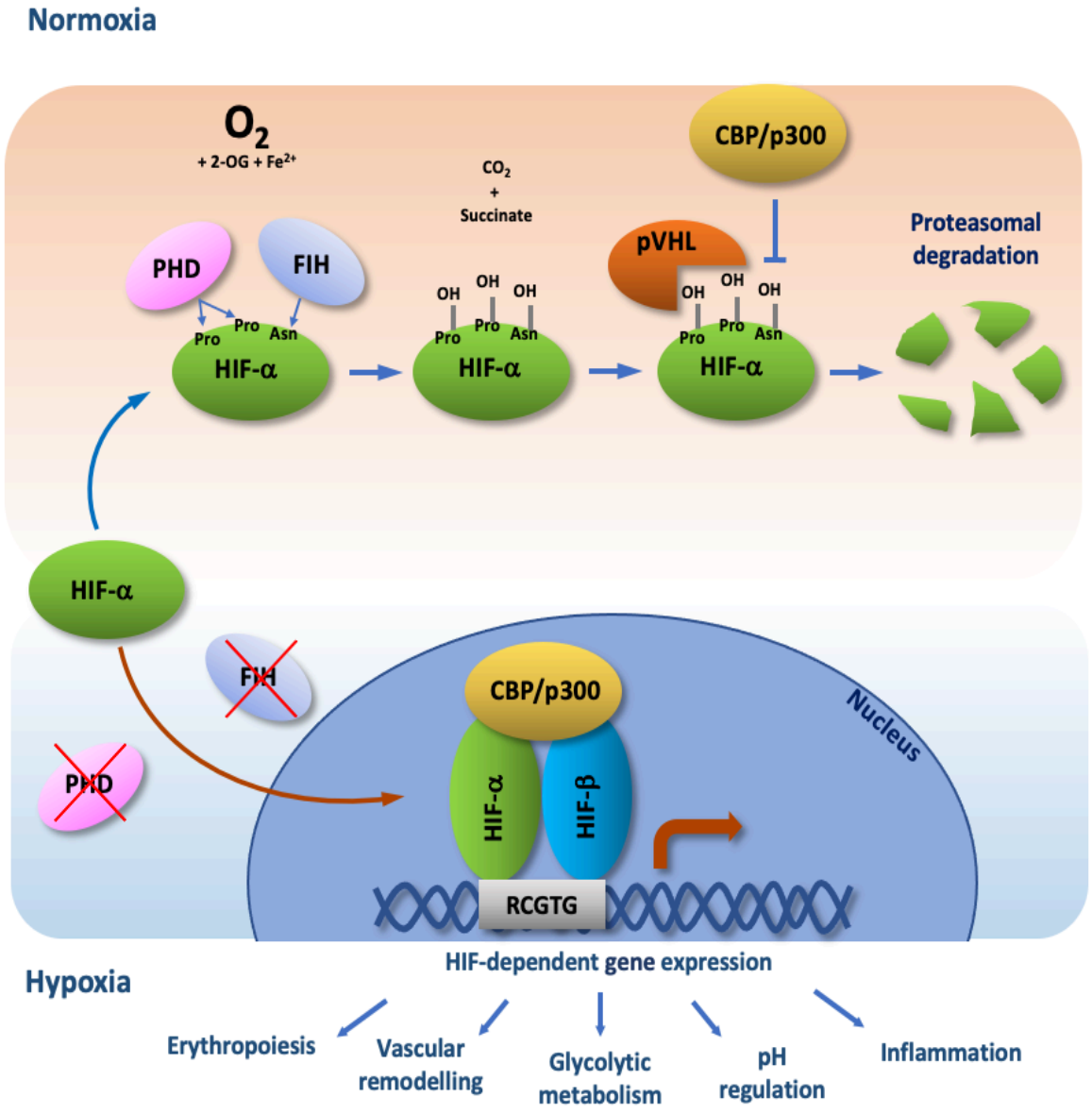


Figure I.2 – Regulation of the hypoxia-inducible factor (HIF) system by oxygen availability

In the presence of molecular oxygen (O_2), 2-oxoglutarate (2-OG), and ferrous iron (Fe^{2+}), the prolyl hydroxylase domain-containing proteins (PHD) hydroxylate specific proline residues within hypoxia-inducible factor alpha (HIFα) (P402 and P564 in human HIF1α and P405 and P531 in human HIF2α) with carbon dioxide (CO_2) and succinate produced as by-products. Three PHD isoforms exist (PHD1, 2 and 3), with PHD2 being most abundant and hence dominant in oxygen sensing. Proline-hydroxylated HIFα is recognised by the von Hippel–Lindau ubiquitin E3 ligase (pVHL) and subsequently undergoes proteasomal degradation. Factor inhibiting HIF (FIH) hydroxylates any HIFα subunits that have escaped proteasomal degradation (at asparagine residue N803), blocking CBP/p300 co-activator recruitment and

thereby limiting their transcriptional activity; conversely, given that HIFα asparaginyl hydroxylation is substantially more resistant to hypoxia than HIFα prolyl hydroxylation, inhibition of FIH further amplifies the HIF transcriptional response under severely hypoxic conditions. PHD and FIH are dioxygen-dependent enzymes; they are inhibited under hypoxic conditions, permitting HIFα subunits to accumulate, heterodimerise with HIFβ, bind to regions of deoxyribonucleic acid (DNA) known as hypoxia response elements (characterised by the consensus motif RCGTG) and activate a myriad of genes including those involved in erythropoiesis, angiogenesis, metabolism and pH regulation. In addition to restoring tissue oxygenation, HIF is involved in numerous other processes such as inflammatory/immunological responses.

Image from [9].

Overall, HIF-mediated transcription entrains a gene expression profile that facilitates cellular adaptation to hypoxia. Examples include up-regulation of processes that increase oxygen delivery to hypoxic tissues (erythropoiesis occurs secondary to increased synthesis of erythropoietin [EPO] [10] and iron transport proteins [11] whilst angiogenesis results from increased vascular endothelial growth factor [VEGF] production [12, 13]) and reduce cellular oxygen consumption by favouring a switch from oxidative phosphorylation to glycolysis through increased synthesis of several glycolytic genes [14-17]. Pangenomic analyses have shown that HIF has many hundreds of direct transcriptional targets including genes involved in a diverse range of functions such as control of cell cycle, cytoskeletal function and epigenetic regulation [18, 19]. The human genome contains approximately 1.1 x 10^6 hypoxia response elements (HRE), deoxyribonucleic acid (DNA) sequences characterised by the consensus motif RCGTG to which the HIF heterodimer can bind, of which about 50000 are located within unmethylated regions (sites of 'open', transcriptionally active chromatin) [19]. However, HIF is only found to be bound to between 500 and 2500 of these accessible HRE (i.e. < 5%) at any one time within a hypoxic cell [20]. In addition, HIF has been reported to influence gene expression through other mechanisms including effects on microRNA (small, non-coding

ribonucleic acid [RNA] molecules, containing about 22 nucleotides, that control gene expression post-transcriptionally by regulating mRNA translation and stability) networks [21, 22] and protein translation [23]. Moreover, the ten-eleven translocation (TET) enzymes [24] and histone lysine demethylases (KDM) [25, 26] are members of the same dioxygenase family as the prolyl hydroxylase domain-containing proteins (PHD) and function as epigenetic regulators that link cellular oxygen levels with HIF-independent transcriptional responses.

Whilst HIF1α shares a high degree of sequence homology with HIF2α, the two isoforms demonstrate distinct patterns of tissue expression (ubiquitous vs. tissue-restricted [HIF2α is expressed primarily in the heart, lung, kidney and liver in addition to specialised cells such as endothelial cells, leukocytes, EPO-producing renal interstitial fibroblasts and type I cells of the carotid body] [27-29]) and time courses of induction (under hypoxia, HIF1α peaks after 12-16 hours and normalises by 24 hours [30-32] whereas it can take up to 72 hours for full stabilisation of HIF2α [31]). Despite recognising the same DNA-binding motif when heterodimerised, HIF1α and HIF2α modulate expression of both overlapping and distinct target genes [19]. For example, glycolytic genes are strict HIF1α targets whereas other genes functioning in the same pathway (namely glucose transporter 1 [GLUT1]) appear to be regulated by both isoforms [33]. In general, HIF1α displays a tendency towards gene-proximal binding (i.e. at gene promoters and transcriptional start sites) whereas HIF2α more commonly binds to gene-distal locations (i.e. at gene enhancers), suggesting that each isoform has inherent properties that contribute to differential binding across the genome [34]. Comparatively little is known about a third isoform, HIF3α, which is expressed only in certain tissues (such as the brain, cornea, thymus, heart, lung and kidney), is hydroxylated by PHD at a single proline residue and lacks the asparagine residue required for hydroxylation by factor inhibiting HIF (FIH) [35, 36]. This isoform, expressed as multiple splice variants [36] including inhibitory

Per-ARNT-Sim domain protein (IPAS) [37] and neonatal and embryonic Per-ARNT-Sim domain protein (NEPAS) [38], is believed to antagonise HIF signalling by either forming inactive or weakly active heterodimers or by sequestering the other HIFα subunit isoforms [39-41]. In summary, the existence of multiple HIFα paralogues endows downstream signalling diversity to a relatively simple core oxygen sensing mechanism.

Under sustained hypoxia, the adaptive effects of HIF stabilisation themselves both increase oxygen supply and reduce oxygen demand and thus eventually down-regulate the pathway. In addition to the inhibitory effects of HIF3α, several other direct HIF targets act collaboratively to negatively regulate the system and thus avoid deleterious consequences of sustained signalling. These include generation of antisense HIF1α (aHIF) [42-44], alternative splice variants [45, 46] and the microRNAs miR-20b [47], miR-155 [48] and miR-210 [49], all of which have been reported to reduce HIF signalling. Furthermore, PHD2 and PHD3 are themselves transcriptional targets of HIF and their increased abundance partially mitigates their reduced function under hypoxia [32, 50-54]. Hypoxic induction of RBX2 [55], a component of the von Hippel–Lindau E3 ubiquitin ligase (pVHL), and CITED2 (also known as p35srj) [56-58], a protein that competes for binding to CBP/p300, favour HIFα degradation and antagonise its transcriptional output, respectively. Conversely, the hypoxia-responsive long non-coding RNA (transcripts with lengths exceeding 200 nucleotides that are not translated into protein) p21 blocks the HIFα-pVHL interaction, acting in a positive feedback mechanism to promote HIFα accumulation under hypoxic conditions [59]. Additionally, ankyrin repeat domain-containing proteins can out-compete HIFα for hydroxylation by FIH, increasing the transcriptional activity of the HIF system [60, 61]. An internal ribosomal entry site in the 5' untranslated region of its mRNA spares HIF1α from the general reduction in protein translation observed under hypoxia [62]. Together, this complex network of feedback loops functions to

modulate the HIF response over time and also has the potential to alter the balance between HIFα isoforms, as exemplified by the predominance of HIF1α during acute hypoxia versus HIF2α during sustained hypoxia. The exact mechanisms of HIF regulation are likely to vary between cell types, permitting oxygen-dependent fine-tuning of HIF across different tissues exposed to a wide range of oxygen tensions (each with their own 'set point' for HIF system activation, a concept termed 'range finding' [63]).

The compensatory changes that follow HIF pathway activation are dependent upon changes in gene-expression patterns and, consequently, must represent medium- to long-term adaptations to hypoxia (i.e. occurring over hours, days and weeks). Therefore, other oxygen sensing systems must exist that mediate acute responses to hypoxia over a period of seconds to minutes (such as occurs in control of ventilation by the carotid body). Recently, a plant oxygen sensor has been demonstrated also to be operative in mammalian cells [64]. This enzyme alters target protein stability directly through post-translational modification and is, therefore, likely to transduce more rapid responses to hypoxia than the transcriptional effects mediated by the HIF system.

Hypoxia and cancer

Given oxygen's critical role in normal physiology, it is not surprising that hypoxia, hyperoxia and dysregulated oxygen sensing are implicated in the pathophysiology of a broad range of diseases (as reviewed in [65]). The existence of hypoxic regions within solid tumours, manifest histologically as necrosis, has long been recognised. In a pioneering study investigating lung squamous cell carcinoma (SCC), Thomlinson and Gray demonstrated that, irrespective of overall tumour size, cancer cell nests always developed central necrosis when their radius exceeded 200 μm [66]. Conversely, cancer cell nests with a radius of less than 160 μm never

developed necrosis. Noting that blood vessels were largely present within adjacent stroma and not within cancer cell nests themselves, the authors proposed that the development of necrosis was driven by hypoxia resulting from insufficient oxygen delivery to tumour cells located at a distance of more than 180 μm from the nearest blood vessel. Supporting this hypothesis, the histological thickness of 'tumour cords' (defined as a functional unit of a blood vessel and its dependent tumour cell volume [67]) is decreased amongst tumour-bearing mice kept under conditions of 10% O_2 as compared to those housed in room air [68]. Several decades later, the development of oxygen sensitive needle electrodes facilitated direct measurement of tumour oxygenation within a range of different human tumours [69-81]. These studies confirmed the presence of profoundly hypoxic regions within solid tumours; indeed, some areas are virtually anoxic.

The development of hypoxia within a tumour depends upon the interaction of a number of complex factors including the oxygen carrying capacity of the patient's blood (cancer patients are often anaemic, with a reduced capacity to deliver oxygen to peripheral tissues [82]), the integrity of vascular beds that perfuse the tumour and the metabolic demands of proliferating tumour cells. Of particular importance, tumour-associated angiogenesis often results in the formation of vasculature that is both structurally and functionally abnormal [83-85]. Two subtypes of tumour hypoxia have been proposed (**Figure I.3**). Acute, or perfusion-limited, hypoxia develops due to a sudden reduction in blood flow, such as occurs upon transient vessel occlusion [86-88]. In contrast, chronic, or diffusion-limited, hypoxia develops due to the irregular nature of tumour vascular beds leading to tumour zones that are too far from blood vessels for diffusion of oxygen [66]. Nevertheless, the exact distinction between acute and chronic tumour hypoxia remains ill-defined and this binary classification is likely to be overly simplistic [89].

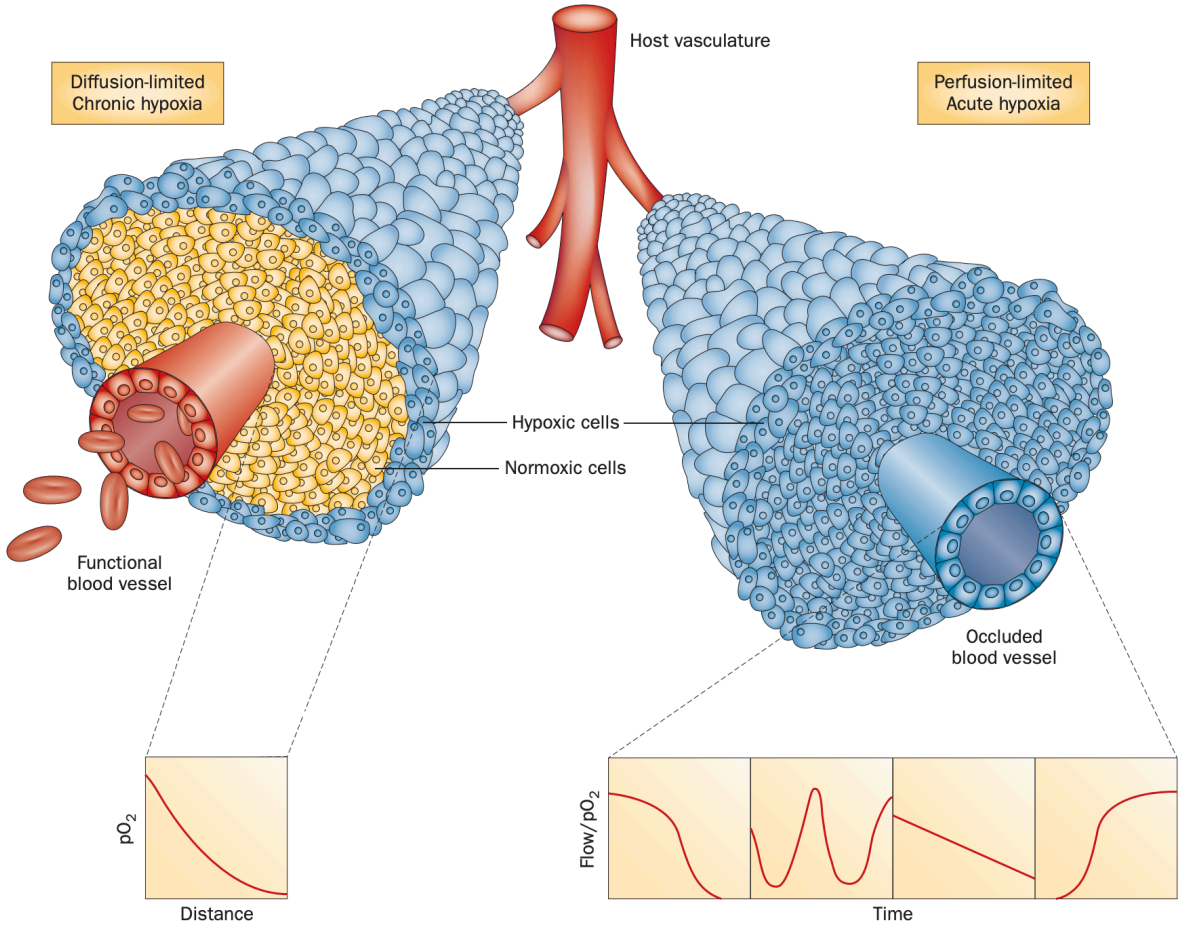


Figure I.3 – Overview of acute and chronic tumour hypoxia

In these illustrations, tumour cells are growing as a cord around a blood vessel from which they obtain oxygen. The left cord depicts chronic (diffusion-limited) tumour hypoxia – as oxygen diffuses from the vessel, it is consumed by perivascular tumour cells, resulting in a decline in oxygen partial pressure (pO_2) with distance, as shown in the insert. This decline results in chronic hypoxia amongst tumour cells located at the periphery of the cord. The right cord depicts acute (perfusion-limited) tumour hypoxia – perfusion has been transiently compromised and all surrounding tumour cells have become acutely hypoxic. Causes include vasospasm, vessel occlusion by blood or circulating tumour cells, vessel collapse due to high interstitial pressure or reversal of blood flow. The insert depicts changes in blood flow/pO_2 over time and demonstrates sudden, complete occlusion (panel 1) and recovery (panel 4), a gradual decrease over time (panel 3) and repeated fluctuations (panel 2).

Image from [90]; reprinted by permission from Nature Publishing Group, copyright 2012.

The presence of hypoxic and necrotic regions within solid human tumours are poor prognostic factors, irrespective of tumour type [91, 92]. The presence of tumour hypoxia may select for a more malignant phenotype through a number of mechanisms including promoting genetic instability [93], resistance to apoptosis [94], angiogenesis [95], invasion [96] and metastasis [97]. Furthermore, tumour hypoxia is associated with resistance to all major types of cancer therapy. Surgery is less likely to be curative due to the increased tendency to local invasion and distant metastasis of hypoxic tumours [75, 98]. Hypoxic tumour cells are less sensitive to radiotherapy, as lethal DNA damage depends upon the generation of reactive oxygen species under aerobic conditions (as reviewed in [99]). Experimental evidence also suggests that perinecrotic, but viable, tumour cells that survive irradiation subsequently acquire HIF1α expression, translocate towards tumour blood vessels and are responsible for disease recurrence [100]. Chemotherapy may be less effective due to the acidic pH of hypoxic tumours, which affects delivery of basic drugs, and the lower proliferation rate, resistance to apoptosis and increased expression of multi-drug resistance transporters observed in hypoxic tumour cells (as reviewed in [101]). Likewise, the irregular vasculature and perturbed perfusion within solid tumours affects the delivery of other anti-cancer drugs to hypoxic cells (as reviewed in [102]). Finally, hypoxic tumours may be less sensitive to immunotherapy (as reviewed in [103] and discussed below). Despite the negative prognostic and predictive significance of tumour hypoxia, this parameter is not routinely evaluated in clinical practice. Approaches to the quantification of tumour hypoxia are discussed in **Appendix 1**, which presents a systematic literature review of immunohistochemical studies comparing the expression of endogenous hypoxia markers (proteins involved in the cellular response to hypoxia) to labelling by exogenous hypoxia markers (chemicals such as pimonidazole and pentafluorinated etanidazole [EF5]) in human malignant tumours.

Anti-tumour immune responses

In addition to neoplastic cells, tumours are composed of an assortment of host-derived non-neoplastic cells including blood vessels, lymphatics, fibroblasts and leukocytes as well as extracellular matrix (collectively referred to as 'tumour stroma'). These various cell types reside within, and contribute to, a shared ecosystem termed the 'tumour microenvironment' (TME) (as reviewed in [104]) (**Figure I.4**). Consequently, initiation, progression and maintenance of the malignant phenotype are affected by events occurring not only within neoplastic cells but also within stromal cells, with these cell types communicating with each other directly, competing for vital elements such as oxygen and nutrients and generating toxic metabolites.

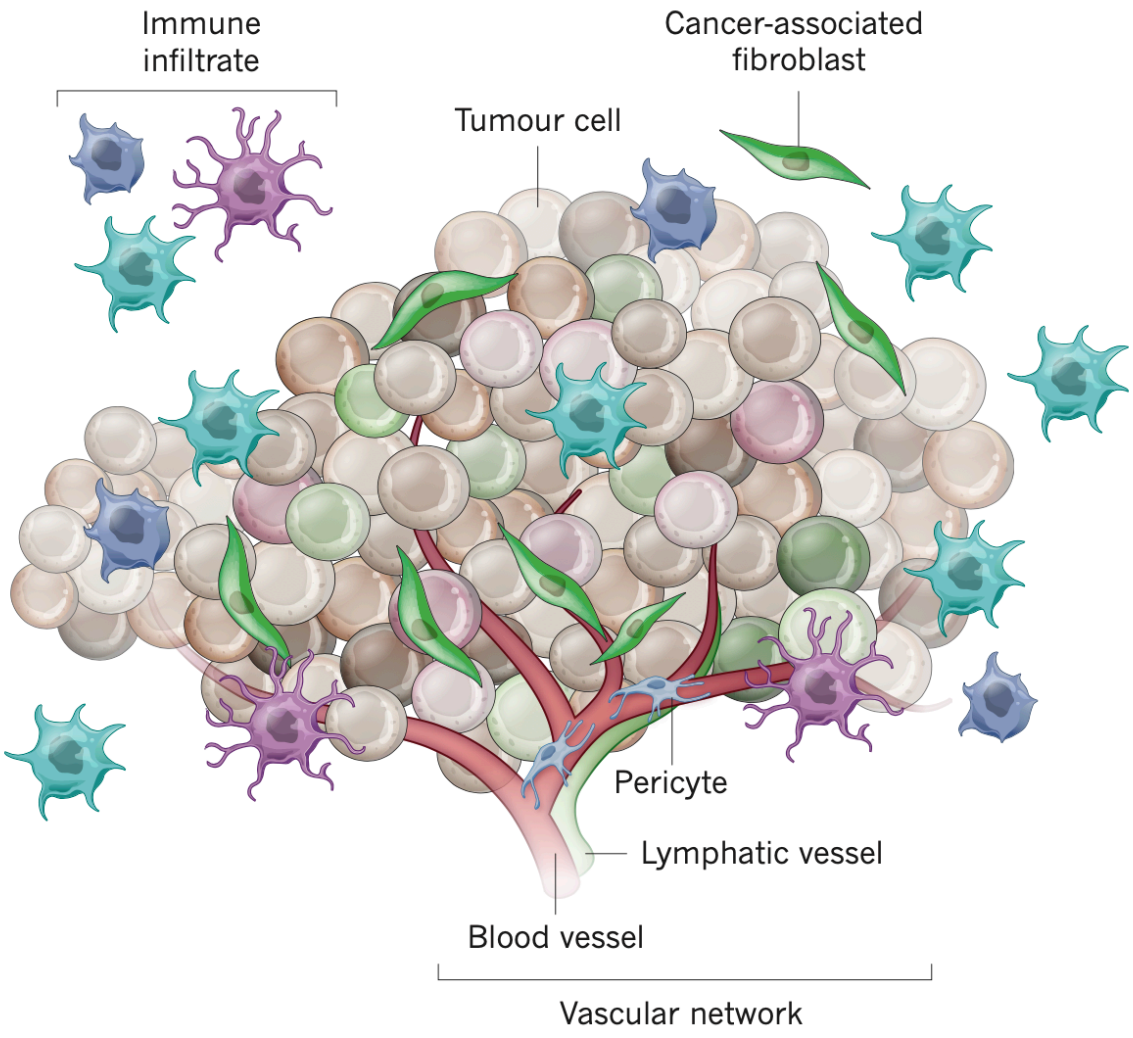


Figure I.4 – Overview of the tumour microenvironment

Tumours are composed of a mixture of neoplastic and non-neoplastic cells including blood vessels, lymphatics, fibroblasts and immune cells. The immune cell infiltrate is composed of multiple different cell types with both pro- and anti-tumour functions. Tumour vasculature can also vary within and between tumours, with more mature vessels displaying greater coverage by supportive pericytes. Cancer-associated fibroblasts are able to remodel extracellular matrix and to secrete cytokines, functions that are largely considered to be pro-tumourigenic.

Image from [105]; reprinted by permission from Nature Publishing Group, copyright 2013.

The human immune system encompasses both innate and adaptive immunity (**Figure I.5 and Table I.1**). The innate immune system provides rapid but non-specific immune responses whilst the adaptive immune system provides slower, but more persistent, antigen-specific immune responses.

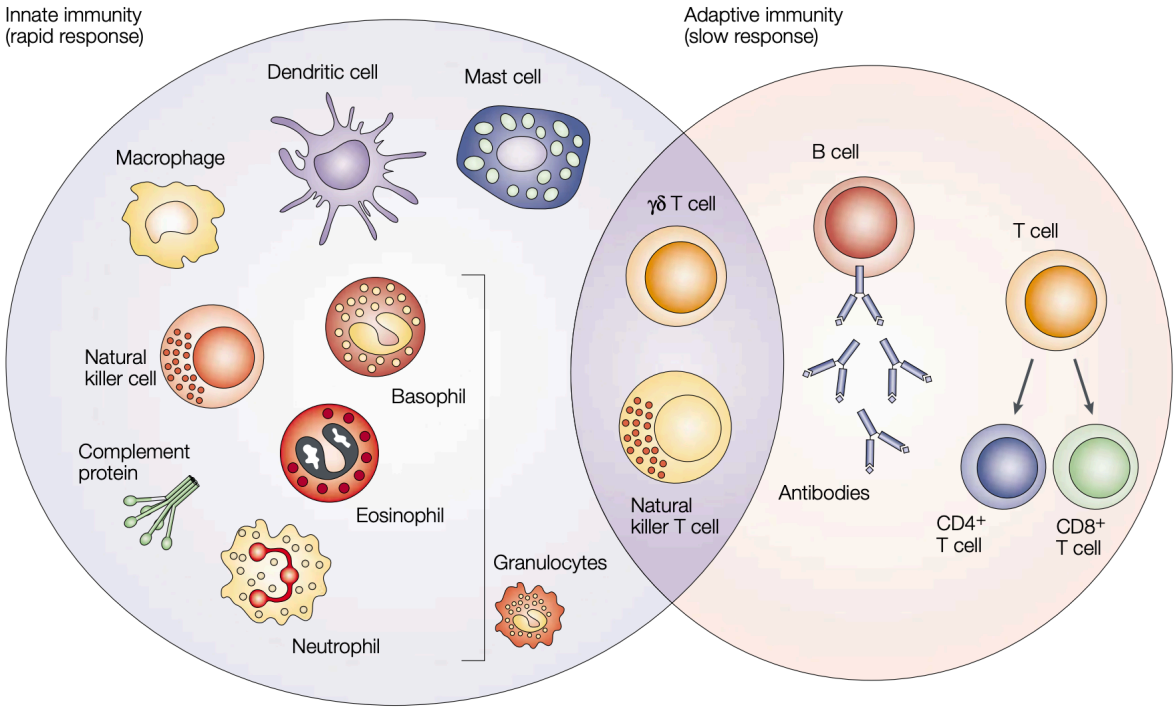


Figure I.5 – Overview of the innate and adaptive immune systems

The innate immune response provides the first line of defence against infection. It consists of soluble factors, such as complement proteins, and diverse cellular components including

granulocytes (basophils, eosinophils, neutrophils and mast cells), macrophages, dendritic cells and natural killer cells. The adaptive immune response is slower but provides antigenic specificity and memory responses upon re-exposure to antigen. It consists of antibodies, B lymphocytes (which, when activated, differentiate into antibody-secreting plasma cells) and $CD4^+$ helper and $CD8^+$ cytotoxic T lymphocytes. However, the two systems are intricately linked. For example, innate immune cells can present antigen to adaptive immune cells whilst antibodies generated by plasma cells can induce phagocytosis by innate immune cells. Natural killer T cells and γδ T cells are cytotoxic lymphocytes that possess characteristics of both innate and adaptive immune cells and are sometimes referred to as innate-like T lymphocytes.
Image from [106]; reprinted by permission from Nature Publishing Group, copyright 2004.

Whilst dynamic interactions take place between neoplastic and immune cells throughout tumour progression, in order for a tumour to develop fully, the neoplastic cells must evade elimination by host immune responses. Indeed, the ability of tumour cells to avoid immune destruction is considered to be one of the 'hallmarks of cancer' [107]. The relationship between neoplastic and immune cells was initially proposed in the theory of 'cancer immunosurveillance' which suggested that the immune system can identify and destroy transformed cells before they progress to a clinically detectable tumour [108]. This notion was further developed by the concept of 'cancer immunoediting' in which host immune responses, now recognised to have both cancer suppressing and promoting properties, act across three sequential phases [109, 110]:

1. Elimination – initially, nascent neoplastic cells are successfully detected and destroyed by host immune cells undertaking 'immunosurveillance' (the acquisition of mutations in protein coding DNA regions, creating neoantigens, or epigenetic alterations, leading to re-expression of embryonic antigens, generate tumour-associated antigens that can be recognised as 'foreign' by the host immune system) [111];

2. Equilibrium – eventually a tumour develops but this is controlled by the immune system (i.e. the rate of neoplastic cell growth is approximately equal to the rate of their destruction by the immune system) [112];
3. Escape – continuous cycles of cell growth, elimination and mutation lead, over time, to a change in tumour immunogenicity under the selective pressure of the immune system ('immunoediting'), eventually generating immunologically sculpted tumour cells that can escape immune destruction, allowing the tumour to grow and metastasise [113, 114].

More recently, the 'cancer-immunity cycle' has outlined seven distinct stages of an anti-tumour immune response [115, 116] (**Figure I.6**).

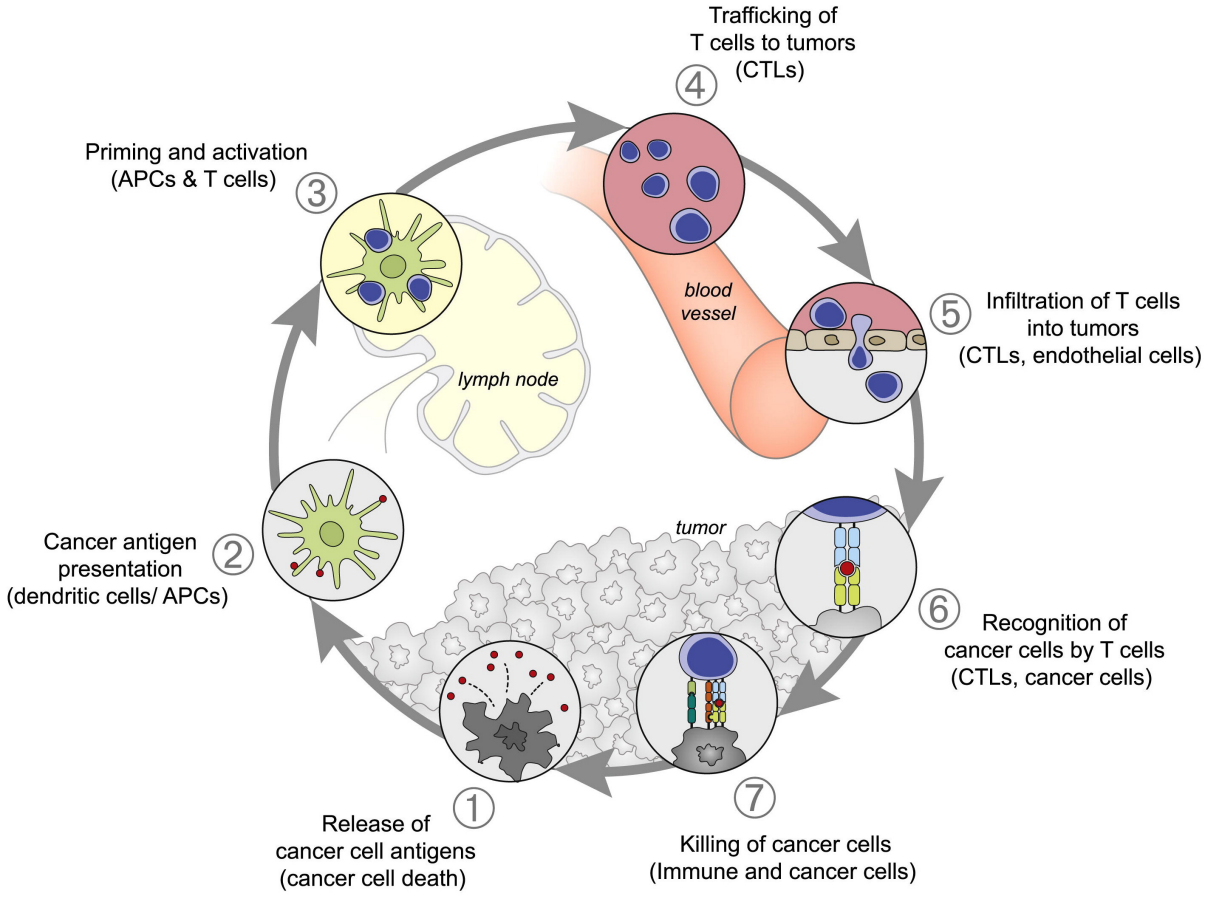


Figure I.6 – Overview of the cancer-immunity cycle

Generation of an anti-tumour immune response is a cyclical process that, under the correct conditions, can be self-propagating leading to amplified and broadened responses. However, numerous inhibitory factors can act to halt this cycle and limit anti-tumour immunity. The cycle can be divided into seven major steps:

1. *Cancer cell death leads to shedding of tumour antigens;*
2. *Antigen-presenting cells (APCs), such as dendritic cells, capture these antigens and migrate to tumour draining lymph nodes via lymphatics;*
3. *Tumour antigens are presented to naïve T lymphocytes by APCs (via major histocompatibility complex [MHC]) with antigen-specific lymphocytes undergoing activation and clonal expansion;*
4. *Activated lymphocytes (most importantly, cytotoxic T lymphocytes [CTLs]) migrate from the lymph node to the tumour site via the bloodstream;*
5. *These lymphocytes leave the bloodstream via high endothelial venules and infiltrate into the core of the tumour along chemotactic gradients;*
6. *Antigen-specific CTLs recognise cognate antigens presented on the surface of tumour cells (via MHC class I);*
7. *CTLs kill cancer cells, releasing further antigens and the cycle recommences.*

Notably, this model is rather simplistic and, for example, fails to recognise fully the role played by innate immune cells and B lymphocytes in anti-tumour immunity.

Image from [115]; reprinted by permission from Elsevier Science, copyright 2013.

However, the observations that many tumours are highly infiltrated by immune cells, can be recognised as immunologically foreign in *ex vivo* assays, yet continue to grow *in situ* by avoiding immune destruction (the 'Hellström paradox') implies that tumour cells are protected *in vivo* by the presence of a highly immunosuppressive TME [117]. Causes of immune escape include lack of effector immune cell infiltration into tumour cell nests (as reviewed in [118]), inhibition of immune responses within the TME by immunosuppressive leukocytes or soluble mediators (as reviewed in [119]) and tumour cell intrinsic resistance to immune destruction (as reviewed in [120]).

The tumour 'immune contexture'

It is now recognised that both quantitative and qualitative aspects of the anti-tumour immune response (collectively described as the tumour 'immune contexture' [121]) are of prognostic and predictive benefit [121-125]). This contexture, which encompasses the composition, density and spatial distribution of tumour infiltrating immune cells, determines whether an immune response is ultimately tumour destructive or tumour supportive. Different types of tumour infiltrating leukocytes, their key functions and protein markers commonly used in their identification are summarised in **Table I.1**.

Table I.1 – Major cell types involved in anti-tumour immune responses

Adapted from [124].

Cell type	Common marker(s)	Key function(s)
Adaptive immune system		
T lymphocytes	CD3	**Mediate the cellular component of adaptive immunity**
Helper T lymphocytes	CD4	**Modulation of immune responses** A heterogenous class of T lymphocytes that recognise extracellular antigen presented by MHC class II on the surface of antigen-presenting cells Modulate immune responses by providing 'help', in the form of cytokines and contact-dependent signals, to cytotoxic T lymphocytes, B lymphocytes and macrophages
Cytotoxic T lymphocytes	CD8	**Elimination of target cells** Induce apoptosis of target cells (i.e. cells expressing cognate antigen in the context of MHC class I) through the release of perforin and granzymes

B lymphocytes	CD19, CD20	**Mediate the humoral component of adaptive immunity** When stimulated, B lymphocytes differentiate into antibody-secreting plasma cells and memory B lymphocytes
Innate immune system		
Macrophages	CD68	**Phagocytosis and cytokine release** Express receptors for antibody, complement and foreign carbohydrates, making them adept phagocytes Also play a role in adaptive immune responses by cytokine release
Neutrophils	Neutrophil elastase	**Phagocytosis and cytokine release** Short-lived phagocytes that can also release inflammatory cytokines
Dendritic cells	CD11c, CD123	**Antigen presentation** Play a key role in linking innate and adaptive immunity by capturing antigen in peripheral tissues, followed by its presentation to T lymphocytes in secondary lymphoid organs Conventional dendritic cells ($CD11c^+$) have a branched morphology that maximises surface area for antigen uptake and presentation; plasmacytoid dendritic cells ($CD123^+$) lack this characteristic morphology
Natural killer cells	CD56	**Cytotoxic elimination of target cells** Cytotoxic lymphocytes that can lyse target cells in an MHC class I-independent manner
MHC – major histocompatibility complex		

Adaptive immune responses

Upon recognition of cognate antigen and appropriate co-stimulation, T lymphocytes transition from a naïve to an activated state. In this process, specialised antigen-presenting cells (APC), such as dendritic cells (DC), present foreign antigens to helper T lymphocytes via major histocompatibility complex (MHC), predominantly within secondary lymphoid organs such as lymph nodes. These helper T lymphocytes subsequently support activation of antigen-specific cytotoxic T lymphocytes (CTL) and B lymphocytes, with the latter differentiating into antibody-secreting plasma cells. Analysis of expression of CD44 (an activation marker) and CD62L (L-selectin; a 'homing receptor' for entry into secondary lymphoid organs via high endothelial venules) on the surface of both $CD4^+$ and $CD8^+$ T lymphocytes permits assessment of their differentiation status. Naïve T lymphocytes express CD62L but not CD44 ($CD44^-$ $CD62L^+$), effector/effector memory T lymphocytes express CD44 but not CD62L ($CD44^+CD62L^-$) whilst central memory T lymphocytes express both markers ($CD44^+CD62L^+$).

Upon activation, naïve helper T lymphocytes can differentiate into a range of mature subsets. Each mature subset is regulated by expression of a 'master' transcription factor which defines their pattern of gene expression and thus functional status (**Figure I.7**).

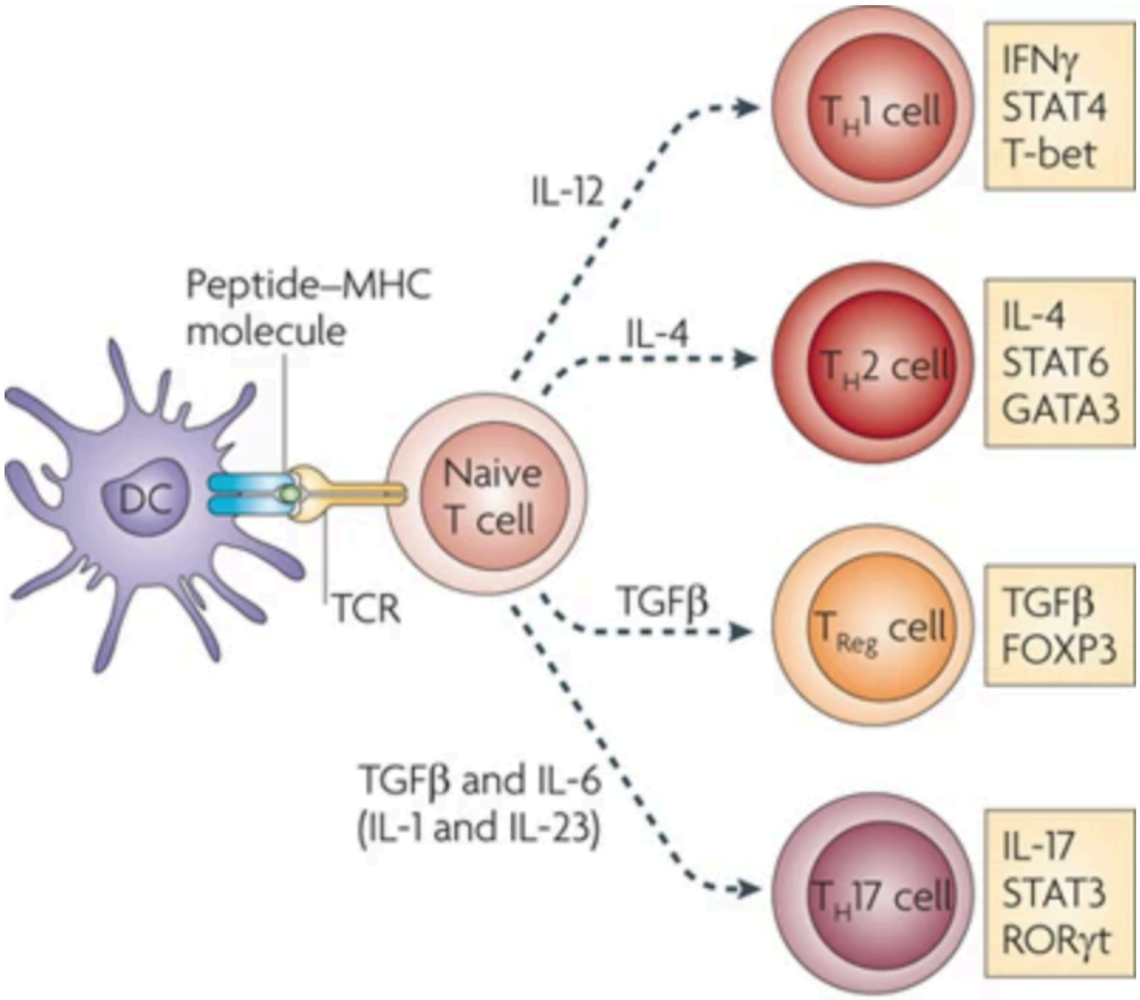


Figure I.7 – Overview of helper T lymphocyte differentiation

Binding of cognate peptide antigen (presented by dendritic cells [DC] via major histocompatibility complex [MHC]) to the T cell receptor (TCR) of a naïve $CD4^+$ helper T lymphocyte leads to its activation and differentiation into one of four main mature subsets – T helper 1 (T_H1), T helper 2 (T_H2), T helper 17 (T_H17) and regulatory T (T_{Reg}) lymphocytes. The differentiation pathway followed by a given helper T lymphocyte depends upon the local cytokine milieu: interleukin 12 (IL-12) favours T_H1 differentiation, IL-4 favours T_H2 differentiation, transforming growth factor beta (TGFβ) favours T_{Reg} differentiation and TGFβ plus IL-6 favour T_H17 differentiation. The gene expression pattern for each subset (and hence function) is regulated by 'master' transcription factors:

- *T_H1 lymphocytes (master transcription factor = T-box expressed in T cells [T-bet], supported by signal transducer and activator of transcription 4 [STAT4]) – produce interferon gamma (IFNγ), tumour necrosis factor alpha (TNFα) and interleukin 2 (IL-2)*

and support cytotoxic T lymphocyte function to protect against intracellular pathogens (such as viruses, bacteria and parasites), as well as contributing to anti-tumour immunity [126];

- *T_H2 lymphocytes (master transcription factor = GATA3, supported by STAT6) – produce IL-4, IL-5, IL-10 and IL-13 and protect against extracellular pathogens (such as helminths) but they have been associated with ineffective anti-tumour immunity [127];*
- *T_H17 lymphocytes (master transcription factor = retinoic acid receptor-related orphan receptor gamma t [RORγt], supported by STAT3) – produce IL-17 and IL-22 and protect against extracellular bacterial and fungal infections as well as contributing to immune responses at mucosal surfaces but also promote autoimmunity and may have both anti- and pro-tumour effects [128];*
- *T_{Reg} lymphocytes (master transcription factor = forkhead box protein 3 [FOXP3]) – anti-inflammatory T lymphocytes that suppress the proliferation and function of pro-inflammatory T lymphocytes, for example through expression of TGFβ, thus preventing autoimmunity but at the risk of promoting tolerance to tumours [129].*

Image from [130]; reprinted by permission from Nature Publishing Group, copyright 2010.

In general, tumour infiltration by $CD3^+$ T lymphocytes and $CD8^+$ T lymphocytes is associated with a good prognosis whereas infiltration by forkhead box protein 3 $(FOXP3)^+$ regulatory T lymphocytes (T_{Reg}) is associated with a poor prognosis in most, but not all, tumour types [121, 122, 124]. Whilst the prognostic significance of B lymphocytes in cancer is not well characterised, they are most commonly reported to be associated with better outcomes [131].

Innate immune responses

Macrophages are highly plastic, multi-functional cells that phagocytose pathogens and secrete a variety of immunomodulatory cytokines. When activated by environmental signals, in a process termed ‘polarisation’, circulating monocyte-derived and tissue resident macrophages adopt one of two broad phenotypes with distinct transcriptional and secretory profiles (as reviewed in [132]) (**Figure I.8**).

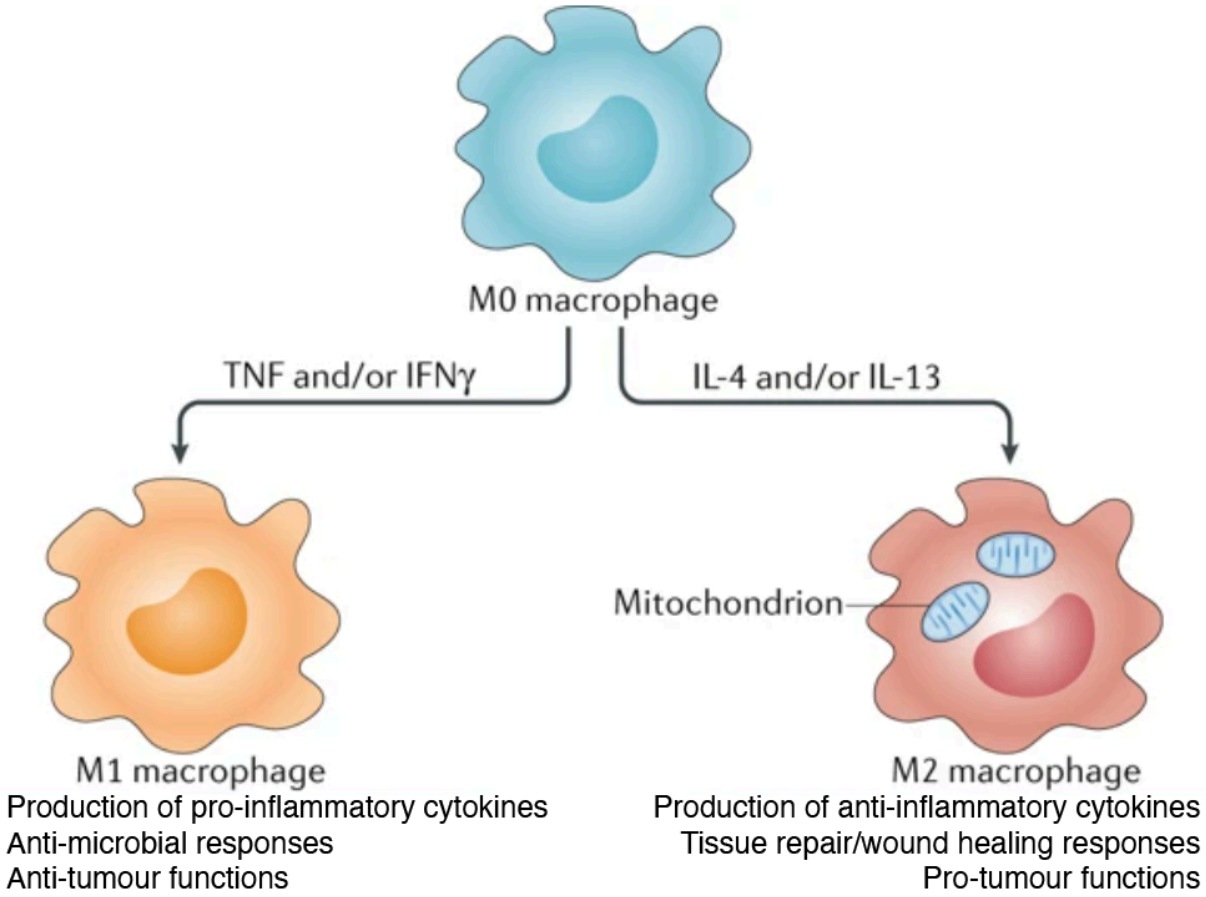


Figure I.8 – Overview of macrophage polarisation

M1 and M2 macrophage polarisation states are an in vitro paradigm that highlights the pro-inflammatory or anti-inflammatory phenotype of these cells but oversimplifies the extremely heterogeneous nature of macrophages in vivo. In brief, naïve M0 macrophages are activated to an M1 phenotype by exposure to pro-inflammatory signals such as lipopolysaccharide and/or the T helper 1 (T_H1) cytokines tumour necrosis factor alpha (TNFα) and interferon gamma (IFNγ) whereas the M2 phenotype is induced by exposure to anti-inflammatory signals such as the T helper 2 (T_H2) cytokines interleukin 4 (IL-4) and IL-13. Classically activated (M1) macrophages release additional TNFα and IFNγ which are immunostimulatory cytokines and thus support anti-tumour immunity. Proposed markers of M1 macrophages include MHC class II (more specifically, HLA-DR) and inducible nitric oxide synthase (iNOS) [133]. Alternatively activated (M2) macrophages produce angiogenic factors (such as vascular endothelial growth factor [VEGF] and platelet-derived growth factor [PDGF]) and cytokines (including transforming growth factor beta [TGFβ], IL-4 and IL-10) that are immunosuppressive and thus inhibit anti-tumour immunity. Proposed markers of M2

macrophages include CD163, CD204 (which are both macrophage scavenger receptors) and CD206 (macrophage mannose receptor C-type 1) [133]. The majority of tumour-associated macrophages (TAM) are believed to adopt a M2-like phenotype.
Image from [134]; reprinted by permission from Nature Publishing Group, copyright 2019.

Tumour-associated neutrophils (TAN) are also able to adopt different phenotypes within the TME. In mice, a dichotomisation of phenotype analogous to that for macrophages has been proposed (N1 possessing anti-tumour and N2 possessing pro-tumour functions) [135, 136], although it is not clear if such a distinction is applicable to humans. A further group of immunosuppressive cells are myeloid-derived suppressor cells (MDSC), a heterogenous population of immature cells of either monocytic or granulocytic origin which can inhibit lymphocyte proliferation and promote tumour growth and metastasis (as reviewed in [137]). Whether these cells represent distinct cell types in their own right, or are simply immature myeloid cells arising secondary to impaired differentiation, is debated. Although multiparametric immunophenotyping is required to accurately identify them, they all express the myeloid marker CD11b [138].

Despite this heterogeneity in function, myeloid cells are generally considered to act in an immunosuppressive manner within the TME (and hence contribute to poor patient outcomes [139-141]) and to have the ability to limit responses to immunotherapy [142] and other cancer treatments [143] (as reviewed in [144]). However, certain innate immune cells are critical to effective anti-tumour immunity. Due to their role in linking the innate and adaptive immune systems, DC are central to stimulating anti-tumour immune responses, although their dysfunction within the TME can lead to tolerance to cancer cell antigens (as reviewed in [145]). Natural killer (NK) cells, a key component of the first line immune defence against pathogens, can recognise stress-inducible damage-associated molecular patterns (DAMP) on the surface

of tumour cells. Unlike CTL, they do not require previous priming and their function is actually inhibited by MHC class I molecules. Therefore, they are particularly important in eliminating tumour cells for which loss of MHC class I expression has contributed to immune escape (as reviewed in [146]).

Cancer immunotherapy

Inspired by regression of an advanced sarcoma in a patient infected with *Streptococcus pyogenes*, efforts to harness the host immune system to produce an anti-cancer response (cancer immunotherapy), through intratumoural administration of mixed bacterial toxins, were initially pioneered by the surgeon William Coley as early as the 1890s [147]. Despite impressive results, this approach was superseded by the development of radiotherapy and chemotherapy (however, retrospective analysis has demonstrated comparable outcomes with Coley's vaccine to these more modern cancer treatments [148]). During this period, progress with cancer immunotherapy was largely limited to use of intravesical Bacillus Calmette-Guérin (BCG) to treat bladder cancer [149] and administration of the immunostimulatory cytokines interleukin 2 (IL-2) in renal cell carcinoma (RCC) and melanoma [150] and interferon alpha (IFNα) in RCC [151]. Lately, there has been a renaissance of interest in the ability to manipulate the host immune response to cancer for therapeutic benefit [152, 153]. In particular, the development of immune checkpoint blockade (ICB) has revolutionised cancer treatment [154]. ICB involves the administration of monoclonal antibodies that prevent transmission of negative signals to tumour-specific T lymphocytes, thus potentiating immune responses. Within secondary lymphoid organs, binding of CD80 (B7-1) or CD86 (B7-2) on the surface of APC to cytotoxic T lymphocyte-associated protein 4 (CTLA-4/CD152) on the surface of T lymphocytes transmits a co-inhibitory signal that constrains activation of the later. Anti-CTLA-4 monoclonal antibodies, such as ipilimumab, block this interaction and increase priming of

naïve tumour-specific T lymphocytes, leading to the generation of new anti-tumour immune responses [155] (**Figure I.9A**). Similarly, ligation of the programmed cell death protein 1 (PD-1/CD279) receptor on the surface of activated T lymphocytes by programmed death-ligand 1 (PD-L1/CD274) or programmed death-ligand 2 (PD-L2/CD273) on the surface of neoplastic or myeloid cells abrogates co-stimulatory signalling via CD28 [156]. Blocking this interaction, with anti-PD-1 (nivolumab and pembrolizumab) or anti-PD-L1 (atezolizumab, avelumab and durvalumab) monoclonal antibodies, reinvigorates existing, but dysfunctional, T lymphocyte responses within the TME (**Figure I.9B**).

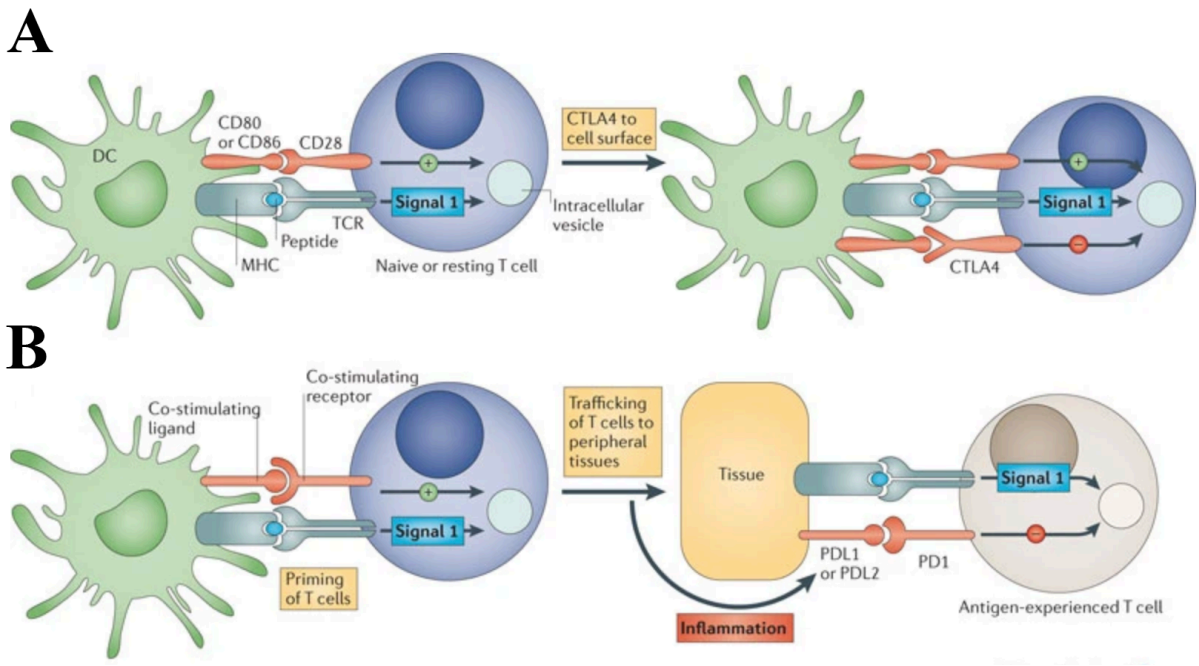


Figure I.9 – Overview of immune checkpoint blockade in cancer immunotherapy

(A) The cytotoxic T lymphocyte-associated protein 4 (CTLA-4)-mediated immune checkpoint is induced in T lymphocytes at the time of their initial response to antigen. Naïve T lymphocytes express high levels of the co-stimulatory molecule CD28 on their surface but do not express the co-inhibitory molecule CTLA-4, which is instead sequestered in intracellular vesicles. Upon T cell receptor (TCR) triggering by cognate antigen presented by major histocompatibility complex (MHC), CTLA-4 is transported to the cell surface, in an amount

which is directly proportional to the strength of TCR/CD28 signalling, where it competes with CD28 for binding to CD80/CD86 on the surface of antigen-presenting cells such as dendritic cells (DC). Therefore, CTLA-4 functions to dampen the amplitude of an initial T lymphocyte response and to maintain a consistent level of T lymphocyte activation despite wide variations in the concentrations and affinities of different antigens for the TCR. In cancer immunotherapy, blocking the interaction between CD80/CD86 and CTLA-4 with an anti-CTLA-4 monoclonal antibody (e.g. ipilimumab) increases priming of naïve tumour-specific T lymphocytes, leading to the generation of new anti-tumour immune responses.
(B) By contrast, the programmed cell death protein 1 (PD-1) pathway regulates T lymphocytes at sites of inflammation. Activated T lymphocytes up-regulate PD-1 and continue to express it within peripheral tissues. Inflammatory signals within these tissues, such as interferon gamma (IFNγ) produced by type 1 helper T lymphocytes, induce the expression of the PD-1 ligands PD-L1 and PD-L2. When these bind to PD-1, T lymphocyte activity is inhibited in order to limit unwanted tissue damage. Excessive induction of PD-1 in the setting of chronic antigen exposure (such as occurs in chronic viral infections and tumours) can induce a state of T lymphocyte dysfunction termed 'exhaustion'. In cancer immunotherapy, these 'exhausted' T lymphocytes can be reinvigorated by blocking this interaction with either anti-PD-1 (e.g. nivolumab and pembrolizumab) or anti-PD-L1 (e.g. atezolizumab, avelumab and durvalumab) monoclonal antibodies.
Image from [157]; reprinted by permission from Nature Publishing Group, copyright 2012.

Other immunotherapeutic approaches include cancer vaccines (as reviewed in [158]), which aim to amplify tumour-specific T lymphocyte responses through active immunisation against cancer cell antigens, and adoptive transfer of chimeric antigen receptor (CAR) T lymphocytes, which have been genetically engineered to express a synthetic receptor that redirects them to recognise and eliminate neoplastic cells expressing the target antigen of interest (as reviewed in [159]). Each of the aforementioned approaches stimulate adaptive anti-tumour immune responses by acting at different stages of the cancer-immunity cycle (**Figure I.10**). Approaches to potentiate innate anti-tumour immune responses have also been proposed but are currently less developed (as reviewed in [160]).

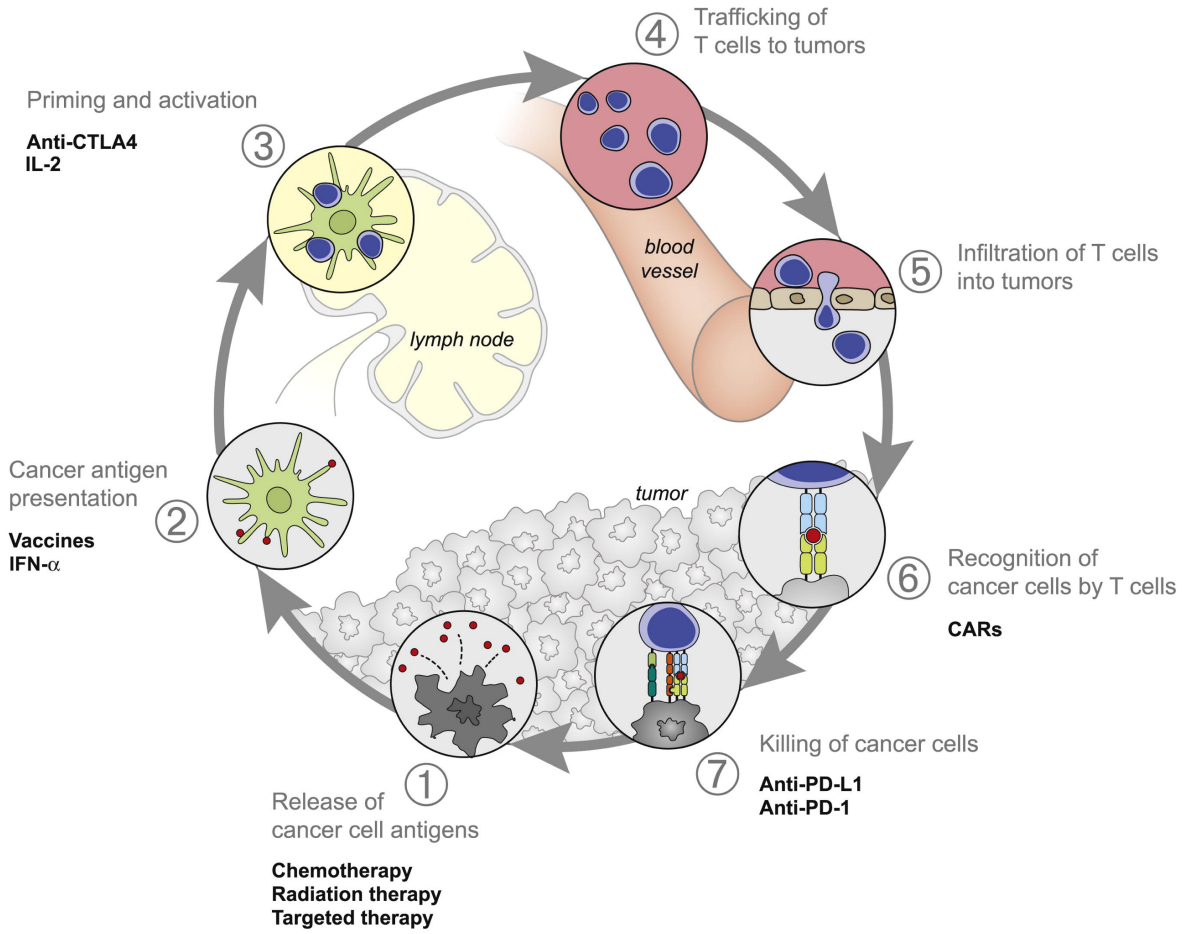


Figure I.10 – Overview of opportunities for immunotherapeutic intervention in cancer

Each step of the cancer-immunity cycle provides an opportunity for immunotherapeutic intervention. Although not developed as immunotherapies, chemotherapy, radiotherapy and targeted therapy can induce tumour cell death and boost release of cancer cell antigens (step 1). Cancer vaccines and interferon alpha (IFNα) stimulate cancer cell antigen presentation by antigen-presenting cells (step 2). Anti-cytotoxic T lymphocyte-associated protein 4 (CTLA-4) antibodies and interleukin 2 (IL-2) boost T lymphocyte priming and activation within tumour draining lymph nodes (step 3). Chimeric antigen receptor (CAR) T lymphocytes are engineered to express a synthetic T cell receptor that increases T lymphocyte recognition of cancer cells (step 6), whilst anti-programmed cell death protein 1 (PD-1) and anti-programmed death-ligand 1 (PD-L1) antibodies potentiate anti-tumour cytotoxicity (step 7). Less progress has been made at improving T lymphocyte trafficking to, and infiltration into, tumours (step 4 and step 5), although this is an area of active investigation.

Image adapted from [115]; reprinted by permission from Elsevier Science, copyright 2013.

Since only a subset of cancer patients benefits from a durable response with immunotherapy, identifying mechanisms of treatment resistance is a key priority (as reviewed in [161, 162]). Whilst the immune TME is highly heterogenous, hypoxia is believed to contribute to local immunosuppression [163-165]. Hypoxia has been associated with resistance to ICB amongst melanoma patients [166] whilst a gene expression signature linking tumour hypoxia, T_{Reg} recruitment and CTL exhaustion is predictive of survival across six common solid tumour types [167], justifying further investigations into the relationship between tumour hypoxia and anti-tumour immunity.

Effects of hypoxia and the hypoxia-inducible factor (HIF) system on immune responses

Recently, it has become apparent that the HIF pathway influences numerous processes that are less intuitively related to oxygen sensing (as reviewed in [168]). The roles of hypoxia and the HIF system in immunological responses is of significant interest because circulating leukocytes are exposed to, and must function within, a wide range of oxygen tensions (from high oxygen levels within the pulmonary circulation to almost anoxia at the site of an abscess or tumour necrosis) and the HIF system is well positioned to mediate many of the homeostatic adaptations necessitated by these microenvironmental changes (as reviewed in [169, 170]).

Leukocyte development

Hypoxia and HIF signalling are implicated in each stage of leukocyte development and functioning. The primary lymphoid organs (bone marrow and thymus) contain regions of profound hypoxia and haematopoietic stem cells (HSC) are enriched within hypoxic bone marrow niches [171-173]. However, HSC have been shown to be hypoxic independently of their spatial proximity to blood vessels, suggesting that hypoxia is a physiological property inherent to this cell type irrespective of their location within the bone marrow [174]. Indeed,

quiescent HSC demonstrate HIF1α stabilisation which contributes to their utilisation of glycolysis for energy provision [175, 176]. Furthermore, whilst HIF signalling is not required for the production of human progenitors engaged in the myeloid lineage, it does support erythroid colony formation [177] and proliferation and differentiation of lymphoid cells within the bone marrow [178].

Adaptive immune responses

In general, type 1 immune responses (which are pro-inflammatory and skewed towards cytotoxicity through potentiation of T helper 1 [T_H1] lymphocytes, CTL, NK cells and M1 macrophages) rely on glycolysis for energy whereas type 2 immune responses (which are anti-inflammatory and dominated by T_{Reg} and M2 macrophages) depend upon oxidative metabolism. During activation, naïve T lymphocytes, which rely on mitochondrial metabolism whilst quiescent, engage aerobic glycolysis to support the immediate (but unsustainable) bioenergetic and biosynthetic demands of the transition to an effector phenotype and subsequent cellular proliferation of clonal expansion. This metabolic shift is maintained by increased HIF1α transcription, secondary to augmented phosphoinositide 3-kinase (PI3K)/mechanistic target of rapamycin (mTOR) signalling [179, 180]. HIF stabilisation is critical to $CD8^+$ T lymphocyte effector differentiation [181-183] and, consequently, HIF1α is essential for *in vivo* CTL-mediated killing of murine tumour cells and its deletion (but not that of HIF2α) leads to accelerated tumour growth [184]. Indeed, ligation of PD-1 or CTLA-4 inhibits glycolysis, contributing to the suppressive function of these immune checkpoint molecules [185]. Glycolytic metabolism appears to be particularly important to T helper 17 (T_H17) lymphocyte differentiation, with T_{Reg} predominantly relying on oxidative phosphorylation and fatty acid oxidation for energy with much lower glycolytic rates [186]. Therefore, HIF1α has been proposed to act as a metabolic ‘switch’ that regulates helper T

lymphocyte lineage commitment along one of these two pathways [187, 188]. Following resolution of inflammation, memory T lymphocytes revert to oxidative metabolism by down-regulating mTOR signalling [189, 190], although they remain 'primed' for rapid activation and proliferation upon re-exposure to antigen, with increased capacity for both oxidative and glycolytic metabolism when compared to naïve T lymphocytes [191, 192].

Developing B lymphocytes are exposed to physiological hypoxia within the bone marrow and HIF activity varies dynamically at different stages of their development, being highest in the early stages and then being suppressed within immature B lymphocytes [193]. Consequently, murine B lymphocytes with either deficiency [194-196] or constitutive activation [193] of HIF1α are developmentally abnormal. The germinal centres of secondary lymphoid organs, the site of antigen-specific B lymphocyte activation, are also regionally hypoxic and germinal centre B lymphocytes engage HIF1α-mediated glycolysis to support rapid growth and proliferation [197]. Whilst one study reported that germinal centre hypoxia potentiates antibody responses [198], another found that germinal centre hypoxia/constitutive B lymphocyte HIF signalling restrains activation of these cells and may play a role in regulating the quality of antibody-mediated immune responses [199]. Thus, further studies are required to characterise more accurately the role of hypoxia and the HIF system in B lymphocyte biology.

Innate immune responses

In a manner analogous to T lymphocyte activation, toll-like receptor (TLR) signalling in myeloid cells (such as occurs in response to bacterial lipopolysaccharide) leads to increased HIF1α transcription (mediated via nuclear factor kappa-light-chain-enhancer of activated B cells [NF-κB] signalling) and stabilisation even when oxygen is available [200-202].

Accordingly, deletion of *Hif1a* within myeloid cells impairs both their glycolytic capacity and function (leading to increased susceptibility to bacterial infection) whereas deletion of *Vhl* in the same cells results in increased inflammation and augmented bactericidal capacity [201, 203]. These observations are consistent with the restriction of the most potent innate inflammatory responses to areas of severe hypoxia, such as within an abscess. Furthermore, hypoxia has been reported to prolong macrophage survival, contributing to their accumulation at sites of chronic inflammation and within tumours [204]. Interestingly, the two main HIFα isoforms have been reported to have opposing effects on macrophage polarisation, with HIF1α being induced by T_H1 cytokines and promoting M1 polarisation (e.g. by up-regulating inducible nitric oxide synthase [*Nos2*] expression) and HIF2α being induced by T helper 2 (T_H2) cytokines and promoting M2 polarisation (e.g. by up-regulating arginase 1 [*Arg1*] expression) [205]. Similarly, hypoxia, acting via HIF, prolongs neutrophil survival and potentiates their inflammatory functions [206-210]. Hypoxia is also reported to enhance the immunosuppressive functions of MDSC, partly through increased expression of *Arg1* [211, 212].

DC encounter antigen and are activated within inflamed tissues in which oxygen availability is limited. Upon TLR ligation, even under experimental conditions of atmospheric oxygen, DC stabilise HIF1α with the consequent glycolytic switch reported to support their maturation and function including increased synthesis of pro-inflammatory cytokines and increased expression of co-stimulatory molecules leading to augmented T lymphocyte stimulation [213-215]. Hypoxia has also been reported to inhibit DC homing to lymph nodes whilst maintaining their pro-inflammatory function at the site of primary disease, thus ‘uncoupling’ localised inflammatory responses and systemic immune responses in a manner that might prevent the development of autoimmunity [216]. However, other studies have reported that hypoxia

inhibits antigen uptake by DC, with immature forms being particularly affected [217, 218], and also contributes to increased apoptosis of immature DC [219]. Furthermore, it appears that the maturation of plasmacytoid DC is particularly sensitive to bone marrow hypoxia, with the process being inhibited in a HIF1α-dependent manner [220]. Thus, the effects of hypoxia on DC are complex and likely to be cell type and context dependent.

After IL-15 priming, short-term hypoxia, acting through HIF1α, supports NK cell glycolysis and augments their cytotoxicity [221]. However, following long-term hypoxia, down-regulation of expression of several major activating surface receptors correlates with impaired killing of virally infected or malignant target cells [222]. Analysis of NK cell transcriptional responses under hypoxia demonstrated increased expression of genes involved in angiogenesis and immunosuppression with decreased expression of pro-inflammatory/anti-tumour genes, such as that encoding interferon gamma (IFNγ) [223].

In summary, numerous pre-clinical studies have utilised either exposure to low levels of oxygen or genetic interventions on the HIF system as tools to study the effects of hypoxia on leukocytes. Although these studies have confirmed an important role for hypoxia and the HIF system in influencing immune cell function, their results have not always been congruent. Explanations for these divergent phenotypes include conducting *in vitro* studies at oxygen tensions that do not accurately reproduce those encountered *in vivo* (as reviewed in [8]) and the use of diverse transgenic animal models that generate abrupt and profound genetic interventions and thus cannot recapitulate the complexity of dynamic immune cell interactions. Therefore, studies utilising approaches that profile the integrative effects of hypoxia/HIF system activation on (anti-tumour) immunity in a more physiologically relevant manner are merited.

Thesis aims and structure

It is my hypothesis that hypoxia contributes to an impaired anti-tumour immune response by influencing the composition and distribution of infiltrating leukocytes, as well as altering their function within the TME. However, a better understanding of how hypoxia, via HIF system activation in tumour cells and leukocytes, impacts upon anti-tumour immune responses is essential to inform the development of more effective immunotherapeutic treatment strategies. In this thesis, I examine the consequences of manipulating hypoxic responses, utilising pharmacological approaches in humans and genetic approaches in mice, on anti-tumour immunity. More specifically:

- In Chapter 1, I utilise immunohistochemistry and a novel image analysis pipeline to evaluate the spatial distribution of tumour infiltrating leukocytes relative to areas of hypoxia in solid human tumours;
- In Chapter 2, I investigate whether the hypoxic TME in human lung cancer can be altered by the administration of the mitochondrial inhibitor atovaquone and whether this pharmacological intervention affects the immune contexture of these tumours;
- In Chapter 3, I characterise an unexpected immunological phenotype arising in a novel mouse model created to study the dynamic HIF response *in vivo*;
- In Chapter 4, I analyse the effects of systemic *Phd2* silencing in mice on the growth of transplantable wild-type tumours and the associated anti-tumour immune response.

Importantly, hypoxia and inflammation co-exist (and may exacerbate each other) in numerous non-malignant conditions including infections, sterile inflammation and autoimmunity. Therefore, work conducted for this thesis may be of relevance to diseases other than cancer.

Materials and Methods

Chapters 1 and 2

Cell pellet samples for immunohistochemistry optimisation/validation

U-2 OS (human osteosarcoma) and HKC-8 (human proximal tubular epithelial) cells were sourced from stocks already available within the Ratcliffe/Pugh Oxygen Sensing Laboratory. Cell culture was performed using aseptic techniques in a high-efficiency particulate air (HEPA) filtered cabinet. Unless otherwise specified, all cell lines were grown at 37 °C in a humidified CO_2 incubator set to 5% CO_2. Both cell lines underwent regular testing for contamination by *Mycoplasma* spp. utilising a MycoAlert™ PLUS Mycoplasma Detection Kit (LT07-703; Lonza, CH), as per manufacturer's instructions.

Cell culture

1. Seed 5.0 x 10^6 U-2 OS cells into a 150 mm dish containing 30 mL Dulbecco's Modified Eagle's Medium (DMEM) culture medium (D6546) supplemented with 10% fetal bovine serum (FBS) (F7524), 2 mM L-glutamine (G7513), 100 IU/mL penicillin and 100 µg/mL streptomycin (P0781) (all from Sigma-Aldrich, UK)
2. Incubate the culture dish in either a standard incubator (as above) or a hypoxia chamber pre-set to the desired level of oxygenation (Invivo$_2$ 400 workstation [Baker Ruskinn, UK]) for 16 hours (when using the hypoxia chamber, add the Eppendorf tube containing pimonidazole [Hypoxyprobe Inc., USA] to the chamber at the same time as the cell culture dish)
3. Add pimonidazole to culture medium to a concentration of approximately 150 µM (12.5 µL of 100 mg/mL [343.9 mM] stock solution diluted in 500 µL phosphate buffered saline [PBS] [P1447; Sigma-Aldrich, UK]) for the final 2 hours

N.B. HKC-8 cells were cultured in a standard incubator only, with the PHD inhibitor dimethyloxalylglycine (DMOG) (CAY71210; Cambridge Bioscience, UK) added to culture medium to a concentration of 1 mM (300 μL of 100 mM stock solution added to 30 mL of medium) for 16 hours. They were not subject to pimonidazole labelling.

Cell harvest

1. Discard culture medium and wash cells in dish with 25 mL room temperature PBS
2. Add 8 mL of trypsin-ethylenediaminetetraacetic acid (EDTA) solution (T3924; Sigma-Aldrich, UK) and return to standard incubator for 5 minutes before terminating cell dissociation by the addition of 17 mL culture medium
3. Transfer medium and dissociated cells into a 50 mL Falcon tube and centrifuge at 180 x g at room temperature for 5 minutes
4. Discard supernatant and wash cells by resuspending them in 25 mL PBS and centrifuging at 180 x g at room temperature for 5 minutes
5. Repeat this washing step for a second time and discard supernatant

Cell fixation

1. Resuspend cells in 5 mL of 10% neutral buffered formalin (NBF) (HT501128; Sigma-Aldrich, UK) and leave to fix in a 15 mL Falcon tube at room temperature for 24 hours
2. Centrifuge at 180 x g at room temperature for 5 minutes, discard supernatant and resuspend cells in 5 mL of 70% ethanol and leave to fix at room temperature for 30 minutes
3. Centrifuge at 180 x g at room temperature for 5 minutes, discard supernatant and resuspend cells in 5 mL of 100% ethanol (32221-M; Sigma-Aldrich, UK) and leave to fix at room temperature for 30 minutes (optional overnight fixation makes a very solid cell pellet)

Cell pellet processing

1. Centrifuge at 180 x g at room temperature for 5 minutes and discard supernatant
2. Heat HistoGel™ (HG-4000; Thermo Fisher Scientific, UK), either by microwaving on a low heat for 15 seconds after loosening the top of the tube or by heating to 60 ± 5 °C on a dry block incubator, and add five drops of liquefied HistoGel™ to the Falcon tube with a Pasteur pipette
3. Resuspend the cells and cool on ice to create a solid cell pellet
4. Transfer the cell pellet to a histology cassette for paraffin embedding (described below in greater detail for murine tissue samples)

Patient tumour samples

The work presented in this thesis was approved under the Oxford Radcliffe Biobank (ORB) research tissue bank ethics, reference 09/H0606/5+5. For each case, all diagnostic haematoxylin and eosin (H&E) stained slides and accompanying formalin-fixed, paraffin-embedded tumour blocks were retrieved from the diagnostic archive of the Department of Cellular Pathology, John Radcliffe Hospital, Oxford. After review of the H&E stained slides with a Consultant Histopathologist with expertise in that specific tumour type, a representative block was selected for each case and tissue sectioning was performed by the Oxford Centre for Histopathology Research (OCHRe).

Head and neck squamous cell carcinoma samples

This cohort of patients has been analysed previously as part of a validation study of a hypoxia gene expression signature [224] (**Appendix 2**). Following ethical approval from the Oxford Local Ethical Review Committee, consecutive patients undergoing potentially curative surgery for head and neck squamous cell carcinoma (HNSCC) were approached and informed consent

obtained for use of their tissue. Patients who were enrolled in the study received an intravenous infusion of 500 mg/m^2 pimonidazole 12-16 hours prior to undergoing surgery.

Clear cell renal cell carcinoma samples

Clear cell renal cell carcinoma (CCRCC) samples containing necrotic foci were identified after review of recent pathology reports from the Department of Cellular Pathology, John Radcliffe Hospital, Oxford and accessed via OCHRe (**Appendix 3**). CCRCC samples assessed for semaphorin 3A (SEMA3A) expression were accessed from OCHRe via Dr Michael Barnkob and Professor Vincenzo Cerundolo (Weatherall Institute of Molecular Medicine, University of Oxford) (**Appendix 4**).

ATOM (Atovaquone as Tumour HypOxia Modifier) study samples

Samples of pimonidazole-treated non-small cell lung cancer (NSCLC) from the ATOM (Atovaquone as Tumour HypOxia Modifier) study were accessed from OCHRe via Dr Michael Skwarski, Mr Marcus Green and Professor Geoff Higgins (Department of Oncology, University of Oxford) (**Appendix 5**). Patients who were enrolled in the study received an oral dose of 500 mg/m^2 pimonidazole 16-24 hours prior to undergoing surgery.

Rectal carcinoma samples

Samples of pimonidazole-treated rectal cancers (presented in Appendix 1) from the RHYTHM-I: Investigating Hypoxia in Rectal Tumours study were accessed from OCHRe via Dr Tessa Greenhalgh and Professor Tim Maughan (Department of Oncology, University of Oxford). Patients who were enrolled in the study received an oral dose of 500 mg/m^2 pimonidazole 16-24 hours prior to undergoing surgery.

Immunohistochemistry

Single staining (head and neck squamous cell carcinoma samples, semaphorin 3A clear cell renal cell carcinoma samples, ATOM study samples, rectal carcinoma samples)

Staining was performed using a Leica BOND-MAX (Leica Biosystems, UK) automated platform using the protocol outlined in **Table M.1**.

Table M.1 – Leica BOND-MAX single staining protocol	
Epitope retrieval*	Variable duration
Peroxide block (3-4% hydrogen peroxide)	5 minutes
Marker (primary antibody)	30 minutes
Post primary (rabbit anti-mouse IgG)	8 minutes
Polymer (anti-rabbit IgG poly-HRP)	8 minutes
Diaminobenzidine	10 minutes
Haematoxylin	5 minutes
*Automated epitope retrieval conducted at 100 °C for the length of time optimised for each primary antibody (see **Table M.3**) *HRP – horseradish peroxidase*	

For the ATOM study samples, PD-L1 immunostaining was performed in the Department of Cellular Pathology, John Radcliffe Hospital, Oxford using the VENTANA PD-L1 (SP263) Assay with the OptiView DAB Immunohistochemistry Detection Kit on the automated VENTANA BenchMark ULTRA slide staining platform, as per manufacturer's instructions [225, 226] (all reagents and equipment from Roche Diagnostics, UK).

Results of p16 immunohistochemistry for the HNSCC cohort, performed using the CINTec® Histology test (Roche Diagnostics, UK) as per manufacturer's instructions, were available

from a previously published study [224]. Tumours with > 70% contiguous, strong nuclear or cytoplasmic staining were scored as positive.

Sequential double staining (clear cell renal cell carcinoma samples with necrosis)

Again, staining was performed using a Leica BOND-MAX automated platform using the protocol outlined in **Table M.2**.

Table M.2 – Leica BOND-MAX double staining protocol	
Epitope retrieval*	20 minutes
Marker (primary antibody 1)	30 minutes
Post primary (rabbit anti-mouse IgG)	20 minutes
Polymer (anti-rabbit IgG poly-AP)	30 minutes
Fast red	10 minutes
Fast red	5 minutes
Epitope retrieval*	20 minutes
Peroxide block (3-4% hydrogen peroxide)	5 minutes
Marker (primary antibody 2)	30 minutes
Post primary (rabbit anti-mouse IgG)	8 minutes
Polymer (anti-rabbit IgG poly-HRP)	8 minutes
Diaminobenzidine	10 minutes
Haematoxylin	5 minutes
*Automated epitope retrieval conducted at 100 °C *AP – alkaline phosphatase, HRP – horseradish peroxidase*	

Primary antibodies

Primary antibodies used in immunohistochemical staining of human tumour specimens are listed in **Table M.3**.

Table M.3 – Primary antibodies used in immunohistochemical staining of human specimens

Antigen	Company	Clone details (catalogue number)	Antibody type	Epitope retrieval protocol*	Duration of epitope retrieval (minutes)	Antibody dilution
CA IX	Abcam, UK	N/A (ab15086)	Rabbit polyclonal	ER1	20	1:2000
CD3	Abcam, UK	N/A (ab5690)	Rabbit polyclonal	ER2	20	1:250
CD4	Leica Biosystems, UK	4B12 (NCL-LCD4-368)	Mouse monoclonal	ER2	20	1:100
CD8	Agilent, UK	C8/144B (M7103)	Mouse monoclonal	ER2	20	1:100
CD11c	Abcam, UK	EP1347Y (ab52632)	Rabbit monoclonal	ER2	20	1:500
CD19	Leica Biosystems, UK	BT51E (NCL-L-CD19-163)	Mouse monoclonal	ER2	20	1:100
CD20	Leica Biosystems, UK	L26 (NCL-L-CD20-L26)	Mouse monoclonal	ER1	20	1:100
CD31	Agilent, UK	JC70A (M0823)	Mouse monoclonal	ER2	20	Variable†
CD68	Agilent, UK	PG-M1 (M0876)	Mouse monoclonal	ER1	20	1:200

CD123	Leica Biosystems, UK	BR4MS (NCL-L-CD123)	Mouse monoclonal	ER2	20	1:100
CD146	Abcam, UK	EPR3208 (ab75769)	Rabbit monoclonal	ER2	20	1:500
CD163	Leica Biosystems, UK	10D6 (NCL-L-CD163)	Mouse monoclonal	ER1	20	1:200
CD204	2BScientific, UK	SRA-E5	Mouse monoclonal	ER1	20	1:250
CD206	Abcam, UK	N/A (ab64693)	Rabbit polyclonal	ER1	20	1:2000
FOXP3	Abcam, UK	236A/E7 (ab20034)	Mouse monoclonal	ER2	20	1:100
GLUT1	Abcam, UK	SPM498 (ab40084)	Mouse monoclonal	ER1	20	1:400
HIF1α	BD Biosciences, UK	Clone 54 (610959)	Mouse monoclonal	ER2	40	1:400
Neutrophil elastase	Abcam, UK	N/A (ab68672)	Rabbit polyclonal	ER1	20	1:500
Pimonidazole	Hypoxyprobe Inc., USA	4.3.11.3 (Mouse-Mab)	Mouse monoclonal	ER1	20	1:1000
Semaphorin 3A	Abcam, UK	EPR19367 (ab199475)	Rabbit monoclonal	ER2	20	1:4000
Wide spectrum cytokeratin	Abcam, UK	N/A (ab9377)	Rabbit polyclonal	ER2	40	1:200

*Automated epitope retrieval conducted at 100 °C

ER1 – citrate-based epitope retrieval solution (pH 6.0)

ER2 – EDTA-based epitope retrieval solution (pH 9.0)

†1:800 for single staining, 1:2500 for double staining of clear cell renal cell carcinoma samples

EDTA – ethylenediaminetetraacetic acid, N/A – not applicable

Secondary antibodies and other reagents

Automated staining requires dewax solution (AR9222), wash solution (AR9590), epitope retrieval solution 1 (AR9961) and epitope retrieval solution 2 (AR9640); all of the other necessary reagents are contained within the BOND Polymer Refine Detection kit (DS9800) and the BOND Polymer Refine Red Detection kit (DS9390) (all from Leica Biosystems, UK).

After completion of staining, slides were mounted in Aquatex (1.08562.0050; VWR, UK) with a 24 x 50 mm glass coverslip (631-0146; VWR, UK) and left to dry overnight before image acquisition.

Positive control samples

Sections of human tonsil acted as positive controls for CD3, CD4, CD8, CD11c, CD19, CD20, CD31, CD68, CD123, CD146, CD163, CD204, CD206, FOXP3, neutrophil elastase and wide spectrum cytokeratin immunostaining. Sections of human CCRCC acted as positive controls for carbonic anhydrase 9 (CA IX) and GLUT1 immunostaining. Sections of non-neoplastic human kidney acted as positive controls for SEMA3A immunostaining. Sections of DMOG-treated HKC-8 cell pellets acted as positive controls for HIF1α immunostaining whilst sections of hypoxic U-2 OS cell pellets, a pimonidazole-treated human rectal cancer sample or a pimonidazole-treated human DLD-1 colorectal cancer xenograft sample acted as positive controls for pimonidazole immunostaining. Sections of human placenta acted as positive

controls for PD-L1 immunostaining. All positive control samples demonstrated patterns and intensities of staining that were consistent between staining runs.

Negative control samples

Negative control samples consisted of the same positive control sample incubated with either a mouse (ab37355; Abcam, UK) or rabbit (GTX47478; GeneTex, UK, or that provided in the SP263 PD-L1 assay kit; Roche Diagnostics, UK) isotype control antibody (ATOM study samples) or omission of the primary antibody (all other samples) and showed no/minimal non-specific staining.

Representative images of human immunohistochemistry control samples are presented in **Appendix 6**.

Image acquisition and analysis

Whole slides were scanned at x200 magnification using the NanoZoomer S210 digital slide scanner (Hamamatsu, Japan). Digital whole slide images were reviewed using NDP.view2 software (Hamamatsu, Japan) and representative images were chosen from these to illustrate key histological findings. All digital image analysis steps were implemented in MATLAB® (MathWorks, USA), automatically performed and visually approved (for more details, image analysis algorithms are described in **Appendices 2, 4, 5 and 7**). PD-L1 immunohistochemistry slides for the ATOM study were scored manually in a blinded manner by a Consultant Histopathologist with expertise in lung cancer pathology (Dr Mark McCole, Department of Cellular Pathology, Oxford University Hospitals NHS Foundation Trust) as per routine clinical practice.

Chapters 3 and 4

Animals

Animal procedures were approved by the University of Oxford Medical Sciences Division Ethical Review Committee and were compliant with the UK Home Office Animals (Scientific Procedures) Act 1986, working under Procedure Project Licence (PPL) P38BE32DE. All mice were housed in the Functional Genetics Facility (Wellcome Centre for Human Genetics, University of Oxford) in individually ventilated cages within a specific-pathogen-free environment under a 12-hour light/dark cycle and were fed a standard pelleted diet and water *ad libitum*. Unless otherwise specified, both male and female mice were used in experiments. Mice included in the autoimmune phenotyping experiments were aged between 8 and 12 weeks at the point of administration of doxycycline whilst mice in the tumour experiments were aged between 10 and 20 weeks at the start of each experiment.

Knockdown mice

Phd2 single knockdown mice carried alleles of *CAG-rtTA*$^{+/-}$*; TRE-shPhd2*$^{+/-}$ whilst control mice carried a single allele of *CAG-rtTA* but no *TRE* allele (*CAG-rtTA*$^{+/-}$*; TRE*$^{-/-}$). For double knockdown experiments, *CAG-rtTA*$^{+/+}$*; TRE-shPhd2*$^{+/-}$ mice were crossed with *CAG-rtTA*$^{-/-}$*; TRE-shHif1a*$^{+/-}$ or *CAG-rtTA*$^{-/-}$*; TRE-shHif2a*$^{+/-}$ mice to produce *CAG-rtTA*$^{+/-}$*; TRE-shPhd2*$^{+}$*/TRE-shHif1a*$^{+}$ or *CAG-rtTA*$^{+/-}$*; TRE-shPhd2*$^{+}$*/TRE-shHif2a*$^{+}$ mice (for further details, see **Appendix 8** and [227]). To induce short hairpin RNA (shRNA) expression, transgenic mice were provided *ad libitum* access to drinking water containing 2.0 mg/mL of doxycycline (D9891) with 3% sucrose (S0389) (both from Sigma-Aldrich, UK). Control mice were also provided the same doxycycline drinking water.

Wild-type mice

Wild-type C57BL/6J mice were obtained from Envigo, UK.

Syngeneic murine tumour experiments

Cell culture

LL/2 (murine Lewis lung carcinoma) cells were purchased from American Type Culture Collection (ATCC) and E0771 (murine mammary gland carcinoma) cells were purchased from CH3 BioSystems™. Both cell lines underwent regular testing for contamination by *Mycoplasma* spp. (as above). Cells were cultured from frozen stocks for at least one week prior to each experiment. LL/2 cells were cultured in DMEM whilst E0771 cells were cultured in Roswell Park Memorial Institute-1640 (RPMI-1640) medium (R0883; Sigma-Aldrich, UK). Both culture media were supplemented with FBS (10% for LL/2 cells and 20% for E0771 cells), 2 mM of L-glutamine, 100 IU/mL of penicillin and 100 μg/mL of streptomycin.

Induction of murine tumours

Mice were shaven over their flanks the day before tumour cell injection, when tumour cells in culture were also split 1:2 in order for them to be maintained within the exponential growth phase. On the day of injection, cells were dissociated by trypsinisation and washed twice in PBS before being counted with a haemocytometer. Cells were then diluted in sterile PBS to produce the desired final concentration. Mice were anaesthetised and cell suspensions were injected bilaterally with a 29G needle as follows:

- LL/2 – 5 x 10^4 cells in 50 μL PBS injected into both male and female mice;
- E0771 –1 x 10^5 cells in 50 μL PBS injected into female mice only.

Assessment of tumour growth

Tumour growth was assessed every other day by measuring their size with digital callipers (15-077-958; Fisher Scientific, UK) in a blinded manner (whilst I conducted the tumour experiments, genotyping was performed by Dr Atsushi Yamamoto). Prior to harvest, tumour surface area (mm^2) was calculated as length x width. After tumour harvest, tumour volume was calculated as length x width x height/2 (mm^3) [228]. Mice were sacrificed when tumours reached the maximum permitted diameter (12.5 mm) or if a humane endpoint was reached (criteria for early endpoint were deteriorating body condition, weight loss and ulcerated or infected tumours).

Pimonidazole administration

Pimonidazole 50 mg/kg (100 μL of 10 mg/mL stock solution for a 20 g mouse) was administered by intraperitoneal injection with a 29G needle two hours before the mice were sacrificed and tissues harvested.

Haematological analyses

When mice were culled, blood was obtained either by cardiac puncture or by venepuncture of the inferior vena cava and collected into heparinised tubes. For serial haematological analyses on individual mice, blood was obtained from the tail vein. Samples were immediately analysed using a Sysmex KX-21N™ Automated Hematology Analyzer (Sysmex Corporation, UK) calibrated for mouse blood. Haematocrits were measured following centrifugation of microhaematocrit capillary tubes.

Anti-nuclear antibody testing

Anti-nuclear antibody (ANA) testing was performed by Ms Tanya Crockford (Nuffield Department of Medicine, University of Oxford) using the following protocol. Mouse serum samples were diluted 100 times in PBS and added to HEp-2000 substrate slides (Immuno Concepts, USA) for 30 minutes. Slides were washed twice with PBS for 5 minutes and once with water for 5 seconds. Slides were then incubated with a fluorescein isothiocyanate (FITC)-labelled goat anti-mouse IgG secondary antibody (ThermoFisher, UK), diluted 1:500 in PBS, for 20 minutes at room temperature in the dark. Slides were washed twice with PBS for 5 minutes and once with water for 5 seconds in the dark before being mounted and imaged with a fluorescence microscope. Acquired images were subject to automated analysis in ImageJ [229] and scored from 0-4 according to fluorescence intensity based on positive and negative control samples on each slide. Samples scored ≥ 2 were considered to be ANA positive. All samples flagged as putative positives were manually cross-checked for *bona fide* nuclear localisation before final scoring.

Histological analyses

Tissue harvesting and processing

Murine tissues for histological processing were immediately transferred to 10% NBF and fixed for 48 hours. Following this, samples were transferred to 70% ethanol before undergoing routine overnight tissue processing in an Excelsior™ AS Tissue Processor (**Table M.4**) and subsequent embedding in paraffin blocks with a HistoStar™ Embedding Workstation (both from ThermoFisher, UK).

Table M.4 – Routine overnight tissue processing programme	
Reagent	Time (hours)
75% alcohol	1.0
90% alcohol	1.0
95% alcohol	1.0
100% alcohol	1.0
100% alcohol	1.0
100% alcohol	1.0
Xylene	1.0
Xylene	1.0
Xylene	1.0
Wax	1.0
Wax	1.0
Wax	1.0

Haematoxylin and eosin staining

Before staining, two troughs (referred to below as #1 and #2) for each of the following fresh reagents were prepared: xylene (247642; Sigma-Aldrich, UK), 100% ethanol, 90% ethanol and 70% ethanol.

1. Specimen sectioning

    1.1. Cut 4 μm sections with a microtome on to adhesive Polysine® slides (631-0107; VWR, UK) and dry overnight in an incubator at 37 °C

2. Dewax and rehydration

    2.1. Melt paraffin wax by placing slides in an incubator at 50 °C for 15 minutes

    2.2. Xylene #1 for 5 minutes

    2.3. Xylene #2 for 5 minutes

    2.4. 100% ethanol #1 for 2 minutes

    2.5. 100% ethanol #2 for 2 minutes

    2.6. 90% ethanol #1 for 2 minutes

    2.7. 90% ethanol #2 for 2 minutes

    2.8. 70% ethanol #1 for 2 minutes

    2.9. 70% ethanol #2 for 2 minutes

    2.10. Tap water for 3 minutes

3. Staining

    3.1. Add slides to Harris haematoyxlin (351945S; VWR, UK) for 4 minutes

    3.2. Wash in running tap water for 3 minutes

    3.3. 10 dips in 1% acid-alcohol (10 mL of concentrated hydrochloric acid + 990 mL of 70% ethanol)

    3.4. 10 dips in tap water

    3.5. 10 dips in Scott's tap water (2 g sodium hydrogen carbonate + 20 g magnesium sulphate + 1 L deionised water)

    3.6. 10 dips in tap water

    3.7. 10 dips in lithium carbonate (15.4 g lithium carbonate + 1 L deionised water)

    3.8. 10 dips in tap water

    3.9. 10 dips in 50% ethanol

    3.10. 10 dips in 70% ethanol

3.11. Add slides to alcoholic eosin Y solution (HT110132; Sigma-Aldrich, UK) for 3 minutes

4. Dehydration and mounting

4.1. 70% ethanol #1 for 2 minutes

4.2. 70% ethanol #2 for 2 minutes

4.3. 90% ethanol #1 for 2 minutes

4.4. 90% ethanol #2 for 2 minutes

4.5. 100% ethanol #1 for 2 minutes

4.6. 100% ethanol #2 for 2 minutes

4.7. Xylene 1 #1 for 2 minutes

4.8. Xylene 2 #2 for 2 minutes

4.9. Mount in dibutylphthalate polystyrene xylene (DPX) mounting solution (06522; Sigma-Aldrich, UK) with a 24 x 50 mm glass coverslip and leave to dry overnight

Immunohistochemistry

1. Specimen sectioning and dewax and rehydration as per H&E staining protocol (above)

2. Antigen retrieval

2.1. Dilute antigen retrieval solution (S1699; Agilent, UK) 1:10 (25 mL of antigen retrieval solution + 225 mL of deionised water) and pre-heat in microwave for 3 minutes in plastic slide box

2.2. Pre-heat pressure cooker (filled with ~2.5 L tap water)

2.3. Place slides in antigen retrieval solution and add to pressure cooker

2.4. Wait for hissing/production of steam and then leave slides for 30 minutes

2.5. Turn off and immediately cool in sink in cold water

2.6. Leave slides to cool for 30 minutes in antigen retrieval solution at room temperature

2.7. Wash in PBS for 5 minutes

3. Peroxidase block

3.1. Place slides on staining tray (Z670146; Sigma-Aldrich, UK)

3.2. Circle tissue with liquid blocking pen (Z672548; Sigma-Aldrich, UK)

3.3. Add one drop of peroxidase block (see below) to each slide and leave for 10 minutes

3.4. Wash in PBS for 5 minutes

4. Primary antibody

4.1. Place slides on staining tray

4.2. Add primary antibody (**Table M.5**) in antibody diluent (ab64211; Abcam, UK) to each slide (~100-300 µL per slide depending upon tissue area)

4.3. Leave for one hour at room temperature or overnight at 4 °C

4.4. Wash 3 times in PBS for 5 minutes each

5. Secondary antibody

5.1. Place slides on staining tray

5.2. Add secondary antibody (see below)

5.3. Leave for 30 minutes at room temperature

5.4. Wash 3 times in PBS for 5 minutes each

6. Chromogen

   6.1. Make diaminobenzidine (DAB) (1 drop of chromogen per 1 mL of substrate buffer as per manufacturer's instructions)

   6.2. Place slides on staining tray

   6.3. Add DAB solution with pipette and leave for time optimised (see below)

   6.4. Wash slides in deionised water for 5 minutes

7. Haematoxylin counterstain

   7.1. Stain with haematoyxlin QS counterstaining kit (H-3404; Vector Laboratories, UK) as per manufacturer's instructions (45 seconds)

   7.2. Rinse two times in tap water (20 dips each)

   7.3. Blue in tap water for 1 minute

8. Dehydration and mounting as per H&E staining protocol (above)

Table M.5 – Primary antibodies used in immunohistochemical staining of murine specimens

Antigen	Company	Clone details (catalogue number)	Antibody type	Antibody dilution	DAB incubation time (mins)
CD3	Abcam, UK	N/A (ab5690)	Rabbit polyclonal	1:100	2
CD4	Stratech, UK	50134-R001	Rabbit monoclonal	1:200	2
CD8a	Synaptic Systems, Germany	N/A (361 003)	Rabbit polyclonal	1:2000	2
CD31	Stratech, UK	DIA-310	Rat monoclonal	1:100	2

CD45	BD Pharmingen, UK	550539	Rat monoclonal	1:100	1.5
F4/80	Abcam, UK	SP115 (ab111101)	Rabbit monoclonal	1:250	4
FOXP3	ThermoFisher, UK	FKJ-16s	Rat monoclonal	1:100	2
GFP	Cell Signaling Technology, UK	2956	Rabbit monoclonal	1:200	1
PAX5	Abcam, UK	EPR3730(2) (ab109443)	Rabbit monoclonal	1:500	2
Pimonidazole	Hypoxyprobe Inc., USA	N/A (PAb2627)	Rabbit polyclonal	1:500	2
DAB – diaminobenzidine, N/A – not applicable					

Caspase 3 and Ki67 immunostaining were performed by Ms Hiromi Kudo and Professor Robert Goldin (Centre for Pathology, Imperial College London).

Secondary antibodies

When performing immunohistochemical staining with a rabbit primary antibody, the peroxidase block, secondary antibody and DAB chromogen were included in the EnVision+ Single Reagents (HRP. Rabbit) kit (K4003; Agilent, UK). When performing immunohistochemical staining with a rat primary antibody, Bloxall® endogenous blocking solution (SP-6000; Vector Laboratories, UK), ImmPRESS® HRP Goat Anti-Rat IgG, Mouse adsorbed Polymer Detection Kit, Peroxidase (MP-7444; Vector Laboratories, UK) and ImmPACT® DAB Substrate, Peroxidase (HRP) (SK-4105; Vector Laboratories, UK) were used.

Representative images of murine immunohistochemistry control samples are presented in **Appendix 9**.

Image acquisition and analysis

Whole slides were scanned at x400 magnification as described above for human samples. Qualitative pathological evaluation of slides was conducted in a semi-blinded manner (reviewing pathologists were aware which samples came from transgenic and control mice but were unaware of the details of the transgenic intervention). Quantification of CD3 (x100 magnification), CD31 (x100 magnification) and pimonidazole (x50 magnification) immunostaining was performed on four randomly chosen areas from each tumour. All digital image analysis steps were implemented in MATLAB® (MathWorks, USA), automatically performed and visually approved.

Flow cytometry

Tissue harvesting and processing

Murine tissues for flow cytometric assessment were immediately transferred to ice-cold PBS.

Leukocyte isolation from tumours

1. Wash excised tumours in PBS, cut into 2-3 mm pieces using a scalpel blade and add tumour dissociation buffer (5 mL of RPMI-1640 medium + 3 mg of collagenase type II [LS004177; Worthington Biochemical, USA] + 5 μL of DNAse I [18047019; ThermoFisher, UK] per sample) followed by dissociation with a gentleMACS™ Octo Dissociator (130-096-427; Miltenyi Biotec, UK)
2. Incubate for 45 minutes at 37 °C under continuous rotation

3. Transfer each sample through a 70 µm cell strainer into a 50 mL Falcon tube; mash any remaining tissue through the strainer with the plunger of a 2.5 mL syringe and rinse with 10 mL of ice-cold fluorescence-activated cell sorting (FACS) buffer (PBS + 5% FBS)
4. Strain for a second time and centrifuge samples at 400 x g at 4 °C for 5 minutes before discarding the supernatant
5. Add 10 mL of ice-cold FACS buffer and centrifuge samples at 400 x g at 4 °C for 5 minutes before discarding the supernatant
6. Vortex mix samples to resuspend cells and add 1 mL of Ammonium-Chloride-Potassium (ACK) lysing buffer (A1049201; ThermoFisher, UK) to samples and incubate for 5 minutes at room temperature to lyse erythrocytes before adding 10 mL of ice-cold FACS buffer to inactivate ACK lysing buffer
7. Centrifuge samples at 400 x g at 4 °C for 5 minutes and discard the supernatant
8. Resuspend the cells in 10 mL of ice-cold FACS buffer and count cells using the Countess™ II automated cell counter (ThermoFisher, UK)
9. Centrifuge samples at 400 x g at 4 °C for 5 minutes and discard the supernatant
10. Resuspend cells in ice-cold FACS buffer to a final concentration of 1 x 10^7 cells per mL and store on ice until antibody staining

Leukocyte isolation from spleen

This is the same protocol as for leukocyte isolation from tumours except that cells are extracted by mashing each spleen into a cell suspension over a petri dish using two glass slides.

Leukocyte isolation from peripheral blood

1. Centrifuge samples at 400 x g at 4 °C for 30 seconds and discard plasma to collect cellular fraction

2. Add 500 µL of ACK lysing buffer to sample and transfer to a 5 mL FACS tube; vortex mix the tubes gently and incubate at room temperature for 5 minutes to lyse erythrocytes before adding 3 mL of ice-cold FACS buffer to inactivate ACK lysing buffer
3. Centrifuge samples at 400 x g at 4 °C for 5 minutes and discard the supernatant
4. Add 500 µL of ACK lysing buffer to sample; vortex mix the tubes gently and incubate at room temperature for 5 minutes before adding 3 mL of ice-cold FACS buffer to inactivate ACK lysing buffer
5. Count cells using the Countess™ II automated cell counter
6. Centrifuge samples at 400 x g at 4 °C for 5 minutes and discard the supernatant
7. Resuspend cells in ice-cold FACS buffer to a final concentration of 1 x 10^7 cells per mL and store on ice until antibody staining

Antibody staining

1. Vortex mix samples and transfer 1 x 10^6 cells (100 µL) from each sample into a 5 mL FACS tube for staining (also prepare additional samples for fluorescence minus one [FMO] controls for CD44, PD-1, F4/80, CD11c and MHC-II)
2. Incubate cells with 100 µL of Fc block (101302; BioLegend, UK) diluted 1:50 in ice-cold FACS buffer on ice for 20 minutes
3. Centrifuge samples at 400 x g at 4 °C for 5 minutes and discard the supernatant
4. Stain cells with 50 µL of antibody cocktail (which includes the antibodies outlined in **Tables M.6-M.10** diluted in ice-cold FACS buffer), including the viability dye 7-aminoactinomycin D (7-AAD) (A1310; ThermoFisher, UK), for 30 minutes at 4 °C in the dark

5. *If required, perform staining for nuclear FOXP3 expression with the FOXP3/Transcription Factor Staining Buffer Set (eBioscience, ThermoFisher, UK) as per manufacturer's instructions*
6. Add 50 µL 1% paraformaldehyde (158127; Sigma-Aldrich, UK) to fix samples and incubate for 30 minutes at 4 °C in the dark
7. Centrifuge samples at 400 x g at 4 °C for 5 minutes; discard the supernatant and resuspend cells in 100 µL of ice-cold PBS (can be left overnight at 4 °C in the dark if analysis will take place the following day)
8. Add 1 x 10^4 counting beads (335925; BD Biosciences, UK) to each sample prior to acquisition on the flow cytometer
9. Prepare single stained samples for compensation set-up using compensation beads (552844; BD Biosciences, UK) on day that test samples are acquired

Antibody panels

Table M.6 – T lymphocyte panel for flow cytometric analysis of spleen and tumour samples

Fluorophore (laser)	Marker	Concentration	Clone
FITC	GFP	N/A	N/A
PerCP-Cy5.5	7-AAD	1:50	N/A
PE	CD8	1:200	53-6.7*
PE-Cy7	CD45	1:200	30-F11*
APC	CD3	1:200	17A2*
BV421	PD-1	1:200	29F.1A12†
BV650	CD44	1:200	IM7†
AF700	CD4	1:200	GK1.5*
BV786	CD62L	1:200	MEL-14‡

N/A – not applicable

*eBioscience, ThermoFisher, UK

†BioLegend, UK

‡BD Biosciences, UK

Table M.7 – Regulatory T lymphocyte panel for flow cytometric analysis of spleen and tumour samples

Fluorophore (laser)	Marker	Concentration	Clone
FITC	GFP	N/A	N/A
PerCP-Cy5.5	7-AAD	1:50	N/A
APC	FOXP3	1:200	FKJ-16s*
BV421	CD45	1:200	30-F11†
BV650	CD25	1:200	PC61‡
AF700	CD4	1:200	GK1.5*

N/A – not applicable

*eBioscience, ThermoFisher, UK

†BioLegend, UK

‡BD Biosciences, UK

Table M.8 – Myeloid cell panel for flow cytometric analysis of spleen and tumour samples

Fluorophore (laser)	Marker	Concentration	Clone
FITC	GFP	N/A	N/A
PerCP-Cy5.5	7-AAD	1:50	N/A
PE	Ly6G	1:200	1A8†
PE-Cy7	CD11b	1:200	M1/70*
APC	Ly6C	1:200	HK1.4†
APC-Cy7	MHC-II	1:200	M5/114.15.2†
BV421	F4/80	1:200	BM8†
BV 605	CD11c	1:200	N418†
BV 711	CD206	1:200	C068C2†

N/A – not applicable

*eBioscience, ThermoFisher, UK

†BioLegend, UK

Table M.9 – Lymphocyte and myeloid cell panel for flow cytometric analysis of peripheral blood

Fluorophore (laser)	Marker	Concentration	Clone
FITC	GFP	N/A	N/A
PerCP-Cy5.5	7-AAD	1:50	N/A
PE	CD3	1:200	17A2*
PE-Cy7	CD11b	1:200	M1/70*
APC	Gr-1	1:200	RB6-8C5*
APC-Cy7	B220	1:200	RA3-6B2†
BV421	CD45	1:200	30-F11†

N/A – not applicable

*eBioscience, ThermoFisher, UK

†BioLegend, UK

Table M.10 – Lymphocyte differentiation panel for flow cytometric analysis of peripheral blood

Fluorophore (laser)	Marker	Concentration	Clone
FITC	GFP	N/A	N/A
PerCP-Cy5.5	7-AAD	1:50	N/A
PE	CD62L	1:200	MEL-14‡
PE-Cy7	CD44	1:200	IM7†
APC	CD8	1:200	53-6.7*
APC-Cy7	CD3	1:200	17A2†
BV421	CD4	1:200	GK1.5†
BV650	CD25	1:200	PC61‡

N/A – not applicable

*eBioscience, ThermoFisher, UK

†BioLegend, UK

‡BD Biosciences, UK

Sample analysis

Cells (to a total of 5 x 10^4-1 x 10^5 live events per sample) were detected using a BD LSRFortessa™ flow cytometer and analysed using BD FACSDiva™ and FlowJo® software (all from BD Biosciences, UK). Gating strategies to analyse populations are depicted in **Appendix 10**.

Statistical analyses

Prior to statistical analysis, all data were subject to normality testing. The mean values of two groups were analysed by either t-test (if data were normally distributed; unpaired if each subject was measured only once or paired if each subject was measured twice) or Mann-Whitney test (if data were not normally distributed and each subject was measured only once). When analysing flow cytometry data, the P values derived by unpaired t-test were adjusted for multiple comparisons. The mean values of more than two groups were analysed either by analysis of variance (ANOVA) (if data were normally distributed and each subject was measured only once), ANOVA with repeated measures (if data were normally distributed and each subject was measured more than once), Kruskal-Wallis test (if data were not normally distributed and each subject was measured only once) or Friedman test (if data were not normally distributed and each subject was measured more than once) with either Tukey's or Dunn's multiple comparisons test applied to compare each group. A mixed-effects analysis was performed instead of an ANOVA with repeated measures when there were missing values in time course experiments. The relationship between two sets of continuous data were analysed by either Pearson correlation (if data were normally distributed) or Spearman's rank correlation (if data were not normally distributed). When appropriate, the agreement between two quantitative measurements was assessed by Bland-Altman analysis. P values of less than 0.05 were considered statistically significant. All statistical analyses were conducted using GraphPad Prism version 8 (GraphPad Software, USA).

Chapter 1

Chapter aim

To validate a novel image analysis pipeline for immune cell counting in histological images and to utilise this to describe the distribution of tumour infiltrating leukocytes relative to areas of hypoxia in solid human tumours.

Introduction

For an anti-tumour immune response to be effective, it must be both of the appropriate specificity and its cellular components must be correctly positioned in order to effect cytotoxicity (as reviewed in [118]). A variety of approaches, such as flow and mass cytometry [230] and gene expression analysis [231, 232], can be used to interrogate a tumour's immune contexture. Whilst these techniques generate in-depth, multi-parametric datasets, they lack spatial resolution, a factor that is best assessed by histology. Whilst international consensus guidelines do exist to facilitate visual enumeration of tumour infiltrating leukocytes [233-235], these have not yet been adopted into routine practice. Furthermore, manual assessment is labour intensive, prone to inter- and intraobserver variation and cannot fully characterise the complex spatial distribution of these cells, a predicament which necessitates a transition from visual to digital assessment [236-238]. To date, computational attempts to quantify spatial distributions have included comparing immune cell densities at the tumour outer margin and inner core [239, 240] and applying established spatial statistics, such as those originally developed in the field of ecology, to immune cell locations [241-248]. Interestingly, such studies have suggested that the spatial distribution of tumour infiltrating leukocytes may reflect both their functional activity [249] and underlying tumour cell molecular aberrations [250, 251]. Nevertheless, the optimal method of assessing these distributions remains to be defined.

As such, further investigation into the best descriptors of the spatial distribution of leukocytes is merited.

The positioning of immune cells within the TME influences their access to oxygen and other nutrients. Therefore, in this chapter, I combine immunohistochemistry and digital image analysis to evaluate how pathophysiological levels of hypoxia relate to the spatial distribution of different leukocyte subsets within human tumours. Specifically, I compare the distributions observed in samples of pimonidazole-treated HNSCC with that observed in CCRCC with the aim of answering the following questions:

1. Are leukocyte subsets non-randomly (and differentially) distributed between hypoxic and non-hypoxic areas within solid tumours?
2. Are discernible patterns likely to be immunosuppressive (e.g. exclusion of effector cells from, and/or recruitment of immunosuppressive cells to, hypoxic areas)?
3. Are leukocyte distributions similar or different when comparing a tumour type in which neoplastic cell HIF-mediated responses are driven by localised microenvironmental hypoxia (HNSCC) as opposed to a tumour type in which neoplastic cell HIF-mediated responses are driven diffusely and constitutively by oncogenic mutation (CCRCC)?

Head and neck squamous cell carcinoma

Head and neck cancer constitutes 4.6% of new cancer cases globally (approximately 835000 cases per year) and is also responsible for 4.6% of annual cancer deaths worldwide (approximately 430000 deaths) [252]. HNSCC is an ideal tumour type to study in the first instance because increasing tumour hypoxia is an established negative prognostic factor [253-256], it is amongst the most highly immune-infiltrated cancer types [257] and is recognised to respond to immunotherapy [258-260].

Clear cell renal cell carcinoma

CCRCC, the commonest form of kidney cancer, may be either sporadic or inherited. In both forms, biallelic inactivation of *VHL* [261] leads to failure of proteasomal degradation of pVHL target proteins and stabilisation of HIFα [262, 263]. Thus, *VHL* null CCRCC tumour cells behave as if they are hypoxic, even when oxygen is available ('pseudohypoxia'). Subsequent activation of HIF-dependent pathways leads to increased expression of a range of target genes including *VEGF* (contributing to the angiogenic phenotype) [264, 265] and *CA IX* [266], which is a useful diagnostic immunohistochemical marker of CCRCC [267]. CCRCC is amongst the most highly immunogenic tumours [268, 269] and responds to ICB [270-272], although its immune contexture is highly heterogeneous [273].

The pseudohypoxic phenotype of CCRCC precludes the use of HIF or HIF-induced proteins as endogenous hypoxia markers. Loss of immunostaining for prolyl hydroxylated HIFα could theoretically be used to identify hypoxic tumour regions. However, in breast cancer spheroid and xenograft models, hydroxylated HIF1α extends to the perinecrotic border [274]. Whether this represents a true biological finding or simply reflects lack of reagent specificity is uncertain but, either way, this is unlikely to be a robust approach to the histological identification of tumour hypoxia in human samples. Consequently, in the absence of pimonidazole-treated samples, in this chapter oxygen levels are assumed to fall with increasing distance along a gradient from blood vessels to necrosis.

Semi-automated ImaGe analysis for HisTology data (SIGHT)

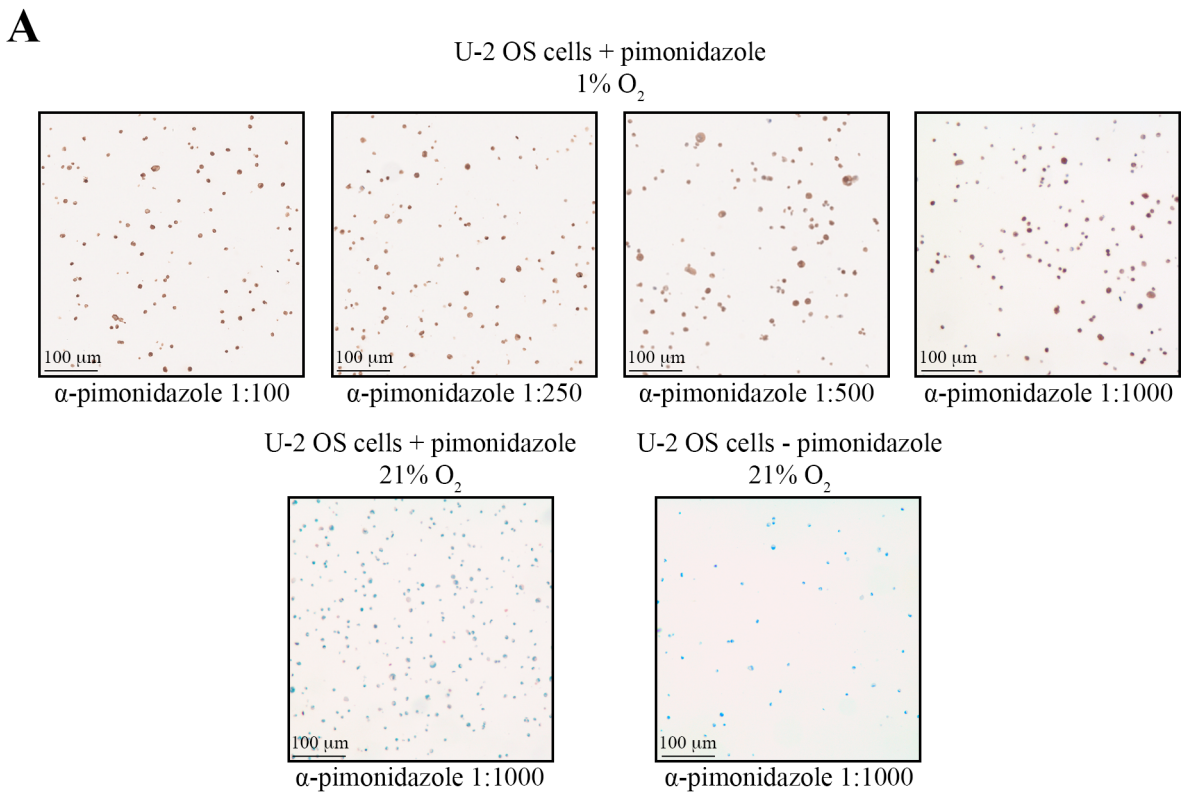
Widespread transition from manual to automated analysis of histology images requires open access to digital pathology software. In this thesis, I have validated and utilised Semi-automated ImaGe analysis for HisTology data (SIGHT), a novel image analysis pipeline

developed by Dr Joshua Bull and Professor Helen Byrne (Wolfson Centre for Mathematical Biology, University of Oxford) to facilitate application of spatial statistics to digital histology images (**Appendix 7**).

Results

Optimisation of pimonidazole immunohistochemistry

U2-OS human osteosarcoma cells were cultured under atmospheric oxygen (21% O_2) and hypoxia (1% O_2) for 16 hours, with pimonidazole added to culture medium for the final two hours. As expected, pimonidazole labelling was only detected in hypoxic cells. Lack of staining observed in cells cultured at atmospheric oxygen was similar to that seen in cells that did not receive pimonidazole (**Figure 1.1A**). Whilst the manufacturer's protocol recommends immunostaining with a primary antibody concentration of 1:50, and the most commonly used dilution in published literature being 1:100, positive signal was detectable at a primary antibody concentration of 1:1000. I next compared staining with 1:100 and 1:1000 primary antibody dilutions on consecutive sections taken from blocks of various human tissues (**Figure 1.1B**). Notably, in human placenta not treated with pimonidazole, background staining within the fibrous stroma of a stem villus was appreciably stronger at the higher concentration. When assessing pimonidazole-treated tumour samples, a concentration of 1:1000 provided clearer demarcation of the hypoxic boundary, with lower signal within tumour cells located at a distance from necrosis and within tumour stroma.


A
U-2 OS cells + pimonidazole
1% O2
100 µm
α-pimonidazole 1:100
100 µm
α-pimonidazole 1:250
100 µm
α-pimonidazole 1:500
100 µm
α-pimonidazole 1:1000
U-2 OS cells + pimonidazole
21% O2
100 µm
α-pimonidazole 1:1000
U-2 OS cells - pimonidazole
21% O2
100 µm
α-pimonidazole 1:1000

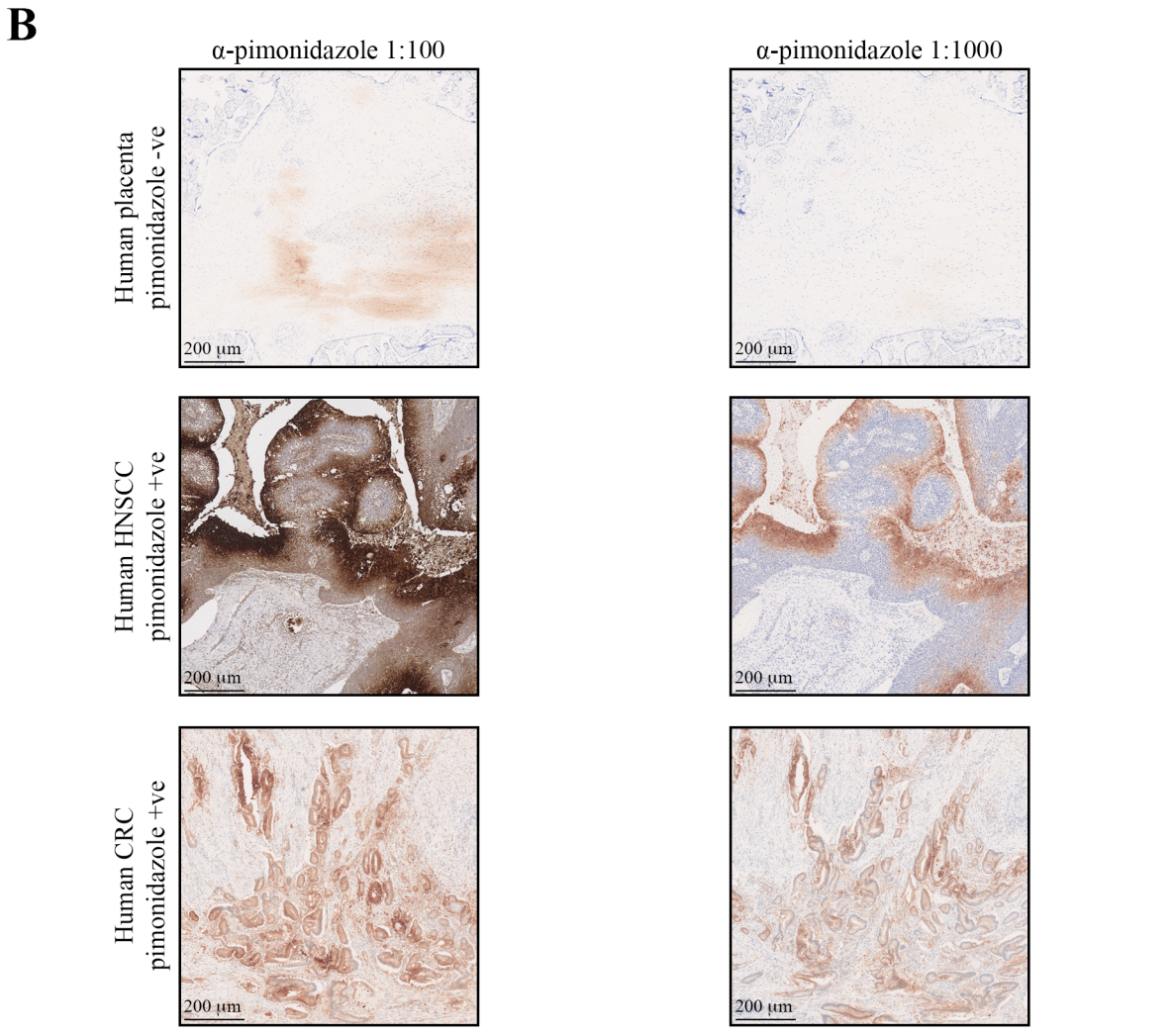

B
α-pimonidazole 1:100
α-pimonidazole 1:1000
Human placenta
pimonidazole -ve
200 µm
200 µm
Human HNSCC
pimonidazole +ve
200 µm
200 µm
Human CRC
pimonidazole +ve
200 µm
200 µm

Figure 1.1 – Optimisation of pimonidazole immunohistochemistry

(A) In vitro validation of pimonidazole immunocytochemistry of U2-OS human osteosarcoma cancer cells. Cells cultured under hypoxic conditions (1% O_2) and treated with pimonidazole show strong cytoplasmic positivity at a range of primary antibody dilutions. By contrast, pimonidazole-treated cells cultured under atmospheric oxygen (21% O_2) show no staining, in line with cells that were not treated with pimonidazole. (B) Comparison of immunohistochemical staining of human tissues using a primary antibody concentration of 1:100 and 1:1000 (from top to bottom: human placenta without pimonidazole treatment, pimonidazole-treated human head and neck squamous cell carcinoma [HNSCC] and colorectal cancer [CRC]).

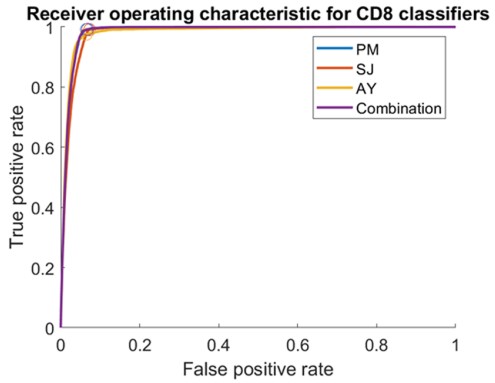
Validation of Semi-automated ImaGe analysis for HisTology data (SIGHT) image analysis pipeline

I next compared the performance of SIGHT to that of humans and other image analysis software in counting leukocytes within histological images. Throughout the validation process, I focused on $CD8^+$ T lymphocytes (cytoplasmic/membranous staining of small, round cells), $FOXP3^+$ T_{Reg} (nuclear staining) and $CD68^+$ macrophages (cytoplasmic/membranous staining of large, irregular cells) as exemplar staining patterns for other commonly used lymphoid and myeloid markers. To identify labelled cells within an image, an accurate classifier must first be trained. Classifiers were trained by three individuals from different professional backgrounds, all of whom were first time users of the software and have variable experience in histology (PM – me, a trainee histopathologist, SJ – a graduate-entry medical student with a doctorate in immunology and AY – a post-doctoral scientist). Training was performed by annotating regions of both positive and negative DAB staining in 4-6 representative images taken at random from HNSCC slides stained for the above markers. Classifiers were then applied to four different images from the same samples, in which I had manually annotated all areas of positive staining to create 'ground truth' data, and receiver operating characteristic (ROC) curves were generated to assess the sensitivity and specificity of each classifier across

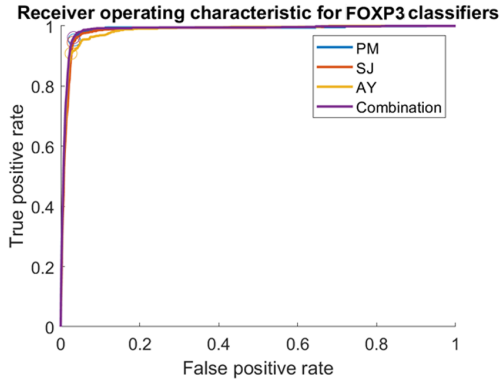
a range of different intensity thresholds for classifying a pixel as positively stained **(Figure 1.2A**). Each classifier performed well, with an area under the curve (AUC) of at least 0.96 (a score of 1 equates to perfect discrimination between positively and negatively stained pixels). Consequently, combining the training data provided by the three individuals did little to improve accuracy of classification. Overall, these results demonstrate that an accurate classifier can be trained quickly (typically 15-30 minutes) by users without significant previous experience of the software. Next, I compared manual and automated cell counting across forty 1.5 mm x 1.5 mm images randomly extracted from HNSCC slides stained for CD8, FOXP3 and CD68. Human intraobserver variation was assessed by counting the cells on two occasions separated by a 12-month washout period (all human counting was performed using the Cell Counter plugin in ImageJ). Repeat counts were highly concordant, with greatest variation in counting $CD68^+$ macrophages, probably due to the indistinct borders of these cells; by comparison, repeat counts using SIGHT were identical (**Figure 1.2B**). Importantly, whilst the mean time to count cells in a single image ranged between 145 and 230 seconds for the human (depending upon the marker analysed), SIGHT only took between 20 and 29 seconds to complete the same task. I then assessed how robust SIGHT counting was to changes in input image. CD8, FOXP3 and CD68 counts were near identical when the same input images were analysed at 0°, 90°, 180° and 270° of rotation (**Figure 1.2C**) with slight differences arising from the superpixellation step. The extent of human interobserver variation was assessed by asking three pathologists to count the number of cells in each of the three sets of 40 images at a single time point. SIGHT counts for each marker largely overlapped with the range of human counts to an extent that was comparable, if not superior, to the overlap observed with counts generated by algorithms developed by local experts in ImageJ and Visiopharm (a commercially available image analysis software) (**Figure 1.2D**). In general, SIGHT counts overlapped with the upper range of human counts. Consequently, whilst comparison of SIGHT counts with the

mean human counts for each image demonstrated strong positive correlations, SIGHT counts tended to be higher (**Figure 1.2E**).

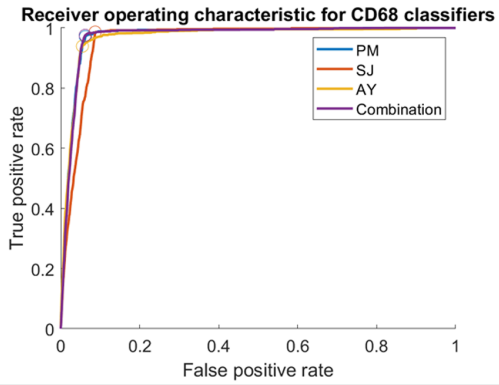
A



AUC
PM - 0.9844
SJ - 0.9804
AY - 0.9821
Combination - 0.9840



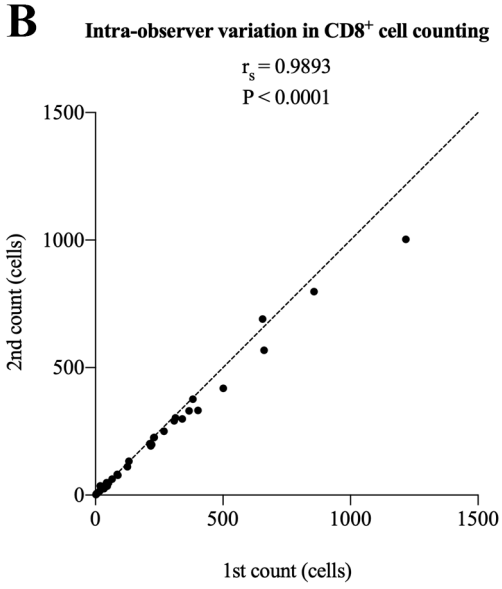
AUC
PM - 0.9857
SJ - 0.9835
AY - 0.9829
Combination - 0.9867

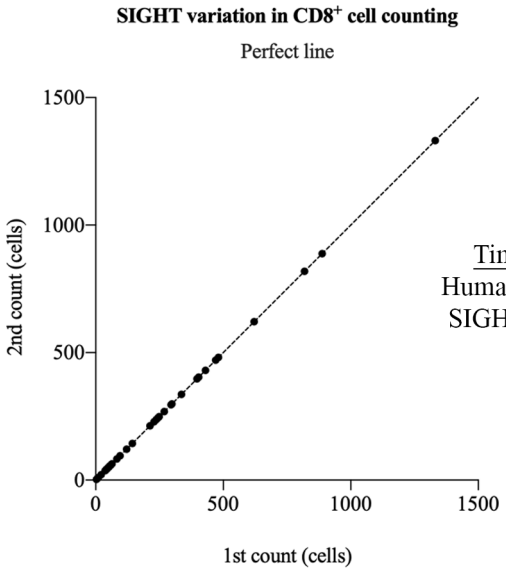


AUC
PM - 0.9728
SJ - 0.9605
AY - 0.9696
Combination - 0.9717

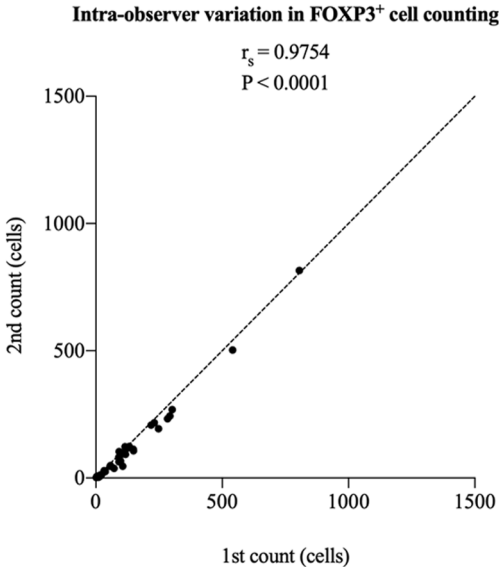
Proportion of annotated superpixels (SP) utilised as support vectors (SV) during image classification				
Classifier / Marker	**PM**	**SJ**	**AY**	**Combined**
CD8	7951 SP → 327 SV (4.1%)	2074 SP → 219 SV (10.6%)	1580 SP → 221 SV (14.0%)	11605 SP → 602 SV (5.2%)
FOXP3	8694 SP → 303 SV (3.5%)	1877 SP → 221 SV (11.8%)	787 SP → 213 SV (27.1%)	11358 SP → 607 SV (5.3%)
CD68	2345 SP → 218 SV (9.3%)	1145 SP → 185 SV (16.2%)	683 SP → 166 SV (24.3%)	4173 SP → 383 SV (9.2%)

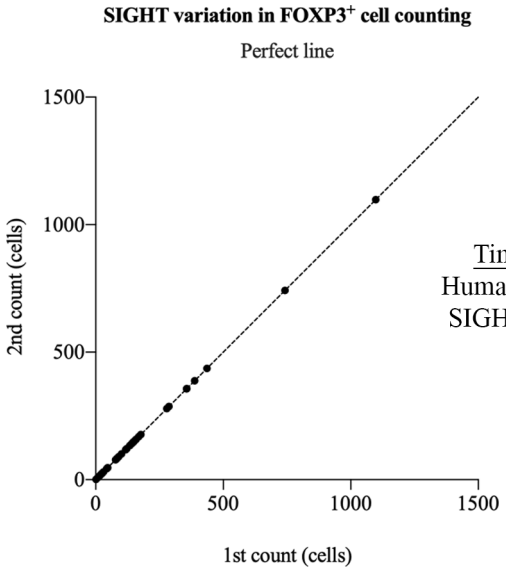
B



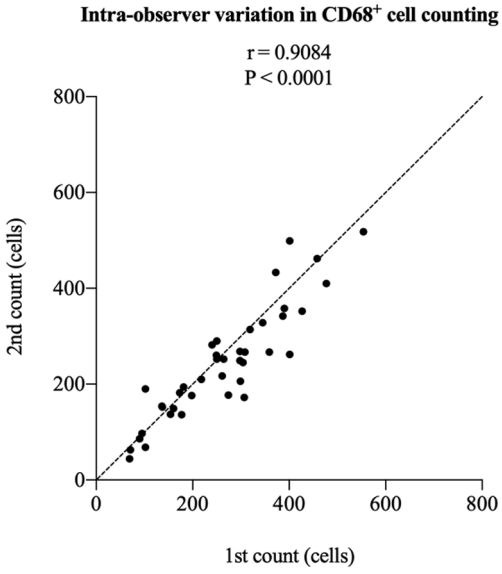


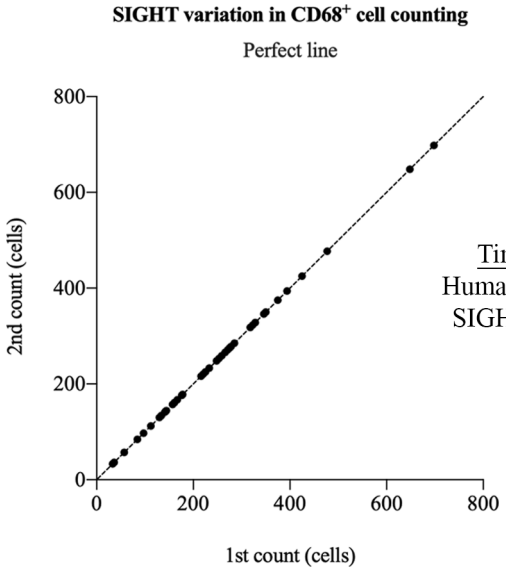
Time per image
Human - 166 seconds
SIGHT - 29 seconds





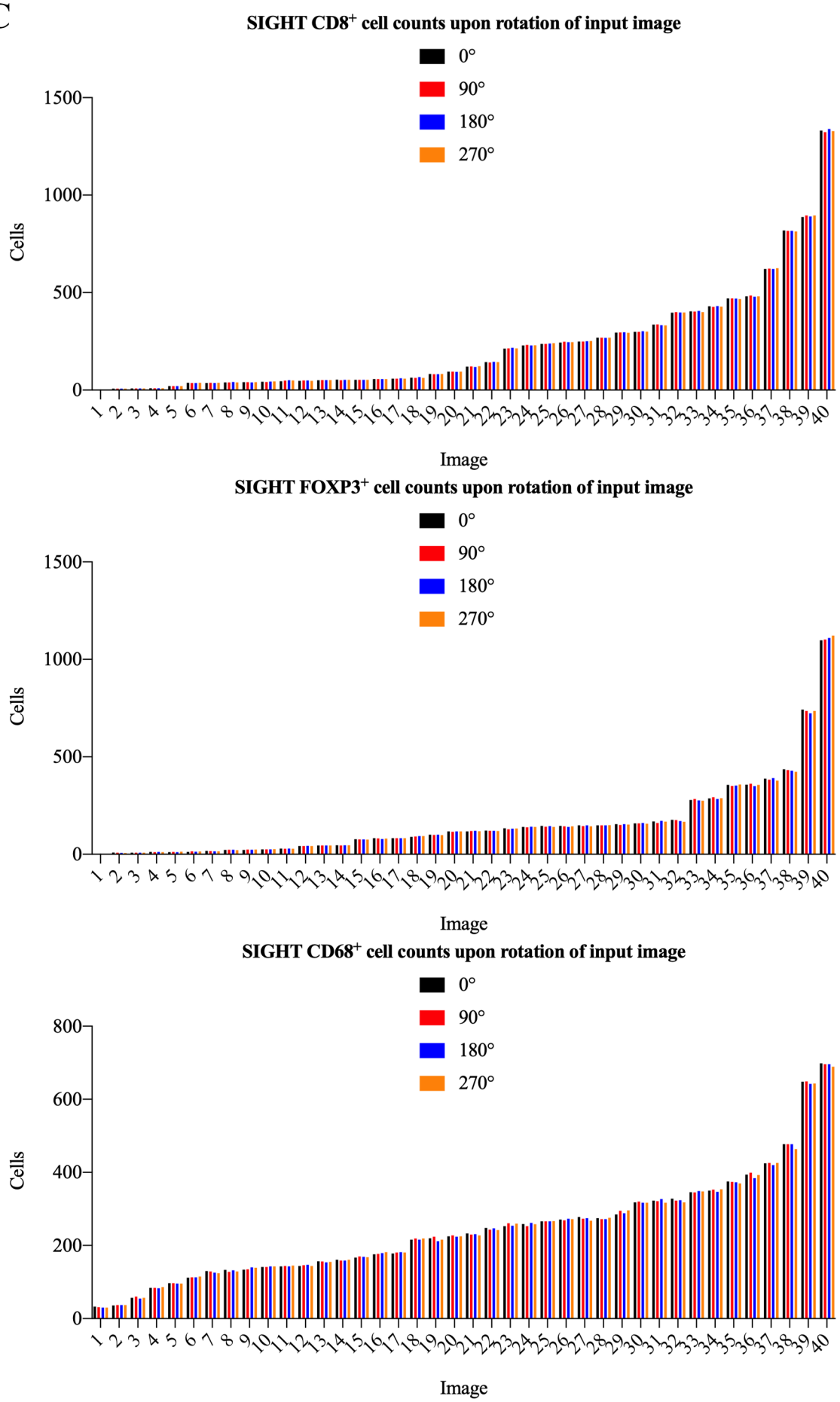
Time per image
Human - 145 seconds
SIGHT - 20 seconds



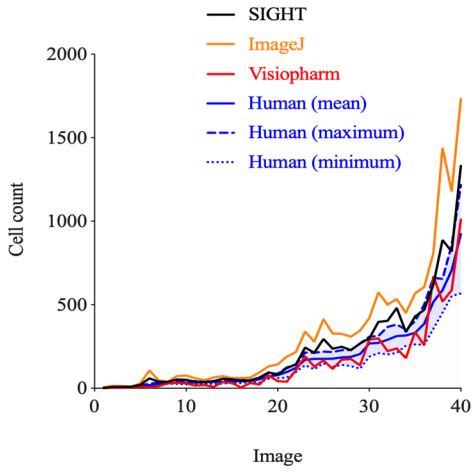


Time per image
Human - 230 seconds
SIGHT - 29 seconds

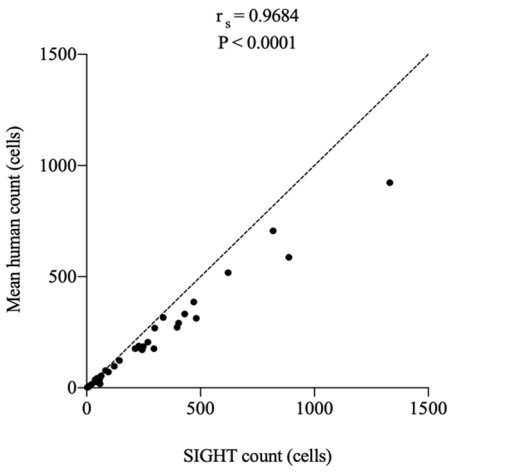
C

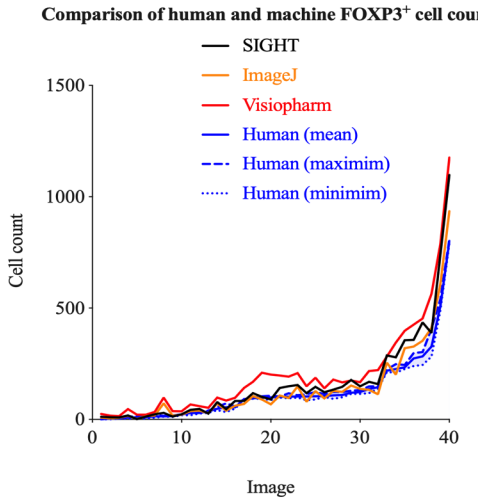

SIGHT CD8+ cell counts upon rotation of input image
0°
90°
180°
270°
Cells
1500
1000
500
0
Image
SIGHT FOXP3+ cell counts upon rotation of input image
0°
90°
180°
270°
Cells
1500
1000
500
0
Image
SIGHT CD68+ cell counts upon rotation of input image
0°
90°
180°
270°
Cells
800
600
400
200
0
Image

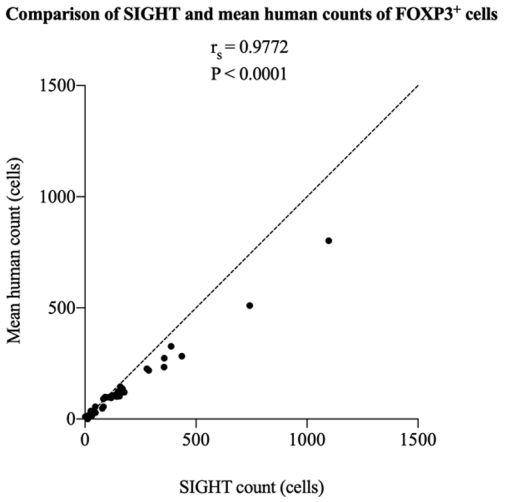
D

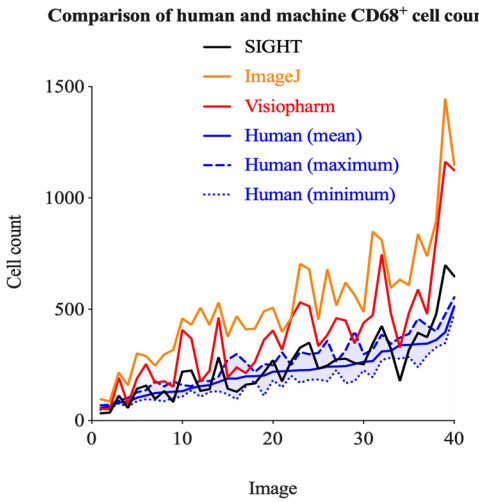

Comparison of human and machine CD8+ cell counts
SIGHT
ImageJ
Visiopharm
Human (mean)
Human (maximum)
Human (minimum)
Cell count
Image

E


Comparison of SIGHT and mean human counts of CD8+ cells
rs = 0.9684
P < 0.0001
Mean human count (cells)
SIGHT count (cells)


Comparison of human and machine FOXP3+ cell counts
SIGHT
ImageJ
Visiopharm
Human (mean)
Human (maximim)
Human (minimim)
Cell count
Image


Comparison of SIGHT and mean human counts of FOXP3+ cells
rs = 0.9772
P < 0.0001
Mean human count (cells)
SIGHT count (cells)


Comparison of human and machine CD68+ cell counts
SIGHT
ImageJ
Visiopharm
Human (mean)
Human (maximum)
Human (minimum)
Cell count
Image

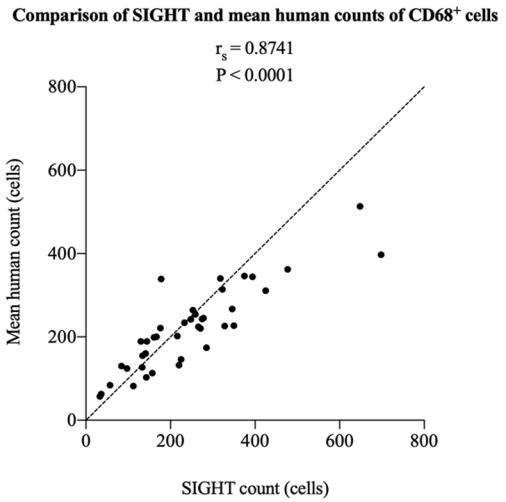

Comparison of SIGHT and mean human counts of CD68+ cells
rs = 0.8741
P < 0.0001
Mean human count (cells)
SIGHT count (cells)

Figure 1.2 – Validation of Semi-automated ImaGe analysis for HisTology data (SIGHT) image analysis pipeline

(A) Receiver operating characteristic (ROC) curves and associated area under the curve (AUC) for CD8, FOXP3 and CD68 classifiers trained by three first-time SIGHT users. The table outlines how many superpixels were annotated during the training of each classifier and what proportion of these contribute to actual classification. (B) Comparison of intraobserver variation in cell counting undertaken by a human and by SIGHT. (C) Effects of rotation of input image on cell counts returned by SIGHT. (D) Comparison of SIGHT, ImageJ and Visiopharm cell counts with counts returned by three pathologists. (E) Correlation between SIGHT cell counts and mean human cell counts. In each scatter (XY) plot, the dashed diagonal line represents the line of equality. Data presented are the Pearson correlation coefficient (r) or Spearman's rank correlation coefficient (r_s) and associated P value.

Analysis of the spatial distribution of tumour infiltrating leukocytes relative to areas of hypoxia in head and neck squamous cell carcinoma

Quantitation and correlation of hypoxia markers

Given concerns about the robustness of endogenous hypoxia markers (**Appendix 1**), I identified a cohort of 16 cases of HNSCC from patients that received the exogenous hypoxia marker pimonidazole as part of a study validating a hypoxia gene expression signature [224]. A representative block of each tumour was selected for analysis and strict serial sections were cut and immunohistochemically stained for CD4, FOXP3, CD8, CD19, CD68, pancytokeratin, pimonidazole and the endogenous hypoxia marker CA IX. The serial sections were stained in a specific order, so that contiguous sections could be overlaid and merged into a single, 'virtually multi-labelled' image (as has been done previously to profile the TME in HNSCC [275]). Each triplet contained an immune cell marker, pancytokeratin and pimonidazole. When possible, a fourth section labelled for CA IX was also included (the number of sections analysed, and the order of their staining, depended upon the amount of tissue available within each block). Subsequently, as many non-overlapping 1.5 mm x 1.5 mm regions of interest

(ROI) as possible were extracted, manually aligned to the corresponding regions on adjacent slides, merged and cropped to a final composite output image. The number of ROI analysed for each tumour varied from 2 to 92 depending upon the size of the tumour (for patient and tumour characteristics, details of immunohistochemistry and image analysis pipeline see **Appendix 2**).

The proportions of pimonidazole and CA IX staining, as well as manually annotated areas of necrosis, were calculated for each ROI from a given tumour, which were then pooled to provide overall values (**Table 1.1**). In keeping with previous studies, the findings are reported as a 'hypoxic fraction', defined as the hypoxia marker positive surface area divided by the total tumour surface area (including both epithelial and stromal components) [276].

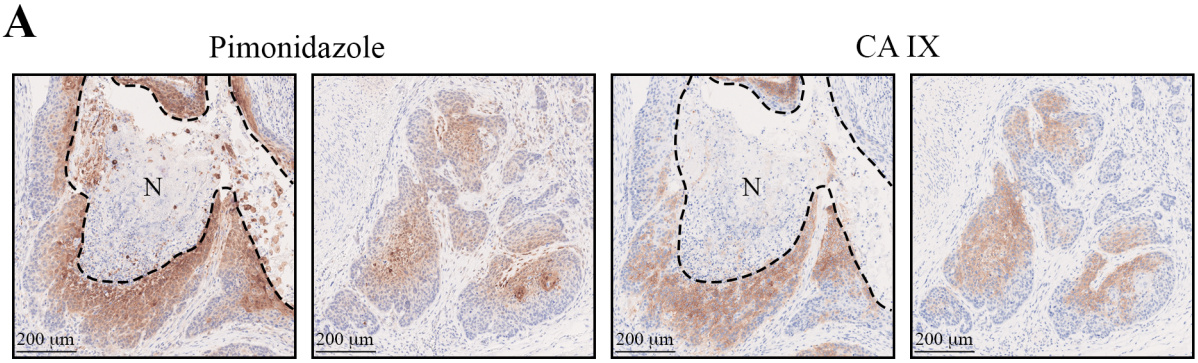
Table 1.1 – Quantification of hypoxia markers in head and neck squamous cell carcinoma cohort

Patient identification	Pimonidazole hypoxic fraction (%)	CA IX hypoxic fraction (%)	Necrosis (%)
#1	5.8	15.4	6.0
#2	1.6	1.7	1.6
#3	1.1	0.4	0.0
#4	4.7	2.0	3.9
#5	2.1	0.6	0.1
#6	14.2	14.5	0.0
#7	3.8	3.0	0.0
#8	3.5	24.6	0.9
#9	9.3	12.9	3.9

#10	2.2	1.0	8.8
#11	2.0	6.3	0.2
#12	13.3	22.8	6.3
#13	8.1	1.6	0.8
#14	6.6	8.0	1.6
#15	1.8	0.1	0.2
#16	2.2	13.6	5.8
Mean	**5.1**	**8.0**	**2.5**
Median	**3.6**	**4.7**	**1.2**
Range	**1.1-14.2**	**0.1-24.6**	**0.0-8.8**
CA IX – carbonic anhydrase 9			

Notably, there was considerable inter- and intratumour variation in the extent of both pimonidazole and CA IX staining. Staining was often observed for both markers in the region immediately adjacent to an area of necrosis but hypoxia without associated necrosis was also apparent (although how this relates to the presence of necrosis in a third dimension is uncertain) (**Figure 1.3A**). Next, I cross-correlated the extent of pimonidazole labelling, CA IX expression and necrosis (**Figure 1.3B**). Moderate positive correlations were observed between pimonidazole and CA IX expression ($r_s = 0.6240$ on a per tumour basis and $r_s = 0.6325$ on a per region basis). However, there were only weak positive correlations between the extent of pimonidazole labelling or CA IX expression and tumour necrosis on a per region basis, largely due to the existence of areas of tumour hypoxia with little/no associated necrosis within the plane of section.

A


Pimonidazole
CA IX
N
N
200 µm
200 µm
200 µm
200 µm

B

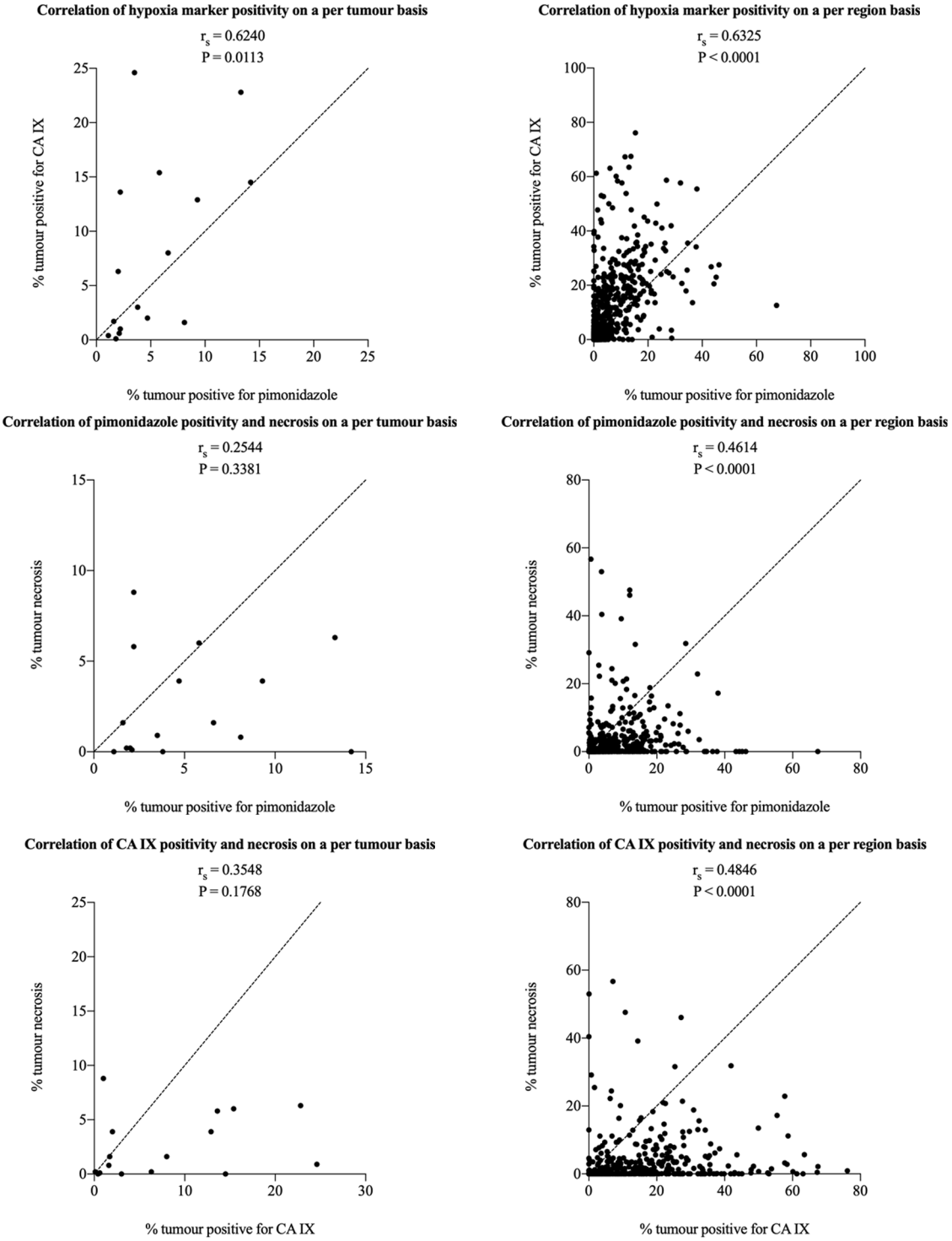

Correlation of hypoxia marker positivity on a per tumour basis
$r_s = 0.6240$
P = 0.0113
% tumour positive for CA IX
% tumour positive for pimonidazole
Correlation of hypoxia marker positivity on a per region basis
$r_s = 0.6325$
P < 0.0001
% tumour positive for CA IX
% tumour positive for pimonidazole
Correlation of pimonidazole positivity and necrosis on a per tumour basis
$r_s = 0.2544$
P = 0.3381
% tumour necrosis
% tumour positive for pimonidazole
Correlation of pimonidazole positivity and necrosis on a per region basis
$r_s = 0.4614$
P < 0.0001
% tumour necrosis
% tumour positive for pimonidazole
Correlation of CA IX positivity and necrosis on a per tumour basis
$r_s = 0.3548$
P = 0.1768
% tumour necrosis
% tumour positive for CA IX
Correlation of CA IX positivity and necrosis on a per region basis
$r_s = 0.4846$
P < 0.0001
% tumour necrosis
% tumour positive for CA IX

Figure 1.3 – Correlation of markers of hypoxia in head and neck squamous cell carcinoma cohort

(A) Exemplar histological images demonstrating comparable patterns of pimonidazole labelling and carbonic anhydrase 9 (CA IX) expression both in relation to, and not in relation to, necrosis (N). (B) Cross-correlation of proportion of tumour area showing pimonidazole labelling, CA IX expression and necrosis in this cohort of 16 head and neck squamous cell carcinoma specimens. In each scatter (XY) plot, the dashed diagonal line represents the line of equality. Data presented are the Spearman's rank correlation coefficient (r_s) and associated P value.

Analysis of the association between tumour hypoxia and immune cell infiltration

Initially, I evaluated whether global tumour hypoxia was associated with immune cell infiltration. However, there was no correlation between the overall extent of pimonidazole labelling and overall density of $CD8^+$, $FOXP3^+$ or $CD68^+$ cells (**Figure 1.4A**). These findings suggest that tumour hypoxia is not a dominant determinant of immune cell infiltration in HNSCC, although statistically significant trends might emerge following analysis of more samples. However, when analysed on a per region basis, there were weak negative correlations between the extent of pimonidazole labelling and microregional density of each immune cell type, suggesting that all three cell types are less abundant in increasingly hypoxic tumour regions (**Figure 1.4B**).

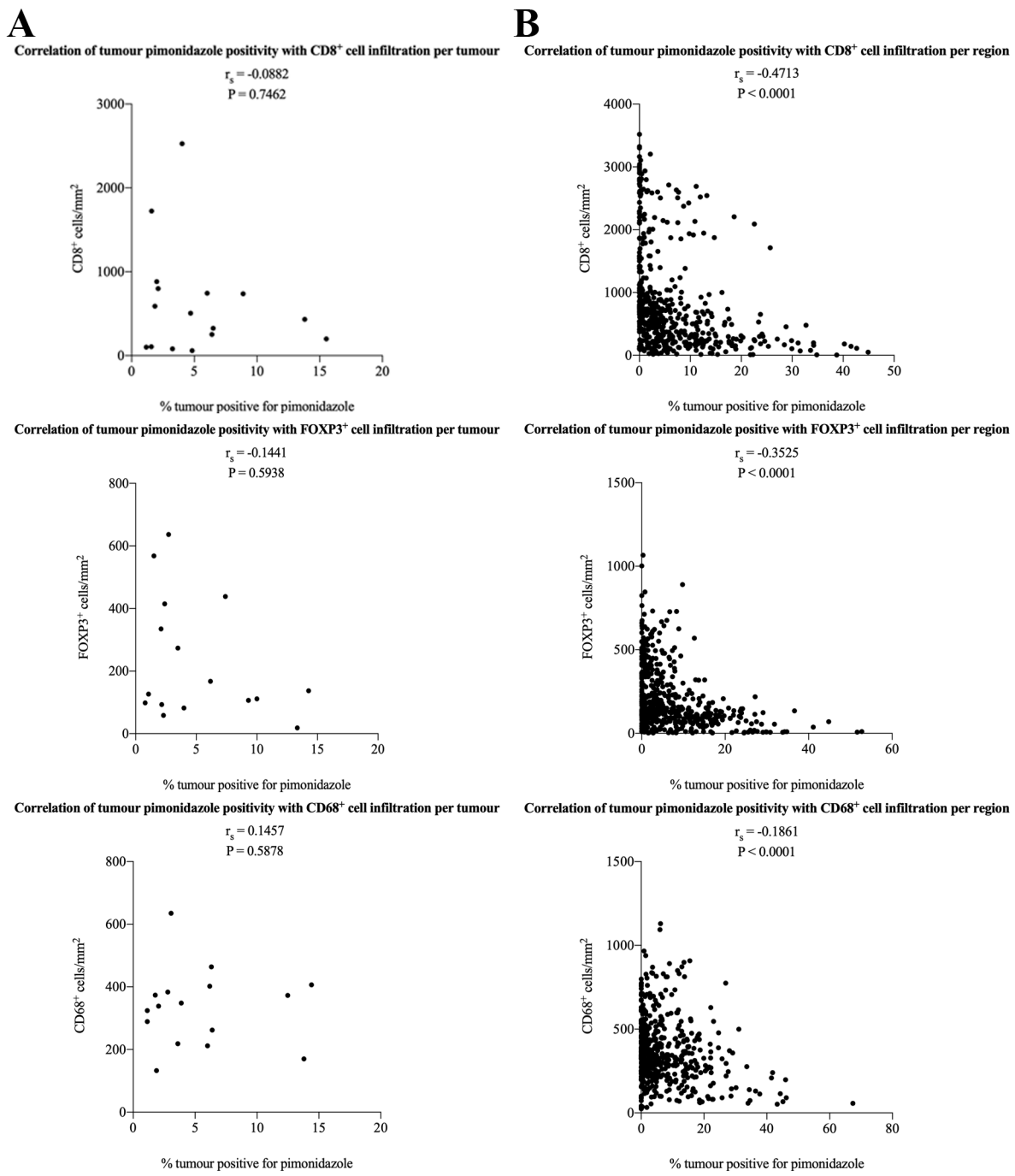


Figure 1.4 – Correlation between tumour hypoxia and immune cell infiltration in head and neck squamous cell carcinoma cohort

(A) Correlation between pimonidazole labelling and immune cell density on a per tumour basis. (B) Correlation between pimonidazole labelling and immune cell density on a per region basis. Data presented are the Spearman's rank correlation coefficient (r_S) and associated P value.

Analysis of the association between tumour hypoxia and immune cell spatial distribution

I subsequently assessed whether these immune cell subsets were distributed differentially between tumour regions that labelled positive for pimonidazole and those that did not. Each type of immune cell was most abundant within the tumour stroma, and, in keeping with the correlations presented above, there were fewer of each of these cells within regions of tumour cell nests that contain pimonidazole adducts as compared to those that did not (**Figure 1.5A**). Interestingly, whilst this decrease in immune cell density was consistent across each tumour for $CD8^+$ and $FOXP3^+$ cells, an increase in $CD68^+$ cells in pimonidazole labelled areas was observed in 3/16 tumours, suggesting that under certain circumstances, macrophages are more able to localise within hypoxic tumour regions than the two T lymphocyte subsets (**Figure 1.5B**). The quantitative results for $CD8^+$ and $FOXP3^+$ cells were in keeping with qualitative observations that cells expressing these markers were predominantly clustered within the stroma at the edge of tumour cells nests with limited penetration towards the centre of these nests; they were rarely observed in perinecrotic/necrotic regions. By comparison, $CD68^+$ cells were more diffusely distributed including within perinecrotic/necrotic regions. These observations are illustrated by an example from one tumour in which a region of necrosis with adjacent perinecrotic pimonidazole labelling is devoid of $CD8^+$ and $FOXP3^+$ cells but does contain $CD68^+$ cells (**Figure 1.5C**).

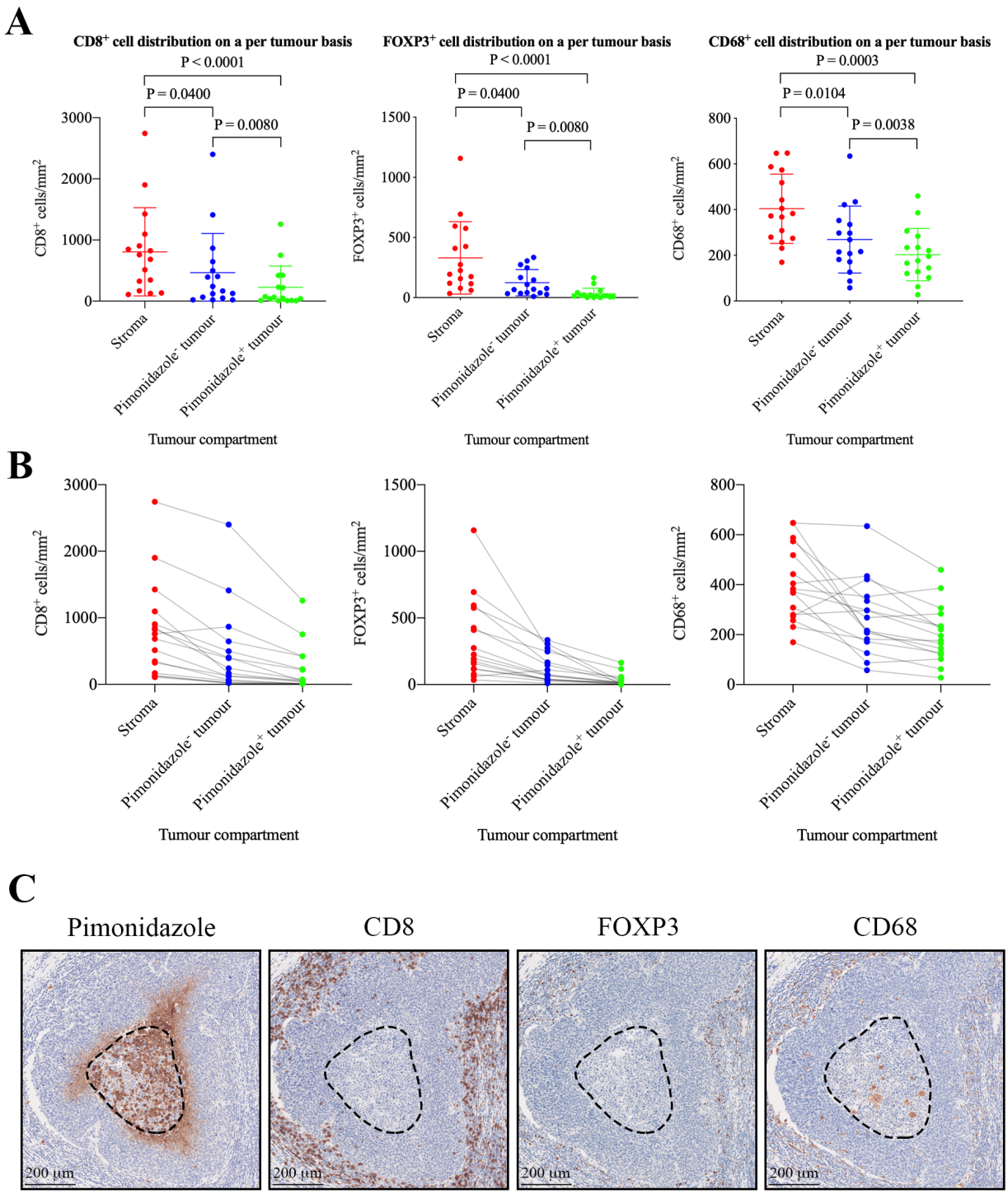


Figure 1.5 – Analysis of immune cell spatial distribution with respect to regions of tumour hypoxia in head and neck squamous cell carcinoma cohort

(A) Comparison of densities of CD8$^+$, FOXP3$^+$ and CD68$^+$ cells in different tumour compartments. Statistical analyses for CD8 and FOXP3 datasets conducted by Friedman test with Dunn's multiple comparisons test. CD68 dataset analysed by repeated measures analysis of variance (ANOVA) with Tukey's multiple comparisons test. (B) Illustration of trends for

each tumour corresponding to the densities presented in (A). (C) Representative histological images demonstrating the presence of $CD68^+$, but not $CD8^+$ or $FOXP3^+$, cells within a tumour region labelled by pimonidazole (necrosis outlined by dashed lines).

Given the discrepancy between my initial qualitative observation of diffuse $CD68^+$ cell distribution and the quantitative analysis demonstrating overall reduction in their numbers in hypoxic tumour regions, I re-evaluated their locations more closely and was able to identify tumour regions labelled with pimonidazole that contained virtually no $CD68^+$ cells (**Figure 1.6A**). By comparison, regions of necrosis always contained $CD68^+$ cells, admixed with cells with morphological features of neutrophils. However, necrotic foci frequently displayed tissue distortion with loss of their cellular contents, precluding accurate quantification of cells within these regions (**Figure 1.6B**). It is possible that inclusion of these foci within the tumour region defined as 'hypoxic' would increase macrophage densities above tumour regions not labelled with pimonidazole.

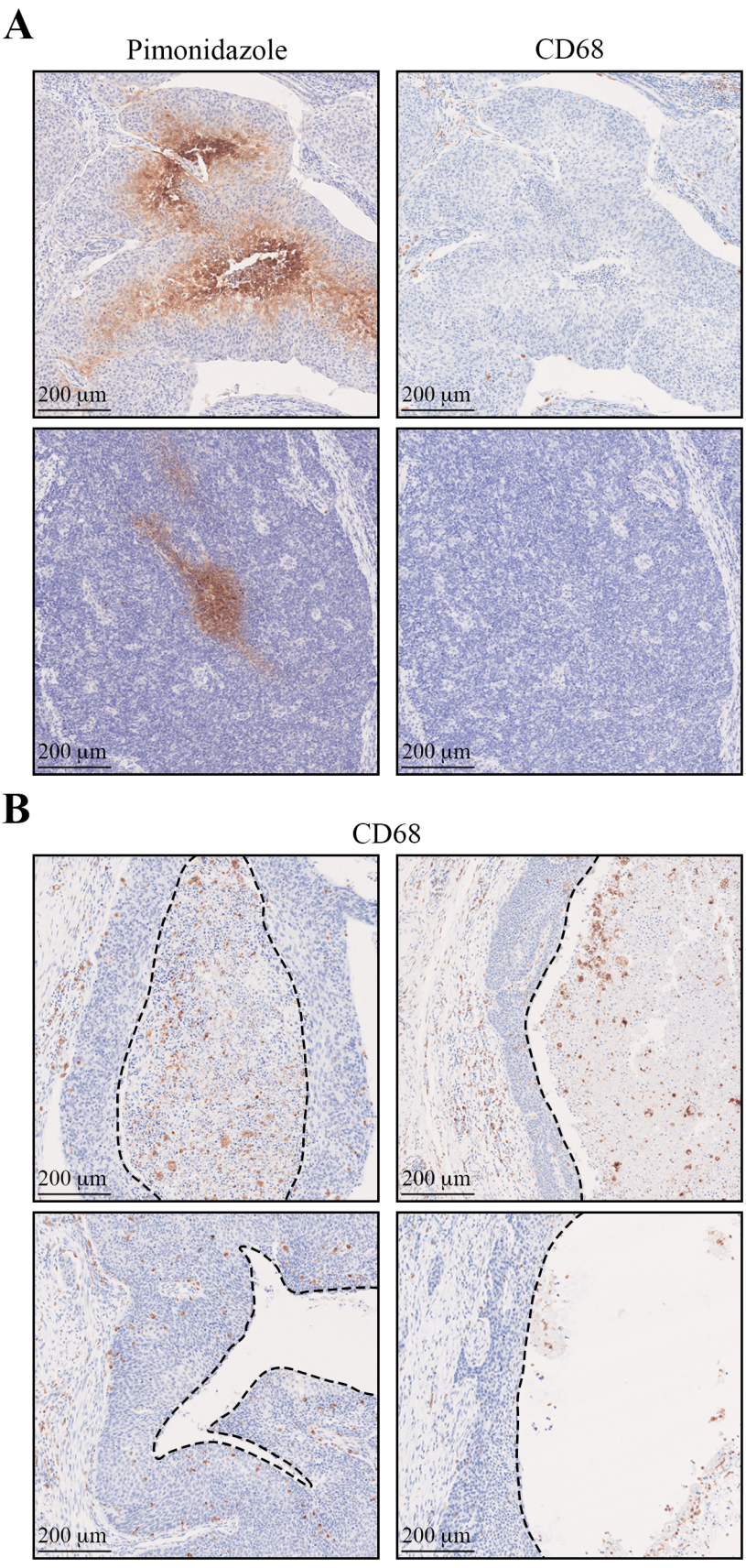

A
Pimonidazole
CD68
200 μm
200 μm
200 μm
200 μm
B
CD68
200 μm
200 μm
200 μm
200 μm

Figure 1.6 – Qualitative analysis of CD68$^+$ cell distribution with respect to regions of tumour hypoxia in head and neck squamous cell carcinoma cohort

(A) Examples of pimonidazole labelled regions from two tumours that are devoid of CD68$^+$ cells. (B) Regions of necrosis (outlined by dashed lines) contain CD68$^+$ cells admixed with polymorphonuclear cells that resemble neutrophils (upper panels). However, tissue retraction within necrotic regions precludes accurate assessment of their cellular contents.

Finally, I analysed the effects of tumour hypoxia on the ratios of the three immune cell subsets within different oxygen environments (**Figure 1.7**). Whilst there were no statistically significant differences between the CD8$^+$:FOXP3$^+$ cell ratios in any of the three compartments, progressive decreases in both the CD8$^+$:CD68$^+$ and FOXP3$^+$:CD68$^+$ cell ratios were observed when moving from more to less oxygenated tumour regions. These findings are in keeping with the qualitative observation that macrophages are more diffusely distributed throughout tumours than both CD8$^+$ and FOXP3$^+$ T lymphocytes.

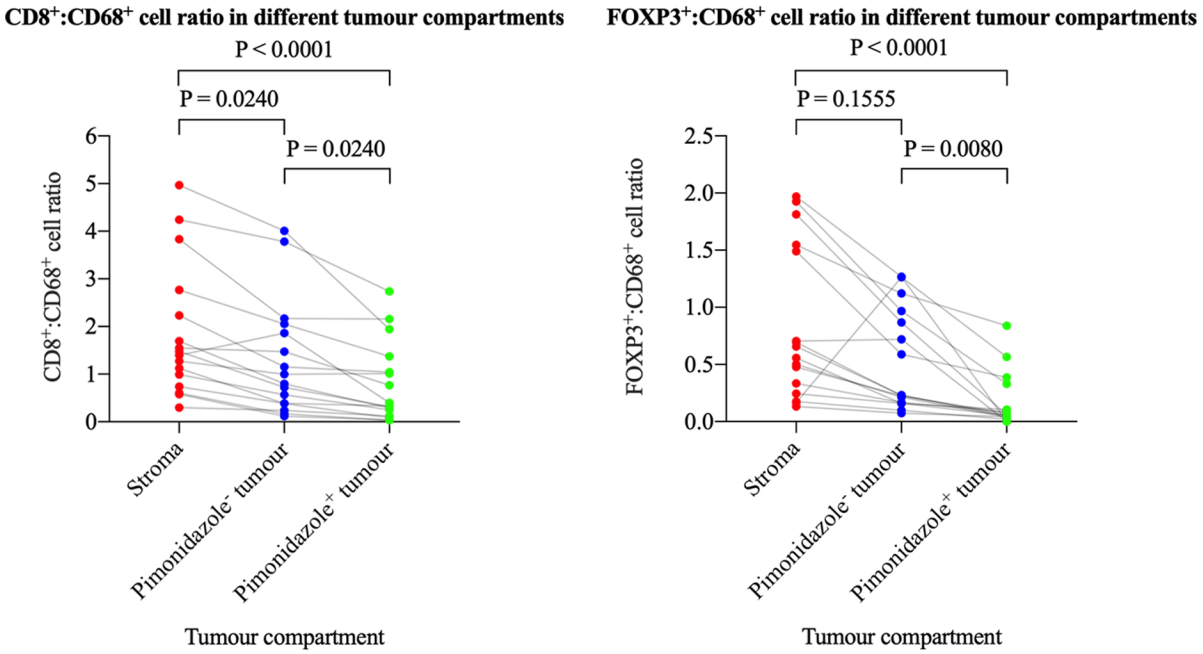


Figure 1.7 – Analysis of T lymphocyte to macrophage ratios with respect to regions of tumour hypoxia in head and neck squamous cell carcinoma cohort

Comparison of $CD8^+$:$CD68^+$ and $FOXP3^+$:$CD68^+$ cell ratios in different tumour compartments. All statistical analyses conducted by Friedman test with Dunn's multiple comparisons test.

Unfortunately, despite using reagents and protocols utilised in diagnostic practice, variability in the intensity of CD4 and CD19 immunostaining precluded quantitative analysis of these markers. Qualitative analysis (**Figure 1.8**) revealed that $CD19^+$ cell distribution demonstrated tight restriction to tumour stroma, often located within tertiary lymphoid structures, with less infiltration into tumour cell nests as compared to $CD8^+$ T lymphocytes. $CD4^+$ cells were also most abundant within tumour stroma but patchy background staining, as reported by others [277], prevented accurate analysis of their distribution within tumour cell nests.

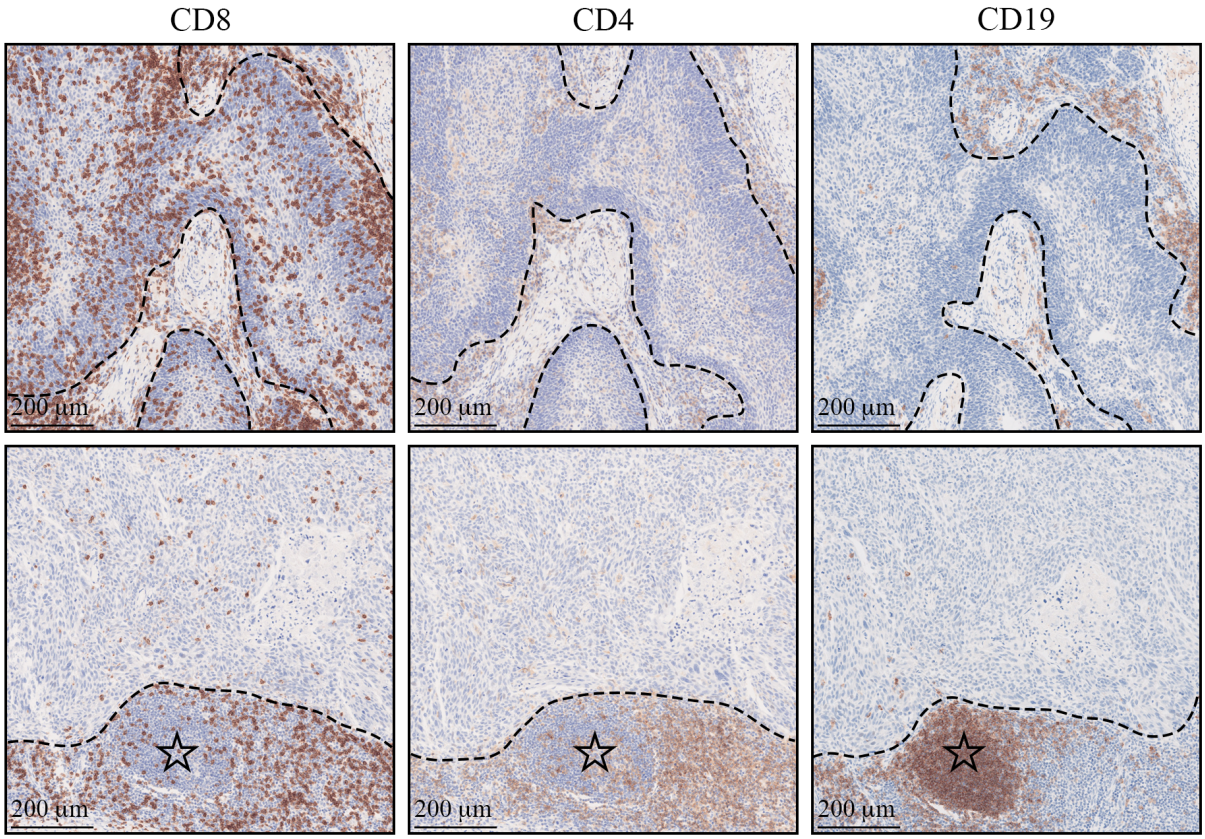


Figure 1.8 – Qualitative analysis of $CD4^+$ and $CD19^+$ cell distributions in head and neck squamous cell carcinoma cohort

Exemplar images from two tumours demonstrating that $CD19^+$ cells are more restricted to stromal regions (outlined by dashed lines) than $CD8^+$ cells. $CD4^+$ cells are also predominantly located within stroma but weak signal, coupled with patchy background staining, precludes accurate analysis of their distribution within tumour cell nests. In the second tumour (lower panel), a tertiary lymphoid structure is present (identified with a star). These ectopic lymphoid organs are composed of a central B lymphocyte follicle surrounded by a T lymphocyte-rich zone which also contains mature dendritic cells. In general, the presence of tertiary lymphoid structures within a tumour portends a more favourable prognosis (as reviewed in [278]).

Analysis of the spatial distribution of tumour infiltrating leukocytes relative to areas of hypoxia in clear cell renal cell carcinoma

Next, I analysed the spatial distribution of leukocytes relative to presumed oxygen gradients in 16 CCRCC samples selected for the presence of tumour necrosis (for patient and tumour

characteristics see **Appendix 3**). Immunohistochemical staining for CA IX demonstrated diffuse expression in all tumours, confirming the presence of a 'pseudohypoxic' phenotype and acting as a surrogate for *VHL* loss (**Figure 1.9**).

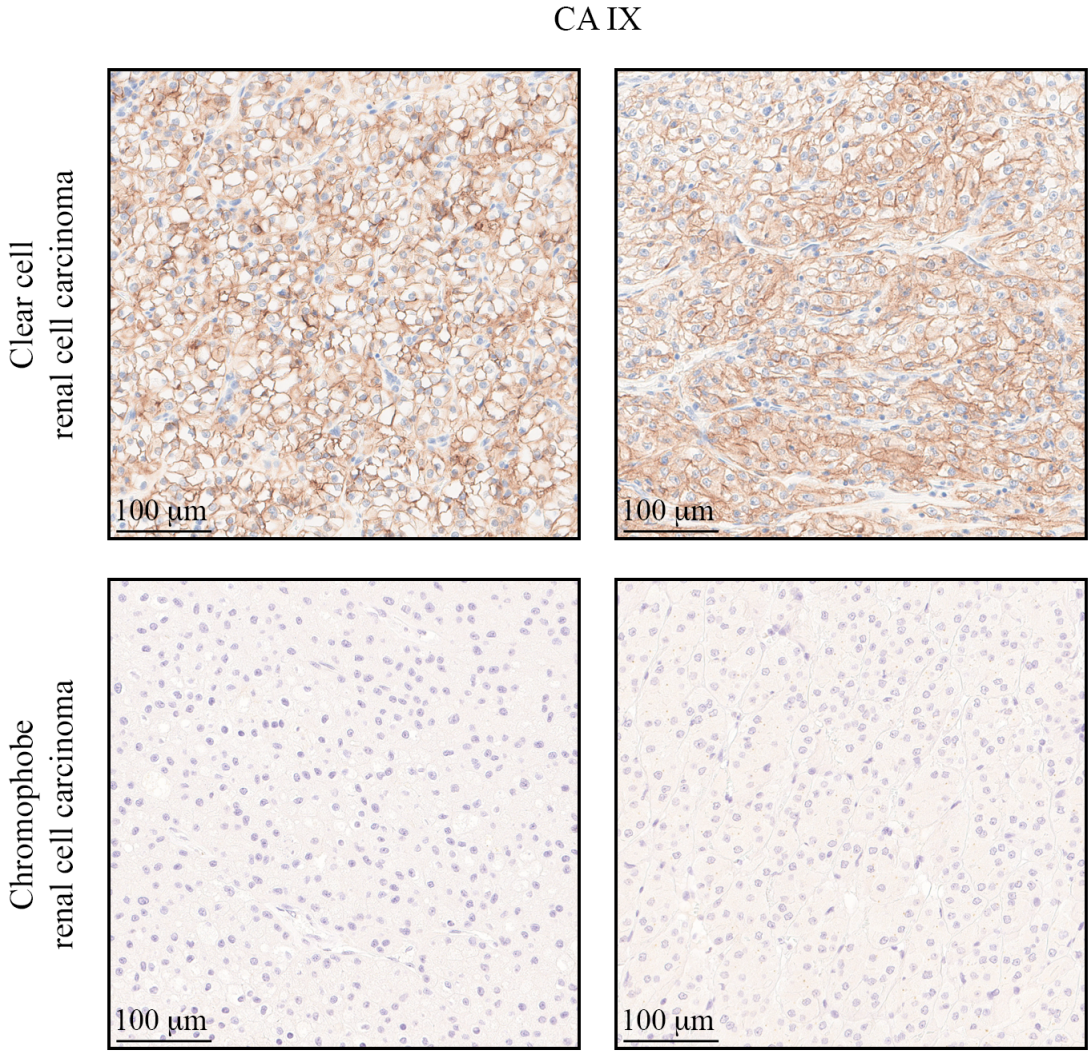


Figure 1.9 – Comparison of carbonic anhydrase 9 expression in clear cell renal cell carcinoma and chromophobe renal cell carcinoma

Exemplar images from two clear cell renal cell carcinoma specimens from this cohort demonstrating diffuse carbonic anhydrase 9 (CA IX) expression, confirming the presence of a 'pseudohypoxic' phenotype and acting as a surrogate for VHL loss; by comparison, no CA IX expression was observed in two cases of chromophobe renal cell carcinoma.

Serial tumour sections then underwent dual immunohistochemical labelling for the leukocyte marker of interest and for the endothelial marker CD31 and the position of these leukocytes between blood vessels (higher oxygen) and necrosis (lower oxygen/anoxia) was described qualitatively. Although the overall extent of leukocyte infiltration varied between different tumours, remarkably similar spatial distributions were observed for all markers analysed across this cohort.

Lymphocytes

Total T lymphocytes ($CD3^+$), CTL ($CD8^+$), T_{Reg} ($FOXP3^+$) and B lymphocytes ($CD20^+$) were more abundant in perivascular, as compared to perinecrotic, tumour regions (**Figure 1.10**). Overall, B lymphocytes were more closely restricted to the perivascular region than T lymphocytes, the latter population demonstrating greater infiltration towards necrotic regions.

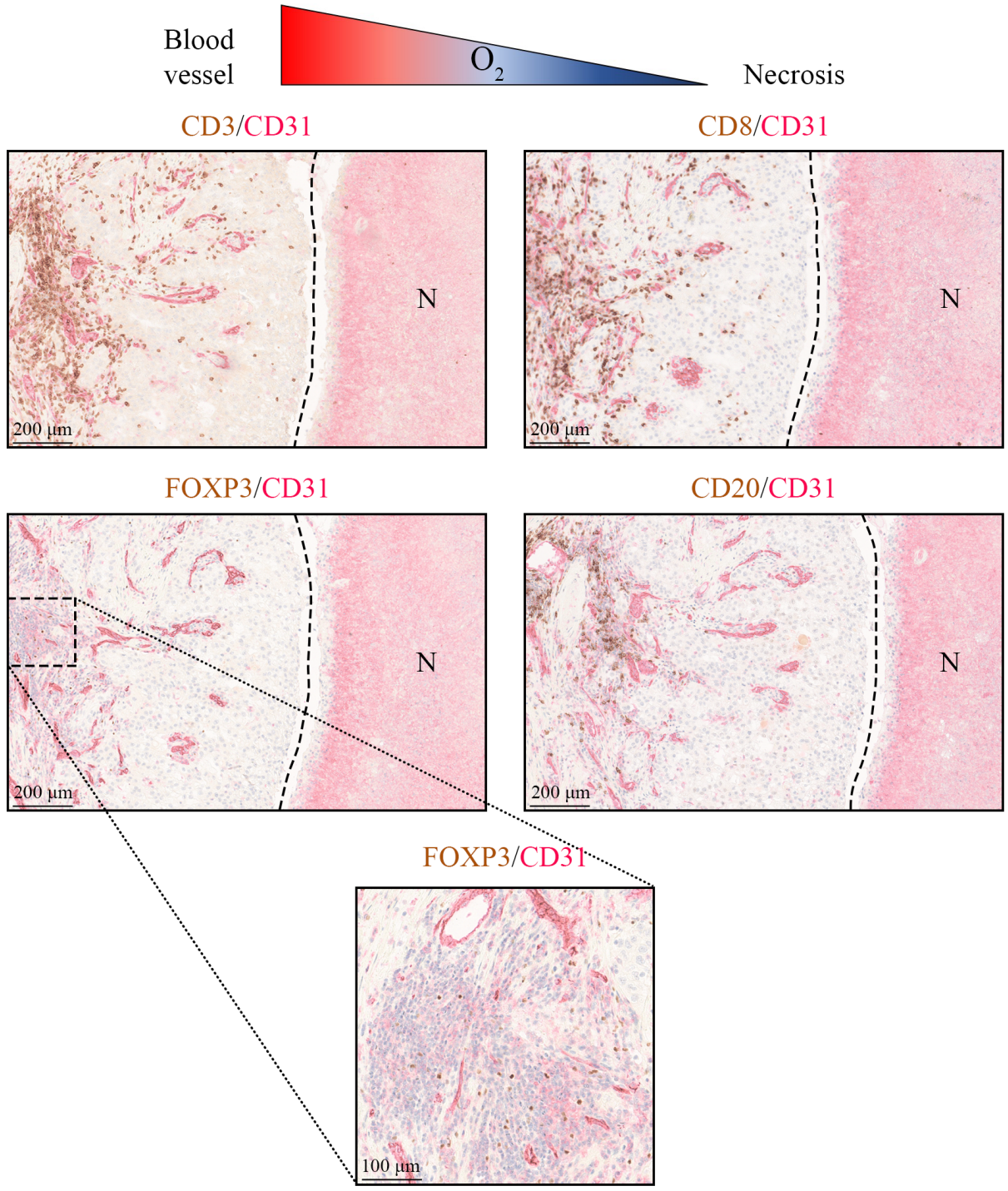


Figure 1.10 – Analysis of the spatial distribution of tumour infiltrating lymphocytes along oxygen gradients in clear cell renal cell carcinoma

Exemplar images from one tumour demonstrating that total T lymphocytes ($CD3^+$), cytotoxic T lymphocytes ($CD8^+$), regulatory T lymphocytes ($FOXP3^+$) and B lymphocytes ($CD20^+$) are located in a perivascular region (as identified by the endothelial marker CD31) at a distance from a region of tumour necrosis (N). In each image, the lymphocytes are labelled by

diaminobenzidine chromogen (brown) whilst the endothelial cells are labelled by Fast Red chromogen (red). The necrotic region is also labelled by Fast Red staining as it contains CD31-expressing myeloid cells [279].

Macrophages

By comparison, macrophages (as identified by the pan-macrophage marker CD68) were diffusely distributed throughout tumours, being abundant in perivascular locations but also accumulating to high density in perinecrotic regions (**Figure 1.11**). In general, tumour infiltrating macrophages expressed the M2 markers CD163 (a haemoglobin-haptoglobin complex receptor) and CD204 (macrophage scavenger receptor 1 [MSR1]), with the latter particularly highly expressed in necrotic regions. However, largely, they did not express the M2 marker CD206 (mannose receptor C-type 1 [MRC1]), which instead labelled macrophages located in well vascularised regions at the edge of tumours.

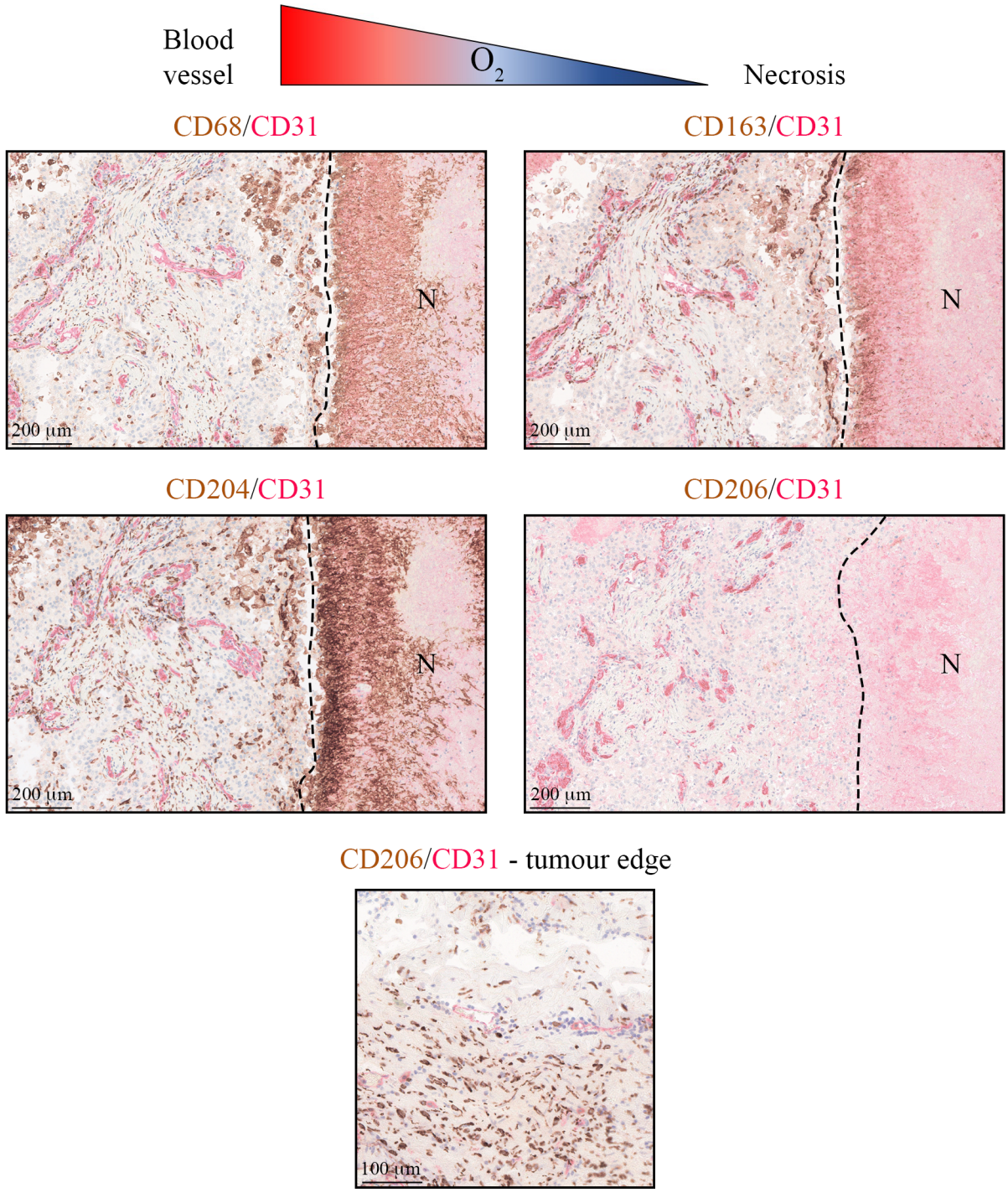


Figure 1.11 – Analysis of the spatial distribution of tumour infiltrating macrophages along oxygen gradients in clear cell renal cell carcinoma

Exemplar images from one tumour demonstrating that macrophages ($CD68^+$) are diffusely distributed throughout tumours but accumulate to highest density in perinecrotic regions. These macrophages express the M2 macrophage markers CD163 (a haemoglobin-haptoglobin complex scavenger receptor) and CD204 (macrophage scavenger receptor 1 [MSR1]).

However, these macrophages do not express the M2 marker CD206 (mannose receptor C-type 1 [MRC1]). Instead, CD206$^+$ macrophages are located in well vascularised regions at the periphery of the tumour. In each image, the macrophages are labelled by diaminobenzidine chromogen (brown) whilst the endothelial cells are labelled by Fast Red chromogen (red). The necrotic region is also labelled by Fast Red staining as it contains CD31-expressing myeloid cells [279].

Neutrophils

Neutrophil infiltration varied widely between different tumours, with some tumours containing very few neutrophils whilst others contained neutrophils that were diffusely distributed throughout the tumour. When present, neutrophils were most prominently located within necrotic regions. Interestingly, in these areas, myeloid cells were observed to conform to a clear topographical arrangement with macrophages palisading around the interface between viable and necrotic tumour cells and neutrophils located in the centre of these necrotic regions (**Figure 1.12**).

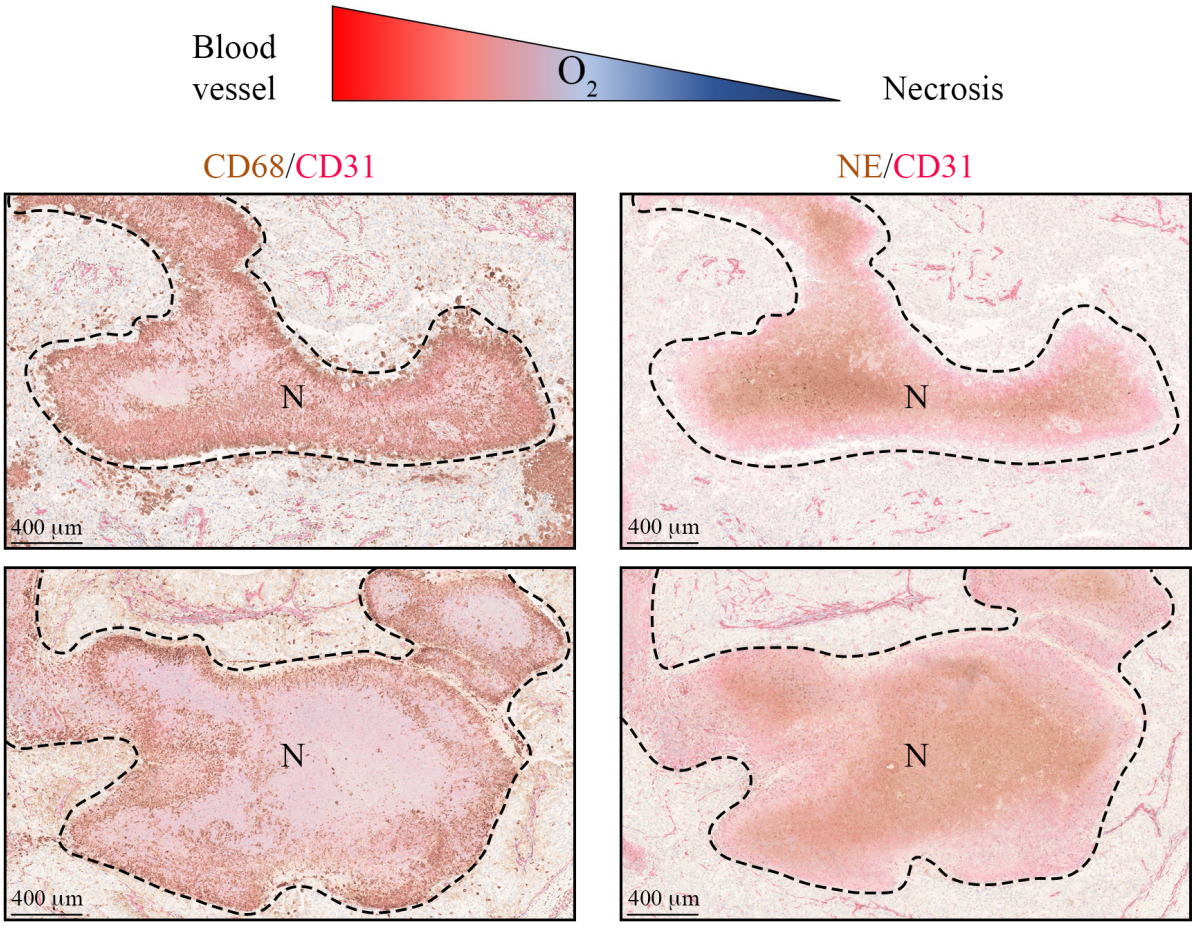


Figure 1.12 – Comparison of the spatial distribution of tumour infiltrating macrophages and neutrophils along oxygen gradients in clear cell renal cell carcinoma

Exemplar images from two tumours demonstrating that macrophages ($CD68^+$) are located at the periphery of necrotic regions whereas neutrophils (neutrophil elastase $[NE]^+$) are located at the centre of necrotic regions. In each image, the macrophages/neutrophils are labelled by diaminobenzidine chromogen (brown) whilst the endothelial cells are labelled by Fast Red chromogen (red). The necrotic region is also labelled by Fast Red staining as it contains CD31-expressing myeloid cells [279].

Dendritic cells

Conventional DC ($CD11c^+$) were abundant within tumours and, like macrophages, were diffusely distributed throughout tumours with accumulation in perinecrotic regions. By comparison, plasmacytoid DC ($CD123^+$) were scarce within tumours. When present, they were

located in perivascular regions but were most abundant in well vascularised regions at the edge of tumours (**Figure 1.13**).

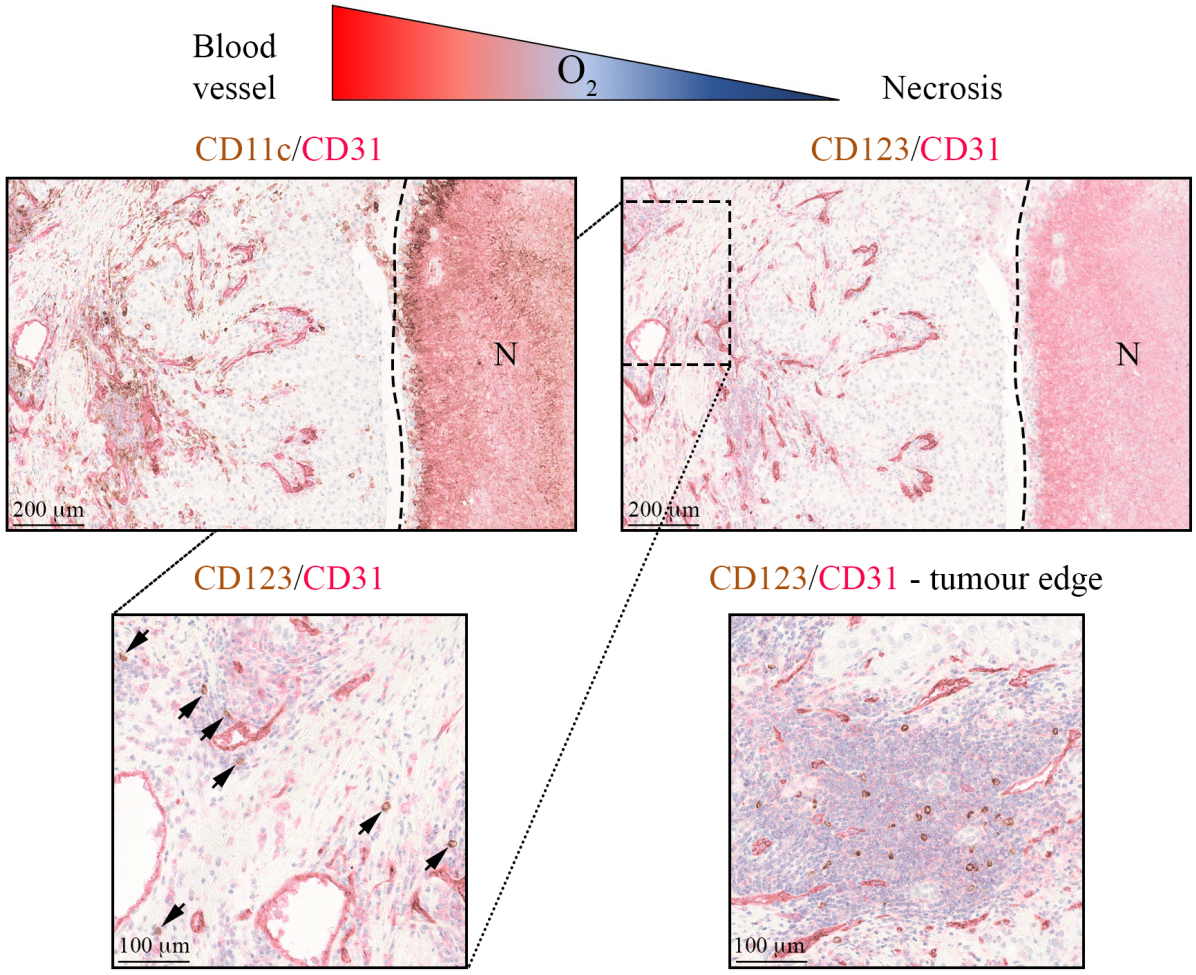


Figure 1.13 – Analysis of the spatial distribution of tumour infiltrating dendritic cells along oxygen gradients in clear cell renal cell carcinoma

Exemplar images from one tumour demonstrating that conventional dendritic cells ($CD11c^+$) are diffusely distributed throughout tumours but accumulate to highest density in perinecrotic regions. By comparison, plasmacytoid dendritic cells ($CD123^+$) are present in lower numbers and are located in perivascular regions. The majority of plasmacytoid dendritic cells are located in well vascularised regions at the periphery of the tumour. In each image, the dendritic cells are labelled by diaminobenzidine chromogen (brown) whilst the endothelial cells are labelled by Fast Red chromogen (red). The necrotic region is also labelled by Fast Red staining as it contains CD31-expressing myeloid cells [279].

Further examples of histology images from this cohort are presented in **Appendix 3**.

Analysis of the spatial distribution of CD8$^+$ T lymphocytes and semaphorin 3A expression relative to tumour vasculature in clear cell renal cell carcinoma

I next wished to explore why CD8$^+$ T lymphocytes are restricted to the perivascular niche in CCRCC. A recent study in lung cancer reported that interaction between SEMA3A, an endothelial and neuronal guidance protein during embryogenesis, and its co-receptor neuropilin-1 on the surface of tumour infiltrating CD8$^+$ T lymphocytes leads to inhibition of their migration and tumour-specific cytotoxicity [280]. I therefore chose to examine the co-localisation of CD8, SEMA3A and CD31 in serial sections from a separate cohort of 12 CCRCC tumours (for patient and tumour characteristics, representative images of immunohistochemical staining and image analysis pipeline see **Appendix 4**). Whilst neuropilin-1 is up-regulated in T lymphocytes upon their activation, its diffuse expression by both tumour cells and non-neoplastic tubular epithelium rendered quantitative analysis non-informative. In the tumours, SEMA3A was predominantly expressed by smooth muscle cells within the tunica media of blood vessels but also in areas of fibromuscular stroma. In adjacent non-neoplastic kidney tissue, glomerular mesangial cells and smooth muscle cells within peritubular capillaries stained positive. Next, images were cropped from the most and least vascularised regions of each tumour's CD31 slide (**Figure 1.14A**) and computationally aligned with the corresponding regions on the SEMA3A and CD8 stained slides. This confirmed that SEMA3A expression co-localised with that of CD31 (**Figure 1.14B**). Furthermore, CD8$^+$ cells were located within regions of high CD31 and SEMA3A expression (**Figure 1.14C**). In 11/12 tumours, there were significantly more CD8$^+$ cells in CD31/SEMA3A-rich areas than in CD31/SEMA3A-poor areas. Additionally, the CD8$^+$ cells that were present in CD31/SEMA3A-poor regions were found to be clustered around any blood vessels/sources of

SEMA3A that were present. Thus, blood vessels, SEMA3A and $CD8^+$ cells co-localise within CCRCC, in keeping with *in vitro* and *in vivo* mechanistic evidence that SEMA3A binding to neuropilin-1 induces cytoskeletal paralysis in tumour-specific $CD8^+$ T lymphocytes and thereby prevents their migration into tumour cell nests [281].

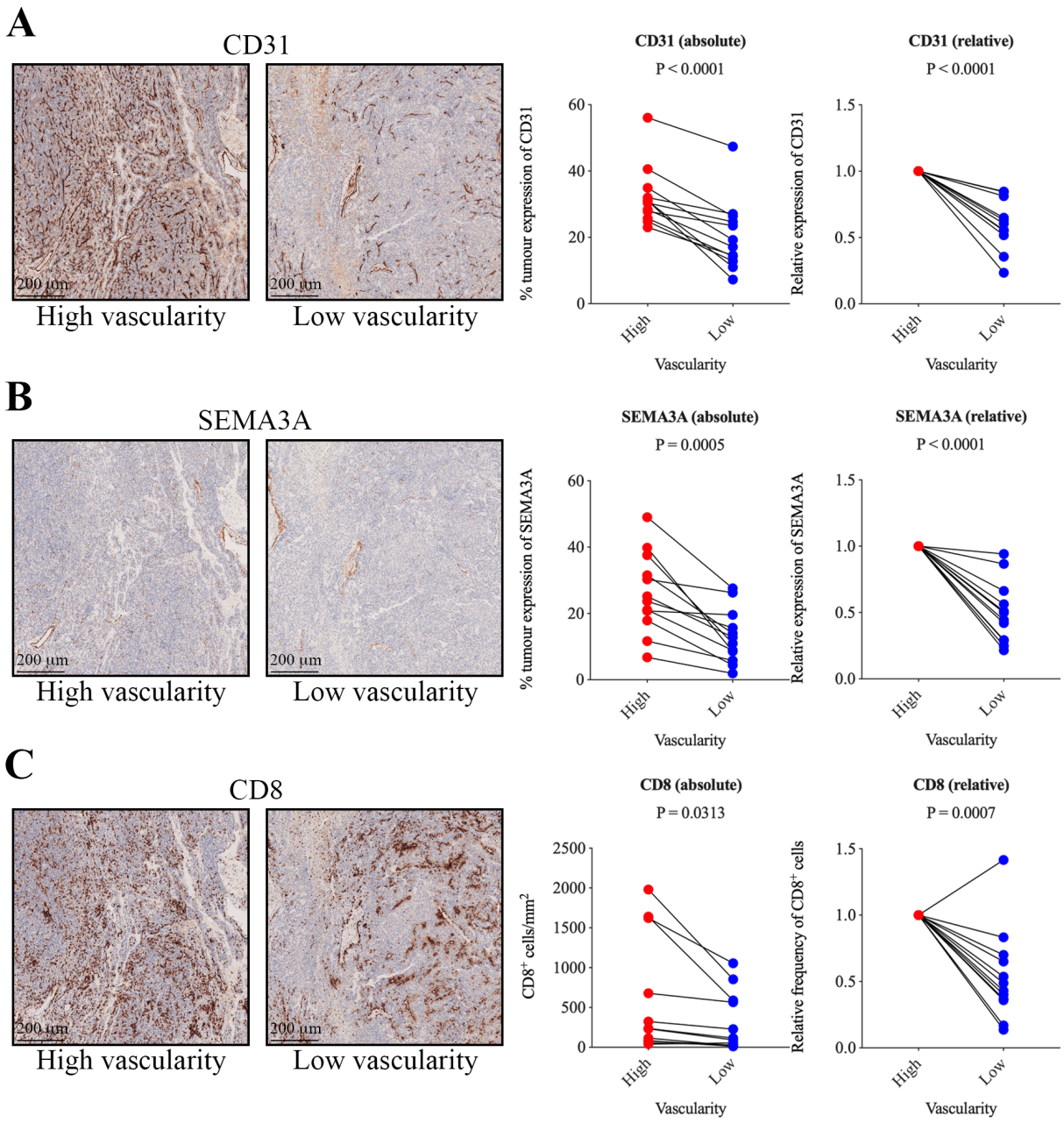


Figure 1.14 – Analysis of the spatial distribution of CD8$^+$ T lymphocytes and semaphorin 3A expression relative to tumour vasculature in clear cell renal cell carcinoma

(*A) Comparison of CD31 immunopositive area in the most and least vascularised regions of clear cell renal cell carcinoma (CCRCC) samples with representative histological images. (B) Comparison of semaphorin 3A (SEMA3A) immunopositive area in the most and least vascularised regions of CCRCC samples with representative histological images. The pattern of SEMA3A expression matches that of CD31. (C) Enumeration of CD8$^+$ cells in the most and least vascularised regions of CCRCC samples with representative histological images. Even in poorly vascularised regions, CD8$^+$ cells are located in the immediate proximity of blood vessels. All statistical analyses conducted by paired t-test.*

Discussion

Summary of findings

In this chapter, I have validated SIGHT, demonstrating broadly comparable performance in cell counting to humans and other available automated approaches. Adding further confidence to this approach is that the values returned for pimonidazole (mean = 5.1%, median = 3.6%, range = 1.1-14.2%) and CA IX (mean = 8.0%, median = 4.7%, range = 0.1-24.6%) hypoxic fractions are comparable to those reported by other HNSCC studies that adopted similar quantitation approaches:

- median pimonidazole hypoxic fraction of 9% (range = 2-29%) in 22 HNSCC samples [276];
- mean pimonidazole hypoxic fraction of 6.0% (range = 0.3-17.2%) and mean CA IX hypoxic fraction of 6.4% (range = 0.6-29.4%) in 43 HNSCC samples [254];
- mean pimonidazole hypoxic fraction of 2.9% (range = 0.0-18.8%) and mean CA IX hypoxic fraction of 2.5% (range = 0.0-34.4%) in 103 laryngeal SCC samples [282];
- median pimonidazole hypoxic fraction of 3.9% (range = 0.0-20.0%) in 41 HNSCC samples [283];

- mean pimonidazole hypoxic fraction of 3.4% (range = 0.0-14.1%) in 45 HNSCC samples [284].

The finding of a moderate positive correlation between pimonidazole labelling and CA IX expression (r_s = 0.6240 on a per tumour basis and r_s = 0.6325 on a per region basis) is also broadly in keeping with other studies, the majority of which report weak positive correlations between the two markers [254, 282, 285-287]. Despite this, some tumours displayed notably greater pimonidazole labelling than CA IX expression including one tumour with necrosis and pimonidazole labelling but virtually no CA IX expression, as has been reported in other HNSCC studies [287, 288]. Therefore, whilst CA IX may provide useful information about tumour hypoxia across large patient cohorts, caution should be exercised when utilising it as a single endogenous hypoxia marker in individual cases, as discussed in Appendix 1. Furthermore, there were only weak positive correlations between the extent of pimonidazole labelling or CA IX expression and tumour necrosis, largely due to the existence of areas of tumour hypoxia with little/no associated necrosis. These findings are consistent with a previous study which also detected tumour hypoxia without necrosis and, conversely, regions of necrosis associated with only moderate hypoxia [289]. The authors of this study concluded that whilst necrosis corresponds to the most hypoxic regions within a given tumour, necrosis alone does not accurately estimate the true extent of tumour hypoxia and thus cannot be utilised to make comparisons of hypoxia across different specimens.

Work presented in this chapter demonstrates that tumour infiltrating lymphocytes are restricted to better oxygenated perivascular regions whilst tumour infiltrating myeloid cells are more able to reside within poorly oxygenated regions. These observations imply that there are profound differences between these cell types with respect to their ability to migrate to, and/or survive

within, hypoxic tumour regions. Furthermore, the existence of broadly comparable distributions between a tumour type in which HIF stabilisation is focal and consequent upon microenvironmental oxygenation (HNSCC) and another with diffuse, oncogenic HIF activation (CCRCC) suggests that these distributions result primarily from leukocyte intrinsic processes, as opposed to as a consequence of HIF activation within tumour cells themselves. Given that most of the data presented in this chapter concern $CD8^+$ CTL, $FOXP3^+$ T_{Reg} and $CD68^+$ macrophages, the remainder of this discussion will predominantly focus on these cell types.

Effector T lymphocytes

Effector T lymphocytes encompass $CD8^+$ CTL and pro-inflammatory $CD4^+$ helper T lymphocytes. Tumour infiltration by $CD8^+$ CTL correlates with improved outcome in HNSCC [290-298]. In contrast to many other tumour types, a high density of $CD8^+$ CTL is associated with poorer survival in CCRCC [299-301], although many of these lymphocytes display an exhausted phenotype [300-302]. Furthermore, T lymphocyte infiltration is higher in tumours that harbour loss of *HIF1A*, which acts as a tumour suppressor gene in CCRCC and thus its loss likely correlates with a more aggressive clinical course independently of the immunological sequelae [303].

To function, effector T lymphocytes must migrate to, and infiltrate, tumours to be physically co-located with their malignant target cells [304]. However, the exact origins of intratumoural lymphocytes are poorly defined. Naïve T lymphocytes may enter, and then differentiate, within the tumour or circulating tumour-specific T lymphocytes may traffic to tumours and subsequently expand *in situ*. A recent study of human kidney tumours demonstrated that these contain stem cell-like T lymphocytes that reside in perivascular niches, also inhabited by

lymphatics and APC, that support continued generation of CTL [305]. These findings are in keeping with the perivascular localisation of T lymphocytes demonstrated in this chapter. Indeed, several murine studies have reported that $CD8^+$ T lymphocytes preferentially localise away from the most hypoxic regions of solid tumours, as identified by pimonidazole or EF5 immunohistochemistry [306-313] or distance from the nearest blood vessel [314]. Similar findings have also been reported in human tumours, although these studies have utilised either necrosis or HIF/HIF-target gene expression as endogenous hypoxia markers and generally report overall correlations as opposed to descriptions of spatial localisation (**Table 1.2**). Additionally, in malignant melanoma, the density of $CD8^+$ T lymphocytes has been reported to be three times higher in vascular, as compared to avascular, tumour areas [313].

Table 1.2 – Summary of human histological studies evaluating the relationship between T lymphocyte infiltration and tumour hypoxia

Author (year)	Cancer type (sample size)	Hypoxia marker	Lymphocyte marker	Comment
Negus (1997) [315]	Ovarian carcinoma (n = 20)	Necrosis	CD3 CD8	T lymphocytes were not present in significant numbers within areas of tumour necrosis (unlike macrophages)
Fiumara (1997) [316]	Papillary thyroid carcinoma (n = 121)	Necrosis	CD45-RO	Tumour necrosis was never associated with T lymphocyte infiltration
Brasanac (1999) [317]	Renal cell carcinoma (n = 26)	Necrosis	CD8	$CD8^+$ lymphocytes were scant in cases with tumour necrosis
Le (2005) [318]	HNSCC (n = 101)	CA IX	CD3	Negative correlation between tumour CA IX expression and $CD3^+$ lymphocyte infiltration (P = 0.05)

Singer (2011) [319]	Renal cell carcinoma (n = 249 including 80 CCRCC)	GLUT1	CD3 CD8	Negative correlation between tumour GLUT1 expression and $CD3^+$ and $CD8^+$ lymphocyte counts in CCRCC only
Ino (2013) [320]	Pancreatic carcinoma (n = 212)	Necrosis	CD4 CD8	Negative correlation between presence of tumour necrosis and $CD4^+$ (P = 0.042) and $CD8^+$ (P = 0.019) lymphocyte counts
Townsend (2013) [321]	Ovarian carcinoma (n = 196)	VEGF	CD4 CD8 Granzyme B TIA1	$CD4^+$ lymphocyte counts were higher in tumours with high VEGF expression as compared to those with low VEGF expression (P = 0.0002) No difference in $CD8^+$ (P = 0.2078), granzyme B^+ (P = 0.0533) or $TIA1^+$ (P = 0.2047) lymphocyte counts between tumours with high and low VEGF expression (granzyme B and TIA1 are markers of cytotoxicity)
Ottensmeier (2016) [322]	HNSCC (n = 308)	HIF1α GLUT1	CD3 CD8	Negative correlation between tumour GLUT1 expression and $CD3^+$ lymphocyte counts (r = -0.43, P < 0.001) Negative correlation between tumour GLUT1 expression and $CD8^+$ lymphocyte counts (r = -0.40, P < 0.001) Negative correlation between tumour HIF1α (r = -0.49, P < 0.001) and GLUT1 (r = -0.42, P < 0.001) expression and TIL counts (based on H&E morphology)

	Lung SCC (n = 34)	HIF1α GLUT1	CD8	Negative correlation between tumour HIF1α (r = -0.54, P < 0.001) and GLUT1 (r = -0.43, P < 0.001) expression and $CD8^+$ lymphocyte counts
Horikawa (2017) [323]	Ovarian carcinoma with peritoneal metastasis (n = 56)	VEGF	CD4 CD8	No correlation between metastatic tumour VEGF expression and $CD4^+$ lymphocyte counts Negative correlation between metastatic tumour VEGF expression and $CD8^+$ lymphocyte counts
Brooks (2019) [324]	HNSCC (n = 15)	CA IX	CD3	Negative correlation between tumour CA IX expression and $CD3^+$ lymphocyte counts within tumour cell nests (r = -0.55, P = 0.0377)
Togo (2020) [325]	HNSCC (n = 59)	HIF1α GLUT1	CD8	Immune 'cold' tumours had low $CD8^+$ lymphocyte counts and high tumour expression of HIF1α and GLUT1
Kuriyama (2020) [326]	Oesophageal SCC (n = 41)	GLUT1	CD8	No association between tumour GLUT1 expression and $CD8^+$ lymphocyte infiltration (P = 0.084)
Craig (2020) [327]	Colorectal carcinoma (n = 316)	CA IX	CD3 CD4 CD8	An increase in CA IX expression was observed in immune 'cold' tumours (defined as having low $CD3^+$, $CD4^+$ and $CD8^+$ lymphocyte counts) (P = 0.0009)

Records separated by a dashed line belong to the same overall study

CA IX – carbonic anhydrase 9, CCRCC – clear cell renal cell carcinoma, H&E – haematoxylin and eosin, HIF1α – hypoxia-inducible factor 1 alpha, HNSCC – head and neck squamous cell carcinoma, GLUT1 – glucose transporter 1, SCC – squamous cell carcinoma, TIA1 – TIA1 cytotoxic granule-associated RNA binding protein 1, TIL – tumour infiltrating lymphocyte, VEGF – vascular endothelial growth factor

Whilst the exact mechanisms underpinning the negative relationship between tumour hypoxia and effector T lymphocyte infiltration are not well defined, possible explanations include:

- failure to enter hypoxic tumour regions (T lymphocyte motility is reduced under hypoxia [313, 314, 328-330] and instead they migrate within tumours outside of, but in close proximity to, blood vessels [331, 332]; furthermore release of the T lymphocyte recruiting chemokines CXCL9 and CXCL10 is reduced under hypoxia [307, 333]);
- rapid exit from hypoxic tumour regions (although I am unaware of any studies reporting this phenomenon);
- reduced proliferation under hypoxic conditions [334-341];
- increased apoptosis under hypoxic conditions [338, 342].

However, many factors other than oxygen availability are perturbed in the TME. Several of these, which are intricately linked to oxygenation, have also been implicated in constraining effective T lymphocyte-mediated anti-tumour immunity including glucose deficiency [343, 344], low pH [345-348] and accumulation of the immunosuppressive substances lactate [349, 350], adenosine [308, 351-353], potassium [354, 355], galectin-1 [318, 356, 357] and VEGF [184, 358-363]. Finally, a number of factors less directly related to oxygenation can also limit T lymphocyte infiltration into tumours including transforming growth factor beta (TGFβ) [364-366], β-catenin [367] and stromal fibroblasts/collagen density [332, 368].

Regulatory T lymphocytes

Analysis of T_{Reg} in human breast cancers and matched non-neoplastic breast tissue revealed low T cell receptor (TCR) repertoire overlap between these sites, suggesting that local expansion of tissue resident T_{Reg} is unlikely to be the primary origin of intratumoural T_{Reg} [369]. Furthermore, low overlap in TCR repertoire between intratumoural T_{Reg} and other intratumoural T lymphocytes also argued against significant conversion of effector T lymphocytes to T_{Reg} within tumours. Instead, these results suggest that the majority of

intratumoural T_{Reg} are recruited from peripheral blood. The prognostic value of tumour infiltrating $FOXP3^+$ cells in HNSCC has not been well characterised, with different studies reporting positive [295, 298, 370-372], neutral [290, 292, 297] and negative [373] associations. By comparison, increasing infiltration by $FOXP3^+$ cells is consistently associated with poorer prognosis in CCRCC [374-376]. In contrast to the observations presented in this chapter, T_{Reg} have been reported to localise within hypoxic regions of murine tumours [377]. Studies in human tumours have largely reported a positive association between tumour hypoxia and T_{Reg} infiltration but, once again, little information has been reported about T_{Reg} distribution (**Table 1.3**).

Table 1.3 – Summary of human histological studies evaluating the relationship between $FOXP3^+$ regulatory T lymphocyte infiltration and tumour hypoxia

Author (year)	Cancer type (sample size)	Hypoxia marker	Comment
Fox (2007) [378]	Prostate carcinoma (n = 146)	HIF1α HIF2α	$FOXP3^+$ cell counts were higher in tumours expressing HIF2α (P = 0.007), but not in tumours expressing HIF1α (P = 0.25), compared to those that did not
Giatromanolaki (2008) [379]	Endometrial carcinoma (n = 79)	HIF1α HIF2α VEGF	No difference in $FOXP3^+$ cell counts between tumours expressing high HIF1α (P = 0.99), HIF2α (P = 0.33) or VEGF (P = 0.80) and those expressing low levels of these proteins
Singer (2011) [319]	Renal cell carcinoma (n = 249 including 80 CCRCC)	GLUT1	No correlation between tumour GLUT1 expression and $FOXP3^+$ cell counts

Yan (2011) [380]	Breast carcinoma (n = 448)	CA IX	$FOXP3^+$ cell counts were higher in tumours that expressed CA IX compared to those that did not ($P < 0.001$)
Ino (2013) [320]	Pancreatic carcinoma (n = 212)	Necrosis	Positive correlation between presence of tumour necrosis and $FOXP3^+$ cell counts ($P = 0.002$)
Deng (2013) [381]	Gastric carcinoma (n = 99)	HIF1α	Positive correlation between tumour HIF1α expression and $FOXP3^+$ cell counts both in patients with metastatic ($r = 0.772$, $P < 0.001$, $n = 47$) and non-metastatic ($r = 0.461$, $P = 0.001$, $n = 52$) disease $FOXP3^+$ cells mainly located close to hypoxic tumour regions with high HIF1α expression
Townsend (2013) [321]	Ovarian carcinoma (n = 196)	VEGF	$FOXP3^+$ cell counts were higher in tumours with high VEGF expression as compared to those with low VEGF expression ($P = 0.0052$)
Giatromanolaki (2020) [382]	NSCLC (n = 98)	CA IX	Positive correlation between tumour CA IX expression and stromal $FOXP3^+$ cell counts ($r = 0.27$, $P = 0.007$)

CA IX – carbonic anhydrase 9, CCRCC – clear cell renal cell carcinoma, FOXP3 – forkhead box P3, GLUT1 – glucose transporter 1, HIF1α – hypoxia-inducible factor 1 alpha, HIF2α – hypoxia-inducible factor 2 alpha, NSCLC – non-small cell lung carcinoma, VEGF – vascular endothelial growth factor

Tumour hypoxia has been reported to promote T_{Reg} recruitment through the induction of the chemokine CCL28 (which binds to CCR10 on T_{Reg}) [383, 384] and VEGF (which binds to neuropilin 1 on T_{Reg}) [385]. In addition to augmented T_{Reg} recruitment, hypoxic exposure has been reported to increase FOXP3 expression by murine splenocytes and human peripheral blood mononuclear cells and to potentiate the immunosuppressive properties of established T_{Reg} [386] (although these findings are at variance with those presented in Chapter 3 of this thesis). Moreover, the culture medium from various cancer cells grown under hypoxic

conditions is capable of augmenting T_{Reg} differentiation [381, 387] whilst hypoxia in murine melanoma tumours leads to increased Nanog-TGFβ signalling, which also promotes T_{Reg} differentiation [388]. Furthermore, VEGF can also drive T_{Reg} proliferation within murine tumours [389]. Unlike effector T lymphocytes, T_{Reg} have been proposed to be endowed with certain properties that favour their survival within hypoxic tumour regions. These include high expression of the stress-responsive anti-apoptotic enzyme haem-oxygenase-1 [377] and the ability to metabolically adapt to conditions of low glucose and high lactate availability [390, 391].

However, in murine prostate cancer, hypoxic tumour regions are devoid of T lymphocytes of all types [310] whilst $CD4^+$ T lymphocytes are less prevalent in hypoxic regions of murine fibrosarcomas [308]. Moreover, gene expression analysis of 126 cases of tongue SCC available through The Cancer Genome Atlas demonstrated that high *CA9* expression was correlated with low T_{Reg} infiltration [392]. On closer inspection of the data included in one of the above studies, it is apparent that T_{Reg} are located in close proximity to, but not primarily within, pimonidazole positive tumour regions [377] whilst another study demonstrates T_{Reg} in close proximity to tumour blood vessels [393]. Intravital imaging in murine breast cancer demonstrated that T_{Reg} do not infiltrate the tumour mass and remain in a perivascular location, in a similar manner to CTL; indeed, exposure of T_{Reg} to acute hypoxia (by lowering inhaled oxygen levels from 21% to 7%) resulted in almost immediate inhibition of their motility [394]. Furthermore, expression of HIF1α by murine T_{Reg} has been proposed to generate 'functional fragility' [395] and to facilitate their migration at the expense of immunosuppression [393], suggesting that T_{Reg} within hypoxic tumour regions may not be fully operative.

Although not corroborated by my own HNSCC data, the majority of studies associate increasing tumour hypoxia with greater numbers of intratumoural T_{Reg}. My observation that T_{Reg} are not located in the most hypoxic tumour regions highlights the value of describing leukocyte localisation in addition to their enumeration. The similar distributions of $CD8^+$ and $FOXP3^+$ T lymphocytes in the HNSCC and CCRCC cohorts suggests that co-localisation of these populations may facilitate suppression of CTL by T_{Reg} (although T_{Reg} utilise both contact-dependent and -independent mechanisms of immunosuppression, as outlined in Chapter 4). Indeed, it has been reported that recruitment of T_{Reg} to tumours follows, and depends upon, CTL infiltration through the release of the T_{Reg} recruiting chemokines CCL1 and CCL22 [396, 397].

Macrophages

Tumour-associated macrophages (TAM) can be derived from both circulating bone marrow-derived monocytes [398] as well as from tissue resident macrophages [399, 400]. Within the TME, TAM are generally considered to inhibit anti-tumour immunity through the suppression of T lymphocyte responses (as reviewed in [401]). Myeloid cells have been reported to accumulate to high densities within hypoxic regions of murine tumours [211, 310, 402-413]. Studies evaluating the relationship between $CD68^+$ macrophage infiltration and hypoxia in human tumours, which report largely comparable findings, are summarised in **Table 1.4**.

Table 1.4 – Summary of human histological studies evaluating the relationship between $CD68^+$ macrophage infiltration and tumour hypoxia			
Author (year)	**Cancer type (sample size)**	**Hypoxia marker**	**Comment**
Torres (1997) [414]	Testicular germ cell tumours (n = 43)	Necrosis	$CD68^+$ macrophages were abundant within areas of tumour necrosis
Negus (1997) [315]	Ovarian carcinoma (n = 20)	Necrosis	$CD68^+$ macrophages were present in significant numbers within areas of tumour necrosis (unlike T lymphocytes)
Fiumara (1997) [316]	Papillary thyroid carcinoma (n = 121)	Necrosis	Tumour necrosis was never associated with infiltration by phagocytosing multinucleated large macrophages
Volodko (1998) [415]	Breast carcinoma (n = 120)	Necrosis	Tumours without necrosis had predominantly weak $CD68^+$ macrophage infiltration whereas the presence of necrosis was associated with moderate/intensive $CD68^+$ macrophage infiltration
Matsumara (1998) [416]	Colorectal carcinoma (n = 148)	Necrosis	$CD68^+$ macrophages were frequently found in tissues within or around the tumour or within areas of tumour necrosis
Leek (1999) [417]	Breast carcinoma (n = 109)	Necrosis	Positive correlation between tumour necrosis and $CD68^+$ macrophage infiltration ($P \leq 0.01$) High numbers of macrophages were observed to palisade around areas of tumour necrosis
Salvesen (1999) [418]	Endometrial carcinoma (n = 60)	VEGF	No correlation between tumour VEGF expression and $CD68^+$ macrophage infiltration

Hemmerlein (2000) [419]	Renal cell carcinoma (n = 36)	Necrosis	$CD68^+$ macrophage counts were higher in tumours with necrosis than in tumours without necrosis The rims of necrotic foci were lined by palisading $CD68^+$ macrophages
Onita (2002) [420]	Bladder carcinoma (n = 67)	HIF2α Necrosis	$CD68^+$ macrophage counts were higher in tumours that expressed HIF2α as compared to those that did not ($P < 0.001$) $CD68^+$ macrophage infiltration was localised near areas of tumour necrosis
Valković (2002) [421]	Breast carcinoma (n = 97)	VEGF	Positive correlation between tumour VEGF expression and $CD68^+$ macrophage infiltration ($P = 0.003$)
Li (2002) [422]	HNSCC (n = 82)	VEGF	$CD68^+$ macrophage counts were higher in tumours that expressed VEGF as compared to those that did not ($P < 0.05$)
Ohta (2002) [423]	Oesophageal SCC (n = 48)	VEGF	Positive correlation between tumour VEGF expression and $CD68^+$ macrophage counts ($P < 0.01$)
Ohno (2003) [424]	Gastric carcinoma (n = 84)	Necrosis	Many $CD68^+$ macrophages were distributed along the invasive margin of the tumours and within areas of tumour necrosis Sometimes, numerous $CD68^+$ macrophages were noted near necrotic areas with large neutrophil clusters
Koga (2004) [425]	Bladder carcinoma (n = 69)	HIF2α Necrosis	No correlation between tumour HIF2α expression and $CD68^+$ macrophage counts Macrophages were particularly concentrated at the tumour invasive front and within areas of tumour necrosis

Ohno (2004) [426]	Endometrial carcinoma (n = 70)	Necrosis	Most $CD68^+$ macrophages were distributed along the invasive tumour margin or within areas of tumour necrosis
Tsutsui (2005) [427]	Breast carcinoma (n = 249)	VEGF	High tumour VEGF expression was associated with high $CD68^+$ macrophage counts (P = 0.0011)
Varney (2005) [428]	Malignant melanoma (n = 98)	VEGF	No correlation between tumour VEGF expression and $CD68^+$ macrophage infiltration
Vicioso (2006) [429]	Breast carcinoma (n = 133)	VEGF	$CD68^+$ macrophage counts were higher in tumours that expressed HIF2α as compared to those that did not but the difference did not reach statistical significance
Bailey (2007) [430]	Colorectal carcinoma (n = 17)	Necrosis	$CD68^+$ macrophage counts were higher in areas of tumour necrosis (P < 0.005) and in areas of stroma (P < 0.005) than in tumour cell nests $CD68^+$ macrophage infiltration was greatest within areas of tumour necrosis
Chai (2008) [431]	Bladder carcinoma (n = 99)	HIF1α	$CD68^+$ macrophage counts were higher in HIF1α high tumours as compared to HIF1α low tumours (P = 0.002)
Kawanaka (2008) [432]	Cervical carcinoma (n = 73)	HIF2α	HIF2α co-localised with $CD68^+$ macrophages in 53/73 (72.6%) samples (but HIF2α staining in tumour cells was reported to be predominantly cytoplasmic rather than nuclear)
Ryder (2008) [433]	Thyroid carcinoma (n = 37)	Necrosis	Tumours with high $CD68^+$ macrophage counts had a trend towards more extensive necrosis (P = 0.149)

Chen (2009) [434]	Bladder carcinoma (n = 216)	HIF1α	$CD68^+$ macrophage counts were higher in tumours with high HIF1α expression as compared to those with low HIF1α expression ($P < 0.0001$)
Zhang (2011) [435]	Lymphoma (n = 38)	VEGF	Positive correlation between tumour VEGF expression and $CD68^+$ macrophage counts ($r = 0.35$, $P < 0.05$)
Muthana (2011) [436]	Prostate carcinoma (n = NR)	Pimonidazole	$CD68^+$ macrophages were detected in both better oxygenated and hypoxic tumour areas Poorly vascularised areas contained higher numbers of $CD68^+$ macrophages than highly vascularised ones ($P < 0.001$)
Cooper (2012) [437]	Glioblastoma (n = 10)	Necrosis	Positive correlation between presence of tumour necrosis and $CD68^+$ macrophage infiltration ($r_s = 0.33$) $CD68^+$ macrophages were seen clustered around blood vessels, within brain tumour stroma individually and in small collections within areas of tumour necrosis
Jiang (2013) [438]	Endometrial carcinoma (n = 95)	VEGF	$CD68^+$ macrophage counts were higher in tumours that expressed VEGF as compared to those that did not ($P = 0.0001$)
Ino (2013) [320]	Pancreatic carcinoma (n = 212)	Necrosis	Positive correlation between presence of tumour necrosis and $CD68^+$ macrophage counts ($P = 0.001$)
Simionescu (2013) [439]	Endometrial carcinoma (n = 52)	Necrosis	$CD68^+$ macrophages were predominantly perivascular or located adjacent to areas of tumour necrosis
Xu (2014) [440]	CCRCC (n = 185)	Necrosis	Positive correlation between presence of tumour necrosis and $CD68^+$ macrophage counts ($P = 0.035$)

Mogoantă (2014) [441]	Colorectal carcinoma (n = 23)	Necrosis	$CD68^+$ macrophages were most numerous within areas of tumour necrosis
Wen (2015) [442]	Ovarian carcinoma (n = 71)	HIF1α	$CD68^+$ macrophage counts were higher in tumours with high HIF1α expression as compared to those with low HIF1α expression ($P < 0.001$)
Li (2016) [443]	Pancreatic carcinoma (n = 131)	HIF1α	Positive correlation between tumour HIF1α expression and $CD68^+$ macrophage counts ($P < 0.05$)
Morita (2017) [444]	Breast carcinoma (n = 53)	Necrosis	Considerable numbers of $CD68^+$ macrophages were present within areas of tumour necrosis $CD68^+$ macrophages were also abundant in the mammary fat adjacent to the tumour, as well as around the luminal surface of vessels
Zhang (2017) [445]	Gastric carcinoma (n = 236)	HIF1α	Positive correlation between tumour HIF1α expression and $CD68^+$ macrophage counts ($r = 0.209$, $P = 0.001$)
Zhang (2018) [446]	Hepatocellular carcinoma (n = 10)	HIF1α	Positive correlation between tumour HIF1α expression and $CD68^+$ macrophage counts but this failed to reach statistical significance ($r = 0.49$, $P = 0.1528$)
Annovazzi (2018) [447]	Glioblastoma (n = 35)	Necrosis	$CD68^+$ macrophages were found in both perivascular and perinecrotic regions (within large areas of tumour necrosis almost all cells were macrophages)

CCRCC – clear cell renal cell carcinoma, HIF1α – hypoxia-inducible factor 1 alpha, HIF2α – hypoxia-inducible factor 2 alpha, HNSCC – head and neck squamous cell carcinoma, NR – not reported, SCC – squamous cell carcinoma, VEGF – vascular endothelial growth factor

Distinct TAM subpopulations are located in different tumour microenvironmental niches. For example, perivascular TAM influence blood vessel function and leukocyte extravasation (as

reviewed in [448]), as well as tumour cell intravasation [449, 450], whereas perinecrotic TAM prevent T lymphocyte infiltration into the centre of tumour cells nests [405].

Perivascular, proangiogenic TAM commonly express the angiopoietin receptor TIE2 which contributes to their recruitment to sites of neoangiogenesis (expression of its ligand angiopoietin-2 is up-regulated by tumour endothelial cells) where they make essential contributions to tumour vascularisation [451-456]. Morphologically, TIE2-expressing monocytes (TEM) are smaller and rounder than the larger and more heterogenous group of phagocytic $TIE2^-$ TAM found in perinecrotic regions [457, 458]. However, TEM are also capable of exerting immunosuppressive effects and are recognised to possess an M2 pattern of gene expression [458]. Indeed, given their perivascular location, TEM are well placed to inhibit effector T lymphocyte activation whilst simultaneously promoting T_{Reg} expansion, processes that are mediated, respectively, through their release of the immunosuppressive cytokine IL-10 and the T_{Reg} chemokine CCL17 [459]. Perivascular TAM have been reported to express CD206/MRC1 [411, 455, 456, 458] in keeping with the presence of small, round $CD206^+$ cells near blood vessels located at the edge of tumours in the CCRCC cohort. Interestingly, low oxygen levels *in vitro* have been associated with increased macrophage expression of the M2 marker ARG1 but reduced expression of the M2 marker CD206/MRC1; accordingly, distinct macrophage populations expressing either one of these markers were found to anti-locate within pimonidazole positive and negative regions of murine tumours [411]. Thus, access to oxygen from adjacent blood vessels supports expression of CD206 in this perivascular population of macrophages.

In general, anti-tumour M1 macrophages are significantly underrepresented in hypoxic tumour regions [307, 460, 461] whereas pro-tumour M2 macrophages are enriched at these sites [361,

410, 411, 460-463]. However, a recent analysis in CCRCC utilising highly multiplexed mass cytometry reported the existence of 17 distinct TAM subpopulations, demonstrating significantly greater complexity than the classical M1/M2 dichotomisation [273]. Whilst CD163, CD204 and CD206 have been used interchangeably as single histological markers of M2 macrophages [133], this study suggested that a population of $CD38^{+}CD204^{+}CD206^{-}$ TAM correlate with the presence of expanded populations of T_{Reg} and exhausted CTL and also contribute directly to immunosuppression through expression of PD-L1 and PD-L2. Data presented in this chapter now demonstrate that this population of pro-tumour macrophages are likely to be enriched in highly hypoxic perinecrotic regions of CCRCC (although expression of CD38, a multi-functional protein expressed by several different types of leukocytes, was not analysed in this cohort). Studies evaluating the relationship between M1 and M2 macrophage infiltration and hypoxia in human tumours are summarised in **Table 1.5**.

Table 1.5 – Summary of human histological studies evaluating the relationship between M1 and M2 macrophage infiltration and tumour hypoxia

Author (year)	Cancer type (sample size)	Hypoxia marker	Macrophage marker	Comment
Ino (2013) [320]	Pancreatic carcinoma (n = 212)	Necrosis	CD163 CD204 HLA-DR	Positive correlation between presence of tumour necrosis and $CD163^{+}$ (P = 0.003) and $CD204^{+}$ (P = 0.001) macrophage counts Negative correlation between presence of necrosis and $HLA\text{-}DR^{+}$ macrophage counts (P = 0.002) The majority of the macrophages within areas of tumour necrosis were of an M2 phenotype

Prosniak (2013) [464]	Glioma (n = 66)	Necrosis	CD68 CD163	$CD68^+$ and $CD163^+$ macrophages were found dispersed throughout the tumour parenchyma Elevated numbers of $CD163^+$ macrophages were seen surrounding areas of tumour necrosis
Lima (2014) [465]	Bladder carcinoma (n = 99)	HIF1α	CD163	Tumours with high numbers of $CD163^+$ macrophages within stroma were associated with low tumour cell HIF1α expression whereas tumours with high numbers of $CD163^+$ macrophages within tumour cells nests were associated with high tumour cell HIF1α expression
Xu (2014) [440]	CCRCC (n = 185)	Necrosis	CD68 CD206	No correlation between presence of tumour necrosis and $CD206^+$ macrophage counts (P = 0.145)
Tripathi (2014) [466]	Breast carcinoma (n = 14)	HIF1α	CD206	$CD206^+$ macrophage counts were much higher in tumour regions expressing HIF1α as compared to those not expressing HIF1α
Cros (2016) [467]	CCRCC (n = 257)	HIF1α	CD163	$CD163^+$ macrophage infiltration was higher in tumours with high HIF1α expression as compared to those with low HIF1α expression (P = 0.02)
Zhang (2017) [445]	Gastric carcinoma (n = 236)	HIF1α	CD163	Positive correlation between tumour HIF1α expression and $CD163^+$ macrophage counts (r = 0.141, P = 0.017)
Kazantseva (2018) [468]	Glioblastoma (n = 20)	CA IX	CD163	Tumour regions expressing CA IX were more infiltrated by $CD163^+$ cells than those not expressing CA IX

Sørensen (2018) [469]	Glioblastoma (n = 193)	Necrosis	CD204	Macrophages tended to accumulate in perivascular and perinecrotic regions 13% $CD204^+$ macrophages co-express HIF1α
Annovazzi (2018) [447]	Glioblastoma (n = 35)	Necrosis	CD163	$CD163^+$ macrophages were found in both perivascular and perinecrotic regions (within large areas of tumour necrosis almost all cells were macrophages)
Chen (2019) [462, 470]	Cervical carcinoma (n = 90)	CA IX	CD163	Positive correlation between tumour CA IX expression and $CD163^+$ macrophage counts ($r = 0.6538$, $P < 0.0001$) $CD163^+$ macrophages infiltrated the stroma surrounding cancer cell nests that expressed CA IX but not around those that did not express CA IX
Maeda-Otsuka (2019) [471]	Angiosarcoma (n = 5)	HIF1α	CD163 CD204	$CD163^+$ and $CD204^+$ macrophage counts were higher in tumour regions expressing HIF1α as compared to those not expressing HIF1α ($P < 0.05$)
Zhu (2019) [472]	Ovarian carcinoma (n = 28)	HIF1α	CD163	$CD163^+$ macrophage infiltration was higher in tumours with high HIF1α expression as compared to those with low HIF1α expression ($P < 0.001$)
Zheng (2020) [473]	NSCLC (n = 104)	HIF1α CA IX	CD163	Positive correlation between tumour HIF1α expression ($r = 0.217$, $P = 0.027$) and tumour CA IX expression ($r = 0.242$, $P = 0.013$) and $CD163^+$ macrophage counts

CA IX – carbonic anhydrase 9, CCRCC – clear cell renal cell carcinoma, HIF1α – hypoxia-inducible factor 1 alpha, HLA-DR – human leukocyte antigen-DR isotype, NSCLC – non-small cell lung carcinoma

A number of different factors contribute to the localisation of TAM within hypoxic tumour regions; examples immediately linked to low oxygenation include VEGF [474-476], CXCL12/stromal cell-derived factor 1 (SDF1) [477] and colony stimulating factor 1 (CSF1)/macrophage colony stimulating factor (M-CSF) [478]. The localisation of M2 TAM within hypoxic tumour regions is critical to their immunosuppressive phenotype, as illustrated by the effects of low oxygen [406, 411], lactic acid/lactate [411, 479, 480] and low pH [481, 482] on TAM gene expression and the observation that myeloid cell-specific deletion of *Nrp1* (a component of the receptor for the macrophage chemoattractant SEMA3A) blocks their recruitment to hypoxic tumour regions and thereby potentiates anti-tumour immunity [405]. Accordingly, murine models indicate that both HIF1α and HIF2α are essential for macrophage-mediated immunosuppression within tumours and loss of either isoform in macrophages delays tumour growth [483, 484]. Indeed, human histological studies have reported that TAM express HIFα, in particular the HIF2α isoform [420, 425, 432, 485-497]. Nevertheless, despite this paradigm, it has been reported that M2 macrophages can also be found within perivascular niches [498, 499], as outlined above.

My observations suggest that low oxygenation alone may be insufficient to recruit macrophages and that necrosis may be the primary mediator driving the recruitment of myeloid cells to hypoxic tumour regions. Indeed, high-mobility group box 1 protein (HMGB1), a nuclear chromatin-associated protein, acts as a DAMP when released by dying cells and promotes migration of macrophages towards areas of tumour hypoxia, where they adopt a M2-like phenotype [500-503]. Once recruited, HMGB1 then decreases expression of CCR2 (the receptor for the chemokine CCL2/monocyte chemoattractant protein 1 [MCP1]) in TAM, contributing to their retention within hypoxic tumour regions [504]. Furthermore, necrotic debris released in hypoxic/anoxic tumour regions also promotes M2 macrophage polarisation

[446]. The precise topographical distribution of macrophages and neutrophils in necrotic regions of human CCRCC demonstrated in this chapter, with neutrophils present in the centre of a necrotic area surrounded by macrophages at the junction between necrotic and hypoxic but viable tumour cells, has previously been reported in murine prostate cancer [505] and likely reflects the ability of neutrophils to survive under severe hypoxia [206-209].

Overall, the results presented in this chapter demonstrate a skewing towards myeloid cells and away from lymphoid cells within hypoxic/necrotic tumour regions. This raises the possibility that hypoxic tumour regions represent immunoprivileged niches which foster immune evasion and resistance to immunotherapy. Thus, influencing the localisation of leukocytes, as well as their number and activity, is likely to contribute to effective immunotherapy. Interestingly, patterns of $CD8^+$ T lymphocyte distribution were fairly consistent across tumours regardless of overall density of these cells (**Figure 1.5B**). This observation suggests that therapies that either overturn these distributions, or simply amplify overall infiltration, are likely to increase absolute $CD8^+$ T lymphocyte numbers within the most hypoxic tumour regions. Importantly, these findings also suggest that analysis of tumour hypoxia at the microregional scale (as provided by histology) will be required to identify small islands of biologically/clinically relevant hypoxia that are likely to be missed by more global assessment strategies (such as cross-sectional imaging).

Clinical relevance

The distinct distributions of different subsets of tumour infiltrating leukocytes are of direct clinical and therapeutic relevance. Administration of pharmacological agents that inhibit HIF signalling can reduce macrophage infiltration into, and thus slow growth of, murine tumours through reduced secretion of VEGF [506] and CSF1 [507] whilst cyclooxygenase-2 inhibition

has been reported to prevent hypoxia-induced M2 polarisation of TAM [508, 509]. Alternatively, the observation that macrophages infiltrate necrotic areas has been exploited to use them to deliver anti-cancer therapies to hypoxic tumour regions [436, 510-513]. Furthermore, the selective accumulation of M2-like TAM within severely hypoxic tumour regions with sub-physiologic oxygen levels means that the administration of macrophage-specific radiolabelled antibodies [404] or genetic engineering of macrophages to express a synthetic reporter on adoption of an M2-like phenotype [413] may facilitate tumour detection via non-invasive imaging.

The hypoxic TME can also be exploited to manipulate CTL function. CAR T lymphocytes are T lymphocytes that have been genetically engineered to possess a modified TCR that recognises an antigen expressed on tumour cells. However, if expression of this antigen is also shared by non-neoplastic tissues, serious toxicity can arise from 'on-target, off-tumour' effects (such as the bile duct damage that prevented further administration of anti-CA IX CAR T lymphocytes in metastatic CCRCC [514]). Given that tumours contain regions of hypoxia that are more profound than normal tissues, oxygen sensitive CAR T lymphocytes have been developed by fusing the CAR component with a HIF1α oxygen-dependent degradation domain (but excluding the domains that endow HIF with transcriptional activity) [515]. In theory, this approach should ensure that the CAR T lymphocytes are only active within areas of hypoxia sufficient to stabilise HIF. Whilst these cells have been shown to be functional in *in vitro* studies, the limited penetration of CTL into hypoxic tumour regions may restrict their *in vivo* efficacy. Indeed, given that hypoxia is generally considered to be detrimental to CTL function, other studies have investigated approaches to potentiate the cytotoxicity of these cells within hypoxic tumour regions. Transgenic engineering of CTL to contain an HRE-IL-2 sequence endows these cells with hypoxia resistance; increased synthesis of IL-2 upon HIF stabilisation

augments their survival and proliferation whilst sustaining their effector functions under oxygen levels as low as 1% [306]. In murine adoptive transfer experiments, pre-conditioning of T lymphocytes by pharmacological PHD inhibition with DMOG [516] or hypoxic culture [314] favours enhanced cytolysis and improves tumour control.

Strengths, limitations and future directions

I have taken great care to optimise and validate SIGHT and, together with collaborators, now intend to use this pipeline to undertake more sophisticated analyses of leukocyte distribution. Simple metrics, such as the cell densities presented here, fail to describe fully the complexity of immune cell spatial patterns. Whilst density provides information as to the number of cells within a given area, it is not informative about how clustered or dispersed they are (**Figure 1.15A**). Although outside of the scope of this thesis, capturing of the exact (x, y) co-ordinates of leukocytes in the samples described in this chapter has been used to develop novel mathematical descriptors of their infiltration into tumours. For example, combining several different spatial statistics, which measure various aspects of clustering and dispersion of points, can derive a single value that is able to categorise tumour images into qualitatively similar groups (**Figure 1.15B**) [517]. In this study, I verified the accuracy of image classification and provided a human assessment of leukocyte infiltration against which to compare the statistical results, thereby ensuring the robustness of our findings. Importantly, the statistical approach adopted provides an estimate of the error associated with each score and we identified parameters that were suggestive of incorrect image classification. Thus, in future, it is conceivable that automated image analysis could proceed without time-consuming visual assessment of its accuracy, with only outliers being flagged as requiring human review. In this way, we could apply our approaches at speed to much larger datasets and correlate different spatial statistics with associated biological or clinical information.

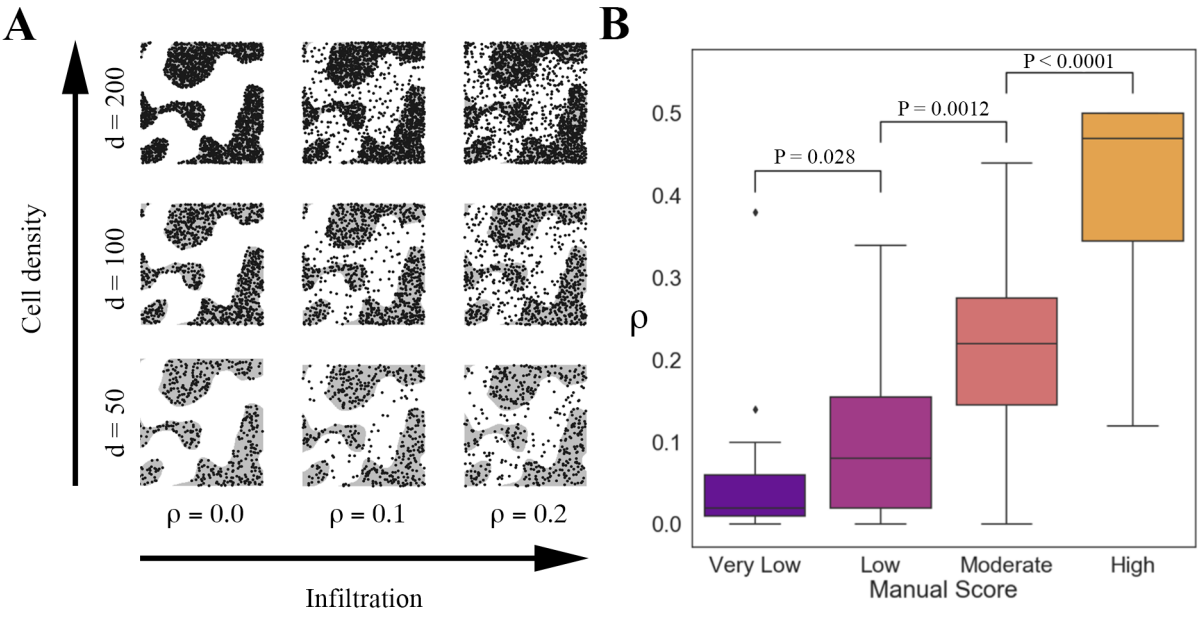


Figure 1.15 – Development of novel mathematical descriptors of immune cell distribution within tumours

(A) A series of images demonstrating how immune cell infiltration into a tumour cell nest changes as the immune cell density (d [cells per mm^2]) and the proportion of cells in the tumour cell nest as compared to stroma (p), vary. In each image, the grey region corresponds to stroma whilst the white region corresponds to the tumour cell nest. These infiltration patterns illustrate that cell density alone does not capture immune cell localisation adequately. (B) By applying a combination of spatial statistics to the (x, y) co-ordinates of immune cells within histology images, the parameter p can be predicted and this value identifies statistically significant differences between manually assigned categories of the extent of immune cell infiltration into tumour cell nests.

In future, we aspire to develop SIGHT into freely available software that integrates advanced statistical tests into the image analysis process in a user-friendly manner. Although computational registration of multiple serial sections cut from the same tissue block is an established methodology to generate virtual multi-labelled output images [275, 518] and a strong correlation exists between pimonidazole scores from two sequential tumour sections

[519], the work presented in this chapter would be improved by adopting multiplex immunohistochemistry/immunofluorescence approaches (as reviewed in [520, 521]), which were not widely available at the beginning of my fellowship four years ago. Importantly, a recent systematic review and meta-analysis demonstrated that multiplexed histological analysis of the spatial distribution and protein co-expression of immune cells across ten different solid tumour types outperformed PD-L1 immunohistochemistry, assessment of tumour mutational burden and gene expression profiling in predicting response to ICB [522]. Reassuringly, the SIGHT pipeline can be easily adapted to analyse such images and future work will focus on images generated through such technologies. Ultimately, we aspire to apply these approaches to larger patient cohorts in order to test the prognostic significance of different descriptors of leukocyte distribution and to undertake in-depth spatial profiling of the changes that occur within the TME as a consequence of therapeutic interventions.

A major limitation of this work is the small sample size, which limits my ability to make wider extrapolations from the results presented. However, administration of pimonidazole to human patients prior to surgery is logistically complex, restricting the number of tumours available for analysis. Thus, firm conclusions cannot be reached until these findings have been verified in a larger cohort of patients. To this end, I have recently gained access to a further 55 pimonidazole-treated HNSCC samples from Manchester, which, together with these Oxford samples, have associated clinical outcome data. The microregional approach that we have adopted will allow in-depth analysis of the spatial heterogeneity of both immune cell infiltration and tumour hypoxia, as well as the interaction between these parameters. However, histological images do not provide information on the highly dynamic changes occurring within tumours. Instead, these histopathological observations should be correlated with

existing, and form the basis for future, mechanistic experimental studies that might better explain tumour infiltrating leukocyte distributions.

Due to the pseudohypoxic phenotype of CCRCC, common endogenous markers cannot be used to identify hypoxic regions. I was unable to identify pimonidazole-treated CCRCC cohorts from which to obtain tissue and time constraints precluded the obtainment of the necessary funding and ethical permissions to accumulate my own cohort *de novo*. Instead I chose to utilise the distance from blood vessels to necrosis as a surrogate for a hypoxic gradient. This is based on the assumptions that (i) tumour vessels are adequately perfused with oxygenated blood and (ii) necrosis has arisen secondary to acute anoxia. However, dysfunction of tumour vessels can also lead to perivascular hypoxia [523] whilst necrosis in CCRCC can occur secondary to events other than microregional hypoxia, for example, widespread thrombo-embolic infarction and immune-related destruction [524]. Furthermore, reliance on CCRCC specimens with necrosis to map hypoxic gradients biases analysis towards a population of clinically more aggressive tumours and precludes analysis of the majority of CCRCC which do not display necrosis [525]. Therefore, administration of pimonidazole or EF5 to CCRCC patients to facilitate accurate mapping of tumour hypoxia would be of significant future interest and allow more direct comparison between tumour types.

Chapter 2

Chapter aim

To investigate whether the hypoxic TME in human NSCLC can be altered by administration of the anti-malarial drug atovaquone and whether this pharmacological intervention affects the immune contexture of these tumours.

Introduction

The importance of oxygen in influencing response to cancer treatment has fostered interest in developing therapies that reduce tumour hypoxia (as reviewed in [91, 526, 527]). Several studies report small but consistent improvements in outcome with this approach, particularly in combination with radiotherapy for the treatment of HNSCC [528]. Despite this evidence, and the clear negative prognostic significance of tumour hypoxia, these treatments have not become established in widespread clinical practice. Given that oxygen availability is the net balance between supply and demand, tumour hypoxia can be reduced, and even eliminated entirely, through increasing oxygen delivery to, and/or reducing oxygen consumption by, cells within a tumour. A number of strategies can be adopted to achieve this, as summarised below.

Improving tumour oxygenation

Increasing oxygen supply

Given the high prevalence of anaemia in cancer patients, several studies have investigated the effects of administering exogenous EPO [529, 530]. Whilst these report mixed results, there is no strong evidence of clinical benefit and several studies have reported adverse effects (most commonly thrombotic in nature) and/or poorer tumour-related outcomes (likely due to the pleiotropic effects of EPO, which might actually promote tumour progression by a number of

mechanisms including stimulating tumour cell proliferation and resistance to apoptosis) [530, 531]. Administering supplemental normobaric oxygen (100% O_2 at sea level pressure of 1 atmosphere) has only a small effect on oxygen supply, since haemoglobin is already saturated when breathing room air, and cannot eradicate tumour hypoxia [532]. Hyperbaric oxygen therapy (HBOT) involves the administration of oxygen above atmospheric pressure, increasing the amount of dissolved oxygen in plasma and thereby improving haemoglobin-independent oxygen supply to hypoxic tumour regions (predominantly targeting diffusion-limited chronic hypoxia) [533, 534]. A systematic review of studies combining HBOT with radiotherapy reported some benefits in head and neck and uterine cancer but with a risk of significant adverse effects including oxygen toxicity seizures and severe radiation injury [535]. Moreover, the practical complexities of administering HBOT [536] have limited its adoption. In some studies, carbogen (95% O_2 and 5% CO_2) is administered instead of pure oxygen; the addition of carbon dioxide maintains tumour perfusion by abrogating oxygen-induced vasoconstriction and also shifts the haemoglobin-oxygen dissociation curve to the right, further helping to increase oxygen delivery [537]. Carbogen can be co-administered with nicotinamide, a form of vitamin B_3 with additional vasodilatory effects [538, 539], and accelerated radiotherapy with this combination is referred to as ARCON (Accelerated Radiotherapy plus CarbOgen and Nicotinamide) [540]. In a randomised phase III clinical trial involving 345 laryngeal cancer patients, ARCON therapy led to improved five-year loco-regional control and disease-free survival as compared to accelerated radiotherapy alone, but only amongst patients with pre-treatment anaemia [541]. Finally, regular exercise has been shown to reduce hypoxia within murine tumours [542-545] and this approach is currently being tested in the setting of human prostate cancer (ClinicalTrials.gov Identifier: NCT03675529).

Reducing oxygen demand

An alternative approach to reducing tumour hypoxia is to lower the oxygen demand of cells within the TME (as reviewed in [546]). In particular, reduction of oxygen consumption by better oxygenated perivascular cells should increase the amount that can diffuse to less oxygenated cells located at a distance from blood vessels. Increasing tumour oxygenation without the administration of supplemental oxygen is an appealing therapeutic strategy, since long-term oxygen administration is associated with significant toxicities including hyperoxic lung and liver injury [547, 548]. Furthermore, mathematical modelling suggests that reducing oxygen consumption may be more effective at alleviating tumour hypoxia than administering supplemental oxygen (potentially up to thirty times more efficient), because it serves to both preserve oxygen levels within distal tumour microvasculature and to reduce oxygen gradients within tumour tissue [549]. In these simulations, a 30% reduction in oxygen consumption by cancer cells was predicted to eliminate tumour hypoxia entirely.

Since the major mechanism of cellular oxygen consumption is oxidative phosphorylation within mitochondria, ETC inhibitors, such as arsenic trioxide [550] and papaverine derivatives [551], have been shown to reduce tumour hypoxia and to sensitise responses to radiotherapy in mouse models but their administration can be associated with significant toxicity [552]. Other compounds, including PI3K inhibitors [553-555], non-steroidal anti-inflammatory drugs [556] and glucocorticoids [557] also alleviate tumour hypoxia by reducing cellular oxygen consumption but the exact mechanisms underpinning their effects are uncertain and concerns exist about toxicities when administered to humans at clinically relevant doses. The commonly prescribed anti-diabetic drug metformin also reduces tumour cell oxygen consumption and tumour hypoxia in murine models through inhibition of mitochondrial complex I [558-560] and is discussed further below.

Targeting tumour vasculature

Whilst anti-VEGF monotherapy has generally not proved to be successful in treating human tumours, VEGF inhibition combined with chemotherapy has been shown to be effective in metastatic colorectal cancer [561]. These apparently contradictory findings suggest that inhibiting angiogenesis can improve tumour perfusion and drug delivery. This process, termed 'vascular normalisation', involves a reduction in microvessel diameter and tortuosity, trimming of immature vasculature and increased pericyte coverage leading to vessel maturation [562, 563]. Furthermore, vascular normalisation can also reduce interstitial fluid pressure within tumours, further improving perfusion and drug penetration [564]. In murine tumour models, this approach has been shown to provide a 'normalisation window' in which tumour hypoxia is reduced and combination therapies, such as radiotherapy [565] and chemotherapy [566], can be administered to best effect. Evidence in glioblastoma demonstrates that whilst only a subset of patients responds to vascular normalisation therapy, overall survival is improved amongst those that do [567]. This is currently a very active field of research, with ongoing studies investigating the effects of combinatorial therapy with a range of other modalities including immunotherapy (as reviewed in [568]).

Effects of altering tumour hypoxia on anti-tumour immunity

As tumour hypoxia is generally believed to inhibit anti-tumour immunity, reducing this may potentiate immune responses. Administration of supplemental oxygen ('respiratory hyperoxia'), has been demonstrated to enhance anti-tumour immune responses in mice [308, 569]. Intradermal MCA205 fibrosarcoma tumours, usually severely hypoxic, displayed a reduction in hypoxia and levels of the immunosuppressive metabolite adenosine, as well as lower angiogenesis and up-regulation in MHC class I expression, amongst mice breathing 60% O_2 as compared to those breathing room air. Mice bearing pulmonary tumours (established by

intravenous injection of MCA205 or B16 melanoma cells) and breathing 60% O_2 also demonstrated reduced tumour size and longer overall survival. These benefits were not observed when tumours were grown in immunocompromised mice, demonstrating that an intact immune system is required. Furthermore, respiratory hyperoxia produced no additional beneficial effects in mice lacking adenosine A2A receptor (A2AR), activation of which interferes with the trafficking and activities of T lymphocytes and NK cells [351, 352, 570], implicating alleviation of the hypoxia-adenosine-A2AR immunosuppressive axis as a key mechanism underpinning the beneficial effects of respiratory hyperoxia. Alleviating tumour hypoxia also affected T lymphocyte trafficking, leading to increased recruitment of $CD8^+$ T lymphocytes (which were also more activated as evidenced by increased expression of CD44, CD69 and IFNγ) and a reduction in T_{Reg} with lower expression of CTLA-4, which is critical for their immunosuppressive function [571]. Eradication of lung metastases could be achieved by the addition of immunotherapy (combined anti-CTLA-4 and anti-PD-1 ICB) to hyperoxic breathing. However, it is possible that the higher affinity for oxygen of human haemoglobin means that the benefits of hyperoxic breathing reported in this study will not directly translate into clinical benefits (haemoglobin P_{50}, the oxygen tension at which haemoglobin is 50% saturated, is ~26 mmHg in humans but ~40 mmHg in mice) [527]. Another approach to increasing tumour oxygenation is through the use of oxygen-delivering nanoplatforms: in pre-clinical studies, these nanoparticles, which can simultaneously facilitate drug delivery, have been shown to alleviate tumour hypoxia and potentiate anti-tumour immunity through synergy with chemotherapy [572, 573], radiotherapy [574-576], photodynamic therapy [577-583] and immunotherapy [584].

Administration of the anti-diabetic drug metformin (which lowers oxygen consumption by tumour cells) also reduced tumour hypoxia and promoted vascular normalisation in murine

B16 melanoma tumours [560]. These changes were accompanied by increased effector T lymphocyte infiltration (with these cells being more proliferative, less apoptotic and expressing higher levels of granzyme B, IFNγ and tumour necrosis factor alpha [TNFα]) and reduced T_{Reg} and MDSC infiltration. Collectively, these effects were associated with an improved tumour response to anti-PD1 ICB. However, biguanides have pleiotropic effects (extending far beyond alteration of cellular metabolism to include effects on angiogenesis and apoptosis) [585-587], meaning that it is unlikely that their influence on anti-tumour immunity is mediated solely through reduced tumour hypoxia (indeed, their immunostimulatory properties have been reported in other murine studies that have not focused on effects on tumour oxygenation [588-594]). Administration of metformin to human HNSCC patients resulted in a significant increase in CTL infiltration and a significant decrease in T_{Reg} [595]; there were no effects on infiltration by $CD163^+$ macrophages or on PD-L1 expression [596]. Metformin has also been reported to inhibit the function of MDSC in human ovarian cancer patients by reducing expression and activity of the adenosine generating ectoenzymes CD39 and CD73, reportedly via HIF1α inhibition [597]. This effect was associated with improved CTL-mediated anti-tumour immunity and correlated with longer overall survival in diabetic ovarian cancer patients. Phase II trials investigating the effects of metformin on tumour hypoxia in locally advanced cervical carcinoma (ClinicalTrials.gov Identifier: NCT02394652) and the combination of metformin and nivolumab for NSCLC (ClinicalTrials.gov Identifier: NCT03048500) are currently in progress.

Finally, several pre-clinical studies have demonstrated that vascular normalisation can improve tumour oxygenation, increase T lymphocyte infiltration into tumours and, when tested, potentiate immunotherapy [360, 361, 566, 598-601]. Importantly, IFNγ-secreting T

lymphocytes are critical in the mutual regulation of vascular normalisation and immunostimulation and their activation via ICB enhances both processes [602, 603].

Overall, the studies discussed above support the concept that drugs that reduce tumour hypoxia can potentiate anti-tumour immunity. Despite these promising pre-clinical results, only a handful of ongoing human studies are investigating whether hypoxia reduces the efficacy of ICB. The ImmunoModulation by the Combination of Ipilimumab and Nivolumab Neoadjuvant to Surgery In Advanced or Recurrent Head and Neck Carcinoma (IMCISION) trial is evaluating neoadjuvant combination ICB with nivolumab and ipilimumab prior to surgery in advanced or recurrent HNSCC and will compare tumour infiltrating leukocytes in pre- and post-treatment biopsies taken from matched hypoxic and non-hypoxic tumour areas as guided by positron emission tomography-computed tomography (PET-CT) imaging (ClinicalTrials.gov Identifier: NCT03003637). In another trial, the addition of metformin to pembrolizumab for the treatment of advanced melanoma is being studied and the effects of this combination on tumour hypoxia will be assessed by immunohistochemistry (ClinicalTrials.gov Identifier: NCT03311308). A further study is evaluating a combination of nivolumab and sitravatinib (a multiple tyrosine kinase inhibitor) for the treatment of oral SCC and will monitor dynamic changes in tumour hypoxia by performing [^{18}F]fluoroazomycinarabinofuranoside (FAZA) PET-CT scanning both before and after immunotherapy (ClinicalTrials.gov Identifier: NCT03575598).

The ATOM (Atovaquone as Tumour HypOxia Modifier) study

Lung cancer is the commonest cause of cancer incidence and mortality worldwide [252]. Traditionally, lung cancer is classified histologically as either small cell lung cancer, a highly aggressive neuroendocrine tumour, or, more commonly, NSCLC, a group which comprises a

heterogenous collection of histological subtypes amongst which adenocarcinoma and SCC predominate [604]. The majority of NSCLC are hypoxic [81, 486], a feature that is associated with poor prognosis [605-608], suggesting that targeting this may be of therapeutic benefit (as reviewed in [609]).

Atovaquone, a ubiquinone analogue traditionally used as an anti-malarial medication, decreases cellular oxygen consumption by inhibiting mitochondrial complex III and has been shown to eradicate hypoxia in tumour spheroids, to reduce hypoxia in tumour xenografts and, when combined with radiotherapy, to slow xenograft growth rate [610]. The ATOM study, designed and co-ordinated by Professor Geoff Higgins (Department of Oncology, University of Oxford), was an open-label, 'window of opportunity' study of the effects of a short course of atovaquone on tumour hypoxia in patients with operable NSCLC (ClinicalTrials.gov Identifier: NCT02628080) (a 'window of opportunity' study involves treatment naïve patients receiving an experimental intervention in the time period between cancer diagnosis and commencement of conventional treatment [611]). Patient eligibility criteria are described in **Table 2.1**.

Table 2.1 – ATOM (Atovaquone as Tumour HypOxia Modifier) study patient eligibility criteria

Inclusion criteria	**Exclusion criteria**
Confirmed or suspected non-small cell lung cancer considered suitable for surgical resection by the lung cancer multidisciplinary team	Previous systemic chemotherapy or biological therapy within 21 days of commencing atovaquone treatment

Age ≥ 18 years	Treatment with other investigational agents, or participation in another interventional clinical trial, within 28 days of recruitment
Eastern Cooperative Oncology Group performance status of 0-2	Known previous adverse reaction to atovaquone or its excipients
At least one measurable lesion > 2 cm in maximal length on diagnostic imaging performed within 60 days of study screening	Co-administration of known electron transport chain inhibitors (including metformin)
No haematological or biochemical blood abnormalities	Impaired gastrointestinal function that may significantly alter absorption of atovaquone
Written informed consent	Administration of warfarin in the 14 days prior to starting atovaquone
Patients willing and able to comply with study protocol	Active hepatitis, gallbladder disease or pancreatitis

The study was designed to enrol two sequential cohorts: Cohort 1 comprising 15 patients receiving atovaquone treatment and Cohort 2 comprising 15 patients not receiving treatment. All patients received oral pimonidazole at a dose of 500 mg/m^2 for self-administration 16-24 hours prior to surgery. The study protocol showing all study interventions is depicted in **Figure 2.1**.

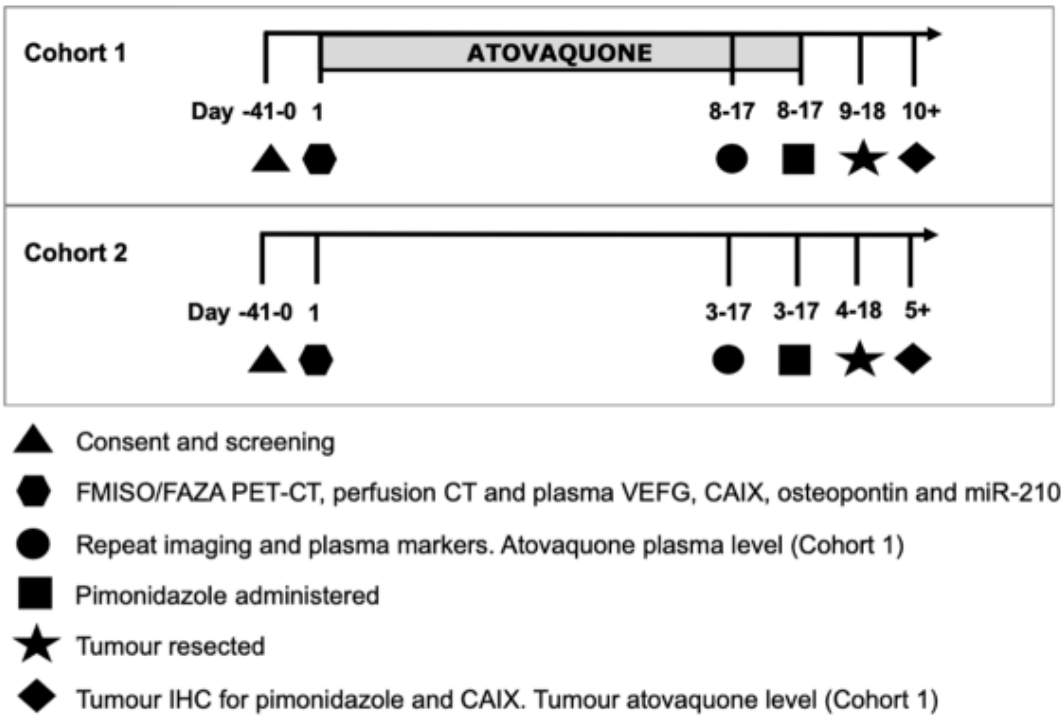


Figure 2.1 – ATOM (Atovaquone as Tumour HypOxia Modifier) study protocol
CAIX – carbonic anhydrase 9, CT – computed tomography, FAZA – [^{18}F]fluoroazomycinarabinofuranoside, FMISO – [^{18}F]fluoromisonidazole, IHC – immunohistochemistry, PET-CT – positron emission tomography-computed tomography, VEGF – vascular endothelial growth factor

In this chapter, I describe the analysis of the immunohistochemistry component of the ATOM study. Immediately after resection, the surgical specimen (usually a lobectomy or pneumonectomy) was inflated with 10% NBF and left to fix at room temperature. During subsequent pathological dissection, the specimen was oriented utilising pre-operative cross-sectional imaging and sutures placed by the surgeon at the time of resection. This was undertaken to facilitate subsequent spatial comparison between results of hypoxia PET-CT imaging, immunohistochemistry and gene expression analysis. Each specimen was cut from

superior to inferior into 5 mm slices (**Figure 2.2**) which were then subdivided into standard tissue cassettes.

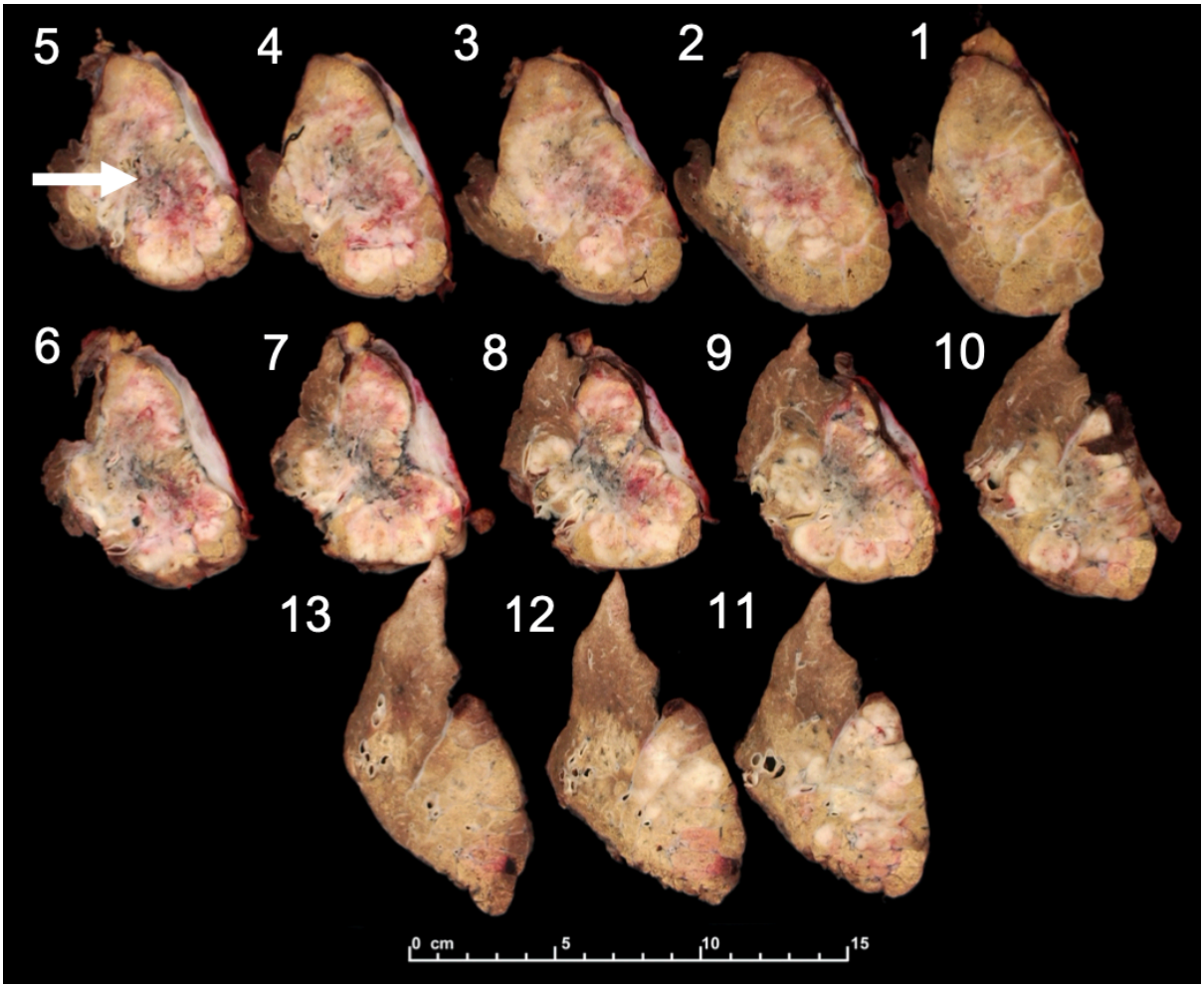


Figure 2.2 – Macroscopic image of a sliced lung resection specimen

In this specimen, a right upper lobectomy cut into thirteen consecutive 5 mm slices, tumour is present in slices 1-12 and measures 80 mm x 60 mm in maximum dimension. Central tumour necrosis is identified in slice five (arrow).

For histological analysis, all blocks from three slices per tumour (representing the superior, middle and inferior thirds of the tumour) were selected for immunohistochemical staining for pimonidazole, CA IX and the vascular markers CD31 and CD146 (for representative images of immunohistochemical staining and image analysis pipeline see **Appendix 5**). Across all patients, the number of blocks per slice ranged from 1 to 9 (median = 4) and the number of

total blocks ranged from 2 to 18 (median = 12). To investigate the effects of atovaquone on anti-tumour immunity, sections from one representative block per patient were also stained for the immunological markers CD8, FOXP3, CD68 and PD-L1.

Results

Patient demographics

29 patients were suitable for full histological analysis (15 patients in Cohort 1 and 14 patients in Cohort 2). All of these patients received oral pimonidazole 16-24 hours before surgery. However, due to last minute rescheduling of surgery, two patients in Cohort 1 and three patients in Cohort 2 could not be included in analysis of pimonidazole labelling. A further group of 14 patients with insufficient hypoxic volume on baseline hypoxia PET-CT imaging were not included in the main study but one block from each of their tumours was processed for limited histological analysis (Cohort 3). Of the 14 Cohort 3 patients, two received both atovaquone and pimonidazole prior to surgery (for patient and tumour characteristics see **Appendix 5**). Overall, treatment groups were reasonably well balanced with regards to age, smoking status and tumour stage; however, there were more males in the non-treatment group. Whilst adenocarcinoma was the commonest histological subtype in both groups, there were proportionally fewer adenocarcinomas in the non-treatment group, which contained more SCC and some rarer subtypes such as giant cell carcinoma, pleomorphic carcinoma and large cell neuroendocrine carcinoma.

Immediately after completion of baseline investigations, patients in Cohort 1 (and the two additional patients in Cohort 3) received 750 mg of oral atovaquone (GlaxoSmithKline, UK) twice a day until the evening prior to surgery. Median length of treatment was 12 days (range = 7-16 days); treatment duration varied due to different lengths of time between completion of

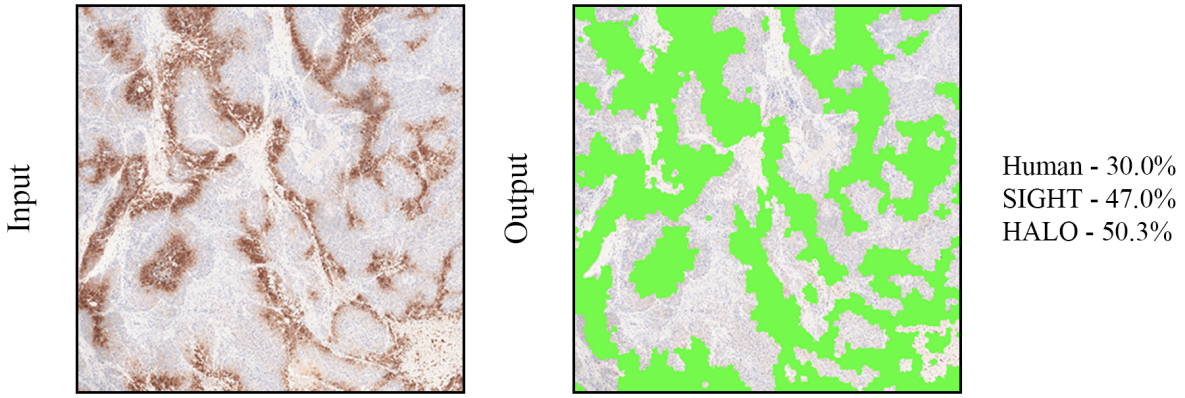
baseline investigations and surgery. Reassuringly, no correlation was found between length of treatment and plasma atovaquone levels and all patients had plasma levels at or above that required to reduce tumour cell oxygen consumption in pre-clinical studies (30 μM) [610].

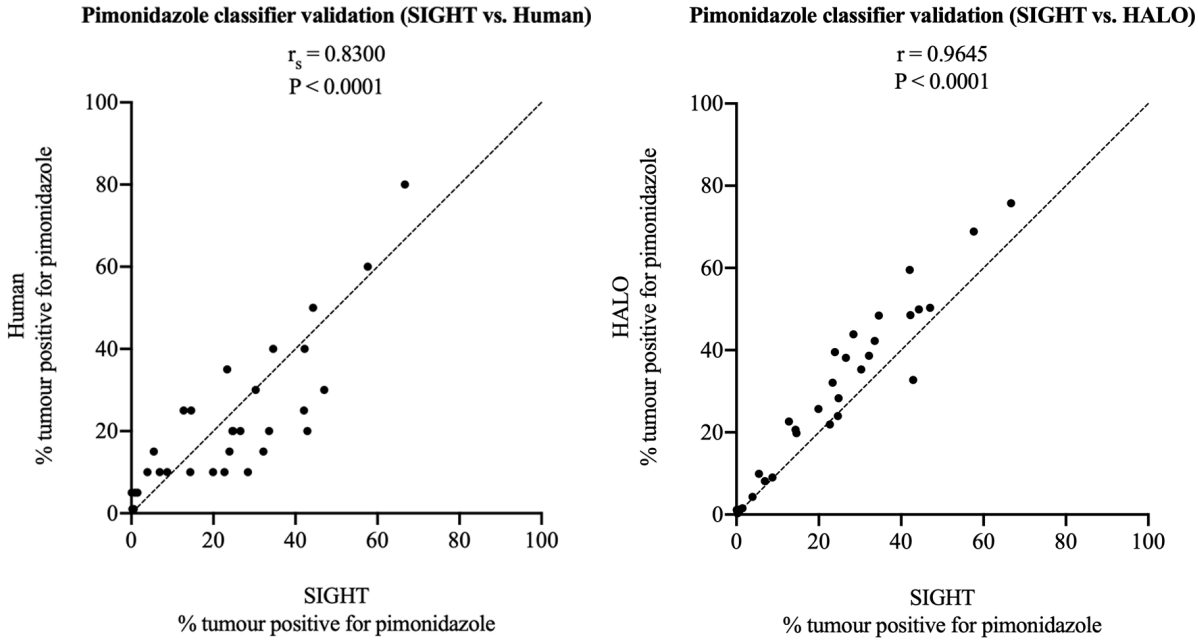
Classifier validation

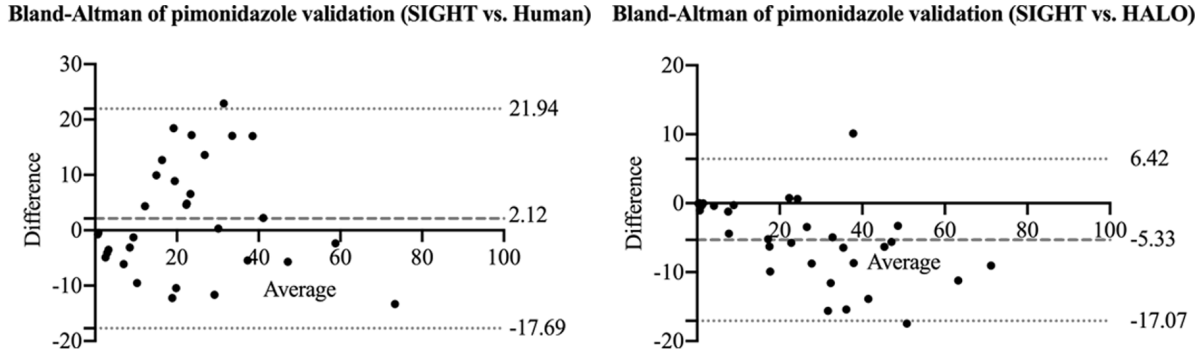
In order to assess the accuracy of our classifiers, we selected at random one representative image for each marker from each tumour. These images were then scored by SIGHT and compared to the manual scores of a Consultant Histopathologist (Dr Alistair Easton, Department of Oncology, University of Oxford) as well as automated scoring using classifiers that he trained in the commercial image analysis platform HALO (Indica Labs, UK). These comparisons demonstrate a strong positive correlation between SIGHT score for pimonidazole and CA IX and those provided by both human and HALO scoring (**Figure 2.3A and 2.3B**). Bland-Altman plots, which assess the agreement between two approaches, demonstrate small mean differences between SIGHT and other scoring methodologies (pimonidazole: +2.12% vs. human and -5.33% vs. HALO; CA IX: +4.25% vs. human and +4.42 vs. HALO). Moderate/strong positive correlations were also observed for scoring of the vascular markers CD31 and CD146 (**Figure 2.3C and 2.3D**). Bland-Altman plots demonstrate that for both markers, SIGHT scores tend to be lower than those provided by either human or HALO assessment (CD31: -8.59% vs. human and -10.64 vs. HALO; CD146: - 11.46% vs. human and -11.58% vs. HALO). A clear advantage of digital image analysis is the ability to provide a precise score whereas human scores display clear terminal digit bias (almost always ending in either 0 or 5) and thus fail to utilise the full continuum of possible values between 0% and 100%.

A

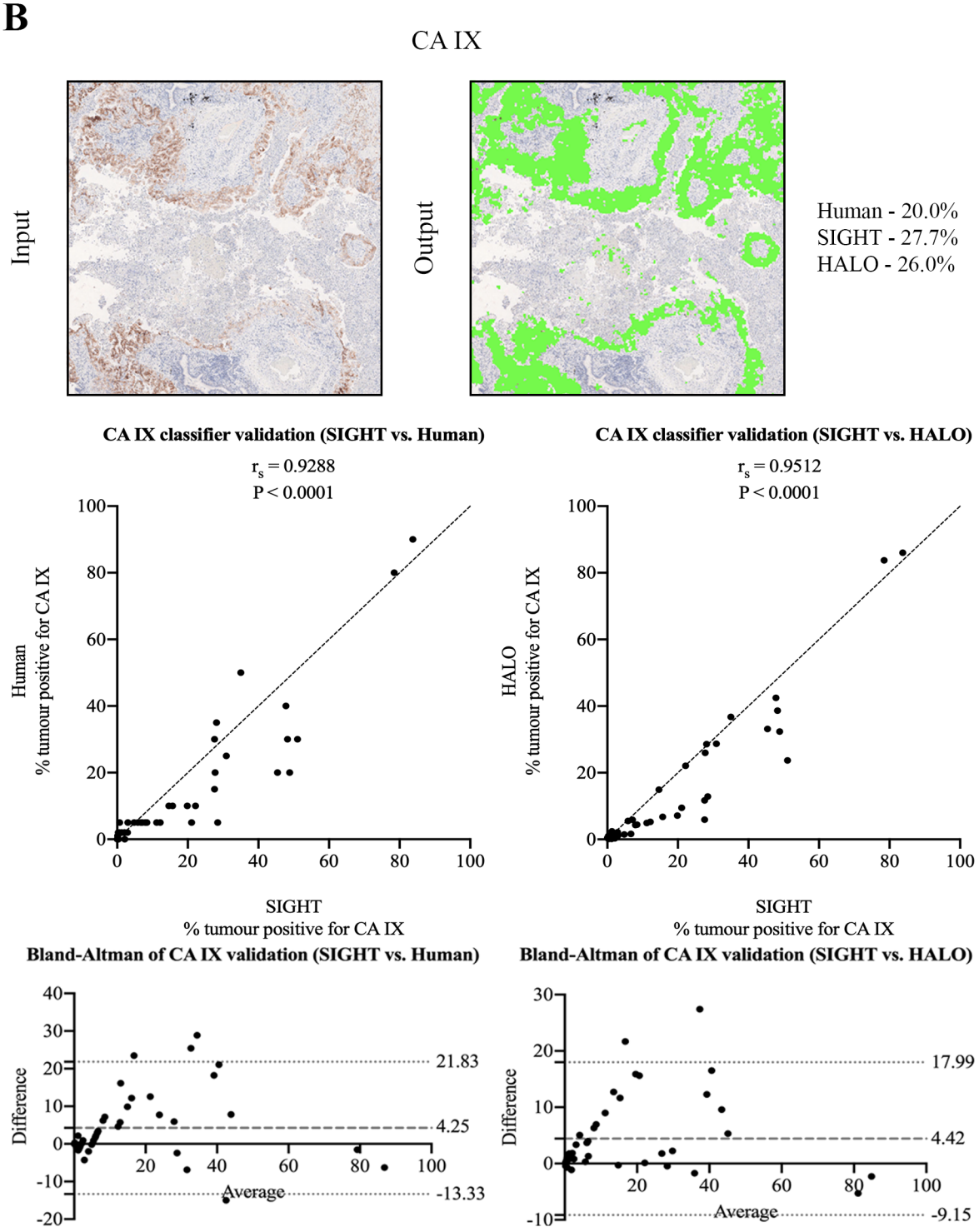
Pimonidazole



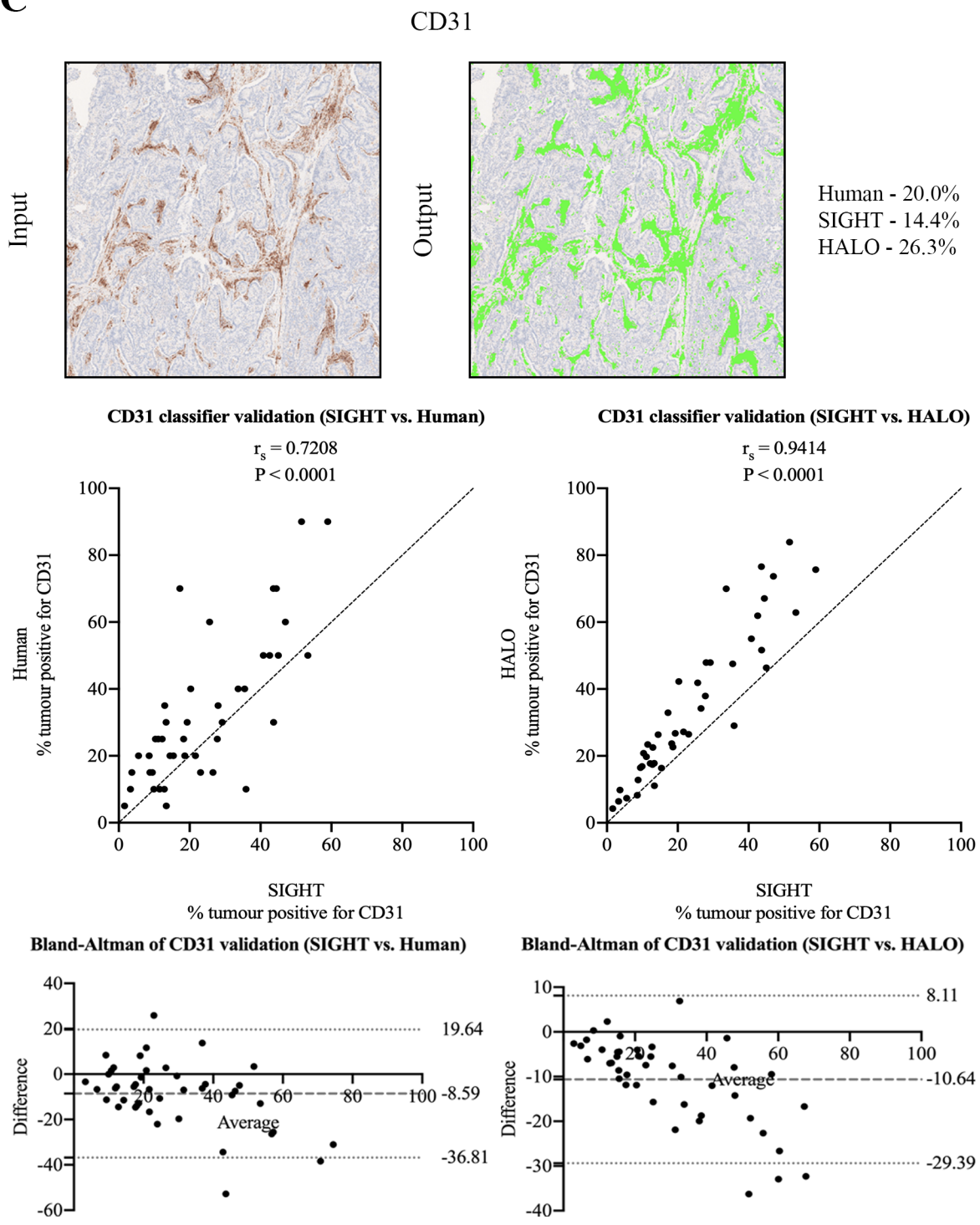




B


CA IX
Input
Output
Human - 20.0%
SIGHT - 27.7%
HALO - 26.0%
CA IX classifier validation (SIGHT vs. Human)
$r_s = 0.9288$
$P < 0.0001$
Human % tumour positive for CA IX
SIGHT % tumour positive for CA IX
CA IX classifier validation (SIGHT vs. HALO)
$r_s = 0.9512$
$P < 0.0001$
HALO % tumour positive for CA IX
SIGHT % tumour positive for CA IX
Bland-Altman of CA IX validation (SIGHT vs. Human)
Difference
Average
21.83
4.25
-13.33
Bland-Altman of CA IX validation (SIGHT vs. HALO)
Difference
Average
17.99
4.42
-9.15

C


CD31
Input
Output
Human - 20.0%
SIGHT - 14.4%
HALO - 26.3%
CD31 classifier validation (SIGHT vs. Human)
r_s = 0.7208
P < 0.0001
Human
% tumour positive for CD31
SIGHT
% tumour positive for CD31
CD31 classifier validation (SIGHT vs. HALO)
r_s = 0.9414
P < 0.0001
HALO
% tumour positive for CD31
SIGHT
% tumour positive for CD31
Bland-Altman of CD31 validation (SIGHT vs. Human)
Difference
Average
19.64
-8.59
-36.81
Bland-Altman of CD31 validation (SIGHT vs. HALO)
Difference
Average
8.11
-10.64
-29.39

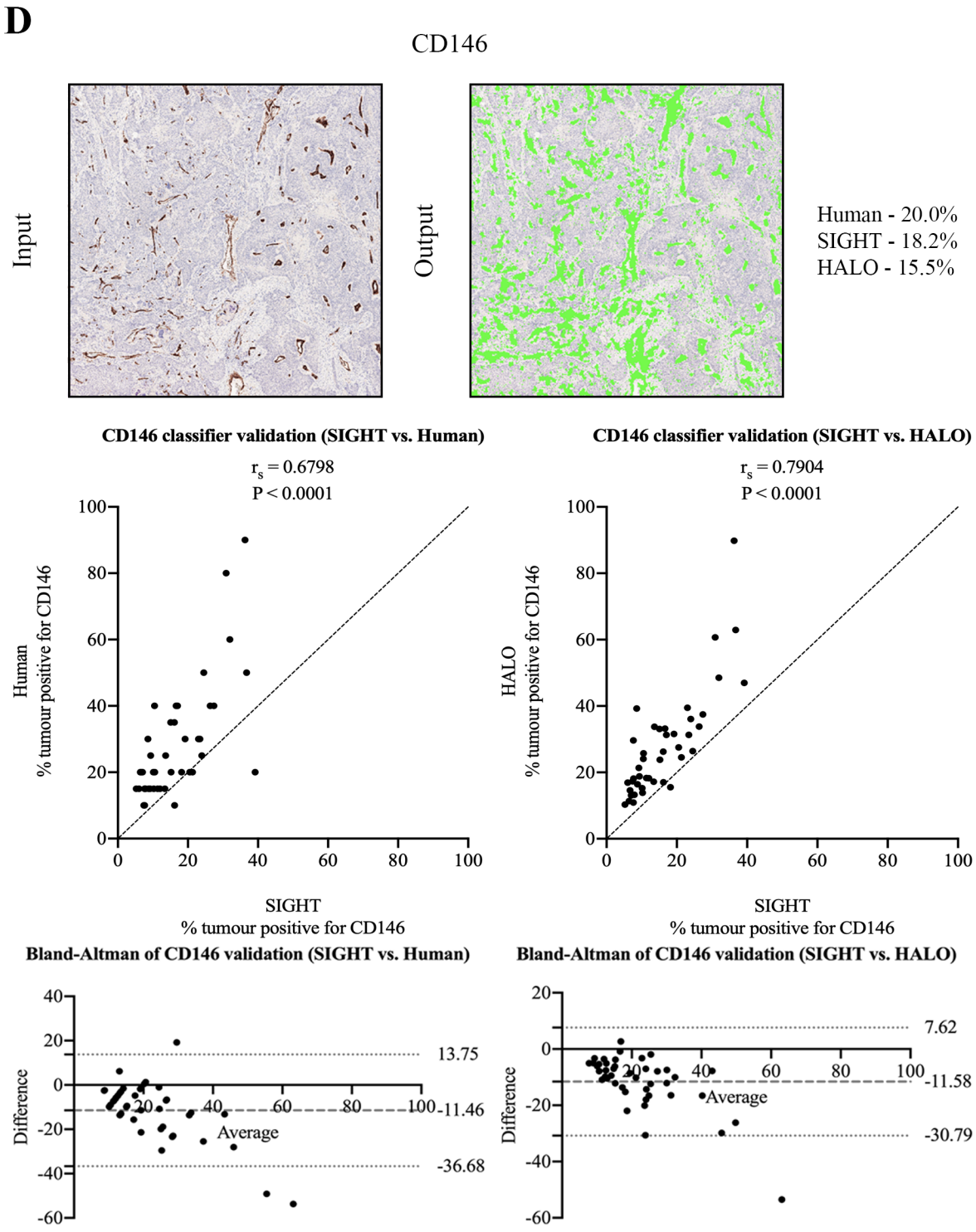


Figure 2.3 – Validation of pimonidazole, carbonic anhydrase 9, CD31 and CD146 classifiers

Correlation and Bland-Altman comparison of scoring performed by SIGHT and both human scoring and automated scoring by HALO software for the hypoxia markers (A) pimonidazole and (B) carbonic anhydrase 9 (CA IX) and the vascular markers (C) CD31 and (D) CD146. In

each scatter (XY) plot, the dashed diagonal line represents the line of equality. Data presented are the Pearson correlation coefficient (r) or Spearman's rank correlation coefficient (r_s) and associated P value. Below each scatter plot is the associated Bland-Altman plot in which the X axis represents the average of the two score ([SIGHT score + comparator score]/2) whilst the Y axis represents the difference between the two scores (SIGHT score – comparator score). In these plots, the dashed horizontal line represents the mean difference in scores between SIGHT and either human or HALO scores whilst the dotted horizontal lines represent the 95% confidence intervals for this difference.

Overall, these data demonstrate that scores provided by SIGHT are comparable to those provided by an expert pathologist when performing either manual scoring or automated scoring with commercial image analysis software.

Tumour hypoxia

Mean whole tumour pimonidazole and CA IX hypoxic fractions for atovaquone treated and untreated patients are shown in **Table 2.2**. Five patients who were subject to an unanticipated delay in surgery after pimonidazole administration were excluded from analysis of this marker.

Table 2.2 – Quantification of hypoxia markers in the ATOM (Atovaquone as Tumour HypOxia Modifier) study

Patient identification	Pimonidazole hypoxic fraction (%)	CA IX hypoxic fraction (%)
Atovaquone treatment		
10001	11.0	15.0
10003^	49.4	2.7
10004	23.3	30.7
10005	16.3	4.2
10006	20.6	15.6
10007^	31.1	9.2
10008	44.8	3.3

10009	50.6	62.6
10010	Unavailable*	27.7
10011	15.2	7.8
10013	Unavailable*	1.4
10014	7.8	25.9
10016	33.6	5.2
10019	18.0	2.6
10020	24.7	3.1
10022	35.5	6.6
10023	6.2	8.0
Mean	**25.9**	**13.6**
Median	**23.3**	**7.8**
Range	**6.2-50.6**	**1.4-62.6**
No atovaquone treatment		
10012^	Unavailable†	1.5
10015^	Unavailable†	1.9
10017^	Unavailable†	6.7
10018^	Unavailable†	6.8
10024	18.4	0.8
10025	Unavailable*	10.1
10026^	Unavailable†	1.2
10027^	Unavailable†	3.6
10028	35.4	2.5
10029	20.9	36.6
10030	14.0	30.5
10031	40.7	6.1
10032^	Unavailable†	34.5
10033	32.7	5.6
10035^	Unavailable†	33.6

10036	19.4	6.5
10037^	Unavailable†	7.0
10038^	Unavailable†	9.1
10039	Unavailable*	24.7
10040^	Unavailable†	14.3
10041	16.2	19.3
10042^	Unavailable†	40.5
10043	22.1	9.2
10044	37.3	8.5
10045	30.4	52.4
10046	Unavailable*	49.7
Mean	**26.1**	**16.3**
Median	**22.1**	**8.8**
Range	**14.0-40.7**	**0.8-52.4**

CA IX – carbonic anhydrase 9

^ Cohort 3 patient

* Unexpected delay to surgery leading to unreliable result

† Pimonidazole not administered due to insufficient baseline hypoxia on imaging

For both pimonidazole and CA IX expression, no statistically significant differences were apparent when compared either by patient cohort or by treatment allocation (**Figure 2.4**).

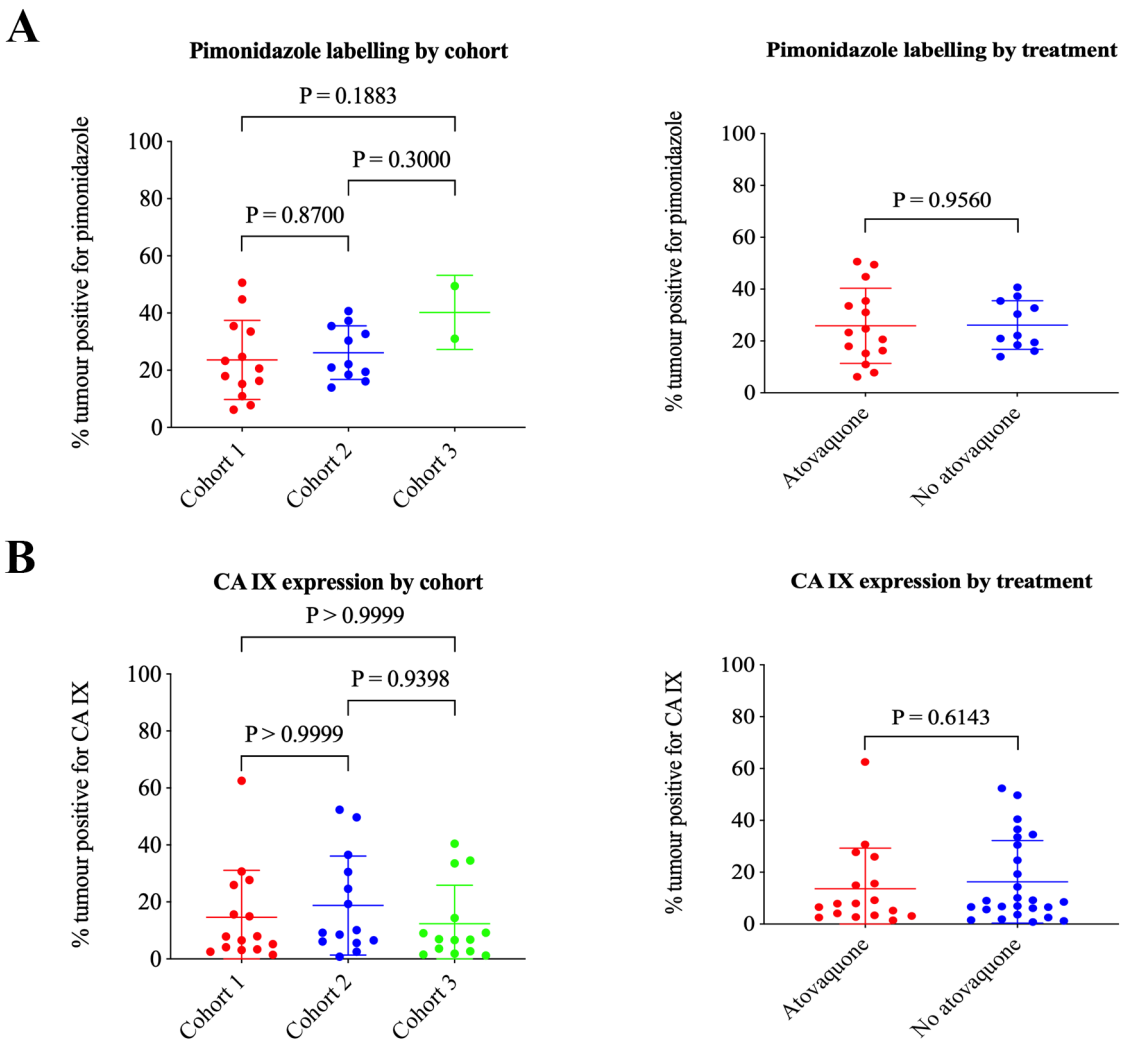


Figure 2.4 – Comparison of hypoxia marker labelling between cohorts and treatment groups

(A) Comparison of pimonidazole labelling on the basis of patient cohort (Cohort 1 n = 13, Cohort 2 n = 11, Cohort 3 n = 2) and treatment allocation (atovaquone group n = 15, no atovaquone group n = 11). (B) Comparison of carbonic anhydrase 9 (CA IX) expression on the basis of patient cohort (Cohort 1 n = 15, Cohort 2 n = 14, Cohort 3 n = 14) and treatment allocation (atovaquone group n = 17, no atovaquone group n = 26). Data are represented as the mean ± standard deviation. For pimonidazole, the data are analysed by either one-way analysis of variance (ANOVA) with Tukey's multiple comparisons post hoc test (when comparing cohorts) or unpaired t-test (when comparing treatment groups). For CA IX, the data are analysed by either Kruskal-Wallis test with Dunn's multiple comparisons post hoc test (when comparing cohorts) or Mann-Whitney test (when comparing treatment groups).

Heterogeneity of tumour hypoxia

The heterogenous nature of tumour hypoxia makes accurate measurement in patients technically challenging. Due to the number of blocks analysed, the ATOM study provides a valuable opportunity to quantify both the inter- and intrapatient heterogeneity of lung cancer hypoxia. In addition to large variations in pimonidazole scoring between patients, notable differences in the extent of pimonidazole labelling were observed between different blocks sampled from the same tumour (**Figure 2.5**). Whilst the range of whole tumour scores was greater for CA IX (0.8%-62.6%) than pimonidazole (6.2%-50.6%), there was slightly more intratumour heterogeneity with pimonidazole (pimonidazole mean range per tumour = 22.8% [6.4%-67.8%] vs. CA IX mean range per tumour = 18.4% [0.0%-70.6%]).

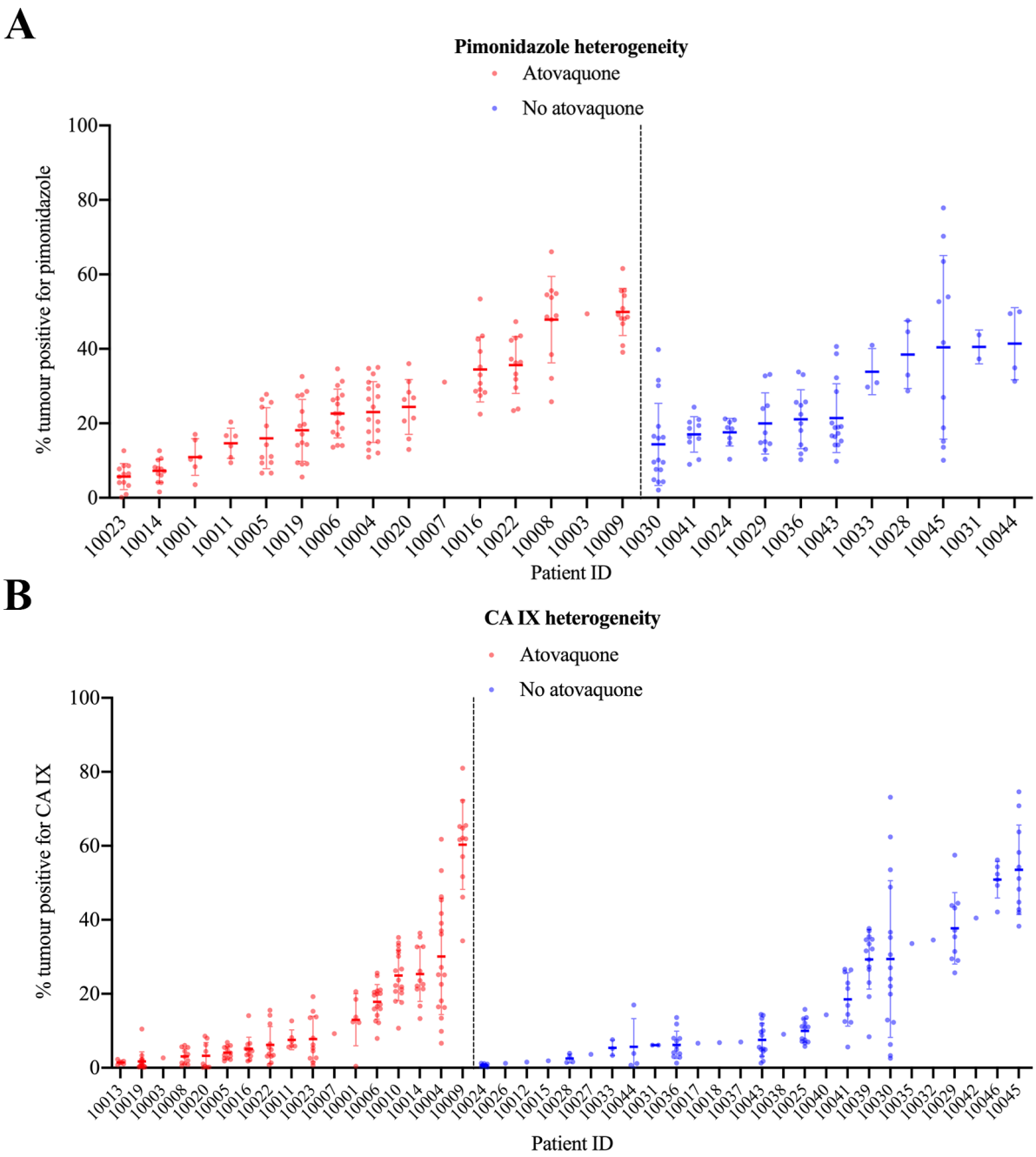


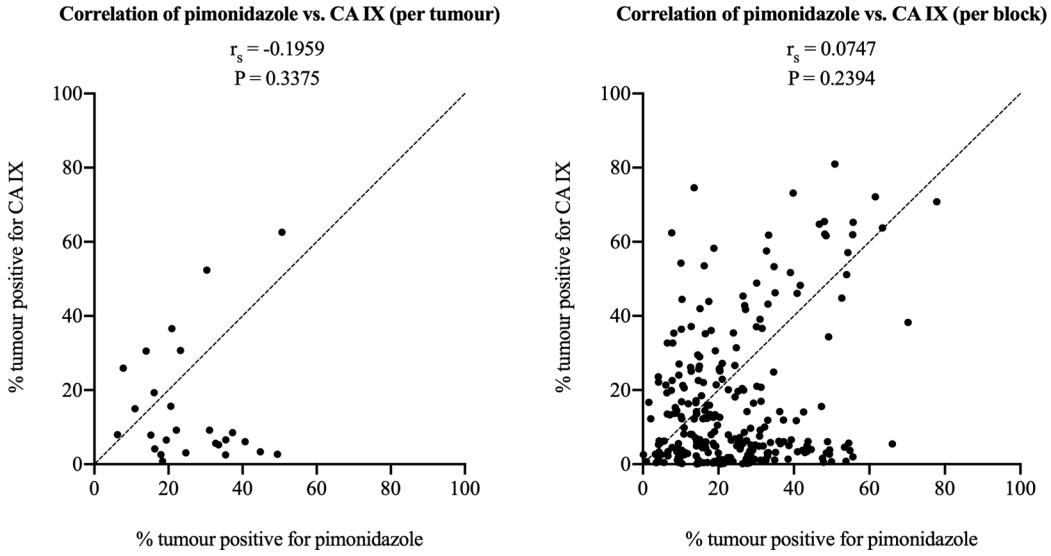
Figure 2.5 – Analysis of inter- and intratumoural heterogeneity of lung cancer hypoxia

Hypoxic percentage defined by either (A) pimonidazole labelling (atovaquone group n = 15, no atovaquone group n = 11) or (B) carbonic anhydrase 9 (CA IX) expression (atovaquone group n = 17, no atovaquone group n = 26). Each dot represents the measurement from a single block and, when present, the horizontal bar and error bars represent the mean value ± standard deviation from analysis of multiple blocks from the same tumour. Patients are ordered by increasing mean value.

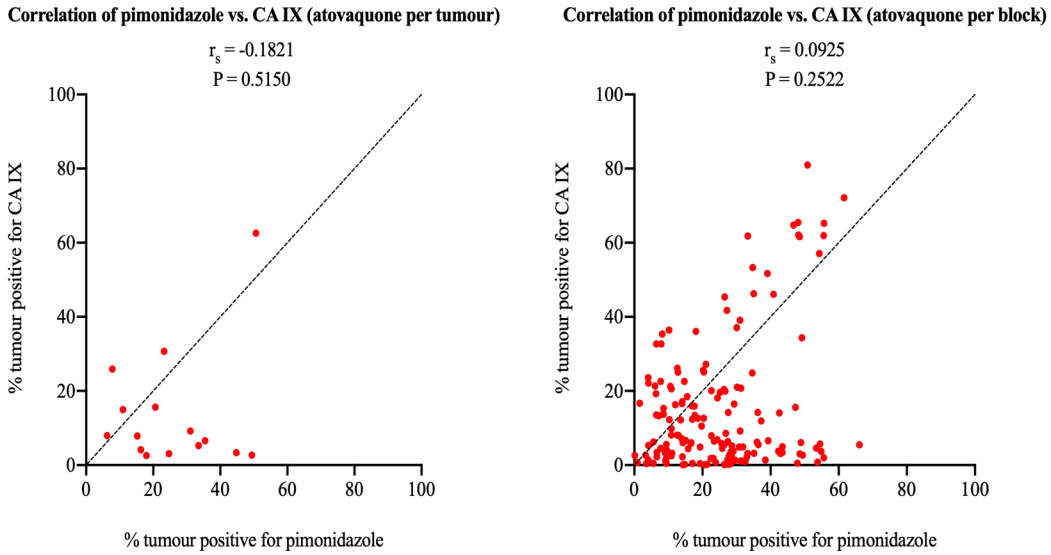
Comparison of hypoxia markers

To assess for an association between pimonidazole labelling and CA IX expression, correlation was performed between the two markers. However, no correlation was found between them on either a per tumour or per block basis (**Figure 2.6A**). Furthermore, this pattern was consistent when analysing these data on the basis of treatment allocation (**Figure 2.6B and 2.6C**). However, when each tumour was analysed in isolation, 11/26 tumours demonstrated broadly concordant expression between the two markers whilst 15/26 tumours displayed varying amounts of pimonidazole labelling but minimal CA IX expression (**Figure 2.6D**). These two distinct patterns of CA IX expression appear to be independent of treatment allocation and tumour histological subtype. The five tumours from patients who had an unanticipated delay to surgery demonstrated variable amounts of CA IX expression but minimal pimonidazole labelling, justifying their exclusion from formal study analysis. This observation is in keeping with the known metabolism of pimonidazole adducts over time due to protein turnover and cell division [612]. Thus, included tumours could be segregated into two distinct groups: one demonstrating a moderate/strong positive correlation between pimonidazole labelling and CA IX expression (**Figure 2.6E**) and another in which there was very little CA IX expression and thus no/only a very weak correlation between these parameters (**Figure 2.6F**).

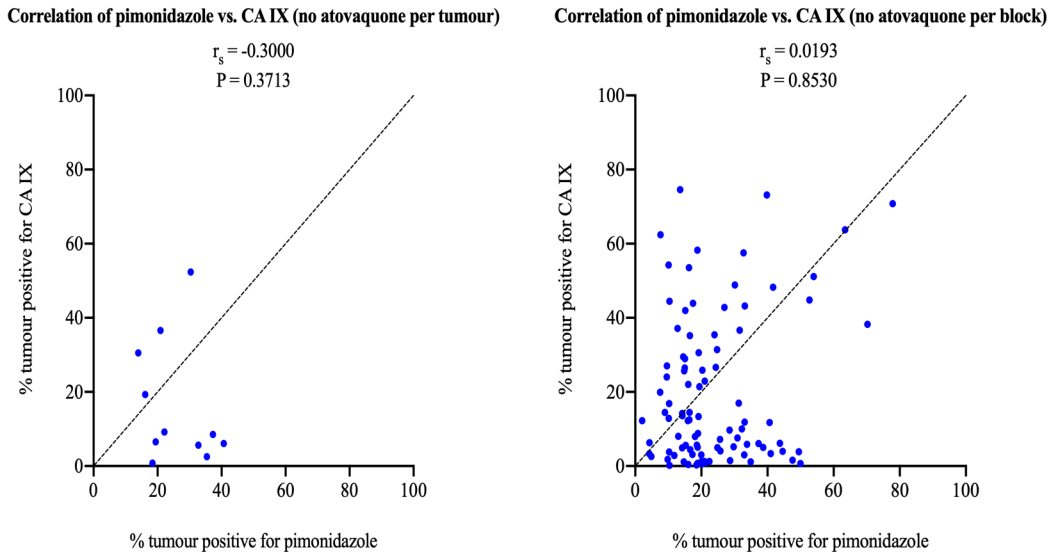
A


Correlation of pimonidazole vs. CA IX (per tumour)
r_s = -0.1959
P = 0.3375
% tumour positive for CA IX
% tumour positive for pimonidazole
Correlation of pimonidazole vs. CA IX (per block)
r_s = 0.0747
P = 0.2394
% tumour positive for CA IX
% tumour positive for pimonidazole

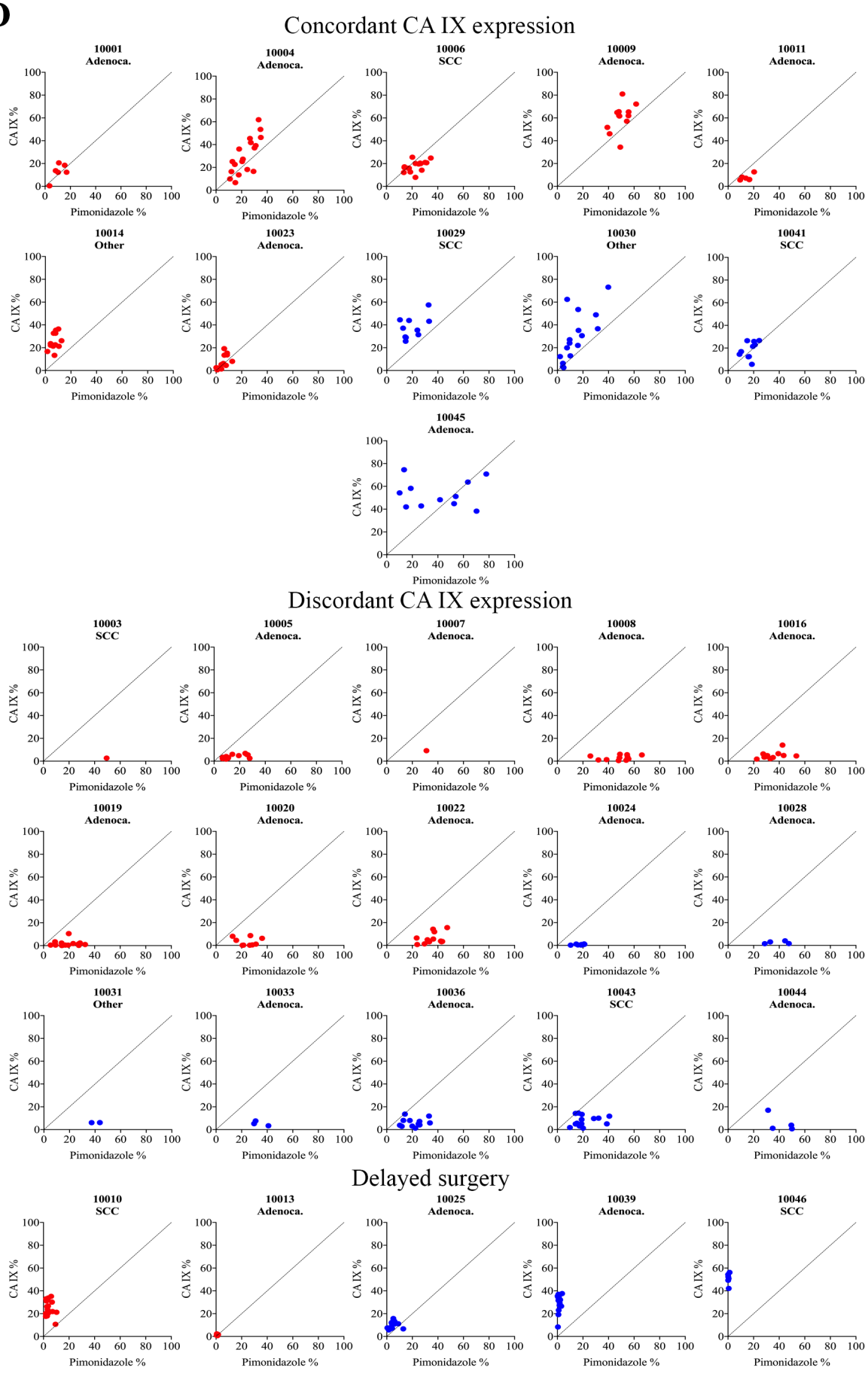
B


Correlation of pimonidazole vs. CA IX (atovaquone per tumour)
r_s = -0.1821
P = 0.5150
% tumour positive for CA IX
% tumour positive for pimonidazole
Correlation of pimonidazole vs. CA IX (atovaquone per block)
r_s = 0.0925
P = 0.2522
% tumour positive for CA IX
% tumour positive for pimonidazole

C


Correlation of pimonidazole vs. CA IX (no atovaquone per tumour)
r_s = -0.3000
P = 0.3713
% tumour positive for CA IX
% tumour positive for pimonidazole
Correlation of pimonidazole vs. CA IX (no atovaquone per block)
r_s = 0.0193
P = 0.8530
% tumour positive for CA IX
% tumour positive for pimonidazole

D


Concordant CA IX expression
10001 Adenoca.
10004 Adenoca.
10006 SCC
10009 Adenoca.
10011 Adenoca.
10014 Other
10023 Adenoca.
10029 SCC
10030 Other
10041 SCC
10045 Adenoca.
Discordant CA IX expression
10003 SCC
10005 Adenoca.
10007 Adenoca.
10008 Adenoca.
10016 Adenoca.
10019 Adenoca.
10020 Adenoca.
10022 Adenoca.
10024 Adenoca.
10028 Adenoca.
10031 Other
10033 Adenoca.
10036 Adenoca.
10043 SCC
10044 Adenoca.
Delayed surgery
10010 SCC
10013 Adenoca.
10025 Adenoca.
10039 Adenoca.
10046 SCC
CA IX %
Pimonidazole %

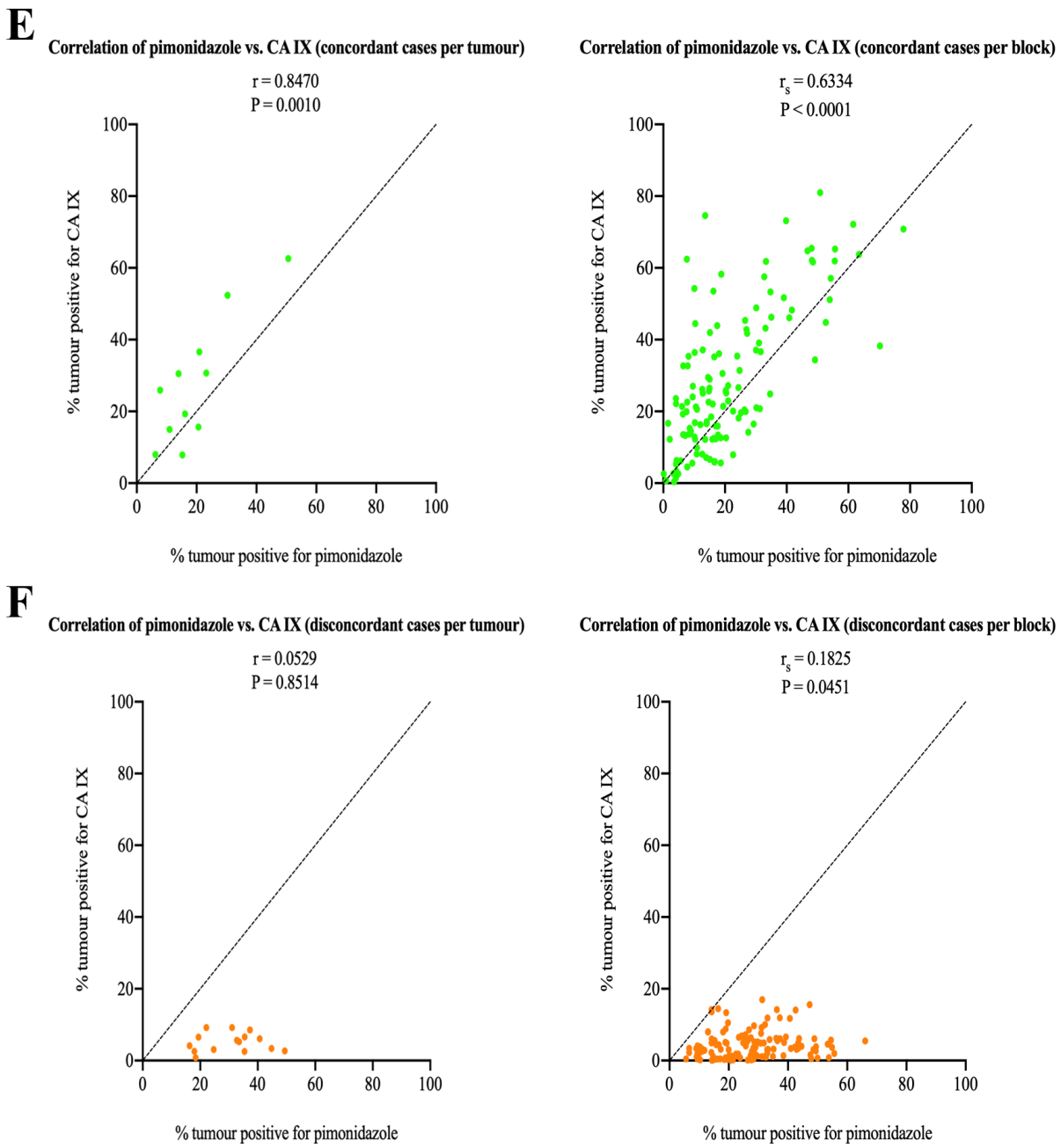


Figure 2.6 – Correlation between pimonidazole labelling and carbonic anhydrase 9 expression

(A) Correlation between pimonidazole labelling and carbonic anhydrase 9 (CA IX) expression across the entire study (n = 26 tumours and 250 blocks). (B) Correlation between pimonidazole labelling and CA IX expression amongst patients who received atovaquone (n = 15 tumours and 155 blocks). (C) Correlation between pimonidazole labelling and CA IX expression amongst patients who did not receive atovaquone (n = 11 tumours and 95 blocks). (D) Correlation between pimonidazole labelling and CA IX expression on an individual tumour

basis. A group of five tumours (n = 55 blocks) in which there was an unexpected delay between pimonidazole administration and surgery are included for comparison purposes (Adenoca. = adenocarcinoma, SCC = squamous cell carcinoma, Other = other histological subtype). (E) Correlation between pimonidazole labelling and CA IX expression amongst tumours displaying concordant marker expression (n = 11 tumours and 129 blocks). (F) Correlation between pimonidazole labelling and CA IX expression amongst tumours displaying discordant marker expression (n = 15 tumours and 121 blocks). Across the figure, black symbols represent all study samples, red symbols represent atovaquone-treated samples, blue symbols represent untreated samples, green symbols represent samples displaying broadly concordant pimonidazole labelling and CA IX expression and orange symbols represent samples displaying discordant pimonidazole labelling and CA IX expression. In each scatter (XY) plot, the dashed diagonal line represents the line of equality. Data presented are the Pearson correlation coefficient (r) or Spearman's rank correlation coefficient (r_s) and associated P value.

Tumour vasculature

Mean whole tumour CD31 and CD146 scores for atovaquone treated and untreated patients are shown in **Table 2.3**.

Table 2.3 – Quantification of vascular markers in the ATOM (Atovaquone as Tumour HypOxia Modifier) study

Patient identification	**CD31 (%)**	**CD146 (%)**
Atovaquone treatment		
10001	17.9	12.7
10003^	29.0	19.6
10004	35.6	16.3
10005	28.7	15.7
10006	31.1	15.8
10007^	33.8	Unavailable*
10008	33.0	22.6

10009	11.1	22.6
10010	4.5	13.5
10011	7.9	8.7
10013	12.3	6.1
10014	10.2	8.2
10016	17.0	22.9
10019	16.3	15.2
10020	12.3	11.9
10022	16.1	15.1
10023	25.7	7.7
Mean	**20.1**	**14.7**
Median	**17.0**	**15.15**
Range	**4.5-35.6**	**6.1-22.9**
No atovaquone treatment		
10012^	34.6	Unavailable*
10015^	56.5	18.4
10017^	34.7	26.2
10018^	36.8	32.8
10024	24.1	4.2
10025	20.4	12.6
10026^	29.4	33.0
10027^	49.9	13.9
10028	15.3	7.8
10029	28.6	14.1
10030	7.1	7.6
10031	4.2	10.3
10032^	20.1	11.3
10033	12.1	10.2

10035^	66.5	20.2
10036	12.8	Unavailable*
10037^	25.1	27.3
10038^	32.2	22.2
10039	9.9	7.3
10040^	49.0	26.5
10041	6.1	7.2
10042^	29.5	33.5
10043	10.9	5.8
10044	36.1	17.2
10045	10.0	14.1
10046	16.5	9.3
Mean	**26.1**	**16.4**
Median	**24.6**	**14.0**
Range	**4.2-66.5**	**4.2-33.5**
^ Cohort 3 patient * Tumour cell expression of CD146 precluded accurate assessment of vasculature		

For both CD31 and CD146, there was no statistically significant difference between treatment groups, although expression of these vascular markers was significantly higher amongst tumours from patients in Cohort 3 (**Figure 2.7A and 2.7B**). CD146, also known as melanoma cell adhesion molecule (MCAM) or cell surface glycoprotein MUC18, is a cell adhesion molecule that is expressed by endothelial cells as well as by smooth muscle cells. In some tumours, it is also expressed by neoplastic cells (**Figure 2.7C**) and in lung cancer this is associated with a poor prognosis [613]. In the ATOM study, 59/334 slides had to be excluded from final analysis due to high CD146 expression by tumour cells that could not be differentiated from vascular expression (leading to unavailable data for 3/43 patients). CD31,

alternatively known as platelet endothelial cell adhesion molecule (PECAM-1), is also a cell adhesion molecule that is expressed by endothelial cells as well as by certain leukocytes including intratumoural [279] and alveolar [614] macrophages (**Figure 2.7D**). Whilst endothelial CD31 expression could often be differentiated from non-vascular tissue expression based on intensity of staining, this was not always possible and likely contributed to the generally higher scoring observed for CD31 as compared to CD146. Nevertheless, comparison of CD31 and CD146 scores demonstrated weak/moderate positive correlations, suggesting that the two markers provide information that is broadly congruent ($r_s = 0.6537$ on a per tumour basis and $r_s = 0.4754$ on a per block basis) (**Figure 2.7E**).

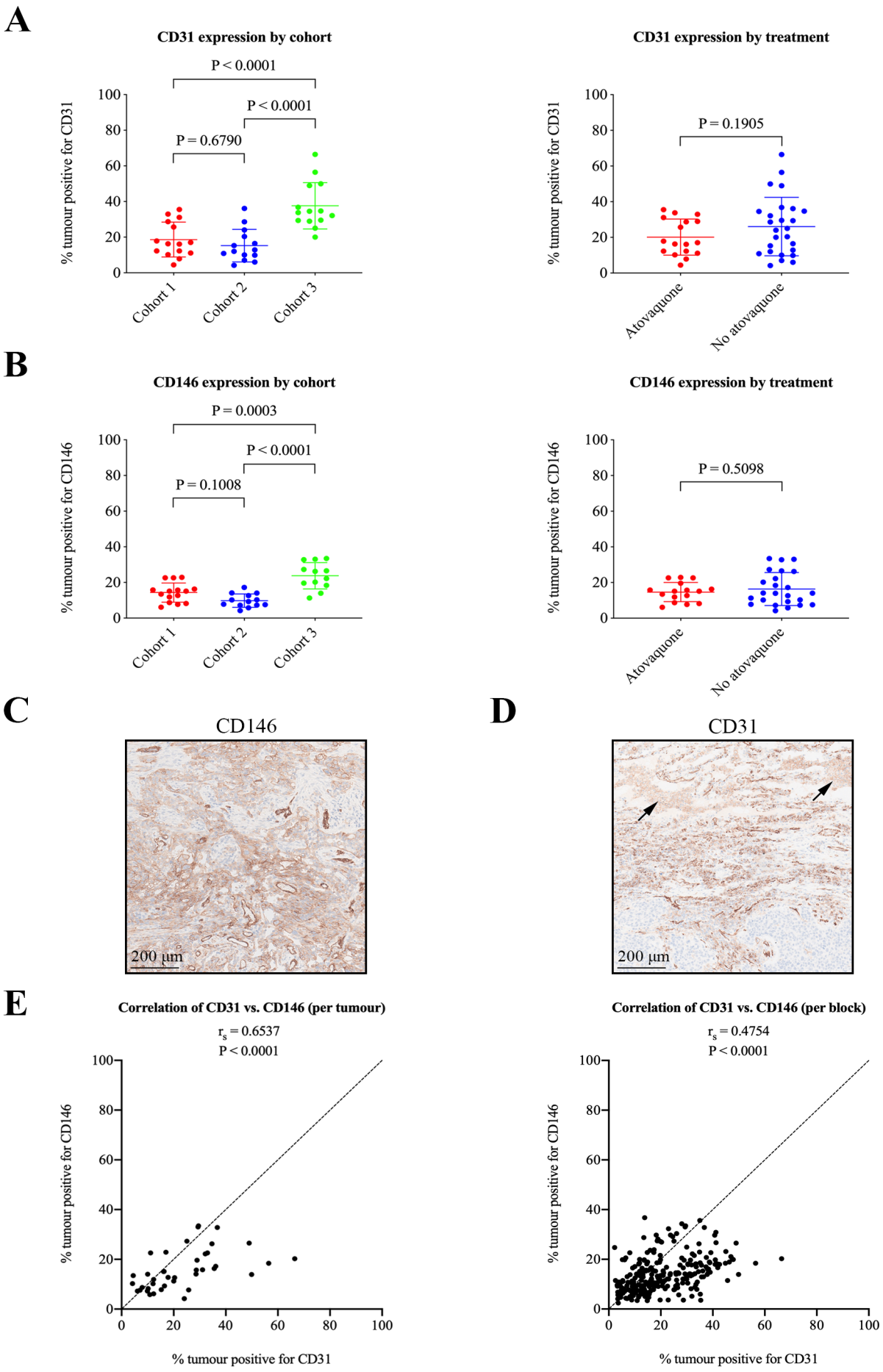

A
CD31 expression by cohort
P < 0.0001
P < 0.0001
P = 0.6790
% tumour positive for CD31
Cohort 1
Cohort 2
Cohort 3
CD31 expression by treatment
P = 0.1905
% tumour positive for CD31
Atovaquone
No atovaquone
B
CD146 expression by cohort
P = 0.0003
P < 0.0001
P = 0.1008
% tumour positive for CD146
Cohort 1
Cohort 2
Cohort 3
CD146 expression by treatment
P = 0.5098
% tumour positive for CD146
Atovaquone
No atovaquone
C
CD146
200 µm
D
CD31
200 µm
E
Correlation of CD31 vs. CD146 (per tumour)
r_s = 0.6537
P < 0.0001
% tumour positive for CD146
% tumour positive for CD31
Correlation of CD31 vs. CD146 (per block)
r_s = 0.4754
P < 0.0001
% tumour positive for CD146
% tumour positive for CD31

Figure 2.7 – Comparison of vascular marker expression between cohorts and treatment groups

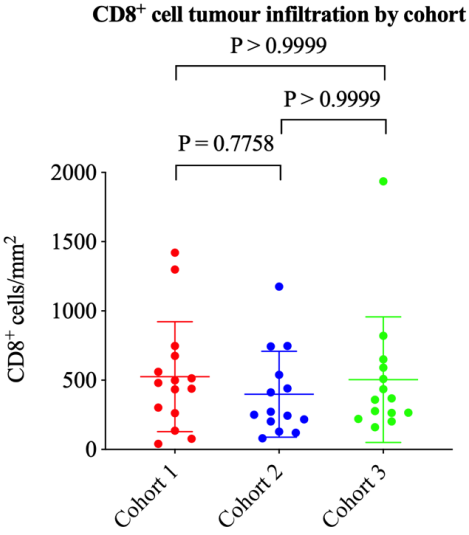
(A) Comparison of CD31 expression on the basis of patient cohort (Cohort 1 n = 15, Cohort 2 n = 14, Cohort 3 n = 14) and treatment allocation (atovaquone group n = 17, no atovaquone group n = 26). (B) Comparison of CD146 expression on the basis of patient cohort (Cohort 1 n = 15, Cohort 2 n = 13, Cohort 3 n = 12) and treatment allocation (atovaquone group n = 16, no atovaquone group n = 24). Data are represented as the mean ± standard deviation and are analysed by either one-way analysis of variance (ANOVA) with Tukey's multiple comparisons post hoc test (when comparing cohorts) or unpaired t-test (when comparing treatment groups). (C) Representative image from a sample demonstrating extensive CD146 expression by tumour cells. Labelled vessels are also apparent admixed with these immunopositive tumour cell nests. (D) Representative image from a sample demonstrating CD31 expression by alveolar macrophages (arrows) located at the interface between tumour invasive margin (lower half of image) and background lung (upper half of image). The intensity of labelling is generally greater on endothelium as compared to non-vascular tissue. (E) Correlation between CD31 and CD146 expression across the entire study (n = 40 tumours and 258 blocks). In the scatter (XY) plot, the dashed diagonal line represents the line of equality. Data presented are the Spearman's rank correlation coefficient (r_s) and associated P value.

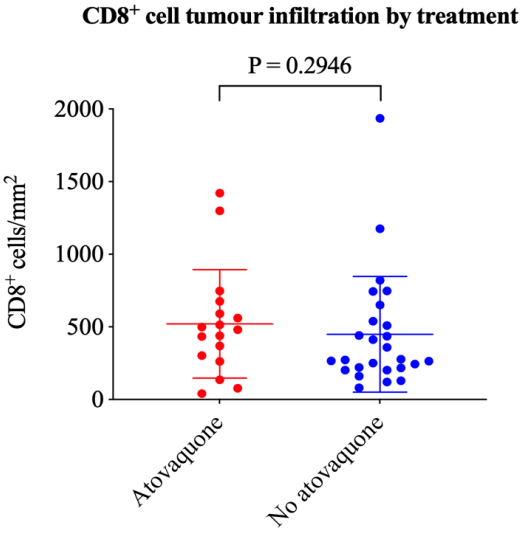
Immunological markers

Immune cell infiltration

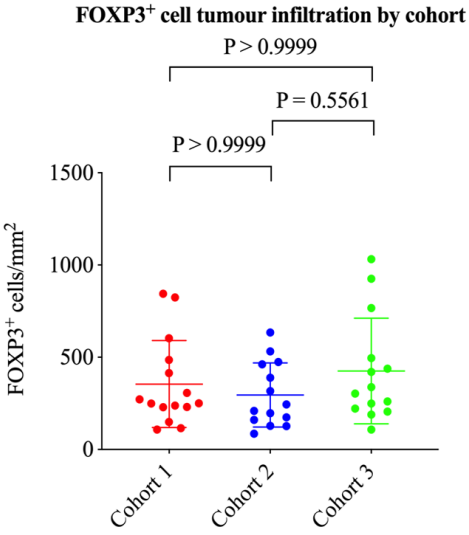
In a related project to evaluate the immunological effects of atovaquone that did not form part of the main study, I quantified the extent of infiltration of $CD8^+$, $FOXP3^+$ and $CD68^+$ cells into these tumours. This was conducted in parallel, and blinded, to the main study analyses and so equivalence of hypoxia and vascular markers between groups was unknown when deciding to profile additional immunological markers. Perhaps unsurprisingly, no statistically significant differences were found for any of these markers when analysed by patient cohort or treatment allocation (**Figure 2.8**).

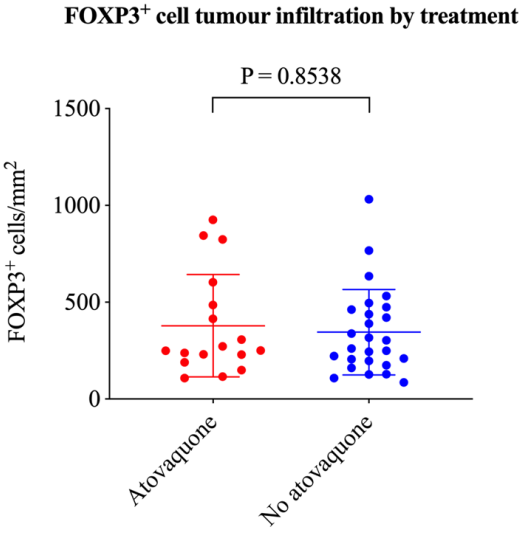
A


CD8+ cell tumour infiltration by cohort
P > 0.9999
P > 0.9999
P = 0.7758
CD8+ cells/mm2
2000
1500
1000
500
0
Cohort 1
Cohort 2
Cohort 3

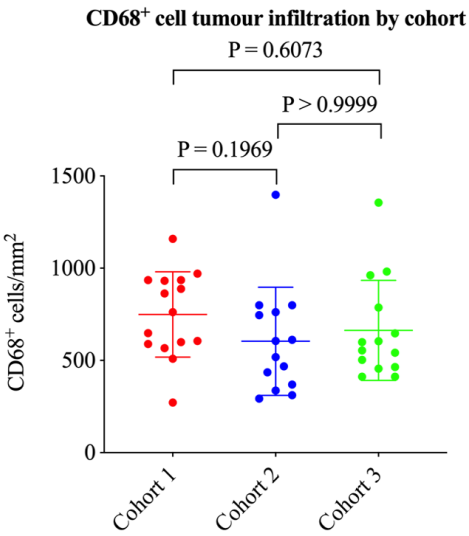

CD8+ cell tumour infiltration by treatment
P = 0.2946
CD8+ cells/mm2
2000
1500
1000
500
0
Atovaquone
No atovaquone

B


FOXP3+ cell tumour infiltration by cohort
P > 0.9999
P = 0.5561
P > 0.9999
FOXP3+ cells/mm2
1500
1000
500
0
Cohort 1
Cohort 2
Cohort 3


FOXP3+ cell tumour infiltration by treatment
P = 0.8538
FOXP3+ cells/mm2
1500
1000
500
0
Atovaquone
No atovaquone

C


CD68+ cell tumour infiltration by cohort
P = 0.6073
P > 0.9999
P = 0.1969
CD68+ cells/mm2
1500
1000
500
0
Cohort 1
Cohort 2
Cohort 3

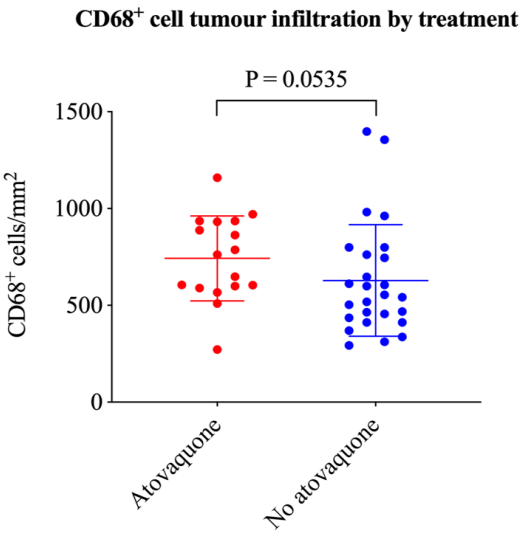
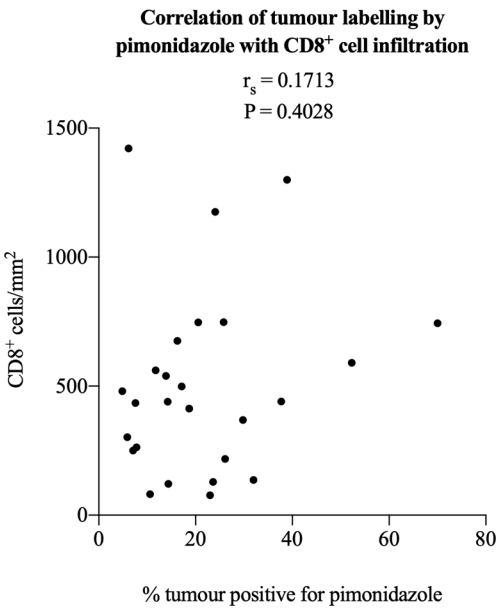
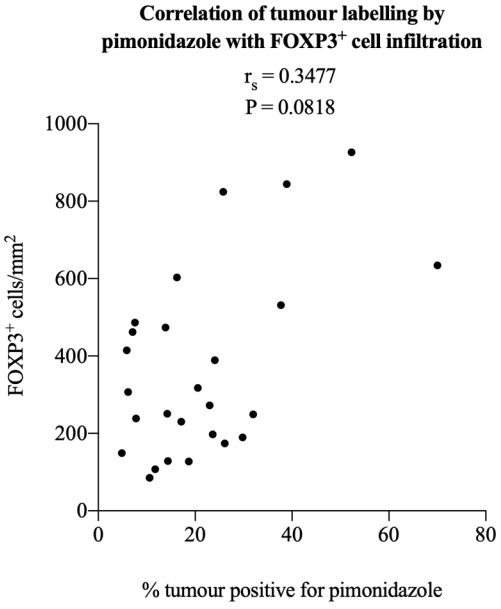

CD68+ cell tumour infiltration by treatment
P = 0.0535
CD68+ cells/mm2
1500
1000
500
0
Atovaquone
No atovaquone

Figure 2.8 – Comparison of immune cell infiltration between cohorts and treatment groups

(A) Comparison of intratumoural $CD8^+$ cell density on the basis of patient cohort (Cohort 1 n = 15, Cohort 2 n = 14, Cohort 3 n = 14) and treatment allocation (atovaquone group n = 17, no atovaquone group n = 26). (B) Comparison of intratumoural $FOXP3^+$ cell density on the basis of patient cohort and treatment allocation. (C) Comparison of intratumoural $CD68^+$ cell density on the basis of patient cohort and treatment allocation. Data are represented as the mean ± standard deviation and are analysed by either Kruskal-Wallis test with Dunn's multiple comparisons post hoc test (when comparing cohorts) or Mann-Whitney test (when comparing treatment groups).

As undertaken for the HNSCC cohort in Chapter 1, I correlated the extent of tumour hypoxia, as assessed by pimonidazole labelling, and intratumoural density of these immune cell populations (**Figure 2.9**). Whilst no correlation was apparent between tumour hypoxia and the intratumoural density of $CD8^+$ and $CD68^+$ cells, a weak positive correlation that just failed to reach statistical significance was observed for $FOXP3^+$ cells.


Correlation of tumour labelling by pimonidazole with CD8+ cell infiltration
rs = 0.1713
P = 0.4028
CD8+ cells/mm2
1500
1000
500
0
0
20
40
60
80
% tumour positive for pimonidazole


Correlation of tumour labelling by pimonidazole with FOXP3+ cell infiltration
rs = 0.3477
P = 0.0818
FOXP3+ cells/mm2
1000
800
600
400
200
0
0
20
40
60
80
% tumour positive for pimonidazole

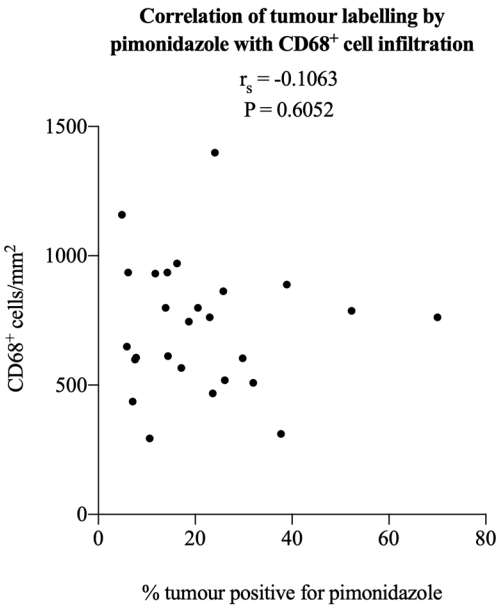

Correlation of tumour labelling by pimonidazole with CD68+ cell infiltration
rs = -0.1063
P = 0.6052
CD68+ cells/mm2
1500
1000
500
0
0
20
40
60
80
% tumour positive for pimonidazole

Figure 2.9 – Correlation between tumour hypoxia and immune cell infiltration

Correlation between pimonidazole labelling and CD8$^+$, FOXP3$^+$and CD68$^+$ cell density for each tumour (n = 26). Data presented are the Spearman's rank correlation coefficient (r_s) and associated P value.

Despite the positive correlation between pimonidazole labelling and FOXP3$^+$ cell density, similar patterns of immune cell localisation as those reported in Chapter 1 were observed (CD8$^+$ and FOXP3$^+$ cells predominantly located outwith regions of pimonidazole labelling with varying, but greater, infiltration of CD68$^+$ cells into these areas) (**Figure 2.10**).

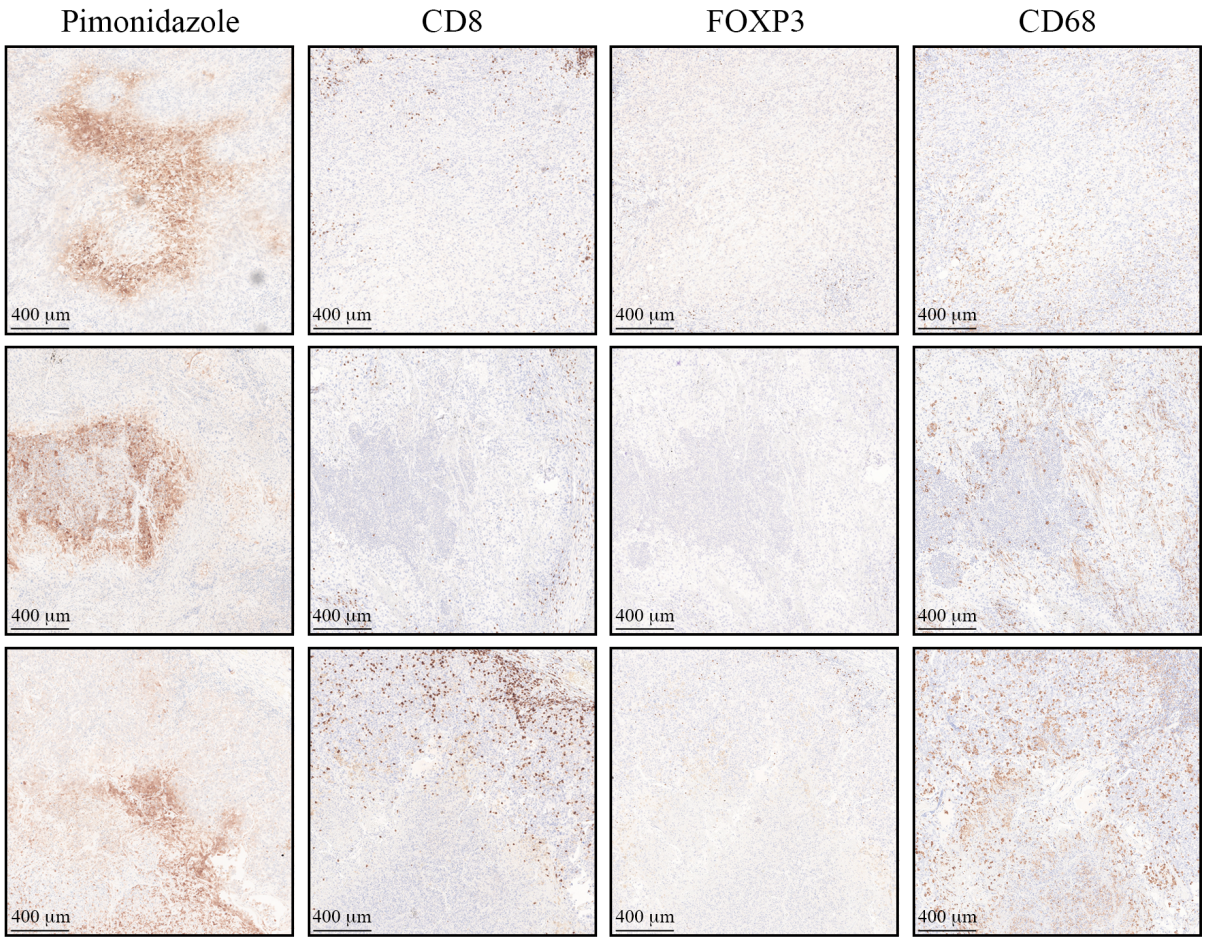


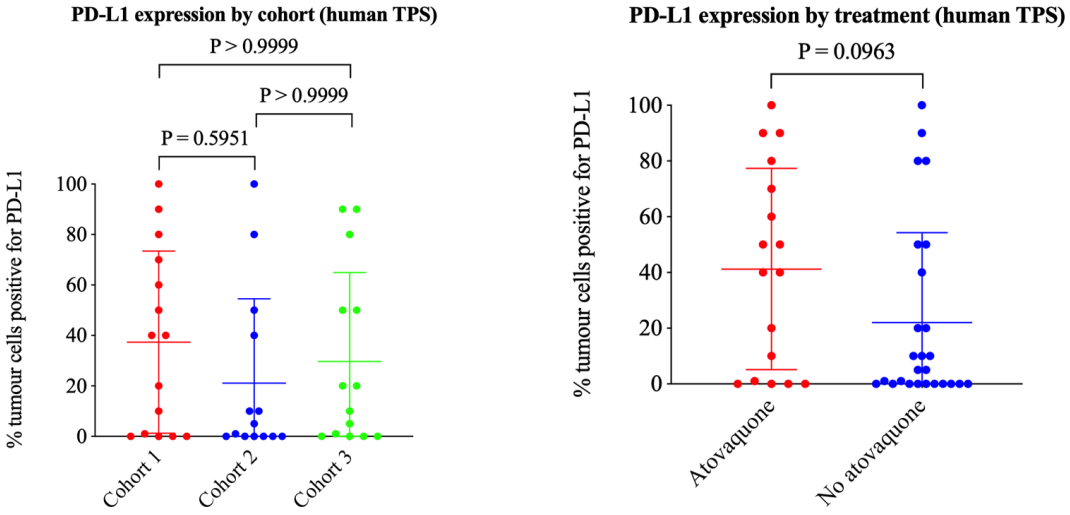
Figure 2.10 – Qualitative analysis of CD8$^+$, FOXP3$^+$ and CD68$^+$ cell distributions with respect to regions of tumour hypoxia

Examples of pimonidazole labelled regions from three tumours that are devoid of CD8$^+$ and FOXP3$^+$ cells but that contain variable numbers of CD68$^+$ cells.

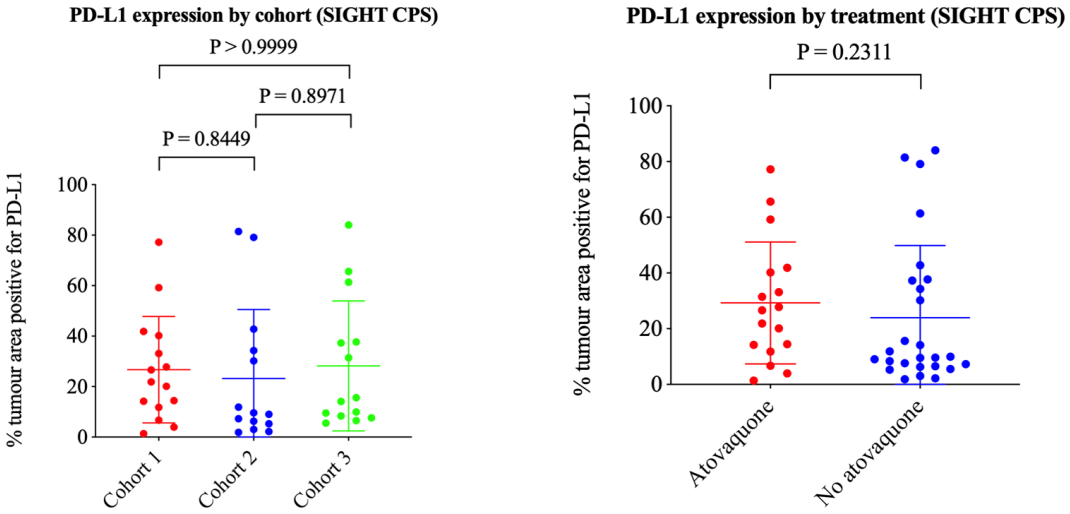
Programmed death-ligand 1 expression

Given that PD-L1 has been reported to be a direct HIF1α target gene [615, 616], I also tested whether its expression was affected by atovaquone administration. Analysis of PD-L1 expression was conducted by two complementary approaches. In the first, PD-L1 expression by tumour cells only (the Tumour Proportion Score [TPS]) was quantified visually by a Consultant Histopathologist in keeping with current clinical practice. In addition, given that other cell types within the TME can express PD-L1 (most notably myeloid cells), I scored overall PD-L1 expression irrespective of cell type using SIGHT (yielding a Combined Positive Score [CPS]). Although no differences were observed between cohorts or treatment groups with either approach, the two types of score were strongly positively correlated (**Figure 2.11**).

A


PD-L1 expression by cohort (human TPS)
P > 0.9999
P > 0.9999
P = 0.5951
% tumour cells positive for PD-L1
100
80
60
40
20
0
Cohort 1
Cohort 2
Cohort 3
PD-L1 expression by treatment (human TPS)
P = 0.0963
% tumour cells positive for PD-L1
100
80
60
40
20
0
Atovaquone
No atovaquone

B


PD-L1 expression by cohort (SIGHT CPS)
P > 0.9999
P = 0.8971
P = 0.8449
% tumour area positive for PD-L1
100
80
60
40
20
0
Cohort 1
Cohort 2
Cohort 3
PD-L1 expression by treatment (SIGHT CPS)
P = 0.2311
% tumour area positive for PD-L1
100
80
60
40
20
0
Atovaquone
No atovaquone

C

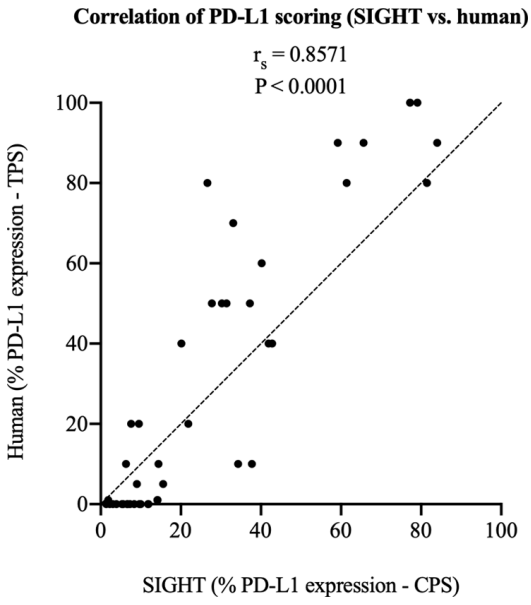

Correlation of PD-L1 scoring (SIGHT vs. human)
$r_s = 0.8571$
P < 0.0001
Human (% PD-L1 expression - TPS)
100
80
60
40
20
0
0
20
40
60
80
100
SIGHT (% PD-L1 expression - CPS)

Figure 2.11 – Comparison of programmed death-ligand 1 expression between cohorts and treatment groups

(A) Comparison of programmed death-ligand 1 (PD-L1) Tumour Proportion Score (TPS) as assessed manually on the basis of patient cohort (Cohort 1 n = 15, Cohort 2 n = 14, Cohort 3 n = 14) and treatment allocation (atovaquone group n = 17, no atovaquone group n = 26). (B) Comparison of PD-L1 Combined Positive Score (CPS) as assessed digitally by Semi-automated ImaGe analysis for HisTology data (SIGHT) on the basis of patient cohort and treatment allocation. Data are represented as the mean ± standard deviation and are analysed by either Kruskal-Wallis test with Dunn's multiple comparisons post hoc test (when comparing cohorts) or Mann-Whitney test (when comparing treatment groups). (C) Correlation of TPS and CPS for each tumour. In the scatter (XY) plot, the dashed diagonal line represents the line of equality. Data presented are the Spearman's rank correlation coefficient (r_s) and associated P value.

Finally, PD-L1 expression was correlated with pimonidazole labelling and immune cell infiltration (**Figure 2.12**). Whilst no correlation between tumour hypoxia and PD-L1 expression was found, moderate/strong positive correlations with $CD8^+$ and $CD68^+$ cell infiltration and a weak positive correlation with $FOXP3^+$ cell infiltration were observed.

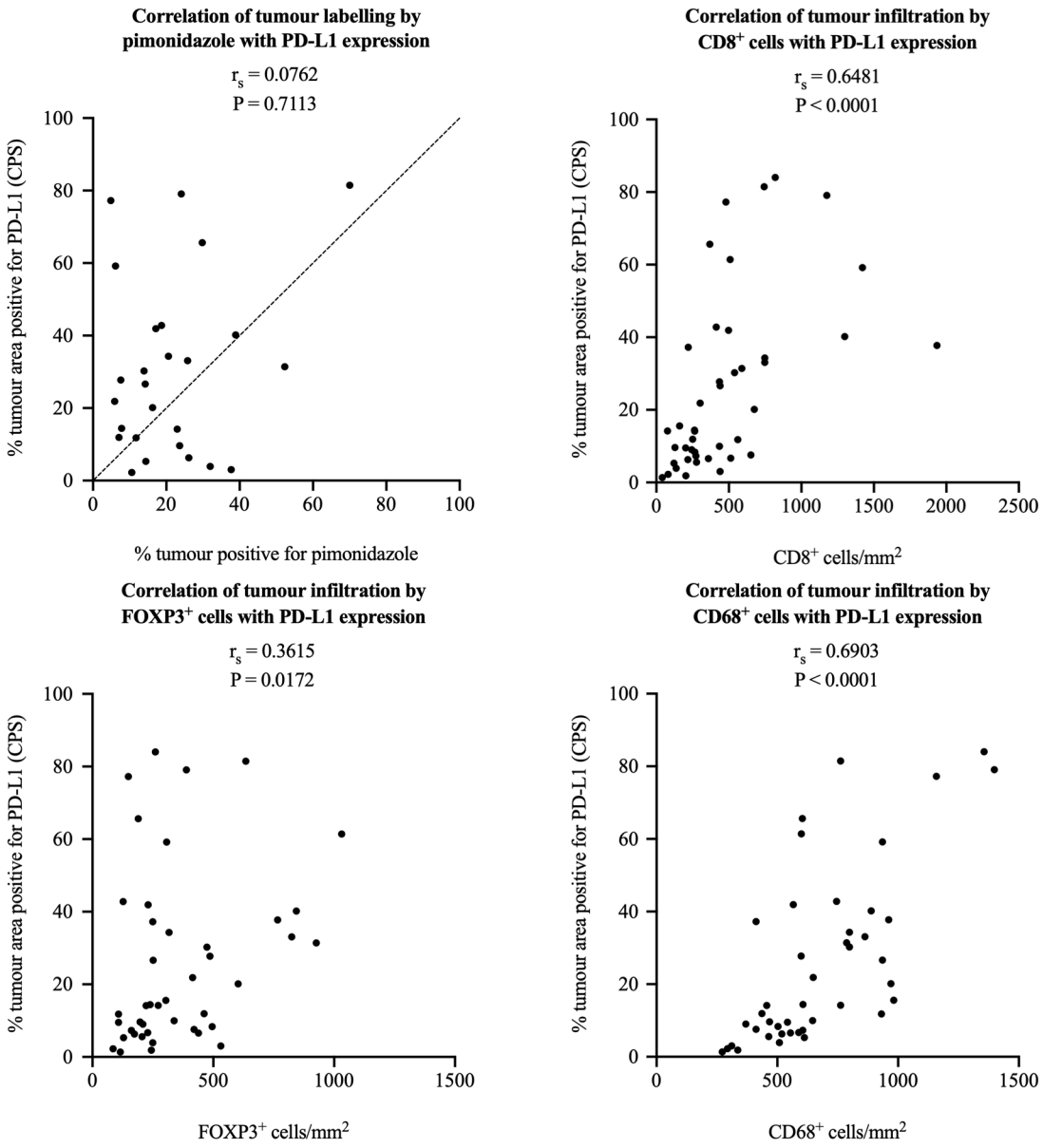


Figure 2.12 – Correlation between programmed death-ligand 1 expression and tumour hypoxia and immune cell infiltration

Correlation of programmed death-ligand 1 (PD-L1) Combined Positive Score (CPS) with tumour hypoxia, as assessed by pimonidazole labelling, (n = 26) and tumour infiltration by CD8$^+$, FOXP3$^+$ and CD68$^+$ cells (n = 43). In the first scatter (XY) plot, the dashed diagonal line represents the line of equality. Data presented are the Spearman's rank correlation coefficient (r_s) and associated P value.

Discussion

Summary of findings

In the work presented in this chapter, I utilised SIGHT to perform in-depth analysis of hypoxia, vascular and immunological markers in a clinical study evaluating the effects of atovaquone as a possible modifier of tumour hypoxia in NSCLC. Whilst seemingly disappointing, equivalent pimonidazole labelling and CA IX expression between treatment groups may actually represent a positive finding. Baseline hypoxia PET-CT imaging (in which the hypoxic volume, as determined by signal derived from the radiolabelled hypoxia tracer FAZA or [^{18}F]fluoromisonidazole [FMISO], is divided by overall tumour volume to determine a hypoxic percentage) demonstrated that, prior to treatment, tumours in the atovaquone treatment group were more hypoxic than control tumours (Cohort 1 mean hypoxia = 33.2% [6.4%-63.0%] vs. Cohort 2 mean hypoxia = 27.9% [4.7%-57.3%]). Following treatment, Cohort 1 mean hypoxia was 24.6% (0.0%-67.9%) as compared to a mean hypoxia of 28.3% (5.6%-59.6%) in Cohort 2. These post-treatment (i.e. immediately pre-surgery) values are broadly comparable to the results presented in this chapter. Overall, 11/15 atovaquone-treated patients had a meaningful reduction in tumour hypoxia (defined *ex ante* by the study oversight committee as at least 10% reduction), as assessed by serial imaging, as compared to only 2/14 patients in Cohort 2 [617]. Tumour vascularity was also similar between Cohort 1 and Cohort 2, in keeping with the hypothesis that atovaquone reduces tumour cell oxygen consumption as opposed to perfusion. Expression of CD31 and CD146 was higher in Cohort 3 tumours, which might explain their low volume of hypoxia on imaging. Why these tumours do not express lower levels of histological hypoxia markers is unclear but it is noteworthy that only one block per tumour was processed for immunohistochemistry, that only two patients received pimonidazole and that CA IX expression may not be a reliable surrogate for tumour hypoxia.

In order to minimise sampling error and to assess tumour hypoxia comprehensively, tumours underwent extensive immunohistochemical analysis. An additional benefit of this approach was the ability to address the issue of tumour hypoxia heterogeneity; overall, wide variations in inter- and intratumour pimonidazole labelling and CA IX expression were observed. These data justify the extent of tumour sampling undertaken in the ATOM study and question the validity of assessing tumour hypoxia by immunohistochemical staining of single tumour sections. In pancreatic cancer, assessment of 4-5 blocks of tumour has been recommended in order to provide an accurate evaluation of pimonidazole labelling [618]. An interesting observation from this chapter's results was the existence of two distinct patterns of CA IX expression in response to the presence of tumour hypoxia as identified by pimonidazole labelling. 15/26 tumours displayed minimal CA IX expression despite clear evidence of pimonidazole labelling. Other studies have reported tumours with lack of CA IX up-regulation despite evidence of hypoxia at either the microregional [619] or whole tumour [620] level, a so-called 'hypoxia-anergic' response. In lung cancer, several studies have reported lower expression of HIF1α [606, 621-623], GLUT1 [623-628] and CA IX [626, 629] amongst cases of adenocarcinoma as compared to SCC. However, in the samples analysed in this study, there was no statistically significant difference in either pimonidazole labelling or CA IX expression between the two histological subtypes (adenocarcinoma vs. SCC: pimonidazole – 27.74% vs. 20.94%, P = 0.8006; CA IX – 7.25% vs. 15.62%, P = 0.2195), although the number of SCC samples was limited. Thus, as outlined in Appendix 1, CA IX may not always be a reliable marker of tumour hypoxia and risks underestimating this parameter in a significant number of cases if assessed in isolation. RNA sequencing data are available for each tumour and it will be of interest to evaluate whether this finding represents failure of the entire HIF response or just failure of up-regulation of certain target genes (for example, carbonic anhydrase 12 [CA XII] is an alternative isoform that can be up-regulated in tumour cells [630] and might

compensate for lack of CA IX expression). Comparable vascularity between samples displaying concordant and discordant patterns of CA IX expression (concordant vs. discordant: CD31 – 17.39% vs. 20.12%, P = 0.5099; CD146 – 12.28% vs. 13.72%, P = 0.5325) suggests that at least some aspects of the HIF signalling pathway remain intact in these tumours.

Given the equivalence between cohorts and treatment groups with respect to both hypoxia and vascular markers, it is perhaps unsurprising that no difference was found for the immunological markers analysed. Although TAM have been reported to enhance tumour hypoxia in a murine lung cancer model [412], no association between these parameters was observed in this patient cohort. However, unlike the HNSCC cohort analysed in Chapter 1, there was a weak positive correlation between tumour hypoxia and $FOXP3^+$ cell density of borderline statistical significance. Whilst the reason for this discrepancy is unclear, it could represent either tumour-specific differences or simply reflect the limited number of samples analysed. The results presented in this chapter are in keeping with other studies that suggest that tumour hypoxia supports T_{Reg} recruitment [383-385] and are in agreement with a recent study in NSCLC that reported a positive correlation between tumour CA IX expression and stromal $FOXP3^+$ cell density [382]. Nevertheless, a consistent observation across all human cohorts analysed in this thesis is that T_{Reg} do not localise to the most hypoxic tumour regions (as identified by pimonidazole labelling and/or necrosis) but instead are enriched in the perivascular niche. A recent study reported that mitochondrial complex III is essential to the immune regulatory function of T_{Reg} and that conditional deletion of an essential subunit of this complex specifically within T_{Reg} inhibits B16 melanoma growth in mice [631]. Whilst no difference in $FOXP3^+$ cell densities could be ascertained between treatment groups within the short timeframe of this study, given that the presence of increased $FOXP3^+$ T lymphocytes is a negative prognostic factor in NSCLC [632], future evaluation of the effects of atovaquone on

T_{Reg} function will be of interest. Atovaquone has been reported to sensitise RCC to chemotherapy (5-fluorouracil) and immunotherapy (IFNα) [633]. However, these experiments were conducted *in vitro* and *in vivo* (the latter utilising xenografts in immunocompromised mice) and so cannot fully assess the immunomodulatory effects of atovaquone and may simply reflect potentiation of the direct cytotoxic effects of these agents.

With the exception of macrophages and the placenta, PD-L1 is not normally expressed by cells under physiological conditions but its expression by tumour cells can be induced to high levels in response to IFNγ produced by tumour-reactive T lymphocytes [634]. More recently, hypoxia/HIF1α stabilisation has been reported to lead to increased PD-L1 expression by both tumour cells [615] and tumour infiltrating myeloid cells [616], including in NSCLC [635, 636]. Furthermore, PD-L1 expression in NSCLC, through the generation of reactive oxygen species, has been reported to up-regulate HIF1α in a positive feedback loop [637]. However, immunohistochemical studies of human NSCLC have reported inconsistent associations between PD-L1 expression and markers of hypoxia. Positive associations have been reported between PD-L1 and HIF1α [635, 638-641], GLUT1 [639, 642] and necrosis [638, 643, 644]. However, other studies have failed to find a statistically significant association between PD-L1 expression and HIF1α [645] and GLUT1 [646] expression. These latter findings mirror reports demonstrating that IFNγ, but not hypoxia, is a key inducer of PD-L1 expression in murine endothelial cells [599] and that PD-L1 is not up-regulated in murine lymphoma cells in response to hypoxic exposure [647]. Thus, hypoxia (acting via HIF) is likely only one of several pathways that regulate PD-L1 expression and may not be central to inducing its expression in certain tumour types. The findings presented in this chapter are in alignment with a recent study in HNSCC which found a positive correlation between PD-L1 expression and $CD3^+$ cell infiltration but no correlation between PD-L1 and CA IX expression, suggesting that IFNγ, and

not hypoxia, is dominant in regulating PD-L1 expression [324]. Supporting this, the correlation between PD-L1 expression and $CD8^+$, $FOXP3^+$ and $CD68^+$ cell infiltration in this study mirrors that reported by others [648-650] and may represent an immune-induced reactive pattern of PD-L1 expression.

Clinical relevance

Whilst no differences were observed between treatment groups in this study, careful consideration must be given to pharmacological approaches to manipulating tumour hypoxia (and tumour cell metabolism) in order to potentiate immunotherapy. Whilst inhibition of tumour cell oxidative metabolism has promoted anti-tumour immunity in murine models [312, 560] and tumour glycolysis has been associated with heightened anti-tumour immunity in humans [651], this finding has not always been replicated. For example, an association between increased glycolysis and decreased $CD8^+$ lymphocyte infiltration in microsatellite instability-high colon cancers has been reported [652] whilst enhancing glycolysis in a murine tumour model ablated T lymphocyte-mediated control of tumour growth [343]. In another study, melanoma and lung tumours with high expression of glycolysis-related genes were also poorly infiltrated by T lymphocytes [653]. Furthermore, in the same study, melanoma samples from patients who failed to respond to adoptive T lymphocyte therapy displayed increased glycolytic activity. Increased glycolysis was associated with lower levels of CXCL10 (a key T lymphocyte chemoattractant) and impaired T lymphocyte trafficking to these tumours, whilst increased lactic acid within the TME has been shown to directly suppresses T lymphocyte and NK cell cytotoxicity [350]. In keeping with these data, administration of a lactate dehydrogenase inhibitor significantly enhanced adoptive T lymphocyte therapy in mice [653]. Whilst initially seeming to be paradoxical, together these observations may hint at the existence of a narrow ‘therapeutic window’ between inhibiting tumour cell oxidative phosphorylation,

in order to increase oxygen availability for leukocytes, and promoting excessive tumour cell glycolysis that utilises glucose and generates an acidic TME and thus undesirably suppresses anti-tumour immunity. Another important factor is that hypoxia modification for radiotherapy and immunotherapy may require different approaches. For radiotherapy, hypoxia may only need to be reduced at the time of treatment (a temporary [hours-days] increase in oxygen would favour the generation of DNA damage) whereas for immune responses to be maximised, longer-term hypoxia reduction (weeks-months) will likely be necessary.

Strengths, limitations and future directions

The patient cohort analysed in this chapter has two key strengths. Firstly, the extensive tissue sampling (multiple blocks from different regions of each tumour) mitigates the risk of sampling error and also provides a unique opportunity to analyse the spatial heterogeneity of pimonidazole labelled hypoxia in NSCLC. Whilst a brief summary of hypoxia heterogeneity has been presented here, future work will focus on a more formal analysis of this parameter, as has already been conducted in pancreatic cancer [618]. Secondly, tumour samples in this study have been subject to extensive characterisation including with pre-operative hypoxia PET-CT imaging and gene expression analysis. Thus, it will be of interest to cross-correlate the findings of these investigations in greater detail. For example, resection specimens were carefully orientated during pathological dissection to ensure that samples analysed for immunohistochemistry are directly comparable with pre-operative cross-sectional imaging. The spatial agreement of the results of these approaches will be compared in order to validate hypoxia PET-CT imaging. Novel mathematical descriptors of leukocyte spatial patterns, developed by collaborators in the Mathematical Institute, will also be applied to this histological dataset given that the distribution of immune cells within NSCLC samples is of prognostic value [246, 248, 251].

A major weakness is the lack of access to pre-treatment tissue samples in order to profile temporal changes with therapy. This occurred because patients proceeded to surgery on the basis of a radiological, and not pathological, diagnosis of cancer. Given the short timeframe between diagnosis and surgery, it was not possible to mandate an invasive tissue biopsy within the study protocol. Further limitations of this study were the relatively small sample size, with heterogeneity of tumour histological sub-type and stage, and non-randomised treatment allocation. Consequently, data presented in this chapter are best considered hypothesis generating and require confirmation in larger studies. In this respect, the Atovaquone with Radical Chemoradiotherapy in Locally Advanced NSCLC (ARCADIAN) trial (a phase I, single arm trial) is currently being established and will include a pre-treatment tumour biopsy.

Chapter 3

Chapter aim

To characterise an unexpected phenotype arising in a novel mouse model created to study the dynamic HIF response *in vivo*.

Introduction

Over recent years, a multitude of pre-clinical studies have been conducted to investigate the *in vivo* cellular response to hypoxia, commonly using transgenic mice to manipulate the PHD-HIF pathway, and these have revealed a wide variety of phenotypes with direct relevance to human disease (as reviewed in [65]). Most of these studies have utilised gene 'knockout' technology which involves the permanent deletion of the target gene(s) of interest. However, such an approach has both large and irreversible effects on gene dosage, may have lethal consequences and does not accurately reproduce the complex changes seen in most disease states. To address these limitations, and to permit more sophisticated investigation of the *in vivo* hypoxic response, colleagues within the Ratcliffe/Pugh Oxygen Sensing Laboratory developed novel transgenic mice lines that permit dynamic manipulation of cellular HIFα levels in either a systemic or tissue-restricted distribution. This transgenic approach utilises an endogenous mechanism of post-transcriptional gene expression regulation called RNA interference (RNAi), triggered through the expression of shRNA to achieve transient target gene silencing ('knockdown' of gene expression occurs due to degradation of complementary mRNA molecules) [654, 655] (**Appendix 8**). Thus, this method allows inducible, bidirectional and reversible manipulation of HIFα levels, which more faithfully recapitulates changes expected to occur as a consequence of pharmacological targeting of this pathway. Silencing of one or both HIFα isoforms reduces levels of the targeted isoform(s) whereas silencing of PHD

leads to HIFα stabilisation; combined silencing of PHD with one HIFα isoform leads to selective stabilisation of the non-targeted HIFα isoform. Activation of the transgenic system, dependent upon the administration of doxycycline (a tetracycline analogue) within drinking water, can be detected at a cellular level by the simultaneous expression of the reporter enhanced green fluorescent protein (GFP), encoded in the same transcript as the targeting shRNA molecule.

As outlined in the Introduction, PHD function as key cellular oxygen sensors [656-658]. PHD suppression leads to HIFα stabilisation and consequent up-regulation of the HIF-dependent adaptive transcriptional response to hypoxia. Pre-clinical studies suggest that pharmacological PHD inhibition may be beneficial in a wide range of human diseases (as reviewed in [659]). In particular, due to their ability to stimulate EPO production, predominantly via HIF2α stabilisation in specific cells of the kidney and liver, several PHD inhibitors are currently being investigated in phase III randomised clinical trials for the treatment of renal anaemia [660-662]. These compounds are structural analogues of 2-oxoglutarate (2-OG), a key reaction co-factor required for PHD activity, and function by blocking entrance of 2-OG and HIFα to the enzymes' catalytic sites. PHD2 is the most abundant PHD isoform and is thus considered to play the most significant role in regulating HIFα levels [663]; however, the different isoforms are recognised to function in a tissue-specific manner [664]. Thus, in preliminary experiments intended to mirror pharmacological PHD inhibition, we elected to silence *Phd2* expression systemically, initially without concomitant interventions on either *Hif1a* or *Hif2a*.

Results

Long-term, systemic silencing of Phd2 in mice causes failure to thrive and autoimmunity

In initial experiments, 7-12-week-old mice continuously receiving doxycycline within their drinking water (2 mg/mL) were observed closely to monitor the effects of long-term, systemic silencing of *Phd2*. After 4-8 weeks of doxycycline administration, *Phd2* knockdown mice (transgenic mice possessing a *Phd2*-targeting shRNA allele) were noted to be failing to thrive, with evidence of skin crusting, mild alopecia and weight loss; in contrast, control mice (transgenic mice lacking a *Phd2*-targeting shRNA allele but treated with doxycycline) remained healthy (**Figure 3.1A**). Differences in body weight between the groups of mice emerged after two weeks and progressively increased (**Figure 3.1B**). Surprisingly, since HIFα stabilisation was expected to induce erythrocytosis, transgenic mice were actually found to be anaemic (with a haematocrit of 36-38% as compared to 51-55% amongst controls). To investigate this observation further, we performed serial peripheral blood sampling in subsequent cohorts of mice: after an initial rise during the first two weeks, red cell count fell sharply thereafter (**Figure 3.1C**). In parallel, we observed a progressive leukocytosis and thrombocytosis amongst transgenic mice only. At necropsy, the most striking macroscopic findings were massive splenomegaly (mean = 157 mg vs. 83 mg per spleen) and peripheral lymphadenopathy (mean = 70 mg vs. 11 mg per four lymph nodes) (**Figure 3.1D**); loss of subcutaneous adipose tissue and increased cutaneous vascularity were also evident.

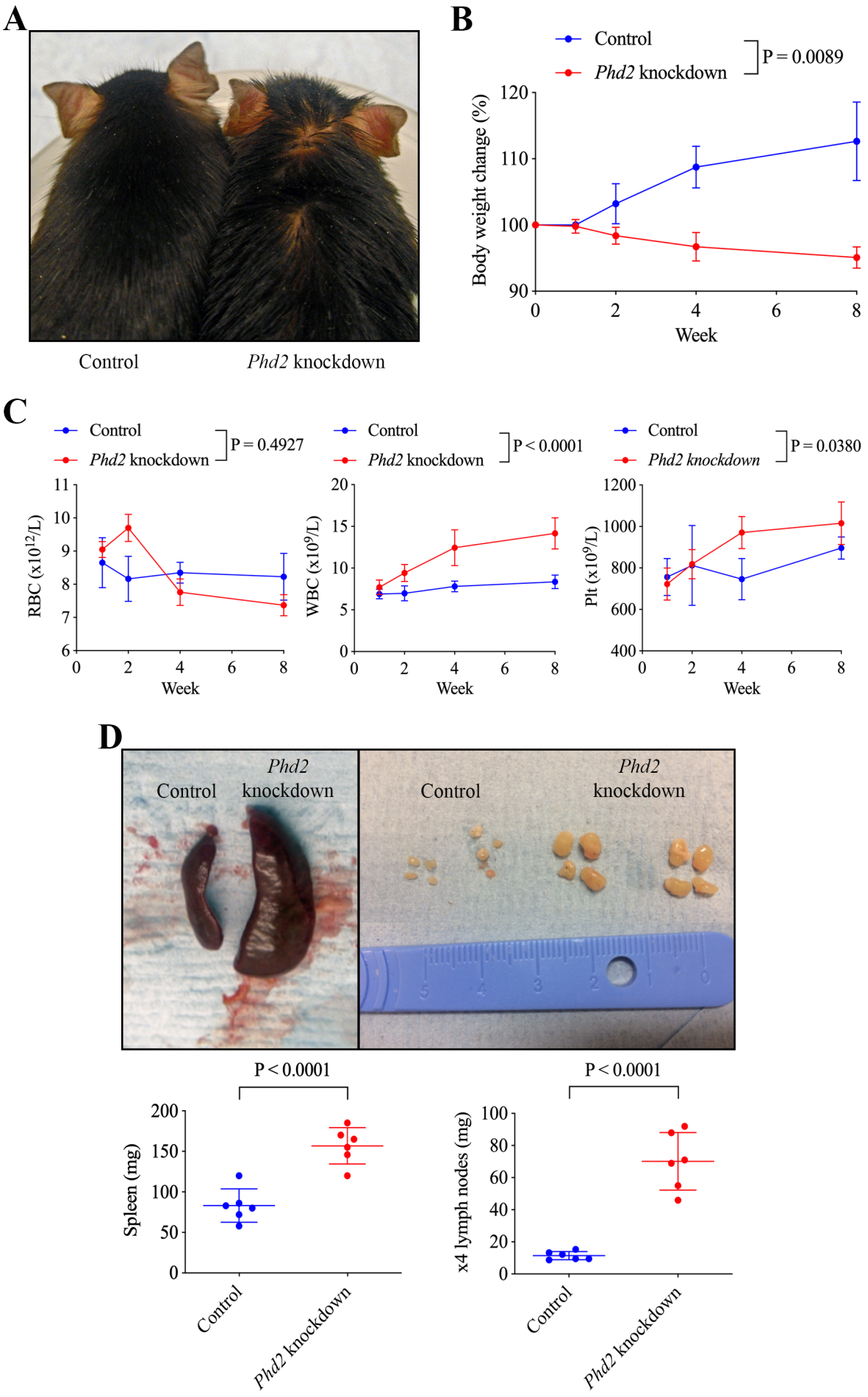

A
Control
Phd2 knockdown
B
Control
Phd2 knockdown
P = 0.0089
Body weight change (%)
Week
C
Control
Phd2 knockdown
P = 0.4927
RBC (x10^12/L)
P < 0.0001
WBC (x10^9/L)
P = 0.0380
Plt (x10^9/L)
Week
D
Control
Phd2 knockdown
P < 0.0001
Spleen (mg)
x4 lymph nodes (mg)
Control
Phd2 knockdown

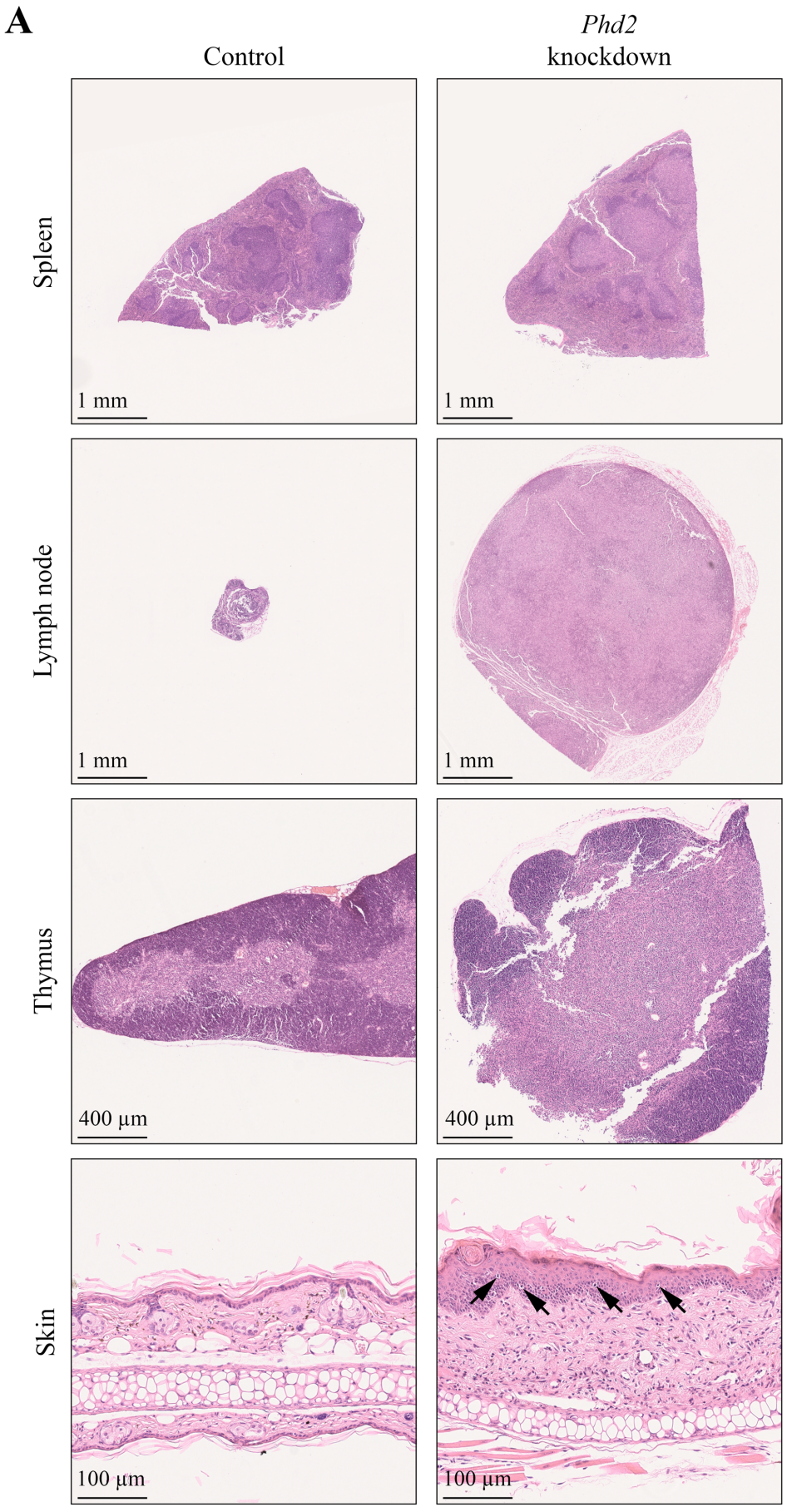
Figure 3.1 – Macroscopic and haematological phenotyping of *Phd2* knockdown mice
(A) Representative image of a Phd2 knockdown mouse and its littermate control following doxycycline administration for 5 weeks. (B) Mean percentage of body weight changes amongst Phd2 knockdown and control mice relative to Day 0 of doxycycline administration. Data are represented as the mean ± standard deviation (SD) and are analysed by two-way analysis of variance (ANOVA) with repeated measures (n = 3 mice per group). (C) Time course of changes in red blood cell (RBC), white blood cell (WBC) and platelet (Plt) counts from Phd2 knockdown and littermate control mice treated with doxycycline for 8 weeks. Data are represented as the mean ± SD and are analysed by two-way ANOVA (n = 3-8 mice per group at each time point). (D) Comparison of masses of spleen and lymph nodes from Phd2 knockdown mice and their littermate controls following doxycycline administration for 5 weeks. Data are represented as the mean ± SD and are analysed by unpaired t-test (n = 6 mice per group). All data at 5 weeks were consistent over three independent experiments whilst data at 8 weeks were consistent over two independent experiments.

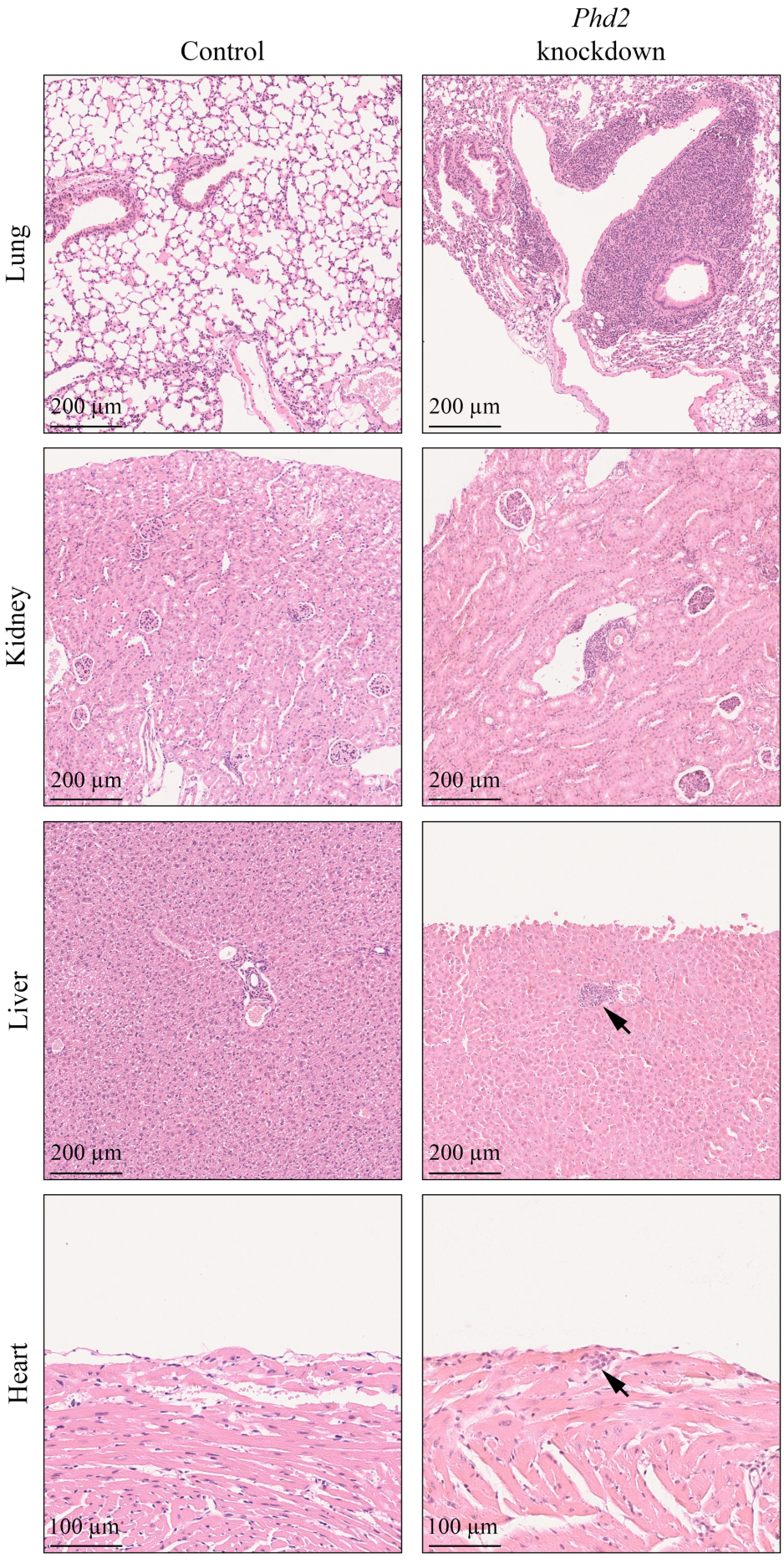
My efforts concentrated on the histopathological characterisation of this phenotype. Microscopic examination of tissue harvested at necropsy (**Figure 3.2A**) confirmed expansion of both spleen and peripheral lymph nodes, with distortion of normal tissue architecture. Eosinophilic mononuclear cells were prominent, expanding the central regions of the lymph nodes and displacing cortical areas to the extreme periphery. At high magnification, large 'centroblast-like' cells with round to oval nuclei, vesicular chromatin and prominent nucleoli were apparent. Similar changes were seen in the white pulp of the spleen and the medulla of the thymus. Examination of the skin of the pinna showed thickening of the keratin layer (hyperkeratosis) and epidermis (acanthosis), dermal fibrosis and loss of subcutaneous fat. In places, empty hair follicles were detected and there was a diffuse lymphohistiocytic (chronic inflammatory cell) infiltrate within the dermis, with focal evidence of exocytosis of lymphocytes into the overlying epidermis. Examination of internal organs revealed further striking changes, with nodular accumulations of leukocytes in bronchovascular regions of the lung and perivascular regions of the kidney. Further examination of the kidney showed an

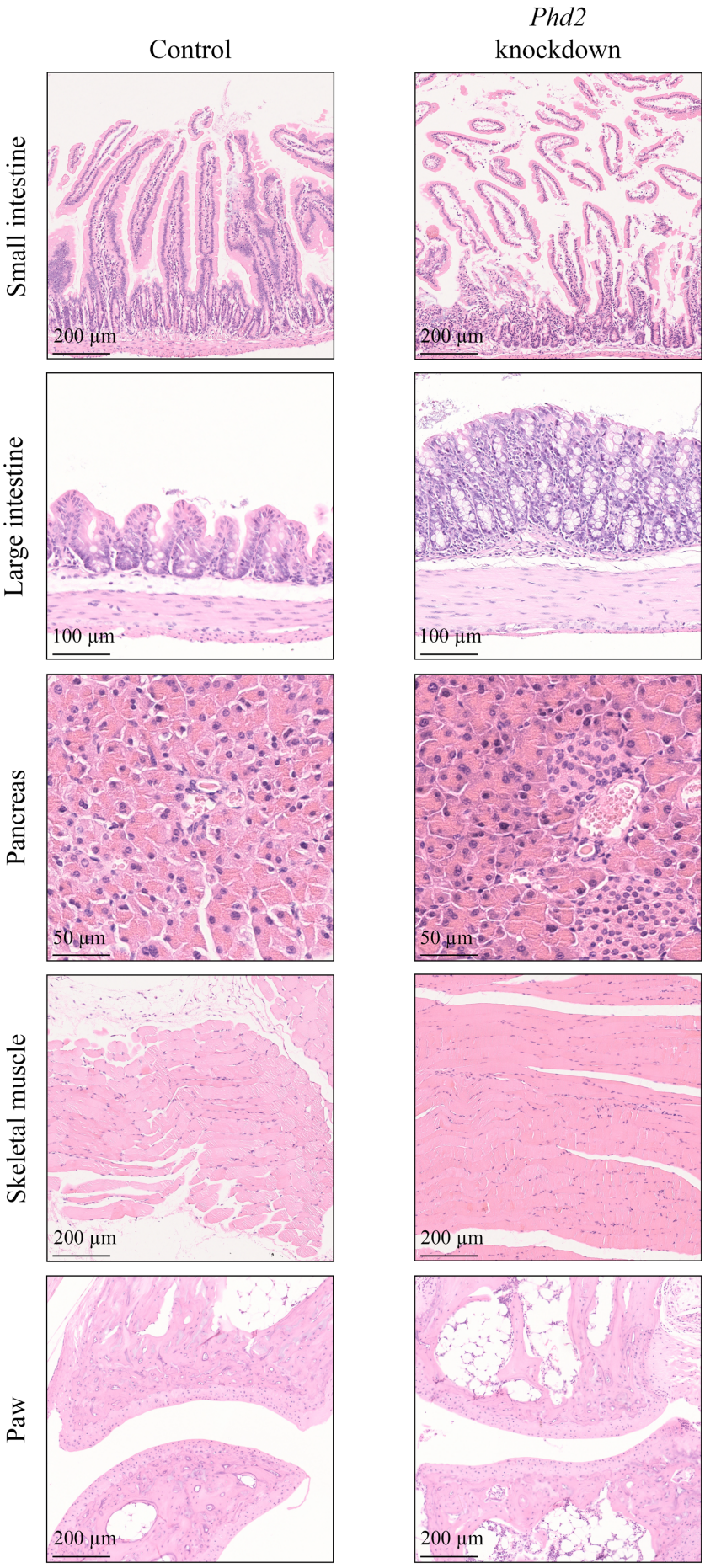
increase in glomerular size and endocapillary hypercellularity suggestive of nephritis; there was no tubulointerstitial inflammation. In the liver, smaller leukocyte clusters were seen in both periportal and perivenous sites. Focal leukocyte infiltration was also found in the epicardial region of the heart. Whilst findings in the small intestine were similar between groups, there was an increase in lymphocytes in the lamina propria, and focally in the crypts and surface epithelium, of the large intestine of transgenic animals only. Samples of the pancreas, skeletal muscle and joints of the paws were comparable between groups. Whilst lymphoid aggregates within internal organs (particularly mucosa-associated lymphoid tissue) are normal and can vary in size depending upon mouse strain [665], in this experiment aggregates were consistently more prominent in *Phd2* knockdown than control mice.

Immunohistochemical staining demonstrated that the mononuclear cells expanding the lymph nodes were predominantly $CD3^+CD4^+$ helper T lymphocytes, with some admixed $CD8^+$ T lymphocytes and $FOXP3^+$ T_{Reg}; paired box protein Pax-5 $(PAX5)^+$ B lymphocytes were displaced to the periphery and few $F4/80^+$ macrophages were identified; transgenic lymph nodes were also more proliferative (as assessed by Ki67 labelling) with reduced apoptosis (as assessed by Caspase 3 labelling) (**Figure 3.2B**). Similar findings were also apparent in the spleen and within the nodular leukocyte collections in the lungs and kidneys. The presence of T lymphocytes within the epidermis was also confirmed by CD3 immunostaining. Overall, given systemic involvement, lack of cellular atypia and necrosis and the admixture of different cell types, these findings were interpreted as being reactive changes with no definitive features of neoplastic transformation. Supporting this conclusion, flow cytometric analysis of peripheral lymph nodes conducted by collaborators demonstrated multi-lineage leukocyte expansion; counts of total leukocytes ($CD45^+$), T lymphocytes ($CD3^+$), B lymphocytes ($B220^+$) and granulocyte lineages ($Gr\text{-}1^+$) were all increased in lymph nodes from transgenic as

compared to control mice [227]. Therefore, the observed phenotype was one of moderate/severe inflammation, with evidence of multi-organ pathology suggestive of autoimmunity. Thus, we arranged testing for the presence of ANA (these are autoantibodies that bind to components of the cell nucleus and act as a marker of autoimmunity) which were detectable in the serum of transgenic, but not of control, mice within the first three weeks of doxycycline administration. All sera of *Phd2* knockdown mice showed a nuclear pattern of reactivity whilst control sera demonstrated either no or only weak reactivity. Using a semi-quantitative scoring system based on both proportion of nuclei stained and intensity of this staining, *Phd2* knockdown mice showed significantly elevated ANA scoring values (**Figure 3.2C**).


A
Control
Phd2 knockdown
Spleen
Lymph node
Thymus
Skin
1 mm
1 mm
1 mm
1 mm
400 µm
400 µm
100 µm
100 µm


Control
Phd2 knockdown
Lung
Kidney
Liver
Heart
200 µm
200 µm
200 µm
200 µm
200 µm
200 µm
100 µm
100 µm


Control
Phd2 knockdown
Small intestine
Large intestine
Pancreas
Skeletal muscle
Paw
200 µm
100 µm
50 µm

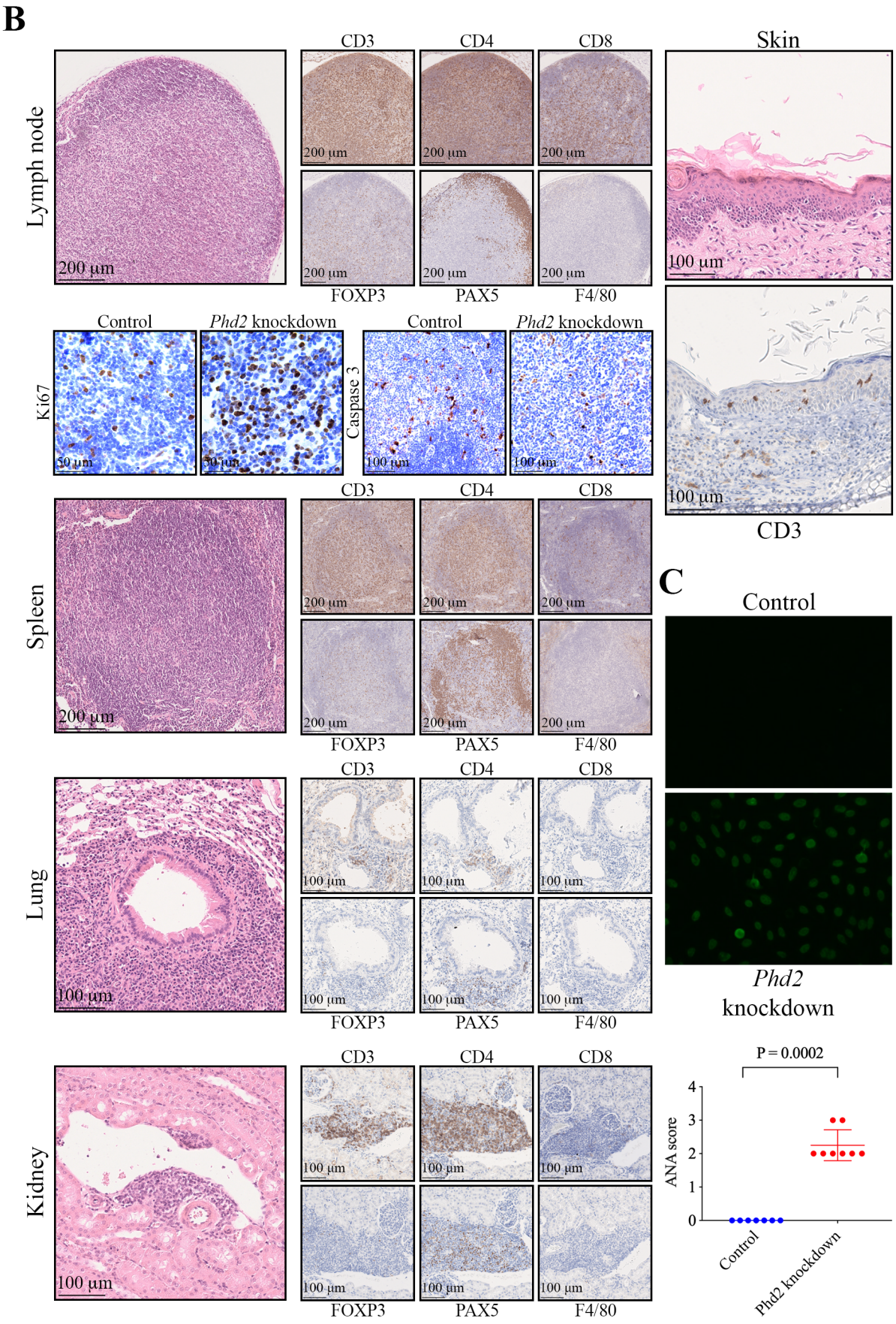

B
Lymph node
CD3
CD4
CD8
200 µm
FOXP3
PAX5
F4/80
Skin
100 µm
Control
Phd2 knockdown
Ki67
Caspase 3
50 µm
100 µm
CD3
Spleen
Lung
Kidney
C
Control
Phd2
knockdown
P = 0.0002
ANA score
0
1
2
3
4
Control
Phd2 knockdown

Figure 3.2 – Histological phenotyping of *Phd2* knockdown mice

(A) Representative haematoxylin and eosin stained tissue sections from Phd2 knockdown and littermate control mice following doxycycline administration for 5 weeks (with the exception of paw tissues, which were collected after 8 weeks). Arrows indicate exocytosis of lymphocytes into the epidermis (skin), a perivascular collection of mononuclear inflammatory cells (liver) and an epicardial collection of mononuclear inflammatory cells (heart) identified in Phd2 knockdown mice only. (B) Immunohistochemical phenotyping of an enlarged lymph node and spleen and inflammatory aggregates in the lung and kidney of Phd2 knockdown mice. (C) Representative fluorescent images and semi-quantitative analysis of anti-nuclear antibody (ANA) testing (0-1 = negative, 2-4 = positive) using serum from Phd2 knockdown and littermate control mice following doxycycline administration for 4-5 weeks. Data are represented as the mean ± standard deviation and are analysed by Mann-Whitney test (n = 7-8 mice per group). All data were consistent over three independent experiments.

The phenotype observed after long-term, systemic silencing of Phd2 represents an 'on-target' effect and is HIFα isoform specific

We then performed a series of further experiments to exclude the possibility that the observed phenotype was an 'off-target' effect caused by systemic shRNA expression. Multi-lineage leukocyte expansion, development of lymphadenopathy (mean = 83 mg vs. 8 mg per four lymph nodes) and splenomegaly (mean = 300 mg vs. 92 mg per spleen) and comparable histological changes were observed in a second transgenic mouse line bearing an independent sequence targeting *Phd2* (**Figure 3.3)**

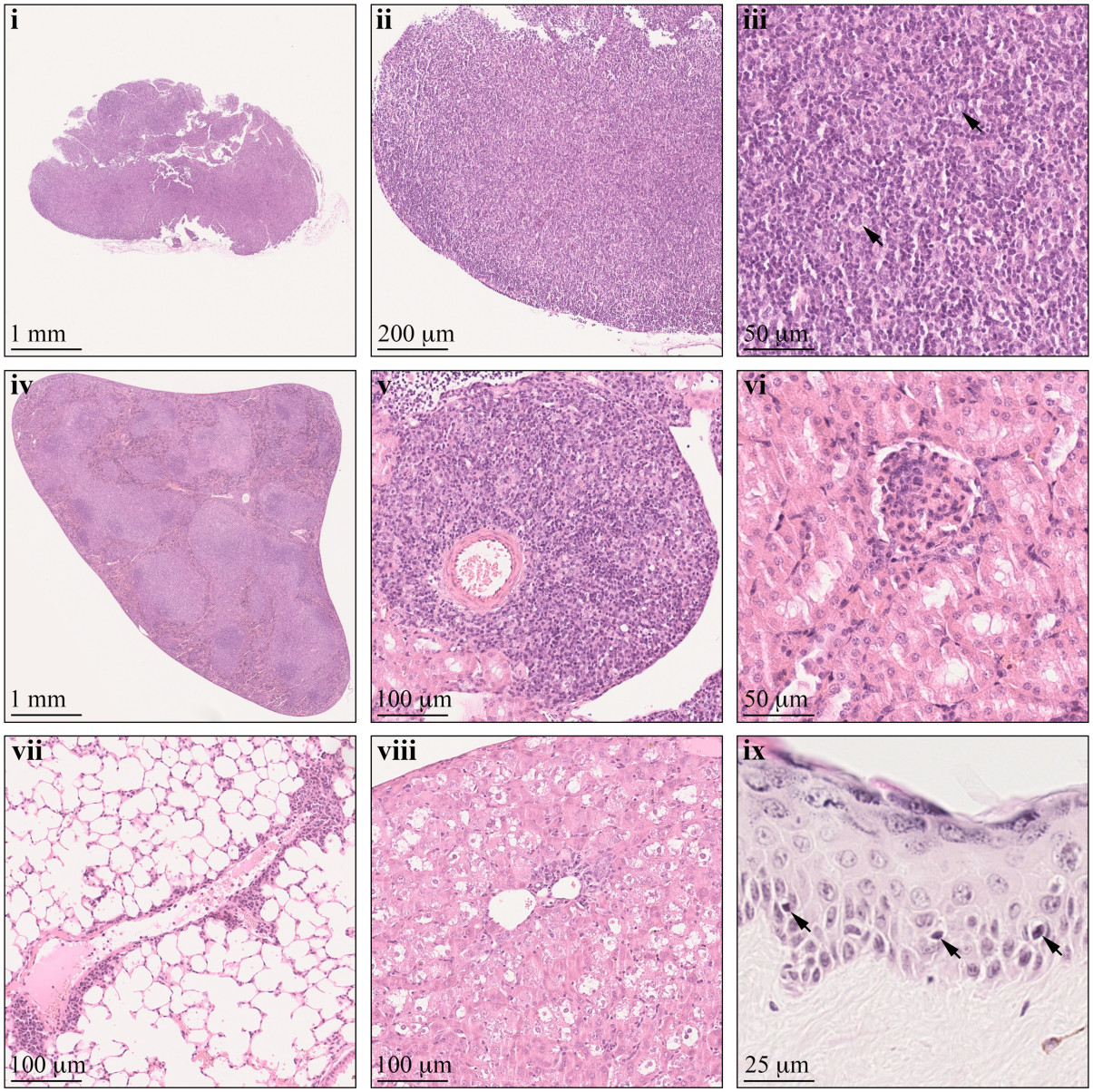
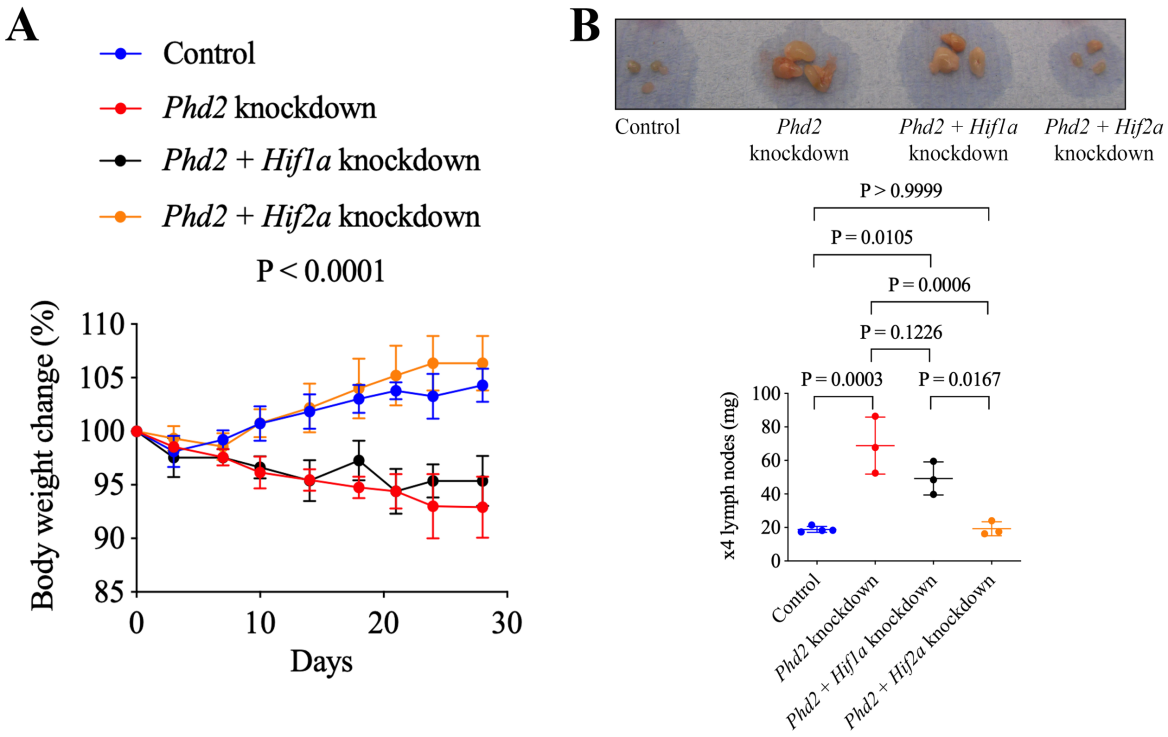


Figure 3.3 – Histological phenotyping of mice bearing a different short hairpin RNA (shRNA) sequence targeting *Phd2* for knockdown

Representative haematoxylin and eosin stained tissue sections from mice bearing a different shRNA sequence targeting Phd2 for knockdown following doxycycline administration for 8 weeks: lymph node (i-iii; arrows indicate 'centroblast-like' cells with oval, vesicular nuclei, prominent nucleoli and eosinophilic cytoplasm), spleen (iv), kidney (v & vi), lung (vii), liver (viii) and skin (ix; arrows demonstrate exocytosis of lymphocytes into the epidermis). All data were consistent over two independent experiments.

In order to assess whether the observed phenotype was dependent on stabilisation of one specific HIFα isoform, double knockdown mice, in which expression of both *Phd2* and either *Hif1a* or *Hif2a* are silenced concomitantly, were developed. I examined histological specimens from mice after four weeks of doxycycline administration and observed that the inflammatory histological changes associated with *Phd2* knockdown were abrogated with concomitant *Hif2a*, but not *Hif1a*, silencing (**Figure 3.4**). Once more, these histological findings were mirrored by flow cytometry results conducted by collaborators [227].


A
Control
Phd2 knockdown
Phd2 + Hif1a knockdown
Phd2 + Hif2a knockdown
P < 0.0001
Body weight change (%)
110
105
100
95
90
85
0
10
20
30
Days
B
Control
Phd2 knockdown
Phd2 + Hif1a knockdown
Phd2 + Hif2a knockdown
P > 0.9999
P = 0.0105
P = 0.0006
P = 0.1226
P = 0.0003
P = 0.0167
x4 lymph nodes (mg)
100
80
60
40
20
0
Control
Phd2 knockdown
Phd2 + Hif1a knockdown
Phd2 + Hif2a knockdown

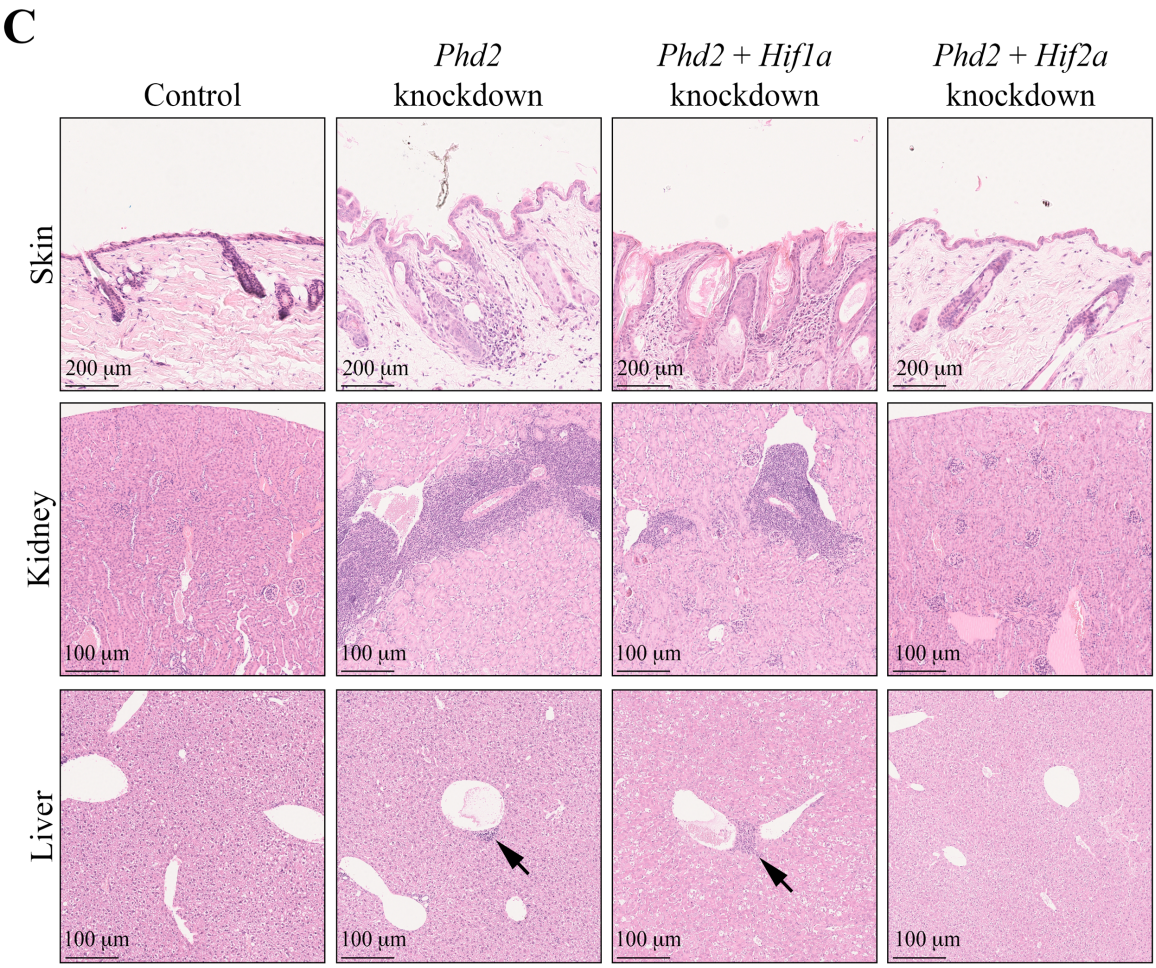

C
Control
Phd2 knockdown
Phd2 + Hif1a knockdown
Phd2 + Hif2a knockdown
Skin
Kidney
Liver
200 µm
100 µm

Figure 3.4 – Reduction of *Hif2a* expression reverses the phenotype in *Phd2* knockdown mice

(A) Mean percentage of body weight changes amongst Phd2, Phd2 + Hif1a, Phd2 + Hif2a knockdown and littermate control mice relative to Day 0 of doxycycline administration. Data are represented as the mean ± standard deviation (SD) and are analysed by two-way analysis of variance (ANOVA) with repeated measures (n = 3-4 mice per group). (B) Comparison of masses of lymph nodes from Phd2, Phd2 + Hif1a, Phd2 + Hif2a knockdown and littermate control mice following 4 weeks of doxycycline administration. Data are represented as the mean ± SD and are analysed by one-way ANOVA with Tukey's multiple comparisons post hoc test (n = 3-4 mice per group). (C) Representative haematoxylin and eosin stained tissue sections from Phd2, Phd2 + Hif1a, Phd2 + Hif2a knockdown and littermate control mice following 4 weeks of doxycycline administration (arrows indicate perivascular collections of mononuclear inflammatory cells).

The effects of long-term, systemic silencing of Phd2 are reversible upon re-expression of Phd2

We next explored the reversibility of the observed phenotype upon re-expression of *Phd2* following withdrawal of doxycycline. Mice were treated with doxycycline for four weeks leading to development of the aforementioned phenotype. At this point, serum and tissues were harvested from a randomly selected subset of mice and administration of doxycycline to the remaining animals was stopped. The latter group were observed for a further seven weeks before their serum and tissues were analysed. After initial administration of doxycycline, mice lost weight, developed lymphadenopathy and generated ANA; amongst animals taken off doxycycline, lost weight was regained, lymphadenopathy regressed and ANA disappeared (**Figure 3.5A-3.5C**). I confirmed the presence of the previously described histological changes amongst mice harvested after four weeks of doxycycline administration. Amongst the mice from which tissue was harvested at the latter time point, my observations showed that the histological features had also improved but, importantly, small residual foci of tissue

inflammation could still be identified in some organs, confirming that this group of mice had also developed autoimmunity during initial administration of doxycycline (**Figure 3.5D**).

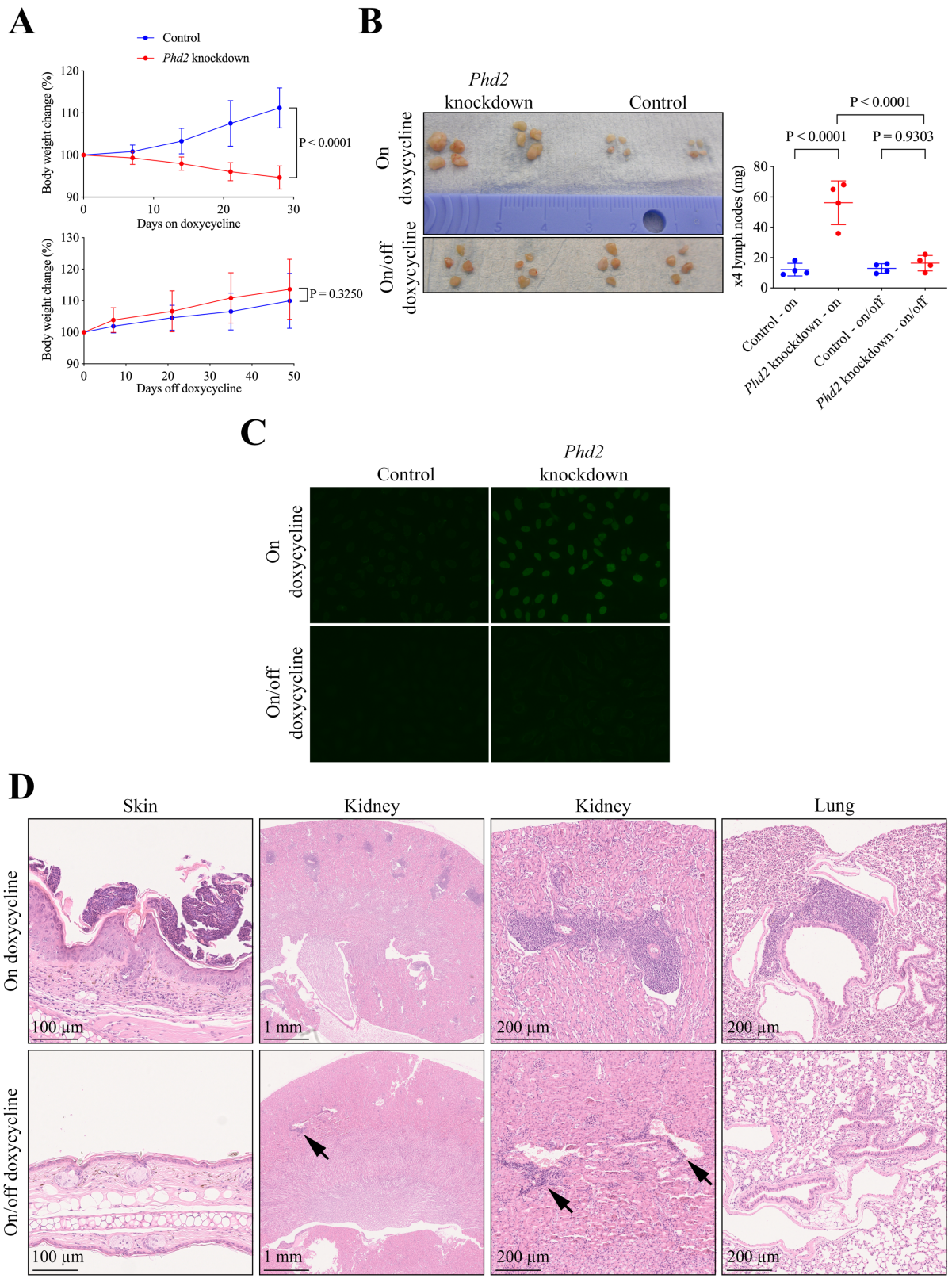


Figure 3.5 – Phenotypic reversal following withdrawal of doxycycline

(A) Mean percentage of body weight changes amongst Phd2 knockdown and control mice relative to Day 0 of doxycycline administration (n = 15 mice per group) or doxycycline withdrawal (n = 8 mice per group). Data are represented as the mean ± standard deviation (SD) and are analysed by mixed-effects analysis (on doxycycline) and two-way analysis of variance (ANOVA) with repeated measures (off doxycycline), respectively. (B) Comparison of masses of lymph nodes from Phd2 knockdown mice and their littermate controls either following doxycycline administration for 4 weeks (on doxycycline) or following doxycycline administration for 4 weeks and then analysed 7 weeks after doxycycline withdrawal (on/off doxycycline). Data are represented as the mean ± SD and are analysed by one-way ANOVA with Tukey's multiple comparisons post hoc test (n = 4 mice per group). (C) Representative fluorescent images from analysis of anti-nuclear antibody (ANA) testing using serum from 'on doxycycline' and 'on/off doxycycline' groups of Phd2 knockdown and littermate control mice. (D) Representative haematoxylin and eosin stained tissue sections from Phd2 knockdown mice in both the 'on doxycycline' and 'on/off doxycycline' groups (arrows indicate perivascular collections of mononuclear inflammatory cells). All data were consistent over two independent experiments.

The Phd2 knockdown phenotype is transferable by bone marrow transplantation

Since silencing of *Phd2* in the transgenic mice was systemic, it was unclear whether the observed autoimmune phenotype was primarily caused by altered leukocyte function or represented a more complex interaction between several different cell types; for example, disrupted epithelial barrier function in the skin, respiratory tract and/or gastrointestinal tract leading to ingress of exogenous alloantigen. To evaluate selectively the role of the immune system in this phenotype, we next performed transplantation of bone marrow from transgenic *Phd2* knockdown donor mice (identified by the pan-leukocyte marker CD45.2) to congenic wild-type recipient mice (identified by the pan-leukocyte marker CD45.1; a five amino acid difference between the CD45.1 and CD45.2 alleles results in altered protein conformation that can be differentiated by antibody-based assays such as flow cytometric analysis of peripheral blood [666, 667]). In parallel, a control group of mice was generated by transplanting bone

marrow from transgenic mice lacking the *Phd2* targeting shRNA sequence. Bone marrow was allowed to engraft for eight weeks following transplantation prior to commencement of doxycycline. Upon treatment with doxycycline, recipients of knockdown, but not control, bone marrow developed lymphadenopathy (**Figure 3.6A**) and generated ANA (**Figure 3.6B**). My examination showed that histological changes were present but were less prominent than in previous experiments (**Figure 3.6C**). In both the knockdown and control groups of animals, all peripheral blood leukocytes were CD45.2^{+} at the point of analysis, confirming complete bone marrow reconstitution by donor marrow. Thus, *Phd2* silencing restricted to bone marrow cells is sufficient to recapitulate the major features of systemic *Phd2* silencing, confirming that the observed autoimmune phenotype primarily results from dysfunction of leukocytes.

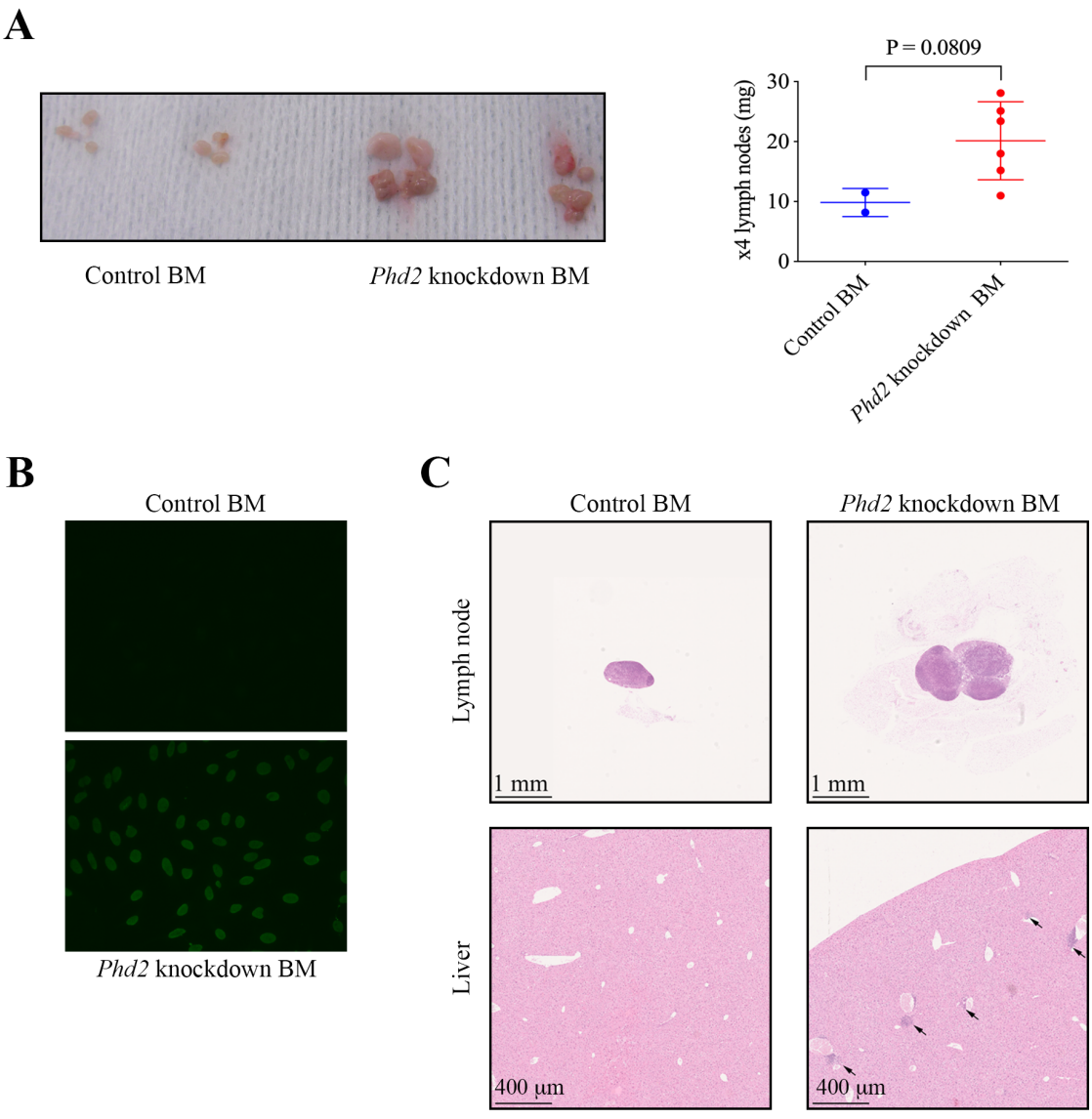


Figure 3.6 – Transfer of the *Phd2* knockdown phenotype by bone marrow transplantation

(A) Comparison of masses of lymph nodes from bone marrow recipient mice following doxycycline administration for 10 weeks. Syngeneic congenically marked (CD45.1$^+$) mice were lethally irradiated before receiving CD45.2$^+$ Phd2 knockdown bone marrow (BM) (n = 6 mice) or CD45.2$^+$ control BM (n = 2 mice) and allowed to reconstitute for 8 weeks prior to commencement of doxycycline administration. Data are represented as the mean ± standard deviation and are analysed by unpaired t-test. (B) Representative fluorescent images of anti-nuclear antibody (ANA) testing using serum from recipients of Phd2 knockdown and control BM. (C) Representative haematoxylin and eosin stained lymph node and liver sections from mice in each group (arrows indicate perivascular collections of mononuclear inflammatory cells). All data were consistent over two independent experiments.

Discussion

Summary of findings

Development of a novel mouse model to study dynamic changes in PHD-HIF hypoxia signalling *in vivo* revealed an unexpected autoimmune phenotype that developed upon systemic silencing of the gene encoding the principal HIF prolyl hydroxylase, PHD2. My contribution to this project was to perform histological assessment of tissue samples. Following 4-8 weeks of shRNA-mediated *Phd2* knockdown, transgenic mice developed multi-lineage leukocytosis and ANA, enlargement of secondary lymphoid organs with associated architectural distortion and nodular leukocyte aggregates within several internal organs. Qualitatively similar phenotypes observed after silencing *Phd2* by means of an alternative shRNA sequence, along with reversal of the phenotype with concomitant *Hif2a* silencing, strongly indicate that this phenotype is a true 'on-target' effect and is not caused by systemic shRNA expression (for example, as a consequence of TLR stimulation [668]). Furthermore, 'off-target' effects have not been reported in several other studies that have used the same RNAi system to silence other genes [669-672].

Several previous studies have investigated the *in vivo* effects of silencing *Phd2* expression by using the well established transgenic approach of gene knockout. At the level of the whole animal, germline deletion of *Phd2* results in developmental defects which are embryonic lethal due to defects in placentation (by comparison, due to their more restricted pattern of tissue expression, *Phd1* and *Phd3* knockout mice are viable) [673], whilst inducible knockout of *Phd2* in adult mice leads to increased angiogenesis [674] and erythrocytosis [675] with ultimately lethal consequences [676]. It is possible that these 'dominant' phenotypes obscured co-existing effects on the immune system which have not been described to date. Of note, one of these

studies did report the development of splenomegaly and leukocytosis in *Phd2* knockout mice [675], which are consistent with the findings presented here.

Taken together, these findings are suggestive of development of autoimmunity upon systemic *Phd2* silencing, with the phenotype being primarily driven by cells originating within the bone marrow. Since the observed phenotype normalises rapidly upon re-establishment of intact hypoxia-sensing machinery when doxycycline is discontinued and shRNA expression ceases, it is not caused by an irreversible change in, or deletion of, cells with immune regulatory function. Intriguingly, the immune dysregulation observed in our mice closely resembles that reported to occur in the Scurfy mouse which arose due to a spontaneous X-linked mutation [677]. Scurfy mice also develop skin crusting, splenomegaly, lymphadenopathy and ultimately die within 3-4 weeks of birth. The line remained poorly characterised for several decades until in-depth phenotyping demonstrated striking autoimmune pathology with prominent leukocyte infiltration in the liver and skin and smaller leukocyte aggregations in the lungs, kidneys, heart, pancreas and salivary glands [678]. Further studies confirmed that these changes were $CD4^+$ T lymphocyte-dependent [679-683] and resembled those occurring in mice deficient in TGFβ [684, 685] and CTLA-4 [686, 687], two critical molecules involved in T lymphocyte regulation. Ultimately, the Scurfy mutation was proven to be a two base pair insertion within the *Foxp3* gene on the X chromosome, leading to a reading frame shift and production of a truncated, non-functional protein [688]. Thereafter, FOXP3 was confirmed to be essential to the function of a newly identified immunoregulatory subset of $CD4^+CD25^+$ T lymphocytes (i.e. T_{Reg}) [689-691]. Thus, Scurfy mice are lacking in functional T_{Reg} required to control effector T lymphocytes, which enter a hyperactivated state and secrete elevated levels of pro-inflammatory cytokines that contribute to the development of autoimmunity [681, 682, 692]. Similarly, inherited mutations in the human *FOXP3* gene cause immune dysregulation

polyendocrinopathy enteropathy X-linked (IPEX) syndrome [693-695]. Individuals affected by this often-fatal disorder develop neonatal autoimmunity leading to thyroiditis, diabetes mellitus, diarrhoea, anaemia and dermatitis.

Similarities in the autoimmune phenotypes observed in *Phd2* knockdown mice and in Scurfy mice led us to examine further T_{Reg} from our mice. In experiments performed by collaborators and thus not presented in this thesis, we found that the absolute number of cells bearing T_{Reg} markers ($CD3^+CD4^+FOXP3^+$) in lymph nodes, spleen and bone marrow from *Phd2* knockdown mice was increased (in proportion to increases in other leukocyte subtypes) when compared with control mice [227]. In keeping with the overall phenotype, this increase was reversible on withdrawal of doxycycline and was totally corrected by simultaneous *Hif2a* silencing and partially corrected by simultaneous *Hif1a* silencing. Similar trends were also found in lymph nodes and bone marrow (but not spleen) of *Phd2* knockout mice. Thus, a deficiency in T_{Reg} numbers was not responsible for the observed phenotype. However, the functional capacity of *Phd2* knockdown T_{Reg} to suppress responder T lymphocyte proliferation *in vitro* (stimulated either polyclonally with anti-CD3/anti-CD28 beads or with allogeneic DC) and effector T lymphocyte-mediated skin allograft rejection *in vivo*, was found to be impaired. Furthermore, skin allograft rejection also occurred when *Phd2* knockdown T_{Reg} alone were adoptively transferred to recipient mice, indicating that transferred $CD4^+CD25^+$ T lymphocytes had in themselves acquired effector functions. Flow cytometric analysis of these cells demonstrated preservation of FOXP3 expression with consistently increased expression of T-box expressed in T cells (T-bet; the T_H1 master transcription factor) and TNFα (a key pro-inflammatory cytokine) but not of GATA3 (the T_H2 master transcription factor), retinoic acid receptor-related orphan receptor gamma t (RORγt; the T_H17 master transcription factor), IFNγ, IL-2, IL-4, IL-10 or IL-17. Furthermore, *Phd2* knockdown led to a reduction of cells with a

$CD44^{-}CD62L^{+}$ naïve phenotype and an increase in cells with a $CD44^{+}CD62L^{-}$ effector memory phenotype amongst both $CD4^{+}FOXP3^{+}$ and $CD4^{+}FOXP3^{-}$ T lymphocyte populations.

These experiments indicate that $CD4^{+}CD25^{+}$ T lymphocytes are intrinsically hypofunctional as immune regulators upon *Phd2* knockdown and demonstrate that deficiency in T_{Reg} function contributes to the autoimmune phenotype observed in systemic *Phd2* knockdown mice, explaining their analogous characteristics to Scurfy mice. However, it is worth highlighting that Scurfy mice lack functional FOXP3 whereas T_{Reg} in our mice maintain expression of wild-type FOXP3. Nevertheless, previous studies providing mechanistic insights into the immune dysregulation occurring in Scurfy mice may be of direct relevance to those occurring in *Phd2* knockdown mice:

1. The Scurfy phenotype is reversed when crossed with a transgenic line in which T lymphocytes express TCR specific for the exogenous antigen ovalbumin [683]. This evidence suggests that the observed phenotype is primarily dependent upon TCR self-reactivity against autoantigen and further allays the concern that the inflammatory phenotype observed in *Phd2* knockdown mice results from alterations in barrier function and ingress of alloantigen.
2. Scurfy mice have been shown to possess dormant autoimmune T lymphocytes that have the potential to induce additional pathologies (such as sialadenitis, gastritis and pancreatitis) upon adoptive transfer of Scurfy lymph node cells to immunodeficient mice [696]. The authors speculate that either lack of time for low-level effector T lymphocyte populations to expand (due to the early mortality of Scurfy mice) or environmental factors (such as passive transfer of antibodies and cytokines from mother to pups in milk), may suppress autoimmune reactions against certain organs and thus explain the tissue-restricted pattern of inflammation observed in Scurfy (and *Phd2* knockdown) mice.

3. Whilst mainly suppressing effector T lymphocytes, there is also evidence that T_{Reg} modulate other leukocyte subsets including B lymphocytes [697] and professional APC such as DC [698]. Scurfy mice have markedly elevated serum levels of polyclonal immunoglobulins, particularly of the IgM, IgG1, IgG3, IgA and IgE (sub)classes [678, 699]. Follicular T_{Reg} are recognised to suppress B lymphocyte responses within the germinal centres of secondary lymphoid organs [700] and dysfunction of Scurfy T_{Reg} leads to a failure of B lymphocyte anergy and consequent autoantibody synthesis [701].
4. Scurfy mice are reported to develop a range of autoantibodies that contribute to the observed pathological changes: antimitochondrial antibodies (reactive to pyruvate dehydrogenase E2) contribute to liver/bile duct inflammation [702], anti-keratin 14 autoantibodies contribute to skin inflammation [703] whilst immunoglobulin and complement deposits are detected in glomeruli [699, 704]. Furthermore, a positive direct Coombs test suggests that autoimmune haemolytic anaemia causes the low haematocrit in Scurfy mice [678]. Whilst not formally tested, the observations of profoundly yellow ('icteric') serum and splenic haemosiderin deposition are supportive of the occurrence of this phenomenon in our *Phd2* knockdown mice. The development of autoantibodies is a critical step in the development of end-organ inflammation in the Scurfy mouse, since genetic or pharmacological depletion of B lymphocytes reverses the autoimmune phenotype without impacting upon systemic T lymphocyte hyperreactivity [699].

Numerous studies have investigated the role of hypoxia in inflammatory/immunological reactions and have reported major HIFα-dependent effects in both innate and adaptive immune cells (as reviewed in [169, 170]). Whilst these experiments have revealed an important role for the PHD-HIF axis in immune cell function, the conclusions have not always been congruent. Several studies, predominantly using *in vitro* hypoxic culture and/or *Hif1a* knockout *in vivo*,

suggest that HIF1α stabilisation increases T_{Reg} abundance and/or immunosuppressive function; in the majority of studies this effect was mediated via up-regulation of FOXP3 expression [341, 386, 705-708]. Alternatively, other studies using similar approaches suggest that hypoxia/HIF1α stabilisation either promotes T_H17 differentiation over T_{Reg} differentiation or inhibits T_{Reg} development and/or function directly [49, 187, 188, 393, 395, 709-715]. Mechanistically, these effects were ascribed to a HIF1α-dependent metabolic shift from oxidative phosphorylation to glycolysis (the preferred metabolic pathways for T_{Reg} and T_H17 lymphocytes, respectively [186]) and/or HIF1α-mediated FOXP3 proteasomal degradation.

Other studies have investigated the effects of manipulation of other components of the PHD-HIF pathway and are, therefore, more directly comparable to the experiments presented in this chapter. T lymphocyte-restricted triple knockout of *Phd1*, *Phd2* and *Phd3* resulted in an increase in pulmonary $CD4^+$ and $CD8^+$ T lymphocytes (which were more activated as determined by increased expression of the markers CD25, CD44, CTLA-4 and IFNγ) but a reduction in pulmonary T_{Reg}, which together contributed to the development of lung-restricted immunopathology manifesting as diffuse alveolar haemorrhage [516]. T_{Reg}-restricted *Vhl* knockout resulted in a HIF1α-dependent reduction of FOXP3 expression, conversion of T_{Reg} to a T_H1-like phenotype (with HIF1α-dependent transcription of *Ifng*) and massive multi-organ inflammation [716] resembling that seen upon systemic *Phd2* silencing in our own mice (however, in our experiments FOXP3 expression was maintained and the phenotype was HIF2α-dependent). In a study currently only published in abstract form, T_{Reg}-restricted *Phd2* knockout also produced a T_H1-like inflammatory response with increased susceptibility to both chemically-induced colitis and experimental autoimmune encephalitis [717]. Interestingly, concomitant *Hif1a* knockout did not reverse this phenotype, which hints at possible HIF2α dependence. PHD3 is highly expressed in T_{Reg} and is reported to enhance T_{Reg} development by

negatively regulating HIF1α levels and thus augmenting FOXP3 levels; silencing *Phd3* alone in murine T_{Reg} reproduces the reciprocal skewing of T_H17:T_{Reg} differentiation described above [718].

Taken together, the weight of evidence from these reports suggests that HIFα stabilisation within T_{Reg} does impair their immunosuppressive capacities and promotes either T_H1- or T_H17-like inflammation. However, the abrupt, cell-restricted interventions they deploy are very un-physiological and the different transgenic interventions and disease models used in these studies may explain, at least in part, the different phenotypes described.

Clinical relevance

The findings reported in this chapter are likely to be of direct relevance to human pathophysiology and to the treatment of human disease in several ways:

1. There are potentially important implications for the advanced pharmaceutical programs aiming to treat renal anaemia with PHD inhibitors. After diabetic nephropathy, glomerulonephritis is the second commonest cause of chronic kidney disease [719]; the hallmark of this disease category is inflammation of glomeruli which can be caused by several forms of autoimmune disease including lupus nephritis, IgA nephritis and anti-glomerular basement membrane (Goodpasture's) disease. Treating such patients with PHD inhibitors might, therefore, exacerbate their underlying autoimmune disease. However, the systemic interventions we used are very large in relation to the low and intermittent doses of PHD inhibitors being administered in current clinical trials and this approach might therefore be expected to have a less profound effect on the host immune system. Furthermore, and of utmost importance from a clinical perspective, the autoimmune

phenotype that we observed was reversible and would thus be expected to resolve upon withdrawal of therapy.

2. Therapeutic manipulation of the PHD-HIF axis could be a potential strategy to treat a range of human diseases characterised by immune dysfunction. Silencing of *PHD2* in T_{Reg} might potentiate immune responses when this is predicted to be of benefit (for example, in the treatment of cancer or chronic infection). However, caution should be exercised upon proceeding with such a strategy in humans due to the risk of severe, albeit most likely reversible, immune-related toxicities. Conversely, HIFα silencing (in particular, HIF2α, potent and selective inhibitors of which are in current clinical trials for the treatment of CCRCC [720]) might potentiate T_{Reg} function and suppress undesirable immune activation (for example, in a variety of autoimmune diseases and in solid organ transplantation).

Strengths, limitations and future directions

The experiments outlined in this chapter are, to my knowledge, the first to interrogate T lymphocyte function in the setting of systemic silencing of *Phd2*, as opposed to cell-specific *Phd2* knockout. This difference is of critical importance given the complexity of 'crosstalk', both between different leukocyte subsets as well as between leukocytes and other cell types, during immunological reactions. The findings presented in this chapter are strengthened by consistency in two transgenic lines with different shRNAs targeting *Phd2* and by similar, although less pronounced, effects in inducible *Phd2* knockout mice [227]. Although the commonalities with Scurfy mice and results of functional assays point to T_{Reg} dysfunction being responsible for the autoimmune phenotype, we have not yet delineated a cell intrinsic mechanism. Therefore, future work should focus on assessing the phenotype of mice in which *Phd2* knockdown is restricted to FOXP3-expressing cells [721], with particular attention paid to the cellular metabolic consequences of this intervention. Furthermore, given that HIF has

been reported to regulate the balance of T_{Reg} with T_H9 [722] and T_H17 lymphocytes [187, 188], in depth examination of these helper T lymphocyte subsets should form part of this work.

The work presented in this chapter identifies a critical role for HIF2α in modulating T_{Reg} function which had not been described previously. Subsequently, HIF2α has been reported to both suppress *in vitro* T_{Reg} differentiation [722] and to be indispensable for T_{Reg} function (since its deletion leads to increased HIF1α expression and T_H17 differentiation) [723]. These discrepant results highlight the complexity of HIF signalling within T_{Reg} and suggest that HIF2α levels must be tightly regulated in these cells, since both its accumulation and complete loss compromise immunosuppressive capacity. Further studies of the role of the PHD2-HIF2α axis in inflammation, autoimmunity and cancer are clearly merited. Thus, in the next chapter, I investigate the effects of systemic *Phd2* knockdown on the growth of syngeneic murine tumours.

Chapter 4

Chapter aim

To analyse the effects of systemic *Phd2* silencing on growth of wild-type tumour grafts and the anti-tumour immune response in mice.

Introduction

T_{Reg} are a subset of $CD4^+$ helper T lymphocytes that function to suppress self-reactive T lymphocytes and thus to maintain immunological self-tolerance and prevent autoimmunity [689-691]. In addition to controlling initial T_{Reg} development, continued expression of FOXP3 is required to maintain the immunosuppressive capacities of mature T_{Reg} [724, 725], which can convert to pro-inflammatory effector T lymphocytes upon loss of FOXP3 expression [726, 727]. FOXP3 is a transcription factor that can directly bind to and activate or repress approximately 700 genes involved in the development and maturation of T_{Reg} [728, 729], although it can also indirectly influence the expression of many more genes through interactions with over 260 other proteins including transcription factors and epigenetic modifiers [730]. Immunosuppression by T_{Reg} is mediated by a range of different contact-dependent and contact-independent mechanisms:

1. Cell surface expression of immune checkpoint molecules including CTLA-4 [571] and lymphocyte activation gene 3 (LAG3; a CD4-related molecule that binds MHC class II) [731] leading to contact-dependent inhibition of APC;
2. Inhibition of production [732, 733], and competitive consumption, of IL-2, an essential cytokine supporting the stimulation and proliferation of effector T lymphocytes (T_{Reg} scarcely produce IL-2 but are highly dependent upon it for survival given their constitutive expression of CD25, a high-affinity IL-2 receptor);

3. Depletion of essential amino acids required for effector T lymphocyte function; for example, through the production of the tryptophan degrading enzyme indoleamine 2,3-dioxygenase (IDO) [734, 735];
4. Production of immune inhibitory cytokines and molecules such as IL-10, IL-35 and TGFβ [736-738];
5. Apoptotic T_{Reg} release large amounts of ATP which is converted by CD73 and CD39, expressed on the T_{Reg} cell surface, to adenosine, a molecule with both T lymphocyte and APC suppressive effects [739];
6. Secretion of granzyme and/or perforin to directly kill effector T lymphocytes [740].

Given that T_{Reg} function to suppress immune responses under physiological conditions, it has been postulated that they also inhibit anti-tumour immunity [741-743]. In support of this concept, several systematic reviews demonstrate that high T_{Reg} infiltration is associated with a poor prognosis across a range of human tumours [121, 744, 745]. On this basis, targeting of T_{Reg}, with the aim of potentiating tumour cell killing by effector T lymphocytes, has emerged as a possible strategy in the treatment of cancer. Supporting such an approach, studies in mice have demonstrated that T_{Reg} do indeed promote tumour development and progression [746, 747]. In these studies, depletion of T_{Reg}, either by administration of anti-CD25 monoclonal antibody or by adoptive transfer of $CD25^+$ cell-depleted splenocytes to T lymphocyte deficient mice, led to regression of syngeneic tumours. T_{Reg} depletion was associated with normalisation of tumour vasculature (reduced vessel dilatation and leakiness) and increased infiltration by tumour-specific CTL. In addition to nullifying their direct immunosuppressive effects, T_{Reg} depletion favours the development of high endothelial venules (specialised blood vessels normally found within secondary lymphoid organs that facilitate lymphocyte extravasation)

within tumours, promoting recruitment of effector T lymphocytes and subsequent tumour eradication [748, 749].

Several pharmacological strategies have been proposed to target T_{Reg} in cancer as summarised below (and reviewed in [743, 750]).

1. Targeting T_{Reg} for depletion

Two main pharmacological strategies exist to deplete T_{Reg} directly: (i) administration of an anti-CD25 monoclonal antibody (e.g. daclizumab) [746, 747] or (ii) administration of a recombinant fusion protein that contains IL-2 linked to diphtheria toxin [751]. In humans, such approaches produced anti-tumour effects when administered either alone in melanoma [752] or in combination with anti-tumour vaccination in melanoma [753, 754] and breast cancer [755]. However, another study failed to report a benefit of daclizumab in combination with vaccination for metastatic melanoma and suggested that this lack of effect related to inhibition of $CD25^{+}FOXP3^{-}$ T lymphocytes (i.e. activated non-T_{Reg} T lymphocytes) [756]. Interestingly, certain chemotherapeutics (such as the alkylating agent cyclophosphamide) also deplete T_{Reg} and this action has been proposed to indirectly potentiate their anti-tumour effects both in rodents [757, 758] and humans [759-761].

2. Targeting immune-checkpoint molecules expressed by T_{Reg}

Tumour infiltrating T_{Reg} express both CTLA-4 and PD-1, suggesting that ICB might target this population of cells. Initially, the efficacy of anti-CTLA-4 therapy (e.g. ipilimumab) was proposed to depend upon reinvigoration of dysfunctional CTLA-4 expressing effector T lymphocytes. However, several studies in both mice [762-765] and humans [766] now suggest that the mechanism of action of these drugs also involves depletion of T_{Reg}, with the overall

effect of increasing the intratumoural CTL:T_{Reg} ratio (although, not all studies have reported this finding [767]). Overall, signalling through PD-1 appears to limit T_{Reg}-mediated immunosuppression within tumours and anti-PD-1 immune checkpoint inhibitors may actually enhance T_{Reg} activity, contributing to the disease hyperprogression observed in a subset of patients that receive this therapy [768, 769].

3. Targeting intracellular signalling in T_{Reg}

Cell signalling cascades, such as the PI3K-protein kinase B (AKT)-mTOR pathway, that are crucial for T_{Reg} survival and function can be inhibited to attenuate their immunosuppressive function [770]. Inhibition of the PI3K delta isoform (PI3Kδ) allows selective elimination of T_{Reg} whilst preserving effector $CD4^+$ T lymphocytes and synergises with vaccination to potentiate anti-tumour immunity in mice (PI3Kδ is functionally redundant with PI3Kα and PI3Kβ in effector $CD4^+$ T lymphocytes but not in T_{Reg}, allowing selective depletion of T_{Reg} upon its inhibition) [771]. Combination therapy of a PI3Kδ inhibitor and anti-PD-1 ICB (pembrolizumab) is currently being tested in advanced solid human tumours (ClinicalTrials.gov Identifier: NCT02646748).

4. Targeting T_{Reg}-modulating factors within the TME

A number of factors within the TME can be manipulated to target T_{Reg} survival and/or function indirectly. For example, IDO is expressed in several cancer types and metabolises the amino acid tryptophan (essential for effector T lymphocyte survival and proliferation) to the immunosuppressive metabolite kynurenine which recruits both immunosuppressive T_{Reg} and MDSC to tumours [772]. Whilst IDO inhibitors (e.g. epacadostat) are currently in clinical trials [773], data relating to their effects on T_{Reg} have not yet been reported. In addition to chemokines including CCL5 [774], CCL22 [741, 775, 776], CCL28 [383] and CXCL12 [777],

the VEGF-A-vascular endothelial growth factor receptor (VEGFR) axis also promotes T_{Reg} accumulation within tumours and its inhibition blocks this, both in animal models [389, 778] and human gastric cancer patients [779]. Finally, tumour-derived TGFβ supports the peripheral conversion of naïve $CD4^+$ T lymphocytes to T_{Reg} in mice [780]. Furthermore, TGFβ secreted by both tumour cells [781] and T_{Reg} [736] directly suppresses effector T lymphocyte function and facilitates murine tumour growth. Consequently, administration of the TGFβ receptor antagonist galunisertib (alone or in combination with anti-PD-L1 immunotherapy) increased the CTL:T_{Reg} ratio in murine tumours and in some cases led to complete tumour regression [782]. Combinations of galunisertib with either anti-PD-1 (nivolumab) or anti-PD-L1 (durvalumab) therapy are currently in clinical trials (ClinicalTrials.gov Identifiers: NCT02423343, NCT02734160).

Based upon the findings presented in Chapter 3 of this thesis, which indicate that the PHD2-HIF2α axis is critical for maintaining T_{Reg} immunosuppressive function, I next elected to test whether systemic *Phd2* knockdown might offer an alternative approach to inhibiting T_{Reg} function and thus enhance anti-tumour immunity. Specific rationale for adopting this experimental approach were:

1. Systemic *Phd2* silencing not only reduces T_{Reg} immunosuppressive function but also causes them to acquire an effector phenotype (with acquisition of expression of the T_H1 transcription factor T-bet and synthesis of the pro-inflammatory cytokine TNFα) [227];
2. Previous reports suggest that stabilisation of HIFα in other T lymphocyte populations can potentiate their effector functions and, when tested, increase their anti-tumour effects [183, 314, 516] (PHD2 is the principal isoform in CTL, which express little or no PHD1 or PHD3 [783]) and during prolonged *Phd2* knockdown in our mice, $CD4^+FOXP3^-$ cells within peripheral lymph nodes demonstrate increased expression of T-bet, TNFα and IFNγ [227],

the latter two being crucial anti-tumour T_H1 cytokines [784] with IFNγ also capable of promoting intratumoural T_{Reg} dysfunction to further potentiate anti-tumour immunity [395] and IFNγ-induced ischaemia leading to tumour collapse [785];

3. PHD2 deficiency in non-neoplastic stromal cells improves tumour perfusion and reduces tumour hypoxia [786];
4. If the approach proves to be effective, it could be replicated pharmacologically by administration of PHD inhibitors.

Furthermore, whilst conducting these experiments, an article was published that reported that murine T_{Reg}-restricted deletion of mitochondrial respiratory chain complex III produces a similar phenotype to that observed in our *Phd2* knockdown mice (i.e. severe multi-organ inflammation despite maintenance of T_{Reg} numbers and preservation of FOXP3 expression) and that these mice were resistant to establishment of tumours upon subcutaneous inoculation of B16 murine melanoma cells [631].

Results

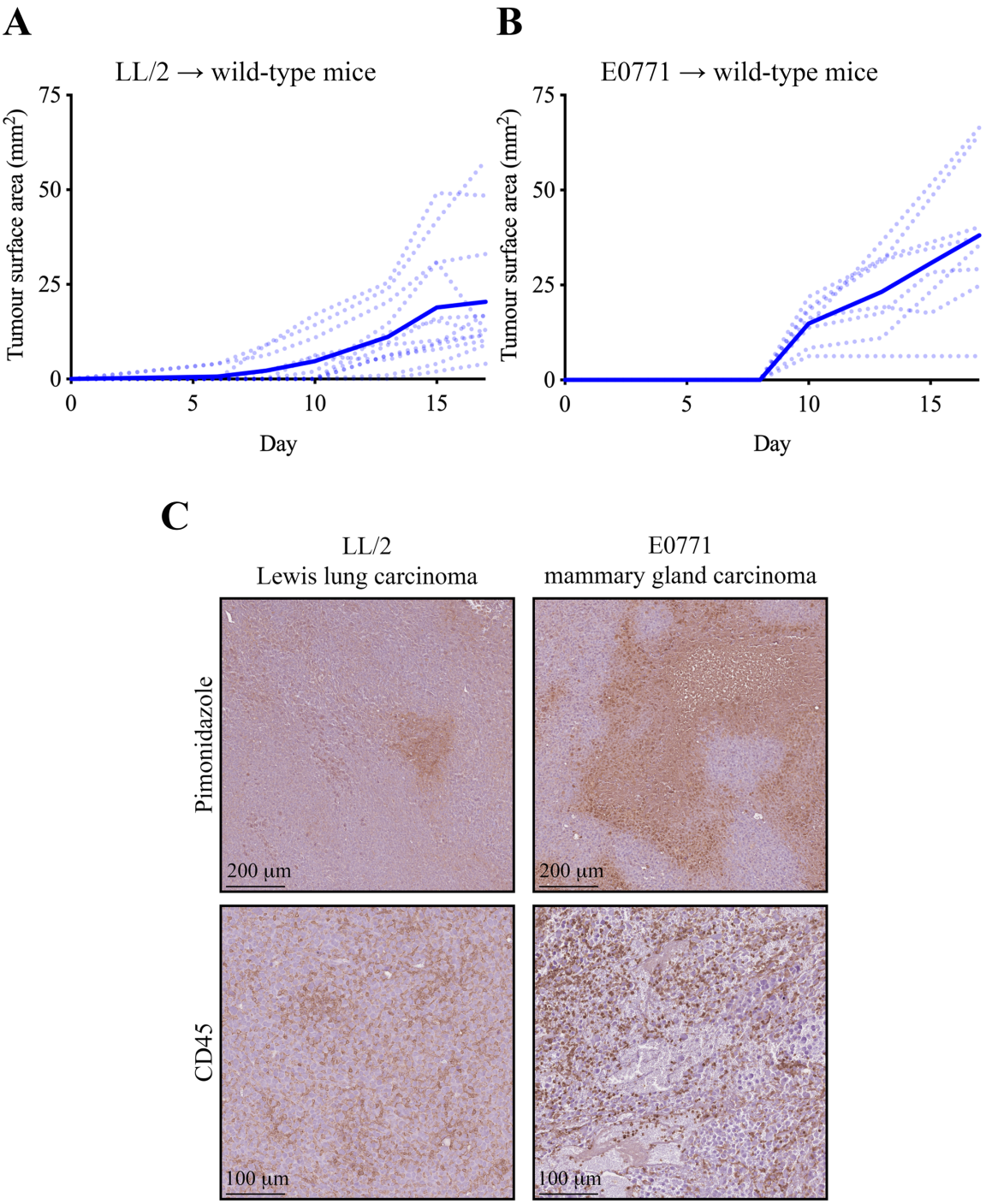
Development of a murine tumour model

Transplantable tumour models, produced by subcutaneous, orthotopic or intravenous inoculation of cultured murine tumour cells into immunocompetent syngeneic recipients, reproducibly generate solid tumours with a short latency period and have thus been a workhorse of cancer immunology research for decades [787, 788]. Importantly, this approach facilitates examination of the effects of manipulation of tumour and/or host cells on anti-tumour immunity in a reasonably high-throughput manner. Furthermore, such models also provide flexibility in the timing of genetic and/or pharmacological interventions. Therefore, it is possible to assess the effects of these interventions both on the treatment of established tumours

as well as part of strategies to optimise anti-tumour immunity in the absence of primary tumour-induced immunosuppression, which might be of relevance in the clinical setting of minimal residual disease after initial treatment with the aim of prevention of subsequent tumour recurrence.

In the experiments presented in this chapter, subcutaneous implantations were performed because of ease of monitoring tumour growth. Preliminary experiments were performed to optimise the establishment of transplantable syngeneic tumours in wild-type C57BL/6J mice (which are of the same murine MHC haplotype, *H2b*, as our knockdown lines). After a review of the literature, I selected two *H2b* murine tumour cell lines (LL/2 and E0771) for optimisation. Importantly, both tumour models have been shown to develop regions of hypoxia (LL/2 [356, 789] and E0771 [790-792]) and to be sensitive to adaptive anti-tumour immune responses (LL/2 [281, 793, 794] and E0771 [795-798]). LL/2 (also known as LLC1 [Lewis lung carcinoma line 1]) is a murine NSCLC cell line, established from a lung tumour arising in a C57BL/6J mouse following implantation of primary Lewis lung carcinoma (LLC) cells, that has the advantage over its parental cells of being adapted to *in vitro* cell culture [799]. It possesses many mutations found commonly in human lung cancer including deletion of *Trp53* and *Cdkn2a* [800] and mutation of *Kras* [801]. E0771, derived from a murine mammary gland adenocarcinoma that developed spontaneously in a C57BL/6J mouse, is a model of human triple negative breast cancer (TNBC) [790, 791]; this aggressive tumour subtype lacks expression of both oestrogen and progesterone receptor and does not harbour human epidermal growth factor receptor 2 (*HER2*) over-amplification and is thus difficult to treat pharmacologically. Importantly, targeting T_{Reg} has been proposed as a credible therapeutic strategy for both human NSCLC [802, 803] and breast cancer [804], particularly TNBC, which is enriched with highly immunosuppressive T_{Reg} [369].

In line with previous studies, injection of both LL/2 cells (5 x 10^4 cells in 50 μL PBS per injection [805]) and E0771 cells (1 x 10^5 cells in 50 μL PBS per injection [806]) into wild-type C57BL/6J recipient mice generated tumours that were first detectable after about two weeks (**Figure 4.1A and 4.1B**); given our Home Office PPL stipulates a maximum tumour diameter of 12.5 mm (156.25 mm^2), this growth rate permits evaluation of anti-tumour immune responses over a 3-4 week period, which should allow an adaptive immune response to develop. Importantly, immunohistochemical staining demonstrated that both tumour models developed regions of hypoxia (as identified by pimonidazole labelling) and immune cell infiltrates (as identified by CD45 [leukocyte common antigen] immunostaining) (**Figure 4.1C**). Our transgenic knockdown mice were generated using parental KH2 embryonic stem cells that contain a 'homing' cassette downstream of the *ColA1* gene for insertion of the desired shRNA sequence [654, 655]. Since these cells are derived from a cross between C57BL/6J and 129/Sv mice (also of murine MHC haplotype *H2b* but with some differences in minor histocompatibility alleles), initial litters of transgenic mice were then backcrossed six times with wild-type C57BL/6J mice to achieve > 99% genetic purity. Nevertheless, given that 129/Sv mice are not considered to be truly inbred and are thus prone to alloimmunity [807], I next confirmed that the same cell lines could be successfully grown as syngeneic tumours in our knockdown mice (experiments performed in mice of varying genotype but all derived from the same transgenic colony) (**Figure 4.1D and 4.1E**). Given evidence that doxycycline itself can have direct cytotoxic effects on murine tumour cell lines *in vitro* [808] and can slow LL/2 tumour growth *in vivo* [809], I then tested whether its administration would dramatically affect tumour growth in our mice. Reassuringly, administration of doxycycline from Day 17 did not eradicate established LL/2 or E0771 tumours (experiments performed in C57BL/6J mice from various colonies available in the Ratcliffe/Pugh laboratory that would not otherwise have been used for experimental work) (**Figure 4.1F and 4.1G**).


A
LL/2 → wild-type mice
Tumour surface area (mm²)
75
50
25
0
0
5
10
15
Day
B
E0771 → wild-type mice
Tumour surface area (mm²)
75
50
25
0
0
5
10
15
Day
C
LL/2
Lewis lung carcinoma
E0771
mammary gland carcinoma
Pimonidazole
CD45
200 µm
200 µm
100 µm
100 µm

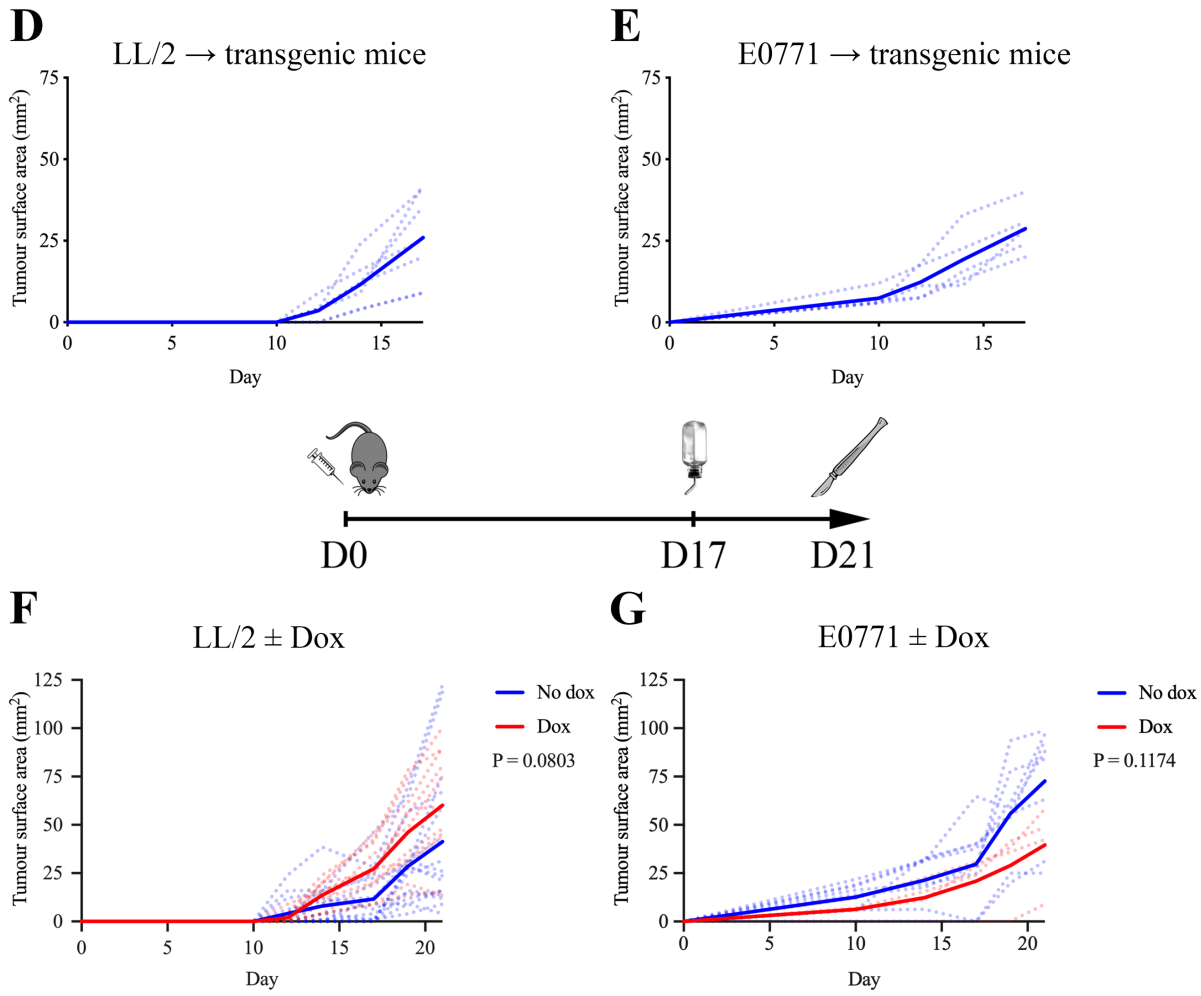


Figure 4.1 – Development of a murine tumour model

(A) Mean (solid line) and individual (dotted lines) growth curves for LL/2 (Lewis lung carcinoma) tumours grown in wild-type recipient mice (n = 12 tumours from 6 mice across two experiments). (B) Mean (solid line) and individual (dotted lines) growth curves for E0771 (murine mammary gland adenocarcinoma) tumours grown in wild-type recipient mice (n = 8 tumours from 6 mice across two experiments). (C) Representative immunohistochemical demonstration of regional hypoxia (pimonidazole) and leukocyte infiltration (CD45) within both LL/2 and E0771 tumours. (D) Mean (solid line) and individual (dotted lines) growth curves for LL/2 tumours grown in transgenic recipient mice (n = 7 tumours from 4 mice in one experiment). (E) Mean (solid line) and individual (dotted lines) growth curves for E0771 tumours grown in transgenic recipient mice (n = 5 tumours from 4 mice in one experiment). (F) Mean (solid line) and individual (dotted lines) growth curves for LL/2 tumours grown in transgenic recipient mice of variable genotype with (red) or without (blue) administration of

doxycycline (Dox) from Day 17. Data are analysed by two-way analysis of variance (ANOVA) with repeated measures (n = 11 tumours from 6 mice treated with doxycycline and 16 tumours from 9 mice not treated with doxycycline across three experiments). (G) Mean (solid line) and individual (dotted lines) growth curves for E0771 tumours grown in transgenic recipient mice of variable genotype with (red) or without (blue) administration of doxycycline from Day 17. Data are analysed by two-way ANOVA with repeated measures (n = 4 tumours from 2 mice treated with doxycycline and 8 tumours from 6 mice not treated with doxycycline across three experiments).

In summary, these small pilot experiments provided evidence that I could generate subcutaneous tumours in both wild-type C57BL/6J and transgenic mice, that these tumours contained regions of hypoxia and immune cell infiltrates and that doxycycline administration did not cause tumour regression. Thus, they confirmed the feasibility of subsequent, larger experiments that evaluated the effect of systemic *Phd2* knockdown on tumour growth.

Systemic *Phd2* knockdown after subcutaneous inoculation of tumour cells

I initially elected to commence *Phd2* knockdown after tumour cell inoculation, as this scenario most closely parallels clinical practice (i.e. beginning treatment after the diagnosis of a tumour). In the first experiment, LL/2 tumours were established in four *Phd2* knockdown mice and in four control mice (all from the same transgenic breeding line but of various different genotypes that would not lead to *Phd2* knockdown upon administration of doxycycline). Doxycycline was administered to both groups from Day 3 after tumour cell inoculation and tumour growth was monitored for a further three weeks, with the aim of allowing enough time to permit the generation of an adaptive immune response. No difference in tumour growth was detected when assessed either by tumour surface area *in vivo* or by tumour volume or tumour mass after tumour explantation (**Figure 4.2A-4.2C**). To evaluate the effects of *Phd2* knockdown on the anti-tumour immune response, I performed immunohistochemical staining

for the pan-T lymphocyte marker CD3. In common with human tumours, there was noticeable heterogeneity in the extent and location of T lymphocyte infiltrates both within and between tumours. Furthermore, tumour infiltrating T lymphocytes were generally more numerous at the tumour periphery, as compared to the centre, and were often arranged in clusters. Overall, there was no quantitative difference in T lymphocyte infiltration between groups, as assessed in four randomly chosen fields of each tumour (**Figure 4.2D**). However, testing of peripheral blood collected at the time of tumour harvest demonstrated that only 1/4 *Phd2* knockdown mice had developed ANA by the end of the experiment (as compared to 0/4 control mice), suggesting that the autoimmune phenotype had not developed in this cohort, perhaps due to the shorter period of knockdown in this experiment (i.e. only 3 weeks as compared to 4-5 weeks in the experiments outlined in Chapter 3).

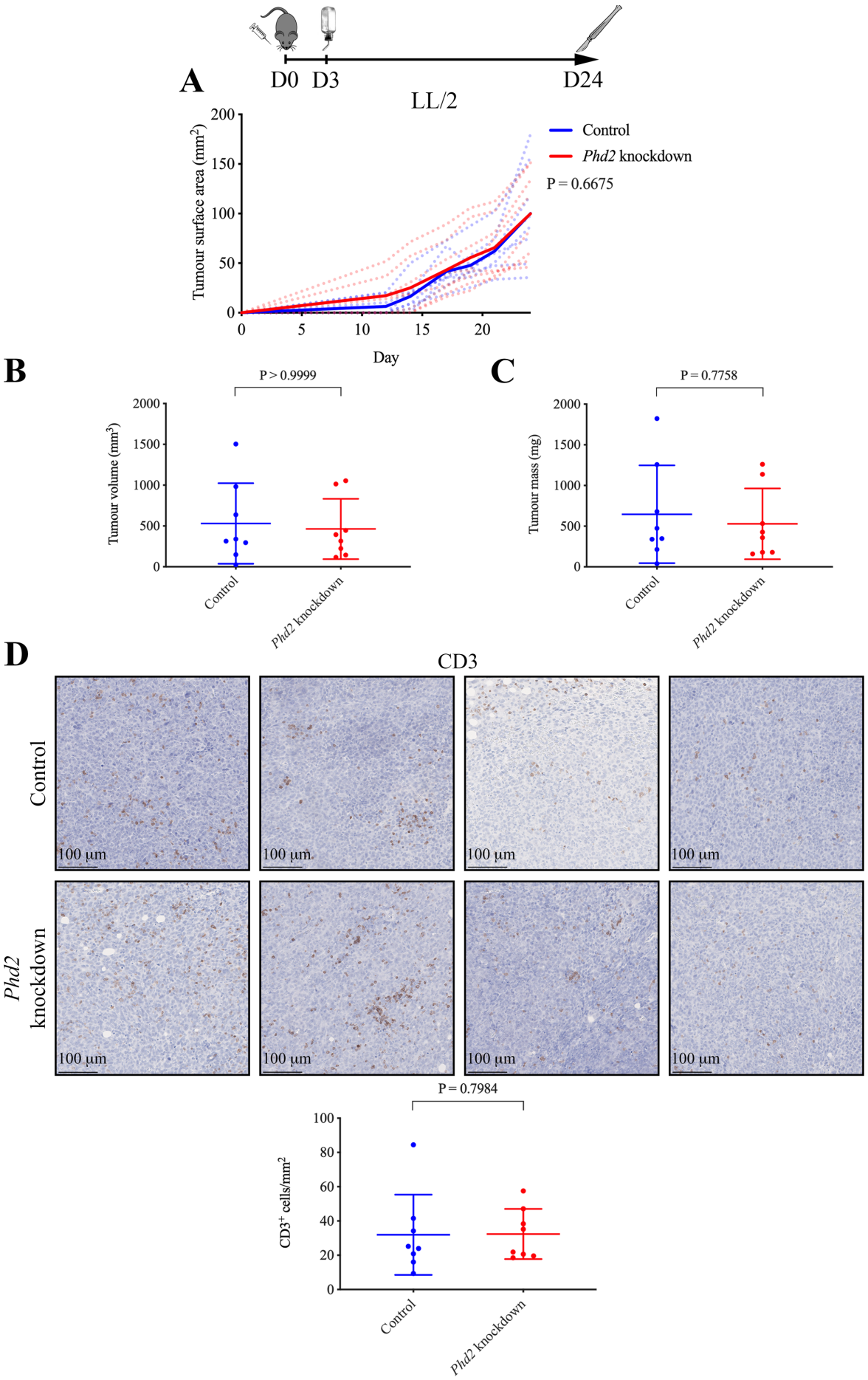

A
D0
D3
D24
LL/2
Tumour surface area (mm²)
Day
Control
Phd2 knockdown
P = 0.6675
B
P > 0.9999
Tumour volume (mm³)
Control
Phd2 knockdown
C
P = 0.7758
Tumour mass (mg)
Control
Phd2 knockdown
D
CD3
Control
Phd2 knockdown
100 µm
P = 0.7984
CD3⁺ cells/mm²
Control
Phd2 knockdown

Figure 4.2 – Effects of systemic *Phd2* knockdown after subcutaneous inoculation of LL/2 tumour cells

(A) Mean (solid line) and individual (dotted lines) growth curves for LL/2 tumours grown in Phd2 knockdown (red) and control mice of various genotypes (blue) following administration of doxycycline from Day 3 after tumour cell inoculation. Data are analysed by two-way analysis of variance (ANOVA) with repeated measures (n = 8 tumours from 4 Phd2 knockdown mice and 8 tumours from 4 control mice in one experiment). (B) Comparison of explanted tumour volumes between groups. Data are represented as the mean ± standard deviation (SD) and are analysed by Mann-Whitney test. (C) Comparison of explanted tumour masses between groups. Data are represented as the mean ± SD and are analysed by Mann-Whitney test. (D) Immunohistochemical comparison of T lymphocyte (CD3) infiltration in representative tumours from each group. Data are represented as the mean ± SD and are analysed by Mann-Whitney test (n = 8 tumours from 4 mice from each group).

Since the lack of effect of *Phd2* knockdown on the growth of LL/2 tumours might have been due to an intrinsic resistance of this cell line to immune destruction, I next repeated the same experiment using the E0771 mammary gland adenocarcinoma model. This time, all experiments were controlled entirely using mice of the *CAG-rtTA*$^{+/-}$*; TRE*$^{-/-}$ genotype. Again, no difference in tumour growth was detected between *Phd2* knockdown and control mice (**Figure 4.3**).

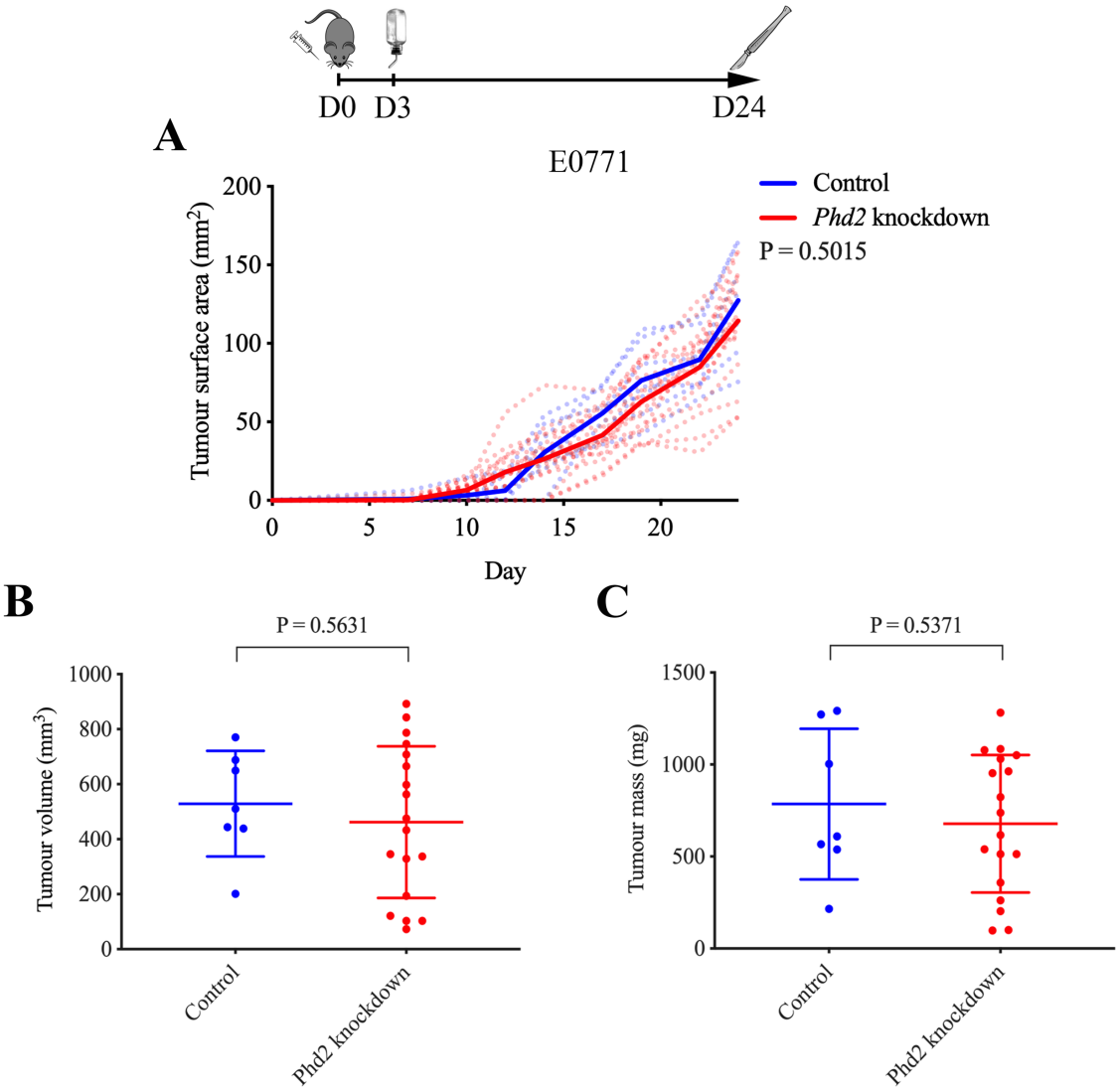


Figure 4.3 – Effects of systemic *Phd2* knockdown after subcutaneous inoculation of E0771 tumour cells

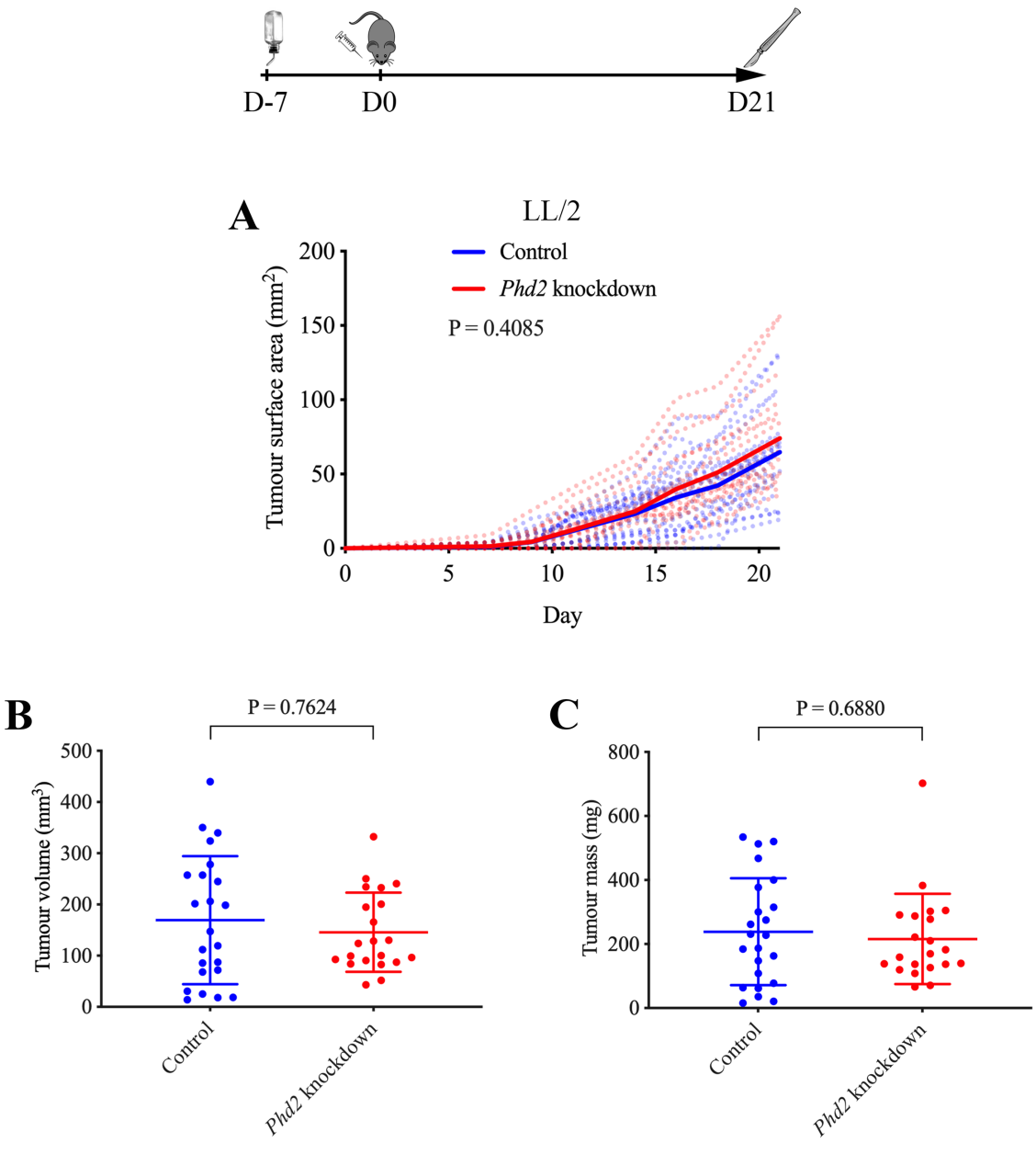
(A) Mean (solid line) and individual (dotted lines) growth curves for E0771 tumours grown in Phd2 knockdown (red) and control (blue) mice following administration of doxycycline from Day 3 after tumour cell inoculation. Data are analysed by two-way analysis of variance (ANOVA) with repeated measures (n = 18 tumours from 9 Phd2 knockdown mice and 7 tumours from 5 control mice across two experiments). (B) Comparison of explanted tumour volumes between groups. Data are represented as the mean ± standard deviation (SD) and are analysed by unpaired t-test. (C) Comparison of explanted tumour masses between groups. Data are represented as the mean ± SD and are analysed by unpaired t-test.

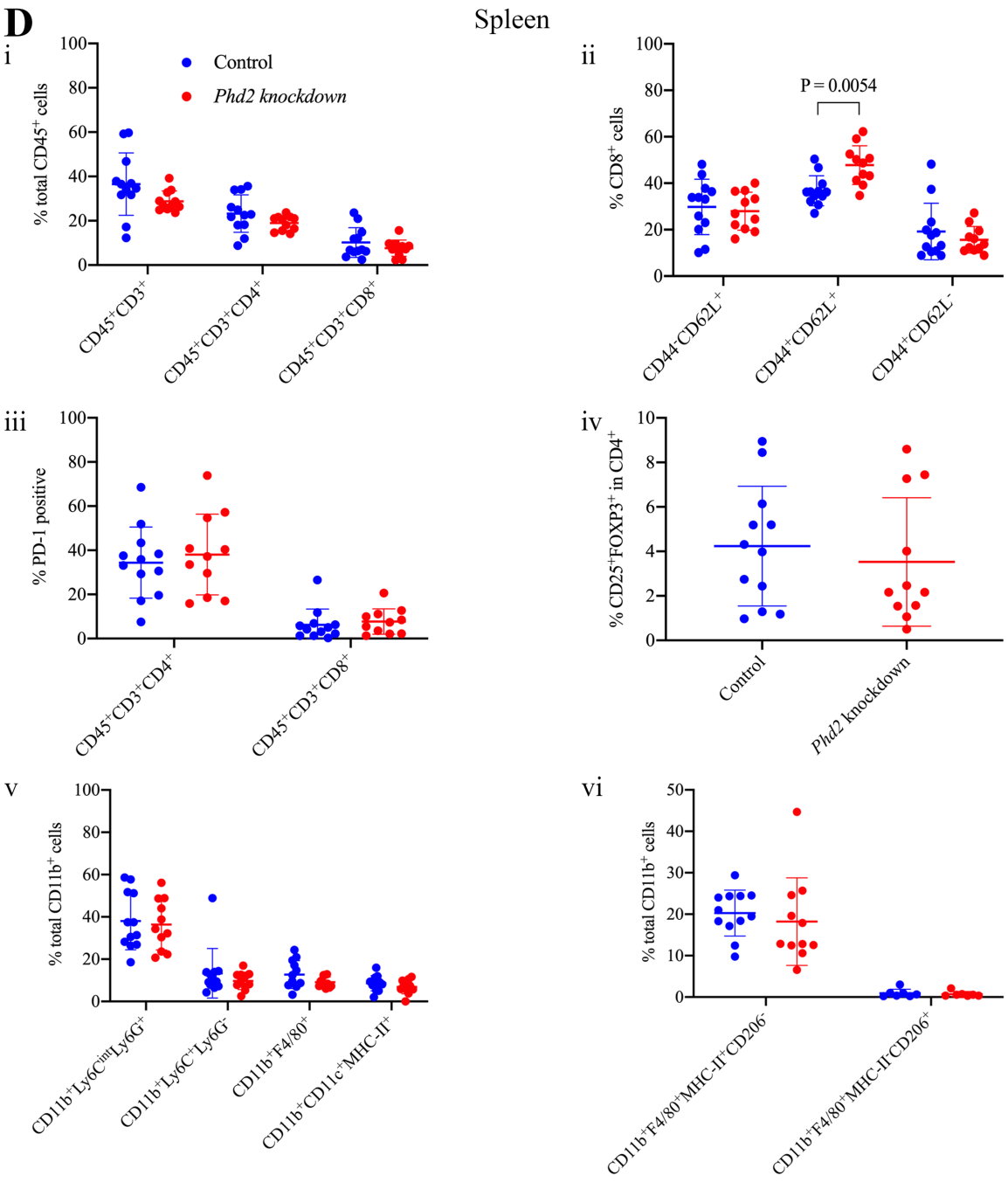
Systemic *Phd2* knockdown before subcutaneous inoculation of tumour cells

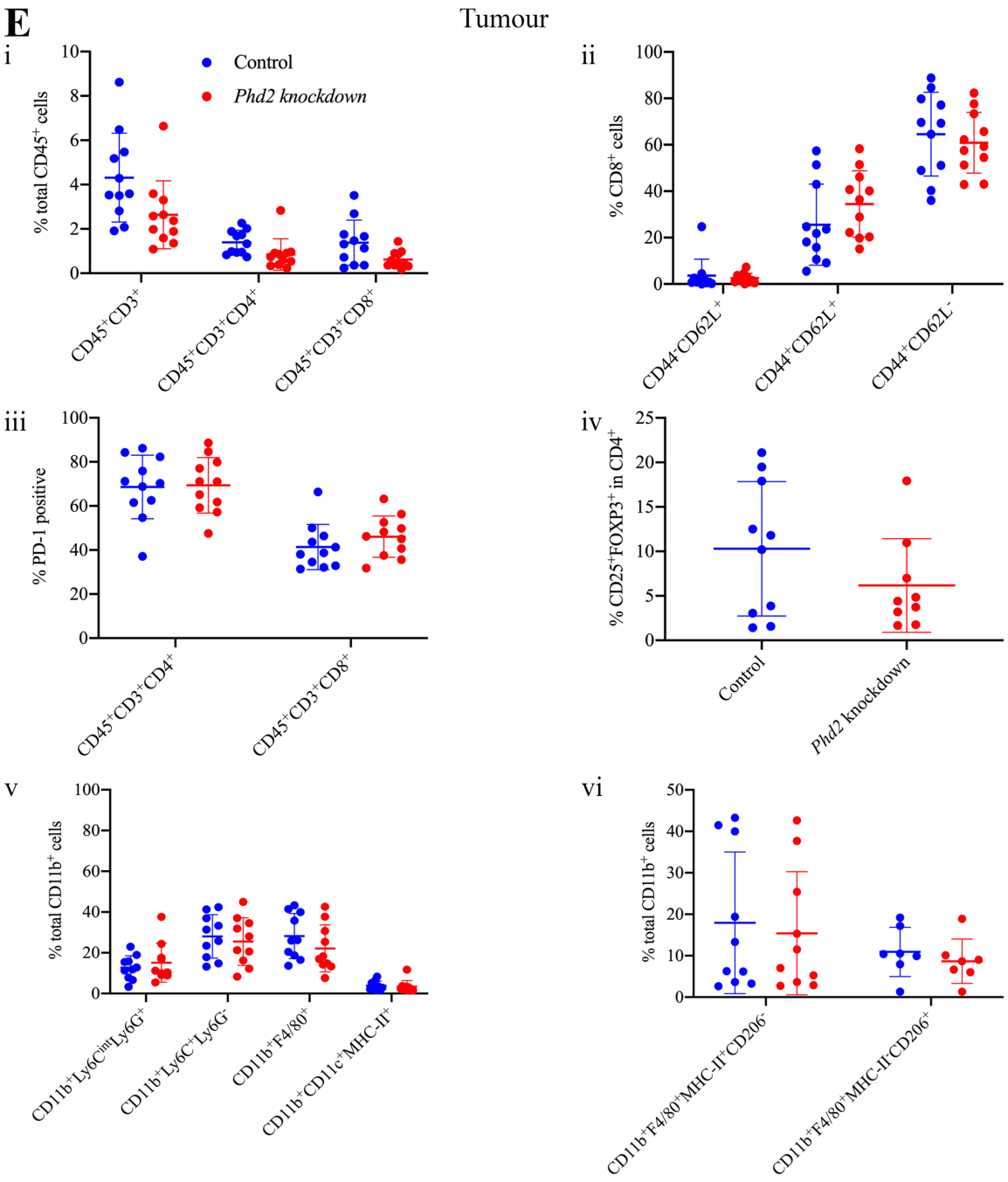
Given the lack of effect on tumour growth of *Phd2* knockdown after tumour cell injection, and since anti-tumour effects have been previously observed when T_{Reg} depletion was achieved either before or at the time of tumour cell inoculation but not later that two days after this [746], I next elected to start doxycycline administration seven days before tumour cell injection. Once again, tumours were harvested at three weeks, meaning that mice in these experiments received four weeks of doxycycline in total. This strategy was selected to facilitate direct comparison with the experiments presented in Chapter 3 and, additionally, to potentiate the strength of host immune responses prior to the establishment of transplantable tumours, which are recognised to perturb immune responses [810, 811].

Despite earlier and longer administration of doxycycline, again no difference in tumour growth was detected between *Phd2* knockdown and control mice (**Figure 4.4A-4.4C**). At Day 21 after doxycycline commencement, mice were culled and tumours and spleens were harvested. In order to profile immune responses, leukocytes were isolated from these and assessed by flow cytometry utilising staining panels that can identify both innate and adaptive cell phenotypes (**Figure 4.4D and 4.4E**). There was a paucity of tumour infiltrating lymphocytes in both groups (**Figure 4.4Ei**), with these largely displaying a $CD44^+CD62L^-$ effector/effector memory phenotype (**Figure 4.4Eii**). Furthermore, both tumour infiltrating $CD4^+$ and $CD8^+$ T lymphocytes demonstrated higher expression of PD-1 than their splenic counterparts (**Figure 4.4Diii and Figure 4.4Eiii**). Whilst PD-1 is expressed transiently during T lymphocyte activation, it is also a marker of dysfunctional ('exhausted') T lymphocytes within the TME [812-814]. T_{Reg} were also enriched in tumours as compared to spleens but only comprised 5-10% of tumour infiltrating $CD4^+$ T lymphocytes, with no statistical difference between groups (**Figure 4.4Div and Figure 4.4Eiv**). LL/2 tumours were also heavily infiltrated by monocytic

MDSC and macrophages but contained few conventional DC (**Figure 4.4Ev**); in addition, more M2 macrophages were detected within tumours as compared to spleens (**Figure 4.4Dvi and Figure 4.4Evi**). Overall, there was almost no difference in tumour or splenic leukocyte populations between groups. Therefore, I next assessed whether *Phd2* knockdown affected tumour vasculature and oxygenation. However, quantification of immunohistochemical staining for CD31 (**Figure 4.4F**) and pimonidazole (**Figure 4.4G**) in four randomly chosen fields of each tumour also demonstrated no differences between groups.




D
Spleen
i
Control
Phd2 knockdown
% total CD45+ cells
CD45+CD3+
CD45+CD3+CD4+
CD45+CD3+CD8+
ii
P = 0.0054
% CD8+ cells
CD44+CD62L+
CD44+CD62L+
CD44+CD62L-
iii
% PD-1 positive
CD45+CD3+CD4+
CD45+CD3+CD8+
iv
% CD25+FOXP3+ in CD4+
Control
Phd2 knockdown
v
% total CD11b+ cells
CD11b+Ly6CintLy6G+
CD11b+Ly6C+Ly6G-
CD11b+F4/80+
CD11b+CD11c+MHC-II+
vi
% total CD11b+ cells
CD11b+F4/80+MHC-II+CD206-
CD11b+F4/80+MHC-II+CD206+


E
Tumour
i
Control
Phd2 knockdown
% total CD45+ cells
CD45+CD3+
CD45+CD3+CD4+
CD45+CD3+CD8+
ii
% CD8+ cells
CD44+CD62L+
CD44+CD62L+
CD44+CD62L-
iii
% PD-1 positive
CD45+CD3+CD4+
CD45+CD3+CD8+
iv
% CD25+FOXP3+ in CD4+
Control
Phd2 knockdown
v
% total CD11b+ cells
CD11b+Ly6Cint Ly6G+
CD11b+Ly6C+Ly6G-
CD11b+F4/80+
CD11b+CD11c+MHC-II+
vi
% total CD11b+ cells
CD11b+F4/80+MHC-II+CD206-
CD11b+F4/80+MHC-II+CD206+

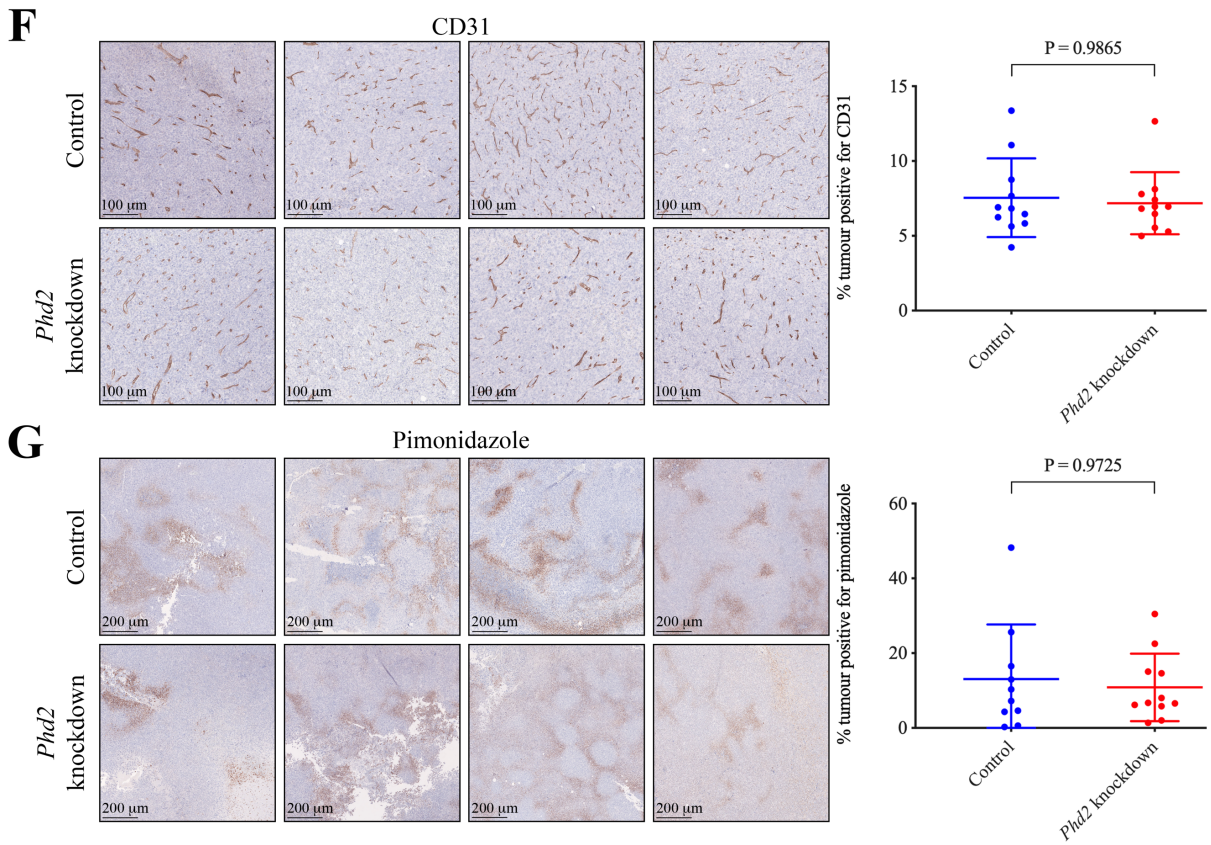


Figure 4.4 – Effects of systemic *Phd2* knockdown before subcutaneous inoculation of LL/2 tumour cells

(A) Mean (solid line) and individual (dotted lines) growth curves for LL/2 tumours grown in Phd2 knockdown (red) and control (blue) mice with administration of doxycycline from Day 7 before tumour cell inoculation. Data are analysed by two-way analysis of variance (ANOVA) with repeated measures (n = 21 tumours from 11 Phd2 knockdown mice and 23 tumours from 12 control mice across two experiments). (B) Comparison of explanted tumour volumes between groups. Data are represented as the mean ± standard deviation (SD) and are analysed by Mann-Whitney test. (C) Comparison of explanted tumour masses between groups. Data are represented as the mean ± SD and are analysed by Mann-Whitney test. (D & E) Flow cytometric analysis of leukocyte populations from spleen (D – n = 11 from Phd2 knockdown mice and 12 from control mice across two experiments) and tumour (E – n = 11 tumours from 11 Phd2 knockdown mice and 11 tumours from 11 control mice across two experiments) with control samples depicted in blue and transgenic samples depicted in red in each graph: (i) proportions of T lymphocytes ($CD45^+CD3^+$), helper T lymphocytes ($CD45^+CD3^+CD4^+$) and cytotoxic T lymphocytes ($CD45^+CD3^+CD8^+$) amongst the total leukocyte population ($CD45^+$),

(ii) differentiation status of $CD8^+$ cytotoxic T lymphocytes ($CD44^-CD62L^+$ = naïve, $CD44^+CD62L^+$ = central memory, $CD44^+CD62L^-$ = effector/effector memory), (iii) PD-1 expression amongst helper T lymphocytes ($CD45^+CD3^+CD4^+$) and cytotoxic T lymphocytes ($CD45^+CD3^+CD8^+$), (iv) proportion of regulatory T lymphocytes ($CD4^+CD25^+FOXP3^+$) amongst the total helper T lymphocyte population ($CD4^+$), (v) proportions of granulocytic myeloid-derived suppressor cells ($CD11b^+Ly6C^{int}Ly6G^+$), monocytic myeloid-derived suppressor cells ($CD11b^+Ly6C^+Ly6G^-$), macrophages ($CD11b^+F4/80^+$) and conventional dendritic cells ($CD11b^+CD11c^+MHC\text{-}II^+$) amongst the total myeloid cell population ($CD11b^+$), (vi) proportions of M1 macrophages ($CD11b^+F4/80^+MHC\text{-}II^+CD206^-$) and M2 macrophages ($CD11b^+F4/80^+MHC\text{-}II^-CD206^+$) amongst the total myeloid cell population ($CD11b^+$). Data are represented as the mean ± SD. With the exception of central memory $CD8^+$ cytotoxic T lymphocytes within the spleen, no statistically significant differences were identified between groups for any cell population when analysed by unpaired t-test and adjusted for multiple comparisons. (F) Immunohistochemical comparison of vascularity (CD31) in tumours from each group. Data are represented as the mean ± SD and are analysed by Mann-Whitney test (n = 11 tumours from 11 mice from each group). (G) Immunohistochemical comparison of hypoxia (pimonidazole) in tumours from each group. Data are represented as the mean ± SD and are analysed by Mann-Whitney test (n = 11 tumours from 11 mice from each group).

The *Phd2* knockdown system is operative in the tumour microenvironment

Given a lack of effect of *Phd2* silencing on tumour growth, it was essential to confirm that the shRNA-mediated knockdown system was fully operative during these experiments. Firstly, results of genotyping were reviewed and found to be accurate. Secondly, immediately prior to final tumour harvest, GFP expression in each mouse was checked at the whole animal level by using a flashlight and filter glasses kit that permits visualisation of green fluorophores in living organisms (BlueStar, NightSea®, USA); in each animal, the presence/absence of GFP expression was in agreement with genotyping results and thus also confirmed that the mice were drinking sufficient amounts of doxycycline to activate the transgenic system and drive transcription of the *Phd2*-targeting shRNA and directly coupled *GFP*. Finally, due to concerns

that poor perfusion might limit delivery of doxycycline to the central cores of tumours, I performed immunohistochemical staining for GFP in tumours derived from both transgenic and control mice. No staining was observed in control tumours but in each tumour from a transgenic mouse there was clear evidence of GFP expression by cells with morphological features of endothelium and infiltrating leukocytes (**Figure 4.5A**). Despite this, assessment of many of the parameters that differed between genotypes in Chapter 3, including body weight (**Figure 4.5B**), spleen and lymph node mass (**Figure 4.5C**), haematocrit (**Figure 4.5D**) and the development of ANA (**Figure 4.5E**), were not significantly different between groups (autoantibodies can develop in both tumour-bearing mice and human cancer patients, likely due to B lymphocyte responses to cellular components, such as DNA, released from dying tumour cells [815, 816]). Flow cytometric analysis of peripheral blood samples taken by tail vein bleeds at weekly intervals from a subset of mice demonstrated no difference in relative counts of circulating $CD3^+$ T lymphocytes, $B220^+$ B lymphocytes, $CD11b^+$ myeloid cells and Gr-1^+ granulocytes between groups (**Figure 4.5F**). Furthermore, no differences were identified with respect to T_{Reg} or differentiation of either $CD4^+$ or $CD8^+$ T lymphocytes as assessed by co-expression of CD44 and CD62L (data not shown).

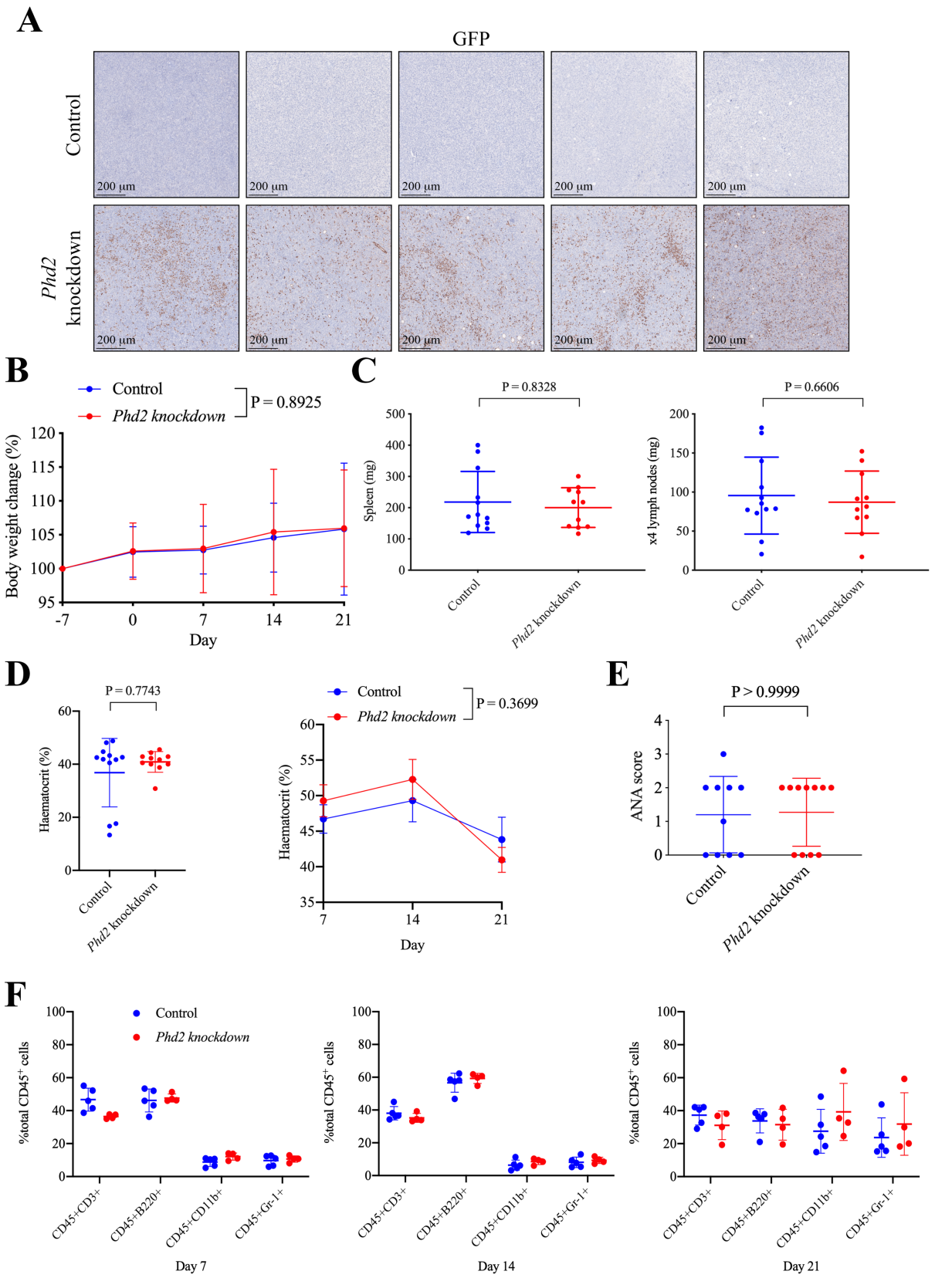

A
GFP
Control
Phd2 knockdown
200 µm
B
Control
Phd2 knockdown
P = 0.8925
Body weight change (%)
Day
C
P = 0.8328
Spleen (mg)
P = 0.6606
x4 lymph nodes (mg)
Control
Phd2 knockdown
D
P = 0.7743
Haematocrit (%)
P = 0.3699
Day
E
P > 0.9999
ANA score
F
%total CD45+ cells
CD45+CD3+
CD45+B220+
CD45+CD11b+
CD45+Gr-1+
Day 7
Day 14
Day 21

Figure 4.5 – Confirmation of transactivation of knockdown system and comparison of phenotypes between groups

(A) Immunohistochemical analysis of enhanced green fluorescent protein (GFP) expression in tumours from each group. (B) Mean percentage of body weight changes amongst tumour-bearing Phd2 knockdown and littermate control mice relative to commencement of doxycycline administration. Data are represented as the mean ± standard deviation (SD) and are analysed by two-way analysis of variance (ANOVA) with repeated measures (n = 11 Phd2 knockdown mice and 12 control mice across two experiments). (C) Comparison of masses of spleen and lymph nodes from tumour-bearing Phd2 knockdown mice and littermate controls. Data are represented as the mean ± SD and are analysed by Mann-Whitney test (spleens) and unpaired t-test (lymph nodes) (n = 11 Phd2 knockdown mice and 12 control mice across two experiments). (D) Comparison of haematocrit values between groups (left panel – n = 11 Phd2 knockdown mice and 12 control mice across two experiments at Day 21, data are represented as the mean ± SD and are analysed by Mann-Whitney test; right panel – n = 4 Phd2 knockdown mice and 5 control mice from one experiment for time course analysis between Day 7 and Day 21, data are represented as the mean ± SD and are analysed by two-way ANOVA with repeated measures). (E) Comparison of anti-nuclear antibody (ANA) scores between groups at Day 21. Data are represented as the mean ± SD and are analysed by Mann-Whitney test. (F) Flow cytometric analysis of peripheral blood at Day 7, Day 14 and Day 21. Data are represented as the mean ± SD (n = 4 Phd2 knockdown mice and 5 control from one experiment). No statistically significant differences were identified between groups for any cell population at any time point when analysed by unpaired t-test and adjusted for multiple comparisons.

Discussion

Summary of findings

The experiments presented in this chapter show no impact on wild-type tumour growth of *Phd2* knockdown within host stromal cells. In contrast to the experiments discussed in Chapter 3, no clear immunological differences could be discerned between *Phd2* knockdown and control mice and thus the tumour-bearing phenotype appears to be dominant to the autoimmune phenotype associated with *Phd2* knockdown in mice without tumours. Several explanations may contribute to this lack of anti-tumour effect. Assuming that GFP expression confirms

adequacy of *Phd2* knockdown and thus possibility of downstream immunological sequalae, this intervention may fail to disrupt the function of T_{Reg} in sufficient numbers to potentiate anti-tumour immune responses (depletion of up to 90-95% of T_{Reg} is required to eradicate large tumours [817]). Importantly, PHD can function redundantly and loss of all three isoforms may be required for optimal anti-tumour immunity [516] (although why this would not also be the case with regards to the development of autoimmunity in mice without tumours is not immediately clear). Alternatively, HIF stabilisation in other cell types may induce pro-tumour effects that counterbalance loss of T_{Reg} function. For example, HIF stabilisation has been reported to promote the development of immunosuppressive, pro-tumourigenic macrophages [479, 483, 484] whilst *Phd2* inactivation also enhances neutrophilic responses [210]. A further possibility for lack of anti-tumour response is the murine tumour model adopted for these experiments. Mouse strain impacts tumour immunogenicity with syngeneic tumours in BALB/c and FVBN mice being more immunogenic and more responsive to immunotherapy than those in C57BL/6J mice [818]. Due to immunoediting, LL/2 cells have low expression of MHC class I and II pathway genes and are predominantly infiltrated by immunosuppressive leukocytes (such as MDSC) [800, 818]. In E0771 tumours, a high proportion of tumour infiltrating leukocytes are monocytes or neutrophils whilst the tumour cells themselves express high levels of PD-L1 [798], features collectively suggestive of an immunosuppressive TME. Nevertheless, given that evaluation of the effects of an intervention on poorly immunogenic tumours is a more stringent test, and is therefore more likely to be of relevance to human disease, we elected to utilise LL/2 and E0771 cells over more immunogenic lines (such as carcinogen-induced MC38 colorectal adenocarcinoma cells which harbour a high burden of non-synonymous mutations [800]). Other considerations include whether duration of pre-treatment was insufficiently long to generate an inflammatory response and whether the presence of a tumour has immunomodulatory effects that negate the autoimmune phenotype

seen in non-tumour-bearing mice. In particular, establishing two tumours per mouse might have caused an excessive tumour burden (initially, this strategy was selected to increase access to samples for optimisation of immunohistochemistry and because future experiments might involve injection of different tumour cell lines into opposing flanks).

Previous studies have analysed the effects of manipulating *Phd2* signalling in host stromal cells on the growth of wild-type tumours. Given that constitutive loss of *Phd2* is embryonic lethal [673], Mazzone and colleagues evaluated *Phd2* haplodeficient mice (i.e. mice with one absent *Phd2* allele [$Phd2^{+/-}$] and, therefore, 50% of wild-type PHD2 protein levels) and noted normal vascular function under physiological conditions [786]. However, whilst there was no effect of *Phd2* haplodeficiency on primary tumour growth (LL/2 and B16 melanoma subcutaneous tumour models and orthotopic Panc02 pancreatic tumour model), haplodeficient mice developed fewer pulmonary metastases. Whilst this could be attributed to immunological effects (which were not profiled), the authors argued that the effect was due to HIF2α-mediated vascular normalisation (ultrastructurally, tumour blood vessels in transgenic mice more closely resembled normal blood vessels, with uniform endothelial cells, well developed basement membranes and more consistent pericyte coverage, leading to improved tumour oxygenation and resistance to tumour cell extravasation). Conditional heterozygosity limited to endothelial cells replicated these effects, suggesting that vascular normalisation initiated by endothelial cells themselves was indeed responsible. Mechanistically, reduction in PHD2 levels led to HIF stabilisation and up-regulation of both soluble and membrane-bound VEGFR1 and VE-cadherin in endothelial cells. Soluble VEGFR1 (sVEGFR1/sFlt1) is a HIF2α target gene [819] and a negative regulator of VEGF signalling [820] (excessive VEGF signalling in hypoxic tumours leads to immature blood vessel formation [821]) whilst VE-cadherin is also a HIF2α target gene [822] and tightens endothelial cell junctions [823], reducing vascular leakage.

Further work demonstrated that the normalisation of tumour vessels associated with *Phd2* haplodeficiency resulted in increased delivery of chemotherapeutics to tumours, potentiating their anti-tumour and anti-metastatic effects [824].

Several studies have also evaluated the consequences of *Phd2* silencing on anti-tumour immunity. Extending upon the above observations, Laoui and colleagues grew LL/2 tumours in *Phd2* haplodeficient mice and found that these were less hypoxic than tumours grown in control mice with this effect again ascribed to vascular normalisation [406]. This reduction in tumour hypoxia was not associated with changes in the abundance of TAM or their expression of M2 macrophage markers but lowered the expression of hypoxia-sensitive genes (such as those involved in glycolysis, angiogenesis and metastasis but not those encoding typical M2 markers such as CD206 and ARG1), thus reducing the angiogenic activity of a subset of TAM characterised by low expression of MHC class II and inhabitancy of hypoxic tumour regions. In order to exclude that the differences in gene expression were caused by *Phd2* haplodeficiency within macrophages themselves, as opposed to alterations in microenvironmental oxygenation within tumours, bone marrow chimeras were created by transferring wild-type bone marrow to transgenic mice. Tumours grown in these chimeras also displayed a reduction in tumour hypoxia (demonstrating that *Phd2* haplodeficiency in non-haematopoietic cells is sufficient to induce vascular normalisation) as well as down-regulation of hypoxia-regulated genes in macrophages with low, but not high, MHC class II expression (high MHC II TAM reside in better oxygenated tumour regions). The authors concluded that hypoxia is not a major driver of TAM differentiation, but instead fine-tunes the phenotype of M2-like TAM. It is notable that these findings are somewhat in contradiction to a previous study from the same group that did find a baseline expansion of M2-like macrophages in *Phd2*

haplodeficient mice in a non-tumour setting, with the arteriogenic capacity of these cells endowing mice with resistance to surgically-induced hindlimb ischaemia [825].

Mamlouk and colleagues demonstrated that conditional deletion of *Phd2* in the haematopoietic system (by crossing a transgenic mouse line with floxed *Phd2* alleles with a second transgenic line possessing Cre-recombinase under the control of the modified human CD68 promoter; whilst CD68 is a monocyte/macrophage marker, phenotyping of these mice demonstrated loss of PHD2 in the entire haematopoietic system and a subset of epithelial cells, but not in endothelium or fibroblasts) leads to reduced volume of both LL/2 and B16 tumours [826]. This finding was replicated upon bone marrow transplantation from transgenic to control mice (definitively limiting *Phd2* knockout to haematopoietic cells) and was partially reversed by concomitant knockout of *Hif1a*. On further evaluation, despite an increase in proliferation and no change in apoptotic rate or vascularity, tumours grown in transgenic mice displayed twice as much necrosis as compared to tumours grown in control mice. Interestingly, whilst flow cytometric profiling of the composition of tumour infiltrating immune cells did not differ between groups (suggesting that there was no effect of *Phd2* deletion on the homing of leukocytes to the tumour site), expression of the majority of both pro- and anti-inflammatory cytokines was reduced in both transgenic macrophages and $CD4^+$ T lymphocytes. When *Phd2* deletion was restricted to either myeloid cells (LysM:Cre), T lymphocytes (CD4:Cre) or B lymphocytes (CD19:Cre), no differences in tumour growth were observed. However, combined *Phd2* knockout in both T lymphocytes and myeloid cells (CD4/LysM:Cre) did reduce tumour growth in a manner comparable to its deletion within the entire haematopoietic compartment. Thus, the authors concluded that ‘crosstalk’ between PHD2 deficient T lymphocytes and myeloid cells was required to induce tumour cell death and reduce tumour growth. Furthermore, they speculated that a shift in balance from pro-tumoural (e.g. IL-4, IL-

10, IL-13, TGFβ) to anti-tumoural (e.g. IL-1, IFNγ, TNFα) cytokines, despite an overall decrease in cytokine synthesis by these cells, may reflect impairment of immunosuppressive tumour infiltrating leukocytes.

Finally, focusing on adaptive immune responses, Clever and colleagues reported that T lymphocyte expression of PHD promotes immunosuppression under well oxygenated conditions such as those found in the lungs, thus maintaining local tolerance to inhaled allergens but permitting colonisation by metastatic tumour cells [516]. Mechanistically, PHD, via repression of HIF1α-driven glycolysis, limit T_H1 lymphocyte and CTL responses whilst promoting T_H2 lymphocyte responses and inducing T_{Reg} formation, effects which together contribute to the development of immunologically tolerant metastatic niches within the lungs. Since PHD can be functionally redundant, in these experiments all three isoforms (i.e. *Phd1*, *Phd2* and *Phd3*) had to be deleted simultaneously within T lymphocytes in order to generate more pulmonary $CD4^+$ and $CD8^+$ T lymphocytes, which were skewed towards an effector phenotype (as assessed by increased expression of IFNγ, granzyme B and perforin) as well as being more activated (as assessed by expression of CD44, CD25, CTLA-4 and glucocorticoid-induced tumour necrosis factor receptor [GITR]). Furthermore, whilst absolute numbers of $FOXP3^+$ T_{Reg} were equivalent between genotypes, there was a reduction in the relative proportion of induced T_{Reg} (a population of T_{Reg}, identified by low expression of neuropilin-1, which are particularly important for maintaining immune tolerance at mucosal sites [827]) in knockout mice. Whilst these immunological changes did not affect the growth of primary subcutaneous tumours, they did suppress the development of lung metastases upon intravenous injection of tumour cells, although this occurred at the expense of sometimes fatal autoimmune lung pathology. From a translational perspective, *ex vivo* treatment of antigen-specific T

lymphocytes with DMOG prior to adoptive cell transfer to tumour-bearing mice led to smaller primary tumours, fewer pulmonary metastases and prolonged survival.

More recently, the effects of pharmacological PHD2 inhibition on tumour growth have been tested in mice. Such treatments will affect both tumour and stromal cell biology. In keeping with previous findings in *Phd2* haplodeficient mice [786, 824], administration of DMOG to subcutaneous LL/2 tumour-bearing mice led to normalisation of tumour vasculature with reduced vessel leakage, improved perfusion and decreased tumour hypoxia [828]. Furthermore, combined treatment with DMOG and cisplatin led to improved efficacy of chemotherapy, which did not alter tumour growth when administered alone. Subsequently, the same group expanded these studies to include the PHD-specific inhibitors roxadustat, daprodustat, molidustat and vadadustat, finding that administration of each of the four inhibitors led to vascular normalisation and a reduction in tumour growth rate (although vadadustat only slowed tumour growth when administered at a dose of 2 mg and not at a higher dose of 4 mg, highlighting the risk of unpredictable effects with this treatment strategy) [829]. However, tumour expression of angiogenic factors and inflammatory cytokines segregated into two discrete treatment-dependent groups with distinct patterns observed with molidustat and vadadustat (generally higher) as compared to roxadustat and daprodustat (generally lower). These discrepancies may relate to differences in potency, inhibition kinetics or preferential HIFα isoform stabilisation between different compounds [830]. Administration of roxadustat has also been demonstrated to inhibit growth of B16 melanoma (but not MC38 colorectal) murine tumours [831]. Assessment of tumour proliferation and apoptosis did not reveal differences between inhibitor and vehicle control treated groups, suggesting that the reduction in tumour growth rate was not a consequence of a direct drug effect on tumour cells. Profiling of tumour infiltrating immune cells demonstrated an increase in leukocytes, particularly $F4/80^{+}$

macrophages, in roxadustat treated tumours (T lymphocyte infiltration was unaffected) and depletion of macrophages by liposome clodronate partially reversed the anti-tumour efficacy of roxadustat. Furthermore, when compared to vehicle control, roxadustat did not affect tumour growth in either *Vhl*$^{fl/fl}$ LysM:Cre mice (which, when untreated, displayed a similar phenotype as roxadustat-treated mice) or *Hif1a*$^{fl/fl}$ LysM:Cre mice, suggesting that its anti-tumour effect is mediated by HIF1α stabilisation within TAM. Subsequent *in vitro* and *in vivo* experiments revealed that the anti-tumour effects of roxadustat were mediated, at least in part, by activation of phagocytosis within these cells.

Clinical relevance

Whilst the experiments presented here focus on the effects of manipulating *Phd2* in host stromal cells, PHD2 also plays important roles in tumour cells. In some experiments, PHD2 has been reported to restrain malignant transformation [832] and tumour growth [833-840]. However, other studies report that PHD2 appears to favour tumour growth [841-844]. This inconsistency extends to immunohistochemical studies performed on human tumour samples, some of which report that high PHD2 expression correlates with increased tumour aggression in head and neck [845], pancreaticobilary [846], lung [847] and liver [848] cancer and others reporting that it correlates with a better prognosis in breast [835], gastric [849] and liver [838] cancer. Thus, care must be exercised in future clinical trials evaluating the administration of PHD inhibitors to human cancer patients, since the effects of such an intervention are likely to be complex and outcomes may vary between different tumour types. In an analogous manner, not all murine tumour models respond to T_{Reg} depletion [746], suggesting that similar resistance is likely to be observed in some humans. Importantly, the prognostic significance of FOXP3^{+} cell infiltration varies between tumour types; whilst generally considered a marker of poor prognosis as outlined in the Introduction to this chapter, their presence has been reported

to be a positive prognostic marker in head and neck, oesophageal, gastric, colorectal and bladder cancer [121, 744, 745]. The explanation for this paradox remains to be confirmed but it has been postulated that T_{Reg} may exert a protective control of pro-tumourigenic inflammation [850, 851] (indeed, this has been demonstrated in mouse models [852-854]) or that FOXP3 may be expressed by effector cells in response to intestinal bacteria residing within colorectal cancers; in contrast, high numbers of *bona fide* T_{Reg} were indeed associated with a poor prognosis in this tumour type [855]. Furthermore, as demonstrated in Chapter 3, therapeutic depletion or inhibition of T_{Reg} risks immune-related adverse events, with skin rash, autoimmune thyroiditis and hepatitis having been reported [856]. These findings underscore the importance of developing robust biomarkers to identify cancer patients most likely to benefit from T_{Reg} manipulation. If achieved, this could facilitate administration of therapeutic agents that specifically target tumour infiltrating T_{Reg}, avoiding 'on-target, off-tumour' effects. If tumour resident T_{Reg} can be manipulated selectively without systemic toxicities, then combinatorial treatment with other therapies including anti-tumour vaccines [753, 755, 857] and ICB [858, 859] may be possible.

Strengths, limitations and future directions

The security of the negative findings presented in this chapter is increased by experimentation with two different cell lines as well as administration of doxycycline both after and before tumour cell injection. Interestingly, several previous studies have reported a similar lack of effect on primary tumour growth but reduction in pulmonary metastases upon reduction of PHD2 in host stromal cells [516, 786, 860, 861]. Of note, metastases were induced either by intravenous injection of tumour cells [516] or by surgical resection of the primary tumour at a specified volume to allow development and further growth of spontaneous metastases [786]. Thus, future experiments should adopt either or both of these approaches and include accurate

analysis of lung tissue to assess for effects of *Phd2* knockdown on the development of pulmonary metastases. Furthermore, it has been speculated that PHD2 inhibition may need to be combined with therapies that are directly cytotoxic (for example, chemotherapy or immunotherapy) in order to control primary tumour growth [862] and this approach merits further investigation. Finally, analysis of T_{Reg} cytokine expression and functionality should also be incorporated into any future work.

Discussion and Future Directions

Although somewhat disparate in their focus and the methodological approaches implemented, each chapter in this thesis is related by the common themes of cellular oxygen sensing, tumour oxygenation and/or immune responses. In particular, I believe that three key strands of work emerge, as discussed below.

1. Histological markers of tumour hypoxia

In Appendix 1, I present the findings of a systematic review comparing the expression of endogenous hypoxia markers with labelling by exogenous hypoxia markers in human tumours. In general, concordance was not strong, highlighting the complexities of quantifying tumour hypoxia by histology. The extreme lability of HIFα itself, coupled with concerns about the specificity of primary antibodies and lack of validated immunostaining protocols, limits its use in specimens that have not been subject to meticulous sample handling. Consequently, HIF targets are commonly used as alternative markers, although these are surrogates of HIF activation and are not entirely hypoxia-specific. These observations, coupled with the inability to utilise HIF and its target genes in 'pseudohypoxic' tumours such as CCRCC, underline the value of pimonidazole-treated tumour samples such as those analysed in Chapters 1 and 2 (although this benefit is counter-balanced by the limited availability of these specimens). Consistent with previous studies [287, 288, 863-866], I identified several tumours that displayed an almost complete lack of CA IX expression despite significant pimonidazole labelling, demonstrating that analysis of a single endogenous hypoxia marker may lead to substantial underestimation of hypoxia in some cases. Whilst this may not impact excessively on the findings of large studies, reliance upon one marker is unlikely to be sufficiently precise for widespread adoption into routine histopathological practice for the quantitation of tumour

hypoxia as a prognostic/predictive factor. Why this occurs is unknown, although interrogation of RNA sequencing data from the ATOM study samples should provide insight into the extent of this phenomenon (e.g. total vs. selective failure of expression of HIF target genes). In future, utilisation of state-of-the-art multiplex immunohistochemistry/immunofluorescence platforms to localise several endogenous hypoxia markers on a single section, in a manner analogous to hypoxia gene expression signatures, should overcome current limitations and provide more comprehensive profiling of the highly complex and dynamic responses of tumour cells to hypoxia. In particular, knowledge of the variation in time course of response of different hypoxia markers may permit distinction between different types of tumour hypoxia, as well as between *in situ* tumour hypoxia and that occurring artefactually during specimen handling.

2. Validation and utilisation of the SIGHT image analysis pipeline

In Chapters 1 and 2, I validated SIGHT, a novel image analysis pipeline created to facilitate the application of spatial statistics to point patterns derived from histology images, such as the (x, y) co-ordinates of leukocytes within tumour sections. Having demonstrated broadly comparable performance in cell counting to humans and other automated approaches, I utilised SIGHT to quantify the distribution of tumour infiltrating leukocytes relative to pimonidazole labelled hypoxia in HNSCC and blood vessels in CCRCC. Overall, these studies demonstrated distinct and consistent patterns of leukocyte distribution in both tumour types, with lymphoid cells largely restricted to better oxygenated perivascular regions and myeloid cells being more diffusely distributed including within profoundly hypoxic necrotic regions. These findings underline the value of histological spatial analysis, which should be used to complement results derived from techniques that require tissue disaggregation such as flow cytometry. Given the deficiency of CTL, and as myeloid cells are generally considered to inhibit anti-tumour immunity, these results suggest that hypoxic regions may represent immunosuppressive niches

within tumours. Broadly comparable patterns of $CD8^+$, $FOXP3^+$ and $CD68^+$ cell distribution relative to oxygen gradients were seen in both tumour types. Since HIF system activation is diffuse in CCRCC but regional in HNSCC, this observation suggests that these distributions result primarily from leukocyte intrinsic processes and/or their interactions with stromal cells, as opposed to as a consequence of HIF-mediated responses within tumour cells. This, in part, motivated my decision to manipulate HIF signalling within leukocytes in the murine tumour experiments described in Chapter 4.

Subsequently, SIGHT was utilised to score immunohistochemically labelled hypoxia, vascular and immunological markers in both lung cancer samples from the ATOM study (Chapter 2) and experimental murine tumours (Chapter 4), further demonstrating the utility of this pipeline. Although beyond the scope of this thesis, the data derived from the HNSCC samples analysed in Chapter 1 have been used to demonstrate that combining multiple spatial statistics provides a more precise description of immune cell localisation within tumours than any single statistic alone and can be used to derive a metric that agrees with a pathologist's semi-quantitative description of leukocyte infiltration [517]. We are currently using SIGHT to demonstrate that topological data analysis, an emerging field of mathematics that studies shape within datasets and provides novel descriptors of spatial data, can be applied to leukocyte point patterns as related to microregional tumour hypoxia (Vipond et al., manuscript under submission). However, due to the effort invested in developing, optimising and validating the image analysis algorithms utilised in these studies, there was insufficient time during my fellowship to apply it to larger patient cohorts. Therefore, future work will focus on the application of SIGHT and these advanced mathematical approaches to bigger image datasets, with particular interest in cohorts with in-depth tumour molecular profiling and well curated patient outcome data and those with pre- and post-therapy tumour samples.

3. *In vivo* studies utilising *Phd2* knockdown mice

The murine studies presented in this thesis provided me with valuable training in conducting and interpreting the results of animal experiments. In Chapter 3, histological evaluation of tissue samples from mice in which the gene encoding PHD2, the principal HIF prolyl hydroxylase, had been silenced contributed to the delineation of an autoimmune phenotype. T_{Reg} with *Phd2* knockdown (and presumed HIF stabilisation) displayed impaired immunosuppressive capacities [227]. These findings are in alignment with observations presented in Chapter 1 that T_{Reg} inhabit a perivascular niche within human tumours and are rarely present within highly hypoxic perinecrotic regions. They also suggest that new drugs that permit manipulation of specific components of the HIF pathway (notably PHD [660-662] and HIF2α [720, 867-869] inhibitors) may have immunological effects if they can be targeted to T_{Reg} in appropriate concentrations. Whilst these effects might be of therapeutic benefit (by either potentiating or inhibiting immunity), significant toxicities could also result if immune responses were perturbed inappropriately in vulnerable individuals (for example, by worsening autoimmunity or immunodeficiency). Rather disappointingly, *Phd2* knockdown did not impact upon growth of subcutaneous tumours in these mice. The reasons for this are unclear but might include insufficient duration of *Phd2* silencing or general lack of immunogenicity of C57BL/6J syngeneic tumours. With regards to the latter, I have developed protocols for the induction of methylcholanthrene-induced tumours in mice. In general, carcinogen-induced tumours have higher mutational burdens than both genetically engineered and spontaneous tumours [800] and thus may be more immunogenic. Furthermore, administration of methylcholanthrene to transgenic mice expressing shRNA targeting different components of the PHD-HIF pathway, either alone or in combination, could generate tumour-derived cell lines for experiments evaluating the (immunological) consequences of manipulation of HIF-mediated responses within neoplastic cells themselves.

Overall, the intersection between tumour hypoxia and anti-tumour immunity has been a fascinating but complex subject to study. Whilst this area has been the subject of intensive investigation, different studies have reported conflicting findings with hypoxia/HIF activation being associated with both augmentation [183, 184, 314, 516] and impairment [211, 484] of anti-tumour immunity. A parsimonious, if perhaps overly simplistic, explanation for these seemingly contradictory findings is that whilst HIF activation is essential for the generation of effective inflammatory/immune responses [183, 184, 201, 203], the profound hypoxia found within tumours, which is associated with a paucity of CTL [308, 313, 322], a scarcity of nutrients such as glucose [343] and tryptophan [870], accumulation of immunosuppressive metabolites including lactic acid [350, 479], adenosine [351] and potassium [354, 355] and enhancement of tumour cell resistance to cytotoxicity [615, 871-874] is detrimental to effective anti-tumour immunity.

Appendix 1 – A systematic review of immunohistochemical studies comparing the expression of endogenous hypoxia markers to exogenous hypoxia marker labelling in malignant human tumours

Introduction

Traditionally, cancer treatment has been based on the histological subtyping of a patient's tumour and a limited number of other factors of prognostic significance such as tumour grade and stage. The advent of 'precision oncology', which attempts to match underlying disease mechanisms to the most appropriate targeted therapy, has the potential to revolutionise patient care and improve outcomes (as reviewed in [875]). Whilst the presence of tumour hypoxia is recognised to be of both of negative predictive and prognostic significance (as reviewed in [91]), it is not routinely evaluated in clinical practice. Therefore, there is a need to develop robust methods to detect regions of hypoxia within solid tumours, in order to facilitate selection of patients who would benefit most from hypoxia-modifying treatments whilst at the same time avoiding over-treatment of patients with better oxygenated tumours [876].

A number of approaches have been developed to identify tumour hypoxia including oxygen sensitive polarographic electrodes (which measure oxygenation directly) (as reviewed in [877]), cross-sectional imaging using techniques including those based on computed tomography (CT), magnetic resonance imaging (MRI) and positron emission tomography (PET) (approaches that permit *in vivo* detection of tumour hypoxia) (as reviewed in [878]), detection of circulating plasma markers of hypoxia such as the secreted proteins osteopontin (OPN) [879, 880] and vascular endothelial growth factor (VEGF) [881, 882] or carbonic anhydrase 9 (CA IX), which is shed from the surface of hypoxic tumour cells [629, 883], (permitting longitudinal assessment of temporal changes in tumour hypoxia, such as might

occur after treatment) and molecular signatures of tumour hypoxia based on gene expression profiles [884].

When compared to the above approaches, histological detection of tumour hypoxia provides unparalleled ability to profile the spatial distribution of hypoxia at a single cell scale (which is arguably the resolution of most biological relevance, due to the clonogenic nature of cancer) and its relation to other architectural parameters such as tumour stroma, blood vessels and areas of necrosis. This is particularly important given tumour hypoxia is recognised to be highly heterogenous not only in time [87, 88], but also in space [289, 618, 885]. Unfortunately, it is not possible to predict the extent of tumour hypoxia purely on the basis of routine histopathological features such as vascularity and the presence of necrosis [289, 886], most likely because these features do not consider the functional status of blood vessels or rate of oxygen consumption by tumour cells. This limitation can be overcome through immunohistochemical detection of hypoxia markers, which can be categorised as either *exogenous* (i.e. requiring the administration of a drug) or *endogenous* (i.e. proteins involved in the cellular response to hypoxia that accumulate under conditions of diminished oxygen supply).

Exogenous hypoxia markers

Immunohistochemical staining for exogenous hypoxia markers, chemicals such as the clinically approved compounds pimonidazole and pentafluorinated etanidazole (EF5) that specifically accumulate within hypoxic cells [612], is considered to be the 'gold standard' approach to the histological identification of tumour hypoxia. These compounds are 2-nitroimidazole derivatives, molecules that contain a nitro group [$–NO_2$] attached to an imidazole ring [$–C_3H_4N_2$], that are administered systemically in advance of tissue sample

collection. In most instances, these compounds are administered intravenously [887, 888] but oral administration of pimonidazole is also possible [889, 890]. These compounds undergo reduction when oxygen levels are profoundly low (below 1.5 kPa/10 mmHg) [891, 892]; when oxygen is present in higher quantities it out-competes these compounds as an electron acceptor. Reduction of these compounds generates highly reactive intermediate species that bind irreversibly to intracellular thiol [–C–SH]-containing molecules such as glutathione and proteins within hypoxic but viable cells (dead cells do not generate a signal because they cannot metabolise these compounds) [893, 894] (**Figure A**). These adducts act as neoepitopes that can subsequently be identified by immunohistochemistry [895, 896], commonly being identified at a distance of approximately 100 μm from the nearest blood vessel [254, 411, 897], and flow cytometry [898, 899].

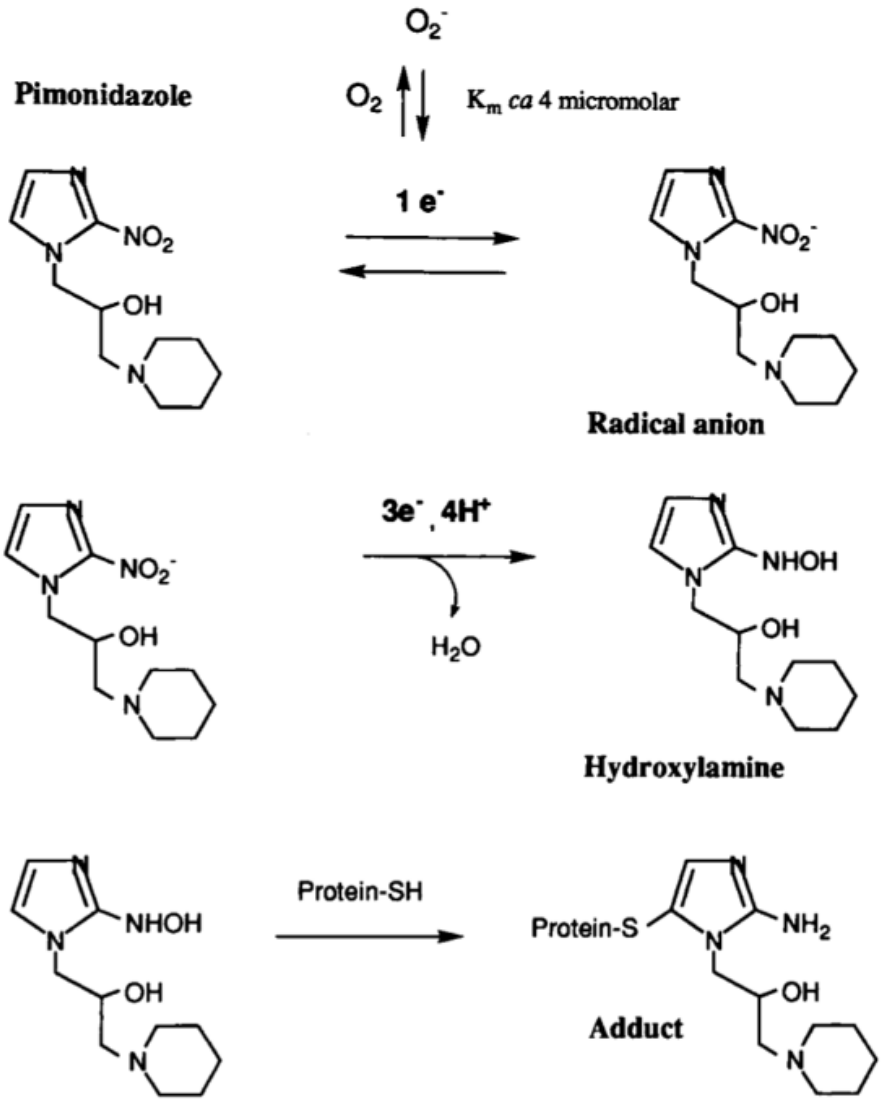


Figure A – Schematic representation of the reductive activation of pimonidazole under hypoxic conditions

The first step is the nitroreductase catalysed addition of an electron to form a nitro radical anion – oxygen (O_2) competes with pimonidazole for the addition of this first electron, which accounts for the pO_2 dependence of activation and binding (top row). Following this, the addition of a further three electrons generates a hydroxylamine intermediate (middle row). The hydroxylamine intermediate reacts with thiol-containing proteins to form stable adducts that can be detected by antibody-based assays, most commonly immunohistochemistry (bottom row).

Image from [900]; reprinted by permission from Elsevier Science, copyright 1998.

Pimonidazole was initially developed as a radiosensitising agent [901] but failed to demonstrate clinical efficacy [902] and was subsequently repurposed as an exogenous hypoxia marker. Whilst primarily influenced by oxygen availability, the avidity of pimonidazole binding can also be affected by other metabolic parameters, such as pH [903]. Consequently, intensity of labelling (e.g. heavy vs light immunohistochemical staining) cannot be related directly to the level of oxygenation across different tumours [904]. Furthermore, batch-to-batch variations in the immunostaining procedure (particularly relevant when this is undertaken by manual, as opposed to automated, immunohistochemistry) can lead to disparity in chromogenic signal intensity between different specimens [519]. Instead, the area of tumour stained by pimonidazole is the most commonly reported metric, being scored either by semi-quantitative manual assessment [905] or fully quantitative digital image analysis [906]. Recognising this limitation of pimonidazole, EF5 was developed with the specific goal of providing a marker that facilitates quantification of both the spatial distribution and severity of hypoxia [888, 907, 908]. A given immunofluorescent staining intensity can be directly translated into an absolute measurement of oxygenation by reference to a calibrated scale derived by incubating fresh tissue cubes from the same sample in the related hypoxia marker EF3 at varying oxygen levels ('cube reference binding' – adducts of the two drugs can be distinguished by specific monoclonal antibodies, thus differentiating *in vitro* from *in vivo* exposure). However, interpretation of EF5 staining is only validated for frozen tissue sections and thus it is less suitable for use in routine histopathological practice and most translational research projects than pimonidazole, which is optimised for detection in formalin-fixed, paraffin-embedded tissue samples.

A major limitation of exogenous hypoxia markers is the requirement to administer these drugs prior to tissue collection. Whilst they are in widespread use in pre-clinical animal studies, only

limited cohorts of human tumours from patients who received these drugs exist. Therefore, a more commonly used approach for histological identification of tumour hypoxia is to stain for *endogenous* markers of tumour hypoxia, which are more easily adopted for use in routine diagnostic pathology laboratories for the retrospective analysis of archival human tumour samples.

Endogenous hypoxia markers

Endogenous hypoxia markers are proteins that are up-regulated during the cellular (patho)physiological response to low oxygen levels, commonly hypoxia-inducible factor (HIF) itself or one of its various downstream target genes (**Table A**).

Table A – Commonly evaluated endogenous markers of tumour hypoxia
Hypoxia-inducible factor (HIF) – regulation of the cellular response to low oxygen availability
• As the master transcription factor coordinating the cellular response to hypoxia, HIF itself acts as an endogenous hypoxia marker • *In vitro*, HIF1α protein stabilisation proceeds dramatically below 6% O_2 (~45 mmHg) with a half maximal response between 1.5-2% O_2 (~10-15 mmHg) and a maximal response at 0.5% O_2 (~3.5 mmHg); the drop in HIF1α protein level observed at 0% O_2 has been attributed to the inhibitory effects of anoxia on overall transcription and translation [909] • Both HIF1α and HIF2α isoforms are detectable with immunohistochemistry in the majority of solid tumours but not in most corresponding non-neoplastic tissues [485, 910] • However, in experiments using cultured cells in suspension, HIF1α induction occurs within two minutes of hypoxia onset, peaks after one hour and becomes undetectable 32 minutes after reoxygenation [911]; these data suggest that meticulous sample

handling and careful analysis are essential for accurate interpretation of HIFα immunohistochemistry

- Therefore, more stable HIF-target genes may be more reliable endogenous markers of hypoxia
- Furthermore, as full HIF transcriptional activity requires co-activator recruitment, HIF target genes may be more specific markers of tumour hypoxia than HIFα itself, since their accumulation requires hypoxic inhibition of both the prolyl hydroxylase domain-containing proteins (PHD) and factor inhibiting HIF (FIH) in parallel

Prolyl hydroxylase domain-containing proteins (PHD) – HIFα regulation

- PHD2 and PHD3, two of the oxygen sensitive hydroxylase enzymes that regulate HIFα subunit stability, are themselves transcriptional targets of HIF [32, 50-54] and thus might act as endogenous hypoxia markers

Carbonic anhydrase 9 (CA IX) – pH regulation

- CA IX is a transmembrane protein, belonging to the zinc metalloenzyme family, that catalyses the reversible hydration of carbon dioxide to carbonic acid and thus contributes to the development of an acidic extracellular tumour microenvironment [912]
- Along with the carbonic anhydrase 12 (CA XII) isoform, CA IX was initially determined to be a HIF1α target gene due to its overexpression in *VHL* defective cell lines and high expression in perinecrotic regions of human tumours [630, 913-915]
- *In vitro*, expression of CA IX increases below oxygen tensions of approximately 20 mmHg, taking about four hours to accumulate under hypoxic conditions and reaching maximal expression after 16 hours [630]
- Immunohistochemical staining demonstrates that the median distance between a blood vessel and the start of CA IX expression in solid human tumours is 80 μm (range = 40-140 μm) [915, 916]
- CA IX is now recognised to be expressed in a wide range of human tumours and, importantly, is not expressed in the majority of matched non-neoplastic tissues, resulting in good ‘signal-to-noise’ upon immunostaining [917]

Glucose transporter 1 (GLUT1) – glucose uptake
• GLUT1 is one of 14 proteins of the GLUT family that facilitates transportation of glucose into cells across their plasma membrane • Due to the increased reliance upon anaerobic glycolysis and consequent requirement for glucose, this protein is up-regulated in cells exposed to low oxygen levels via both HIF1α and HIF2α [33] • Immunohistochemical staining demonstrates that GLUT1 is expressed by a significant proportion of solid tumours [918]
Vascular endothelial growth factor (VEGF) – angiogenesis
• VEGF (VEGF-A), a well characterised HIF-target gene [12, 13], is a secreted protein involved in angiogenesis, the formation of new blood vessels, through supporting the proliferation and migration of endothelial cells • Other than VEGF-A, the VEGF family includes placental growth factor (PlGF) and VEGF-B (which predominantly contribute to angiogenesis under stressed/pathological conditions) and VEGF-C and VEGF-D (which mainly function to stimulate lymphangiogenesis) (as reviewed in [919]) • Although up-regulation of these other VEGF family members under hypoxia has been reported, the exact mechanisms remain unclear and are not solely dependent upon HIF
Erythropoietin (EPO) and erythropoietin receptor (EPOR) – red blood cell production
• EPO, a glycoprotein that functions as a haematopoietic growth factor by stimulating red blood cell production within bone marrow and hence supports oxygen delivery to peripheral tissues, was the first HIF target gene to be identified [10] • Subsequently, its receptor EPOR was also demonstrated to be a hypoxia-sensitive gene [920, 921]
Lactate dehydrogenase (LDH) and monocarboxylate transporters (MCT) – metabolism and export of lactate
• LDH catalyses the interconversion of pyruvate, the final product of glycolysis, to lactate and is induced by HIF1α under hypoxic conditions [14, 922]

- LDH is a tetramer composed of LDH-M and LDH-H subunits (encoded by the *LDHA* and *LDHB* genes, respectively); thus, five isoforms, each with different tissue distributions, exist:
    - LDH1 (4H) – heart, erythrocytes and brain
    - LDH2 (3H1M) – reticuloendothelial system
    - LDH3 (2H2M) – lung
    - LDH4 (1H3M) – kidney, pancreas and placenta
    - LDH5 (4M) – liver, striated muscle and brain
- MCT are a family of plasma membrane transporters that transport monocarboxylates across plasma membranes; for example, exporting lactate which is a toxic by-product of glycolysis
- The MCT4, but not the MCT1, isoform has been reported to be induced by HIF1α under hypoxic conditions [16]

Osteopontin (OPN) – a multi-functional structural protein

- OPN is a secreted glycoprotein that plays roles in bone remodelling, inflammation and immune responses and is known to be over-expressed in various human tumours, promoting the development of metastases (as reviewed in [923])
- Analysis of gene expression microarray data from sixty different human tumour cell lines demonstrated an inverse correlation between *OPN* and *VHL* expression [879]
- Under hypoxic conditions *in vitro*, OPN accumulates more slowly than CA IX, GLUT1 and LDH, suggesting that it might be a marker of chronic hypoxia [924], although regulation proceeds at least in part via a HIF-independent mechanism [925]

Whilst exogenous and endogenous markers of tumour hypoxia have been the subject of several previous review articles [926-930], a systematic review of the topic is lacking. Thus, a comprehensive overview of all immunohistochemical studies that compare the expression of endogenous hypoxia markers to exogenous hypoxia marker labelling in malignant human

tumours is merited, with the objective of identifying robust endogenous hypoxia markers for use in future studies.

Methods

This systematic review was conducted in accordance with the recommendations of the Preferred Reporting Items for Systematic Reviews and Meta-analyses (PRISMA) statement [931] and the PRISMA Extension for Scoping Reviews (PRISMA-ScR) checklist [932].

Eligibility criteria

The following framework was used to develop eligibility criteria for the review:

- Population – malignant human tumours;
- Index test – immunohistochemical staining for endogenous markers of hypoxia (including HIF, its target genes and other proteins induced by low levels of oxygen);
- Comparison test ('reference standard') – immunohistochemical staining for exogenous markers of hypoxia (pimonidazole or EF5);
- Outcome/target condition – identification of tumour hypoxia (to what extent does the expression of endogenous markers of hypoxia correlate and/or co-localise with labelling by exogenous markers of hypoxia?).

Inclusion criteria specified all immunohistochemical studies comparing the expression of endogenous hypoxia markers to exogenous hypoxia marker labelling in malignant human tumours. Exclusion criteria included studies on non-malignant human tissues, *ex vivo* tumour/cell line cultures, xenograft models and non-human tissues. No date or language limits were applied and studies reported as both conference abstracts and full papers were eligible for inclusion.

Information sources

A systematic literature search was performed in Ovid MEDLINE and Embase. The final date for searching was 9th March 2017 but manual searching was continued until thesis submission in order to identify newly published records. Reference lists of identified studies and pertinent review articles were assessed for relevant records not identified by the initial search. I also reviewed lists of publications available from the manufacturers of pimonidazole (http://www.hypoxyprobe.com) and EF5 (https://hypoxia-imaging.org).

Search

The search strategy was drafted in collaboration with an experienced librarian (Ms Eli Harriss, Bodleian Health Care Libraries, University of Oxford). Search terms included free text terms for pimonidazole and EF5 and their aliases, along with Medical Subject Headings (MeSH) terms and free text alternatives for neoplasms/cancer (**Table B**).

Table B – Systematic review search strategy	
Exogenous hypoxia markers (pimonidazole [Hypoxyprobe = trade name, Ro-038799 = chemical name]/EF5)	
1.	nitroimidazole.mp. [mp=title, abstract, original title, name of substance word, subject heading word, keyword heading word, protocol supplementary concept word, rare disease supplementary concept word, unique identifier, synonyms]
2.	2-nitroimidazole.mp. [mp=title, abstract, original title, name of substance word, subject heading word, keyword heading word, protocol supplementary concept word, rare disease supplementary concept word, unique identifier, synonyms]
3.	pimonidazole.mp. [mp=title, abstract, original title, name of substance word, subject heading word, keyword heading word, protocol supplementary concept word, rare disease supplementary concept word, unique identifier, synonyms]

4.	hypoxyprobe.mp. [mp=title, abstract, original title, name of substance word, subject heading word, keyword heading word, protocol supplementary concept word, rare disease supplementary concept word, unique identifier, synonyms]
5.	Ro-038799.mp.
6.	Ro 038799.mp.
7.	Ro 03-8799.mp.
8.	Ro-03-8799.mp.
9.	R0 038799.mp.
10.	Ro o38799.mp.
11.	R0 o38799.mp.
12.	R0 03-8799.mp.
13.	R0 o3-8799.mp.
14.	Ro o3-8799.mp.
15.	EF5.mp. [mp=title, abstract, original title, name of substance word, subject heading word, keyword heading word, protocol supplementary concept word, rare disease supplementary concept word, unique identifier, synonyms]
16.	EF-5.mp. [mp=title, abstract, original title, name of substance word, subject heading word, keyword heading word, protocol supplementary concept word, rare disease supplementary concept word, unique identifier, synonyms]
17.	1 or 2 or 3 or 4 or 5 or 6 or 7 or 8 or 9 or 10 or 11 or 12 or 13 or 14 or 15 or 16
Cancer	
18.	neoplasms by histologic type/ or neoplasms by site/ or neoplasms, experimental/ or neoplasms, hormone-dependent/ or neoplasms, multiple primary/ or neoplasms, post-traumatic/ or neoplasms, radiation-induced/ or neoplasms, second primary/ or neoplastic processes/ or neoplastic syndromes, hereditary/ or paraneoplastic syndromes/ or pregnancy complications, neoplastic/

19.	neoplas*.mp. [mp=title, abstract, original title, name of substance word, subject heading word, keyword heading word, protocol supplementary concept word, rare disease supplementary concept word, unique identifier, synonyms]
20.	tumo*.mp. [mp=title, abstract, original title, name of substance word, subject heading word, keyword heading word, protocol supplementary concept word, rare disease supplementary concept word, unique identifier, synonyms]
21.	cancer*.mp. [mp=title, abstract, original title, name of substance word, subject heading word, keyword heading word, protocol supplementary concept word, rare disease supplementary concept word, unique identifier, synonyms]
22.	carcinoma*.mp. [mp=title, abstract, original title, name of substance word, subject heading word, keyword heading word, protocol supplementary concept word, rare disease supplementary concept word, unique identifier, synonyms]
23.	malignan*.mp. [mp=title, abstract, original title, name of substance word, subject heading word, keyword heading word, protocol supplementary concept word, rare disease supplementary concept word, unique identifier, synonyms]
24.	sarcoma*.mp. [mp=title, abstract, original title, name of substance word, subject heading word, keyword heading word, protocol supplementary concept word, rare disease supplementary concept word, unique identifier, synonyms]
25.	lymphoma*.mp. [mp=title, abstract, original title, name of substance word, subject heading word, keyword heading word, protocol supplementary concept word, rare disease supplementary concept word, unique identifier, synonyms]
26.	18 or 19 or 20 or 21 or 22 or 23 or 24 or 25
Combination of exogenous hypoxia marker and cancer	
27.	17 and 26

Selection of sources of evidence

Duplicates were discarded from initial search results. The titles and abstracts of remaining records were screened for relevance by two individuals (myself and Dr Tessa Greenhalgh,

Department of Oncology, University of Oxford). The full text of potentially relevant studies was reviewed prior to confirming their inclusion.

Data charting process

Relevant data from included studies were abstracted into a database by means of a pro forma. The aforementioned individuals charted the data, discussed the results and any inconsistencies in data charting and continuously updated the data charting form in an iterative process.

Data items

Data relating to record identification details (e.g. first author, year of publication, PubMed ID, host institution), numbers of included patients, details of pimonidazole administration, sample types analysed, immunohistochemistry protocols and scoring methods and relevant results relating to the extent of marker correlation and co-localisation were collated. Studies are referred to by the first author and year of their first full publication or published abstract (if no full publication is available).

Data are the Pearson correlation co-efficient (r) or Spearman's rank correlation coefficient (r_s). All results and P values are recorded as reported by each study. If not explicitly stated, and raw data were available within the manuscript, these parameters were calculated.

Synthesis of results

Given that several identified studies described only qualitative findings, a narrative synthesis of evidence was deemed to be more appropriate than a formal meta-analysis.

Results

Study selection

43 records met inclusion criteria (38 full articles [254, 282-288, 519, 523, 625, 630, 863-866, 933-954] and 5 abstracts [890, 955-958], relating to 34 separate studies. Amongst these, manual searching identified two additional records [946, 954] including one that was published after the systematic search was undertaken [954]. All studies utilised pimonidazole as the exogenous hypoxia marker and none utilised EF5. A flow diagram summarising the study selection process is depicted in **Figure B**.

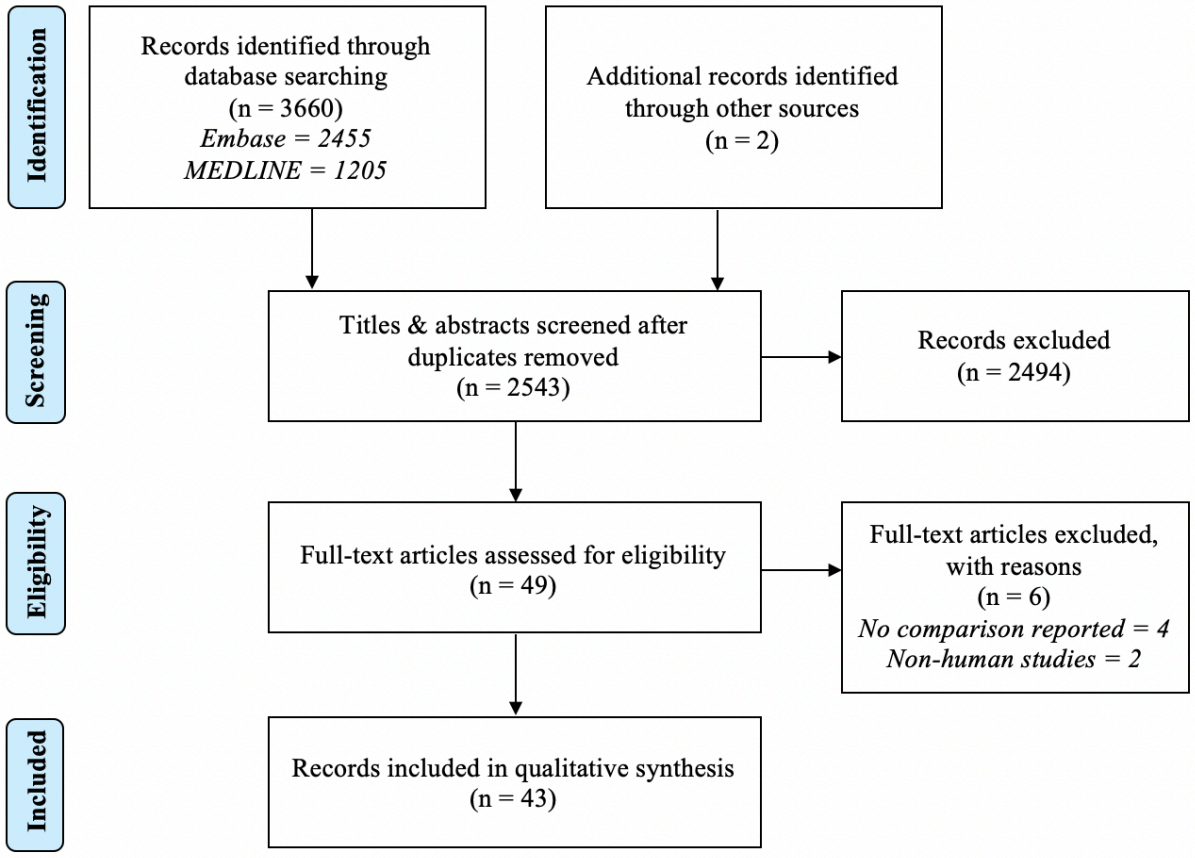


Figure B – Flow diagram to show inclusion and exclusion of records in systematic review

Study findings

The findings of each study, grouped by endogenous marker, are presented in **Table C.**

Table C – Summary of findings of studies included in systematic review				
Author (year)	**Cancer type**	**Sample size**	**Correlation of area of staining**	**Co-localisation of staining**
αβ-crystallin				
van de Schootbrugge (2014) [951]	HNSCC	n = 38	NR	Large overlap, although αβ-crystallin can be detected in pimonidazole negative regions
Protein kinase B (AKT)				
Wennemers (2013) [948]	Breast carcinoma	n = 38	NR	AKT staining observed in pimonidazole positive areas
Nijkamp (2011) [283]	HNSCC	n = 41	No correlation	AKT expressed in both pimonidazole positive and negative cells
Nijkamp (2013) [949]	HNSCC	n = 69	NR	AKT expression higher in pimonidazole positive areas
Stegeman (2014) [950]	HNSCC	n = 9	NR	Hypoxic pattern of AKT expression in 89% of tumours, non-hypoxic pattern of AKT expression in 11% of tumours
Carbonic anhydrase 9 (CA IX)				
Wykoff (2000) [630]	Bladder carcinoma/ non-melanoma skin cancer	n = 20 (14/6)	$r_s = 0.28$ P = 0.2360	Substantial, although incomplete, overlap

Hoskin (2003) [864]	Bladder carcinoma	n = 21	r = 0.86 P < 0.0001	Good co-localisation
Airley (2003) [938]	Cervical carcinoma	n = 42	r_s = 0.10 P = 0.52	Distinctly similar patterns of staining, although the precise area of staining differed slightly
Olive (2001) [863]	Cervical carcinoma	n = 18	r = 0.87 P < 0.0001	Excellent co-localisation but CA IX positive area twice as large as pimonidazole positive area
Jankovic (2006) [519]	Cervical carcinoma	n = 67	r = 0.6 P < 0.01	> 70% regions analysed demonstrated co-localisation
van Laarhoven (2006) [865]	Colorectal carcinoma (liver metastases)	n = 24	No correlation	Co-localisation observed but microregional areas of mismatch also identified
Goethals (2006) [866]	Colorectal carcinoma	n = 20	r_s = 0.07 P = 0.76	Good co-localisation in only 25-30% of tumours
Verstraete (2013) [947]	Colorectal carcinoma	n = 17	No correlation	Heterogenous patch-like pattern of CA IX expression but not overlapping
Brenner (2018) [954, 958]	Glioblastoma	n = 11	r = 0.84 P = 0.001	Strong co-localisation
Lal (2001) [935]	HNSCC	n = 2	NR	Nearly identical patterns of staining

Kaanders (2002) [254]	HNSCC	n = 42	r = 0.36 P = 0.02	Similar distribution but CA IX signal generally observed at shorter distances from blood vessels; areas of mismatch observed
De Schutter (2006) [285]	HNSCC	n = 48	r_s = 0.36 P = 0.01	NR
Hoogsteen (2009) [282]	HNSCC	n = 103	r_s = 0.2 P = 0.047	Variable co-localisation with large variation between biopsies
Rademakers (2013) [287]	HNSCC	n = 79	r = 0.36 P < 0.01	CA IX displayed either a perinecrotic (16%), diffuse (56%) or low/absent (28%) staining pattern whilst pimonidazole displayed a predominantly diffusion-limited staining pattern
Rademakers (2011) [286]	HNSCC	n = 18	r_s = 0.42 P = 0.06	Significantly higher CA IX expression in pimonidazole stained areas (P = 0.005) CA IX expression closely followed the pimonidazole pattern in some tumours, in others its expression showed less spatial correlation
Stegeman (2014) [950]	HNSCC	n = 11	NR	Hypoxic pattern of CA IX expression in 73% of tumours, non-hypoxic pattern of CA IX expression in 27% of tumours
Bruine de Bruin (2015) [288]	HNSCC	n = 11	r_s = -0.25 P = 0.4467	NR

Konopleva (2015) [952]	Leukaemia (bone marrow)	n = 3 (pre-treatment) n = 9 (post-treatment)	r = NR P = 0.66 r = NR P = 0.73	NR
Epidermal growth factor receptor (EGFR)				
Goethals (2006) [866]	Colorectal carcinoma	n = 20	$r_s = 0.36$ P = 0.21	Totally different staining patterns (EGFR – diffuse, pimonidazole – perinecrotic at a distance from blood vessels)
Nijkamp (2011) [283]	HNSCC	n = 41	No correlation	EGFR expressed in both pimonidazole positive and negative cells
Hoogsteen (2012) [284]	HNSCC	n = 45	$r_s = 0.35$ P = 0.018	Varying degrees of co-localisation with areas of mismatch observed, pimonidazole labelling in a perinecrotic distribution at a distance from blood vessels whereas EGFR was mainly expressed at an intermediate distance from blood vessels
Nijkamp (2013) [949]	HNSCC	n = 69	NR	EGFR predominantly expressed in better oxygenated areas close to blood vessels
Stegeman (2014) [950]	HNSCC	n = 12	NR	Hypoxic pattern of EGFR expression in 67% of tumours, non-hypoxic pattern of EGFR expression in 33% of tumours
Erythropoietin (EPO)				
Arcasoy 2002 [937, 955]	Breast carcinoma	n = 38	r = 0.60 P < 0.0001	Microregional analysis demonstrated patterns of complete overlap, some overlap and little/no overlap

Arcasoy (2005) [941]	HNSCC	n = 20	$r_s = 0.74$ P < 0.001	Significant microregional overlap but staining did not always co-localise (overlap in 19% of biopsies, mixed overlap/no overlap in 51% of biopsies, no overlap in 30% of biopsies)
Erythropoietin receptor (EPOR)				
Arcasoy (2002) [937, 955]	Breast carcinoma	n = 38	r = 0.63 P < 0.0001	Microregional analysis demonstrated patterns of complete overlap, some overlap and little/no overlap
Arcasoy (2005) [941]	HNSCC	n = 20	r = NR P > 0.2	NR
Hoogsteen (2005) [943]	HNSCC	n = 34	NR	Lack of co-localisation, EPOR staining showed an almost reverse relationship to pimonidazole labelling
Glucose transporter 1 (GLUT1)				
Hoskin (2003) [864]	Bladder carcinoma	n = 21	r = 0.91 P < 0.0001	Good co-localisation
Airley (2003) [938]	Cervical carcinoma	n = 42	$r_s = 0.45$ P < 0.003	Distinctly similar patterns of staining, although the precise area of staining differed slightly
Varia (2011)* [890]	Cervical carcinoma	n = 11	NR	No co-localisation (GLUT1 – peripheral tumour cells, pimonidazole – central tumour cells)
van Laarhoven (2006) [865]	Colorectal carcinoma (liver metastases)	n = 24	No correlation	Co-localisation observed but microregional areas of mismatch also identified

Verstraete (2013) [947]	Colorectal carcinoma	n = 17	No correlation	Heterogenous patch-like pattern of GLUT1 expression but not overlapping
De Schutter (2006) [285]	HNSCC	n = 48	No correlation	NR
Rademakers (2011) [286]	HNSCC	n = 18	$r_s = 0.16$ P = 0.51	Diffuse pattern of GLUT1 expression but with more staining at increasing distance from vessels
Stegeman (2014) [950]	HNSCC	n = 16	NR	Hypoxic pattern of GLUT1 expression in 37% of tumours, non-hypoxic pattern of GLUT1 expression in 63% of tumours
Bruine de Bruin (2015) [288]	HNSCC	n = 11	r = -0.24 P = 0.4743	NR
Mandeville (2012) [625, 956]	Lung carcinoma	n = 14	$r_s = 0.03$ P = 0.85	Co-localisation but also regional differences
Rupp (2016) [953]	Prostate carcinoma	n = 15	$r_s = 0.53$ P = NR	Partial co-localisation
Hypoxia-inducible factor 1 alpha (HIF1α)				
Hutchison (2004) [523]	Cervical carcinoma	n = 36	$r_s = 0.34$ P = 0.04	Partial co-localisation, both perinecrotic and perivascular HIF1α nuclear positive cells identified

Sobhanifar (2005) [942]	Cervical carcinoma	n = 3	NR	HIF1α expression detected closer to blood vessels than pimonidazole labelling but HIF1α expression significantly reduced in perinecrotic cells containing pimonidazole adducts
Jankovic (2006) [519]	Cervical carcinoma	n = 67	r = 0.34 P ≤ 0.01	> 70% regions analysed demonstrated co-localisation
Janssen (2002) [936]	HNSCC	n = 10	r = 0.24 P = 0.51	Low co-localisation, range of overlap of HIF1α with pimonidazole = 0.02-25.0%
Rademakers (2011) [286]	HNSCC	n = 18	NR	HIF1α expressed in 75% of samples, mostly around pimonidazole positive areas with large variation in intensity of expression
Bruine de Bruin (2015) [288]	HNSCC	n = 10	r = -0.63 P = 0.05	NR
Konopleva (2015) [952]	Leukaemia (bone marrow)	n = 3 (pre-treatment) n = 8 (post-treatment)	r = NR P = 0.33 r = NR P = 0.78	NR
Rupp (2016) [953]	Prostate carcinoma	n = 15	r_s = 0.62 P = NR	Partial co-localisation
Involucrin				
Raleigh (2000) [934, 940]	Cervical carcinoma/ HNSCC	n = 20 (13/7)	NR	Microregional analysis demonstrated complete overlap in 82% of sections, some overlap in 14% of sections and little/no overlap in 4% of sections

Azuma (2003) [939]	Cervical carcinoma	n = 34	r_s = -0.10 P = 0.69	Co-localisation observed in intermediate grade tumours but not in well or poorly differentiated tumours
Lactate dehydrogenase 5 (LDH5)				
Rademakers (2011) [286]	Cervical carcinoma	n = 18	r_s = 0.66 P = 0.002	Significantly higher expression of LDH5 in pimonidazole labelled areas (P < 0.0001) Extensive LDH5 expression in most tumours with more intense staining in hypoxic areas
Monocarboxylate transporter 1 (MCT1)				
Verstraete (2013) [947, 957]	Colorectal carcinoma	n = 17	No correlation	Heterogenous patch-like pattern of MCT1 expression but not overlapping
Rademakers (2011) [286]	HNSCC	n = 18	r_s = 0.16 P = 0.51	No statistically significant difference in MCT1 expression between pimonidazole labelled and unlabelled areas (P = 0.11) MCT1 expression observed adjacent to and within pimonidazole positive areas but substantial variation in extent and intensity of expression between tumours
Stegeman (2014) [950]	HNSCC	n = 15	NR	Hypoxic pattern of MCT1 expression in 47% of tumours, non-hypoxic pattern of MCT1 expression in 53% of tumours
Monocarboxylate transporter 4 (MCT4)				
Verstraete (2013) [947, 957]	Colorectal carcinoma	n = 17	No correlation	Heterogenous patch-like pattern of MCT4 expression but not overlapping

Rademakers (2011) [286]	HNSCC	n = 18	r_s = 0.21 P = 0.37	Significantly higher MCT4 expression in pimonidazole labelled areas (P < 0.001) Diffuse pattern of MCT4 expression but with more staining at increasing distance from vessels
Stegeman (2014) [950]	HNSCC	n = 13	NR	Hypoxic pattern of MCT4 expression in 38% of tumours, non-hypoxic pattern of MCT4 expression in 62% of tumours
Metallothionein 1 and 2 (MT I & MT II)				
Raleigh (2000) [934]	Cervical carcinoma/ HNSCC	n = 20 (13/7)	r_s = 0.15 P = 0.5198	Microregional analysis demonstrated complete overlap in 11% of sections, some overlap in 22% of sections and little/no overlap in 67% of sections
Myoglobin				
Kristiansen (2011) [946]	Breast carcinoma	n = 2	NR	No co-localisation
Osteopontin (OPN)				
Rupp (2016) [953]	Prostate carcinoma	n = 15	r_s = 0.61 P = NR	Partial co-localisation
Prolyl hydroxylase domain-containing protein 2 (PHD2)				
Verstraete (2013) [947]	Colorectal carcinoma	n = 17	No correlation	Homogenous PHD2 expression in > 90% of tumour cells, thus not marking hypoxic cells

Thymidine phosphorylase (TP)				
Kabuubi (2006) [944]	Cervical carcinoma	n = 38	r_s = 0.13 P = 0.45	Higher levels of TP expression adjacent to areas of necrosis but no pattern in relation to tumour vasculature
Tribbles homolog 3 (TRIB3)				
Wennemers (2011) [945, 948]	Breast carcinoma	n = 38	NR	TRIB3 staining observed in pimonidazole positive areas
Vascular endothelial growth factor (VEGF)				
Raleigh (1998) [933]	Cervical carcinoma/ HNSCC	n = 18 (13/5)	No correlation	In some instances, VEGF and pimonidazole co-localised but this was not the predominant pattern
Goethals (2006) [866]	Colorectal carcinoma	n = 20	r_s = -0.15 P = 0.51	Totally different patterns of staining (VEGF – diffuse, pimonidazole – perinecrotic at a distance from blood vessels)

*Abstract only

Records separated by a dashed line belong to the same overall study. Data presented are the Pearson correlation coefficient (r) or Spearman's rank correlation coefficient (r_s) and associated P value.

HNSCC – head and neck squamous cell carcinoma, NR – not reported

Discussion

Summary of findings

Hypoxia-inducible factor alpha

Eight records compared HIF1α expression to pimonidazole labelling [286, 288, 519, 523, 936, 942, 952, 953]. The majority of these studies reported either a weak positive correlation or no correlation between the extent of HIF1α and pimonidazole immunostaining. In general, partial co-localisation of marker expression was noted but HIF1α expression tended to be observed

more proximally to blood vessels than pimonidazole [523, 936, 942]. Indeed, double staining for HIF1α and the endothelial markers CD31/CD34 in one study demonstrated both perinecrotic and perivascular HIF1α nuclear positive cells (with the latter population perhaps indicative of acutely hypoxic cells caused by a transient decrease in blood flow within the adjacent vessel) [523]. Furthermore, HIF1α expression was reported to be lost in the most hypoxic tumour cells located in immediately perinecrotic areas [942] (**Figure C**). *In vitro* mechanistic studies indicated that nutrient deprivation was responsible for the loss of HIF1α expression in these cells (in keeping with other studies that indicate a requirement for glucose and glutamine for HIFα stabilisation [959, 960]), with the longer half-life of CA IX explaining its ongoing expression despite the absence of HIF1α stabilisation. Of note, when correlated with polarographic electrode oxygen measurements, HIF1α immunostaining displays at best a weak positive association [519, 523, 961-963].

These discrepancies may reflect the fact that static, two-dimensional histological images cannot fully capture the dynamic, three-dimensional nature of tumour hypoxia. In addition, several important biological factors may also contribute including the different oxygen tensions required for HIFα stabilisation (~20 mmHg) and pimonidazole reduction (< 10 mmHg) and the existence of stimuli, such as activation of certain growth factor signalling pathways, specific oncogenic mutations and generation of reactive oxygen species, that can stabilise HIFα in an oxygen-independent manner (as reviewed in [964]). Interestingly, no records were identified that compared the expression of HIF2α with exogenous hypoxia markers, raising the possibility that the actual extent of HIFα stabilisation might have been underestimated in the studies included in this review. Of note, immunostaining for HIFα is technically demanding and several caveats must be carefully considered when performing this. Due to the exquisitely

oxygen sensitive nature of HIFα stability and its short half-life, HIFα expression may be artefactually acquired or lost at the time of tissue harvest. The choice of fixative and length of fixation have also been reported to strongly influence results [485, 961] (**Figure C**). Unfortunately, immediate specimen processing with standardised tissue fixation is seldom achieved in routine pathological practice. Furthermore, HIFα antigenicity is recognised to deteriorate with increasing age of the paraffin block [965]. By extension, it is also sensible to minimise the length of time between block sectioning and performing HIFα immunohistochemistry. Furthermore, staining protocols require careful validation [927, 966] and great care must be taken when interpreting patterns of HIFα expression. Overall, HIFα is unlikely to be a robust endogenous hypoxia marker when analysing archival clinical samples.

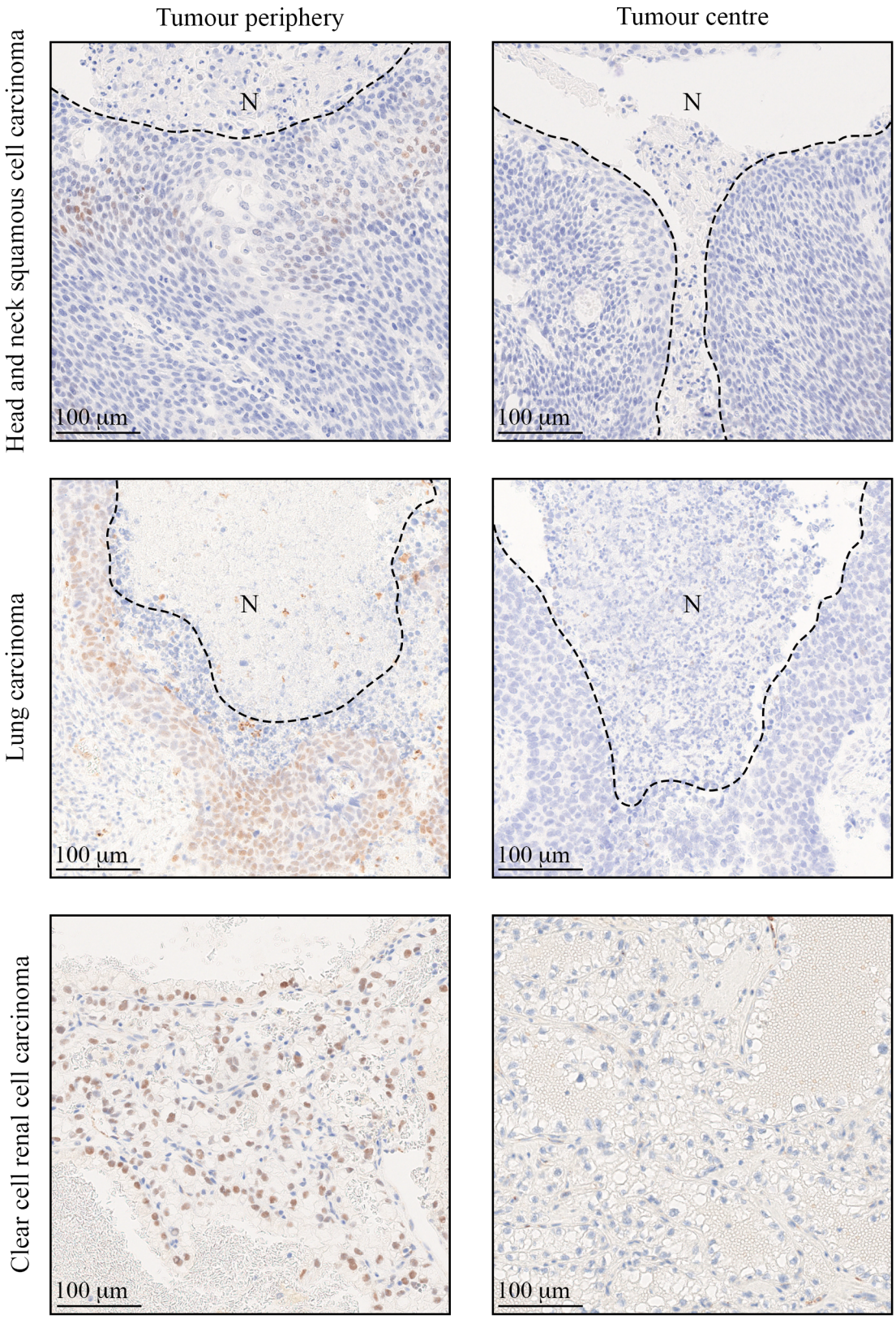

Tumour periphery
Tumour centre
Head and neck squamous cell carcinoma
Lung carcinoma
Clear cell renal cell carcinoma
N
N
N
N
100 µm
100 µm
100 µm
100 µm
100 µm
100 µm

Figure C – Variability in hypoxia-inducible factor 1 alpha expression within and between different human tumours

Immunohistochemical staining for hypoxia-inducible factor 1 alpha (HIF1α) in perinecrotic regions from the periphery and centre of a case of head and neck squamous cell carcinoma and a case of lung carcinoma and regions not related to necrosis (N) in a case of clear cell renal cell carcinoma. There is marked variation in strength of staining between and within samples. Whilst biological effects may contribute to these differences, the observation that staining is stronger in peripheral, as compared to central, regions of each tumour suggests that immunodetection of HIF1α is particularly sensitive to tissue fixation and/or antigen retrieval. Furthermore, nuclear expression is less suitable than cytoplasmic or membranous expression for the delineation of boundaries of hypoxic tumour regions and HIF1α expression is lost in the cells immediately adjacent to necrosis.

Prolyl hydroxylase domain-containing proteins

Only one study was identified that compared the expression of prolyl hydroxylase domain-containing protein 2 (PHD2) to pimonidazole [947]. In 17 colorectal cancer samples, the diffuse nature of PHD2 expression resulted in no correlation with pimonidazole. This finding is perhaps unsurprising given that expression of PHD2 is in part regulated by HIF1α [52-54], which itself shows only partial co-localisation with pimonidazole immunostaining.

Carbonic anhydrase 9

CA IX was the most extensively studied endogenous hypoxia marker, being reported on by 19 records [254, 282, 285-288, 519, 630, 863-866, 935, 938, 947, 950, 952, 954, 958]. The observed correlations with pimonidazole labelling varied from none at all to very strong. Whilst most studies reported co-localisation of marker expression, CA IX tended to extend beyond the boundary of pimonidazole adduct formation (thus labelling both profoundly hypoxic cells as well as those that are intermediate in oxygenation, in keeping with its HIFα dependency). Other potential biological explanations for a lack of correlation include the time period required

for induction of CA IX expression (16-24 hours *in vitro* [630, 935]) and its relatively long half-life (approximately 38 hours [967]) meaning that its expression may preferentially detect regions of chronic tumour hypoxia and miss regions of acute hypoxia labelled by pimonidazole adducts. Furthermore, CA IX expression can be modulated by factors other than oxygen availability, such as extracellular pH [967-970]. Studies in human tumours comparing CA IX expression with polarographic electrode oxygen measurements have reported inconsistent results, with some demonstrating a significant positive association [81, 971] and yet others reporting no correlation at all [519, 963, 972, 973].

Of note, no records comparing the expression of the hypoxia-inducible carbonic anhydrase 12 (CA XII) isoform to pimonidazole were identified.

Glucose transporter 1

12 records compared glucose transporter 1 (GLUT1) expression to pimonidazole labelling [285, 286, 288, 625, 864, 865, 890, 938, 947, 950, 953, 956]. Whilst some studies reported moderate-to-strong correlation with pimonidazole, most did not. As with other endogenous markers, several studies reported partial co-localisation with pimonidazole but others observed a more diffuse expression pattern. Importantly, as GLUT1 can be basally expressed in well oxygenated cancer cells [974] and some non-neoplastic cells such as red blood cells, its histological expression in tumours is more diffuse and less demarcated than that of CA IX [975] (**Figure D**). Consequently, the delineation of the boundaries of its expression involves a degree of subjectivity. Additionally, GLUT1 expression has been reported to correlate only weakly, at best, with polarographic electrode oxygen measurements [976-978]. This may relate to oxygen-independent regulation of expression by factors including hormones [979] and pH [980].

Of note, no records comparing the expression of the hypoxia-inducible glucose transporter 3 (GLUT3) isoform to pimonidazole were identified.

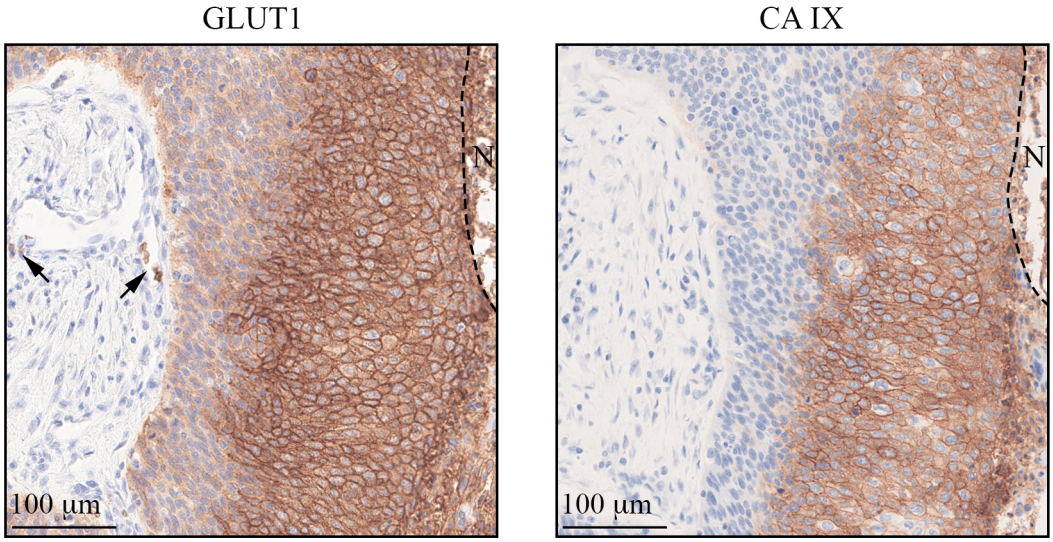


Figure D – Comparison of patterns of glucose transporter 1 and carbonic anhydrase 9 expression in human head and neck squamous cell carcinoma

Immunohistochemical staining for perinecrotic glucose transporter 1 (GLUT1) and carbonic anhydrase 9 (CA IX) in serial sections from a case of human head and neck squamous cell carcinoma. As compared to CA IX, which displays a distinct boundary between positive and negative regions, GLUT1 is basally expressed by non-hypoxic tumour cells and some non-neoplastic cells including red blood cells (arrows) (N – necrosis).

Vascular endothelial growth factor

Two records compared VEGF expression to pimonidazole labelling [866, 933]. Neither study demonstrated correlation or co-localisation between the markers and VEGF immunostaining does not correlate with polarographic electrode oxygen measurements [978]. VEGF levels are also regulated by oxygen-independent mechanisms, including phosphatase and tensin homolog (PTEN)-phosphoinositide 3-kinase (PI3K)-protein kinase B (AKT) signalling [981]. Furthermore, VEGF is a secreted protein and immunohistochemistry is therefore not the best

technique to identify its cells of origin. Indeed, tumoural VEGF mRNA levels, as measured by quantitative real-time polymerase chain reaction, do correlate with pimonidazole immunostaining [982] and several studies have used mRNA *in situ* hybridisation to identify producer cells which are indeed located in perinecrotic tumour regions [630, 983, 984] and co-localise with EF5 labelling [985] and CA IX expression [916].

Erythropoietin and erythropoietin receptor

Three records compared erythropoietin (EPO) expression [937, 941, 955] and four records compared erythropoietin receptor (EPOR) expression [937, 941, 943, 955] to pimonidazole labelling. For EPO, moderate and strong correlation was observed in breast and head and neck squamous cell carcinoma (HNSCC), respectively, but lack of overlap was also observed in a proportion of samples. Whilst EPOR expression did correlate with pimonidazole in breast cancer, it did not in two studies in HNSCC. A similar finding has been reported in a further study in HNSCC in which EPO, but nor EPOR, correlated with HIF1α and CA IX immunostaining [986]. Subsequently, the C-20 rabbit polyclonal antibody used to identify EPOR in the above studies has been demonstrated to cross-react with non-EPOR proteins and is thus unsuitable for immunohistochemistry [987, 988]. Indeed, when probed by immunoblotting with a more specific and sensitive monoclonal antibody, no EPOR expression was detected in both benign and malignant human breast, lung, colon, ovary and skin tissue [989]. Thus, whilst EPO merits further investigation as an endogenous hypoxia marker in cancer, the results of studies of EPOR expression are unlikely to be reliable.

Lactate dehydrogenase

A single record compared lactate dehydrogenase five (LDH5) expression to pimonidazole labelling [286]. This found moderate correlation between the markers and that LDH5

expression was significantly increased in pimonidazole positive as compared to negative areas. In light of these findings, further studies of the role of LDH5 as an endogenous hypoxia marker are warranted.

Monocarboxylate transporters

Four records compared monocarboxylate transporter 1 (MCT1) and monocarboxylate transporter 4 (MCT4) expression to pimonidazole labelling [286, 947, 950, 957]. Overall, neither marker appears to be informative of tumour hypoxia.

Osteopontin

A single record compared OPN expression to pimonidazole labelling and reported moderate correlation and partial co-localisation between the two markers [953]. Whilst circulating plasma levels of OPN have been reported to correlate weakly with polarographic electrode measurements of tumour hypoxia [879, 963], immunostaining for OPN does not appear to correlate with this parameter [963, 978, 990].

Several studies evaluating the expression of proteins less intuitively associated with oxygenation were also identified.

Epidermal growth factor receptor and protein kinase B

Epidermal growth factor receptor (EGFR) is a transmembrane tyrosine kinase that acts as a receptor for a family of protein ligands including epidermal growth factor (EGF) and transforming growth factor alpha (TGFα). Ligand binding activates intracellular signalling pathways that control a panoply of critical cellular processes such as DNA synthesis and proliferation. Exposure of human cells to hypoxia *in vitro* has been shown to augment

expression of EGFR by increasing protein synthesis [991-993], possibly in a HIF2α-dependent manner [994], although this induction has not always been reported [924]. AKT is a serine/threonine-specific protein kinase that plays a key role in multiple fundamental cellular processes such as proliferation, metabolism and apoptosis; it is a downstream mediator of EGFR pathway signalling, amongst others. Activation of AKT by hypoxia has been observed both *in vitro* and in tumour xenografts [995]. Five records compared EGFR expression [283, 284, 866, 949, 950] and four records compared AKT expression [283, 948-950] to pimonidazole labelling. No correlation was reported for EGFR, which appears to be predominantly expressed in better oxygenated tumour regions, as was reported by a study which compared its expression to that of CA IX [619]. AKT has been reported to co-localise with pimonidazole but also appears to be expressed in tumour regions that do not form adducts.

Tribbles homolog 3

Expression of Tribbles homolog 3 (TRIB3), a pseudokinase that acts as a negative regulator of the PTEN-PI3K-AKT, mitogen-activated protein kinase (MAPK) and nuclear factor kappa-light-chain-enhancer of activated B cells (NF-κB) signalling pathways, is up-regulated by hypoxia [996]. Two records compared TRIB3 expression to pimonidazole labelling and reported qualitative overlap between the two markers [945, 948]. Therefore, further studies of TRIB3 as a possible endogenous hypoxia marker in breast cancer are merited.

Involucrin

Involucrin, a structural protein expressed in mature keratinocytes, is a useful marker of stratified squamous epithelial differentiation. Three records compared involucrin expression to pimonidazole labelling [934, 939, 940]. Although initially reported to demonstrate a large degree of overlap with pimonidazole [934], subsequent studies questioned this co-localisation,

particularly in well differentiated tumours (which tend to display diffuse involucrin expression) and poorly differentiated tumours (which generally show weak or absent expression) [939, 940]. Accordingly, *in vitro*, involucrin expression could be induced by hypoxic exposure in a moderately differentiated squamous cell carcinoma (SCC) cell line but not in a poorly differentiated SCC cell line [940]. Furthermore, involucrin immunostaining does not correlate with polarographic electrode oxygen measurements [978]. Thus, it is likely that differentiation status modulates the effects of hypoxia on the induction of involucrin, making it an unreliable marker of tumour hypoxia.

αβ-crystallin

αβ-crystallin is a small heat shock protein, also known as HspB5, that acts as a chaperone for VEGF, facilitating correct folding of this protein and thus supporting angiogenesis [997]. Its expression has been reported to be up-regulated *in vivo* after hypoxic exposure [998]. A single record compared αβ-crystallin expression to pimonidazole labelling and noted overlapping distributions [951]. *In vitro* studies suggested that up-regulation is not directly caused by hypoxia itself, rather by generation of reactive oxygen species upon reoxygenation leading to prolonged αβ-crystallin expression that promotes cell survival. If correct, this mechanism is likely to limit its use as an endogenous hypoxia marker.

Metallothioneins

Metallothioneins (MT) are a family of metal binding proteins that are localised to the Golgi apparatus and play a key role in cellular handling of zinc. Expression of both class I and class II metallothioneins have been reported to be induced by hypoxia, most likely in a HIF-independent manner [999-1002]. A single record compared MT I/MT II expression to pimonidazole labelling in cervical carcinoma and HNSCC (the antibody utilised in the study

recognises both isoforms) [934]. Extent of staining did not correlate with pimonidazole labelling and little or no overlap was observed in 67% of samples. In another study included in this review, MT II mRNA was also noted to be expressed in the peripheral, better oxygenated, regions of cervical cancer samples [939].

Myoglobin

Myoglobin is a cytoplasmic iron- and oxygen-binding protein, predominantly found within muscle. In addition, it can also be detected by immunohistochemistry in breast cancer samples, displaying a positive correlation with HIF2α and CA IX (but not HIF1α or GLUT1) expression, suggesting a possible role for hypoxia in regulation of myoglobin expression [1003]. A single record compared myoglobin expression to pimonidazole labelling and found no evidence of co-localisation in breast cancer [946]. Furthermore, in a larger cohort of 137 ductal carcinoma *in situ* (DCIS) samples from patients who did not receive pimonidazole, a perinecrotic expression of myoglobin was observed in only 27% of cases whereas expression was diffuse in 73% of cases. As such, the authors concluded that myoglobin expression was not predominantly regulated by tumour oxygenation in the majority of cases.

Thymidine phosphorylase

Thymidine phosphorylase (TP) contributes to pyrimidine salvage by recovering nucleosides after DNA and RNA degradation and has also been reported to have angiogenic properties [1004]. Its expression has been reported to be induced by hypoxia both *in vitro* and in tumour xenografts [1005] and correlates with HIF2α immunostaining in human endometrial carcinoma [1006]. A single record compared TP expression to pimonidazole labelling in cervical cancer [944]. Whilst TP was identified in perinecrotic tumour regions, its expression did not correlate with that of pimonidazole immunostaining. Furthermore, there was no association with tumour

oxygenation as measured by Eppendorf electrode, microvascular density or HIF1α and HIF2α immunostaining; statistically significant but weak positive correlations were observed with CA IX, GLUT1 and VEGF immunostaining.

Other markers

Several records were identified that compared exogenous hypoxia marker labelling to markers that were deemed not to be hypoxia-inducible and thus were not formally included in this review. The expression of both pimonidazole [254, 276, 282-284, 286, 287, 864, 865, 897, 906, 936, 943, 949, 953, 1007-1010] and EF5 [289, 985, 1011] were compared to blood vessels markers including CD31, CD34 and PAL-E. Furthermore, both pimonidazole [864, 865, 887, 897, 900, 934, 936, 1007, 1010, 1012] and EF5 [289, 1013] were also compared to markers of cellular proliferation including the endogenous markers Ki67, cyclin A and proliferating cell nuclear antigen (PCNA) as well as the exogenously administered thymidine analogues iododeoxyuridine (IdUrd) and bromodeoxyuridine (BrdUrd), chemicals that are incorporated into the DNA of cells in the S phase of the cell cycle. In general, markers of proliferation and hypoxia were inversely correlated, with proliferating cells located in proximity to blood vessels whilst exogenous hypoxia marker labelling was greatest at a distance from vessels, confirming that these substances preferentially mark regions of diffusion-limited, chronic hypoxia. Finally, expression of the endogenous DNA damage marker γH2AX was enriched in pimonidazole positive regions in cervical cancer samples [1014] whilst the differentiation marker CK19 was expressed in pimonidazole negative regions in the same tumour type [1015].

Limitations of included studies

The results of this systematic review demonstrate varying degrees of correlation and co-localisation between different endogenous hypoxia markers and pimonidazole, with

comparison of the geographic distribution of these markers frequently revealing areas of both overlapping and non-overlapping staining even within the same tumour. The extent to which these discrepancies are attributable to the biological heterogeneity inherent to both cancer and hypoxia or variations in methodological approaches between studies remains unclear.

Whilst most records included clear inclusion and exclusion criteria for patient enrolment, none described whether this enrolment involved either all consecutive, or a random sample of, eligible patients. The included studies were performed by a small number of academic institutions, complicating assessment of whether a given record represented a genuinely new study or simply re-analysis of samples that had been included in previous publications. Sample dropout was evident in some records, suggesting depletion of available tumour material for certain patients. This observation raises the possibility of selection bias towards larger tumours, which is a common problem with retrospective tissue-based studies [1016]. Given the complexities of pimonidazole administration within routine clinical practice, relatively few patients were included in the studies identified by this review. Therefore, there is a risk that these studies are underpowered to detect subtle but clinically significant findings. Conversely, testing of multiple markers with *post hoc* subset analyses and cut-point optimisation risks generating false positive findings and over-enthusiastic conclusions. Furthermore, there is a high risk of publication bias in that studies with negative findings may remain unpublished.

Significant methodological weaknesses were apparent across the included records and several records failed to provide sufficient detail in their methods section to permit accurate quality assessment and to facilitate reproduction by external laboratories, limiting the generalisability of their findings. In particular, greater detail about specimen handling (for example, type of fixative used and approximate length of fixation time) and immunohistochemistry protocols is

desirable. Selection of sample type for analysis (such as biopsy versus resection and single sample versus multiple samples per tumour) varied between studies and likely contributes to lack of correlation between markers [885]. When reported fully, immunohistochemical assays varied between studies with respect to antigen retrieval, type and concentration of primary antibodies used and visualisation technique. All but one study performed manual immunohistochemical staining, an approach that is not consistent with contemporary pathological practice, which utilises automated platforms to reduce variation in staining both within and between batches of slides. In addition, only one study stated the time between block sectioning and immunostaining. This is particularly important due to concerns about long-term stability/antigenicity of oxygen sensitive proteins. Compounding this concern, many studies either included sub-optimal controls (such as omission of the primary antibody as a negative control when use of an isotype control antibody would be more informative) or failed to include information about control specimens entirely. Lastly, approaches to histological interpretation and scoring varied greatly between studies (for example, qualitative versus semi-quantitative versus fully quantitative analysis and visual inspection versus digital image analysis). These differences are likely to be of utmost importance given that scoring and correlating putative hypoxia markers has been reported to be extremely sensitive to the scoring system used [938]. In conclusion, future studies should conform to accepted publishing standards. Whilst this is not a review of the prognostic significance of these markers, the Reporting Recommendations for Tumour Marker Prognostic Studies (REMARK) guidelines provide helpful information regarding the conduct and reporting of tumour immunohistochemistry studies [1017, 1018].

A further issue for consideration are the limitations inherent to the reference standard test. Although considered the ‘gold standard’ approach to the detection of hypoxia in tissue sections, exogenous hypoxia markers suffers from important limitations. Several studies have reported

a lack of correlation between pimonidazole [519, 1019-1022] or EF5 [888, 1023] labelling and tumour oxygenation as measured by polarographic electrode. This discrepancy may relate to a number of factors, particularly the presence of tumour necrosis which is classified as anoxic by polarographic electrode measurement but is not stained by exogenous hypoxia markers which only label viable tumour cells [1024]. Furthermore, pimonidazole adducts are recognised to form around areas of keratinisation in well differentiated SCC, regions that may or may not be hypoxic [1025] (**Figure E**). Also, the impact on exogenous marker labelling of a delay between drug administration and tissue collection (which could conceivably occur during routine clinical practice) is not well described and was not discussed in detail in any of the identified records. Nevertheless, the extent of pimonidazole staining has been reported to be of both prognostic and predictive value in HNSCC [254] and to correlate with an aggressive hypoxic phenotype in prostate cancer [1012], suggesting that exogenous markers do label clinically relevant tumour hypoxia.

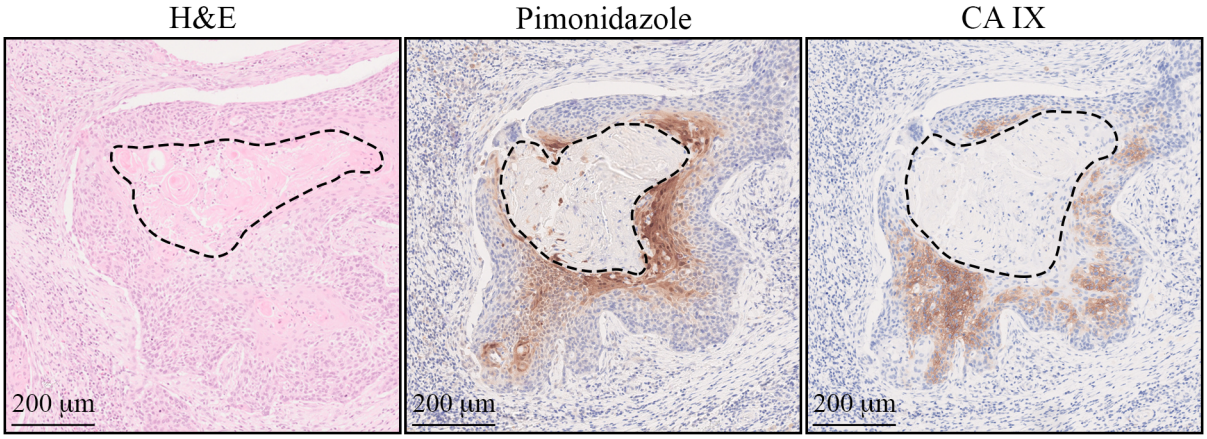


Figure E – Differentiation-associated pimonidazole labelling in human head and neck squamous cell carcinoma

Haematoxylin and eosin (H&E) and pimonidazole and carbonic anhydrase 9 (CA IX) immunohistochemistry staining on serial sections from a case of well differentiated human head and neck squamous cell carcinoma displaying central keratinisation (dashed lines). Hypoxia-independent pimonidazole binding has been reported to occur in more differentiated

head and neck tumours, necessitating caution in hypoxia quantification. However, overlap between pimonidazole labelling and CA IX expression suggests that, in this instance, the region is truly hypoxic.

Finally, a limitation of both endogenous and exogenous histological markers of hypoxia is a tendency for researchers to dichotomise tumour regions as either 'hypoxic' (positively stained) or 'non-hypoxic/normoxic' (negatively stained). Rather, it is more appropriate to consider staining patterns in the context of hypoxic gradients that exist within solid tumours, from the best oxygenated perivascular regions (~30 mmHg [1026]) to virtually anoxic necrotic areas, and hypoxia is thus best reported as a quantitative value along this continuum [1027, 1028] (**Figure F**).

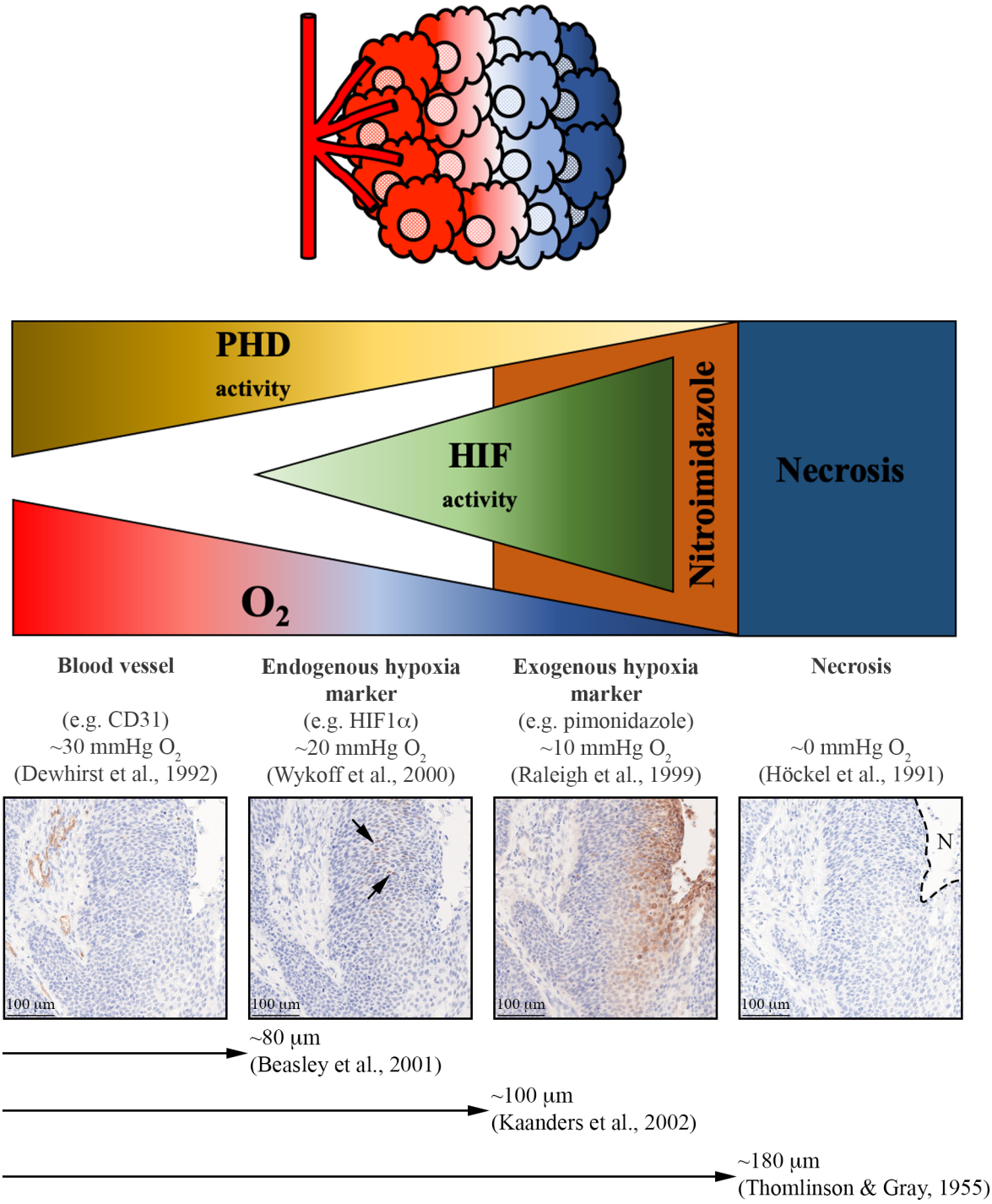


Figure F – Gradients of oxygen availability exist within solid tumours

Gradients of oxygen (O_2) availability exist in solid tumours and arise through a complex interaction of a number of factors including the blood's oxygen carrying capacity, the integrity and function of tumour blood vessels and the metabolic demands of tumour and stromal cells. In general, perivascular regions are the best oxygenated areas within tumours. As oxygen availability decreases, so too does the enzymatic activity of the prolyl hydroxylase domain-

containing proteins (PHD). Endogenous hypoxia markers are activated via the hypoxia-inducible factor (HIF) system at an oxygen partial pressure of approximately 20 mmHg (reported to arise at about 80 μm from the nearest blood vessel) whereas exogenous hypoxia markers, such as pimonidazole, label more profoundly hypoxic regions (approximately 10 mmHg/100 μm from the nearest blood vessel). Necrosis (N) occurs within tumour regions that are virtually anoxic (approximately 180 μm from the nearest blood vessel). This figure sequentially illustrates immunohistochemical labelling of stromal blood vessel endothelium with CD31 (to the left), nuclear accumulation of HIF1α (arrows), the hypoxic adducts formed by pimonidazole and an area of necrosis (top right). It is important to note that this schematic representation is rather simplistic and fails to account for acute changes in tumour perfusion, such as occur upon blood vessel blockage or reversal of blood flow (references: Dewhirst et al., 1992 [1026]; Wykoff et al., 2000 [630]; Raleigh et al., 1999 [892]; Höckel et al., 1991 [70]; Beasley et al., 2001 [915]; Kaanders et al., 2002 [254]; Thomlinson & Gray, 1955 [66]).

Conclusions

When undertaking histological studies of tumour oxygenation, regions of tumour hypoxia must be detected with certainty in order to generate reliable findings. Unfortunately, this review has failed to identify a robust endogenous hypoxia marker that correlates with an exogenous hypoxia marker (or polarographic electrode measurements of tumour oxygenation) across studies. Clearly, no endogenous marker is absolutely hypoxia-specific, rather they are indirect surrogate markers of hypoxia. Concerningly, several studies reported a complete lack of detection of endogenous hypoxia marker expression despite significant pimonidazole labelling [287, 288, 863-866, 933] (**Figure G**). Why this occurs is unknown but *in vitro* studies have previously demonstrated a non-uniform response in a panel of tumour cells with regards to CA IX induction following hypoxic exposure. Such an observation means that reliance upon a single endogenous hypoxia marker may lead to substantial underestimation of hypoxia in a proportion of tumours. Thus, identification of absence of endogenous marker expression in the presence of tumour necrosis should raise the possibility of this occurrence. Ideally, it is good

practice to confirm the presence of tumour hypoxia by staining for at least two, and preferably more, different endogenous markers.

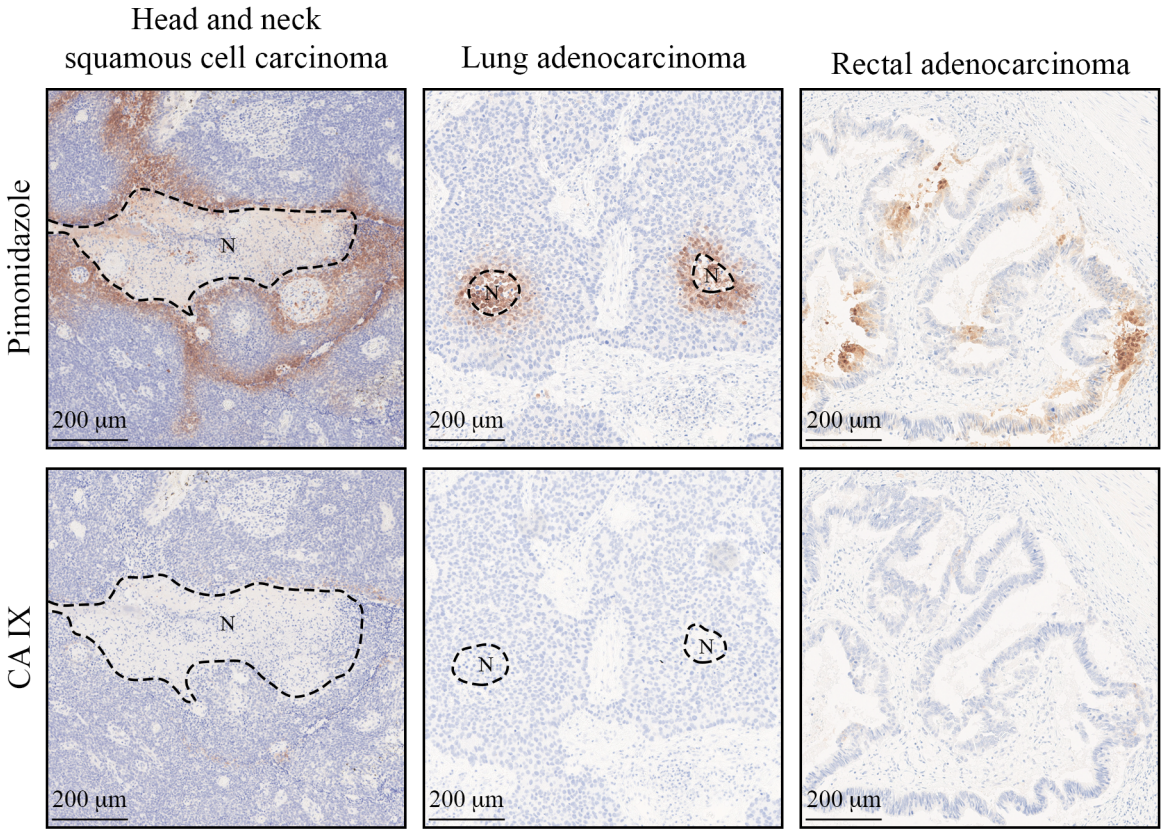


Figure G – Lack of carbonic anhydrase 9 expression in hypoxic human head and neck squamous cell carcinoma, lung adenocarcinoma and rectal adenocarcinoma

Despite the presence of pimonidazole adducts and necrosis (N), immunostaining of serial sections from samples of human head and neck squamous cell carcinoma, lung adenocarcinoma and rectal adenocarcinoma demonstrate that these tumours do not express carbonic anhydrase 9 (CA IX), illustrating the benefit of analysing more than one marker when assessing tumour hypoxia by immunohistochemistry.

Future studies using existing samples should be conducted on larger cohorts of patients (which will require multi-centre collaborations) and should utilise standardised, contemporary immunohistochemistry techniques and scoring. Whilst immunostaining of serial sections for

the assessment of tumour hypoxia has been validated [519], the recent development of robust multiplex immunohistochemistry/immunofluorescence platforms (as reviewed in [520, 521]) facilitates analysis of several markers on a single section. Not only will this permit more accurate co-localisation of markers, but it also offers the potential to combine several endogenous markers to generate oxygen supply maps [953] and improve prognostication [1029]. This approach will overcome the limitations of relying upon a single endogenous hypoxia marker to interrogate what is a dynamic and heterogenous pathophysiological process, has the potential to facilitate distinction between pre-existing tissue oxygenation and effects occurring during specimen handling [1030, 1031] and may obviate the need for exogenous markers in future studies. Combining immunohistochemistry with *in situ* RNA analysis [1032] will facilitate accurate localisation of the hypoxic cells that are synthesising secreted proteins such as EPO, OPN and VEGF, as well as detection of microRNAs that are hypoxia-inducible and thus might also act as endogenous markers (for example, miR-210) [21]. If prospective studies are being undertaken with recruitment of new patients, separate injection of two or more hypoxia or perfusion markers may provide additional information about spatiotemporal fluctuations in tumour oxygenation, as has been achieved in animal studies [1033-1037]. In order for such studies to be informative, tissue handling and fixation will need to follow strict protocols. Furthermore, as the complexity of data increases, more advanced analytical approaches will be required. Whilst approaches to comparing the distribution of different histological markers in tumour sections have been proposed (for example, parametric mapping [1038]), these have not been adopted in the studies identified by this review. Whole slide imaging and digital image analysis offer the ability to undertake consistent and sophisticated analysis of histology images to generate results that can be integrated with the findings from *in vitro* studies, animal experiments and mathematical modelling. By combining these

techniques, it may be possible to extrapolate findings generated from two-dimensional histology images to the three-dimensional complexity of human tumours.

Appendix 2 – Head and neck squamous cell carcinoma cohort

Patient characteristics	
Mean age in years (range)	55.6 (39-80)
Gender (male/female)	15 (93.8%)/ 1 (6.3%)
Alcohol (currently heavy/previously heavy/never heavy/no alcohol)	3 (18.8%)/ 3 (18.8%)/ 9 (56.3%)/ 1 (6.3%)
Smoker (current/previous/never)	10 (62.5%)/ 1 (6.3%)/ 5 (31.3%)
Tumour history (primary/recurrence)	15 (93.8%)/ 1 (6.3%)
Neoadjuvant chemotherapy or radiotherapy (yes/no)	1 (6.3%)/ 15 (93.8%)
Tumour characteristics	
Tumour site	
Oral cavity	1 (6.3%)
Oropharynx	10 (62.5%)
Hypopharynx	3 (18.8%)
Larynx	2 (12.5%)
Histological grade	
Well differentiated	0 (0.0%)
Moderately differentiated	6 (37.5%)
Poorly differentiated	9 (56.3%)
Unknown	1 (6.3%)

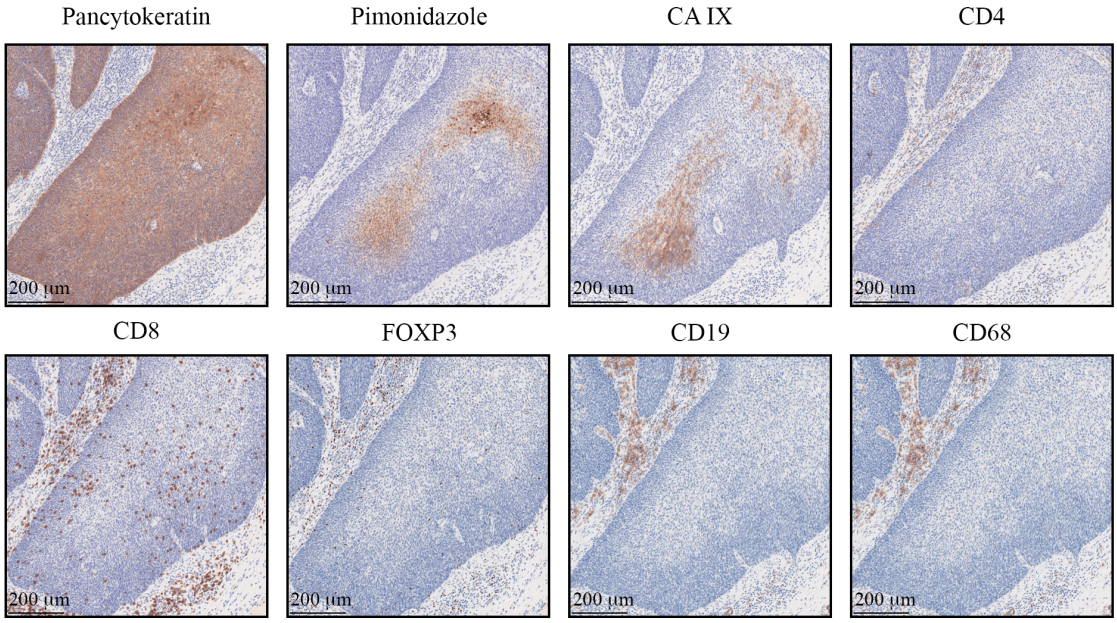
Tumour stage (Union for International Cancer Control [UICC] TNM Classification of Malignant Tumours, 6th edition)	
pT1	2 (12.5%)
pT2	6 (37.5%)
pT3	6 (37.5%)
pT4	1 (6.3%)
Unknown	1 (6.3%)
Human papilloma virus (HPV) status (p16 immunohistochemistry)	
Positive	6 (37.5%)
Negative	2 (12.5%)
Unknown	8 (50.0%)

Histological preparation and image analysis

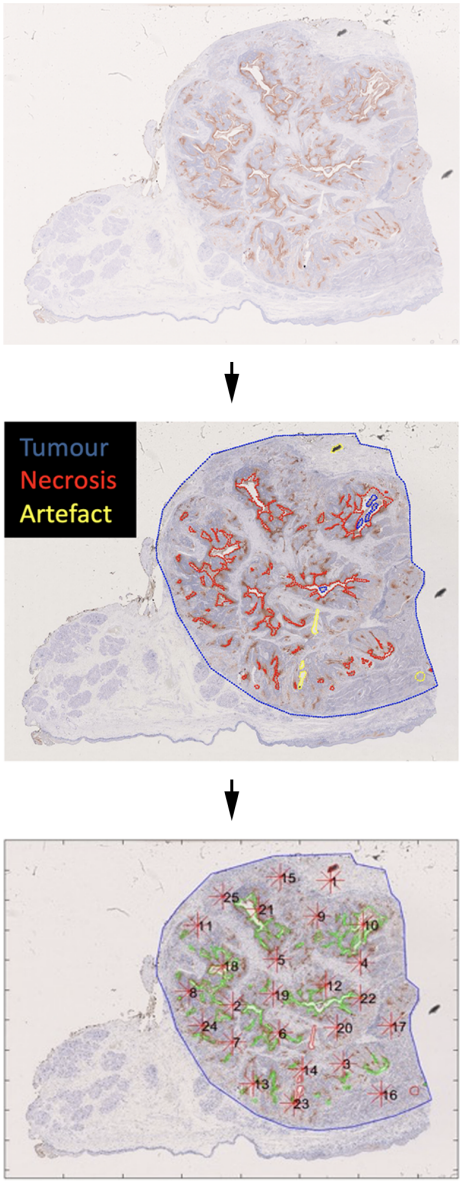


11 cases:
1. Haematoxylin & eosin
2. CA IX
3. CD4
4. Pimonidazole
5. Pancytokeratin
6. Pimonidazole
7. CD8
8. CA IX
9. FOXP3
10. Pimonidazole
11. Pancytokeratin
12. Pimonidazole
13. CD19
14. CA IX
15. CD68
16. Pimonidazole
17. Pancytokeratin

5 cases:
1. Haematoxylin & eosin
2. CD4
3. Pimonidazole
4. Pancytokeratin
5. Pimonidazole
6. CD8
7. FOXP3
8. Pimonidazole
9. Pancytokeratin
10. Pimonidazole
11. CD19
12. CD68
13. Pimonidazole
14. Pancytokeratin
15. Pimonidazole
16. CA IX



Strict serial sections were cut and stained in a specific order, so that either three and four contiguous sections could be overlaid and merged into a single, 'virtually multi-labelled' image. Each triplet contained an immune cell marker of interest (either CD4 [a marker of helper T lymphocytes], FOXP3 [a marker of regulatory T lymphocytes], CD8 [a marker of cytotoxic T lymphocytes], CD19 [a marker of B lymphocytes] or CD68 [a pan-macrophage marker]), pancytokeratin (to differentiate tumour epithelium and stroma) and pimonidazole (to detect areas of hypoxia). When possible, a fourth section labelled for the endogenous hypoxia marker carbonic anhydrase 9 (CA IX) was also included.



Manual annotations and selection of regions of interest

Each section is manually annotated to identify the tumour boundary (blue) and areas of necrosis (red) and artefactual changes for exclusion (yellow). Care is taken to exclude pre-existing lymphoid stroma from the assessment. Annotations can be applied using MATLAB®'s inbuilt annotation tools or can be imported from other software as an XML file. The tumour boundary annotation is used to direct random placement of non-overlapping 1.5 mm x 1.5 mm regions of interest (ROI). ROI are created until it is impossible to generate more without overlap.

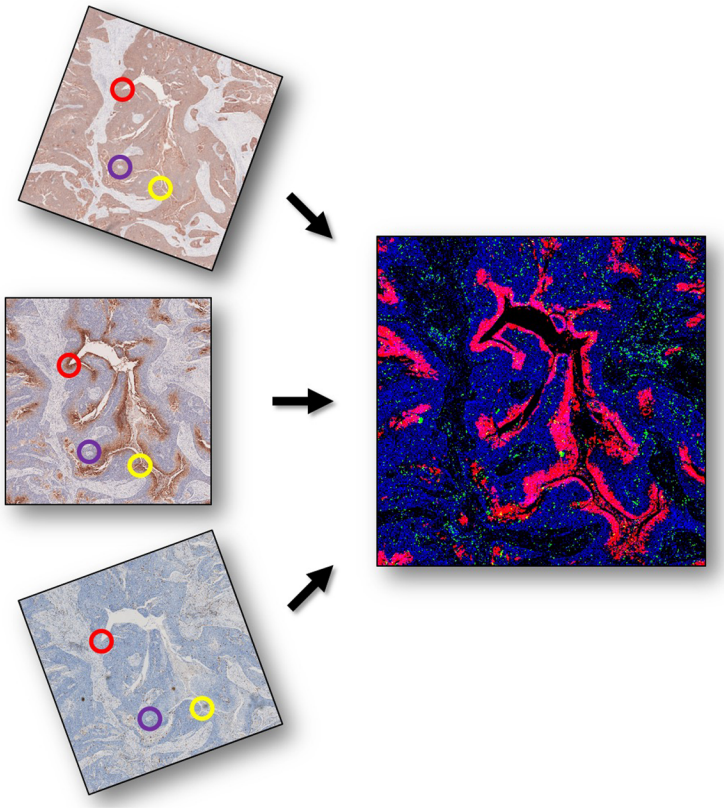


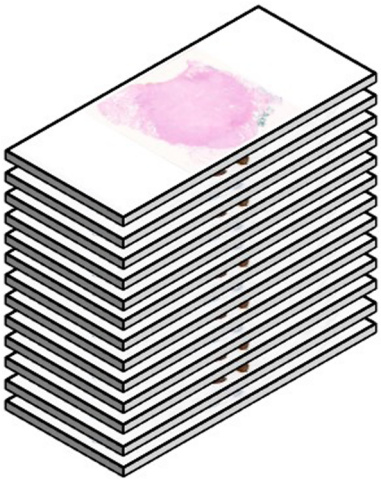
Image registration and creation of a final composite output image

3 mm x 3 mm images are extracted around each ROI at x10 objective magnification in each serial section. These consecutive images are then registered semi-automatically, using manually identified control points to ensure correct image alignment. Finally, the aligned images are cropped to a final 1.5 mm x 1.5 mm composite image. After visual assessment to confirm accuracy of classification, quantitative summary statistics, such as immune cell counts and densities, are extracted.

Appendix 3 – Clear cell renal cell carcinoma with necrosis cohort

Patient characteristics	
Mean age in years (range)	64.4 (52-80)
Gender (male/female)	15 (93.8%)/1 (6.3%)
Tumour characteristics	
Tumour site	
Left/right kidney	6 (37.5%)/10 (62.5%)
Tumour grade (World Health Organization [WHO]/International Society of Urological Pathology [ISUP] grading system)	
1	1 (6.3%)
2	1 (6.3%)
3	4 (25.0%)
4	10 (62.5%)
Tumour stage (Union for International Cancer Control [UICC] TNM Classification of Malignant Tumours, 8th edition)	
pT1a	0 (0.0%)
pT1b	1 (6.3%)
pT2a	2 (12.5%)
pT2b	0 (0.0%)
pT3a	13 (81.3%)
pT3b	0 (0.0%)
pT3c	0 (0.0%)
pT4	0 (0.0%)

Histological preparation

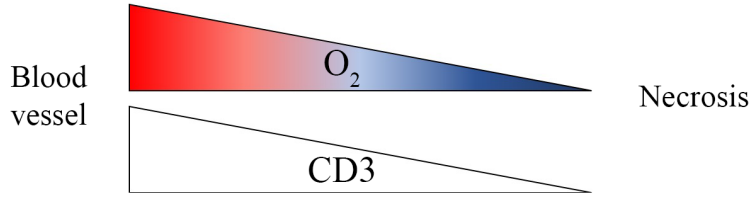


1. Haematoxylin & eosin
2. CA IX
3. CD31/CD3
4. CD31/CD8
5. CD31/FOXP3
6. CD31/CD20
7. CD31/CD68
8. CD31/CD163
9. CD31/CD204
10. CD31/CD206
11. CD31/Neutrophil elastase
12. CD31/CD11c
13. CD31/CD123

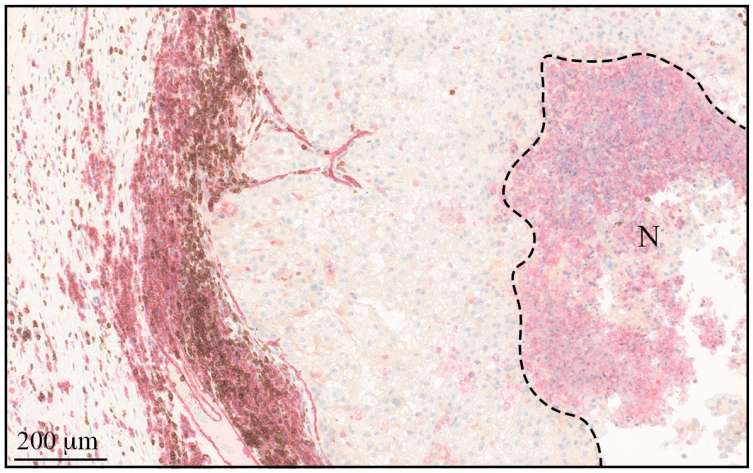
Haematoxylin and eosin stained slides were reviewed to identify tumour blocks containing necrosis. Sections were cut from one block per case and the first block was stained for carbonic anhydrase 9 (CA IX) to confirm the presence of a 'pseudohypoxic' phenotype, a surrogate for *VHL* loss. Serial sections subsequently underwent dual immunohistochemical labelling for the endothelial marker CD31 and an immune cell marker of interest:

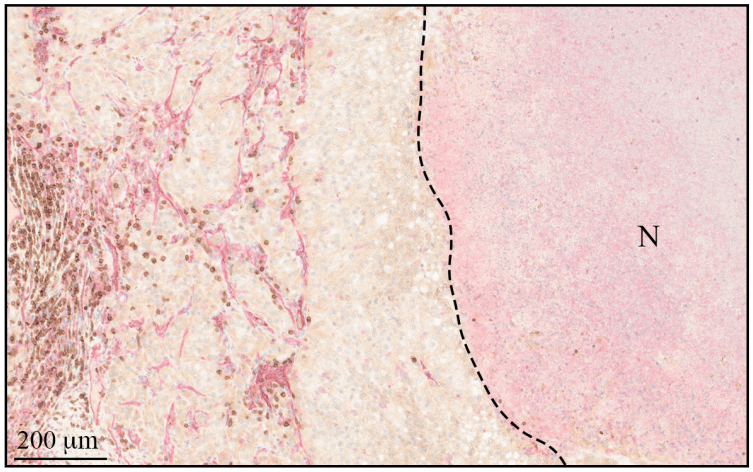
- CD3 – a pan-T lymphocyte marker;
- CD8 – a marker of cytotoxic T lymphocytes;
- FOXP3 – a marker of regulatory T lymphocytes;
- CD20 – a marker of B lymphocytes;
- CD68 – a pan-macrophage marker;
- CD163 – a marker of M2 macrophages;
- CD204 – a marker of M2 macrophages;
- CD206 – a marker of M2 macrophages;
- Neutrophil elastase – a marker of neutrophils;
- CD11c – a marker of conventional dendritic cells;
- CD123 – a marker of plasmacytoid dendritic cell.

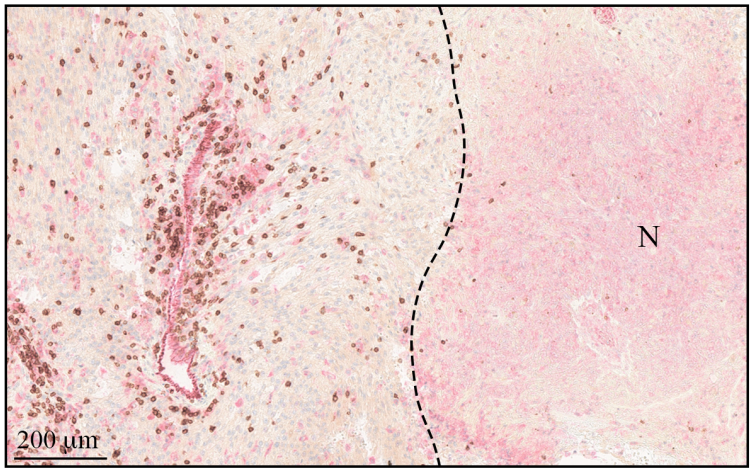
CD3⁺ T lymphocytes



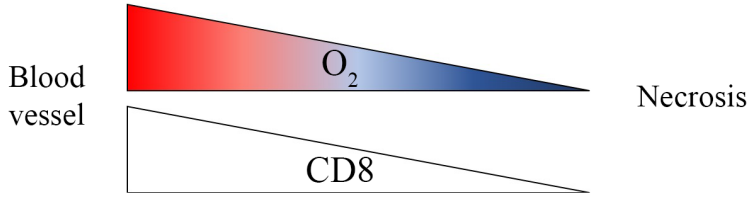
CD3/CD31



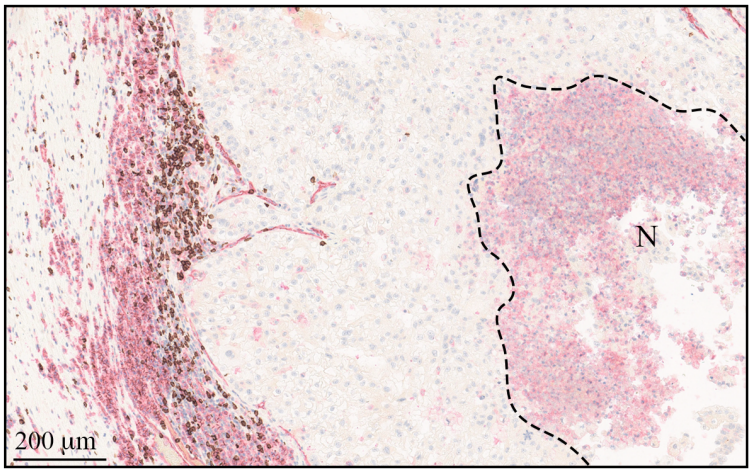


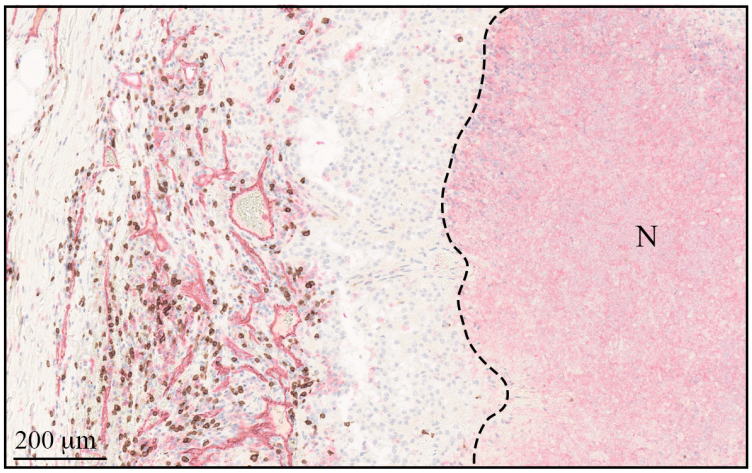


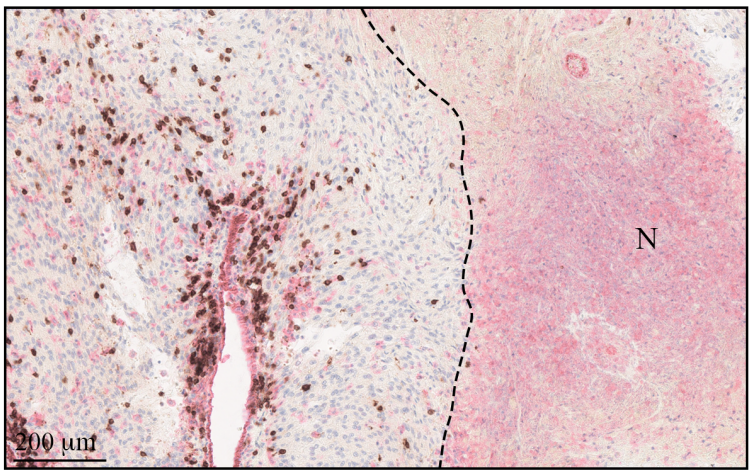
CD8⁺ T lymphocytes



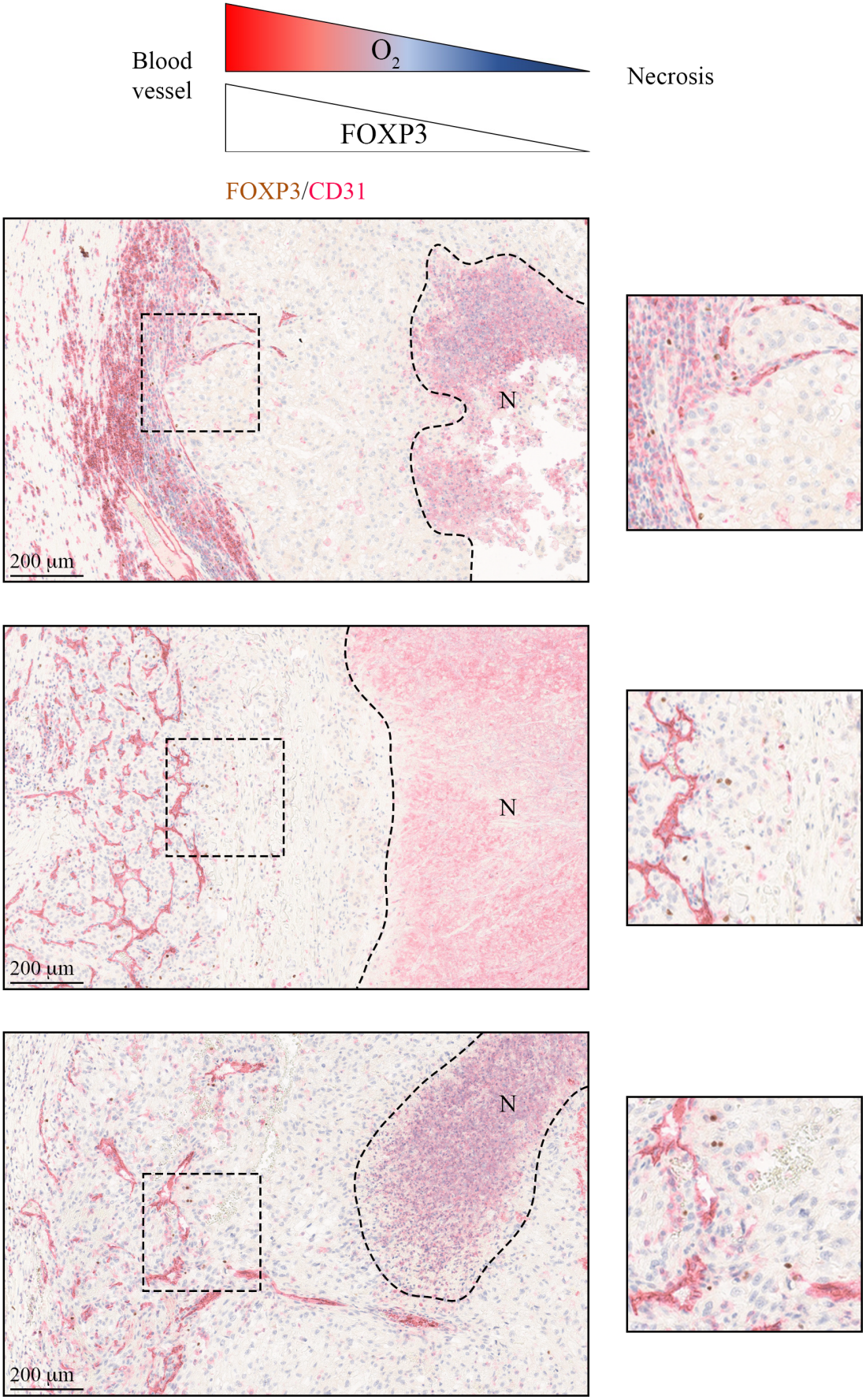
CD8/CD31



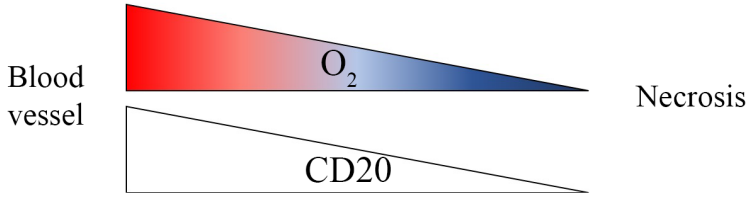




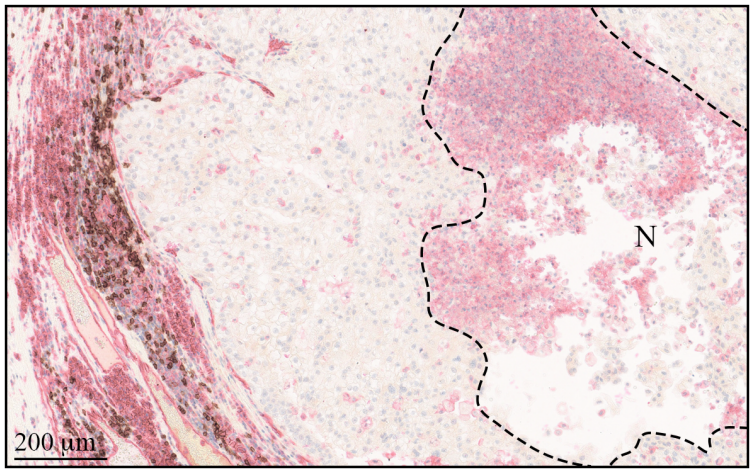
FOXP3^{+} T lymphocytes

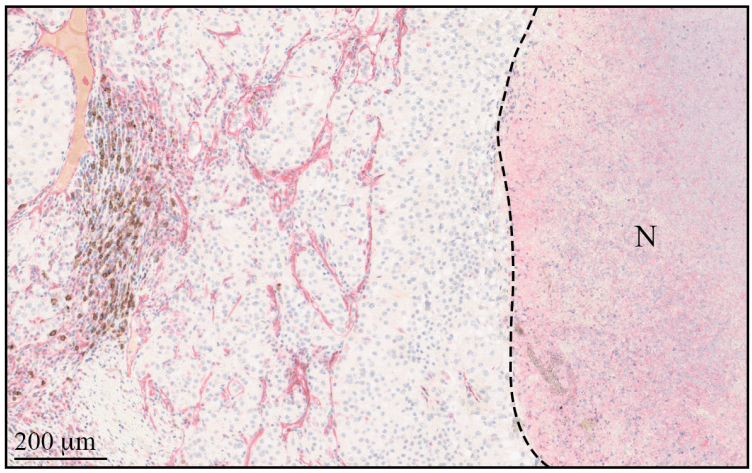


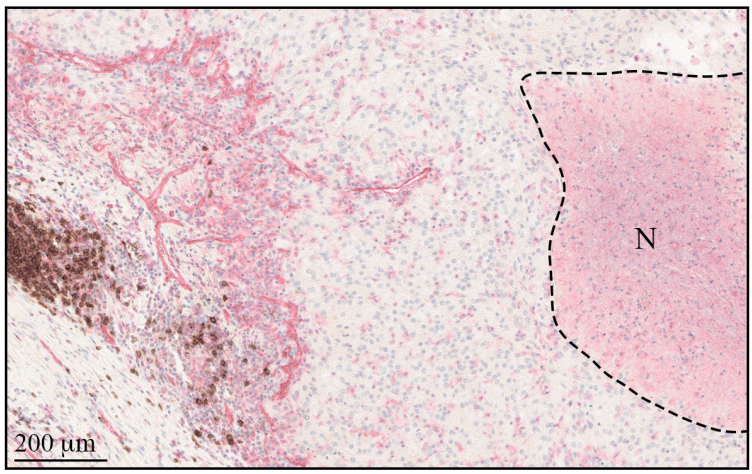
CD20⁺ B lymphocytes



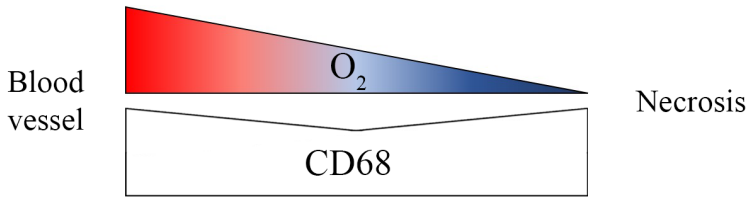
CD20/CD31



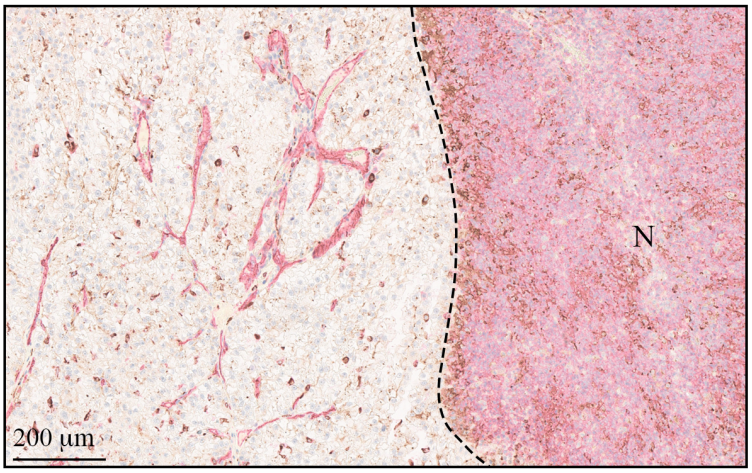


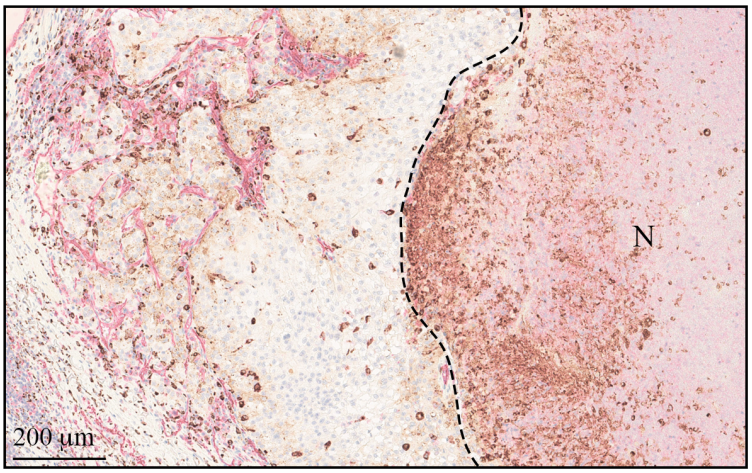


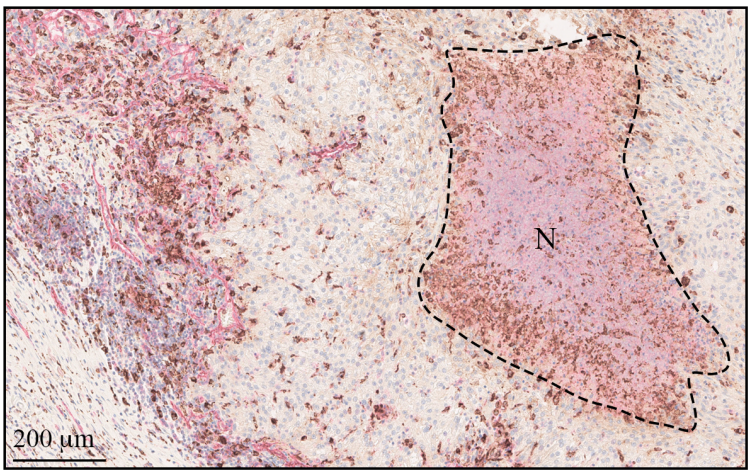
CD68^{+} macrophages



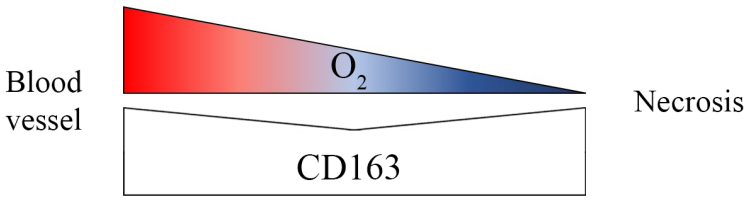
CD68/CD31



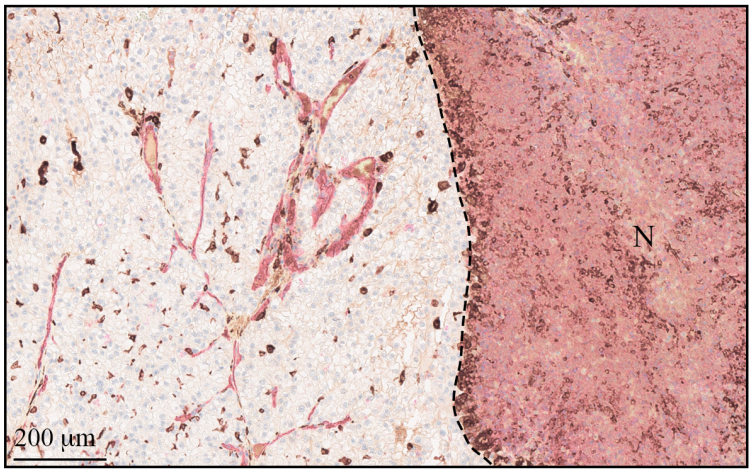


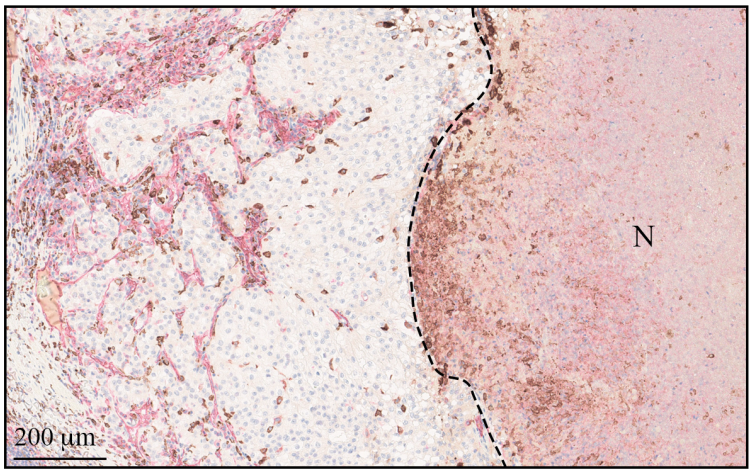


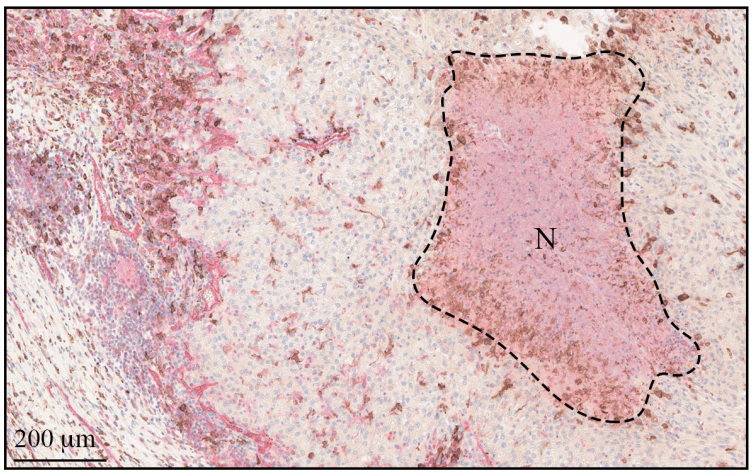
CD163^{+} macrophages



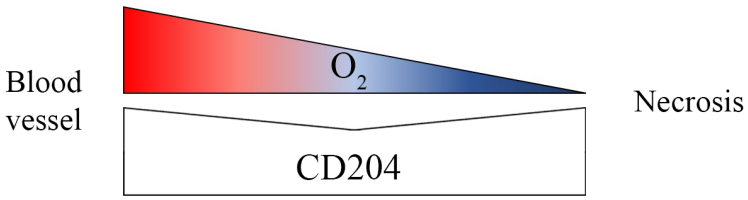
CD163/CD31



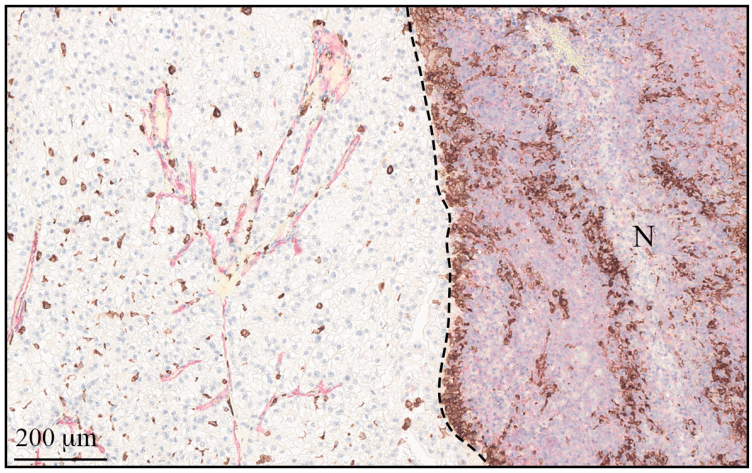


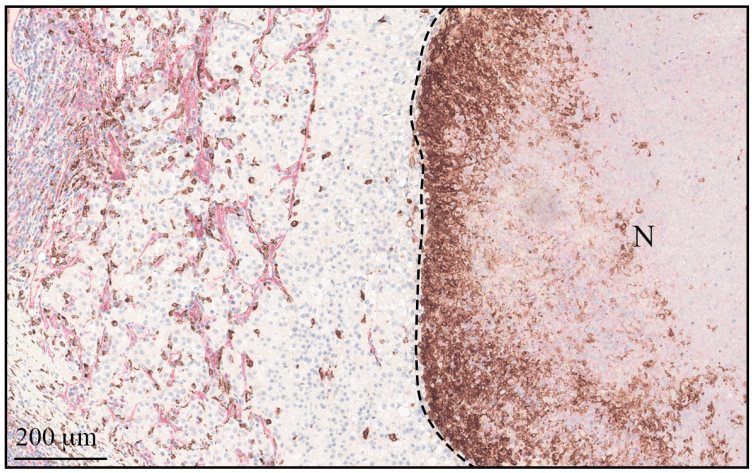


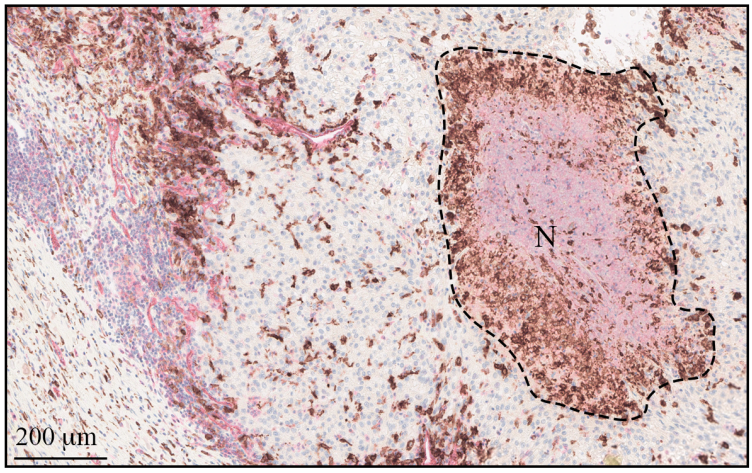
CD204⁺ macrophages



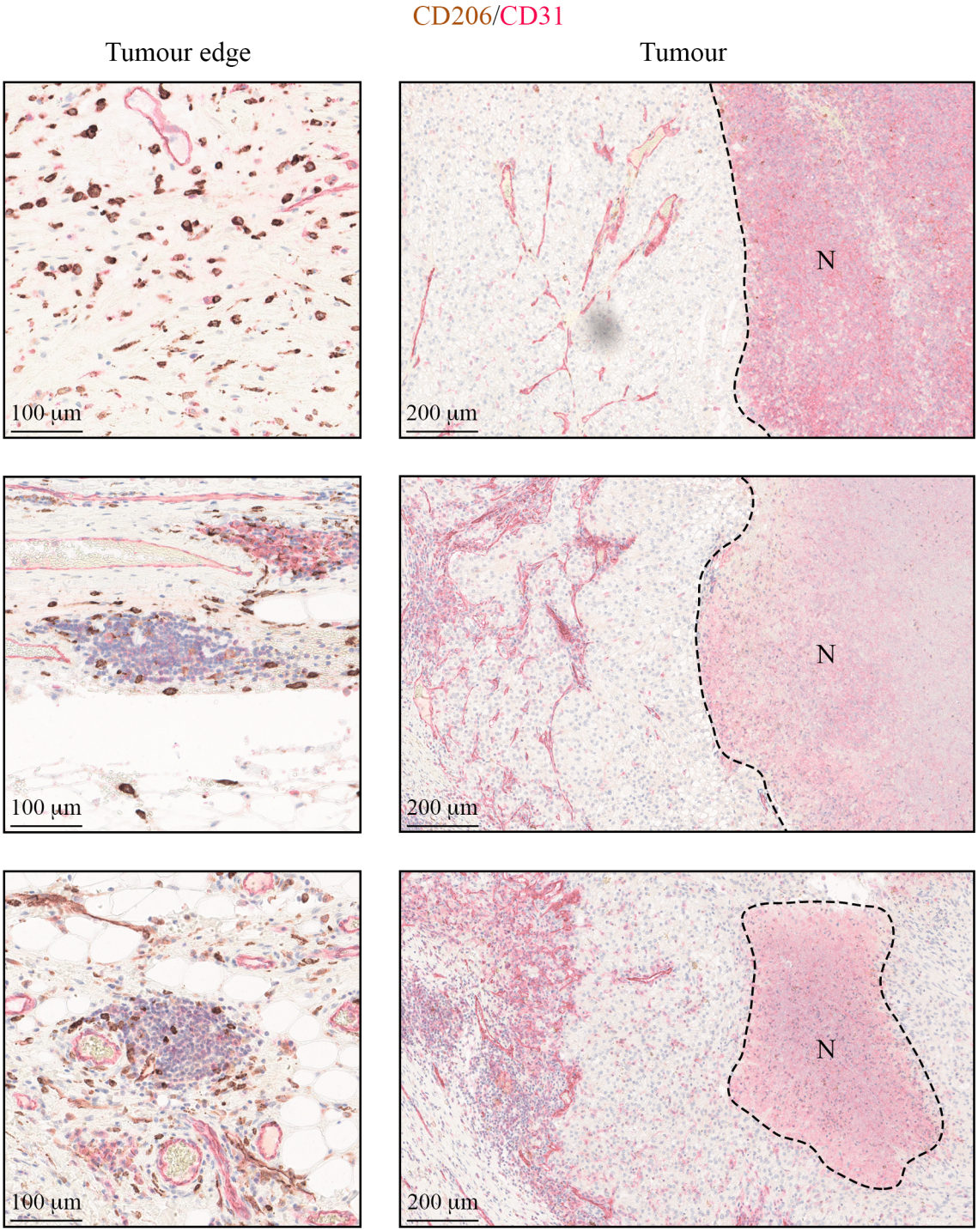
CD204/CD31



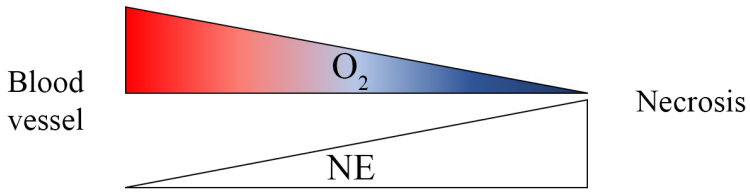




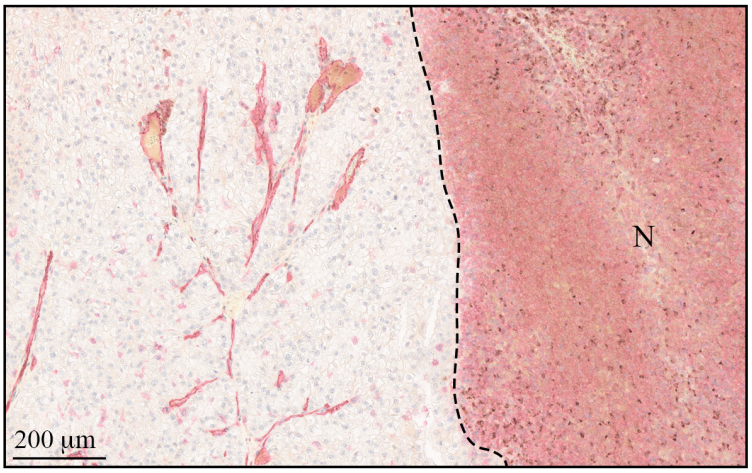
CD206^{+} macrophages

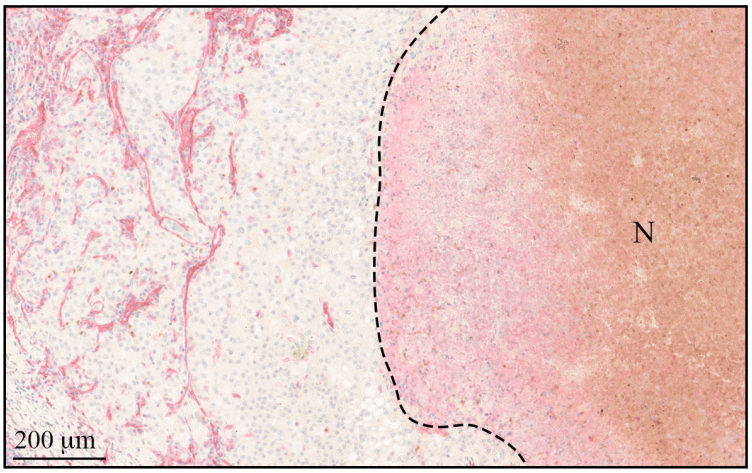


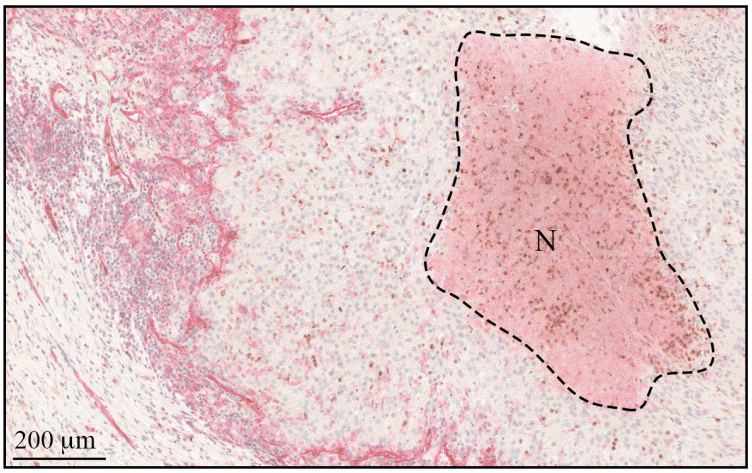
Neutrophil elastase$^+$ neutrophils



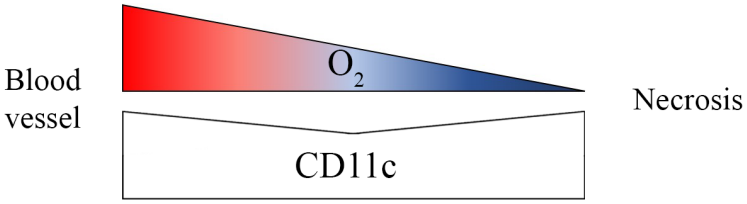
NE/CD31



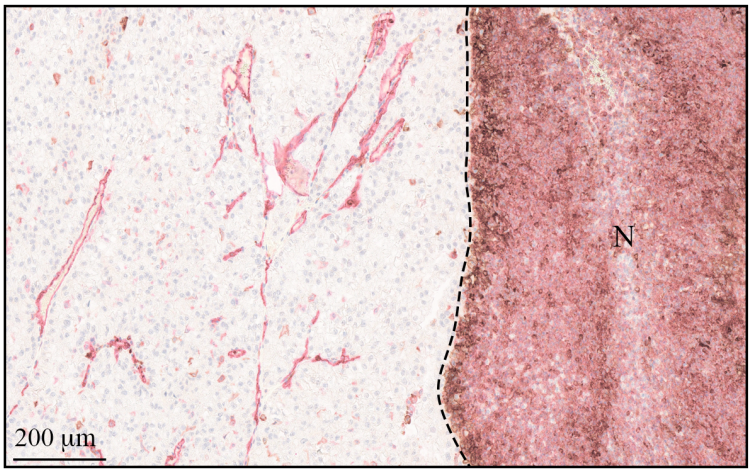


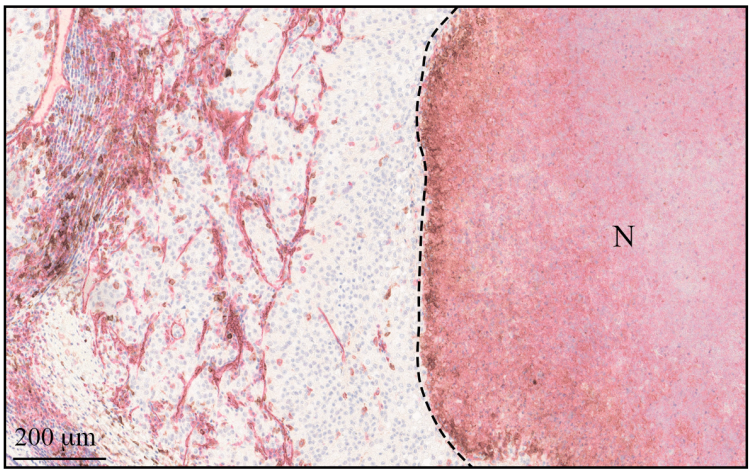


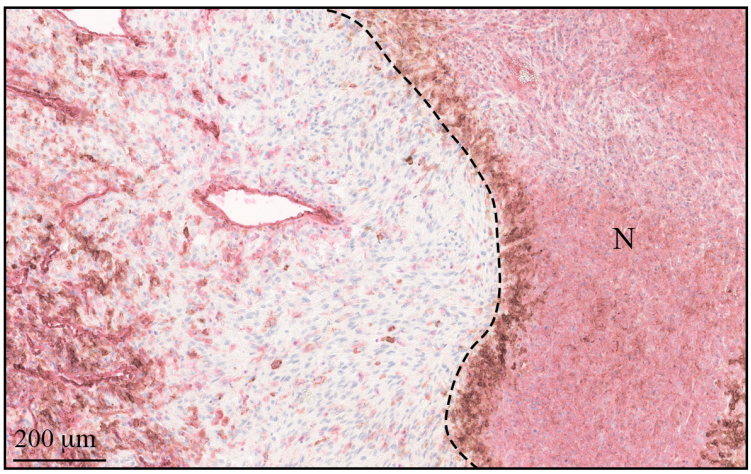
CD11c^{+} dendritic cells



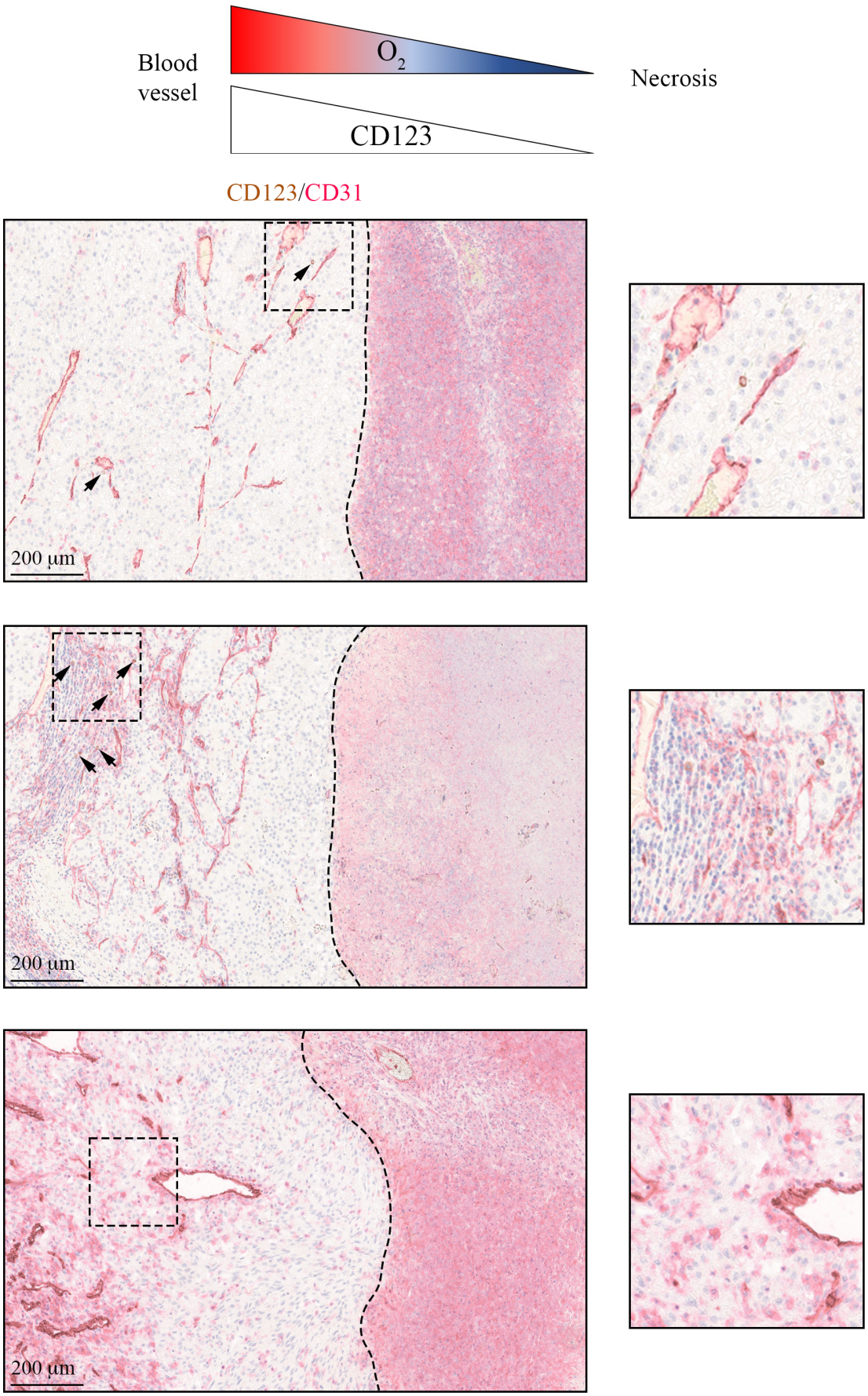
CD11c/CD31







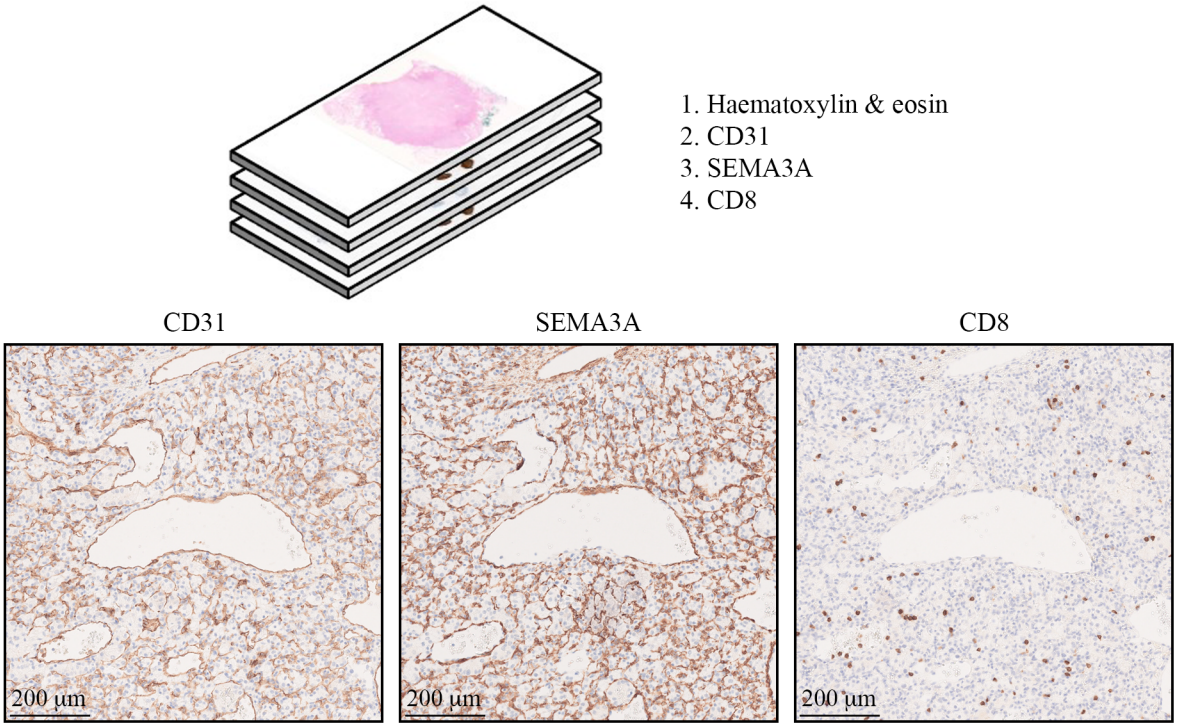
CD123⁺ dendritic cells



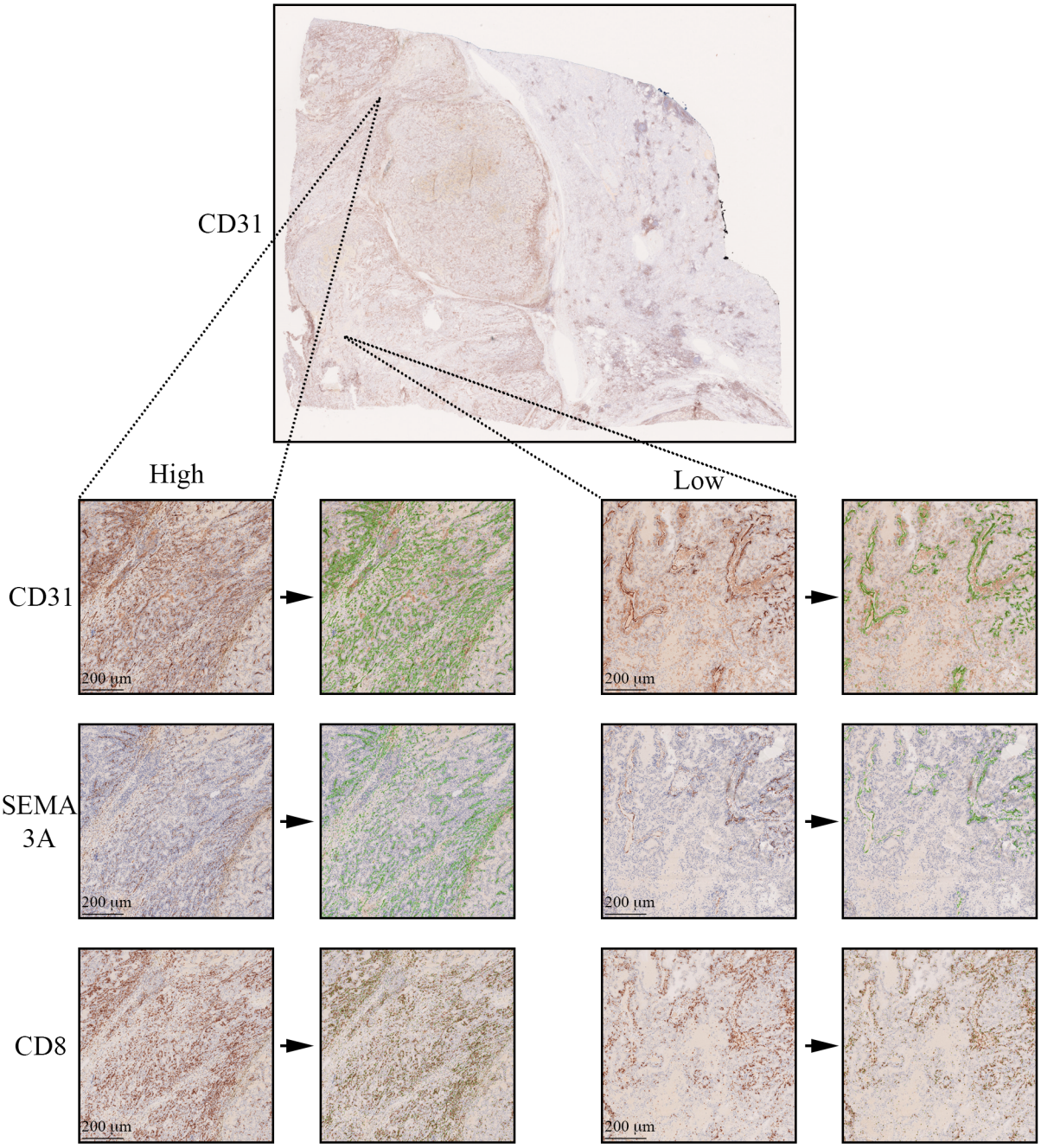
Appendix 4 – Semaphorin 3A clear cell renal cell carcinoma cohort

Patient characteristics	
Mean age in years (range)	67.0 (48-86)
Gender (male/female)	6 (50.0%)/6 (50.0%)
Tumour characteristics	
Tumour site	
Left/right kidney	5 (41.7%)/7 (58.3%)
Tumour grade (World Health Organization [WHO]/International Society of Urological Pathology [ISUP] grading system)	
1	0 (0.0%)
2	1 (8.3%)
3	10 (83.3%)
4	1 (8.3%)
Tumour stage (Union for International Cancer Control [UICC] TNM Classification of Malignant Tumours, 8th edition)	
pT1a	0 (0.0%)
pT1b	4 (33.3%)
pT2a	1 (8.3%)
pT2b	0 (0.0%)
pT3a	7 (58.3)
pT3b	0 (0.0%)
pT3c	0 (0.0%)
pT4	0 (0.0%)

Histological preparation and image analysis



Strict serial sections were cut and stained for CD31 (a marker of blood vessel endothelial cells), semaphorin 3A (SEMA3A) and CD8 (a marker of cytotoxic T lymphocytes). For each case, the CD31 stained slide was reviewed and the extent of staining was quantified in the regions where expression was deemed to be highest and lowest (% stained area = positively stained pixels/total pixels x 100). This analysis was repeated in the same regions on adjacent serial sections for SEMA3A (% stained area = positively stained pixels/total pixels x 100) and CD8 (discrete cell counts were calculated from positively stained regions using a watershedding process).

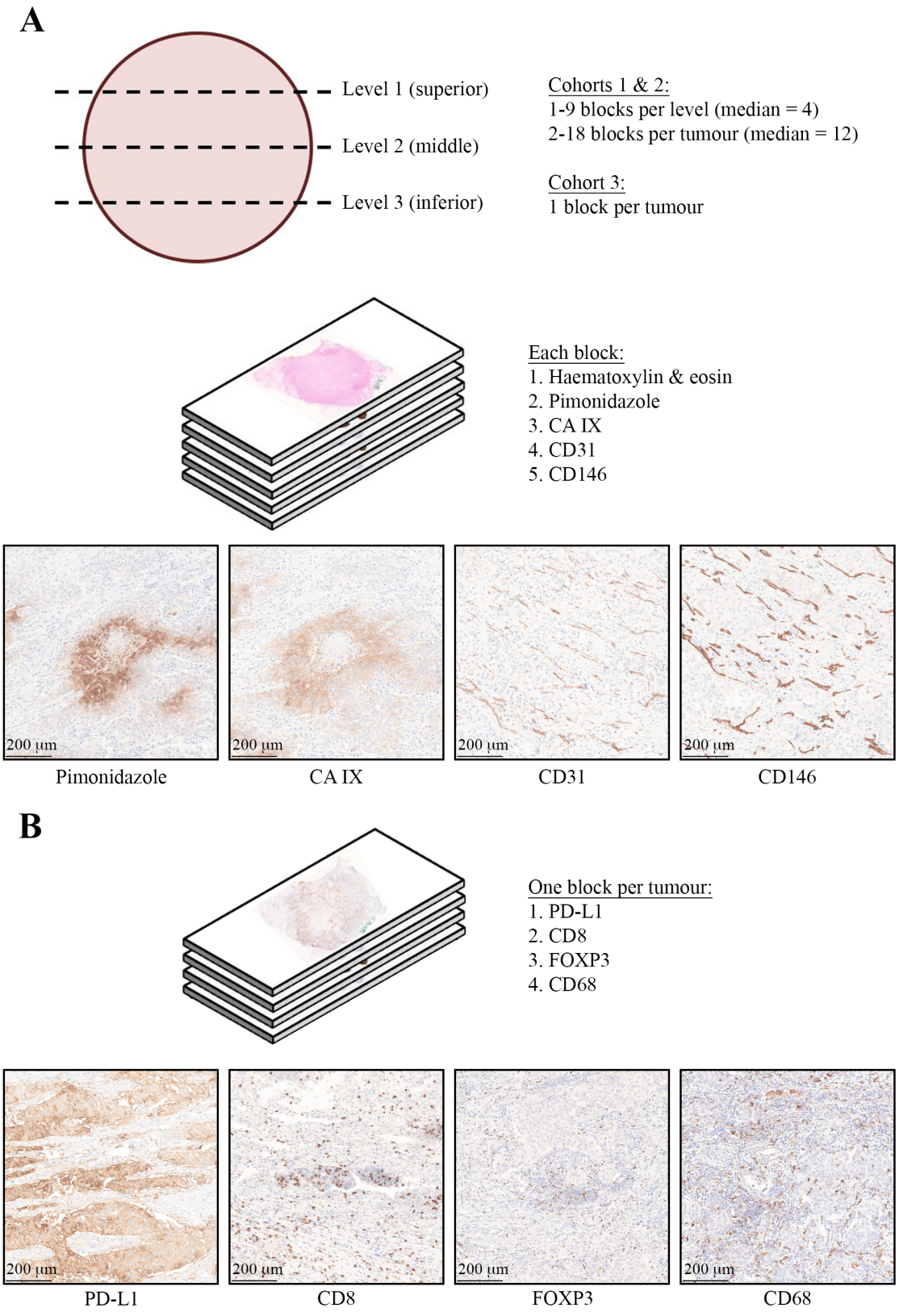

CD31
High
Low
CD31
SEMA 3A
CD8
200 μm
200 μm
200 μm
200 μm
200 μm
200 μm

Appendix 5 – ATOM (Atovaquone as Tumour HypOxia Modifier) study cohort

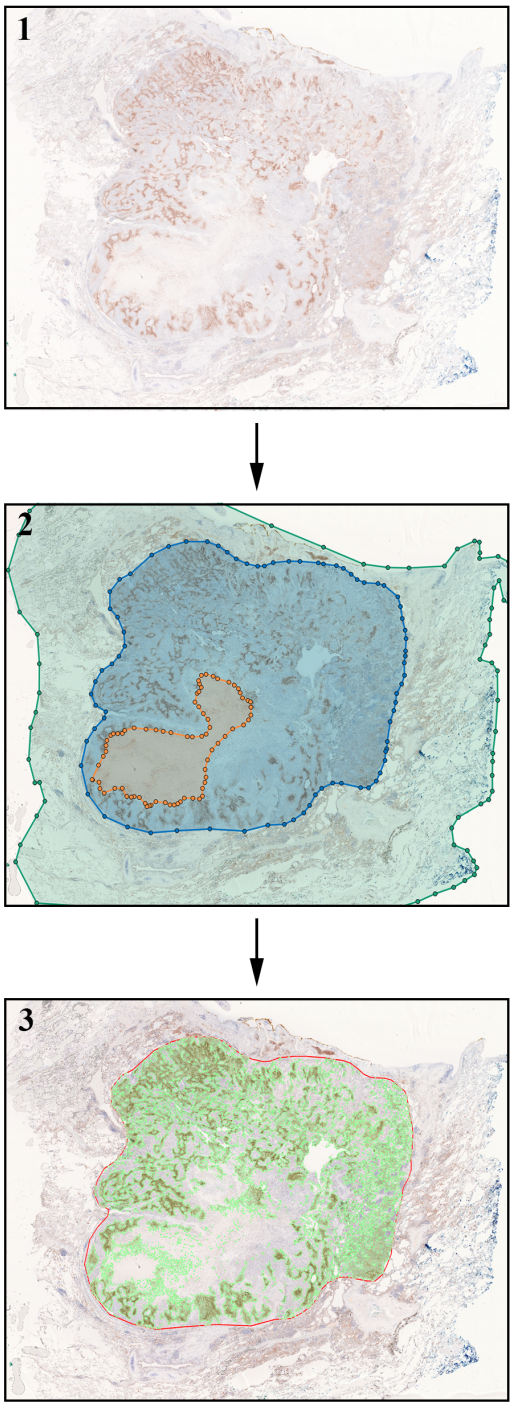
Patient and tumour characteristics by cohort			
	Cohort 1 (n = 15)	**Cohort 2 (n = 14)**	**Cohort 3 (n = 14)**
Patient characteristics			
Mean age in years (range)	65.2 (54-77)	66.7 (49-87)	70.7 (61-79)
Gender (male/female)	7 (46.7%)/ 8 (53.3%)	9 (64.3%)/ 5 (35.7%)	9 (64.3%)/ 5 (35.7%)
Smoker (current/previous/never)	1/14/0	0/14/0	0/12/2
Tumour characteristics			
Histological subtype			
Adenocarcinoma	12 (80.0%)	8 (57.1%)	6 (42.9%)
Squamous cell carcinoma	2 (13.3%)	4 (28.6%)	7 (50.0%)
Adenosquamous carcinoma	1 (6.7%)	0 (0.0%)	0 (0.0%)
Giant cell carcinoma	0 (0.0%)	0 (0.0%)	1 (7.1%)
Pleomorphic carcinoma	0 (0.0%)	1 (7.1%)	0 (0.0%)
Large cell neuroendocrine carcinoma	0 (0.0%)	1 (7.1%)	0 (0.0%)
Tumour stage (Union for International Cancer Control [UICC] TNM Classification of Malignant Tumours, 8th edition)			
pT1a	0 (0.0%)	0 (0.0%)	0 (0.0%)
pT1b	0 (0.0%)	0 (0.0%)	0 (0.0%)
pT1c	1 (6.7%)	0 (0.0%)	1 (7.1%)
pT2a	0 (0.0%)	2 (14.3%)	6 (42.9%)
pT2b	4 (26.7%)	2 (14.3%)	2 (14.3%)
pT3	6 (40.0%)	4 (28.6%)	3 (21.4%)
pT4	4 (26.7%)	6 (42.9%)	2 (14.3%)

Patient and tumour characteristics by treatment		
	Atovaquone (n = 17)	**No atovaquone (n = 26)**
Patient characteristics		
Mean age in years (range)	65.4 (54-77)	68.8 (49-87)
Gender (male/female)	7 (41.2%)/ 10 (58.8%)	18 (69.2%)/ 8 (30.8%)
Smoker (current/previous/never)	1/16/0	0/24/2
Tumour characteristics		
Histological subtype		
Adenocarcinoma	13 (76.5%)	13 (50.0%)
Squamous cell carcinoma	3 (17.6%)	10 (38.5%)
Adenosquamous carcinoma	1 (5.9%)	0 (0.0%)
Giant cell carcinoma	0 (0.0%)	1 (3.8%)
Pleomorphic carcinoma	0 (0.0%)	1 (3.8%)
Large cell neuroendocrine carcinoma	0 (0.0%)	1 (3.8%)
Tumour stage (Union for International Cancer Control [UICC] TNM Classification of Malignant Tumours, 8th edition)		
pT1a	0 (0.0%)	0 (0.0%)
pT1b	0 (0.0%)	0 (0.0%)
pT1c	1 (5.9%)	1 (3.8%)
pT2a	1 (5.9%)	7 (26.9%)
pT2b	4 (23.5%)	4 (15.4%)
pT3	7 (41.2%)	6 (23.1%)
pT4	4 (23.5%)	8 (30.8%)

Histological preparation and image analysis



Histological preparation for the main study analysis (A) and for the analysis of immunological markers (B).



1. Whole slide imaging is performed for each sample.

2. Manual annotation of the tissue edge (green), tumour margin (blue) and regions of necrosis (orange) is performed.

3. Image analysis is undertaken, with regions of positive staining within the tumour area identified in green. After visual assessment to confirm accuracy of classification, quantitative summary statistics, such as percentage tumour area expressing a given marker, are extracted.

Appendix 6 – Human immunohistochemistry optimisation/validation

Hypoxia markers

Clonal populations of HKC-8 (human proximal tubular epithelial) cells in which Clustered Regularly Interspaced Short Palindromic Repeats (CRISPR)-Cas9 technology had been used to introduce frameshift mutations that disrupt the production of key components of the hypoxia-inducible factor (HIF) pathway [34] were cultured under atmospheric oxygen, with the prolyl hydroxylase domain-containing protein (PHD) inhibitor dimethyloxalylglycine (DMOG) added to medium for 16 hours in order to stabilise HIFα. Cell pellets were then created from these populations, embedded within paraffin and sectioned on to glass slides for immunohistochemical staining.

Hypoxia-inducible factor one alpha

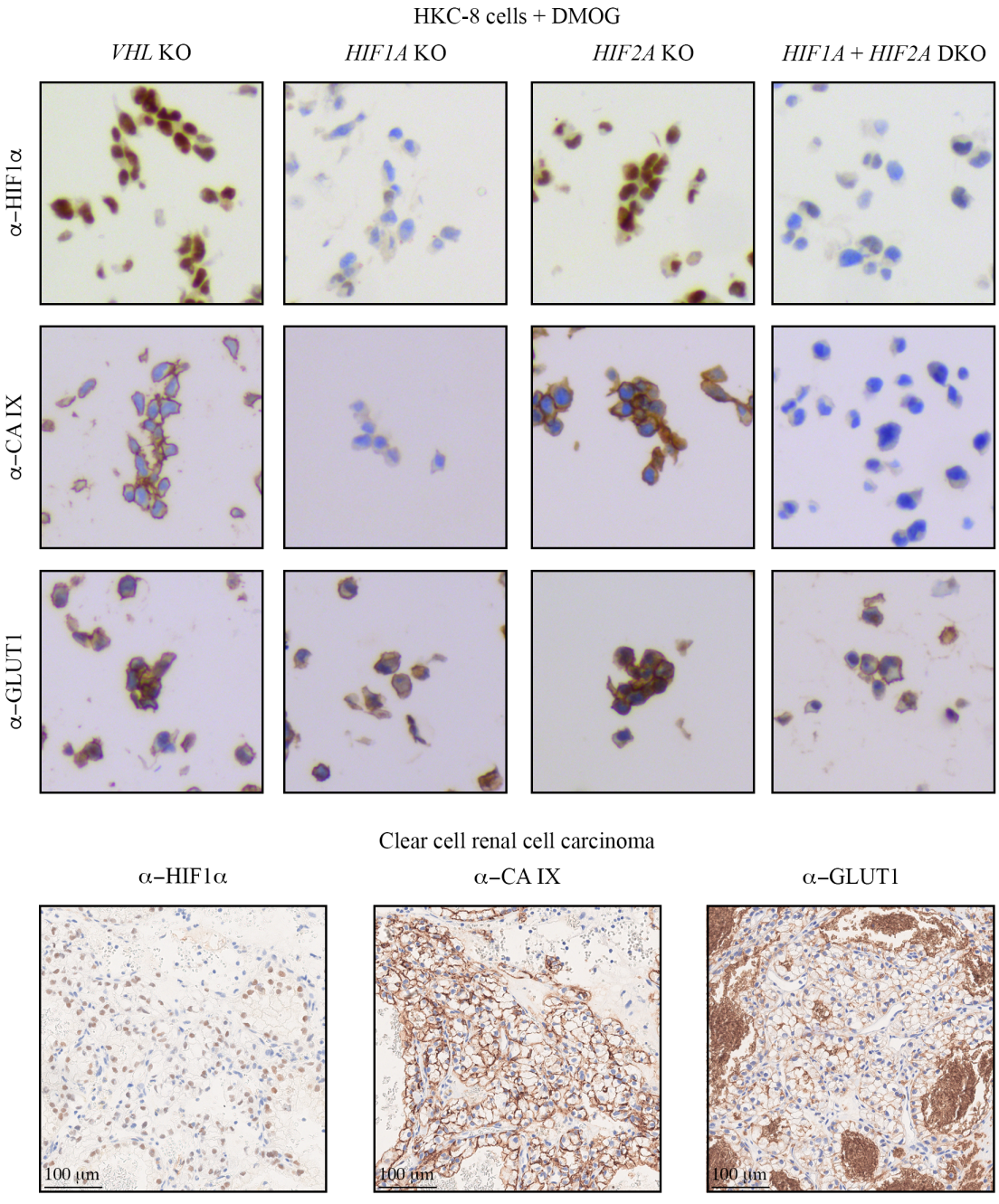
HKC-8 cells with disruption of *VHL* (*VHL* KO) demonstrated strong nuclear immunopositivity for hypoxia-inducible factor one alpha (HIF1α). This pattern of expression was maintained in cells with disruption of *HIF2A* alone (*HIF2A* KO) but was lost in those with disruption of *HIF1A* alone (*HIF1A* KO) and *HIF1A* and *HIF2A* in combination (*HIF1A* + *HIF2A* DKO), confirming specificity of the primary antibody.

Carbonic anhydrase 9 and glucose transporter 1

The same cell pellets were then used to validate immunostaining protocols for carbonic anhydrase 9 (CA IX) and glucose transporter 1 (GLUT1). A similar pattern of positivity was observed for CA IX as for HIF1α, in keeping with this gene being a strict HIF1α target gene [266]. By comparison, GLUT1 was detected in all populations, in keeping with this gene being

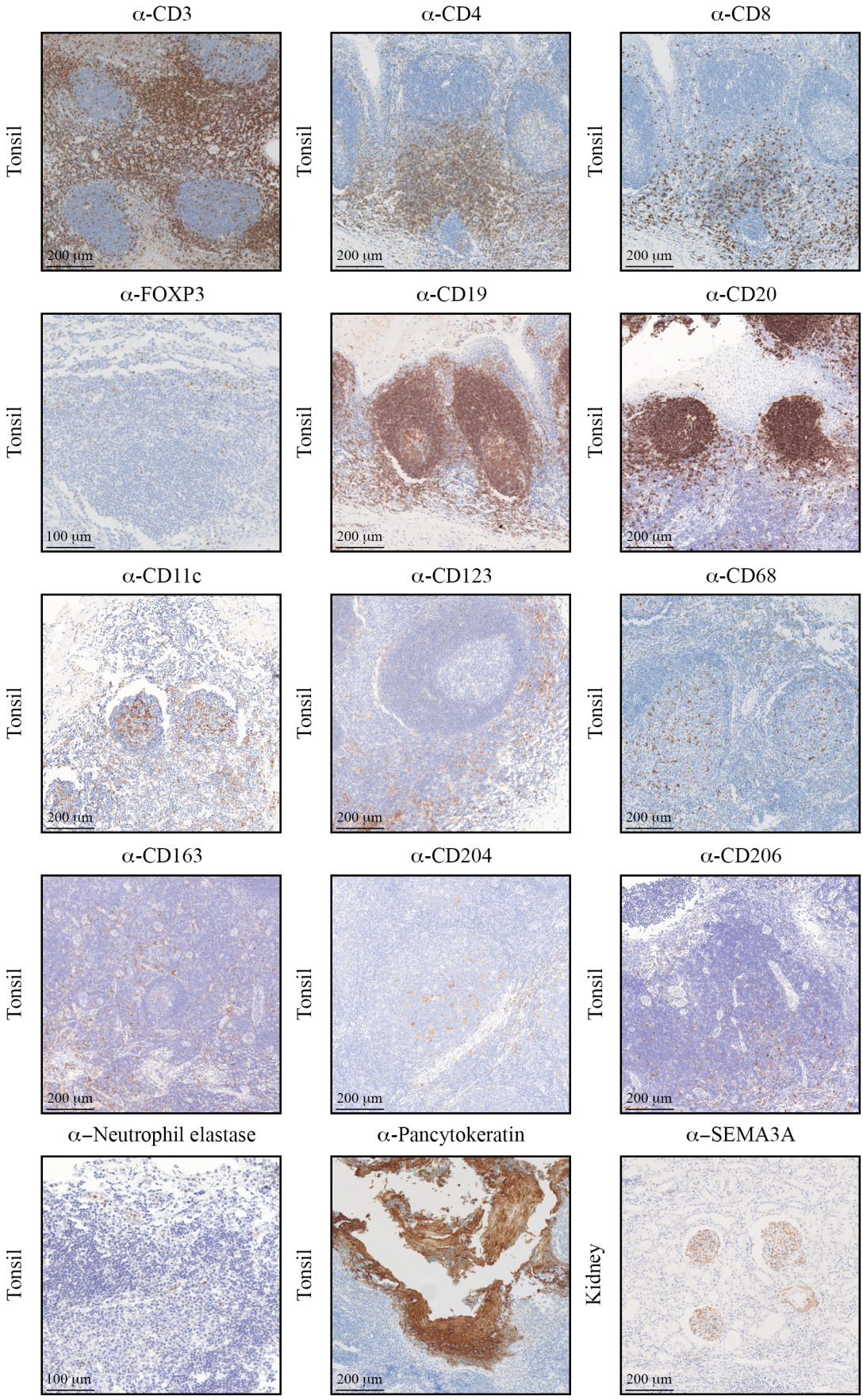
subject to HIF-independent regulation of expression in this cell type (the proximal tubule is responsible for renal glucose reabsorption).

Thereafter, immunostaining was performed on serial sections from a specimen of human VHL syndrome-associated clear cell renal cell carcinoma. As expected, diffuse tumour cell expression of all three markers was observed, although marked GLUT1 expression by erythrocytes was also apparent.



Other markers

Sections of human palatine tonsil tissue were used as positive control samples for most other markers. The B lymphocyte markers CD19 and CD20 are highly expressed within lymphoid follicles whilst the T lymphocyte markers CD3, CD4, CD8 and FOXP3 are predominantly expressed by cells located in interfollicular regions. The dendritic cell markers CD11c and CD123 and the macrophage markers CD68, CD163, CD204 and CD206 are expressed by cells variably located both within lymphoid follicles and interfollicular regions. Only occasional cells expressing the neutrophil marker neutrophil elastase are evident. Pancytokeratin is expressed by stratified squamous epithelium lining tonsillar crypts. Semaphorin 3A (SEMA3A) is expressed by vascular smooth muscle cells and podocytes within non-neoplastic human kidney.

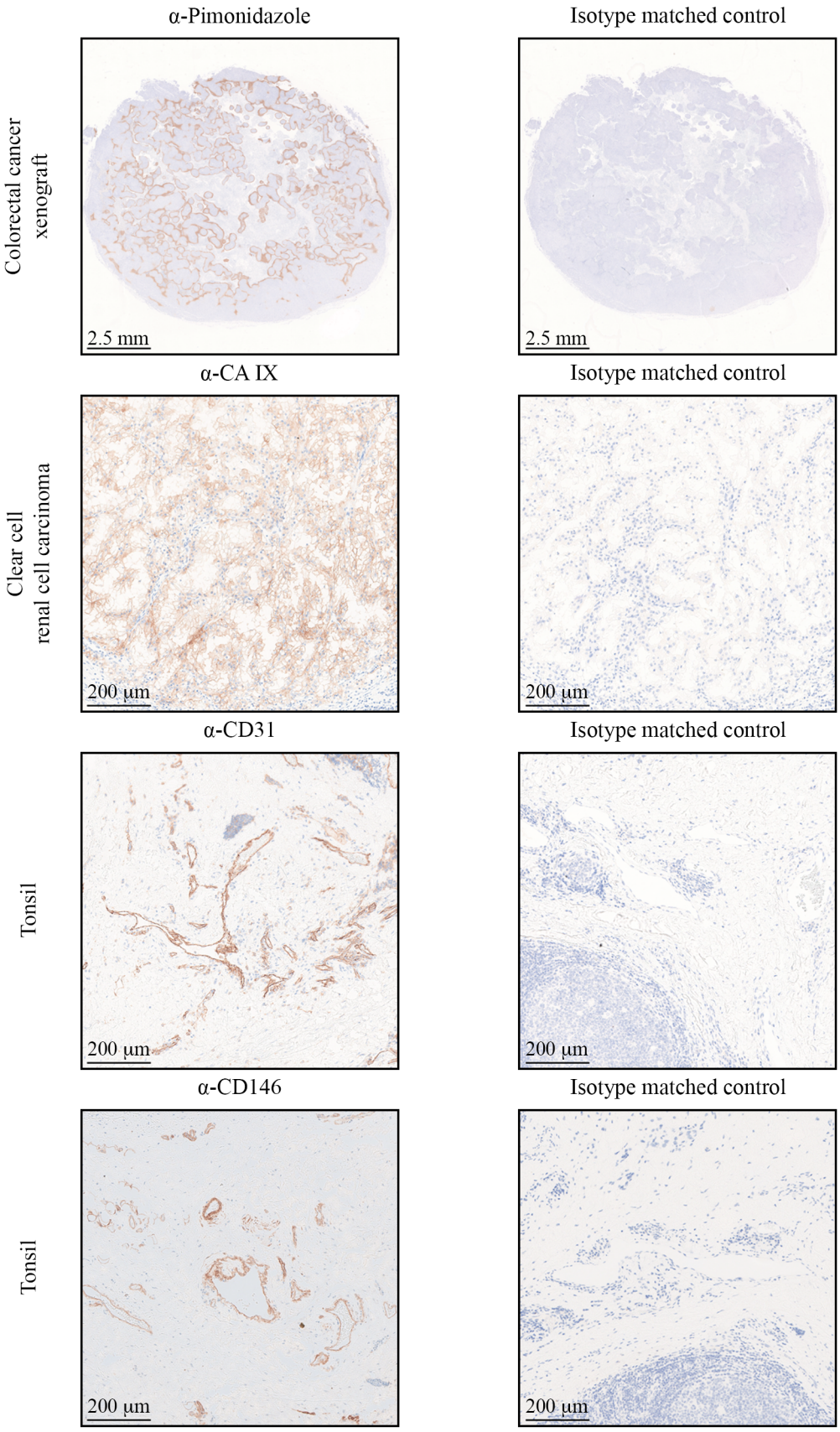

α-CD3
α-CD4
α-CD8
α-FOXP3
α-CD19
α-CD20
α-CD11c
α-CD123
α-CD68
α-CD163
α-CD204
α-CD206
α–Neutrophil elastase
α-Pancytokeratin
α–SEMA3A
Tonsil
Kidney
200 µm
100 µm

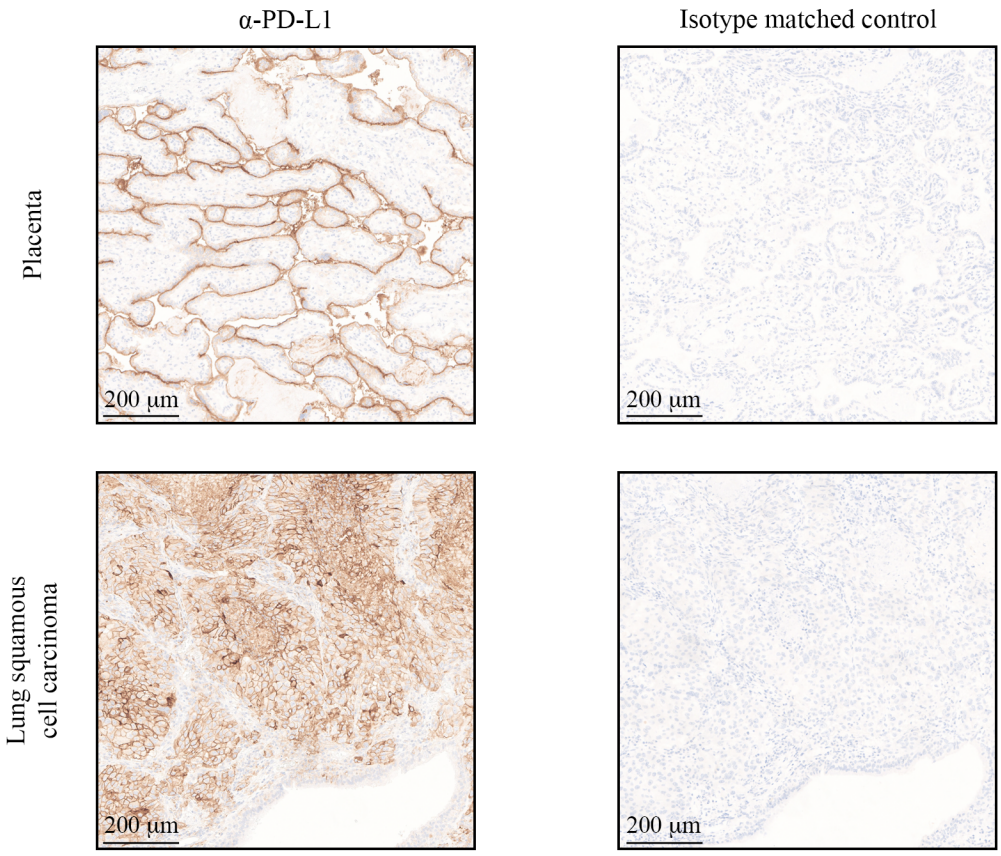
ATOM (Atovaquone as Tumour HypOxia Modifier) study markers

When immunohistochemistry was performed on ATOM study specimens, the following samples were used as positive controls:

- pimonidazole – human DLD-1 colorectal cancer xenograft from a pimonidazole-treated mouse;
- CA IX – human clear cell renal cell carcinoma;
- CD31 – human palatine tonsil;
- CD146 – human palatine tonsil;
- PD-L1 – human placenta.

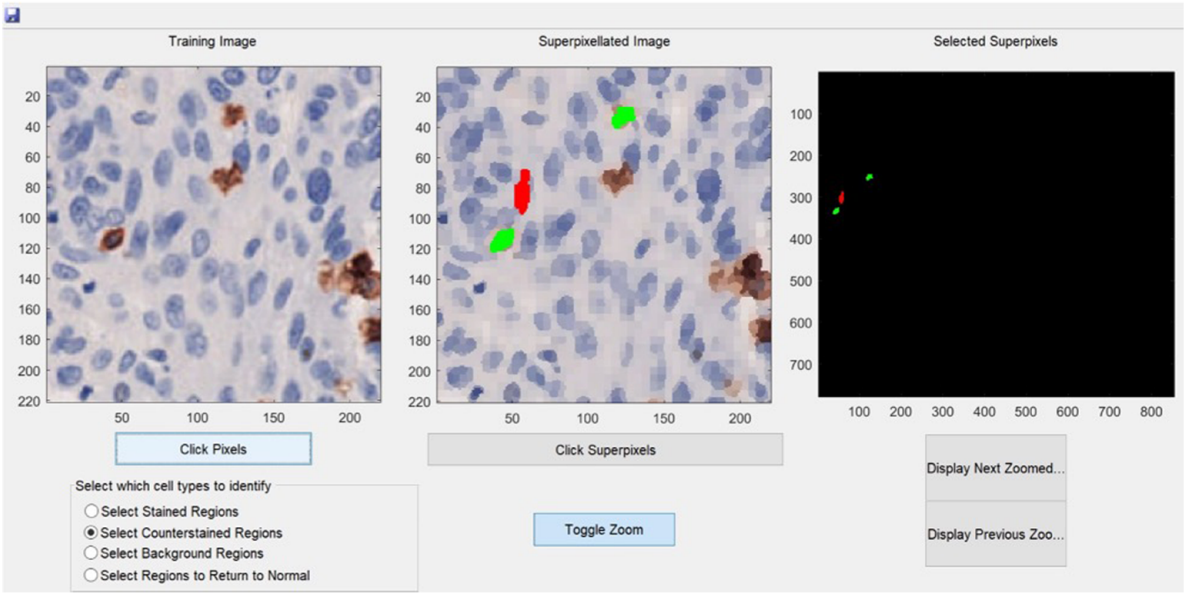
After each staining run, the positive control sample displayed the predicted pattern of immunopositivity. By comparison, no/minimal staining was observed when the primary antibody was substituted for an isotype control antibody.


α-Pimonidazole
Isotype matched control
Colorectal cancer xenograft
2.5 mm
2.5 mm
α-CA IX
Isotype matched control
Clear cell renal cell carcinoma
200 µm
200 µm
α-CD31
Isotype matched control
Tonsil
200 µm
200 µm
α-CD146
Isotype matched control
Tonsil
200 µm
200 µm


α-PD-L1
Isotype matched control
Placenta
Lung squamous cell carcinoma
200 μm
200 μm
200 μm
200 μm

Appendix 7 – Semi-automated ImaGe analysis for HisTology data (SIGHT) pipeline

All analyses performed by SIGHT are implemented in MATLAB® (MathWorks, USA) employing scripts developed by Dr Joshua Bull and Professor Helen Byrne (Wolfson Centre for Mathematical Biology, University of Oxford). The modular nature of this pipeline means that alternative approaches can be substituted at each stage.



Classifier training

A graphical user interface (GUI) provides a convenient and quick way to identify areas of positive and negative staining in representative training images for each marker of interest. Commonly, training data are derived from between 4 and 12 representative images from different slides to account for variability in staining. These training data are subsequently used to generate a Support Vector Machine (SVM) classifier that facilitates rapid, consistent and reproducible analysis of a larger number of images.

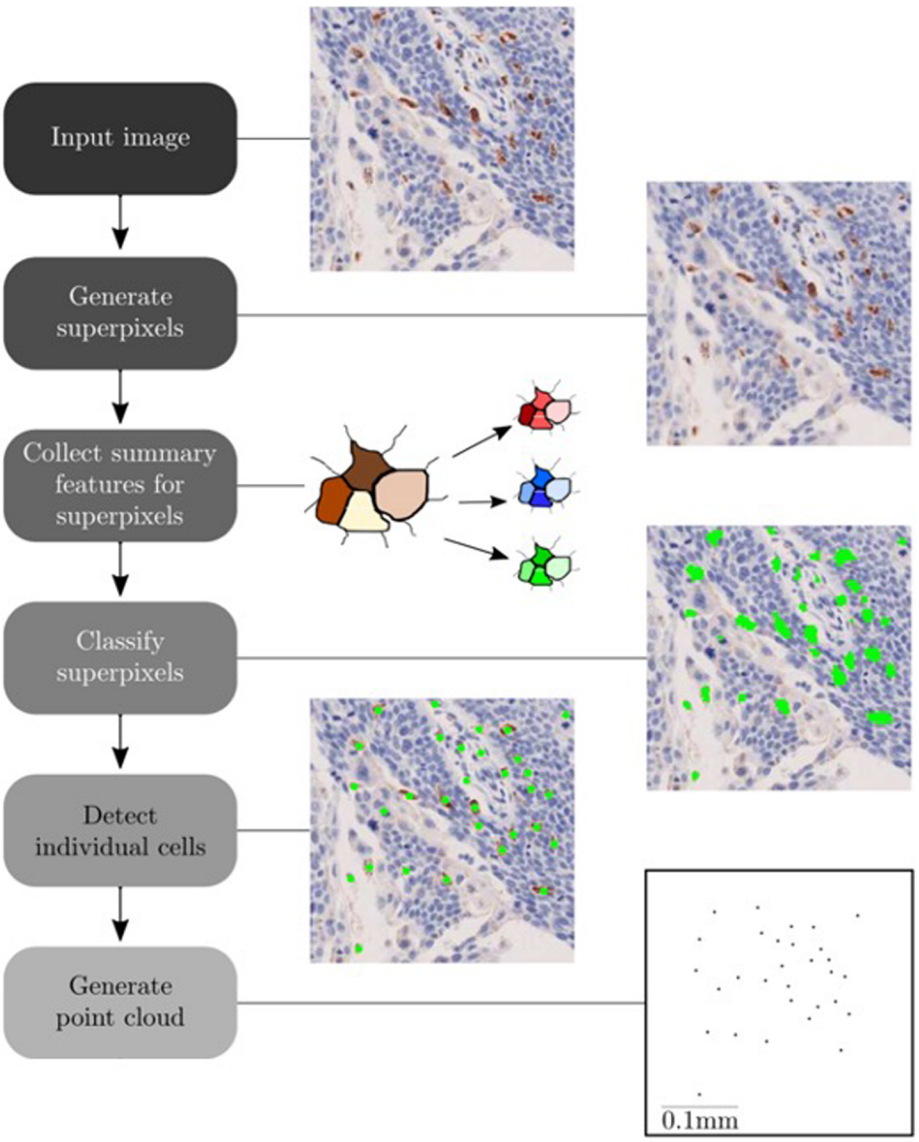


Image analysis

Input image

The maximum image scale of a histological slide scan is typically 0.2205 μm per pixel (x40 effective magnification). Consequently, a tissue section measuring 3.5 cm x 2 cm may generate an image containing approximately 1.4 x 10^{10} pixels. This presents a challenge for image analysis algorithms, which must classify each pixel. Before beginning digital image analysis, we compress the image to 0.882 μm per pixel (x10 effective magnification), which is often captured by digital pathology scanners as part of the image stack. To further increase the speed

of image analysis for whole slide images, we decompose each image into tiles of approximately 1000 pixels x 1000 pixels which can be analysed in parallel using multiple computational cores, if desired.

Generate superpixels

The SIGHT pipeline minimises the effective size of each image by using superpixels (clusters of adjacent pixels with similar colour intensities). A wide range of superpixellation algorithms exist, providing varying degrees of control over properties such as the size and shape of a superpixel. We utilise the Simple Linear Iterative Clustering (SLIC) algorithm [1039], a particularly fast algorithm which provides control over the size of superpixels and generates superpixels which adhere well to the boundaries of objects in images. Our pipeline generates superpixels with an area of approximately 20 μm^2.

Collect summary features for superpixels

We collect a range of summary features which describe the colour and shape of each superpixel, as well as some of the context of surrounding superpixels. These features are the same as those gained during the training of classifiers. The SLIC algorithm operates in the CIELAB colour space, in which the colour of each superpixel is described by the colour channels L (for lightness, from black to white), a (from green to red) and b (from blue to yellow).

Classify superpixels

These features are used to classify each superpixel as either positively or negatively stained using a binary SVM. This uses previous training data to locate a hyperplane which optimally

separates the classes in a high dimensional feature space. Superpixels are then assigned to a class based on their location in feature space relative to the hyperplane.

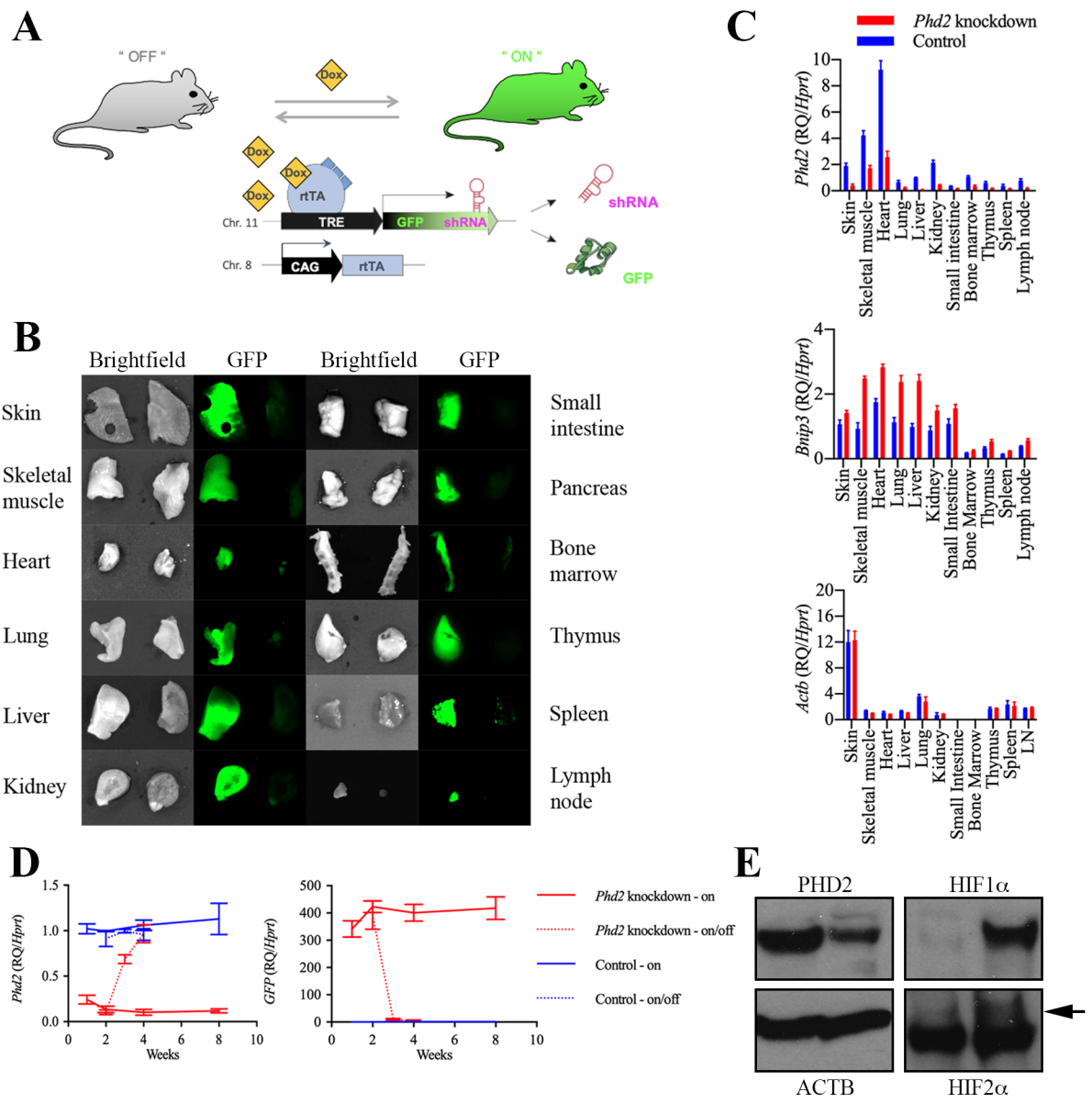
Detect individual cells

We use a watershedding algorithm to segment individual cells within positively classified regions. Watershedding algorithms have been shown to perform well at cell counting tasks in spite of their speed and simplicity [1040].

Generate point cloud

The watershedding approach produces a labelled segmentation of individual cells. The predicted cell centroids are then returned as the minima of the watershedding catchment basins. The resulting point cloud consists of (x, y) coordinates for each cell centre. This point cloud can then be used to derive simple quantitative summary statistics, such as cell counts and densities, as well as supporting more sophisticated analyses of the spatial distribution of cells.

Appendix 8 – Inducible knockdown transgenic mice



(**A**) Schematic representation of *Phd2*-targeted short hairpin RNA (shRNA) transgenic mice that utilise inducible RNA interference to control gene expression. These mice possess a CAG (a strong synthetic promoter comprising the cytomegalovirus early enhancer element, the promoter, first exon and first intron of the chicken beta-actin gene and the splice acceptor of the rabbit beta-globin gene)-promoted reverse tetracycline transactivator (rtTA) transgene located on chromosome 8 and an enhanced green fluorescent protein (GFP)-shRNA cassette

located downstream of the collagen type I gene (*Col1a1*) on chromosome 11. Whilst the rtTA is constitutively expressed, it is only capable of binding to the tetracycline response element (TRE) within the GFP-shRNA cassette in the presence of doxycycline (Dox). Thus, when transgenic mice receive Dox in their drinking water, transcription of a silencing shRNA directed against *Phd2* occurs with concomitant transcription of GFP which acts as a reporter protein that facilitates tracking of shRNA expression. After processing, the shRNA is loaded onto the cytosolic RNA-induced silencing complex (RISC) and complementary mRNA is degraded, leading to repression of the desired target gene. Control mice express CAG-rtTA but not the GFP-shRNA cassette.

(**B**) Representative brightfield and fluorescent images of organs harvested from *Phd2* knockdown and littermate control mice after two weeks of Dox treatment (2 mg/mL in 3% sucrose drinking water *ad libitum*). GFP expression was detected in all organs examined. In each pair of samples, the organ from the transgenic mouse is located on the left of the image whilst the organ from the control mouse is on the right of the image.

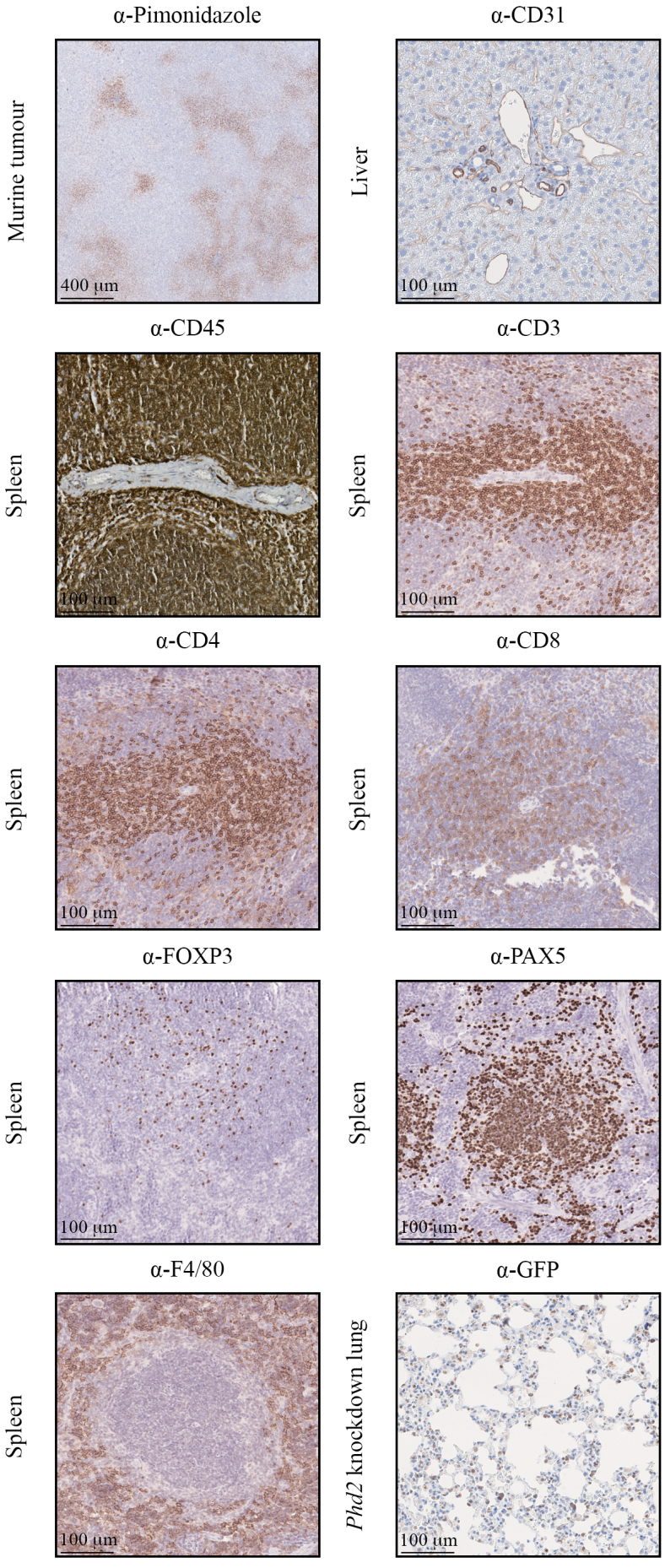
(**C**) Tissue distribution of mRNA for *Phd2*, the HIF target gene *Bnip3* and *Actb*, a housekeeping gene not considered to be a HIF target, in organs harvested following two weeks of Dox treatment to both knockdown and littermate control mice (n = 3 in each group; values calculated as the relative quantity [RQ] when compared to *Hprt* expression in the liver of control mice). Data are presented as mean ± standard deviation (SD).

(**D**) Reversibility of changes to *Phd2* and *GFP* mRNA levels in the liver of knockdown and littermate control mice treated with Dox (ON group = 8 weeks of Dox treatment, ON-OFF group = 2 weeks of Dox treatment followed by 2 weeks without Dox; n = 3 in each group). Data are presented as mean ± SD.

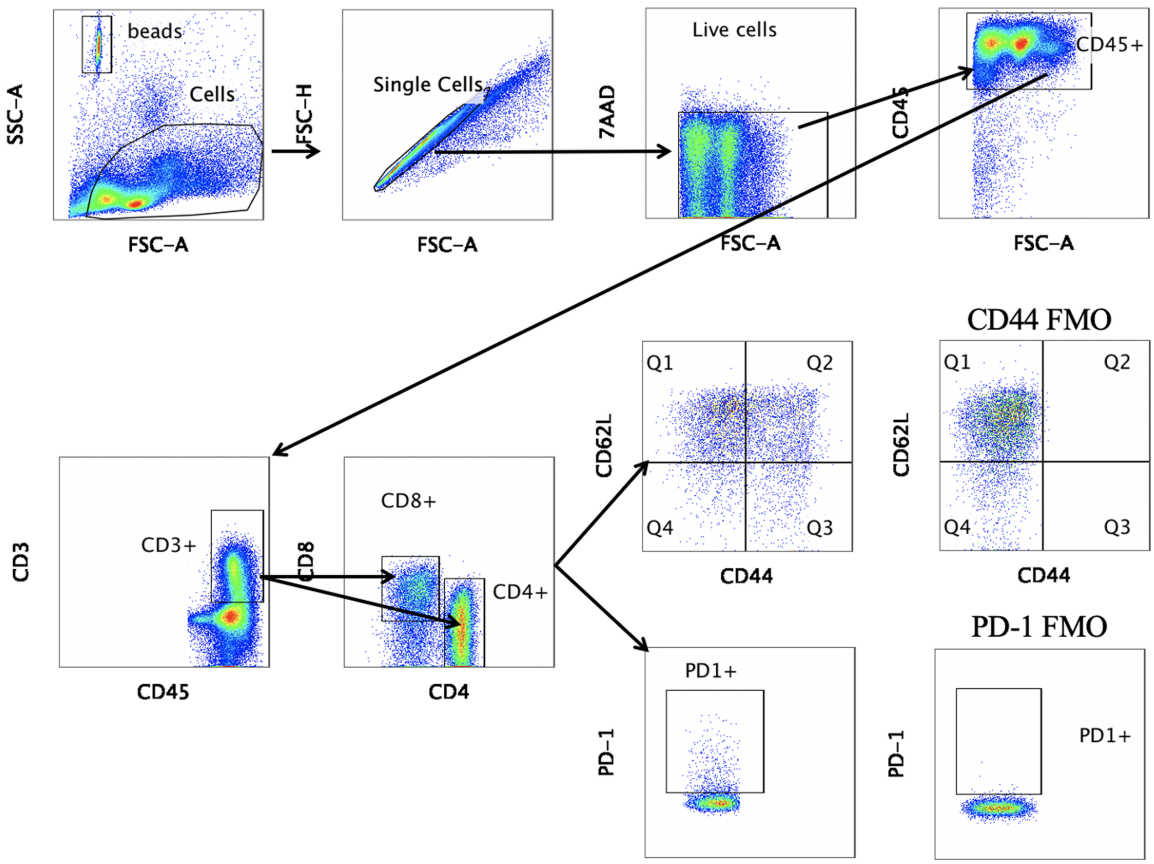
(**E**) Western blots demonstrating protein levels of PHD2, HIF1α, HIF2α and ACTB (loading control) in livers harvested from a knockdown and littermate control mouse following two weeks of Dox treatment. In each image, the sample from the transgenic mouse is located on the right whilst the sample from the control mouse is on the left (note that the HIF2α blot displays a lower non-specific band, with the HIF2α-specific band identified by the black arrow).

Appendix 9 – Murine immunohistochemistry optimisation/validation

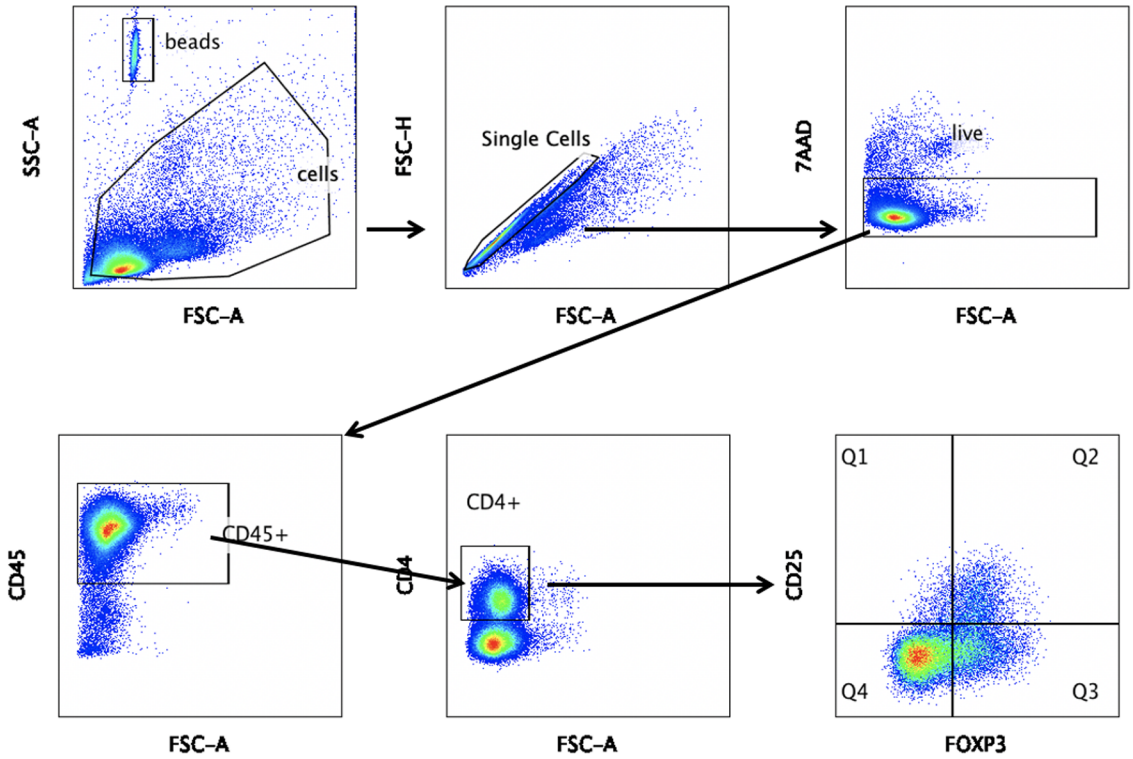
A murine tumour with known labelling acted as a positive control sample for pimonidazole immunohistochemistry. CD31 is expressed by blood vessels within murine liver. CD45 (leukocyte common antigen) is expressed by all leukocytes within murine spleen. The T lymphocyte markers CD3, CD4, CD8 and FOXP3 and the B lymphocyte marker PAX5 were expressed by cells surrounding a central artery within the white pulp. By comparison, the macrophage marker F4/80 was expressed by cells within the red pulp. Lung tissue from a doxycycline-treated *Phd2* knockdown mouse acted as a positive control sample for enhanced green fluorescent protein (GFP) immunohistochemistry; no staining was detected in lung tissue from a doxycycline-treated control mouse (data not shown).


α-Pimonidazole
α-CD31
Murine tumour
Liver
400 µm
100 µm
α-CD45
α-CD3
Spleen
Spleen
100 µm
100 µm
α-CD4
α-CD8
Spleen
Spleen
100 µm
100 µm
α-FOXP3
α-PAX5
Spleen
Spleen
100 µm
100 µm
α-F4/80
α-GFP
Spleen
Phd2 knockdown lung
100 µm
100 µm

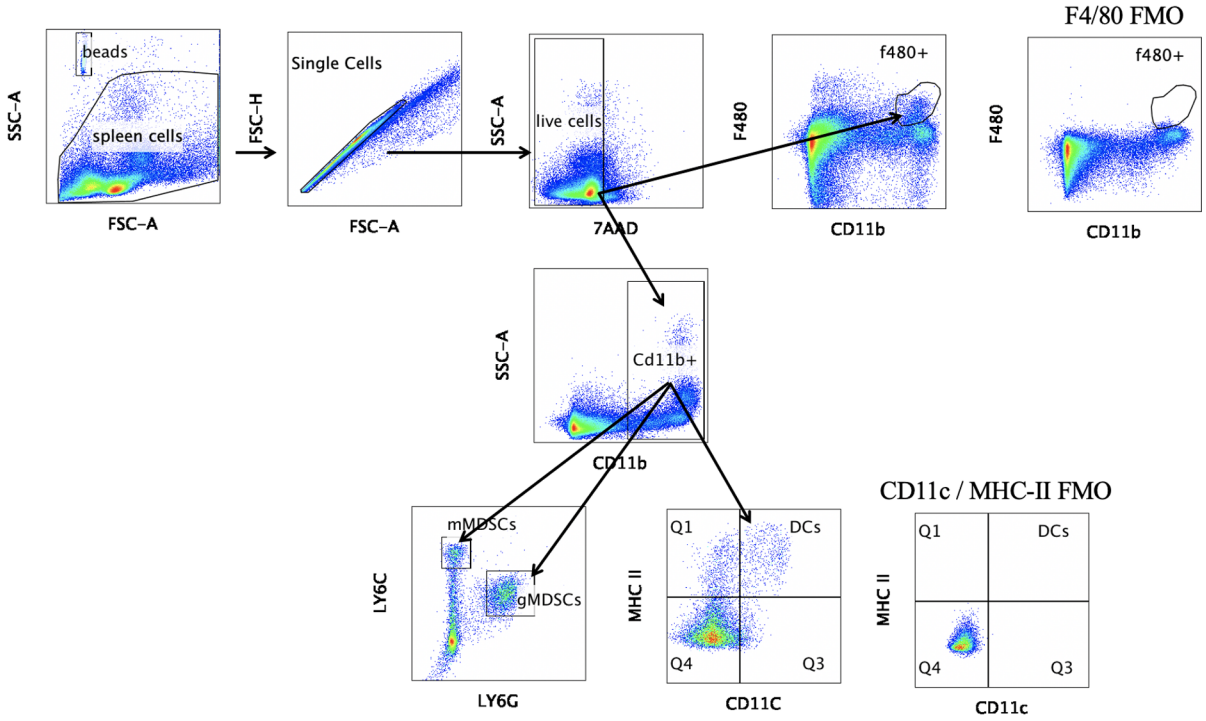
Appendix 10 – Flow cytometry gating strategies



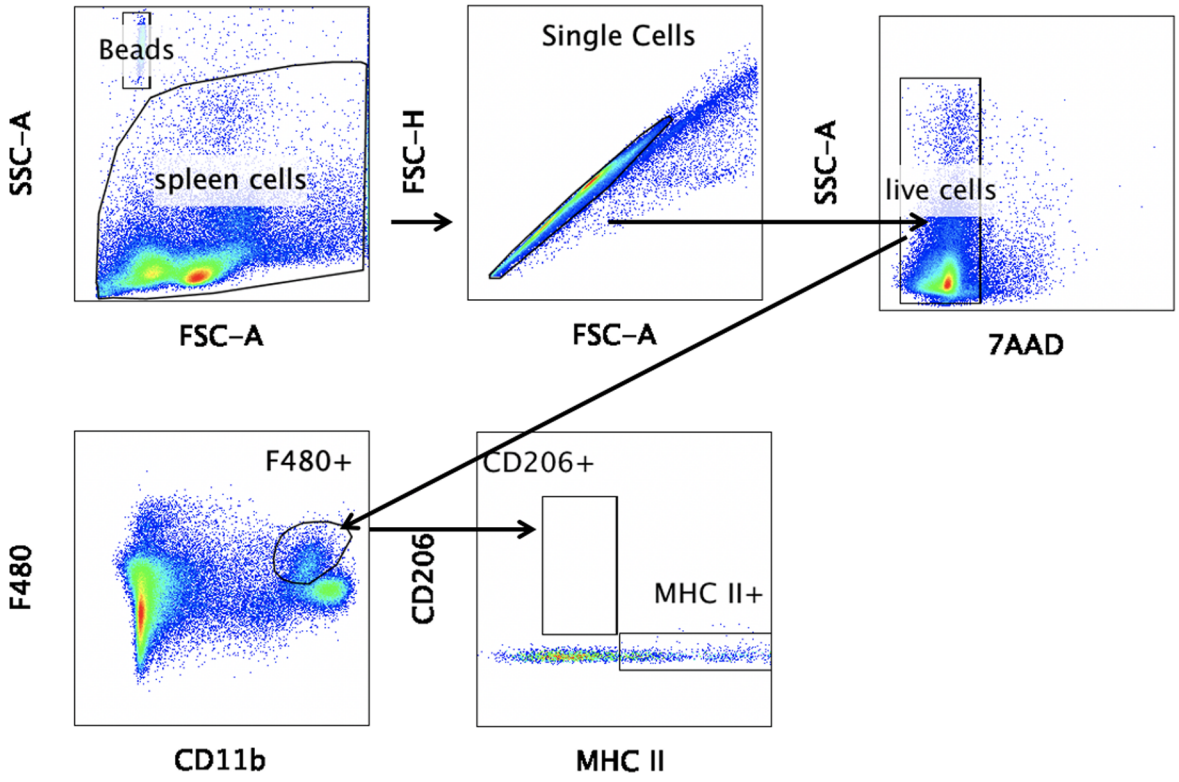
Representative flow cytometry dot plots indicating the gating strategy for identification of T lymphocyte populations, their differentiation status and PD-1 expression within spleen and tumour in **Figure 4.4Di-iii** and **Figure 4.4Ei-iii** (FMO = Fluorescence Minus One control).



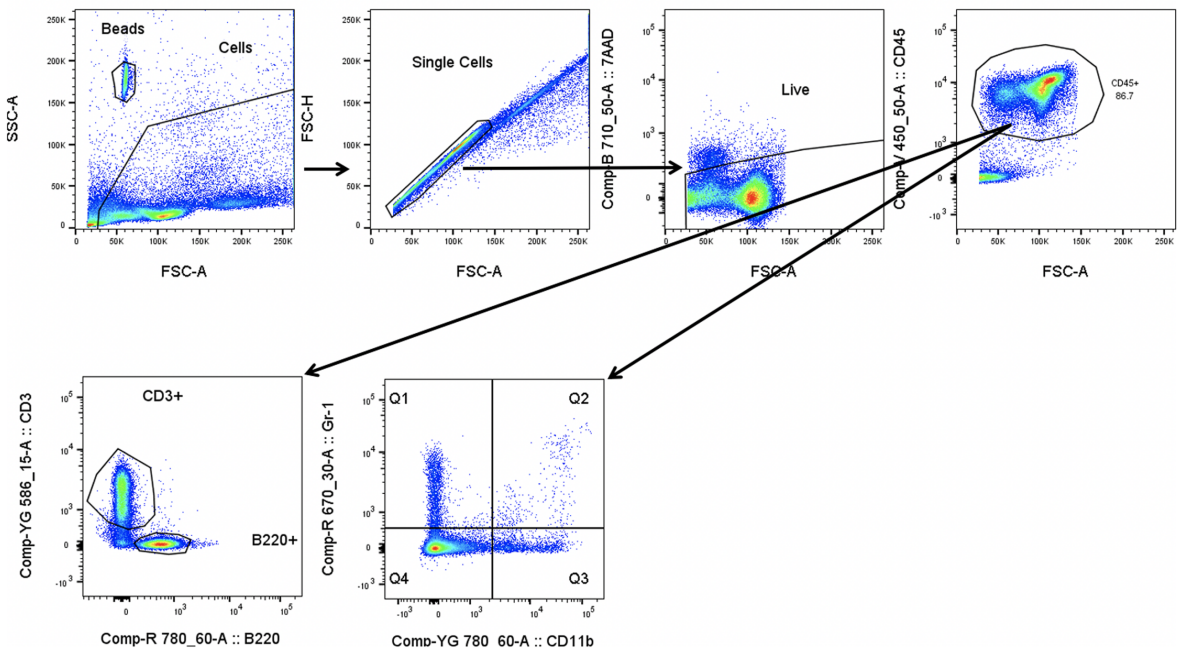
Representative flow cytometry dot plots indicating the gating strategy for identification of regulatory T lymphocytes within spleen and tumour in **Figure 4.4Div** and **Figure 4.4Eiv**.



Representative flow cytometry dot plots indicating the gating strategy for identification of myeloid cell populations within spleen and tumour in **Figure 4. 4Dv** and **Figure 4.4Ev** (FMO = Fluorescence Minus One control).



Representative flow cytometry dot plots indicating the gating strategy for identification of macrophage polarisation within spleen and tumour in **Figure 4. 4Dvi** and **Figure 4.4Evi**.



Representative flow cytometry dot plots indicating the gating strategy for identification of lymphocyte and myeloid populations within peripheral blood in **Figure 4.5F**.

Publications

The following publications have arisen from the work presented in this thesis:

Introduction

'Hypoxia and HIF pathway in cancer and the placenta' **Macklin P**, McAuliffe J, Pugh C, Yamamoto A (2017), *Placenta*, 56:8-13

'Recent advances in the biology of tumour hypoxia with relevance to diagnostic practice and tissue-based research' **Macklin P**, Yamamoto A, Browning L, Hofer M, Adam J, Pugh C (2020), *Journal of Pathology*, 250(5):593-611

Chapter 1

'Combining multiple spatial statistics enhances the description of immune cell localisation within tumours' Bull J, **Macklin P**, Quaiser T, Braun F, Waters S, Pugh C, Byrne H (2020), *Scientific Reports*, 10(1):18624

Chapter 2

'Mitochondrial inhibitor atovaquone increases tumor oxygenation and inhibits hypoxic gene expression in patients with non-small cell lung cancer' Skwarski M, McGowan D, Belcher E, Di Chiara F, Stavroulias D, McCole M, Derham J, Chu K-Y, Teoh E, Chauhan J, O'Reilly D, Harris B, **Macklin P**, Bull J, Green M, Rodriguez-Berriguete G, Prevo R, Folkes L, Campo L, Ferencz P, Croal P, Flight H, Qi C, Holmes J, O'Connor J, Gleeson F, McKenna W, Harris A, Bulte D, Buffa F, Macpherson R, Higgins G (2021), *Clinical Cancer Research*, In press

Chapter 3

'Systemic silencing of PHD2 causes reversible immune regulatory dysfunction' Yamamoto A, Hester J, **Macklin P**, Kawai K, Uchiyama M, Biggs D, Bishop T, Bull K, Cheng X, Cawthorne E, Coleman M, Crockford T, Davies B, Dow L, Goldin R, Kranc K, Kudo H, Lawson H, McAuliffe J, Milward K, Scudamore C, Soilleux E, Issa F, Ratcliffe P, Pugh C (2019), *Journal of Clinical Investigation*, 129(9):3640-3656

The following manuscripts are either in preparation for submission or undergoing journal review:

Chapter 1

'Semaphorin 3A induces cytoskeletal paralysis in tumor-specific $CD8^+$ T cells' Barnkob M, Michaels Y, André V, **Macklin P**, Gileadi U, Valvo S, Rei M, Kulicke C, Chen J, Jain V, Woodcock V, Colin-York H, Hadjinicolaou A, Kong Y, Mayya V, Bull J, Rijal P, Pugh C, Townsend A, Olsen L, Fritzsche M, Fulga T, Dustin M, Jones Y, Cerundolo V (2019), bioRxiv doi: https://doi.org/10.1101/849083

'Multiparameter persistent homology landscapes distinguish spatial patterns of immune cells' Vipond O, Bull J, **Macklin P**, Tillmann U, Pugh C, Byrne H, Harrington H (2021)

During my Clinical Research Fellowship, I published the following articles that are not related to work presented in this thesis:

'A systematic review of the use of rituximab for the treatment of antibody-mediated renal transplant rejection' **Macklin P**, Morris P, Knight S (2017), *Transplantation Reviews*, 31(2):87-95

'An incidental clear cell lesion of the kidney found at the time of cadaveric renal transplantation' **Macklin P**, Soares M, Roberts I, Browning L (2018), *Diagnostic Histopathology*, 24(6):223-226

'Barriers to the release of human tissue for clinical trials research in the UK: a national survey of cellular pathology laboratories on behalf of the National Cancer Research Institute's Cellular Molecular Pathology (CM-Path) initiative' **Macklin P**, Hall A, Lee J, Hair J, Speirs V, Thomas G, Oien K, Verrill C (2019), *Journal of Clinical Pathology*, 72(1):52-57

'Tumour Seeding in the Tract of Percutaneous Renal Tumour Biopsy: A Report on Seven Cases from a UK Tertiary Referral Centre' **Macklin P**, Sullivan M, Tapping C, Cranston D, Webster G, Roberts I, Verrill C, Browning L (2019), *European Urology*, 75(5):861-867

'An unusual cause of a right nasal mass in a 73-year-old male' **Macklin P**, Turner G, Royston D (2019), *Diagnostic Histopathology*, 25(6):260-263

‘Artificial intelligence in digital pathology: a roadmap to routine use in clinical practice’ Colling R, Pitman H, Oien K, Rajpoot N, **Macklin P**, Snead D, Sackville T, Verrill C (2019), *Journal of Pathology*, 249(2):143-150

‘CM-Path Molecular Diagnostics Forum – consensus statement on the development and implementation of molecular diagnostic tests in the United Kingdom’ **Macklin P**, Pillay N, Lee J, Pitman H, Scott S, Wang J, Craig C, Jones L, Oien K, Colling R, Coupland S, Verrill C (2019), *British Journal of Cancer*, 121(9):738-743

‘Tumour seeding of the renal tumour biopsy tract – a histologically under-recognised feature?’ **Macklin P**, Verrill C, Roberts I, Colling R, Sullivan M, Webster G, Cranston D, Tapping C, Browning L (2019), *Histopathology*, 76(5):763-766

References

1. Lyons TW, Reinhard CT, Planavsky NJ. The rise of oxygen in Earth's early ocean and atmosphere. Nature. 2014;506(7488):307-15.

2. Chellan P, Sadler PJ. The elements of life and medicines. Philos Trans A Math Phys Eng Sci. 2015;373(2037).

3. Hedges SB, Blair JE, Venturi ML, et al. A molecular timescale of eukaryote evolution and the rise of complex multicellular life. BMC Evol Biol. 2004;4:2.

4. Sitkovsky M, Lukashev D. Regulation of immune cells by local-tissue oxygen tension: HIF1 alpha and adenosine receptors. Nat Rev Immunol. 2005;5(9):712-21.

5. Thomson L, Paton J. Oxygen toxicity. Paediatr Respir Rev. 2014;15(2):120-3.

6. Ortiz-Prado E, Dunn JF, Vasconez J, et al. Partial pressure of oxygen in the human body: a general review. Am J Blood Res. 2019;9(1):1-14.

7. Ledford H, Callaway E. Biologists who decoded how cells sense oxygen win medicine Nobel. Nature. 2019;574(7777):161-2.

8. Keeley TP, Mann GE. Defining Physiological Normoxia for Improved Translation of Cell Physiology to Animal Models and Humans. Physiol Rev. 2019;99(1):161-234.

9. Macklin PS, Yamamoto A, Browning L, et al. Recent advances in the biology of tumour hypoxia with relevance to diagnostic practice and tissue-based research. J Pathol. 2020;250(5):593-611.

10. Semenza GL, Wang GL. A nuclear factor induced by hypoxia via de novo protein synthesis binds to the human erythropoietin gene enhancer at a site required for transcriptional activation. Mol Cell Biol. 1992;12(12):5447-54.

11. Rolfs A, Kvietikova I, Gassmann M, et al. Oxygen-regulated transferrin expression is mediated by hypoxia-inducible factor-1. J Biol Chem. 1997;272(32):20055-62.

12. Goldberg MA, Schneider TJ. Similarities between the oxygen-sensing mechanisms regulating the expression of vascular endothelial growth factor and erythropoietin. J Biol Chem. 1994;269(6):4355-9.

13. Forsythe JA, Jiang BH, Iyer NV, et al. Activation of vascular endothelial growth factor gene transcription by hypoxia-inducible factor 1. Mol Cell Biol. 1996;16(9):4604-13.

14. Firth JD, Ebert BL, Pugh CW, et al. Oxygen-regulated control elements in the phosphoglycerate kinase 1 and lactate dehydrogenase A genes: similarities with the erythropoietin 3' enhancer. Proc Natl Acad Sci U S A. 1994;91(14):6496-500.

15. Ebert BL, Firth JD, Ratcliffe PJ. Hypoxia and mitochondrial inhibitors regulate expression of glucose transporter-1 via distinct Cis-acting sequences. J Biol Chem. 1995;270(49):29083-9.

16. Ullah MS, Davies AJ, Halestrap AP. The plasma membrane lactate transporter MCT4, but not MCT1, is up-regulated by hypoxia through a HIF-1alpha-dependent mechanism. J Biol Chem. 2006;281(14):9030-7.

17. Kim JW, Tchernyshyov I, Semenza GL, et al. HIF-1-mediated expression of pyruvate dehydrogenase kinase: a metabolic switch required for cellular adaptation to hypoxia. Cell Metab. 2006;3(3):177-85.

18. Mole DR, Blancher C, Copley RR, et al. Genome-wide association of hypoxia-inducible factor (HIF)-1alpha and HIF-2alpha DNA binding with expression profiling of hypoxia-inducible transcripts. J Biol Chem. 2009;284(25):16767-75.

19. Schodel J, Oikonomopoulos S, Ragoussis J, et al. High-resolution genome-wide mapping of HIF-binding sites by ChIP-seq. Blood. 2011;117(23):e207-17.

20. Xia X, Lemieux ME, Li W, et al. Integrative analysis of HIF binding and transactivation reveals its role in maintaining histone methylation homeostasis. Proc Natl Acad Sci U S A. 2009;106(11):4260-5.

21. Kulshreshtha R, Ferracin M, Wojcik SE, et al. A microRNA signature of hypoxia. Mol Cell Biol. 2007;27(5):1859-67.

22. Camps C, Saini HK, Mole DR, et al. Integrated analysis of microRNA and mRNA expression and association with HIF binding reveals the complexity of microRNA expression regulation under hypoxia. Mol Cancer. 2014;13:28.

23. Uniacke J, Holterman CE, Lachance G, et al. An oxygen-regulated switch in the protein synthesis machinery. Nature. 2012;486(7401):126-9.

24. Thienpont B, Steinbacher J, Zhao H, et al. Tumour hypoxia causes DNA hypermethylation by reducing TET activity. Nature. 2016;537(7618):63-8.

25. Chakraborty AA, Laukka T, Myllykoski M, et al. Histone demethylase KDM6A directly senses oxygen to control chromatin and cell fate. Science. 2019;363(6432):1217-22.

26. Batie M, Frost J, Frost M, et al. Hypoxia induces rapid changes to histone methylation and reprograms chromatin. Science. 2019;363(6432):1222-6.

27. Ema M, Taya S, Yokotani N, et al. A novel bHLH-PAS factor with close sequence similarity to hypoxia-inducible factor 1alpha regulates the VEGF expression and is potentially involved in lung and vascular development. Proc Natl Acad Sci U S A. 1997;94(9):4273-8.

28. Wiesener MS, Turley H, Allen WE, et al. Induction of endothelial PAS domain protein-1 by hypoxia: characterization and comparison with hypoxia-inducible factor-1alpha. Blood. 1998;92(7):2260-8.

29. Wiesener MS, Jurgensen JS, Rosenberger C, et al. Widespread hypoxia-inducible expression of HIF-2alpha in distinct cell populations of different organs. FASEB J. 2003;17(2):271-3.

30. Wang GL, Jiang BH, Rue EA, et al. Hypoxia-inducible factor 1 is a basic-helix-loop-helix-PAS heterodimer regulated by cellular O2 tension. Proc Natl Acad Sci U S A. 1995;92(12):5510-4.

31. Holmquist-Mengelbier L, Fredlund E, Lofstedt T, et al. Recruitment of HIF-1alpha and HIF-2alpha to common target genes is differentially regulated in neuroblastoma: HIF-2alpha promotes an aggressive phenotype. Cancer Cell. 2006;10(5):413-23.

32. Ginouves A, Ilc K, Macias N, et al. PHDs overactivation during chronic hypoxia "desensitizes" HIFalpha and protects cells from necrosis. Proc Natl Acad Sci U S A. 2008;105(12):4745-50.

33. Hu CJ, Wang LY, Chodosh LA, et al. Differential roles of hypoxia-inducible factor 1alpha (HIF-1alpha) and HIF-2alpha in hypoxic gene regulation. Mol Cell Biol. 2003;23(24):9361-74.

34. Smythies JA, Sun M, Masson N, et al. Inherent DNA-binding specificities of the HIF-1alpha and HIF-2alpha transcription factors in chromatin. EMBO Rep. 2019;20(1).

35. Gu YZ, Moran SM, Hogenesch JB, et al. Molecular characterization and chromosomal localization of a third alpha-class hypoxia inducible factor subunit, HIF3alpha. Gene Expr. 1998;7(3):205-13.

36. Maynard MA, Qi H, Chung J, et al. Multiple splice variants of the human HIF-3 alpha locus are targets of the von Hippel-Lindau E3 ubiquitin ligase complex. J Biol Chem. 2003;278(13):11032-40.

37. Makino Y, Uenishi R, Okamoto K, et al. Transcriptional up-regulation of inhibitory PAS domain protein gene expression by hypoxia-inducible factor 1 (HIF-1): a negative feedback regulatory circuit in HIF-1-mediated signaling in hypoxic cells. J Biol Chem. 2007;282(19):14073-82.

38. Yamashita T, Ohneda O, Nagano M, et al. Abnormal heart development and lung remodeling in mice lacking the hypoxia-inducible factor-related basic helix-loop-helix PAS protein NEPAS. Mol Cell Biol. 2008;28(4):1285-97.

39. Hara S, Hamada J, Kobayashi C, et al. Expression and characterization of hypoxia-inducible factor (HIF)-3alpha in human kidney: suppression of HIF-mediated gene expression by HIF-3alpha. Biochem Biophys Res Commun. 2001;287(4):808-13.

40. Makino Y, Cao R, Svensson K, et al. Inhibitory PAS domain protein is a negative regulator of hypoxia-inducible gene expression. Nature. 2001;414(6863):550-4.

41. Makino Y, Kanopka A, Wilson WJ, et al. Inhibitory PAS domain protein (IPAS) is a hypoxia-inducible splicing variant of the hypoxia-inducible factor-3alpha locus. J Biol Chem. 2002;277(36):32405-8.

42. Thrash-Bingham CA, Tartof KD. aHIF: a natural antisense transcript overexpressed in human renal cancer and during hypoxia. J Natl Cancer Inst. 1999;91(2):143-51.

43. Rossignol F, Vache C, Clottes E. Natural antisense transcripts of hypoxia-inducible factor 1alpha are detected in different normal and tumour human tissues. Gene. 2002;299(1-2):135-40.

44. Uchida T, Rossignol F, Matthay MA, et al. Prolonged hypoxia differentially regulates hypoxia-inducible factor (HIF)-1alpha and HIF-2alpha expression in lung epithelial cells: implication of natural antisense HIF-1alpha. J Biol Chem. 2004;279(15):14871-8.

45. Gothie E, Richard DE, Berra E, et al. Identification of alternative spliced variants of human hypoxia-inducible factor-1alpha. J Biol Chem. 2000;275(10):6922-7.

46. Chun YS, Choi E, Kim TY, et al. A dominant-negative isoform lacking exons 11 and 12 of the human hypoxia-inducible factor-1alpha gene. Biochem J. 2002;362(Pt 1):71-9.

47. Lei Z, Li B, Yang Z, et al. Regulation of HIF-1alpha and VEGF by miR-20b tunes tumor cells to adapt to the alteration of oxygen concentration. PLoS One. 2009;4(10):e7629.

48. Bruning U, Cerone L, Neufeld Z, et al. MicroRNA-155 promotes resolution of hypoxia-inducible factor 1alpha activity during prolonged hypoxia. Mol Cell Biol. 2011;31(19):4087-96.

49. Wang H, Flach H, Onizawa M, et al. Negative regulation of Hif1a expression and TH17 differentiation by the hypoxia-regulated microRNA miR-210. Nat Immunol. 2014;15(4):393-401.

50. D'Angelo G, Duplan E, Boyer N, et al. Hypoxia up-regulates prolyl hydroxylase activity: a feedback mechanism that limits HIF-1 responses during reoxygenation. J Biol Chem. 2003;278(40):38183-7.

51. del Peso L, Castellanos MC, Temes E, et al. The von Hippel Lindau/hypoxia-inducible factor (HIF) pathway regulates the transcription of the HIF-proline hydroxylase genes in response to low oxygen. J Biol Chem. 2003;278(49):48690-5.

52. Marxsen JH, Stengel P, Doege K, et al. Hypoxia-inducible factor-1 (HIF-1) promotes its degradation by induction of HIF-alpha-prolyl-4-hydroxylases. Biochem J. 2004;381(Pt 3):761-7.

53. Aprelikova O, Chandramouli GV, Wood M, et al. Regulation of HIF prolyl hydroxylases by hypoxia-inducible factors. J Cell Biochem. 2004;92(3):491-501.

54. Stiehl DP, Wirthner R, Koditz J, et al. Increased prolyl 4-hydroxylase domain proteins compensate for decreased oxygen levels. Evidence for an autoregulatory oxygen-sensing system. J Biol Chem. 2006;281(33):23482-91.

55. Tan M, Gu Q, He H, et al. SAG/ROC2/RBX2 is a HIF-1 target gene that promotes HIF-1 alpha ubiquitination and degradation. Oncogene. 2008;27(10):1404-11.

56. Bhattacharya S, Michels CL, Leung MK, et al. Functional role of p35srj, a novel p300/CBP binding protein, during transactivation by HIF-1. Genes Dev. 1999;13(1):64-75.

57. Yin Z, Haynie J, Yang X, et al. The essential role of Cited2, a negative regulator for HIF-1alpha, in heart development and neurulation. Proc Natl Acad Sci U S A. 2002;99(16):10488-93.

58. Berlow RB, Dyson HJ, Wright PE. Hypersensitive termination of the hypoxic response by a disordered protein switch. Nature. 2017;543(7645):447-51.

59. Yang F, Zhang H, Mei Y, et al. Reciprocal regulation of HIF-1alpha and lincRNA-p21 modulates the Warburg effect. Mol Cell. 2014;53(1):88-100.

60. Coleman ML, McDonough MA, Hewitson KS, et al. Asparaginyl hydroxylation of the Notch ankyrin repeat domain by factor inhibiting hypoxia-inducible factor. J Biol Chem. 2007;282(33):24027-38.

61. Webb JD, Muranyi A, Pugh CW, et al. MYPT1, the targeting subunit of smooth-muscle myosin phosphatase, is a substrate for the asparaginyl hydroxylase factor inhibiting hypoxia-inducible factor (FIH). Biochem J. 2009;420(2):327-33.

62. Lang KJ, Kappel A, Goodall GJ. Hypoxia-inducible factor-1alpha mRNA contains an internal ribosome entry site that allows efficient translation during normoxia and hypoxia. Mol Biol Cell. 2002;13(5):1792-801.

63. Ratcliffe PJ. Oxygen sensing and hypoxia signalling pathways in animals: the implications of physiology for cancer. J Physiol. 2013;591(8):2027-42.

64. Masson N, Keeley TP, Giuntoli B, et al. Conserved N-terminal cysteine dioxygenases transduce responses to hypoxia in animals and plants. Science. 2019;365(6448):65-9.

65. Semenza GL. Oxygen sensing, hypoxia-inducible factors, and disease pathophysiology. Annu Rev Pathol. 2014;9:47-71.

66. Thomlinson RH, Gray LH. The histological structure of some human lung cancers and the possible implications for radiotherapy. Br J Cancer. 1955;9(4):539-49.

67. Hirst DG. Anemia: a problem or an opportunity in radiotherapy? Int J Radiat Oncol Biol Phys. 1986;12(11):2009-17.

68. Tannock IF. The relation between cell proliferation and the vascular system in a transplanted mouse mammary tumour. Br J Cancer. 1968;22(2):258-73.

69. Gatenby RA, Kessler HB, Rosenblum JS, et al. Oxygen distribution in squamous cell carcinoma metastases and its relationship to outcome of radiation therapy. Int J Radiat Oncol Biol Phys. 1988;14(5):831-8.

70. Hockel M, Schlenger K, Knoop C, et al. Oxygenation of carcinomas of the uterine cervix: evaluation by computerized O2 tension measurements. Cancer Res. 1991;51(22):6098-102.

71. Kayama T, Yoshimoto T, Fujimoto S, et al. Intratumoral oxygen pressure in malignant brain tumor. J Neurosurg. 1991;74(1):55-9.

72. Vaupel P, Schlenger K, Knoop C, et al. Oxygenation of human tumors: evaluation of tissue oxygen distribution in breast cancers by computerized O2 tension measurements. Cancer Res. 1991;51(12):3316-22.

73. Lartigau E, Le Ridant AM, Lambin P, et al. Oxygenation of head and neck tumors. Cancer. 1993;71(7):2319-25.

74. Nordsmark M, Bentzen SM, Overgaard J. Measurement of human tumour oxygenation status by a polarographic needle electrode. An analysis of inter- and intratumour heterogeneity. Acta Oncol. 1994;33(4):383-9.

75. Hockel M, Schlenger K, Aral B, et al. Association between tumor hypoxia and malignant progression in advanced cancer of the uterine cervix. Cancer Res. 1996;56(19):4509-15.

76. Wong RK, Fyles A, Milosevic M, et al. Heterogeneity of polarographic oxygen tension measurements in cervix cancer: an evaluation of within and between tumor variability, probe position, and track depth. Int J Radiat Oncol Biol Phys. 1997;39(2):405-12.

77. Adam MF, Gabalski EC, Bloch DA, et al. Tissue oxygen distribution in head and neck cancer patients. Head Neck. 1999;21(2):146-53.

78. Koong AC, Mehta VK, Le QT, et al. Pancreatic tumors show high levels of hypoxia. Int J Radiat Oncol Biol Phys. 2000;48(4):919-22.

79. Movsas B, Chapman JD, Hanlon AL, et al. Hypoxia in human prostate carcinoma: an Eppendorf PO2 study. Am J Clin Oncol. 2001;24(5):458-61.

80. Beppu T, Kamada K, Yoshida Y, et al. Change of oxygen pressure in glioblastoma tissue under various conditions. J Neurooncol. 2002;58(1):47-52.

81. Le QT, Chen E, Salim A, et al. An evaluation of tumor oxygenation and gene expression in patients with early stage non-small cell lung cancers. Clin Cancer Res. 2006;12(5):1507-14.

82. Aapro M, Osterborg A, Gascon P, et al. Prevalence and management of cancer-related anaemia, iron deficiency and the specific role of i.v. iron. Ann Oncol. 2012;23(8):1954-62.

83. Eberhard A, Kahlert S, Goede V, et al. Heterogeneity of angiogenesis and blood vessel maturation in human tumors: implications for antiangiogenic tumor therapies. Cancer Res. 2000;60(5):1388-93.

84. Morikawa S, Baluk P, Kaidoh T, et al. Abnormalities in pericytes on blood vessels and endothelial sprouts in tumors. Am J Pathol. 2002;160(3):985-1000.

85. McDonald DM, Baluk P. Significance of blood vessel leakiness in cancer. Cancer Res. 2002;62(18):5381-5.

86. Brown JM. Evidence for acutely hypoxic cells in mouse tumours, and a possible mechanism of reoxygenation. Br J Radiol. 1979;52(620):650-6.

87. Dewhirst MW, Braun RD, Lanzen JL. Temporal changes in PO2 of R3230AC tumors in Fischer-344 rats. Int J Radiat Oncol Biol Phys. 1998;42(4):723-6.

88. Cardenas-Navia LI, Mace D, Richardson RA, et al. The pervasive presence of fluctuating oxygenation in tumors. Cancer Res. 2008;68(14):5812-9.

89. Bayer C, Vaupel P. Acute versus chronic hypoxia in tumors: Controversial data concerning time frames and biological consequences. Strahlenther Onkol. 2012;188(7):616-27.

90. Horsman MR, Mortensen LS, Petersen JB, et al. Imaging hypoxia to improve radiotherapy outcome. Nat Rev Clin Oncol. 2012;9(12):674-87.

91. Wilson WR, Hay MP. Targeting hypoxia in cancer therapy. Nat Rev Cancer. 2011;11(6):393-410.

92. Richards CH, Mohammed Z, Qayyum T, et al. The prognostic value of histological tumor necrosis in solid organ malignant disease: a systematic review. Future Oncol. 2011;7(10):1223-35.

93. Bhandari V, Hoey C, Liu LY, et al. Molecular landmarks of tumor hypoxia across cancer types. Nat Genet. 2019;51(2):308-18.

94. Graeber TG, Osmanian C, Jacks T, et al. Hypoxia-mediated selection of cells with diminished apoptotic potential in solid tumours. Nature. 1996;379(6560):88-91.

95. Carmeliet P, Dor Y, Herbert JM, et al. Role of HIF-1alpha in hypoxia-mediated apoptosis, cell proliferation and tumour angiogenesis. Nature. 1998;394(6692):485-90.

96. Pennacchietti S, Michieli P, Galluzzo M, et al. Hypoxia promotes invasive growth by transcriptional activation of the met protooncogene. Cancer Cell. 2003;3(4):347-61.

97. Godet I, Shin YJ, Ju JA, et al. Fate-mapping post-hypoxic tumor cells reveals a ROS-resistant phenotype that promotes metastasis. Nat Commun. 2019;10(1):4862.

98. Vergis R, Corbishley CM, Norman AR, et al. Intrinsic markers of tumour hypoxia and angiogenesis in localised prostate cancer and outcome of radical treatment: a retrospective analysis of two randomised radiotherapy trials and one surgical cohort study. Lancet Oncol. 2008;9(4):342-51.

99. Dewhirst MW, Cao Y, Moeller B. Cycling hypoxia and free radicals regulate angiogenesis and radiotherapy response. Nat Rev Cancer. 2008;8(6):425-37.

100. Harada H, Inoue M, Itasaka S, et al. Cancer cells that survive radiation therapy acquire HIF-1 activity and translocate towards tumour blood vessels. Nat Commun. 2012;3:783.

101. Cosse JP, Michiels C. Tumour hypoxia affects the responsiveness of cancer cells to chemotherapy and promotes cancer progression. Anticancer Agents Med Chem. 2008;8(7):790-7.

102. Minchinton AI, Tannock IF. Drug penetration in solid tumours. Nat Rev Cancer. 2006;6(8):583-92.

103. Chouaib S, Noman MZ, Kosmatopoulos K, et al. Hypoxic stress: obstacles and opportunities for innovative immunotherapy of cancer. Oncogene. 2017;36(4):439-45.

104. Balkwill FR, Capasso M, Hagemann T. The tumor microenvironment at a glance. J Cell Sci. 2012;125(Pt 23):5591-6.

105. Junttila MR, de Sauvage FJ. Influence of tumour micro-environment heterogeneity on therapeutic response. Nature. 2013;501(7467):346-54.

106. Dranoff G. Cytokines in cancer pathogenesis and cancer therapy. Nat Rev Cancer. 2004;4(1):11-22.

107. Hanahan D, Weinberg RA. Hallmarks of cancer: the next generation. Cell. 2011;144(5):646-74.

108. Burnet FM. The concept of immunological surveillance. Prog Exp Tumor Res. 1970;13:1-27.

109. Dunn GP, Bruce AT, Ikeda H, et al. Cancer immunoediting: from immunosurveillance to tumor escape. Nat Immunol. 2002;3(11):991-8.

110. Mittal D, Gubin MM, Schreiber RD, et al. New insights into cancer immunoediting and its three component phases--elimination, equilibrium and escape. Curr Opin Immunol. 2014;27:16-25.

111. Shankaran V, Ikeda H, Bruce AT, et al. IFNgamma and lymphocytes prevent primary tumour development and shape tumour immunogenicity. Nature. 2001;410(6832):1107-11.

112. Koebel CM, Vermi W, Swann JB, et al. Adaptive immunity maintains occult cancer in an equilibrium state. Nature. 2007;450(7171):903-7.

113. Matsushita H, Vesely MD, Koboldt DC, et al. Cancer exome analysis reveals a T-cell-dependent mechanism of cancer immunoediting. Nature. 2012;482(7385):400-4.

114. Angelova M, Mlecnik B, Vasaturo A, et al. Evolution of Metastases in Space and Time under Immune Selection. Cell. 2018;175(3):751-65 e16.

115. Chen DS, Mellman I. Oncology meets immunology: the cancer-immunity cycle. Immunity. 2013;39(1):1-10.

116. Chen DS, Mellman I. Elements of cancer immunity and the cancer-immune set point. Nature. 2017;541(7637):321-30.

117. Hellstrom I, Hellstrom KE, Pierce GE, et al. Cellular and humoral immunity to different types of human neoplasms. Nature. 1968;220(5174):1352-4.

118. Joyce JA, Fearon DT. T cell exclusion, immune privilege, and the tumor microenvironment. Science. 2015;348(6230):74-80.

119. Anderson KG, Stromnes IM, Greenberg PD. Obstacles Posed by the Tumor Microenvironment to T cell Activity: A Case for Synergistic Therapies. Cancer Cell. 2017;31(3):311-25.

120. Kalbasi A, Ribas A. Tumour-intrinsic resistance to immune checkpoint blockade. Nat Rev Immunol. 2020;20(1):25-39.

121. Fridman WH, Zitvogel L, Sautes-Fridman C, et al. The immune contexture in cancer prognosis and treatment. Nat Rev Clin Oncol. 2017;14(12):717-34.

122. Gooden MJ, de Bock GH, Leffers N, et al. The prognostic influence of tumour-infiltrating lymphocytes in cancer: a systematic review with meta-analysis. Br J Cancer. 2011;105(1):93-103.

123. Gentles AJ, Newman AM, Liu CL, et al. The prognostic landscape of genes and infiltrating immune cells across human cancers. Nat Med. 2015;21(8):938-45.

124. Barnes TA, Amir E. HYPE or HOPE: the prognostic value of infiltrating immune cells in cancer. Br J Cancer. 2017;117(4):451-60.

125. Thorsson V, Gibbs DL, Brown SD, et al. The Immune Landscape of Cancer. Immunity. 2018;48(4):812-30 e14.

126. Alspach E, Lussier DM, Miceli AP, et al. MHC-II neoantigens shape tumour immunity and response to immunotherapy. Nature. 2019;574(7780):696-701.

127. DeNardo DG, Barreto JB, Andreu P, et al. CD4(+) T cells regulate pulmonary metastasis of mammary carcinomas by enhancing protumor properties of macrophages. Cancer Cell. 2009;16(2):91-102.

128. Asadzadeh Z, Mohammadi H, Safarzadeh E, et al. The paradox of Th17 cell functions in tumor immunity. Cell Immunol. 2017;322:15-25.

129. Chen ML, Pittet MJ, Gorelik L, et al. Regulatory T cells suppress tumor-specific CD8 T cell cytotoxicity through TGF-beta signals in vivo. Proc Natl Acad Sci U S A. 2005;102(2):419-24.

130. Zou W, Restifo NP. T(H)17 cells in tumour immunity and immunotherapy. Nat Rev Immunol. 2010;10(4):248-56.

131. Wouters MCA, Nelson BH. Prognostic Significance of Tumor-Infiltrating B Cells and Plasma Cells in Human Cancer. Clin Cancer Res. 2018;24(24):6125-35.

132. Lawrence T, Natoli G. Transcriptional regulation of macrophage polarization: enabling diversity with identity. Nat Rev Immunol. 2011;11(11):750-61.

133. Jayasingam SD, Citartan M, Thang TH, et al. Evaluating the Polarization of Tumor-Associated Macrophages Into M1 and M2 Phenotypes in Human Cancer Tissue: Technicalities and Challenges in Routine Clinical Practice. Front Oncol. 2019;9:1512.

134. Russell DG, Huang L, VanderVen BC. Immunometabolism at the interface between macrophages and pathogens. Nat Rev Immunol. 2019;19(5):291-304.

135. Fridlender ZG, Sun J, Kim S, et al. Polarization of tumor-associated neutrophil phenotype by TGF-beta: "N1" versus "N2" TAN. Cancer Cell. 2009;16(3):183-94.

136. Shaul ME, Levy L, Sun J, et al. Tumor-associated neutrophils display a distinct N1 profile following TGFbeta modulation: A transcriptomics analysis of pro- vs. antitumor TANs. Oncoimmunology. 2016;5(11):e1232221.

137. Kumar V, Patel S, Tcyganov E, et al. The Nature of Myeloid-Derived Suppressor Cells in the Tumor Microenvironment. Trends Immunol. 2016;37(3):208-20.

138. Bronte V, Brandau S, Chen SH, et al. Recommendations for myeloid-derived suppressor cell nomenclature and characterization standards. Nat Commun. 2016;7:12150.

139. Zhang QW, Liu L, Gong CY, et al. Prognostic significance of tumor-associated macrophages in solid tumor: a meta-analysis of the literature. PLoS One. 2012;7(12):e50946.

140. Shen M, Hu P, Donskov F, et al. Tumor-associated neutrophils as a new prognostic factor in cancer: a systematic review and meta-analysis. PLoS One. 2014;9(6):e98259.

141. Chittezhath M, Dhillon MK, Lim JY, et al. Molecular profiling reveals a tumor-promoting phenotype of monocytes and macrophages in human cancer progression. Immunity. 2014;41(5):815-29.

142. Zhu Y, Knolhoff BL, Meyer MA, et al. CSF1/CSF1R blockade reprograms tumor-infiltrating macrophages and improves response to T-cell checkpoint immunotherapy in pancreatic cancer models. Cancer Res. 2014;74(18):5057-69.

143. Rivera LB, Meyronet D, Hervieu V, et al. Intratumoral myeloid cells regulate responsiveness and resistance to antiangiogenic therapy. Cell Rep. 2015;11(4):577-91.

144. De Palma M, Lewis CE. Macrophage regulation of tumor responses to anticancer therapies. Cancer Cell. 2013;23(3):277-86.

145. Wculek SK, Cueto FJ, Mujal AM, et al. Dendritic cells in cancer immunology and immunotherapy. Nat Rev Immunol. 2020;20(1):7-24.

146. Chiossone L, Dumas PY, Vienne M, et al. Natural killer cells and other innate lymphoid cells in cancer. Nat Rev Immunol. 2018;18(11):671-88.

147. Coley WB. The Treatment of Inoperable Sarcoma by Bacterial Toxins (the Mixed Toxins of the Streptococcus erysipelas and the Bacillus prodigiosus). Proc R Soc Med. 1910;3(Surg Sect):1-48.

148. Richardson MA, Ramirez T, Russell NC, et al. Coley toxins immunotherapy: a retrospective review. Altern Ther Health Med. 1999;5(3):42-7.

149. Redelman-Sidi G, Glickman MS, Bochner BH. The mechanism of action of BCG therapy for bladder cancer--a current perspective. Nat Rev Urol. 2014;11(3):153-62.

150. Rosenberg SA, Yang JC, Topalian SL, et al. Treatment of 283 consecutive patients with metastatic melanoma or renal cell cancer using high-dose bolus interleukin 2. JAMA. 1994;271(12):907-13.

151. Canil C, Hotte S, Mayhew LA, et al. Interferon-alfa in the treatment of patients with inoperable locally advanced or metastatic renal cell carcinoma: a systematic review. Can Urol Assoc J. 2010;4(3):201-8.

152. Couzin-Frankel J. Breakthrough of the year 2013. Cancer immunotherapy. Science. 2013;342(6165):1432-3.

153. Ledford H, Else H, Warren M. Cancer immunologists scoop medicine Nobel prize. Nature. 2018;562(7725):20-1.

154. Sharma P, Allison JP. The future of immune checkpoint therapy. Science. 2015;348(6230):56-61.

155. Kvistborg P, Philips D, Kelderman S, et al. Anti-CTLA-4 therapy broadens the melanoma-reactive CD8+ T cell response. Sci Transl Med. 2014;6(254):254ra128.

156. Hui E, Cheung J, Zhu J, et al. T cell costimulatory receptor CD28 is a primary target for PD-1-mediated inhibition. Science. 2017;355(6332):1428-33.

157. Pardoll DM. The blockade of immune checkpoints in cancer immunotherapy. Nat Rev Cancer. 2012;12(4):252-64.

158. Hu Z, Ott PA, Wu CJ. Towards personalized, tumour-specific, therapeutic vaccines for cancer. Nat Rev Immunol. 2018;18(3):168-82.

159. Jackson HJ, Rafiq S, Brentjens RJ. Driving CAR T-cells forward. Nat Rev Clin Oncol. 2016;13(6):370-83.

160. Kather JN, Halama N. Harnessing the innate immune system and local immunological microenvironment to treat colorectal cancer. Br J Cancer. 2019;120(9):871-82.

161. Pitt JM, Vetizou M, Daillere R, et al. Resistance Mechanisms to Immune-Checkpoint Blockade in Cancer: Tumor-Intrinsic and -Extrinsic Factors. Immunity. 2016;44(6):1255-69.

162. Sharma P, Hu-Lieskovan S, Wargo JA, et al. Primary, Adaptive, and Acquired Resistance to Cancer Immunotherapy. Cell. 2017;168(4):707-23.

163. Duechler M, Peczek L, Zuk K, et al. The heterogeneous immune microenvironment in breast cancer is affected by hypoxia-related genes. Immunobiology. 2014;219(2):158-65.

164. Duechler M, Peczek L, Szubert M, et al. Influence of hypoxia inducible factors on the immune microenvironment in ovarian cancer. Anticancer Res. 2014;34(6):2811-9.

165. Lin W, Wu S, Chen X, et al. Characterization of Hypoxia Signature to Evaluate the Tumor Immune Microenvironment and Predict Prognosis in Glioma Groups. Front Oncol. 2020;10:796.

166. Hugo W, Zaretsky JM, Sun L, et al. Genomic and Transcriptomic Features of Response to Anti-PD-1 Therapy in Metastatic Melanoma. Cell. 2016;165(1):35-44.

167. Chang WH, Forde D, Lai AG. A novel signature derived from immunoregulatory and hypoxia genes predicts prognosis in liver and five other cancers. J Transl Med. 2019;17(1):14.

168. Pugh CW, Ratcliffe PJ. New horizons in hypoxia signaling pathways. Exp Cell Res. 2017;356(2):116-21.

169. Palazon A, Goldrath AW, Nizet V, et al. HIF transcription factors, inflammation, and immunity. Immunity. 2014;41(4):518-28.

170. Watts ER, Walmsley SR. Inflammation and Hypoxia: HIF and PHD Isoform Selectivity. Trends Mol Med. 2019;25(1):33-46.

171. Parmar K, Mauch P, Vergilio JA, et al. Distribution of hematopoietic stem cells in the bone marrow according to regional hypoxia. Proc Natl Acad Sci U S A. 2007;104(13):5431-6.

172. Kubota Y, Takubo K, Suda T. Bone marrow long label-retaining cells reside in the sinusoidal hypoxic niche. Biochem Biophys Res Commun. 2008;366(2):335-9.

173. Spencer JA, Ferraro F, Roussakis E, et al. Direct measurement of local oxygen concentration in the bone marrow of live animals. Nature. 2014;508(7495):269-73.

174. Nombela-Arrieta C, Pivarnik G, Winkel B, et al. Quantitative imaging of haematopoietic stem and progenitor cell localization and hypoxic status in the bone marrow microenvironment. Nat Cell Biol. 2013;15(5):533-43.

175. Simsek T, Kocabas F, Zheng J, et al. The distinct metabolic profile of hematopoietic stem cells reflects their location in a hypoxic niche. Cell Stem Cell. 2010;7(3):380-90.

176. Takubo K, Goda N, Yamada W, et al. Regulation of the HIF-1alpha level is essential for hematopoietic stem cells. Cell Stem Cell. 2010;7(3):391-402.

177. Rouault-Pierre K, Lopez-Onieva L, Foster K, et al. HIF-2alpha protects human hematopoietic stem/progenitors and acute myeloid leukemic cells from apoptosis induced by endoplasmic reticulum stress. Cell Stem Cell. 2013;13(5):549-63.

178. Chabi S, Uzan B, Naguibneva I, et al. Hypoxia Regulates Lymphoid Development of Human Hematopoietic Progenitors. Cell Rep. 2019;29(8):2307-20 e6.

179. Nakamura H, Makino Y, Okamoto K, et al. TCR engagement increases hypoxia-inducible factor-1 alpha protein synthesis via rapamycin-sensitive pathway under hypoxic conditions in human peripheral T cells. J Immunol. 2005;174(12):7592-9.

180. Menk AV, Scharping NE, Moreci RS, et al. Early TCR Signaling Induces Rapid Aerobic Glycolysis Enabling Distinct Acute T Cell Effector Functions. Cell Rep. 2018;22(6):1509-21.

181. Wang R, Dillon CP, Shi LZ, et al. The transcription factor Myc controls metabolic reprogramming upon T lymphocyte activation. Immunity. 2011;35(6):871-82.

182. Finlay DK, Rosenzweig E, Sinclair LV, et al. PDK1 regulation of mTOR and hypoxia-inducible factor 1 integrate metabolism and migration of CD8+ T cells. J Exp Med. 2012;209(13):2441-53.

183. Doedens AL, Phan AT, Stradner MH, et al. Hypoxia-inducible factors enhance the effector responses of CD8(+) T cells to persistent antigen. Nat Immunol. 2013;14(11):1173-82.

184. Palazon A, Tyrakis PA, Macias D, et al. An HIF-1alpha/VEGF-A Axis in Cytotoxic T Cells Regulates Tumor Progression. Cancer Cell. 2017;32(5):669-83 e5.

185. Patsoukis N, Bardhan K, Chatterjee P, et al. PD-1 alters T-cell metabolic reprogramming by inhibiting glycolysis and promoting lipolysis and fatty acid oxidation. Nat Commun. 2015;6:6692.

186. Michalek RD, Gerriets VA, Jacobs SR, et al. Cutting edge: distinct glycolytic and lipid oxidative metabolic programs are essential for effector and regulatory CD4+ T cell subsets. J Immunol. 2011;186(6):3299-303.

187. Shi LZ, Wang R, Huang G, et al. HIF1alpha-dependent glycolytic pathway orchestrates a metabolic checkpoint for the differentiation of TH17 and Treg cells. J Exp Med. 2011;208(7):1367-76.

188. Dang EV, Barbi J, Yang HY, et al. Control of T(H)17/T(reg) balance by hypoxia-inducible factor 1. Cell. 2011;146(5):772-84.

189. Pearce EL, Walsh MC, Cejas PJ, et al. Enhancing CD8 T-cell memory by modulating fatty acid metabolism. Nature. 2009;460(7251):103-7.

190. Araki K, Turner AP, Shaffer VO, et al. mTOR regulates memory CD8 T-cell differentiation. Nature. 2009;460(7251):108-12.

191. van der Windt GJ, O'Sullivan D, Everts B, et al. CD8 memory T cells have a bioenergetic advantage that underlies their rapid recall ability. Proc Natl Acad Sci U S A. 2013;110(35):14336-41.

192. Gubser PM, Bantug GR, Razik L, et al. Rapid effector function of memory CD8+ T cells requires an immediate-early glycolytic switch. Nat Immunol. 2013;14(10):1064-72.

193. Burrows N, Bashford-Rogers RJM, Bhute VJ, et al. Dynamic regulation of hypoxia-inducible factor-1alpha activity is essential for normal B cell development. Nat Immunol. 2020;21(11):1408-20.

194. Kojima H, Gu H, Nomura S, et al. Abnormal B lymphocyte development and autoimmunity in hypoxia-inducible factor 1alpha -deficient chimeric mice. Proc Natl Acad Sci U S A. 2002;99(4):2170-4.

195. Kojima H, Kobayashi A, Sakurai D, et al. Differentiation stage-specific requirement in hypoxia-inducible factor-1alpha-regulated glycolytic pathway during murine B cell development in bone marrow. J Immunol. 2010;184(1):154-63.

196. Meng X, Grotsch B, Luo Y, et al. Hypoxia-inducible factor-1alpha is a critical transcription factor for IL-10-producing B cells in autoimmune disease. Nat Commun. 2018;9(1):251.

197. Jellusova J, Cato MH, Apgar JR, et al. Gsk3 is a metabolic checkpoint regulator in B cells. Nat Immunol. 2017;18(3):303-12.

198. Abbott RK, Thayer M, Labuda J, et al. Germinal Center Hypoxia Potentiates Immunoglobulin Class Switch Recombination. J Immunol. 2016;197(10):4014-20.

199. Cho SH, Raybuck AL, Stengel K, et al. Germinal centre hypoxia and regulation of antibody qualities by a hypoxia response system. Nature. 2016;537(7619):234-8.

200. Blouin CC, Page EL, Soucy GM, et al. Hypoxic gene activation by lipopolysaccharide in macrophages: implication of hypoxia-inducible factor 1alpha. Blood. 2004;103(3):1124-30.

201. Peyssonnaux C, Datta V, Cramer T, et al. HIF-1alpha expression regulates the bactericidal capacity of phagocytes. J Clin Invest. 2005;115(7):1806-15.

202. Rius J, Guma M, Schachtrup C, et al. NF-kappaB links innate immunity to the hypoxic response through transcriptional regulation of HIF-1alpha. Nature. 2008;453(7196):807-11.

203. Cramer T, Yamanishi Y, Clausen BE, et al. HIF-1alpha is essential for myeloid cell-mediated inflammation. Cell. 2003;112(5):645-57.

204. Roiniotis J, Dinh H, Masendycz P, et al. Hypoxia prolongs monocyte/macrophage survival and enhanced glycolysis is associated with their maturation under aerobic conditions. J Immunol. 2009;182(12):7974-81.

205. Takeda N, O'Dea EL, Doedens A, et al. Differential activation and antagonistic function of HIF-{alpha} isoforms in macrophages are essential for NO homeostasis. Genes Dev. 2010;24(5):491-501.

206. Hannah S, Mecklenburgh K, Rahman I, et al. Hypoxia prolongs neutrophil survival in vitro. FEBS Lett. 1995;372(2-3):233-7.

207. Mecklenburgh KI, Walmsley SR, Cowburn AS, et al. Involvement of a ferroprotein sensor in hypoxia-mediated inhibition of neutrophil apoptosis. Blood. 2002;100(8):3008-16.

208. Walmsley SR, Print C, Farahi N, et al. Hypoxia-induced neutrophil survival is mediated by HIF-1alpha-dependent NF-kappaB activity. J Exp Med. 2005;201(1):105-15.

209. Thompson AA, Elks PM, Marriott HM, et al. Hypoxia-inducible factor 2alpha regulates key neutrophil functions in humans, mice, and zebrafish. Blood. 2014;123(3):366-76.

210. Sadiku P, Willson JA, Dickinson RS, et al. Prolyl hydroxylase 2 inactivation enhances glycogen storage and promotes excessive neutrophilic responses. J Clin Invest. 2017;127(9):3407-20.

211. Corzo CA, Condamine T, Lu L, et al. HIF-1alpha regulates function and differentiation of myeloid-derived suppressor cells in the tumor microenvironment. J Exp Med. 2010;207(11):2439-53.

212. Noman MZ, Janji B, Hu S, et al. Tumor-Promoting Effects of Myeloid-Derived Suppressor Cells Are Potentiated by Hypoxia-Induced Expression of miR-210. Cancer Res. 2015;75(18):3771-87.

213. Jantsch J, Chakravortty D, Turza N, et al. Hypoxia and hypoxia-inducible factor-1 alpha modulate lipopolysaccharide-induced dendritic cell activation and function. J Immunol. 2008;180(7):4697-705.

214. Bosco MC, Pierobon D, Blengio F, et al. Hypoxia modulates the gene expression profile of immunoregulatory receptors in human mature dendritic cells: identification of TREM-1 as a novel hypoxic marker in vitro and in vivo. Blood. 2011;117(9):2625-39.

215. Jantsch J, Wiese M, Schodel J, et al. Toll-like receptor activation and hypoxia use distinct signaling pathways to stabilize hypoxia-inducible factor 1alpha (HIF1A) and result in differential HIF1A-dependent gene expression. J Leukoc Biol. 2011;90(3):551-62.

216. Mancino A, Schioppa T, Larghi P, et al. Divergent effects of hypoxia on dendritic cell functions. Blood. 2008;112(9):3723-34.

217. Elia AR, Cappello P, Puppo M, et al. Human dendritic cells differentiated in hypoxia down-modulate antigen uptake and change their chemokine expression profile. J Leukoc Biol. 2008;84(6):1472-82.

218. Yang M, Ma C, Liu S, et al. Hypoxia skews dendritic cells to a T helper type 2-stimulating phenotype and promotes tumour cell migration by dendritic cell-derived osteopontin. Immunology. 2009;128(1 Suppl):e237-49.

219. Naldini A, Morena E, Pucci A, et al. Hypoxia affects dendritic cell survival: role of the hypoxia-inducible factor-1alpha and lipopolysaccharide. J Cell Physiol. 2012;227(2):587-95.

220. Weigert A, Weichand B, Sekar D, et al. HIF-1alpha is a negative regulator of plasmacytoid DC development in vitro and in vivo. Blood. 2012;120(15):3001-6.

221. Velasquez SY, Killian D, Schulte J, et al. Short Term Hypoxia Synergizes with Interleukin 15 Priming in Driving Glycolytic Gene Transcription and Supports Human Natural Killer Cell Activities. J Biol Chem. 2016;291(25):12960-77.

222. Balsamo M, Manzini C, Pietra G, et al. Hypoxia downregulates the expression of activating receptors involved in NK-cell-mediated target cell killing without affecting ADCC. Eur J Immunol. 2013;43(10):2756-64.

223. Parodi M, Raggi F, Cangelosi D, et al. Hypoxia Modifies the Transcriptome of Human NK Cells, Modulates Their Immunoregulatory Profile, and Influences NK Cell Subset Migration. Front Immunol. 2018;9:2358.

224. Betts GN, Eustace A, Patiar S, et al. Prospective technical validation and assessment of intra-tumour heterogeneity of a low density array hypoxia gene profile in head and neck squamous cell carcinoma. Eur J Cancer. 2013;49(1):156-65.

225. Rebelatto MC, Midha A, Mistry A, et al. Development of a programmed cell death ligand-1 immunohistochemical assay validated for analysis of non-small cell lung cancer and head and neck squamous cell carcinoma. Diagn Pathol. 2016;11(1):95.

226. Scorer P, Scott M, Lawson N, et al. Consistency of tumor and immune cell programmed cell death ligand-1 expression within and between tumor blocks using the VENTANA SP263 assay. Diagn Pathol. 2018;13(1):47.

227. Yamamoto A, Hester J, Macklin PS, et al. Systemic silencing of PHD2 causes reversible immune regulatory dysfunction. J Clin Invest. 2019;129(9):3640-56.

228. Tomayko MM, Reynolds CP. Determination of subcutaneous tumor size in athymic (nude) mice. Cancer Chemother Pharmacol. 1989;24(3):148-54.

229. Schneider CA, Rasband WS, Eliceiri KW. NIH Image to ImageJ: 25 years of image analysis. Nat Methods. 2012;9(7):671-5.

230. Gadalla R, Noamani B, MacLeod BL, et al. Validation of CyTOF Against Flow Cytometry for Immunological Studies and Monitoring of Human Cancer Clinical Trials. Front Oncol. 2019;9:415.

231. Newman AM, Liu CL, Green MR, et al. Robust enumeration of cell subsets from tissue expression profiles. Nat Methods. 2015;12(5):453-7.

232. Newman AM, Steen CB, Liu CL, et al. Determining cell type abundance and expression from bulk tissues with digital cytometry. Nat Biotechnol. 2019;37(7):773-82.

233. Salgado R, Denkert C, Demaria S, et al. The evaluation of tumor-infiltrating lymphocytes (TILs) in breast cancer: recommendations by an International TILs Working Group 2014. Ann Oncol. 2015;26(2):259-71.

234. Hendry S, Salgado R, Gevaert T, et al. Assessing Tumor-infiltrating Lymphocytes in Solid Tumors: A Practical Review for Pathologists and Proposal for a Standardized Method From the International Immunooncology Biomarkers Working Group: Part 1: Assessing the Host Immune Response, TILs in Invasive Breast Carcinoma and Ductal Carcinoma In Situ, Metastatic Tumor Deposits and Areas for Further Research. Adv Anat Pathol. 2017;24(5):235-51.

235. Hendry S, Salgado R, Gevaert T, et al. Assessing Tumor-Infiltrating Lymphocytes in Solid Tumors: A Practical Review for Pathologists and Proposal for a Standardized Method from the International Immuno-Oncology Biomarkers Working Group: Part 2: TILs in Melanoma, Gastrointestinal Tract Carcinomas, Non-Small Cell Lung Carcinoma and Mesothelioma, Endometrial and Ovarian Carcinomas, Squamous Cell Carcinoma of the Head and Neck, Genitourinary Carcinomas, and Primary Brain Tumors. Adv Anat Pathol. 2017;24(6):311-35.

236. Heindl A, Nawaz S, Yuan Y. Mapping spatial heterogeneity in the tumor microenvironment: a new era for digital pathology. Lab Invest. 2015;95(4):377-84.

237. Klauschen F, Muller KR, Binder A, et al. Scoring of tumor-infiltrating lymphocytes: From visual estimation to machine learning. Semin Cancer Biol. 2018;52(Pt 2):151-7.

238. Koelzer VH, Sirinukunwattana K, Rittscher J, et al. Precision immunoprofiling by image analysis and artificial intelligence. Virchows Arch. 2019;474(4):511-22.

239. Galon J, Costes A, Sanchez-Cabo F, et al. Type, density, and location of immune cells within human colorectal tumors predict clinical outcome. Science. 2006;313(5795):1960-4.

240. Kather JN, Suarez-Carmona M, Charoentong P, et al. Topography of cancer-associated immune cells in human solid tumors. Elife. 2018;7.

241. Yuan Y. Modelling the spatial heterogeneity and molecular correlates of lymphocytic infiltration in triple-negative breast cancer. J R Soc Interface. 2015;12(103).

242. Nawaz S, Heindl A, Koelble K, et al. Beyond immune density: critical role of spatial heterogeneity in estrogen receptor-negative breast cancer. Mod Pathol. 2015;28(6):766-77.

243. Maley CC, Koelble K, Natrajan R, et al. An ecological measure of immune-cancer colocalization as a prognostic factor for breast cancer. Breast Cancer Res. 2015;17(1):131.

244. Carstens JL, Correa de Sampaio P, Yang D, et al. Spatial computation of intratumoral T cells correlates with survival of patients with pancreatic cancer. Nat Commun. 2017;8:15095.

245. Heindl A, Sestak I, Naidoo K, et al. Relevance of Spatial Heterogeneity of Immune Infiltration for Predicting Risk of Recurrence After Endocrine Therapy of ER+ Breast Cancer. J Natl Cancer Inst. 2018;110(2).

246. Barua S, Fang P, Sharma A, et al. Spatial interaction of tumor cells and regulatory T cells correlates with survival in non-small cell lung cancer. Lung Cancer. 2018;117:73-9.

247. Gong C, Anders RA, Zhu Q, et al. Quantitative Characterization of CD8+ T Cell Clustering and Spatial Heterogeneity in Solid Tumors. Front Oncol. 2018;8:649.

248. Corredor G, Wang X, Zhou Y, et al. Spatial Architecture and Arrangement of Tumor-Infiltrating Lymphocytes for Predicting Likelihood of Recurrence in Early-Stage Non-Small Cell Lung Cancer. Clin Cancer Res. 2019;25(5):1526-34.

249. Posselt R, Erlenbach-Wunsch K, Haas M, et al. Spatial distribution of FoxP3+ and CD8+ tumour infiltrating T cells reflects their functional activity. Oncotarget. 2016;7(37):60383-94.

250. Saltz J, Gupta R, Hou L, et al. Spatial Organization and Molecular Correlation of Tumor-Infiltrating Lymphocytes Using Deep Learning on Pathology Images. Cell Rep. 2018;23(1):181-93 e7.

251. AbdulJabbar K, Raza SEA, Rosenthal R, et al. Geospatial immune variability illuminates differential evolution of lung adenocarcinoma. Nat Med. 2020;26(7):1054-62.

252. Bray F, Ferlay J, Soerjomataram I, et al. Global cancer statistics 2018: GLOBOCAN estimates of incidence and mortality worldwide for 36 cancers in 185 countries. CA Cancer J Clin. 2018;68(6):394-424.

253. Brizel DM, Sibley GS, Prosnitz LR, et al. Tumor hypoxia adversely affects the prognosis of carcinoma of the head and neck. Int J Radiat Oncol Biol Phys. 1997;38(2):285-9.

254. Kaanders JH, Wijffels KI, Marres HA, et al. Pimonidazole binding and tumor vascularity predict for treatment outcome in head and neck cancer. Cancer Res. 2002;62(23):7066-74.

255. Nordsmark M, Bentzen SM, Rudat V, et al. Prognostic value of tumor oxygenation in 397 head and neck tumors after primary radiation therapy. An international multi-center study. Radiother Oncol. 2005;77(1):18-24.

256. Koukourakis MI, Bentzen SM, Giatromanolaki A, et al. Endogenous markers of two separate hypoxia response pathways (hypoxia inducible factor 2 alpha and carbonic anhydrase 9) are associated with radiotherapy failure in head and neck cancer patients recruited in the CHART randomized trial. J Clin Oncol. 2006;24(5):727-35.

257. Mandal R, Senbabaoglu Y, Desrichard A, et al. The head and neck cancer immune landscape and its immunotherapeutic implications. JCI Insight. 2016;1(17):e89829.

258. Ferris RL, Blumenschein G, Jr., Fayette J, et al. Nivolumab for Recurrent Squamous-Cell Carcinoma of the Head and Neck. N Engl J Med. 2016;375(19):1856-67.

259. Cohen EEW, Soulieres D, Le Tourneau C, et al. Pembrolizumab versus methotrexate, docetaxel, or cetuximab for recurrent or metastatic head-and-neck squamous cell carcinoma (KEYNOTE-040): a randomised, open-label, phase 3 study. Lancet. 2019;393(10167):156-67.

260. Ghanizada M, Jakobsen KK, Gronhoj C, et al. The effects of checkpoint inhibition on head and neck squamous cell carcinoma: A systematic review. Oral Oncol. 2019;90:67-73.

261. Gnarra JR, Tory K, Weng Y, et al. Mutations of the VHL tumour suppressor gene in renal carcinoma. Nat Genet. 1994;7(1):85-90.

262. Maxwell PH, Wiesener MS, Chang GW, et al. The tumour suppressor protein VHL targets hypoxia-inducible factors for oxygen-dependent proteolysis. Nature. 1999;399(6733):271-5.

263. Krieg M, Haas R, Brauch H, et al. Up-regulation of hypoxia-inducible factors HIF-1alpha and HIF-2alpha under normoxic conditions in renal carcinoma cells by von Hippel-Lindau tumor suppressor gene loss of function. Oncogene. 2000;19(48):5435-43.

264. Wiesener MS, Munchenhagen PM, Berger I, et al. Constitutive activation of hypoxia-inducible genes related to overexpression of hypoxia-inducible factor-1alpha in clear cell renal carcinomas. Cancer Res. 2001;61(13):5215-22.

265. Turner KJ, Moore JW, Jones A, et al. Expression of hypoxia-inducible factors in human renal cancer: relationship to angiogenesis and to the von Hippel-Lindau gene mutation. Cancer Res. 2002;62(10):2957-61.

266. Grabmaier K, MC AdW, Verhaegh GW, et al. Strict regulation of CAIX(G250/MN) by HIF-1alpha in clear cell renal cell carcinoma. Oncogene. 2004;23(33):5624-31.

267. Shen SS, Truong LD, Scarpelli M, et al. Role of immunohistochemistry in diagnosing renal neoplasms: when is it really useful? Arch Pathol Lab Med. 2012;136(4):410-7.

268. Rooney MS, Shukla SA, Wu CJ, et al. Molecular and genetic properties of tumors associated with local immune cytolytic activity. Cell. 2015;160(1-2):48-61.

269. Senbabaoglu Y, Gejman RS, Winer AG, et al. Tumor immune microenvironment characterization in clear cell renal cell carcinoma identifies prognostic and immunotherapeutically relevant messenger RNA signatures. Genome Biol. 2016;17(1):231.

270. Motzer RJ, Tannir NM, McDermott DF, et al. Nivolumab plus Ipilimumab versus Sunitinib in Advanced Renal-Cell Carcinoma. N Engl J Med. 2018;378(14):1277-90.

271. Rini BI, Plimack ER, Stus V, et al. Pembrolizumab plus Axitinib versus Sunitinib for Advanced Renal-Cell Carcinoma. N Engl J Med. 2019;380(12):1116-27.

272. Motzer RJ, Penkov K, Haanen J, et al. Avelumab plus Axitinib versus Sunitinib for Advanced Renal-Cell Carcinoma. N Engl J Med. 2019;380(12):1103-15.

273. Chevrier S, Levine JH, Zanotelli VRT, et al. An Immune Atlas of Clear Cell Renal Cell Carcinoma. Cell. 2017;169(4):736-49 e18.

274. Snell CE, Turley H, McIntyre A, et al. Proline-hydroxylated hypoxia-inducible factor 1alpha (HIF-1alpha) upregulation in human tumours. PLoS One. 2014;9(2):e88955.

275. Lee SL, Cabanero M, Hyrcza M, et al. Computer-assisted image analysis of the tumor microenvironment on an oral tongue squamous cell carcinoma tissue microarray. Clin Transl Radiat Oncol. 2019;17:32-9.

276. Wijffels KI, Kaanders JH, Rijken PF, et al. Vascular architecture and hypoxic profiles in human head and neck squamous cell carcinomas. Br J Cancer. 2000;83(5):674-83.

277. Parra ER, Uraoka N, Jiang M, et al. Validation of multiplex immunofluorescence panels using multispectral microscopy for immune-profiling of formalin-fixed and paraffin-embedded human tumor tissues. Sci Rep. 2017;7(1):13380.

278. Sautes-Fridman C, Petitprez F, Calderaro J, et al. Tertiary lymphoid structures in the era of cancer immunotherapy. Nat Rev Cancer. 2019;19(6):307-25.

279. McKenney JK, Weiss SW, Folpe AL. CD31 expression in intratumoral macrophages: a potential diagnostic pitfall. Am J Surg Pathol. 2001;25(9):1167-73.

280. Leclerc M, Voilin E, Gros G, et al. Regulation of antitumour CD8 T-cell immunity and checkpoint blockade immunotherapy by Neuropilin-1. Nat Commun. 2019;10(1):3345.

281. Barnkob MB, Michaels YS, André V, et al. Semaphorin 3A induces cytoskeletal paralysis in tumor-specific CD8+ T cells. bioRxiv. 2019:849083.

282. Hoogsteen IJ, Lok J, Marres HA, et al. Hypoxia in larynx carcinomas assessed by pimonidazole binding and the value of CA-IX and vascularity as surrogate markers of hypoxia. Eur J Cancer. 2009;45(16):2906-14.

283. Nijkamp MM, Hoogsteen IJ, Span PN, et al. Spatial relationship of phosphorylated epidermal growth factor receptor and activated AKT in head and neck squamous cell carcinoma. Radiother Oncol. 2011;101(1):165-70.

284. Hoogsteen IJ, Marres HA, van den Hoogen FJ, et al. Expression of EGFR under tumor hypoxia: identification of a subpopulation of tumor cells responsible for aggressiveness and treatment resistance. Int J Radiat Oncol Biol Phys. 2012;84(3):807-14.

285. De Schutter H, Barbe B, Spaepen M, et al. Microsatellite alterations in head and neck squamous cell carcinoma and relation to expression of pimonidazole, CA IX and GLUT-1. Radiother Oncol. 2006;80(2):143-50.

286. Rademakers SE, Lok J, van der Kogel AJ, et al. Metabolic markers in relation to hypoxia; staining patterns and colocalization of pimonidazole, HIF-1alpha, CAIX, LDH-5, GLUT-1, MCT1 and MCT4. BMC Cancer. 2011;11:167.

287. Rademakers SE, Hoogsteen IJ, Rijken PF, et al. Pattern of CAIX expression is prognostic for outcome and predicts response to ARCON in patients with laryngeal cancer treated in a phase III randomized trial. Radiother Oncol. 2013;108(3):517-22.

288. Bruine de Bruin L, Bollineni VR, Wachters JE, et al. Assessment of hypoxic subvolumes in laryngeal cancer with (18)F-fluoroazomycinarabinoside ((18)F-FAZA)-PET/CT scanning and immunohistochemistry. Radiother Oncol. 2015;117(1):106-12.

289. Evans SM, Hahn SM, Magarelli DP, et al. Hypoxic heterogeneity in human tumors: EF5 binding, vasculature, necrosis, and proliferation. Am J Clin Oncol. 2001;24(5):467-72.

290. Nasman A, Romanitan M, Nordfors C, et al. Tumor infiltrating CD8+ and Foxp3+ lymphocytes correlate to clinical outcome and human papillomavirus (HPV) status in tonsillar cancer. PLoS One. 2012;7(6):e38711.

291. Nordfors C, Grun N, Tertipis N, et al. CD8+ and CD4+ tumour infiltrating lymphocytes in relation to human papillomavirus status and clinical outcome in tonsillar and base of tongue squamous cell carcinoma. Eur J Cancer. 2013;49(11):2522-30.

292. Balermpas P, Michel Y, Wagenblast J, et al. Tumour-infiltrating lymphocytes predict response to definitive chemoradiotherapy in head and neck cancer. Br J Cancer. 2014;110(2):501-9.

293. Oguejiofor K, Hall J, Slater C, et al. Stromal infiltration of CD8 T cells is associated with improved clinical outcome in HPV-positive oropharyngeal squamous carcinoma. Br J Cancer. 2015;113(6):886-93.

294. Balermpas P, Rodel F, Rodel C, et al. CD8+ tumour-infiltrating lymphocytes in relation to HPV status and clinical outcome in patients with head and neck cancer after postoperative chemoradiotherapy: A multicentre study of the German cancer consortium radiation oncology group (DKTK-ROG). Int J Cancer. 2016;138(1):171-81.

295. Nguyen N, Bellile E, Thomas D, et al. Tumor infiltrating lymphocytes and survival in patients with head and neck squamous cell carcinoma. Head Neck. 2016;38(7):1074-84.

296. Oguejiofor K, Galletta-Williams H, Dovedi SJ, et al. Distinct patterns of infiltrating CD8+ T cells in HPV+ and CD68 macrophages in HPV- oropharyngeal squamous cell

carcinomas are associated with better clinical outcome but PD-L1 expression is not prognostic. Oncotarget. 2017;8(9):14416-27.

297. Feng Z, Bethmann D, Kappler M, et al. Multiparametric immune profiling in HPV- oral squamous cell cancer. JCI Insight. 2017;2(14).

298. de Ruiter EJ, Ooft ML, Devriese LA, et al. The prognostic role of tumor infiltrating T-lymphocytes in squamous cell carcinoma of the head and neck: A systematic review and meta-analysis. Oncoimmunology. 2017;6(11):e1356148.

299. Nakano O, Sato M, Naito Y, et al. Proliferative activity of intratumoral CD8(+) T-lymphocytes as a prognostic factor in human renal cell carcinoma: clinicopathologic demonstration of antitumor immunity. Cancer Res. 2001;61(13):5132-6.

300. Giraldo NA, Becht E, Pages F, et al. Orchestration and Prognostic Significance of Immune Checkpoints in the Microenvironment of Primary and Metastatic Renal Cell Cancer. Clin Cancer Res. 2015;21(13):3031-40.

301. Giraldo NA, Becht E, Vano Y, et al. Tumor-Infiltrating and Peripheral Blood T-cell Immunophenotypes Predict Early Relapse in Localized Clear Cell Renal Cell Carcinoma. Clin Cancer Res. 2017;23(15):4416-28.

302. Menard LC, Fischer P, Kakrecha B, et al. Renal Cell Carcinoma (RCC) Tumors Display Large Expansion of Double Positive (DP) CD4+CD8+ T Cells With Expression of Exhaustion Markers. Front Immunol. 2018;9:2728.

303. Hoefflin R, Harlander S, Schafer S, et al. HIF-1alpha and HIF-2alpha differently regulate tumour development and inflammation of clear cell renal cell carcinoma in mice. Nat Commun. 2020;11(1):4111.

304. Mrass P, Takano H, Ng LG, et al. Random migration precedes stable target cell interactions of tumor-infiltrating T cells. J Exp Med. 2006;203(12):2749-61.

305. Jansen CS, Prokhnevska N, Master VA, et al. An intra-tumoral niche maintains and differentiates stem-like CD8 T cells. Nature. 2019;576(7787):465-70.

306. Kim H, Peng G, Hicks JM, et al. Engineering human tumor-specific cytotoxic T cells to function in a hypoxic environment. Mol Ther. 2008;16(3):599-606.

307. Marotta D, Karar J, Jenkins WT, et al. In vivo profiling of hypoxic gene expression in gliomas using the hypoxia marker EF5 and laser-capture microdissection. Cancer Res. 2011;71(3):779-89.

308. Hatfield SM, Kjaergaard J, Lukashev D, et al. Immunological mechanisms of the antitumor effects of supplemental oxygenation. Sci Transl Med. 2015;7(277):277ra30.

309. Zhang S, Zhong M, Wang C, et al. CCL5-deficiency enhances intratumoral infiltration of CD8(+) T cells in colorectal cancer. Cell Death Dis. 2018;9(7):766.

310. Jayaprakash P, Ai M, Liu A, et al. Targeted hypoxia reduction restores T cell infiltration and sensitizes prostate cancer to immunotherapy. J Clin Invest. 2018;128(11):5137-49.

311. Xie G, Cheng T, Lin J, et al. Local angiotensin II contributes to tumor resistance to checkpoint immunotherapy. J Immunother Cancer. 2018;6(1):88.

312. Najjar YG, Menk AV, Sander C, et al. Tumor cell oxidative metabolism as a barrier to PD-1 blockade immunotherapy in melanoma. JCI Insight. 2019;4(5).

313. Manaster Y, Shipony Z, Hutzler A, et al. Reduced CTL motility and activity in avascular tumor areas. Cancer Immunol Immunother. 2019;68(8):1287-301.

314. Gropper Y, Feferman T, Shalit T, et al. Culturing CTLs under Hypoxic Conditions Enhances Their Cytolysis and Improves Their Anti-tumor Function. Cell Rep. 2017;20(11):2547-55.

315. Negus RP, Stamp GW, Hadley J, et al. Quantitative assessment of the leukocyte infiltrate in ovarian cancer and its relationship to the expression of C-C chemokines. Am J Pathol. 1997;150(5):1723-34.

316. Fiumara A, Belfiore A, Russo G, et al. In situ evidence of neoplastic cell phagocytosis by macrophages in papillary thyroid cancer. J Clin Endocrinol Metab. 1997;82(5):1615-20.

317. Brasanac D, Muller CA, Muller GA, et al. HLA class I antigens expression in renal cell carcinoma: histopathological and clinical correlation. J Exp Clin Cancer Res. 1999;18(4):505-10.

318. Le QT, Shi G, Cao H, et al. Galectin-1: a link between tumor hypoxia and tumor immune privilege. J Clin Oncol. 2005;23(35):8932-41.

319. Singer K, Kastenberger M, Gottfried E, et al. Warburg phenotype in renal cell carcinoma: high expression of glucose-transporter 1 (GLUT-1) correlates with low CD8(+) T-cell infiltration in the tumor. Int J Cancer. 2011;128(9):2085-95.

320. Ino Y, Yamazaki-Itoh R, Shimada K, et al. Immune cell infiltration as an indicator of the immune microenvironment of pancreatic cancer. Br J Cancer. 2013;108(4):914-23.

321. Townsend KN, Spowart JE, Huwait H, et al. Markers of T cell infiltration and function associate with favorable outcome in vascularized high-grade serous ovarian carcinoma. PLoS One. 2013;8(12):e82406.

322. Ottensmeier CH, Perry KL, Harden EL, et al. Upregulated Glucose Metabolism Correlates Inversely with CD8+ T-cell Infiltration and Survival in Squamous Cell Carcinoma. Cancer Res. 2016;76(14):4136-48.

323. Horikawa N, Abiko K, Matsumura N, et al. Expression of Vascular Endothelial Growth Factor in Ovarian Cancer Inhibits Tumor Immunity through the Accumulation of Myeloid-Derived Suppressor Cells. Clin Cancer Res. 2017;23(2):587-99.

324. Brooks JM, Menezes AN, Ibrahim M, et al. Development and Validation of a Combined Hypoxia and Immune Prognostic Classifier for Head and Neck Cancer. Clin Cancer Res. 2019;25(17):5315-28.

325. Togo M, Yokobori T, Shimizu K, et al. Diagnostic value of (18)F-FDG-PET to predict the tumour immune status defined by tumoural PD-L1 and CD8(+)tumour-infiltrating lymphocytes in oral squamous cell carcinoma. Br J Cancer. 2020;122(11):1686-94.

326. Kuriyama K, Higuchi T, Yokobori T, et al. Uptake of positron emission tomography tracers reflects the tumor immune status in esophageal squamous cell carcinoma. Cancer Sci. 2020;111(6):1969-78.

327. Craig SG, Humphries MP, Alderdice M, et al. Immune status is prognostic for poor survival in colorectal cancer patients and is associated with tumour hypoxia. Br J Cancer. 2020;123(8):1280-8.

328. Huang JH, Cardenas-Navia LI, Caldwell CC, et al. Requirements for T lymphocyte migration in explanted lymph nodes. J Immunol. 2007;178(12):7747-55.

329. Pavesi A, Tan AT, Koh S, et al. A 3D microfluidic model for preclinical evaluation of TCR-engineered T cells against solid tumors. JCI Insight. 2017;2(12).

330. Rytelewski M, Haryutyunan K, Nwajei F, et al. Merger of dynamic two-photon and phosphorescence lifetime microscopy reveals dependence of lymphocyte motility on oxygen in solid and hematological tumors. J Immunother Cancer. 2019;7(1):78.

331. Boissonnas A, Fetler L, Zeelenberg IS, et al. In vivo imaging of cytotoxic T cell infiltration and elimination of a solid tumor. J Exp Med. 2007;204(2):345-56.

332. Salmon H, Franciszkiewicz K, Damotte D, et al. Matrix architecture defines the preferential localization and migration of T cells into the stroma of human lung tumors. J Clin Invest. 2012;122(3):899-910.

333. Murthy A, Gerber SA, Koch CJ, et al. Intratumoral Hypoxia Reduces IFN-gamma-Mediated Immunity and MHC Class I Induction in a Preclinical Tumor Model. Immunohorizons. 2019;3(4):149-60.

334. Loeffler DA, Juneau PL, Masserant S. Influence of tumour physico-chemical conditions on interleukin-2-stimulated lymphocyte proliferation. Br J Cancer. 1992;66(4):619-22.

335. Naldini A, Carraro F, Silvestri S, et al. Hypoxia affects cytokine production and proliferative responses by human peripheral mononuclear cells. J Cell Physiol. 1997;173(3):335-42.

336. Atkuri KR, Herzenberg LA, Herzenberg LA. Culturing at atmospheric oxygen levels impacts lymphocyte function. Proc Natl Acad Sci U S A. 2005;102(10):3756-9.

337. Atkuri KR, Herzenberg LA, Niemi AK, et al. Importance of culturing primary lymphocytes at physiological oxygen levels. Proc Natl Acad Sci U S A. 2007;104(11):4547-52.

338. Larbi A, Zelba H, Goldeck D, et al. Induction of HIF-1alpha and the glycolytic pathway alters apoptotic and differentiation profiles of activated human T cells. J Leukoc Biol. 2010;87(2):265-73.

339. Ohta A, Diwanji R, Kini R, et al. In vivo T cell activation in lymphoid tissues is inhibited in the oxygen-poor microenvironment. Front Immunol. 2011;2:27.

340. Ohta A, Madasu M, Subramanian M, et al. Hypoxia-induced and A2A adenosine receptor-independent T-cell suppression is short lived and easily reversible. Int Immunol. 2014;26(2):83-91.

341. Westendorf AM, Skibbe K, Adamczyk A, et al. Hypoxia Enhances Immunosuppression by Inhibiting CD4+ Effector T Cell Function and Promoting Treg Activity. Cell Physiol Biochem. 2017;41(4):1271-84.

342. Youssef MM, Symonds P, Ellis IO, et al. EMAP-II-dependent lymphocyte killing is associated with hypoxia in colorectal cancer. Br J Cancer. 2006;95(6):735-43.

343. Chang CH, Qiu J, O'Sullivan D, et al. Metabolic Competition in the Tumor Microenvironment Is a Driver of Cancer Progression. Cell. 2015;162(6):1229-41.

344. Ho PC, Bihuniak JD, Macintyre AN, et al. Phosphoenolpyruvate Is a Metabolic Checkpoint of Anti-tumor T Cell Responses. Cell. 2015;162(6):1217-28.

345. Calcinotto A, Filipazzi P, Grioni M, et al. Modulation of microenvironment acidity reverses anergy in human and murine tumor-infiltrating T lymphocytes. Cancer Res. 2012;72(11):2746-56.

346. Nakagawa Y, Negishi Y, Shimizu M, et al. Effects of extracellular pH and hypoxia on the function and development of antigen-specific cytotoxic T lymphocytes. Immunol Lett. 2015;167(2):72-86.

347. Pilon-Thomas S, Kodumudi KN, El-Kenawi AE, et al. Neutralization of Tumor Acidity Improves Antitumor Responses to Immunotherapy. Cancer Res. 2016;76(6):1381-90.

348. Johnston RJ, Su LJ, Pinckney J, et al. VISTA is an acidic pH-selective ligand for PSGL-1. Nature. 2019;574(7779):565-70.

349. Fischer K, Hoffmann P, Voelkl S, et al. Inhibitory effect of tumor cell-derived lactic acid on human T cells. Blood. 2007;109(9):3812-9.

350. Brand A, Singer K, Koehl GE, et al. LDHA-Associated Lactic Acid Production Blunts Tumor Immunosurveillance by T and NK Cells. Cell Metab. 2016;24(5):657-71.

351. Ohta A, Gorelik E, Prasad SJ, et al. A2A adenosine receptor protects tumors from antitumor T cells. Proc Natl Acad Sci U S A. 2006;103(35):13132-7.

352. Chimote AA, Hajdu P, Kucher V, et al. Selective inhibition of KCa3.1 channels mediates adenosine regulation of the motility of human T cells. J Immunol. 2013;191(12):6273-80.

353. Chimote AA, Balajthy A, Arnold MJ, et al. A defect in KCa3.1 channel activity limits the ability of CD8(+) T cells from cancer patients to infiltrate an adenosine-rich microenvironment. Sci Signal. 2018;11(527).

354. Eil R, Vodnala SK, Clever D, et al. Ionic immune suppression within the tumour microenvironment limits T cell effector function. Nature. 2016;537(7621):539-43.

355. Vodnala SK, Eil R, Kishton RJ, et al. T cell stemness and dysfunction in tumors are triggered by a common mechanism. Science. 2019;363(6434).

356. Banh A, Zhang J, Cao H, et al. Tumor galectin-1 mediates tumor growth and metastasis through regulation of T-cell apoptosis. Cancer Res. 2011;71(13):4423-31.

357. Nambiar DK, Aguilera T, Cao H, et al. Galectin-1-driven T cell exclusion in the tumor endothelium promotes immunotherapy resistance. J Clin Invest. 2019;129(12):5553-67.

358. Gabrilovich DI, Chen HL, Girgis KR, et al. Production of vascular endothelial growth factor by human tumors inhibits the functional maturation of dendritic cells. Nat Med. 1996;2(10):1096-103.

359. Zhang L, Conejo-Garcia JR, Katsaros D, et al. Intratumoral T cells, recurrence, and survival in epithelial ovarian cancer. N Engl J Med. 2003;348(3):203-13.

360. Shrimali RK, Yu Z, Theoret MR, et al. Antiangiogenic agents can increase lymphocyte infiltration into tumor and enhance the effectiveness of adoptive immunotherapy of cancer. Cancer Res. 2010;70(15):6171-80.

361. Huang Y, Yuan J, Righi E, et al. Vascular normalizing doses of antiangiogenic treatment reprogram the immunosuppressive tumor microenvironment and enhance immunotherapy. Proc Natl Acad Sci U S A. 2012;109(43):17561-6.

362. Motz GT, Santoro SP, Wang LP, et al. Tumor endothelium FasL establishes a selective immune barrier promoting tolerance in tumors. Nat Med. 2014;20(6):607-15.

363. Voron T, Colussi O, Marcheteau E, et al. VEGF-A modulates expression of inhibitory checkpoints on CD8+ T cells in tumors. J Exp Med. 2015;212(2):139-48.

364. Chou CK, Schietinger A, Liggitt HD, et al. Cell-intrinsic abrogation of TGF-beta signaling delays but does not prevent dysfunction of self/tumor-specific CD8 T cells in a murine model of autochthonous prostate cancer. J Immunol. 2012;189(8):3936-46.

365. Mariathasan S, Turley SJ, Nickles D, et al. TGFbeta attenuates tumour response to PD-L1 blockade by contributing to exclusion of T cells. Nature. 2018;554(7693):544-8.

366. Tauriello DVF, Palomo-Ponce S, Stork D, et al. TGFbeta drives immune evasion in genetically reconstituted colon cancer metastasis. Nature. 2018;554(7693):538-43.

367. Spranger S, Bao R, Gajewski TF. Melanoma-intrinsic beta-catenin signalling prevents anti-tumour immunity. Nature. 2015;523(7559):231-5.

368. Feig C, Jones JO, Kraman M, et al. Targeting CXCL12 from FAP-expressing carcinoma-associated fibroblasts synergizes with anti-PD-L1 immunotherapy in pancreatic cancer. Proc Natl Acad Sci U S A. 2013;110(50):20212-7.

369. Plitas G, Konopacki C, Wu K, et al. Regulatory T Cells Exhibit Distinct Features in Human Breast Cancer. Immunity. 2016;45(5):1122-34.

370. Badoual C, Hans S, Rodriguez J, et al. Prognostic value of tumor-infiltrating CD4+ T-cell subpopulations in head and neck cancers. Clin Cancer Res. 2006;12(2):465-72.

371. Wansom D, Light E, Thomas D, et al. Infiltrating lymphocytes and human papillomavirus-16--associated oropharyngeal cancer. Laryngoscope. 2012;122(1):121-7.

372. Bron L, Jandus C, Andrejevic-Blant S, et al. Prognostic value of arginase-II expression and regulatory T-cell infiltration in head and neck squamous cell carcinoma. Int J Cancer. 2013;132(3):E85-93.

373. Sun DS, Zhao MQ, Xia M, et al. The correlation between tumor-infiltrating Foxp3+ regulatory T cells and cyclooxygenase-2 expression and their association with recurrence in resected head and neck cancers. Med Oncol. 2012;29(2):707-13.

374. Li JF, Chu YW, Wang GM, et al. The prognostic value of peritumoral regulatory T cells and its correlation with intratumoral cyclooxygenase-2 expression in clear cell renal cell carcinoma. BJU Int. 2009;103(3):399-405.

375. Liotta F, Gacci M, Frosali F, et al. Frequency of regulatory T cells in peripheral blood and in tumour-infiltrating lymphocytes correlates with poor prognosis in renal cell carcinoma. BJU Int. 2011;107(9):1500-6.

376. Kang MJ, Kim KM, Bae JS, et al. Tumor-infiltrating PD1-Positive Lymphocytes and FoxP3-Positive Regulatory T Cells Predict Distant Metastatic Relapse and Survival of Clear Cell Renal Cell Carcinoma. Transl Oncol. 2013;6(3):282-9.

377. Dey M, Chang AL, Wainwright DA, et al. Heme oxygenase-1 protects regulatory T cells from hypoxia-induced cellular stress in an experimental mouse brain tumor model. J Neuroimmunol. 2014;266(1-2):33-42.

378. Fox SB, Launchbury R, Bates GJ, et al. The number of regulatory T cells in prostate cancer is associated with the androgen receptor and hypoxia-inducible factor (HIF)-2alpha but not HIF-1alpha. Prostate. 2007;67(6):623-9.

379. Giatromanolaki A, Bates GJ, Koukourakis MI, et al. The presence of tumor-infiltrating FOXP3+ lymphocytes correlates with intratumoral angiogenesis in endometrial cancer. Gynecol Oncol. 2008;110(2):216-21.

380. Yan M, Jene N, Byrne D, et al. Recruitment of regulatory T cells is correlated with hypoxia-induced CXCR4 expression, and is associated with poor prognosis in basal-like breast cancers. Breast Cancer Res. 2011;13(2):R47.

381. Deng B, Zhu JM, Wang Y, et al. Intratumor hypoxia promotes immune tolerance by inducing regulatory T cells via TGF-beta1 in gastric cancer. PLoS One. 2013;8(5):e63777.

382. Giatromanolaki A, Harris AL, Banham AH, et al. Carbonic anhydrase 9 (CA9) expression in non-small-cell lung cancer: correlation with regulatory FOXP3+T-cell tumour stroma infiltration. Br J Cancer. 2020;122(8):1205-10.

383. Facciabene A, Peng X, Hagemann IS, et al. Tumour hypoxia promotes tolerance and angiogenesis via CCL28 and T(reg) cells. Nature. 2011;475(7355):226-30.

384. Ren L, Yu Y, Wang L, et al. Hypoxia-induced CCL28 promotes recruitment of regulatory T cells and tumor growth in liver cancer. Oncotarget. 2016;7(46):75763-73.

385. Hansen W, Hutzler M, Abel S, et al. Neuropilin 1 deficiency on CD4+Foxp3+ regulatory T cells impairs mouse melanoma growth. J Exp Med. 2012;209(11):2001-16.

386. Ben-Shoshan J, Maysel-Auslender S, Mor A, et al. Hypoxia controls CD4+CD25+ regulatory T-cell homeostasis via hypoxia-inducible factor-1alpha. Eur J Immunol. 2008;38(9):2412-8.

387. Wei J, Wu A, Kong LY, et al. Hypoxia potentiates glioma-mediated immunosuppression. PLoS One. 2011;6(1):e16195.

388. Hasmim M, Noman MZ, Messai Y, et al. Cutting edge: Hypoxia-induced Nanog favors the intratumoral infiltration of regulatory T cells and macrophages via direct regulation of TGF-beta1. J Immunol. 2013;191(12):5802-6.

389. Terme M, Pernot S, Marcheteau E, et al. VEGFA-VEGFR pathway blockade inhibits tumor-induced regulatory T-cell proliferation in colorectal cancer. Cancer Res. 2013;73(2):539-49.

390. Angelin A, Gil-de-Gomez L, Dahiya S, et al. Foxp3 Reprograms T Cell Metabolism to Function in Low-Glucose, High-Lactate Environments. Cell Metab. 2017;25(6):1282-93 e7.

391. Wang H, Franco F, Tsui YC, et al. CD36-mediated metabolic adaptation supports regulatory T cell survival and function in tumors. Nat Immunol. 2020;21(3):298-308.

392. Guan C, Ouyang D, Qiao Y, et al. CA9 transcriptional expression determines prognosis and tumour grade in tongue squamous cell carcinoma patients. J Cell Mol Med. 2020;24(10):5832-41.

393. Miska J, Lee-Chang C, Rashidi A, et al. HIF-1alpha Is a Metabolic Switch between Glycolytic-Driven Migration and Oxidative Phosphorylation-Driven Immunosuppression of Tregs in Glioblastoma. Cell Rep. 2019;27(1):226-37 e4.

394. Egeblad M, Ewald AJ, Askautrud HA, et al. Visualizing stromal cell dynamics in different tumor microenvironments by spinning disk confocal microscopy. Dis Model Mech. 2008;1(2-3):155-67.

395. Overacre-Delgoffe AE, Chikina M, Dadey RE, et al. Interferon-gamma Drives Treg Fragility to Promote Anti-tumor Immunity. Cell. 2017;169(6):1130-41 e11.

396. Spranger S, Spaapen RM, Zha Y, et al. Up-regulation of PD-L1, IDO, and T(regs) in the melanoma tumor microenvironment is driven by CD8(+) T cells. Sci Transl Med. 2013;5(200):200ra116.

397. Williams JB, Horton BL, Zheng Y, et al. The EGR2 targets LAG-3 and 4-1BB describe and regulate dysfunctional antigen-specific CD8+ T cells in the tumor microenvironment. J Exp Med. 2017;214(2):381-400.

398. Shand FH, Ueha S, Otsuji M, et al. Tracking of intertissue migration reveals the origins of tumor-infiltrating monocytes. Proc Natl Acad Sci U S A. 2014;111(21):7771-6.

399. Zhu Y, Herndon JM, Sojka DK, et al. Tissue-Resident Macrophages in Pancreatic Ductal Adenocarcinoma Originate from Embryonic Hematopoiesis and Promote Tumor Progression. Immunity. 2017;47(2):323-38 e6.

400. Loyher PL, Hamon P, Laviron M, et al. Macrophages of distinct origins contribute to tumor development in the lung. J Exp Med. 2018;215(10):2536-53.

401. DeNardo DG, Ruffell B. Macrophages as regulators of tumour immunity and immunotherapy. Nat Rev Immunol. 2019;19(6):369-82.

402. Collingridge DR, Hill SA, Chaplin DJ. Proportion of infiltrating IgG-binding immune cells predict for tumour hypoxia. Br J Cancer. 2001;84(5):626-30.

403. Wang SC, Hong JH, Hsueh C, et al. Tumor-secreted SDF-1 promotes glioma invasiveness and TAM tropism toward hypoxia in a murine astrocytoma model. Lab Invest. 2012;92(1):151-62.

404. Movahedi K, Schoonooghe S, Laoui D, et al. Nanobody-based targeting of the macrophage mannose receptor for effective in vivo imaging of tumor-associated macrophages. Cancer Res. 2012;72(16):4165-77.

405. Casazza A, Laoui D, Wenes M, et al. Impeding macrophage entry into hypoxic tumor areas by Sema3A/Nrp1 signaling blockade inhibits angiogenesis and restores antitumor immunity. Cancer Cell. 2013;24(6):695-709.

406. Laoui D, Van Overmeire E, Di Conza G, et al. Tumor hypoxia does not drive differentiation of tumor-associated macrophages but rather fine-tunes the M2-like macrophage population. Cancer Res. 2014;74(1):24-30.

407. Zhu G, Tang Y, Geng N, et al. HIF-alpha/MIF and NF-kappaB/IL-6 axes contribute to the recruitment of CD11b+Gr-1+ myeloid cells in hypoxic microenvironment of HNSCC. Neoplasia. 2014;16(2):168-79.

408. Zhang J, Cao J, Ma S, et al. Tumor hypoxia enhances Non-Small Cell Lung Cancer metastasis by selectively promoting macrophage M2 polarization through the activation of ERK signaling. Oncotarget. 2014;5(20):9664-77.

409. Wenes M, Shang M, Di Matteo M, et al. Macrophage Metabolism Controls Tumor Blood Vessel Morphogenesis and Metastasis. Cell Metab. 2016;24(5):701-15.

410. Jeong SK, Kim JS, Lee CG, et al. Tumor associated macrophages provide the survival resistance of tumor cells to hypoxic microenvironmental condition through IL-6 receptor-mediated signals. Immunobiology. 2017;222(1):55-65.

411. Carmona-Fontaine C, Deforet M, Akkari L, et al. Metabolic origins of spatial organization in the tumor microenvironment. Proc Natl Acad Sci U S A. 2017;114(11):2934-9.

412. Jeong H, Kim S, Hong BJ, et al. Tumor-Associated Macrophages Enhance Tumor Hypoxia and Aerobic Glycolysis. Cancer Res. 2019;79(4):795-806.

413. Aalipour A, Chuang HY, Murty S, et al. Engineered immune cells as highly sensitive cancer diagnostics. Nat Biotechnol. 2019;37(5):531-9.

414. Torres A, Casanova JF, Nistal M, et al. Quantification of immunocompetent cells in testicular germ cell tumours. Histopathology. 1997;30(1):23-30.

415. Volodko N, Reiner A, Rudas M, et al. Tumour-associated macrophages in breast cancer and their prognostic correlations. The Breast. 1998;7(2):99-105.

416. Matsumura M, Chiba Y, Lu C, et al. Platelet-derived endothelial cell growth factor/thymidine phosphorylase expression correlated with tumor angiogenesis and macrophage infiltration in colorectal cancer. Cancer Lett. 1998;128(1):55-63.

417. Leek RD, Landers RJ, Harris AL, et al. Necrosis correlates with high vascular density and focal macrophage infiltration in invasive carcinoma of the breast. Br J Cancer. 1999;79(5-6):991-5.

418. Salvesen HB, Akslen LA. Significance of tumour-associated macrophages, vascular endothelial growth factor and thrombospondin-1 expression for tumour angiogenesis and prognosis in endometrial carcinomas. Int J Cancer. 1999;84(5):538-43.

419. Hemmerlein B, Markus A, Wehner M, et al. Expression of acute and late-stage inflammatory antigens, c-fms, CSF-1, and human monocytic serine esterase 1, in tumor-associated macrophages of renal cell carcinomas. Cancer Immunol Immunother. 2000;49(9):485-92.

420. Onita T, Ji PG, Xuan JW, et al. Hypoxia-induced, perinecrotic expression of endothelial Per-ARNT-Sim domain protein-1/hypoxia-inducible factor-2alpha correlates with tumor progression, vascularization, and focal macrophage infiltration in bladder cancer. Clin Cancer Res. 2002;8(2):471-80.

421. Valkovic T, Dobrila F, Melato M, et al. Correlation between vascular endothelial growth factor, angiogenesis, and tumor-associated macrophages in invasive ductal breast carcinoma. Virchows Arch. 2002;440(6):583-8.

422. Li C, Shintani S, Terakado N, et al. Infiltration of tumor-associated macrophages in human oral squamous cell carcinoma. Oncol Rep. 2002;9(6):1219-23.

423. Ohta M, Kitadai Y, Tanaka S, et al. Monocyte chemoattractant protein-1 expression correlates with macrophage infiltration and tumor vascularity in human esophageal squamous cell carcinomas. Int J Cancer. 2002;102(3):220-4.

424. Ohno S, Inagawa H, Dhar DK, et al. The degree of macrophage infiltration into the cancer cell nest is a significant predictor of survival in gastric cancer patients. Anticancer Res. 2003;23(6D):5015-22.

425. Koga F, Kageyama Y, Kawakami S, et al. Prognostic significance of endothelial Per-Arnt-sim domain protein 1/hypoxia-inducible factor-2alpha expression in a subset of tumor associated macrophages in invasive bladder cancer. J Urol. 2004;171(3):1080-4.

426. Ohno S, Ohno Y, Suzuki N, et al. Correlation of histological localization of tumor-associated macrophages with clinicopathological features in endometrial cancer. Anticancer Res. 2004;24(5C):3335-42.

427. Tsutsui S, Yasuda K, Suzuki K, et al. Macrophage infiltration and its prognostic implications in breast cancer: the relationship with VEGF expression and microvessel density. Oncol Rep. 2005;14(2):425-31.

428. Varney ML, Johansson SL, Singh RK. Tumour-associated macrophage infiltration, neovascularization and aggressiveness in malignant melanoma: role of monocyte chemotactic protein-1 and vascular endothelial growth factor-A. Melanoma Res. 2005;15(5):417-25.

429. Vicioso L, Gonzalez FJ, Alvarez M, et al. Elevated serum levels of vascular endothelial growth factor are associated with tumor-associated macrophages in primary breast cancer. Am J Clin Pathol. 2006;125(1):111-8.

430. Bailey C, Negus R, Morris A, et al. Chemokine expression is associated with the accumulation of tumour associated macrophages (TAMs) and progression in human colorectal cancer. Clin Exp Metastasis. 2007;24(2):121-30.

431. Chai CY, Chen WT, Hung WC, et al. Hypoxia-inducible factor-1alpha expression correlates with focal macrophage infiltration, angiogenesis and unfavourable prognosis in urothelial carcinoma. J Clin Pathol. 2008;61(5):658-64.

432. Kawanaka T, Kubo A, Ikushima H, et al. Prognostic significance of HIF-2alpha expression on tumor infiltrating macrophages in patients with uterine cervical cancer undergoing radiotherapy. J Med Invest. 2008;55(1-2):78-86.

433. Ryder M, Ghossein RA, Ricarte-Filho JC, et al. Increased density of tumor-associated macrophages is associated with decreased survival in advanced thyroid cancer. Endocr Relat Cancer. 2008;15(4):1069-74.

434. Chen WT, Hung WC, Kang WY, et al. Overexpression of cyclooxygenase-2 in urothelial carcinoma in conjunction with tumor-associated-macrophage infiltration, hypoxia-inducible factor-1alpha expression, and tumor angiogenesis. APMIS. 2009;117(3):176-84.

435. Zhang W, Wang L, Zhou D, et al. Expression of tumor-associated macrophages and vascular endothelial growth factor correlates with poor prognosis of peripheral T-cell lymphoma, not otherwise specified. Leuk Lymphoma. 2011;52(1):46-52.

436. Muthana M, Giannoudis A, Scott SD, et al. Use of macrophages to target therapeutic adenovirus to human prostate tumors. Cancer Res. 2011;71(5):1805-15.

437. Cooper LA, Gutman DA, Chisolm C, et al. The tumor microenvironment strongly impacts master transcriptional regulators and gene expression class of glioblastoma. Am J Pathol. 2012;180(5):2108-19.

438. Jiang XF, Tang QL, Li HG, et al. Tumor-associated macrophages correlate with progesterone receptor loss in endometrial endometrioid adenocarcinoma. J Obstet Gynaecol Res. 2013;39(4):855-63.

439. Simionescu C, Margaritescu C, Stepan A, et al. Tumor angiogenesis, macrophages and mast cell microdensities in endometrioid endometrial carcinoma. Oncol Lett. 2013;6(2):415-20.

440. Xu L, Zhu Y, Chen L, et al. Prognostic value of diametrically polarized tumor-associated macrophages in renal cell carcinoma. Ann Surg Oncol. 2014;21(9):3142-50.

441. Mogoanta SS, Lungu C, Ilie C, et al. Peritumoral inflammatory reaction in colon cancer. Histological and immunohistochemical study. Rom J Morphol Embryol. 2014;55(4):1429-35.

442. Wen Z, Liu H, Li M, et al. Increased metabolites of 5-lipoxygenase from hypoxic ovarian cancer cells promote tumor-associated macrophage infiltration. Oncogene. 2015;34(10):1241-52.

443. Li N, Li Y, Li Z, et al. Hypoxia Inducible Factor 1 (HIF-1) Recruits Macrophage to Activate Pancreatic Stellate Cells in Pancreatic Ductal Adenocarcinoma. Int J Mol Sci. 2016;17(6).

444. Morita Y, Zhang R, Leslie M, et al. Pathologic evaluation of tumor-associated macrophage density and vessel inflammation in invasive breast carcinomas. Oncol Lett. 2017;14(2):2111-8.

445. Zhang WJ, Chen C, Zhou ZH, et al. Hypoxia-inducible factor-1 alpha Correlates with Tumor-Associated Macrophages Infiltration, Influences Survival of Gastric Cancer Patients. J Cancer. 2017;8(10):1818-25.

446. Zhang J, Zhang Q, Lou Y, et al. Hypoxia-inducible factor-1alpha/interleukin-1beta signaling enhances hepatoma epithelial-mesenchymal transition through macrophages in a hypoxic-inflammatory microenvironment. Hepatology. 2018;67(5):1872-89.

447. Annovazzi L, Mellai M, Bovio E, et al. Microglia immunophenotyping in gliomas. Oncol Lett. 2018;15(1):998-1006.

448. Lewis CE, Harney AS, Pollard JW. The Multifaceted Role of Perivascular Macrophages in Tumors. Cancer Cell. 2016;30(1):18-25.

449. Wyckoff JB, Wang Y, Lin EY, et al. Direct visualization of macrophage-assisted tumor cell intravasation in mammary tumors. Cancer Res. 2007;67(6):2649-56.

450. Harney AS, Arwert EN, Entenberg D, et al. Real-Time Imaging Reveals Local, Transient Vascular Permeability, and Tumor Cell Intravasation Stimulated by TIE2hi Macrophage-Derived VEGFA. Cancer Discov. 2015;5(9):932-43.

451. De Palma M, Venneri MA, Roca C, et al. Targeting exogenous genes to tumor angiogenesis by transplantation of genetically modified hematopoietic stem cells. Nat Med. 2003;9(6):789-95.

452. De Palma M, Venneri MA, Galli R, et al. Tie2 identifies a hematopoietic lineage of proangiogenic monocytes required for tumor vessel formation and a mesenchymal population of pericyte progenitors. Cancer Cell. 2005;8(3):211-26.

453. Venneri MA, De Palma M, Ponzoni M, et al. Identification of proangiogenic TIE2-expressing monocytes (TEMs) in human peripheral blood and cancer. Blood. 2007;109(12):5276-85.

454. Murdoch C, Tazzyman S, Webster S, et al. Expression of Tie-2 by human monocytes and their responses to angiopoietin-2. J Immunol. 2007;178(11):7405-11.

455. Coffelt SB, Tal AO, Scholz A, et al. Angiopoietin-2 regulates gene expression in TIE2-expressing monocytes and augments their inherent proangiogenic functions. Cancer Res. 2010;70(13):5270-80.

456. Mazzieri R, Pucci F, Moi D, et al. Targeting the ANG2/TIE2 axis inhibits tumor growth and metastasis by impairing angiogenesis and disabling rebounds of proangiogenic myeloid cells. Cancer Cell. 2011;19(4):512-26.

457. De Palma M, Mazzieri R, Politi LS, et al. Tumor-targeted interferon-alpha delivery by Tie2-expressing monocytes inhibits tumor growth and metastasis. Cancer Cell. 2008;14(4):299-311.

458. Pucci F, Venneri MA, Biziato D, et al. A distinguishing gene signature shared by tumor-infiltrating Tie2-expressing monocytes, blood "resident" monocytes, and embryonic macrophages suggests common functions and developmental relationships. Blood. 2009;114(4):901-14.

459. Coffelt SB, Chen YY, Muthana M, et al. Angiopoietin 2 stimulates TIE2-expressing monocytes to suppress T cell activation and to promote regulatory T cell expansion. J Immunol. 2011;186(7):4183-90.

460. Movahedi K, Laoui D, Gysemans C, et al. Different tumor microenvironments contain functionally distinct subsets of macrophages derived from Ly6C(high) monocytes. Cancer Res. 2010;70(14):5728-39.

461. Jerby-Arnon L, Shah P, Cuoco MS, et al. A Cancer Cell Program Promotes T Cell Exclusion and Resistance to Checkpoint Blockade. Cell. 2018;175(4):984-97 e24.

462. Chen XJ, Wu S, Yan RM, et al. The role of the hypoxia-Nrp-1 axis in the activation of M2-like tumor-associated macrophages in the tumor microenvironment of cervical cancer. Mol Carcinog. 2019;58(3):388-97.

463. Ma B, Cheng H, Mu C, et al. The SIAH2-NRF1 axis spatially regulates tumor microenvironment remodeling for tumor progression. Nat Commun. 2019;10(1):1034.

464. Prosniak M, Harshyne LA, Andrews DW, et al. Glioma grade is associated with the accumulation and activity of cells bearing M2 monocyte markers. Clin Cancer Res. 2013;19(14):3776-86.

465. Lima L, Oliveira D, Tavares A, et al. The predominance of M2-polarized macrophages in the stroma of low-hypoxic bladder tumors is associated with BCG immunotherapy failure. Urol Oncol. 2014;32(4):449-57.

466. Tripathi C, Tewari BN, Kanchan RK, et al. Macrophages are recruited to hypoxic tumor areas and acquire a pro-angiogenic M2-polarized phenotype via hypoxic cancer cell derived cytokines Oncostatin M and Eotaxin. Oncotarget. 2014;5(14):5350-68.

467. Cros J, Sbidian E, Posseme K, et al. Nestin expression on tumour vessels and tumour-infiltrating macrophages define a poor prognosis subgroup of pt1 clear cell renal cell carcinoma. Virchows Arch. 2016;469(3):331-7.

468. Kazantseva M, Eiholzer RA, Mehta S, et al. Elevation of the TP53 isoform Delta133p53beta in glioblastomas: an alternative to mutant p53 in promoting tumor development. J Pathol. 2018;246(1):77-88.

469. Sorensen MD, Dahlrot RH, Boldt HB, et al. Tumour-associated microglia/macrophages predict poor prognosis in high-grade gliomas and correlate with an aggressive tumour subtype. Neuropathol Appl Neurobiol. 2018;44(2):185-206.

470. Chen XJ, Deng YR, Wang ZC, et al. Hypoxia-induced ZEB1 promotes cervical cancer progression via CCL8-dependent tumour-associated macrophage recruitment. Cell Death Dis. 2019;10(7):508.

471. Maeda-Otsuka S, Kajihara I, Tasaki Y, et al. Hypoxia accelerates the progression of angiosarcoma through the regulation of angiosarcoma cells and tumor microenvironment. J Dermatol Sci. 2019;93(2):123-32.

472. Zhu X, Shen H, Yin X, et al. Macrophages derived exosomes deliver miR-223 to epithelial ovarian cancer cells to elicit a chemoresistant phenotype. J Exp Clin Cancer Res. 2019;38(1):81.

473. Zheng X, Weigert A, Reu S, et al. Spatial Density and Distribution of Tumor-Associated Macrophages Predict Survival in Non-Small Cell Lung Carcinoma. Cancer Res. 2020;80(20):4414-25.

474. Lewis JS, Landers RJ, Underwood JC, et al. Expression of vascular endothelial growth factor by macrophages is up-regulated in poorly vascularized areas of breast carcinomas. J Pathol. 2000;192(2):150-8.

475. Lin EY, Li JF, Bricard G, et al. Vascular endothelial growth factor restores delayed tumor progression in tumors depleted of macrophages. Mol Oncol. 2007;1(3):288-302.

476. Muramatsu M, Yamamoto S, Osawa T, et al. Vascular endothelial growth factor receptor-1 signaling promotes mobilization of macrophage lineage cells from bone marrow and stimulates solid tumor growth. Cancer Res. 2010;70(20):8211-21.

477. Du R, Lu KV, Petritsch C, et al. HIF1alpha induces the recruitment of bone marrow-derived vascular modulatory cells to regulate tumor angiogenesis and invasion. Cancer Cell. 2008;13(3):206-20.

478. Chaturvedi P, Gilkes DM, Takano N, et al. Hypoxia-inducible factor-dependent signaling between triple-negative breast cancer cells and mesenchymal stem cells promotes macrophage recruitment. Proc Natl Acad Sci U S A. 2014;111(20):E2120-9.

479. Colegio OR, Chu NQ, Szabo AL, et al. Functional polarization of tumour-associated macrophages by tumour-derived lactic acid. Nature. 2014;513(7519):559-63.

480. Zhang D, Tang Z, Huang H, et al. Metabolic regulation of gene expression by histone lactylation. Nature. 2019;574(7779):575-80.

481. Bohn T, Rapp S, Luther N, et al. Tumor immunoevasion via acidosis-dependent induction of regulatory tumor-associated macrophages. Nat Immunol. 2018;19(12):1319-29.

482. El-Kenawi A, Gatenbee C, Robertson-Tessi M, et al. Acidity promotes tumour progression by altering macrophage phenotype in prostate cancer. Br J Cancer. 2019;121(7):556-66.

483. Imtiyaz HZ, Williams EP, Hickey MM, et al. Hypoxia-inducible factor 2alpha regulates macrophage function in mouse models of acute and tumor inflammation. J Clin Invest. 2010;120(8):2699-714.

484. Doedens AL, Stockmann C, Rubinstein MP, et al. Macrophage expression of hypoxia-inducible factor-1 alpha suppresses T-cell function and promotes tumor progression. Cancer Res. 2010;70(19):7465-75.

485. Talks KL, Turley H, Gatter KC, et al. The expression and distribution of the hypoxia-inducible factors HIF-1alpha and HIF-2alpha in normal human tissues, cancers, and tumor-associated macrophages. Am J Pathol. 2000;157(2):411-21.

486. Giatromanolaki A, Koukourakis MI, Sivridis E, et al. Relation of hypoxia inducible factor 1 alpha and 2 alpha in operable non-small cell lung cancer to angiogenic/molecular profile of tumours and survival. Br J Cancer. 2001;85(6):881-90.

487. Burke B, Tang N, Corke KP, et al. Expression of HIF-1alpha by human macrophages: implications for the use of macrophages in hypoxia-regulated cancer gene therapy. J Pathol. 2002;196(2):204-12.

488. Leek RD, Talks KL, Pezzella F, et al. Relation of hypoxia-inducible factor-2 alpha (HIF-2 alpha) expression in tumor-infiltrative macrophages to tumor angiogenesis and the oxidative thymidine phosphorylase pathway in human breast cancer. Cancer Res. 2002;62(5):1326-9.

489. Stewart M, Talks K, Leek R, et al. Expression of angiogenic factors and hypoxia inducible factors HIF 1, HIF 2 and CA IX in non-Hodgkin's lymphoma. Histopathology. 2002;40(3):253-60.

490. Beasley NJ, Leek R, Alam M, et al. Hypoxia-inducible factors HIF-1alpha and HIF-2alpha in head and neck cancer: relationship to tumor biology and treatment outcome in surgically resected patients. Cancer Res. 2002;62(9):2493-7.

491. Xia G, Kageyama Y, Hayashi T, et al. Positive expression of HIF-2alpha/EPAS1 in invasive bladder cancer. Urology. 2002;59(5):774-8.

492. Hui EP, Chan AT, Pezzella F, et al. Coexpression of hypoxia-inducible factors 1alpha and 2alpha, carbonic anhydrase IX, and vascular endothelial growth factor in nasopharyngeal carcinoma and relationship to survival. Clin Cancer Res. 2002;8(8):2595-604.

493. Bangoura G, Yang LY, Huang GW, et al. Expression of HIF-2alpha/EPAS1 in hepatocellular carcinoma. World J Gastroenterol. 2004;10(4):525-30.

494. Couvelard A, O'Toole D, Leek R, et al. Expression of hypoxia-inducible factors is correlated with the presence of a fibrotic focus and angiogenesis in pancreatic ductal adenocarcinomas. Histopathology. 2005;46(6):668-76.

495. Winter SC, Shah KA, Han C, et al. The relation between hypoxia-inducible factor (HIF)-1alpha and HIF-2alpha expression with anemia and outcome in surgically treated head and neck cancer. Cancer. 2006;107(4):757-66.

496. Osada R, Horiuchi A, Kikuchi N, et al. Expression of hypoxia-inducible factor 1alpha, hypoxia-inducible factor 2alpha, and von Hippel-Lindau protein in epithelial ovarian neoplasms and allelic loss of von Hippel-Lindau gene: nuclear expression of hypoxia-inducible factor 1alpha is an independent prognostic factor in ovarian carcinoma. Hum Pathol. 2007;38(9):1310-20.

497. Bangoura G, Liu ZS, Qian Q, et al. Prognostic significance of HIF-2alpha/EPAS1 expression in hepatocellular carcinoma. World J Gastroenterol. 2007;13(23):3176-82.

498. Hughes R, Qian BZ, Rowan C, et al. Perivascular M2 Macrophages Stimulate Tumor Relapse after Chemotherapy. Cancer Res. 2015;75(17):3479-91.

499. Wang Q, He Z, Huang M, et al. Vascular niche IL-6 induces alternative macrophage activation in glioblastoma through HIF-2alpha. Nat Commun. 2018;9(1):559.

500. Rojas A, Delgado-Lopez F, Perez-Castro R, et al. HMGB1 enhances the protumoral activities of M2 macrophages by a RAGE-dependent mechanism. Tumour Biol. 2016;37(3):3321-9.

501. Huber R, Meier B, Otsuka A, et al. Tumour hypoxia promotes melanoma growth and metastasis via High Mobility Group Box-1 and M2-like macrophages. Sci Rep. 2016;6:29914.

502. Jiang J, Wang GZ, Wang Y, et al. Hypoxia-induced HMGB1 expression of HCC promotes tumor invasiveness and metastasis via regulating macrophage-derived IL-6. Exp Cell Res. 2018;367(1):81-8.

503. Yu S, Li Q, Yu Y, et al. Activated HIF1alpha of tumor cells promotes chemoresistance development via recruiting GDF15-producing tumor-associated macrophages in gastric cancer. Cancer Immunol Immunother. 2020;69(10):1973-87.

504. Araya P, Romero J, Delgado-Lopez F, et al. HMGB1 decreases CCR-2 expression and migration of M2 macrophages under hypoxia. Inflamm Res. 2019;68(8):639-42.

505. Chiang CS, Fu SY, Wang SC, et al. Irradiation promotes an M2 macrophage phenotype in tumor hypoxia. Front Oncol. 2012;2:89.

506. Shay JE, Imtiyaz HZ, Sivanand S, et al. Inhibition of hypoxia-inducible factors limits tumor progression in a mouse model of colorectal cancer. Carcinogenesis. 2014;35(5):1067-77.

507. Yin M, Guo Y, Hu R, et al. Potent BRD4 inhibitor suppresses cancer cell-macrophage interaction. Nat Commun. 2020;11(1):1833.

508. Na YR, Yoon YN, Son DI, et al. Cyclooxygenase-2 inhibition blocks M2 macrophage differentiation and suppresses metastasis in murine breast cancer model. PLoS One. 2013;8(5):e63451.

509. Dubey P, Shrivastava R, Tripathi C, et al. Cyclooxygenase-2 inhibition attenuates hypoxic cancer cells induced M2-polarization of macrophages. Cell Mol Biol (Noisy-le-grand). 2014;60(3):10-5.

510. Griffiths L, Binley K, Iqball S, et al. The macrophage - a novel system to deliver gene therapy to pathological hypoxia. Gene Ther. 2000;7(3):255-62.

511. Owen MR, Stamper IJ, Muthana M, et al. Mathematical modeling predicts synergistic antitumor effects of combining a macrophage-based, hypoxia-targeted gene therapy with chemotherapy. Cancer Res. 2011;71(8):2826-37.

512. Muthana M, Rodrigues S, Chen YY, et al. Macrophage delivery of an oncolytic virus abolishes tumor regrowth and metastasis after chemotherapy or irradiation. Cancer Res. 2013;73(2):490-5.

513. An L, Wang Y, Lin J, et al. Macrophages-Mediated Delivery of Small Gold Nanorods for Tumor Hypoxia Photoacoustic Imaging and Enhanced Photothermal Therapy. ACS Appl Mater Interfaces. 2019;11(17):15251-61.

514. Lamers CH, Sleijfer S, van Steenbergen S, et al. Treatment of metastatic renal cell carcinoma with CAIX CAR-engineered T cells: clinical evaluation and management of on-target toxicity. Mol Ther. 2013;21(4):904-12.

515. Juillerat A, Marechal A, Filhol JM, et al. An oxygen sensitive self-decision making engineered CAR T-cell. Sci Rep. 2017;7:39833.

516. Clever D, Roychoudhuri R, Constantinides MG, et al. Oxygen Sensing by T Cells Establishes an Immunologically Tolerant Metastatic Niche. Cell. 2016;166(5):1117-31 e14.

517. Bull JA, Macklin PS, Quaiser T, et al. Combining multiple spatial statistics enhances the description of immune cell localisation within tumours. Sci Rep. 2020;10(1):18624.

518. Wang CW, Ka SM, Chen A. Robust image registration of biological microscopic images. Sci Rep. 2014;4:6050.

519. Jankovic B, Aquino-Parsons C, Raleigh JA, et al. Comparison between pimonidazole binding, oxygen electrode measurements, and expression of endogenous hypoxia markers in cancer of the uterine cervix. Cytometry B Clin Cytom. 2006;70(2):45-55.

520. Decalf J, Albert ML, Ziai J. New tools for pathology: a user's review of a highly multiplexed method for in situ analysis of protein and RNA expression in tissue. J Pathol. 2019;247(5):650-61.

521. Tan WCC, Nerurkar SN, Cai HY, et al. Overview of multiplex immunohistochemistry/immunofluorescence techniques in the era of cancer immunotherapy. Cancer Commun (Lond). 2020;40(4):135-53.

522. Lu S, Stein JE, Rimm DL, et al. Comparison of Biomarker Modalities for Predicting Response to PD-1/PD-L1 Checkpoint Blockade: A Systematic Review and Meta-analysis. JAMA Oncol. 2019.

523. Hutchison GJ, Valentine HR, Loncaster JA, et al. Hypoxia-inducible factor 1alpha expression as an intrinsic marker of hypoxia: correlation with tumor oxygen, pimonidazole measurements, and outcome in locally advanced carcinoma of the cervix. Clin Cancer Res. 2004;10(24):8405-12.

524. Delahunt B, Eble JN, Egevad L, et al. Grading of renal cell carcinoma. Histopathology. 2019;74(1):4-17.

525. Sengupta S, Lohse CM, Leibovich BC, et al. Histologic coagulative tumor necrosis as a prognostic indicator of renal cell carcinoma aggressiveness. Cancer. 2005;104(3):511-20.

526. Wigerup C, Pahlman S, Bexell D. Therapeutic targeting of hypoxia and hypoxia-inducible factors in cancer. Pharmacol Ther. 2016;164:152-69.

527. Dewhirst MW, Mowery YM, Mitchell JB, et al. Rationale for hypoxia assessment and amelioration for precision therapy and immunotherapy studies. J Clin Invest. 2019;129(2):489-91.

528. Overgaard J. Hypoxic modification of radiotherapy in squamous cell carcinoma of the head and neck--a systematic review and meta-analysis. Radiother Oncol. 2011;100(1):22-32.

529. Henke M, Laszig R, Rube C, et al. Erythropoietin to treat head and neck cancer patients with anaemia undergoing radiotherapy: randomised, double-blind, placebo-controlled trial. Lancet. 2003;362(9392):1255-60.

530. Debeljak N, Solar P, Sytkowski AJ. Erythropoietin and cancer: the unintended consequences of anemia correction. Front Immunol. 2014;5:563.

531. Szenajch J, Wcislo G, Jeong JY, et al. The role of erythropoietin and its receptor in growth, survival and therapeutic response of human tumor cells: From clinic to bench - a critical review. Biochim Biophys Acta. 2010;1806(1):82-95.

532. Thews O, Vaupel P. Spatial oxygenation profiles in tumors during normo- and hyperbaric hyperoxia. Strahlenther Onkol. 2015;191(11):875-82.

533. Churchill-Davidson I, Sanger C, Thomlinson RH. High-pressure oxygen and radiotherapy. Lancet. 1955;268(6874):1091-5.

534. Moen I, Stuhr LE. Hyperbaric oxygen therapy and cancer--a review. Target Oncol. 2012;7(4):233-42.

535. Bennett MH, Feldmeier J, Smee R, et al. Hyperbaric oxygenation for tumour sensitisation to radiotherapy. Cochrane Database Syst Rev. 2012(4):CD005007.

536. Tobin DA. Explosive decompression in a hyperbaric oxygen chamber. Am J Roentgenol Radium Ther Nucl Med. 1971;111(3):622-4.

537. Falk SJ, Ward R, Bleehen NM. The influence of carbogen breathing on tumour tissue oxygenation in man evaluated by computerised p02 histography. Br J Cancer. 1992;66(5):919-24.

538. Horsman MR, Brown JM, Hirst VK, et al. Mechanism of action of the selective tumor radiosensitizer nicotinamide. Int J Radiat Oncol Biol Phys. 1988;15(3):685-90.

539. Chaplin DJ, Horsman MR, Trotter MJ. Effect of nicotinamide on the microregional heterogeneity of oxygen delivery within a murine tumor. J Natl Cancer Inst. 1990;82(8):672-6.

540. Kaanders JH, Bussink J, van der Kogel AJ. ARCON: a novel biology-based approach in radiotherapy. Lancet Oncol. 2002;3(12):728-37.

541. Janssens GO, Rademakers SE, Terhaard CH, et al. Improved recurrence-free survival with ARCON for anemic patients with laryngeal cancer. Clin Cancer Res. 2014;20(5):1345-54.

542. Jones LW, Viglianti BL, Tashjian JA, et al. Effect of aerobic exercise on tumor physiology in an animal model of human breast cancer. J Appl Physiol (1985). 2010;108(2):343-8.

543. Jones LW, Antonelli J, Masko EM, et al. Exercise modulation of the host-tumor interaction in an orthotopic model of murine prostate cancer. J Appl Physiol (1985). 2012;113(2):263-72.

544. McCullough DJ, Nguyen LM, Siemann DW, et al. Effects of exercise training on tumor hypoxia and vascular function in the rodent preclinical orthotopic prostate cancer model. J Appl Physiol (1985). 2013;115(12):1846-54.

545. Betof AS, Lascola CD, Weitzel D, et al. Modulation of murine breast tumor vascularity, hypoxia and chemotherapeutic response by exercise. J Natl Cancer Inst. 2015;107(5).

546. Gallez B, Neveu MA, Danhier P, et al. Manipulation of tumor oxygenation and radiosensitivity through modification of cell respiration. A critical review of approaches and imaging biomarkers for therapeutic guidance. Biochim Biophys Acta Bioenerg. 2017;1858(8):700-11.

547. Kallet RH, Matthay MA. Hyperoxic acute lung injury. Respir Care. 2013;58(1):123-41.

548. Zangl Q, Martignoni A, Jackson SH, et al. Postoperative hyperoxia (60%) worsens hepatic injury in mice. Anesthesiology. 2014;121(6):1217-25.

549. Secomb TW, Hsu R, Ong ET, et al. Analysis of the effects of oxygen supply and demand on hypoxic fraction in tumors. Acta Oncol. 1995;34(3):313-6.

550. Diepart C, Karroum O, Magat J, et al. Arsenic trioxide treatment decreases the oxygen consumption rate of tumor cells and radiosensitizes solid tumors. Cancer Res. 2012;72(2):482-90.

551. Benej M, Hong X, Vibhute S, et al. Papaverine and its derivatives radiosensitize solid tumors by inhibiting mitochondrial metabolism. Proc Natl Acad Sci U S A. 2018;115(42):10756-61.

552. Heinz S, Freyberger A, Lawrenz B, et al. Mechanistic Investigations of the Mitochondrial Complex I Inhibitor Rotenone in the Context of Pharmacological and Safety Evaluation. Sci Rep. 2017;7:45465.

553. Fokas E, Im JH, Hill S, et al. Dual inhibition of the PI3K/mTOR pathway increases tumor radiosensitivity by normalizing tumor vasculature. Cancer Res. 2012;72(1):239-48.

554. Kelly CJ, Hussien K, Fokas E, et al. Regulation of O2 consumption by the PI3K and mTOR pathways contributes to tumor hypoxia. Radiother Oncol. 2014;111(1):72-80.

555. McGowan DR, Skwarski M, Bradley KM, et al. Buparlisib with thoracic radiotherapy and its effect on tumour hypoxia: A phase I study in patients with advanced non-small cell lung carcinoma. Eur J Cancer. 2019;113:87-95.

556. Crokart N, Radermacher K, Jordan BF, et al. Tumor radiosensitization by antiinflammatory drugs: evidence for a new mechanism involving the oxygen effect. Cancer Res. 2005;65(17):7911-6.

557. Crokart N, Jordan BF, Baudelet C, et al. Glucocorticoids modulate tumor radiation response through a decrease in tumor oxygen consumption. Clin Cancer Res. 2007;13(2 Pt 1):630-5.

558. Zannella VE, Dal Pra A, Muaddi H, et al. Reprogramming metabolism with metformin improves tumor oxygenation and radiotherapy response. Clin Cancer Res. 2013;19(24):6741-50.

559. Chowdhury S, Yung E, Pintilie M, et al. MATE2 Expression Is Associated with Cancer Cell Response to Metformin. PLoS One. 2016;11(12):e0165214.

560. Scharping NE, Menk AV, Whetstone RD, et al. Efficacy of PD-1 Blockade Is Potentiated by Metformin-Induced Reduction of Tumor Hypoxia. Cancer Immunol Res. 2017;5(1):9-16.

561. Hurwitz H, Fehrenbacher L, Novotny W, et al. Bevacizumab plus irinotecan, fluorouracil, and leucovorin for metastatic colorectal cancer. N Engl J Med. 2004;350(23):2335-42.

562. Jain RK. Normalizing tumor vasculature with anti-angiogenic therapy: a new paradigm for combination therapy. Nat Med. 2001;7(9):987-9.

563. Jain RK. Normalization of tumor vasculature: an emerging concept in antiangiogenic therapy. Science. 2005;307(5706):58-62.

564. Tong RT, Boucher Y, Kozin SV, et al. Vascular normalization by vascular endothelial growth factor receptor 2 blockade induces a pressure gradient across the vasculature and improves drug penetration in tumors. Cancer Res. 2004;64(11):3731-6.

565. Winkler F, Kozin SV, Tong RT, et al. Kinetics of vascular normalization by VEGFR2 blockade governs brain tumor response to radiation: role of oxygenation, angiopoietin-1, and matrix metalloproteinases. Cancer Cell. 2004;6(6):553-63.

566. Park JS, Kim IK, Han S, et al. Normalization of Tumor Vessels by Tie2 Activation and Ang2 Inhibition Enhances Drug Delivery and Produces a Favorable Tumor Microenvironment. Cancer Cell. 2016;30(6):953-67.

567. Batchelor TT, Gerstner ER, Emblem KE, et al. Improved tumor oxygenation and survival in glioblastoma patients who show increased blood perfusion after cediranib and chemoradiation. Proc Natl Acad Sci U S A. 2013;110(47):19059-64.

568. Martin JD, Seano G, Jain RK. Normalizing Function of Tumor Vessels: Progress, Opportunities, and Challenges. Annu Rev Physiol. 2019;81:505-34.

569. Hatfield SM, Kjaergaard J, Lukashev D, et al. Systemic oxygenation weakens the hypoxia and hypoxia inducible factor 1alpha-dependent and extracellular adenosine-mediated tumor protection. J Mol Med (Berl). 2014;92(12):1283-92.

570. Raskovalova T, Huang X, Sitkovsky M, et al. Gs protein-coupled adenosine receptor signaling and lytic function of activated NK cells. J Immunol. 2005;175(7):4383-91.

571. Wing K, Onishi Y, Prieto-Martin P, et al. CTLA-4 control over Foxp3+ regulatory T cell function. Science. 2008;322(5899):271-5.

572. Song M, Liu T, Shi C, et al. Bioconjugated Manganese Dioxide Nanoparticles Enhance Chemotherapy Response by Priming Tumor-Associated Macrophages toward M1-like Phenotype and Attenuating Tumor Hypoxia. ACS Nano. 2016;10(1):633-47.

573. Zou MZ, Liu WL, Li CX, et al. A Multifunctional Biomimetic Nanoplatform for Relieving Hypoxia to Enhance Chemotherapy and Inhibit the PD-1/PD-L1 Axis. Small. 2018;14(28):e1801120.

574. Meng L, Cheng Y, Tong X, et al. Tumor Oxygenation and Hypoxia Inducible Factor-1 Functional Inhibition via a Reactive Oxygen Species Responsive Nanoplatform for Enhancing Radiation Therapy and Abscopal Effects. ACS Nano. 2018;12(8):8308-22.

575. Song X, Xu J, Liang C, et al. Self-Supplied Tumor Oxygenation through Separated Liposomal Delivery of H2O2 and Catalase for Enhanced Radio-Immunotherapy of Cancer. Nano Lett. 2018;18(10):6360-8.

576. Chen Q, Chen J, Yang Z, et al. Nanoparticle-Enhanced Radiotherapy to Trigger Robust Cancer Immunotherapy. Adv Mater. 2019;31(10):e1802228.

577. Chen Z, Liu L, Liang R, et al. Bioinspired Hybrid Protein Oxygen Nanocarrier Amplified Photodynamic Therapy for Eliciting Anti-tumor Immunity and Abscopal Effect. ACS Nano. 2018;12(8):8633-45.

578. Xing L, Gong JH, Wang Y, et al. Hypoxia alleviation-triggered enhanced photodynamic therapy in combination with IDO inhibitor for preferable cancer therapy. Biomaterials. 2019;206:170-82.

579. Wang T, Zhang H, Han Y, et al. Light-Enhanced O2-Evolving Nanoparticles Boost Photodynamic Therapy To Elicit Antitumor Immunity. ACS Appl Mater Interfaces. 2019;11(18):16367-79.

580. Zhou TJ, Xing L, Fan YT, et al. Inhibition of breast cancer proliferation and metastasis by strengthening host immunity with a prolonged oxygen-generating phototherapy hydrogel. J Control Release. 2019;309:82-93.

581. Li W, Yang J, Luo L, et al. Targeting photodynamic and photothermal therapy to the endoplasmic reticulum enhances immunogenic cancer cell death. Nat Commun. 2019;10(1):3349.

582. Liu Y, Pan Y, Cao W, et al. A tumor microenvironment responsive biodegradable CaCO3/MnO2- based nanoplatform for the enhanced photodynamic therapy and improved PD-L1 immunotherapy. Theranostics. 2019;9(23):6867-84.

583. Shen Z, Xia J, Ma Q, et al. Tumor Microenvironment-triggered Nanosystems as dual-relief Tumor Hypoxia Immunomodulators for enhanced Phototherapy. Theranostics. 2020;10(20):9132-52.

584. Hei Y, Teng B, Zeng Z, et al. Multifunctional Immunoliposomes Combining Catalase and PD-L1 Antibodies Overcome Tumor Hypoxia and Enhance Immunotherapeutic Effects Against Melanoma. Int J Nanomedicine. 2020;15:1677-91.

585. Bromage DI, Yellon DM. The pleiotropic effects of metformin: time for prospective studies. Cardiovasc Diabetol. 2015;14:109.

586. Schulten HJ. Pleiotropic Effects of Metformin on Cancer. Int J Mol Sci. 2018;19(10).

587. Prattichizzo F, Giuliani A, Mensa E, et al. Pleiotropic effects of metformin: Shaping the microbiome to manage type 2 diabetes and postpone ageing. Ageing Res Rev. 2018;48:87-98.

588. Eikawa S, Nishida M, Mizukami S, et al. Immune-mediated antitumor effect by type 2 diabetes drug, metformin. Proc Natl Acad Sci U S A. 2015;112(6):1809-14.

589. Kim SH, Li M, Trousil S, et al. Phenformin Inhibits Myeloid-Derived Suppressor Cells and Enhances the Anti-Tumor Activity of PD-1 Blockade in Melanoma. J Invest Dermatol. 2017;137(8):1740-8.

590. Kunisada Y, Eikawa S, Tomonobu N, et al. Attenuation of CD4(+)CD25(+) Regulatory T Cells in the Tumor Microenvironment by Metformin, a Type 2 Diabetes Drug. EBioMedicine. 2017;25:154-64.

591. Wang JC, Sun X, Ma Q, et al. Metformin's antitumour and anti-angiogenic activities are mediated by skewing macrophage polarization. J Cell Mol Med. 2018.

592. Pereira FV, Melo ACL, Low JS, et al. Metformin exerts antitumor activity via induction of multiple death pathways in tumor cells and activation of a protective immune response. Oncotarget. 2018;9(40):25808-25.

593. Cha JH, Yang WH, Xia W, et al. Metformin Promotes Antitumor Immunity via Endoplasmic-Reticulum-Associated Degradation of PD-L1. Mol Cell. 2018;71(4):606-20 e7.

594. Yin X, Han S, Song C, et al. Metformin enhances gefitinib efficacy by interfering with interactions between tumor-associated macrophages and head and neck squamous cell carcinoma cells. Cell Oncol (Dordr). 2019;42(4):459-75.

595. Amin D, Richa T, Mollaee M, et al. Metformin Effects on FOXP3(+) and CD8(+) T Cell Infiltrates of Head and Neck Squamous Cell Carcinoma. Laryngoscope. 2020;130(9):E490-E8.

596. Curry JM, Johnson J, Mollaee M, et al. Metformin Clinical Trial in HPV+ and HPV- Head and Neck Squamous Cell Carcinoma: Impact on Cancer Cell Apoptosis and Immune Infiltrate. Front Oncol. 2018;8:436.

597. Li L, Wang L, Li J, et al. Metformin-Induced Reduction of CD39 and CD73 Blocks Myeloid-Derived Suppressor Cell Activity in Patients with Ovarian Cancer. Cancer Res. 2018;78(7):1779-91.

598. Gabrilovich DI, Ishida T, Nadaf S, et al. Antibodies to vascular endothelial growth factor enhance the efficacy of cancer immunotherapy by improving endogenous dendritic cell function. Clin Cancer Res. 1999;5(10):2963-70.

599. Schmittnaegel M, Rigamonti N, Kadioglu E, et al. Dual angiopoietin-2 and VEGFA inhibition elicits antitumor immunity that is enhanced by PD-1 checkpoint blockade. Sci Transl Med. 2017;9(385).

600. Allen E, Jabouille A, Rivera LB, et al. Combined antiangiogenic and anti-PD-L1 therapy stimulates tumor immunity through HEV formation. Sci Transl Med. 2017;9(385).

601. Zhao S, Ren S, Jiang T, et al. Low-Dose Apatinib Optimizes Tumor Microenvironment and Potentiates Antitumor Effect of PD-1/PD-L1 Blockade in Lung Cancer. Cancer Immunol Res. 2019;7(4):630-43.

602. Tian L, Goldstein A, Wang H, et al. Mutual regulation of tumour vessel normalization and immunostimulatory reprogramming. Nature. 2017;544(7649):250-4.

603. Zheng X, Fang Z, Liu X, et al. Increased vessel perfusion predicts the efficacy of immune checkpoint blockade. J Clin Invest. 2018;128(5):2104-15.

604. Travis WD, Brambilla E, Nicholson AG, et al. The 2015 World Health Organization Classification of Lung Tumors: Impact of Genetic, Clinical and Radiologic Advances Since the 2004 Classification. J Thorac Oncol. 2015;10(9):1243-60.

605. Li C, Lu HJ, Na FF, et al. Prognostic role of hypoxic inducible factor expression in non-small cell lung cancer: a meta-analysis. Asian Pac J Cancer Prev. 2013;14(6):3607-12.

606. Ren W, Mi D, Yang K, et al. The expression of hypoxia-inducible factor-1alpha and its clinical significance in lung cancer: a systematic review and meta-analysis. Swiss Med Wkly. 2013;143:w13855.

607. Yang SL, Ren QG, Wen L, et al. Clinicopathological and prognostic significance of hypoxia-inducible factor-1 alpha in lung cancer: a systematic review with meta-analysis. J Huazhong Univ Sci Technolog Med Sci. 2016;36(3):321-7.

608. Gao ZJ, Wang Y, Yuan WD, et al. HIF-2alpha not HIF-1alpha overexpression confers poor prognosis in non-small cell lung cancer. Tumour Biol. 2017;39(6):1010428317709637.

609. Salem A, Asselin MC, Reymen B, et al. Targeting Hypoxia to Improve Non-Small Cell Lung Cancer Outcome. J Natl Cancer Inst. 2018;110(1).

610. Ashton TM, Fokas E, Kunz-Schughart LA, et al. The anti-malarial atovaquone increases radiosensitivity by alleviating tumour hypoxia. Nat Commun. 2016;7:12308.

611. Aroldi F, Lord SR. Window of opportunity clinical trial designs to study cancer metabolism. Br J Cancer. 2020;122(1):45-51.

612. Ljungkvist AS, Bussink J, Kaanders JH, et al. Dynamics of tumor hypoxia measured with bioreductive hypoxic cell markers. Radiat Res. 2007;167(2):127-45.

613. Zeng P, Li H, Lu PH, et al. Prognostic value of CD146 in solid tumor: A Systematic Review and Meta-analysis. Sci Rep. 2017;7(1):4223.

614. Pusztaszeri MP, Seelentag W, Bosman FT. Immunohistochemical expression of endothelial markers CD31, CD34, von Willebrand factor, and Fli-1 in normal human tissues. J Histochem Cytochem. 2006;54(4):385-95.

615. Barsoum IB, Smallwood CA, Siemens DR, et al. A mechanism of hypoxia-mediated escape from adaptive immunity in cancer cells. Cancer Res. 2014;74(3):665-74.

616. Noman MZ, Desantis G, Janji B, et al. PD-L1 is a novel direct target of HIF-1alpha, and its blockade under hypoxia enhanced MDSC-mediated T cell activation. J Exp Med. 2014;211(5):781-90.

617. Skwarski M, McGowan DR, Belcher E, et al. Mitochondrial Inhibitor Atovaquone Increases Tumor Oxygenation and Inhibits Hypoxic Gene Expression in Patients with Non-Small Cell Lung Cancer. Clin Cancer Res. 2021.

618. Dhani NC, Serra S, Pintilie M, et al. Analysis of the intra- and intertumoral heterogeneity of hypoxia in pancreatic cancer patients receiving the nitroimidazole tracer pimonidazole. Br J Cancer. 2015;113(6):864-71.

619. Mayer A, Zahnreich S, Brieger J, et al. Downregulation of EGFR in hypoxic, diffusion-limited areas of squamous cell carcinomas of the head and neck. Br J Cancer. 2016;115(11):1351-8.

620. Giatromanolaki A, Koukourakis MI, Sivridis E, et al. Expression of hypoxia-inducible carbonic anhydrase-9 relates to angiogenic pathways and independently to poor outcome in non-small cell lung cancer. Cancer Res. 2001;61(21):7992-8.

621. Lee CH, Lee MK, Kang CD, et al. Differential expression of hypoxia inducible factor-1 alpha and tumor cell proliferation between squamous cell carcinomas and adenocarcinomas among operable non-small cell lung carcinomas. J Korean Med Sci. 2003;18(2):196-203.

622. Karetsi E, Ioannou MG, Kerenidi T, et al. Differential expression of hypoxia-inducible factor 1alpha in non-small cell lung cancer and small cell lung cancer. Clinics (Sao Paulo). 2012;67(12):1373-8.

623. Furukawa T, Miyata Y, Kushitani K, et al. Association between [18F]-fluoro-2-deoxyglucose uptake and expressions of hypoxia-induced factor 1alpha and glucose transporter 1 in non-small cell lung cancer. Jpn J Clin Oncol. 2015;45(12):1154-61.

624. Meijer TW, Schuurbiers OC, Kaanders JH, et al. Differences in metabolism between adeno- and squamous cell non-small cell lung carcinomas: spatial distribution and prognostic value of GLUT1 and MCT4. Lung Cancer. 2012;76(3):316-23.

625. Mandeville HC, Ng QS, Daley FM, et al. Operable non-small cell lung cancer: correlation of volumetric helical dynamic contrast-enhanced CT parameters with immunohistochemical markers of tumor hypoxia. Radiology. 2012;264(2):581-9.

626. Schuurbiers OC, Meijer TW, Kaanders JH, et al. Glucose metabolism in NSCLC is histology-specific and diverges the prognostic potential of 18FDG-PET for adenocarcinoma and squamous cell carcinoma. J Thorac Oncol. 2014;9(10):1485-93.

627. Koh YW, Lee SJ, Park SY. Differential expression and prognostic significance of GLUT1 according to histologic type of non-small-cell lung cancer and its association with volume-dependent parameters. Lung Cancer. 2017;104:31-7.

628. Goodwin J, Neugent ML, Lee SY, et al. The distinct metabolic phenotype of lung squamous cell carcinoma defines selective vulnerability to glycolytic inhibition. Nat Commun. 2017;8:15503.

629. Ilie M, Mazure NM, Hofman V, et al. High levels of carbonic anhydrase IX in tumour tissue and plasma are biomarkers of poor prognostic in patients with non-small cell lung cancer. Br J Cancer. 2010;102(11):1627-35.

630. Wykoff CC, Beasley NJ, Watson PH, et al. Hypoxia-inducible expression of tumor-associated carbonic anhydrases. Cancer Res. 2000;60(24):7075-83.

631. Weinberg SE, Singer BD, Steinert EM, et al. Mitochondrial complex III is essential for suppressive function of regulatory T cells. Nature. 2019;565(7740):495-9.

632. Geng Y, Shao Y, He W, et al. Prognostic Role of Tumor-Infiltrating Lymphocytes in Lung Cancer: a Meta-Analysis. Cell Physiol Biochem. 2015;37(4):1560-71.

633. Chen D, Sun X, Zhang X, et al. Targeting mitochondria by anthelmintic drug atovaquone sensitizes renal cell carcinoma to chemotherapy and immunotherapy. J Biochem Mol Toxicol. 2018;32(9):e22195.

634. Dong H, Strome SE, Salomao DR, et al. Tumor-associated B7-H1 promotes T-cell apoptosis: a potential mechanism of immune evasion. Nat Med. 2002;8(8):793-800.

635. Koh J, Jang JY, Keam B, et al. EML4-ALK enhances programmed cell death-ligand 1 expression in pulmonary adenocarcinoma via hypoxia-inducible factor (HIF)-1alpha and STAT3. Oncoimmunology. 2016;5(3):e1108514.

636. Zhao Y, Wang XX, Wu W, et al. EZH2 regulates PD-L1 expression via HIF-1alpha in non-small cell lung cancer cells. Biochem Biophys Res Commun. 2019;517(2):201-9.

637. Tung JN, Lin PL, Wang YC, et al. PD-L1 confers resistance to EGFR mutation-independent tyrosine kinase inhibitors in non-small cell lung cancer via upregulation of YAP1 expression. Oncotarget. 2018;9(4):4637-46.

638. Chang YL, Yang CY, Lin MW, et al. High co-expression of PD-L1 and HIF-1alpha correlates with tumour necrosis in pulmonary pleomorphic carcinoma. Eur J Cancer. 2016;60:125-35.

639. Kasahara N, Kaira K, Bao P, et al. Correlation of tumor-related immunity with 18F-FDG-PET in pulmonary squamous-cell carcinoma. Lung Cancer. 2018;119:71-7.

640. Kaira K, Shimizu K, Kitahara S, et al. 2-Deoxy-2-[fluorine-18] fluoro-d-glucose uptake on positron emission tomography is associated with programmed death ligand-1 expression in patients with pulmonary adenocarcinoma. Eur J Cancer. 2018;101:181-90.

641. Koh YW, Lee SJ, Han JH, et al. PD-L1 protein expression in non-small-cell lung cancer and its relationship with the hypoxia-related signaling pathways: A study based on immunohistochemistry and RNA sequencing data. Lung Cancer. 2019;129:41-7.

642. Cui Y, Li X, Du B, et al. PD-L1 in Lung Adenocarcinoma: Insights into the Role of (18)F-FDG PET/CT. Cancer Manag Res. 2020;12:6385-95.

643. Wang H, Li Z, Dong B, et al. Prognostic significance of PD-L1 expression and CD8+ T cell infiltration in pulmonary neuroendocrine tumors. Diagn Pathol. 2018;13(1):30.

644. Jreige M, Letovanec I, Chaba K, et al. (18)F-FDG PET metabolic-to-morphological volume ratio predicts PD-L1 tumour expression and response to PD-1 blockade in non-small-cell lung cancer. Eur J Nucl Med Mol Imaging. 2019;46(9):1859-68.

645. Guo R, Li Y, Wang Z, et al. Hypoxia-inducible factor-1alpha and nuclear factor-kappaB play important roles in regulating programmed cell death ligand 1 expression by epidermal growth factor receptor mutants in non-small-cell lung cancer cells. Cancer Sci. 2019;110(5):1665-75.

646. Shimizu K, Kaira K, Higuchi T, et al. Relationship Between Tumor Immune Markers and Fluorine-18-alpha-Methyltyrosine ([(18)F]FAMT) Uptake in Patients with Lung Cancer. Mol Imaging Biol. 2020;22(4):1078-86.

647. Kajiwara T, Tanaka T, Kukita K, et al. Hypoxia augments MHC class I antigen presentation via facilitation of ERO1-alpha-mediated oxidative folding in murine tumor cells. Eur J Immunol. 2016;46(12):2842-51.

648. Lopci E, Toschi L, Grizzi F, et al. Correlation of metabolic information on FDG-PET with tissue expression of immune markers in patients with non-small cell lung cancer (NSCLC) who are candidates for upfront surgery. Eur J Nucl Med Mol Imaging. 2016;43(11):1954-61.

649. Silva MA, Ryall KA, Wilm C, et al. PD-L1 immunostaining scoring for non-small cell lung cancer based on immunosurveillance parameters. PLoS One. 2018;13(6):e0196464.

650. Shima T, Shimoda M, Shigenobu T, et al. Infiltration of tumor-associated macrophages is involved in tumor programmed death-ligand 1 expression in early lung adenocarcinoma. Cancer Sci. 2020;111(2):727-38.

651. Jiang Z, Liu Z, Li M, et al. Increased glycolysis correlates with elevated immune activity in tumor immune microenvironment. EBioMedicine. 2019;42:431-42.

652. Vasaikar S, Huang C, Wang X, et al. Proteogenomic Analysis of Human Colon Cancer Reveals New Therapeutic Opportunities. Cell. 2019;177(4):1035-49 e19.

653. Cascone T, McKenzie JA, Mbofung RM, et al. Increased Tumor Glycolysis Characterizes Immune Resistance to Adoptive T Cell Therapy. Cell Metab. 2018;27(5):977-87 e4.

654. Premsrirut PK, Dow LE, Kim SY, et al. A rapid and scalable system for studying gene function in mice using conditional RNA interference. Cell. 2011;145(1):145-58.

655. Dow LE, Premsrirut PK, Zuber J, et al. A pipeline for the generation of shRNA transgenic mice. Nat Protoc. 2012;7(2):374-93.

656. Jaakkola P, Mole DR, Tian YM, et al. Targeting of HIF-alpha to the von Hippel-Lindau ubiquitylation complex by O2-regulated prolyl hydroxylation. Science. 2001;292(5516):468-72.

657. Ivan M, Kondo K, Yang H, et al. HIFalpha targeted for VHL-mediated destruction by proline hydroxylation: implications for O2 sensing. Science. 2001;292(5516):464-8.

658. Epstein AC, Gleadle JM, McNeill LA, et al. C. elegans EGL-9 and mammalian homologs define a family of dioxygenases that regulate HIF by prolyl hydroxylation. Cell. 2001;107(1):43-54.

659. Koivunen P, Kietzmann T. Hypoxia-Inducible Factor Prolyl 4-Hydroxylases and Metabolism. Trends Mol Med. 2018;24(12):1021-35.

660. Haase VH. HIF-prolyl hydroxylases as therapeutic targets in erythropoiesis and iron metabolism. Hemodial Int. 2017;21(Supplement 1):S110-24.

661. Chen N, Hao C, Peng X, et al. Roxadustat for Anemia in Patients with Kidney Disease Not Receiving Dialysis. N Engl J Med. 2019;381(11):1001-10.

662. Chen N, Hao C, Liu BC, et al. Roxadustat Treatment for Anemia in Patients Undergoing Long-Term Dialysis. N Engl J Med. 2019;381(11):1011-22.

663. Berra E, Benizri E, Ginouves A, et al. HIF prolyl-hydroxylase 2 is the key oxygen sensor setting low steady-state levels of HIF-1alpha in normoxia. EMBO J. 2003;22(16):4082-90.

664. Appelhoff RJ, Tian YM, Raval RR, et al. Differential function of the prolyl hydroxylases PHD1, PHD2, and PHD3 in the regulation of hypoxia-inducible factor. J Biol Chem. 2004;279(37):38458-65.

665. Cesta MF. Normal structure, function, and histology of mucosa-associated lymphoid tissue. Toxicol Pathol. 2006;34(5):599-608.

666. Seldin MF, D'Hoostelaere LA, Steinberg AD, et al. Allelic variants of Ly-5 in inbred and natural populations of mice. Immunogenetics. 1987;26(1-2):74-8.

667. Zebedee SL, Barritt DS, Raschke WC. Comparison of mouse Ly5a and Ly5b leucocyte common antigen alleles. Dev Immunol. 1991;1(4):243-54.

668. Kariko K, Bhuyan P, Capodici J, et al. Small interfering RNAs mediate sequence-independent gene suppression and induce immune activation by signaling through toll-like receptor 3. J Immunol. 2004;172(11):6545-9.

669. Nasr Z, Dow LE, Paquet M, et al. Suppression of eukaryotic initiation factor 4E prevents chemotherapy-induced alopecia. BMC Pharmacol Toxicol. 2013;14:58.

670. Miething C, Scuoppo C, Bosbach B, et al. PTEN action in leukaemia dictated by the tissue microenvironment. Nature. 2014;510(7505):402-6.

671. Bolden JE, Tasdemir N, Dow LE, et al. Inducible in vivo silencing of Brd4 identifies potential toxicities of sustained BET protein inhibition. Cell Rep. 2014;8(6):1919-29.

672. Ebbesen SH, Scaltriti M, Bialucha CU, et al. Pten loss promotes MAPK pathway dependency in HER2/neu breast carcinomas. Proc Natl Acad Sci U S A. 2016;113(11):3030-5.

673. Takeda K, Ho VC, Takeda H, et al. Placental but not heart defects are associated with elevated hypoxia-inducible factor alpha levels in mice lacking prolyl hydroxylase domain protein 2. Mol Cell Biol. 2006;26(22):8336-46.

674. Takeda K, Cowan A, Fong GH. Essential role for prolyl hydroxylase domain protein 2 in oxygen homeostasis of the adult vascular system. Circulation. 2007;116(7):774-81.

675. Takeda K, Aguila HL, Parikh NS, et al. Regulation of adult erythropoiesis by prolyl hydroxylase domain proteins. Blood. 2008;111(6):3229-35.

676. Minamishima YA, Moslehi J, Bardeesy N, et al. Somatic inactivation of the PHD2 prolyl hydroxylase causes polycythemia and congestive heart failure. Blood. 2008;111(6):3236-44.

677. Russell WL, Russell LB, Gower JS. Exceptional Inheritance of a Sex-Linked Gene in the Mouse Explained on the Basis That the X/O Sex-Chromosome Constitution Is Female. Proc Natl Acad Sci U S A. 1959;45(4):554-60.

678. Godfrey VL, Wilkinson JE, Russell LB. X-linked lymphoreticular disease in the scurfy (sf) mutant mouse. Am J Pathol. 1991;138(6):1379-87.

679. Godfrey VL, Wilkinson JE, Rinchik EM, et al. Fatal lymphoreticular disease in the scurfy (sf) mouse requires T cells that mature in a sf thymic environment: potential model for thymic education. Proc Natl Acad Sci U S A. 1991;88(13):5528-32.

680. Godfrey VL, Rouse BT, Wilkinson JE. Transplantation of T cell-mediated, lymphoreticular disease from the scurfy (sf) mouse. Am J Pathol. 1994;145(2):281-6.

681. Blair PJ, Bultman SJ, Haas JC, et al. CD4+CD8- T cells are the effector cells in disease pathogenesis in the scurfy (sf) mouse. J Immunol. 1994;153(8):3764-74.

682. Kanangat S, Blair P, Reddy R, et al. Disease in the scurfy (sf) mouse is associated with overexpression of cytokine genes. Eur J Immunol. 1996;26(1):161-5.

683. Zahorsky-Reeves JL, Wilkinson JE. The murine mutation scurfy (sf) results in an antigen-dependent lymphoproliferative disease with altered T cell sensitivity. Eur J Immunol. 2001;31(1):196-204.

684. Shull MM, Ormsby I, Kier AB, et al. Targeted disruption of the mouse transforming growth factor-beta 1 gene results in multifocal inflammatory disease. Nature. 1992;359(6397):693-9.

685. Kulkarni AB, Huh CG, Becker D, et al. Transforming growth factor beta 1 null mutation in mice causes excessive inflammatory response and early death. Proc Natl Acad Sci U S A. 1993;90(2):770-4.

686. Waterhouse P, Penninger JM, Timms E, et al. Lymphoproliferative disorders with early lethality in mice deficient in Ctla-4. Science. 1995;270(5238):985-8.

687. Tivol EA, Borriello F, Schweitzer AN, et al. Loss of CTLA-4 leads to massive lymphoproliferation and fatal multiorgan tissue destruction, revealing a critical negative regulatory role of CTLA-4. Immunity. 1995;3(5):541-7.

688. Brunkow ME, Jeffery EW, Hjerrild KA, et al. Disruption of a new forkhead/winged-helix protein, scurfin, results in the fatal lymphoproliferative disorder of the scurfy mouse. Nat Genet. 2001;27(1):68-73.

689. Hori S, Nomura T, Sakaguchi S. Control of regulatory T cell development by the transcription factor Foxp3. Science. 2003;299(5609):1057-61.

690. Fontenot JD, Gavin MA, Rudensky AY. Foxp3 programs the development and function of CD4+CD25+ regulatory T cells. Nat Immunol. 2003;4(4):330-6.

691. Khattri R, Cox T, Yasayko SA, et al. An essential role for Scurfin in CD4+CD25+ T regulatory cells. Nat Immunol. 2003;4(4):337-42.

692. Clark LB, Appleby MW, Brunkow ME, et al. Cellular and molecular characterization of the scurfy mouse mutant. J Immunol. 1999;162(5):2546-54.

693. Powell BR, Buist NR, Stenzel P. An X-linked syndrome of diarrhea, polyendocrinopathy, and fatal infection in infancy. J Pediatr. 1982;100(5):731-7.

694. Wildin RS, Ramsdell F, Peake J, et al. X-linked neonatal diabetes mellitus, enteropathy and endocrinopathy syndrome is the human equivalent of mouse scurfy. Nat Genet. 2001;27(1):18-20.

695. Bennett CL, Christie J, Ramsdell F, et al. The immune dysregulation, polyendocrinopathy, enteropathy, X-linked syndrome (IPEX) is caused by mutations of FOXP3. Nat Genet. 2001;27(1):20-1.

696. Sharma R, Jarjour WN, Zheng L, et al. Large functional repertoire of regulatory T-cell suppressible autoimmune T cells in scurfy mice. J Autoimmun. 2007;29(1):10-9.

697. Zhao DM, Thornton AM, DiPaolo RJ, et al. Activated CD4+CD25+ T cells selectively kill B lymphocytes. Blood. 2006;107(10):3925-32.

698. Misra N, Bayry J, Lacroix-Desmazes S, et al. Cutting edge: human CD4+CD25+ T cells restrain the maturation and antigen-presenting function of dendritic cells. J Immunol. 2004;172(8):4676-80.

699. Aschermann S, Lehmann CH, Mihai S, et al. B cells are critical for autoimmune pathology in Scurfy mice. Proc Natl Acad Sci U S A. 2013;110(47):19042-7.

700. Chung Y, Tanaka S, Chu F, et al. Follicular regulatory T cells expressing Foxp3 and Bcl-6 suppress germinal center reactions. Nat Med. 2011;17(8):983-8.

701. Leonardo SM, Josephson JA, Hartog NL, et al. Altered B cell development and anergy in the absence of Foxp3. J Immunol. 2010;185(4):2147-56.

702. Zhang W, Sharma R, Ju ST, et al. Deficiency in regulatory T cells results in development of antimitochondrial antibodies and autoimmune cholangitis. Hepatology. 2009;49(2):545-52.

703. Huter EN, Natarajan K, Torgerson TR, et al. Autoantibodies in scurfy mice and IPEX patients recognize keratin 14. J Invest Dermatol. 2010;130(5):1391-9.

704. Hadaschik EN, Wei X, Leiss H, et al. Regulatory T cell-deficient scurfy mice develop systemic autoimmune features resembling lupus-like disease. Arthritis Res Ther. 2015;17:35.

705. Higashiyama M, Hokari R, Hozumi H, et al. HIF-1 in T cells ameliorated dextran sodium sulfate-induced murine colitis. J Leukoc Biol. 2012;91(6):901-9.

706. Clambey ET, McNamee EN, Westrich JA, et al. Hypoxia-inducible factor-1 alpha-dependent induction of FoxP3 drives regulatory T-cell abundance and function during inflammatory hypoxia of the mucosa. Proc Natl Acad Sci U S A. 2012;109(41):E2784-93.

707. Wu J, Cui H, Zhu Z, et al. Effect of HIF1alpha on Foxp3 expression in CD4+ CD25- T lymphocytes. Microbiol Immunol. 2014;58(7):409-15.

708. Neildez-Nguyen TMA, Bigot J, Da Rocha S, et al. Hypoxic culture conditions enhance the generation of regulatory T cells. Immunology. 2015;144(3):431-43.

709. Yang S, Wang B, Guan C, et al. Foxp3+IL-17+ T cells promote development of cancer-initiating cells in colorectal cancer. J Leukoc Biol. 2011;89(1):85-91.

710. Ikejiri A, Nagai S, Goda N, et al. Dynamic regulation of Th17 differentiation by oxygen concentrations. Int Immunol. 2012;24(3):137-46.

711. Bollinger T, Gies S, Naujoks J, et al. HIF-1alpha- and hypoxia-dependent immune responses in human CD4+CD25high T cells and T helper 17 cells. J Leukoc Biol. 2014;96(2):305-12.

712. Hsiao HW, Hsu TS, Liu WH, et al. Deltex1 antagonizes HIF-1alpha and sustains the stability of regulatory T cells in vivo. Nat Commun. 2015;6:6353.

713. Shehade H, Acolty V, Moser M, et al. Cutting Edge: Hypoxia-Inducible Factor 1 Negatively Regulates Th1 Function. J Immunol. 2015;195(4):1372-6.

714. Yao Y, Wang L, Zhou J, et al. HIF-1alpha inhibitor echinomycin reduces acute graft-versus-host disease and preserves graft-versus-leukemia effect. J Transl Med. 2017;15(1):28.

715. Feldhoff LM, Rueda CM, Moreno-Fernandez ME, et al. IL-1beta induced HIF-1alpha inhibits the differentiation of human FOXP3(+) T cells. Sci Rep. 2017;7(1):465.

716. Lee JH, Elly C, Park Y, et al. E3 Ubiquitin Ligase VHL Regulates Hypoxia-Inducible Factor-1alpha to Maintain Regulatory T Cell Stability and Suppressive Capacity. Immunity. 2015;42(6):1062-74.

717. Ajouaou Y, Hussein H, Denanglaire S, et al. Expression of PHD2 regulates regulatory T cell capacity to control Th1-like inflammatory responses. 5th European Congress of Immunology, 2018; Amsterdam, Netherlands. p. 389.

718. Singh Y, Shi X, Zhang S, et al. Prolyl hydroxylase 3 (PHD3) expression augments the development of regulatory T cells. Mol Immunol. 2016;76:7-12.

719. Segelmark M, Hellmark T. Autoimmune kidney diseases. Autoimmun Rev. 2010;9(5):A366-71.

720. Courtney KD, Infante JR, Lam ET, et al. Phase I Dose-Escalation Trial of PT2385, a First-in-Class Hypoxia-Inducible Factor-2alpha Antagonist in Patients With Previously Treated Advanced Clear Cell Renal Cell Carcinoma. J Clin Oncol. 2018;36(9):867-74.

721. Dow LE, Nasr Z, Saborowski M, et al. Conditional reverse tet-transactivator mouse strains for the efficient induction of TRE-regulated transgenes in mice. PLoS One. 2014;9(4):e95236.

722. Singh Y, Garden OA, Lang F, et al. MicroRNAs regulate T-cell production of interleukin-9 and identify hypoxia-inducible factor-2alpha as an important regulator of T helper 9 and regulatory T-cell differentiation. Immunology. 2016;149(1):74-86.

723. Hsu TS, Lin YL, Wang YA, et al. HIF-2alpha is indispensable for regulatory T cell function. Nat Commun. 2020;11(1):5005.

724. Wan YY, Flavell RA. Regulatory T-cell functions are subverted and converted owing to attenuated Foxp3 expression. Nature. 2007;445(7129):766-70.

725. Williams LM, Rudensky AY. Maintenance of the Foxp3-dependent developmental program in mature regulatory T cells requires continued expression of Foxp3. Nat Immunol. 2007;8(3):277-84.

726. Zhou X, Bailey-Bucktrout SL, Jeker LT, et al. Instability of the transcription factor Foxp3 leads to the generation of pathogenic memory T cells in vivo. Nat Immunol. 2009;10(9):1000-7.

727. Oldenhove G, Bouladoux N, Wohlfert EA, et al. Decrease of Foxp3+ Treg cell number and acquisition of effector cell phenotype during lethal infection. Immunity. 2009;31(5):772-86.

728. Marson A, Kretschmer K, Frampton GM, et al. Foxp3 occupancy and regulation of key target genes during T-cell stimulation. Nature. 2007;445(7130):931-5.

729. Zheng Y, Josefowicz SZ, Kas A, et al. Genome-wide analysis of Foxp3 target genes in developing and mature regulatory T cells. Nature. 2007;445(7130):936-40.

730. Rudra D, deRoos P, Chaudhry A, et al. Transcription factor Foxp3 and its protein partners form a complex regulatory network. Nat Immunol. 2012;13(10):1010-9.

731. Huang CT, Workman CJ, Flies D, et al. Role of LAG-3 in regulatory T cells. Immunity. 2004;21(4):503-13.

732. Thornton AM, Shevach EM. CD4+CD25+ immunoregulatory T cells suppress polyclonal T cell activation in vitro by inhibiting interleukin 2 production. J Exp Med. 1998;188(2):287-96.

733. Takahashi T, Kuniyasu Y, Toda M, et al. Immunologic self-tolerance maintained by CD25+CD4+ naturally anergic and suppressive T cells: induction of autoimmune disease by breaking their anergic/suppressive state. Int Immunol. 1998;10(12):1969-80.

734. Fallarino F, Grohmann U, Hwang KW, et al. Modulation of tryptophan catabolism by regulatory T cells. Nat Immunol. 2003;4(12):1206-12.

735. Cobbold SP, Adams E, Farquhar CA, et al. Infectious tolerance via the consumption of essential amino acids and mTOR signaling. Proc Natl Acad Sci U S A. 2009;106(29):12055-60.

736. Jarnicki AG, Lysaght J, Todryk S, et al. Suppression of antitumor immunity by IL-10 and TGF-beta-producing T cells infiltrating the growing tumor: influence of tumor environment on the induction of CD4+ and CD8+ regulatory T cells. J Immunol. 2006;177(2):896-904.

737. Collison LW, Workman CJ, Kuo TT, et al. The inhibitory cytokine IL-35 contributes to regulatory T-cell function. Nature. 2007;450(7169):566-9.

738. Turnis ME, Sawant DV, Szymczak-Workman AL, et al. Interleukin-35 Limits Anti-Tumor Immunity. Immunity. 2016;44(2):316-29.

739. Deaglio S, Dwyer KM, Gao W, et al. Adenosine generation catalyzed by CD39 and CD73 expressed on regulatory T cells mediates immune suppression. J Exp Med. 2007;204(6):1257-65.

740. Grossman WJ, Verbsky JW, Barchet W, et al. Human T regulatory cells can use the perforin pathway to cause autologous target cell death. Immunity. 2004;21(4):589-601.

741. Curiel TJ, Coukos G, Zou L, et al. Specific recruitment of regulatory T cells in ovarian carcinoma fosters immune privilege and predicts reduced survival. Nat Med. 2004;10(9):942-9.

742. Antony PA, Piccirillo CA, Akpinarli A, et al. CD8+ T cell immunity against a tumor/self-antigen is augmented by CD4+ T helper cells and hindered by naturally occurring T regulatory cells. J Immunol. 2005;174(5):2591-601.

743. Togashi Y, Shitara K, Nishikawa H. Regulatory T cells in cancer immunosuppression - implications for anticancer therapy. Nat Rev Clin Oncol. 2019;16(6):356-71.

744. deLeeuw RJ, Kost SE, Kakal JA, et al. The prognostic value of FoxP3+ tumor-infiltrating lymphocytes in cancer: a critical review of the literature. Clin Cancer Res. 2012;18(11):3022-9.

745. Shang B, Liu Y, Jiang SJ, et al. Prognostic value of tumor-infiltrating FoxP3+ regulatory T cells in cancers: a systematic review and meta-analysis. Sci Rep. 2015;5:15179.

746. Onizuka S, Tawara I, Shimizu J, et al. Tumor rejection by in vivo administration of anti-CD25 (interleukin-2 receptor alpha) monoclonal antibody. Cancer Res. 1999;59(13):3128-33.

747. Shimizu J, Yamazaki S, Sakaguchi S. Induction of tumor immunity by removing CD25+CD4+ T cells: a common basis between tumor immunity and autoimmunity. J Immunol. 1999;163(10):5211-8.

748. Hindley JP, Jones E, Smart K, et al. T-cell trafficking facilitated by high endothelial venules is required for tumor control after regulatory T-cell depletion. Cancer Res. 2012;72(21):5473-82.

749. Colbeck EJ, Jones E, Hindley JP, et al. Treg Depletion Licenses T Cell-Driven HEV Neogenesis and Promotes Tumor Destruction. Cancer Immunol Res. 2017;5(11):1005-15.

750. Shitara K, Nishikawa H. Regulatory T cells: a potential target in cancer immunotherapy. Ann N Y Acad Sci. 2018;1417(1):104-15.

751. Litzinger MT, Fernando R, Curiel TJ, et al. IL-2 immunotoxin denileukin diftitox reduces regulatory T cells and enhances vaccine-mediated T-cell immunity. Blood. 2007;110(9):3192-201.

752. Rasku MA, Clem AL, Telang S, et al. Transient T cell depletion causes regression of melanoma metastases. J Transl Med. 2008;6:12.

753. Dannull J, Su Z, Rizzieri D, et al. Enhancement of vaccine-mediated antitumor immunity in cancer patients after depletion of regulatory T cells. J Clin Invest. 2005;115(12):3623-33.

754. Mahnke K, Schonfeld K, Fondel S, et al. Depletion of CD4+CD25+ human regulatory T cells in vivo: kinetics of Treg depletion and alterations in immune functions in vivo and in vitro. Int J Cancer. 2007;120(12):2723-33.

755. Rech AJ, Mick R, Martin S, et al. CD25 blockade depletes and selectively reprograms regulatory T cells in concert with immunotherapy in cancer patients. Sci Transl Med. 2012;4(134):134ra62.

756. Jacobs JF, Punt CJ, Lesterhuis WJ, et al. Dendritic cell vaccination in combination with anti-CD25 monoclonal antibody treatment: a phase I/II study in metastatic melanoma patients. Clin Cancer Res. 2010;16(20):5067-78.

757. Ghiringhelli F, Larmonier N, Schmitt E, et al. CD4+CD25+ regulatory T cells suppress tumor immunity but are sensitive to cyclophosphamide which allows immunotherapy of established tumors to be curative. Eur J Immunol. 2004;34(2):336-44.

758. Wu J, Waxman DJ. Metronomic cyclophosphamide eradicates large implanted GL261 gliomas by activating antitumor Cd8(+) T-cell responses and immune memory. Oncoimmunology. 2015;4(4):e1005521.

759. Ghiringhelli F, Menard C, Puig PE, et al. Metronomic cyclophosphamide regimen selectively depletes CD4+CD25+ regulatory T cells and restores T and NK effector functions in end stage cancer patients. Cancer Immunol Immunother. 2007;56(5):641-8.

760. Ladoire S, Arnould L, Apetoh L, et al. Pathologic complete response to neoadjuvant chemotherapy of breast carcinoma is associated with the disappearance of tumor-infiltrating Foxp3+ regulatory T cells. Clin Cancer Res. 2008;14(8):2413-20.

761. Scurr M, Pembroke T, Bloom A, et al. Low-Dose Cyclophosphamide Induces Antitumor T-Cell Responses, which Associate with Survival in Metastatic Colorectal Cancer. Clin Cancer Res. 2017;23(22):6771-80.

762. Simpson TR, Li F, Montalvo-Ortiz W, et al. Fc-dependent depletion of tumor-infiltrating regulatory T cells co-defines the efficacy of anti-CTLA-4 therapy against melanoma. J Exp Med. 2013;210(9):1695-710.

763. Bulliard Y, Jolicoeur R, Windman M, et al. Activating Fc gamma receptors contribute to the antitumor activities of immunoregulatory receptor-targeting antibodies. J Exp Med. 2013;210(9):1685-93.

764. Selby MJ, Engelhardt JJ, Quigley M, et al. Anti-CTLA-4 antibodies of IgG2a isotype enhance antitumor activity through reduction of intratumoral regulatory T cells. Cancer Immunol Res. 2013;1(1):32-42.

765. Arce Vargas F, Furness AJS, Litchfield K, et al. Fc Effector Function Contributes to the Activity of Human Anti-CTLA-4 Antibodies. Cancer Cell. 2018;33(4):649-63 e4.

766. Romano E, Kusio-Kobialka M, Foukas PG, et al. Ipilimumab-dependent cell-mediated cytotoxicity of regulatory T cells ex vivo by nonclassical monocytes in melanoma patients. Proc Natl Acad Sci U S A. 2015;112(19):6140-5.

767. Sharma A, Subudhi SK, Blando J, et al. Anti-CTLA-4 Immunotherapy Does Not Deplete FOXP3(+) Regulatory T Cells (Tregs) in Human Cancers. Clin Cancer Res. 2019;25(4):1233-8.

768. Dodagatta-Marri E, Meyer DS, Reeves MQ, et al. alpha-PD-1 therapy elevates Treg/Th balance and increases tumor cell pSmad3 that are both targeted by alpha-TGFbeta antibody to promote durable rejection and immunity in squamous cell carcinomas. J Immunother Cancer. 2019;7(1):62.

769. Kamada T, Togashi Y, Tay C, et al. PD-1(+) regulatory T cells amplified by PD-1 blockade promote hyperprogression of cancer. Proc Natl Acad Sci U S A. 2019;116(20):9999-10008.

770. Ali K, Soond DR, Pineiro R, et al. Inactivation of PI(3)K p110delta breaks regulatory T-cell-mediated immune tolerance to cancer. Nature. 2014;510(7505):407-11.

771. Ahmad S, Abu-Eid R, Shrimali R, et al. Differential PI3Kdelta Signaling in CD4(+) T-cell Subsets Enables Selective Targeting of T Regulatory Cells to Enhance Cancer Immunotherapy. Cancer Res. 2017;77(8):1892-904.

772. Holmgaard RB, Zamarin D, Li Y, et al. Tumor-Expressed IDO Recruits and Activates MDSCs in a Treg-Dependent Manner. Cell Rep. 2015;13(2):412-24.

773. Beatty GL, O'Dwyer PJ, Clark J, et al. First-in-Human Phase I Study of the Oral Inhibitor of Indoleamine 2,3-Dioxygenase-1 Epacadostat (INCB024360) in Patients with Advanced Solid Malignancies. Clin Cancer Res. 2017;23(13):3269-76.

774. Tan MC, Goedegebuure PS, Belt BA, et al. Disruption of CCR5-dependent homing of regulatory T cells inhibits tumor growth in a murine model of pancreatic cancer. J Immunol. 2009;182(3):1746-55.

775. Gobert M, Treilleux I, Bendriss-Vermare N, et al. Regulatory T cells recruited through CCL22/CCR4 are selectively activated in lymphoid infiltrates surrounding primary breast tumors and lead to an adverse clinical outcome. Cancer Res. 2009;69(5):2000-9.

776. Svensson H, Olofsson V, Lundin S, et al. Accumulation of CCR4(+)CTLA-4 FOXP3(+)CD25(hi) regulatory T cells in colon adenocarcinomas correlate to reduced activation of conventional T cells. PLoS One. 2012;7(2):e30695.

777. Wei S, Kryczek I, Edwards RP, et al. Interleukin-2 administration alters the CD4+FOXP3+ T-cell pool and tumor trafficking in patients with ovarian carcinoma. Cancer Res. 2007;67(15):7487-94.

778. Roland CL, Lynn KD, Toombs JE, et al. Cytokine levels correlate with immune cell infiltration after anti-VEGF therapy in preclinical mouse models of breast cancer. PLoS One. 2009;4(11):e7669.

779. Tada Y, Togashi Y, Kotani D, et al. Targeting VEGFR2 with Ramucirumab strongly impacts effector/activated regulatory T cells and CD8(+) T cells in the tumor microenvironment. J Immunother Cancer. 2018;6(1):106.

780. Moo-Young TA, Larson JW, Belt BA, et al. Tumor-derived TGF-beta mediates conversion of CD4+Foxp3+ regulatory T cells in a murine model of pancreas cancer. J Immunother. 2009;32(1):12-21.

781. Thomas DA, Massague J. TGF-beta directly targets cytotoxic T cell functions during tumor evasion of immune surveillance. Cancer Cell. 2005;8(5):369-80.

782. Holmgaard RB, Schaer DA, Li Y, et al. Targeting the TGFbeta pathway with galunisertib, a TGFbetaRI small molecule inhibitor, promotes anti-tumor immunity leading to

durable, complete responses, as monotherapy and in combination with checkpoint blockade. J Immunother Cancer. 2018;6(1):47.

783. Rollings CM, Sinclair LV, Brady HJM, et al. Interleukin-2 shapes the cytotoxic T cell proteome and immune environment-sensing programs. Sci Signal. 2018;11(526).

784. Braumuller H, Wieder T, Brenner E, et al. T-helper-1-cell cytokines drive cancer into senescence. Nature. 2013;494(7437):361-5.

785. Kammertoens T, Friese C, Arina A, et al. Tumour ischaemia by interferon-gamma resembles physiological blood vessel regression. Nature. 2017;545(7652):98-102.

786. Mazzone M, Dettori D, de Oliveira RL, et al. Heterozygous deficiency of PHD2 restores tumor oxygenation and inhibits metastasis via endothelial normalization. Cell. 2009;136(5):839-51.

787. Dranoff G. Experimental mouse tumour models: what can be learnt about human cancer immunology? Nat Rev Immunol. 2011;12(1):61-6.

788. Gengenbacher N, Singhal M, Augustin HG. Preclinical mouse solid tumour models: status quo, challenges and perspectives. Nat Rev Cancer. 2017;17(12):751-65.

789. Furuta C, Miyamoto T, Takagi T, et al. Transforming growth factor-beta signaling enhancement by long-term exposure to hypoxia in a tumor microenvironment composed of Lewis lung carcinoma cells. Cancer Sci. 2015;106(11):1524-33.

790. Johnstone CN, Smith YE, Cao Y, et al. Functional and molecular characterisation of EO771.LMB tumours, a new C57BL/6-mouse-derived model of spontaneously metastatic mammary cancer. Dis Model Mech. 2015;8(3):237-51.

791. Yang Y, Yang HH, Hu Y, et al. Immunocompetent mouse allograft models for development of therapies to target breast cancer metastasis. Oncotarget. 2017;8(19):30621-43.

792. Buss LA, Mandani A, Phillips E, et al. Characterisation of a Mouse Model of Breast Cancer with Metabolic Syndrome. In Vivo. 2018;32(5):1071-80.

793. Carmi Y, Spitzer MH, Linde IL, et al. Allogeneic IgG combined with dendritic cell stimuli induce antitumour T-cell immunity. Nature. 2015;521(7550):99-104.

794. Sun QF, Zhao XN, Peng CL, et al. Immunotherapy for Lewis lung carcinoma utilizing dendritic cells infected with CK19 gene recombinant adenoviral vectors. Oncol Rep. 2015;34(5):2289-95.

795. Stagg J, Divisekera U, McLaughlin N, et al. Anti-CD73 antibody therapy inhibits breast tumor growth and metastasis. Proc Natl Acad Sci U S A. 2010;107(4):1547-52.

796. Gray MJ, Gong J, Hatch MM, et al. Phosphatidylserine-targeting antibodies augment the anti-tumorigenic activity of anti-PD-1 therapy by enhancing immune activation and downregulating pro-oncogenic factors induced by T-cell checkpoint inhibition in murine triple-negative breast cancers. Breast Cancer Res. 2016;18(1):50.

797. Liu J, Blake SJ, Harjunpaa H, et al. Assessing Immune-Related Adverse Events of Efficacious Combination Immunotherapies in Preclinical Models of Cancer. Cancer Res. 2016;76(18):5288-301.

798. Crosby EJ, Wei J, Yang XY, et al. Complimentary mechanisms of dual checkpoint blockade expand unique T-cell repertoires and activate adaptive anti-tumor immunity in triple-negative breast tumors. Oncoimmunology. 2018;7(5):e1421891.

799. Bertram JS, Janik P. Establishment of a cloned line of Lewis Lung Carcinoma cells adapted to cell culture. Cancer Lett. 1980;11(1):63-73.

800. Mosely SI, Prime JE, Sainson RC, et al. Rational Selection of Syngeneic Preclinical Tumor Models for Immunotherapeutic Drug Discovery. Cancer Immunol Res. 2017;5(1):29-41.

801. Li HY, McSharry M, Bullock B, et al. The Tumor Microenvironment Regulates Sensitivity of Murine Lung Tumors to PD-1/PD-L1 Antibody Blockade. Cancer Immunol Res. 2017;5(9):767-77.

802. Zhang D, Chen Z, Wang DC, et al. Regulatory T cells and potential inmmunotherapeutic targets in lung cancer. Cancer Metastasis Rev. 2015;34(2):277-90.

803. De Simone M, Arrigoni A, Rossetti G, et al. Transcriptional Landscape of Human Tissue Lymphocytes Unveils Uniqueness of Tumor-Infiltrating T Regulatory Cells. Immunity. 2016;45(5):1135-47.

804. Bohling SD, Allison KH. Immunosuppressive regulatory T cells are associated with aggressive breast cancer phenotypes: a potential therapeutic target. Mod Pathol. 2008;21(12):1527-32.

805. Cai Y, Xiong S, Zheng Y, et al. Trichosanthin enhances anti-tumor immune response in a murine Lewis lung cancer model by boosting the interaction between TSLC1 and CRTAM. Cell Mol Immunol. 2011;8(4):359-67.

806. Priceman SJ, Shen S, Wang L, et al. S1PR1 is crucial for accumulation of regulatory T cells in tumors via STAT3. Cell Rep. 2014;6(6):992-9.

807. Simpson EM, Linder CC, Sargent EE, et al. Genetic variation among 129 substrains and its importance for targeted mutagenesis in mice. Nat Genet. 1997;16(1):19-27.

808. Xie J, Nair A, Hermiston TW. A comparative study examining the cytotoxicity of inducible gene expression system ligands in different cell types. Toxicol In Vitro. 2008;22(1):261-6.

809. Fainaru O, Adini I, Benny O, et al. Doxycycline induces membrane expression of VE-cadherin on endothelial cells and prevents vascular hyperpermeability. FASEB J. 2008;22(10):3728-35.

810. Ewens A, Mihich E, Ehrke MJ. Distant metastasis from subcutaneously grown E0771 medullary breast adenocarcinoma. Anticancer Res. 2005;25(6B):3905-15.

811. Mittal R, Chen CW, Lyons JD, et al. Murine lung cancer induces generalized T-cell exhaustion. J Surg Res. 2015;195(2):541-9.

812. Ahmadzadeh M, Johnson LA, Heemskerk B, et al. Tumor antigen-specific CD8 T cells infiltrating the tumor express high levels of PD-1 and are functionally impaired. Blood. 2009;114(8):1537-44.

813. Zhang Y, Huang S, Gong D, et al. Programmed death-1 upregulation is correlated with dysfunction of tumor-infiltrating CD8+ T lymphocytes in human non-small cell lung cancer. Cell Mol Immunol. 2010;7(5):389-95.

814. Goods BA, Hernandez AL, Lowther DE, et al. Functional differences between PD-1+ and PD-1- CD4+ effector T cells in healthy donors and patients with glioblastoma multiforme. PLoS One. 2017;12(9):e0181538.

815. Lv S, Zhang J, Wu J, et al. Origin and anti-tumor effects of anti-dsDNA autoantibodies in cancer patients and tumor-bearing mice. Immunol Lett. 2005;99(2):217-27.

816. Madrid FF, Maroun MC. Serologic laboratory findings in malignancy. Rheum Dis Clin North Am. 2011;37(4):507-25.

817. Li X, Kostareli E, Suffner J, et al. Efficient Treg depletion induces T-cell infiltration and rejection of large tumors. Eur J Immunol. 2010;40(12):3325-35.

818. Lechner MG, Karimi SS, Barry-Holson K, et al. Immunogenicity of murine solid tumor models as a defining feature of in vivo behavior and response to immunotherapy. J Immunother. 2013;36(9):477-89.

819. Dutta D, Ray S, Vivian JL, et al. Activation of the VEGFR1 chromatin domain: an angiogenic signal-ETS1/HIF-2alpha regulatory axis. J Biol Chem. 2008;283(37):25404-13.

820. Kendall RL, Thomas KA. Inhibition of vascular endothelial cell growth factor activity by an endogenously encoded soluble receptor. Proc Natl Acad Sci U S A. 1993;90(22):10705-9.

821. Benjamin LE, Golijanin D, Itin A, et al. Selective ablation of immature blood vessels in established human tumors follows vascular endothelial growth factor withdrawal. J Clin Invest. 1999;103(2):159-65.

822. Le Bras A, Lionneton F, Mattot V, et al. HIF-2alpha specifically activates the VE-cadherin promoter independently of hypoxia and in synergy with Ets-1 through two essential ETS-binding sites. Oncogene. 2007;26(53):7480-9.

823. Taddei A, Giampietro C, Conti A, et al. Endothelial adherens junctions control tight junctions by VE-cadherin-mediated upregulation of claudin-5. Nat Cell Biol. 2008;10(8):923-34.

824. Leite de Oliveira R, Deschoemaeker S, Henze AT, et al. Gene-targeting of Phd2 improves tumor response to chemotherapy and prevents side-toxicity. Cancer Cell. 2012;22(2):263-77.

825. Takeda Y, Costa S, Delamarre E, et al. Macrophage skewing by Phd2 haplodeficiency prevents ischaemia by inducing arteriogenesis. Nature. 2011;479(7371):122-6.

826. Mamlouk S, Kalucka J, Singh RP, et al. Loss of prolyl hydroxylase-2 in myeloid cells and T-lymphocytes impairs tumor development. Int J Cancer. 2014;134(4):849-58.

827. Josefowicz SZ, Niec RE, Kim HY, et al. Extrathymically generated regulatory T cells control mucosal TH2 inflammation. Nature. 2012;482(7385):395-9.

828. Koyama S, Matsunaga S, Imanishi M, et al. Tumour blood vessel normalisation by prolyl hydroxylase inhibitor repaired sensitivity to chemotherapy in a tumour mouse model. Sci Rep. 2017;7:45621.

829. Nishide S, Uchida J, Matsunaga S, et al. Prolyl-hydroxylase inhibitors reconstitute tumor blood vessels in mice. J Pharmacol Sci. 2020;143(2):122-6.

830. Yeh TL, Leissing TM, Abboud MI, et al. Molecular and cellular mechanisms of HIF prolyl hydroxylase inhibitors in clinical trials. Chem Sci. 2017;8(11):7651-68.

831. Nishide S, Matsunaga S, Shiota M, et al. Controlling the Phenotype of Tumor-Infiltrating Macrophages via the PHD-HIF Axis Inhibits Tumor Growth in a Mouse Model. iScience. 2019;19:940-54.

832. Lee KA, Lynd JD, O'Reilly S, et al. The biphasic role of the hypoxia-inducible factor prolyl-4-hydroxylase, PHD2, in modulating tumor-forming potential. Mol Cancer Res. 2008;6(5):829-42.

833. Chan DA, Kawahara TL, Sutphin PD, et al. Tumor vasculature is regulated by PHD2-mediated angiogenesis and bone marrow-derived cell recruitment. Cancer Cell. 2009;15(6):527-38.

834. Matsumoto K, Obara N, Ema M, et al. Antitumor effects of 2-oxoglutarate through inhibition of angiogenesis in a murine tumor model. Cancer Sci. 2009;100(9):1639-47.

835. Bordoli MR, Stiehl DP, Borsig L, et al. Prolyl-4-hydroxylase PHD2- and hypoxia-inducible factor 2-dependent regulation of amphiregulin contributes to breast tumorigenesis. Oncogene. 2011;30(5):548-60.

836. Su Y, Loos M, Giese N, et al. Prolyl hydroxylase-2 (PHD2) exerts tumor-suppressive activity in pancreatic cancer. Cancer. 2012;118(4):960-72.

837. Li Y, Zhang D, Wang X, et al. Hypoxia-inducible miR-182 enhances HIF1alpha signaling via targeting PHD2 and FIH1 in prostate cancer. Sci Rep. 2015;5:12495.

838. Tao Y, Lin F, Li R, et al. Prolyl hydroxylase-2 inhibits liver tumor cell proliferation and cyclin D1 expression in a hydroxylase-dependent manner. Int J Biochem Cell Biol. 2016;77(Pt A):129-40.

839. Di Conza G, Trusso Cafarello S, Zheng X, et al. PHD2 Targeting Overcomes Breast Cancer Cell Death upon Glucose Starvation in a PP2A/B55alpha-Mediated Manner. Cell Rep. 2017;18(12):2836-44.

840. Wang L, Niu Z, Wang X, et al. PHD2 exerts anti-cancer and anti-inflammatory effects in colon cancer xenografts mice via attenuating NF-kappaB activity. Life Sci. 2020;242:117167.

841. Klotzsche-von Ameln A, Muschter A, Mamlouk S, et al. Inhibition of HIF prolyl hydroxylase-2 blocks tumor growth in mice through the antiproliferative activity of TGFbeta. Cancer Res. 2011;71(9):3306-16.

842. Klotzsche-von Ameln A, Muschter A, Heimesaat MM, et al. HIF prolyl hydroxylase-2 inhibition diminishes tumor growth through matrix metalloproteinase-induced TGFbeta activation. Cancer Biol Ther. 2012;13(4):216-23.

843. Naba A, Clauser KR, Lamar JM, et al. Extracellular matrix signatures of human mammary carcinoma identify novel metastasis promoters. Elife. 2014;3:e01308.

844. Jiang W, Zhou X, Li Z, et al. Prolyl 4-hydroxylase 2 promotes B-cell lymphoma progression via hydroxylation of Carabin. Blood. 2018;131(12):1325-36.

845. Jokilehto T, Rantanen K, Luukkaa M, et al. Overexpression and nuclear translocation of hypoxia-inducible factor prolyl hydroxylase PHD2 in head and neck squamous cell carcinoma is associated with tumor aggressiveness. Clin Cancer Res. 2006;12(4):1080-7.

846. Gossage L, Zaitoun A, Fareed KR, et al. Expression of key hypoxia sensing prolyl-hydroxylases PHD1, -2 and -3 in pancreaticobiliary cancer. Histopathology. 2010;56(7):908-20.

847. Andersen S, Donnem T, Stenvold H, et al. Overexpression of the HIF hydroxylases PHD1, PHD2, PHD3 and FIH are individually and collectively unfavorable prognosticators for NSCLC survival. PLoS One. 2011;6(8):e23847.

848. Zhen L, Shijie N, Shuijun Z. Tumor PHD2 expression is correlated with clinical features and prognosis of patients with HCC receiving liver resection. Medicine (Baltimore). 2014;93(29):e179.

849. Kamphues C, Wittschieber D, Klauschen F, et al. Prolyl hydroxylase domain 2 protein is a strong prognostic marker in human gastric cancer. Pathobiology. 2012;79(1):11-7.

850. Haas M, Dimmler A, Hohenberger W, et al. Stromal regulatory T-cells are associated with a favourable prognosis in gastric cancer of the cardia. BMC Gastroenterol. 2009;9:65.

851. Ladoire S, Martin F, Ghiringhelli F. Prognostic role of FOXP3+ regulatory T cells infiltrating human carcinomas: the paradox of colorectal cancer. Cancer Immunol Immunother. 2011;60(7):909-18.

852. Erdman SE, Poutahidis T, Tomczak M, et al. CD4+ CD25+ regulatory T lymphocytes inhibit microbially induced colon cancer in Rag2-deficient mice. Am J Pathol. 2003;162(2):691-702.

853. Erdman SE, Rao VP, Poutahidis T, et al. CD4(+)CD25(+) regulatory lymphocytes require interleukin 10 to interrupt colon carcinogenesis in mice. Cancer Res. 2003;63(18):6042-50.

854. Erdman SE, Sohn JJ, Rao VP, et al. CD4+CD25+ regulatory lymphocytes induce regression of intestinal tumors in ApcMin/+ mice. Cancer Res. 2005;65(10):3998-4004.

855. Saito T, Nishikawa H, Wada H, et al. Two FOXP3(+)CD4(+) T cell subpopulations distinctly control the prognosis of colorectal cancers. Nat Med. 2016;22(6):679-84.

856. Kurose K, Ohue Y, Wada H, et al. Phase Ia Study of FoxP3+ CD4 Treg Depletion by Infusion of a Humanized Anti-CCR4 Antibody, KW-0761, in Cancer Patients. Clin Cancer Res. 2015;21(19):4327-36.

857. Morse MA, Hobeika AC, Osada T, et al. Depletion of human regulatory T cells specifically enhances antigen-specific immune responses to cancer vaccines. Blood. 2008;112(3):610-8.

858. Taylor NA, Vick SC, Iglesia MD, et al. Treg depletion potentiates checkpoint inhibition in claudin-low breast cancer. J Clin Invest. 2017;127(9):3472-83.

859. Di Pilato M, Kim EY, Cadilha BL, et al. Targeting the CBM complex causes Treg cells to prime tumours for immune checkpoint therapy. Nature. 2019;570(7759):112-6.

860. Kuchnio A, Moens S, Bruning U, et al. The Cancer Cell Oxygen Sensor PHD2 Promotes Metastasis via Activation of Cancer-Associated Fibroblasts. Cell Rep. 2015;12(6):992-1005.

861. Madsen CD, Pedersen JT, Venning FA, et al. Hypoxia and loss of PHD2 inactivate stromal fibroblasts to decrease tumour stiffness and metastasis. EMBO Rep. 2015;16(10):1394-408.

862. Jain RK. A new target for tumor therapy. N Engl J Med. 2009;360(25):2669-71.

863. Olive PL, Aquino-Parsons C, MacPhail SH, et al. Carbonic anhydrase 9 as an endogenous marker for hypoxic cells in cervical cancer. Cancer Res. 2001;61(24):8924-9.

864. Hoskin PJ, Sibtain A, Daley FM, et al. GLUT1 and CAIX as intrinsic markers of hypoxia in bladder cancer: relationship with vascularity and proliferation as predictors of outcome of ARCON. Br J Cancer. 2003;89(7):1290-7.

865. van Laarhoven HW, Kaanders JH, Lok J, et al. Hypoxia in relation to vasculature and proliferation in liver metastases in patients with colorectal cancer. Int J Radiat Oncol Biol Phys. 2006;64(2):473-82.

866. Goethals L, Debucquoy A, Perneel C, et al. Hypoxia in human colorectal adenocarcinoma: comparison between extrinsic and potential intrinsic hypoxia markers. Int J Radiat Oncol Biol Phys. 2006;65(1):246-54.

867. Cho H, Du X, Rizzi JP, et al. On-target efficacy of a HIF-2alpha antagonist in preclinical kidney cancer models. Nature. 2016;539(7627):107-11.

868. Chen W, Hill H, Christie A, et al. Targeting renal cell carcinoma with a HIF-2 antagonist. Nature. 2016;539(7627):112-7.

869. Wallace EM, Rizzi JP, Han G, et al. A Small-Molecule Antagonist of HIF2alpha Is Efficacious in Preclinical Models of Renal Cell Carcinoma. Cancer Res. 2016;76(18):5491-500.

870. Uyttenhove C, Pilotte L, Theate I, et al. Evidence for a tumoral immune resistance mechanism based on tryptophan degradation by indoleamine 2,3-dioxygenase. Nat Med. 2003;9(10):1269-74.

871. Noman MZ, Janji B, Kaminska B, et al. Blocking hypoxia-induced autophagy in tumors restores cytotoxic T-cell activity and promotes regression. Cancer Res. 2011;71(18):5976-86.

872. Hasmim M, Noman MZ, Lauriol J, et al. Hypoxia-dependent inhibition of tumor cell susceptibility to CTL-mediated lysis involves NANOG induction in target cells. J Immunol. 2011;187(8):4031-9.

873. Baginska J, Viry E, Berchem G, et al. Granzyme B degradation by autophagy decreases tumor cell susceptibility to natural killer-mediated lysis under hypoxia. Proc Natl Acad Sci U S A. 2013;110(43):17450-5.

874. Messai Y, Noman MZ, Hasmim M, et al. ITPR1 protects renal cancer cells against natural killer cells by inducing autophagy. Cancer Res. 2014;74(23):6820-32.

875. Collins DC, Sundar R, Lim JSJ, et al. Towards Precision Medicine in the Clinic: From Biomarker Discovery to Novel Therapeutics. Trends Pharmacol Sci. 2017;38(1):25-40.

876. Janssens GO, Rademakers SE, Terhaard CH, et al. Accelerated radiotherapy with carbogen and nicotinamide for laryngeal cancer: results of a phase III randomized trial. J Clin Oncol. 2012;30(15):1777-83.

877. Vaupel P, Hockel M, Mayer A. Detection and characterization of tumor hypoxia using pO2 histography. Antioxid Redox Signal. 2007;9(8):1221-35.

878. Gaertner FC, Souvatzoglou M, Brix G, et al. Imaging of hypoxia using PET and MRI. Curr Pharm Biotechnol. 2012;13(4):552-70.

879. Le QT, Sutphin PD, Raychaudhuri S, et al. Identification of osteopontin as a prognostic plasma marker for head and neck squamous cell carcinomas. Clin Cancer Res. 2003;9(1):59-67.

880. Overgaard J, Eriksen JG, Nordsmark M, et al. Plasma osteopontin, hypoxia, and response to the hypoxia sensitiser nimorazole in radiotherapy of head and neck cancer: results from the DAHANCA 5 randomised double-blind placebo-controlled trial. Lancet Oncol. 2005;6(10):757-64.

881. Chen Z, Malhotra PS, Thomas GR, et al. Expression of proinflammatory and proangiogenic cytokines in patients with head and neck cancer. Clin Cancer Res. 1999;5(6):1369-79.

882. Shariat SF, Anwuri VA, Lamb DJ, et al. Association of preoperative plasma levels of vascular endothelial growth factor and soluble vascular cell adhesion molecule-1 with lymph node status and biochemical progression after radical prostatectomy. J Clin Oncol. 2004;22(9):1655-63.

883. Zavada J, Zavadova Z, Zat'ovicova M, et al. Soluble form of carbonic anhydrase IX (CA IX) in the serum and urine of renal carcinoma patients. Br J Cancer. 2003;89(6):1067-71.

884. Buffa FM, Harris AL, West CM, et al. Large meta-analysis of multiple cancers reveals a common, compact and highly prognostic hypoxia metagene. Br J Cancer. 2010;102(2):428-35.

885. Iakovlev VV, Pintilie M, Morrison A, et al. Effect of distributional heterogeneity on the analysis of tumor hypoxia based on carbonic anhydrase IX. Lab Invest. 2007;87(12):1206-17.

886. West CM, Cooper RA, Loncaster JA, et al. Tumor vascularity: a histological measure of angiogenesis and hypoxia. Cancer Res. 2001;61(7):2907-10.

887. Kennedy AS, Raleigh JA, Perez GM, et al. Proliferation and hypoxia in human squamous cell carcinoma of the cervix: first report of combined immunohistochemical assays. Int J Radiat Oncol Biol Phys. 1997;37(4):897-905.

888. Evans SM, Hahn S, Pook DR, et al. Detection of hypoxia in human squamous cell carcinoma by EF5 binding. Cancer Res. 2000;60(7):2018-24.

889. Varia MA, Lee DYW, Raleigh JA. Oral Pimonidazole HCl as Tumor Hypoxia Marker: Report of First Clinical Use - Pharmacokinetics and Tolerance. Int J Radiat Oncol Biol Phys. 2009;75(3 Supplement):S539-40.

890. Varia MA, Lee DY, Raleigh JA. Comparison between Glut-1 Expression and Hypoxia in Squamous Cell Carcinoma of the Uterine Cervix Using Oral Pimonidazole as Hypoxia Marker. Int J Radiat Oncol Biol Phys. 2011;81(2 Supplement):S705.

891. Gross MW, Karbach U, Groebe K, et al. Calibration of misonidazole labeling by simultaneous measurement of oxygen tension and labeling density in multicellular spheroids. Int J Cancer. 1995;61(4):567-73.

892. Raleigh JA, Chou SC, Arteel GE, et al. Comparisons among pimonidazole binding, oxygen electrode measurements, and radiation response in C3H mouse tumors. Radiat Res. 1999;151(5):580-9.

893. Varghese AJ, Gulyas S, Mohindra JK. Hypoxia-dependent reduction of 1-(2-nitro-1-imidazolyl)-3-methoxy-2-propanol by Chinese hamster ovary cells and KHT tumor cells in vitro and in vivo. Cancer Res. 1976;36(10):3761-5.

894. Chapman JD, Franko AJ, Sharplin J. A marker for hypoxic cells in tumours with potential clinical applicability. Br J Cancer. 1981;43(4):546-50.

895. Lord EM, Harwell L, Koch CJ. Detection of hypoxic cells by monoclonal antibody recognizing 2-nitroimidazole adducts. Cancer Res. 1993;53(23):5721-6.

896. Arteel GE, Thurman RG, Yates JM, et al. Evidence that hypoxia markers detect oxygen gradients in liver: pimonidazole and retrograde perfusion of rat liver. Br J Cancer. 1995;72(4):889-95.

897. Hoskin PJ, Sibtain A, Daley FM, et al. The immunohistochemical assessment of hypoxia, vascularity and proliferation in bladder carcinoma. Radiother Oncol. 2004;72(2):159-68.

898. Olive PL, Durand RE, Raleigh JA, et al. Comparison between the comet assay and pimonidazole binding for measuring tumour hypoxia. Br J Cancer. 2000;83(11):1525-31.

899. Koch CJ. Importance of antibody concentration in the assessment of cellular hypoxia by flow cytometry: EF5 and pimonidazole. Radiat Res. 2008;169(6):677-88.

900. Varia MA, Calkins-Adams DP, Rinker LH, et al. Pimonidazole: a novel hypoxia marker for complementary study of tumor hypoxia and cell proliferation in cervical carcinoma. Gynecol Oncol. 1998;71(2):270-7.

901. Dische S, Saunders MI, Bennett MH, et al. A comparison of the tumour concentrations obtainable with misonidazole and Ro 03-8799. Br J Radiol. 1986;59(705):911-7.

902. Dische S, Chassagne D, Hope-Stone HF, et al. A trial of Ro 03-8799 (pimonidazole) in carcinoma of the uterine cervix: an interim report from the Medical Research Council Working Party on advanced carcinoma of the cervix. Radiother Oncol. 1993;26(2):93-103.

903. Kleiter MM, Thrall DE, Malarkey DE, et al. A comparison of oral and intravenous pimonidazole in canine tumors using intravenous CCI-103F as a control hypoxia marker. Int J Radiat Oncol Biol Phys. 2006;64(2):592-602.

904. Durand RE, Raleigh JA. Identification of nonproliferating but viable hypoxic tumor cells in vivo. Cancer Res. 1998;58(16):3547-50.

905. Raleigh JA, Chou SC, Bono EL, et al. Semiquantitative immunohistochemical analysis for hypoxia in human tumors. Int J Radiat Oncol Biol Phys. 2001;49(2):569-74.

906. Haustermans K, Hofland I, Van de Pavert L, et al. Diffusion limited hypoxia estimated by vascular image analysis: comparison with pimonidazole staining in human tumors. Radiother Oncol. 2000;55(3):325-33.

907. Woods ML, Koch CJ, Lord EM. Detection of individual hypoxic cells in multicellular spheroids by flow cytometry using the 2-nitroimidazole, EF5, and monoclonal antibodies. Int J Radiat Oncol Biol Phys. 1996;34(1):93-101.

908. Koch CJ. Measurement of absolute oxygen levels in cells and tissues using oxygen sensors and 2-nitroimidazole EF5. Methods Enzymol. 2002;352:3-31.

909. Jiang BH, Semenza GL, Bauer C, et al. Hypoxia-inducible factor 1 levels vary exponentially over a physiologically relevant range of O2 tension. Am J Physiol. 1996;271(4 Pt 1):C1172-80.

910. Zhong H, De Marzo AM, Laughner E, et al. Overexpression of hypoxia-inducible factor 1alpha in common human cancers and their metastases. Cancer Res. 1999;59(22):5830-5.

911. Jewell UR, Kvietikova I, Scheid A, et al. Induction of HIF-1alpha in response to hypoxia is instantaneous. FASEB J. 2001;15(7):1312-4.

912. Lee SH, McIntyre D, Honess D, et al. Carbonic anhydrase IX is a pH-stat that sets an acidic tumour extracellular pH in vivo. Br J Cancer. 2018;119(5):622-30.

913. Ivanov SV, Kuzmin I, Wei MH, et al. Down-regulation of transmembrane carbonic anhydrases in renal cell carcinoma cell lines by wild-type von Hippel-Lindau transgenes. Proc Natl Acad Sci U S A. 1998;95(21):12596-601.

914. Wykoff CC, Beasley N, Watson PH, et al. Expression of the hypoxia-inducible and tumor-associated carbonic anhydrases in ductal carcinoma in situ of the breast. Am J Pathol. 2001;158(3):1011-9.

915. Beasley NJ, Wykoff CC, Watson PH, et al. Carbonic anhydrase IX, an endogenous hypoxia marker, expression in head and neck squamous cell carcinoma and its relationship to hypoxia, necrosis, and microvessel density. Cancer Res. 2001;61(13):5262-7.

916. Turner KJ, Crew JP, Wykoff CC, et al. The hypoxia-inducible genes VEGF and CA9 are differentially regulated in superficial vs invasive bladder cancer. Br J Cancer. 2002;86(8):1276-82.

917. Ivanov S, Liao SY, Ivanova A, et al. Expression of hypoxia-inducible cell-surface transmembrane carbonic anhydrases in human cancer. Am J Pathol. 2001;158(3):905-19.

918. Younes M, Lechago LV, Somoano JR, et al. Wide expression of the human erythrocyte glucose transporter Glut1 in human cancers. Cancer Res. 1996;56(5):1164-7.

919. Shibuya M. Vascular Endothelial Growth Factor (VEGF) and Its Receptor (VEGFR) Signaling in Angiogenesis: A Crucial Target for Anti- and Pro-Angiogenic Therapies. Genes Cancer. 2011;2(12):1097-105.

920. Acs G, Zhang PJ, McGrath CM, et al. Hypoxia-inducible erythropoietin signaling in squamous dysplasia and squamous cell carcinoma of the uterine cervix and its potential role in cervical carcinogenesis and tumor progression. Am J Pathol. 2003;162(6):1789-806.

921. Beleslin-Cokic BB, Cokic VP, Yu X, et al. Erythropoietin and hypoxia stimulate erythropoietin receptor and nitric oxide production by endothelial cells. Blood. 2004;104(7):2073-80.

922. Firth JD, Ebert BL, Ratcliffe PJ. Hypoxic regulation of lactate dehydrogenase A. Interaction between hypoxia-inducible factor 1 and cAMP response elements. J Biol Chem. 1995;270(36):21021-7.

923. Rangaswami H, Bulbule A, Kundu GC. Osteopontin: role in cell signaling and cancer progression. Trends Cell Biol. 2006;16(2):79-87.

924. Sorensen BS, Hao J, Overgaard J, et al. Influence of oxygen concentration and pH on expression of hypoxia induced genes. Radiother Oncol. 2005;76(2):187-93.

925. Zhu Y, Denhardt DT, Cao H, et al. Hypoxia upregulates osteopontin expression in NIH-3T3 cells via a Ras-activated enhancer. Oncogene. 2005;24(43):6555-63.

926. Bussink J, Kaanders JH, van der Kogel AJ. Tumor hypoxia at the micro-regional level: clinical relevance and predictive value of exogenous and endogenous hypoxic cell markers. Radiother Oncol. 2003;67(1):3-15.

927. Vordermark D, Brown JM. Endogenous markers of tumor hypoxia predictors of clinical radiation resistance? Strahlenther Onkol. 2003;179(12):801-11.

928. Williams KJ, Parker CA, Stratford IJ. Exogenous and endogenous markers of tumour oxygenation status: definitive markers of tumour hypoxia? Adv Exp Med Biol. 2005;566:285-94.

929. Moon EJ, Brizel DM, Chi JT, et al. The potential role of intrinsic hypoxia markers as prognostic variables in cancer. Antioxid Redox Signal. 2007;9(8):1237-94.

930. Mayer A, Hockel M, Vaupel P. Endogenous hypoxia markers: case not proven! Adv Exp Med Biol. 2008;614:127-36.

931. Moher D, Liberati A, Tetzlaff J, et al. Preferred reporting items for systematic reviews and meta-analyses: the PRISMA statement. PLoS Med. 2009;6(7):e1000097.

932. Tricco AC, Lillie E, Zarin W, et al. PRISMA Extension for Scoping Reviews (PRISMA-ScR): Checklist and Explanation. Ann Intern Med. 2018;169(7):467-73.

933. Raleigh JA, Calkins-Adams DP, Rinker LH, et al. Hypoxia and vascular endothelial growth factor expression in human squamous cell carcinomas using pimonidazole as a hypoxia marker. Cancer Res. 1998;58(17):3765-8.

934. Raleigh JA, Chou SC, Calkins-Adams DP, et al. A clinical study of hypoxia and metallothionein protein expression in squamous cell carcinomas. Clin Cancer Res. 2000;6(3):855-62.

935. Lal A, Peters H, St Croix B, et al. Transcriptional response to hypoxia in human tumors. J Natl Cancer Inst. 2001;93(17):1337-43.

936. Janssen HL, Haustermans KM, Sprong D, et al. HIF-1A, pimonidazole, and iododeoxyuridine to estimate hypoxia and perfusion in human head-and-neck tumors. Int J Radiat Oncol Biol Phys. 2002;54(5):1537-49.

937. Arcasoy MO, Amin K, Karayal AF, et al. Functional significance of erythropoietin receptor expression in breast cancer. Lab Invest. 2002;82(7):911-8.

938. Airley RE, Loncaster J, Raleigh JA, et al. GLUT-1 and CAIX as intrinsic markers of hypoxia in carcinoma of the cervix: relationship to pimonidazole binding. Int J Cancer. 2003;104(1):85-91.

939. Azuma Y, Chou SC, Lininger RA, et al. Hypoxia and differentiation in squamous cell carcinomas of the uterine cervix: pimonidazole and involucrin. Clin Cancer Res. 2003;9(13):4944-52.

940. Chou SC, Azuma Y, Varia MA, et al. Evidence that involucrin, a marker for differentiation, is oxygen regulated in human squamous cell carcinomas. Br J Cancer. 2004;90(3):728-35.

941. Arcasoy MO, Amin K, Chou SC, et al. Erythropoietin and erythropoietin receptor expression in head and neck cancer: relationship to tumor hypoxia. Clin Cancer Res. 2005;11(1):20-7.

942. Sobhanifar S, Aquino-Parsons C, Stanbridge EJ, et al. Reduced expression of hypoxia-inducible factor-1alpha in perinecrotic regions of solid tumors. Cancer Res. 2005;65(16):7259-66.

943. Hoogsteen IJ, Peeters WJ, Marres HA, et al. Erythropoietin receptor is not a surrogate marker for tumor hypoxia and does not correlate with survival in head and neck squamous cell carcinomas. Radiother Oncol. 2005;76(2):213-8.

944. Kabuubi P, Loncaster JA, Davidson SE, et al. No relationship between thymidine phosphorylase (TP, PD-ECGF) expression and hypoxia in carcinoma of the cervix. Br J Cancer. 2006;94(1):115-20.

945. Wennemers M, Bussink J, Scheijen B, et al. Tribbles homolog 3 denotes a poor prognosis in breast cancer and is involved in hypoxia response. Breast Cancer Res. 2011;13(4):R82.

946. Kristiansen G, Hu J, Wichmann D, et al. Endogenous myoglobin in breast cancer is hypoxia-inducible by alternative transcription and functions to impair mitochondrial activity: a role in tumor suppression? J Biol Chem. 2011;286(50):43417-28.

947. Verstraete M, Debucquoy A, Devos E, et al. Investigation of possible endogenous hypoxia markers in colorectal cancer. Int J Radiat Biol. 2013;89(1):9-15.

948. Wennemers M, Stegeman H, Bussink J, et al. Hypoxia regulation of phosphokinases and the prognostic value of pAKT in breast cancer. Int J Biol Markers. 2013;28(2):151-60.

949. Nijkamp MM, Span PN, Stegeman H, et al. Low phosphorylated AKT expression in laryngeal cancer: indications for a higher metastatic risk. Int J Radiat Oncol Biol Phys. 2013;87(2):349-55.

950. Stegeman H, Rademakers SE, Span PN, et al. Hypoxia, metabolism, and growth factor signaling in head and neck squamous cell carcinoma: correlation between primary and xenograft tumors. Head Neck. 2014;36(9):1288-95.

951. van de Schootbrugge C, Schults EM, Bussink J, et al. Effect of hypoxia on the expression of alphaB-crystallin in head and neck squamous cell carcinoma. BMC Cancer. 2014;14:252.

952. Konopleva M, Thall PF, Yi CA, et al. Phase I/II study of the hypoxia-activated prodrug PR104 in refractory/relapsed acute myeloid leukemia and acute lymphoblastic leukemia. Haematologica. 2015;100(7):927-34.

953. Rupp NJ, Schuffler PJ, Zhong Q, et al. Oxygen supply maps for hypoxic microenvironment visualization in prostate cancer. J Pathol Inform. 2016;7:3.

954. Brenner A, Zuniga R, Sun JD, et al. Hypoxia-activated evofosfamide for treatment of recurrent bevacizumab-refractory glioblastoma: a phase I surgical study. Neuro Oncol. 2018;20(9):1231-9.

955. Raleigh JA, Arcasoy MO, Amin K, et al. Comparison between exogenous and endogenous hypoxia markers in human cancer: Pimonidazole and erythropoietin. Cancer Res. 2006;66(8 Supplement):S852-3.

956. Mandeville H, Goh V, Daley F, et al. Validation of volumetric DCE-CT as a biomarker of tumour hypoxia and vascularity in NSCLC. Radiother Oncol. 2010;96(Supplement 1):S82-3.

957. Debucquoy A, Khan NA, Saqaert X, et al. The use of MCT1 and MCT4 as endogenous hypoxia markers in colorectal cancer. Radiother Oncol. 2010;96(Supplement 1):S613-4.

958. Cavazos D, Gruslova A, Sun J, et al. Pharmacodynamic biomarker assessments in a phase I/II trial of the hypoxia-activated prodrug TH-302 and bevacizumab in bevacizumab-refractory recurrent glioblastoma. Neuro-Oncology. 2014;16(Supplement 5):v60.

959. Kwon SJ, Lee YJ. Effect of low glutamine/glucose on hypoxia-induced elevation of hypoxia-inducible factor-1alpha in human pancreatic cancer MiaPaCa-2 and human prostatic cancer DU-145 cells. Clin Cancer Res. 2005;11(13):4694-700.

960. Vordermark D, Kraft P, Katzer A, et al. Glucose requirement for hypoxic accumulation of hypoxia-inducible factor-1alpha (HIF-1alpha). Cancer Lett. 2005;230(1):122-33.

961. Haugland HK, Vukovic V, Pintilie M, et al. Expression of hypoxia-inducible factor-1alpha in cervical carcinomas: correlation with tumor oxygenation. Int J Radiat Oncol Biol Phys. 2002;53(4):854-61.

962. Mayer A, Wree A, Hockel M, et al. Lack of correlation between expression of HIF-1alpha protein and oxygenation status in identical tissue areas of squamous cell carcinomas of the uterine cervix. Cancer Res. 2004;64(16):5876-81.

963. Nordsmark M, Eriksen JG, Gebski V, et al. Differential risk assessments from five hypoxia specific assays: The basis for biologically adapted individualized radiotherapy in advanced head and neck cancer patients. Radiother Oncol. 2007;83(3):389-97.

964. Iommarini L, Porcelli AM, Gasparre G, et al. Non-Canonical Mechanisms Regulating Hypoxia-Inducible Factor 1 Alpha in Cancer. Front Oncol. 2017;7:286.

965. Biswas S, Charlesworth PJ, Turner GD, et al. CD31 angiogenesis and combined expression of HIF-1alpha and HIF-2alpha are prognostic in primary clear-cell renal cell carcinoma (CC-RCC), but HIFalpha transcriptional products are not: implications for antiangiogenic trials and HIFalpha biomarker studies in primary CC-RCC. Carcinogenesis. 2012;33(9):1717-25.

966. Trastour C, Benizri E, Ettore F, et al. HIF-1alpha and CA IX staining in invasive breast carcinomas: prognosis and treatment outcome. Int J Cancer. 2007;120(7):1451-8.

967. Rafajova M, Zatovicova M, Kettmann R, et al. Induction by hypoxia combined with low glucose or low bicarbonate and high posttranslational stability upon reoxygenation contribute to carbonic anhydrase IX expression in cancer cells. Int J Oncol. 2004;24(4):995-1004.

968. Willam C, Warnecke C, Schefold JC, et al. Inconsistent effects of acidosis on HIF-alpha protein and its target genes. Pflugers Arch. 2006;451(4):534-43.

969. Ihnatko R, Kubes M, Takacova M, et al. Extracellular acidosis elevates carbonic anhydrase IX in human glioblastoma cells via transcriptional modulation that does not depend on hypoxia. Int J Oncol. 2006;29(4):1025-33.

970. Sorensen BS, Alsner J, Overgaard J, et al. Hypoxia induced expression of endogenous markers in vitro is highly influenced by pH. Radiother Oncol. 2007;83(3):362-6.

971. Loncaster JA, Harris AL, Davidson SE, et al. Carbonic anhydrase (CA IX) expression, a potential new intrinsic marker of hypoxia: correlations with tumor oxygen measurements and prognosis in locally advanced carcinoma of the cervix. Cancer Res. 2001;61(17):6394-9.

972. Hedley D, Pintilie M, Woo J, et al. Carbonic anhydrase IX expression, hypoxia, and prognosis in patients with uterine cervical carcinomas. Clin Cancer Res. 2003;9(15):5666-74.

973. Mayer A, Hockel M, Vaupel P. Carbonic anhydrase IX expression and tumor oxygenation status do not correlate at the microregional level in locally advanced cancers of the uterine cervix. Clin Cancer Res. 2005;11(20):7220-5.

974. Clavo AC, Brown RS, Wahl RL. Fluorodeoxyglucose uptake in human cancer cell lines is increased by hypoxia. J Nucl Med. 1995;36(9):1625-32.

975. Jonathan RA, Wijffels KI, Peeters W, et al. The prognostic value of endogenous hypoxia-related markers for head and neck squamous cell carcinomas treated with ARCON. Radiother Oncol. 2006;79(3):288-97.

976. Airley R, Loncaster J, Davidson S, et al. Glucose transporter glut-1 expression correlates with tumor hypoxia and predicts metastasis-free survival in advanced carcinoma of the cervix. Clin Cancer Res. 2001;7(4):928-34.

977. Mayer A, Hockel M, Wree A, et al. Microregional expression of glucose transporter-1 and oxygenation status: lack of correlation in locally advanced cervical cancers. Clin Cancer Res. 2005;11(7):2768-73.

978. Sakata K, Someya M, Nagakura H, et al. A clinical study of hypoxia using endogenous hypoxic markers and polarographic oxygen electrodes. Strahlenther Onkol. 2006;182(9):511-7.

979. Medina RA, Meneses AM, Vera JC, et al. Differential regulation of glucose transporter expression by estrogen and progesterone in Ishikawa endometrial cancer cells. J Endocrinol. 2004;182(3):467-78.

980. Hakimian J, Ismail-Beigi F. Enhancement of glucose transport in clone 9 cells by exposure to alkaline pH: studies on potential mechanisms. J Membr Biol. 1991;120(1):29-39.

981. Pore N, Liu S, Shu HK, et al. Sp1 is involved in Akt-mediated induction of VEGF expression through an HIF-1-independent mechanism. Mol Biol Cell. 2004;15(11):4841-53.

982. Donaldson SB, Betts G, Bonington SC, et al. Perfusion estimated with rapid dynamic contrast-enhanced magnetic resonance imaging correlates inversely with vascular endothelial growth factor expression and pimonidazole staining in head-and-neck cancer: a pilot study. Int J Radiat Oncol Biol Phys. 2011;81(4):1176-83.

983. Shweiki D, Itin A, Soffer D, et al. Vascular endothelial growth factor induced by hypoxia may mediate hypoxia-initiated angiogenesis. Nature. 1992;359(6398):843-5.

984. Plate KH, Breier G, Weich HA, et al. Vascular endothelial growth factor is a potential tumour angiogenesis factor in human gliomas in vivo. Nature. 1992;359(6398):845-8.

985. Ziemer LS, Koch CJ, Maity A, et al. Hypoxia and VEGF mRNA expression in human tumors. Neoplasia. 2001;3(6):500-8.

986. Winter SC, Shah KA, Campo L, et al. Relation of erythropoietin and erythropoietin receptor expression to hypoxia and anemia in head and neck squamous cell carcinoma. Clin Cancer Res. 2005;11(21):7614-20.

987. Elliott S, Busse L, Bass MB, et al. Anti-Epo receptor antibodies do not predict Epo receptor expression. Blood. 2006;107(5):1892-5.

988. Brown WM, Maxwell P, Graham AN, et al. Erythropoietin receptor expression in non-small cell lung carcinoma: a question of antibody specificity. Stem Cells. 2007;25(3):718-22.

989. Elliott S, Swift S, Busse L, et al. Epo receptors are not detectable in primary human tumor tissue samples. PLoS One. 2013;8(7):e68083.

990. Bache M, Reddemann R, Said HM, et al. Immunohistochemical detection of osteopontin in advanced head-and-neck cancer: prognostic role and correlation with oxygen electrode measurements, hypoxia-inducible-factor-1alpha-related markers, and hemoglobin levels. Int J Radiat Oncol Biol Phys. 2006;66(5):1481-7.

991. Wing DA, Talley GD, Storch TG. Oxygen concentration regulates EGF-induced proliferation and EGF-receptor down regulation. Biochem Biophys Res Commun. 1988;153(3):952-8.

992. Laderoute KR, Grant TD, Murphy BJ, et al. Enhanced epidermal growth factor receptor synthesis in human squamous carcinoma cells exposed to low levels of oxygen. Int J Cancer. 1992;52(3):428-32.

993. Nishi H, Nishi KH, Johnson AC. Early Growth Response-1 gene mediates up-regulation of epidermal growth factor receptor expression during hypoxia. Cancer Res. 2002;62(3):827-34.

994. Franovic A, Gunaratnam L, Smith K, et al. Translational up-regulation of the EGFR by tumor hypoxia provides a nonmutational explanation for its overexpression in human cancer. Proc Natl Acad Sci U S A. 2007;104(32):13092-7.

995. Stegeman H, Kaanders JH, Wheeler DL, et al. Activation of AKT by hypoxia: a potential target for hypoxic tumors of the head and neck. BMC Cancer. 2012;12:463.

996. Bowers AJ, Scully S, Boylan JF. SKIP3, a novel Drosophila tribbles ortholog, is overexpressed in human tumors and is regulated by hypoxia. Oncogene. 2003;22(18):2823-35.

997. Kase S, He S, Sonoda S, et al. alphaB-crystallin regulation of angiogenesis by modulation of VEGF. Blood. 2010;115(16):3398-406.

998. Louapre P, Grongnet JF, Tanguay RM, et al. Effects of hypoxia on stress proteins in the piglet heart at birth. Cell Stress Chaperones. 2005;10(1):17-23.

999. Murphy BJ, Laderoute KR, Chin RJ, et al. Metallothionein IIA is up-regulated by hypoxia in human A431 squamous carcinoma cells. Cancer Res. 1994;54(22):5808-10.

1000. Mattern J, Kallinowski F, Herfarth C, et al. Association of resistance-related protein expression with poor vascularization and low levels of oxygen in human rectal cancer. Int J Cancer. 1996;67(1):20-3.

1001. Raleigh JA, Chou SC, Tables L, et al. Relationship of hypoxia to metallothionein expression in murine tumors. Int J Radiat Oncol Biol Phys. 1998;42(4):727-30.

1002. Murphy BJ, Andrews GK, Bittel D, et al. Activation of metallothionein gene expression by hypoxia involves metal response elements and metal transcription factor-1. Cancer Res. 1999;59(6):1315-22.

1003. Kristiansen G, Rose M, Geisler C, et al. Endogenous myoglobin in human breast cancer is a hallmark of luminal cancer phenotype. Br J Cancer. 2010;102(12):1736-45.

1004. Haraguchi M, Miyadera K, Uemura K, et al. Angiogenic activity of enzymes. Nature. 1994;368(6468):198.

1005. Griffiths L, Dachs GU, Bicknell R, et al. The influence of oxygen tension and pH on the expression of platelet-derived endothelial cell growth factor/thymidine phosphorylase in human breast tumor cells grown in vitro and in vivo. Cancer Res. 1997;57(4):570-2.

1006. Sivridis E, Giatromanolaki A, Gatter KC, et al. Association of hypoxia-inducible factors 1alpha and 2alpha with activated angiogenic pathways and prognosis in patients with endometrial carcinoma. Cancer. 2002;95(5):1055-63.

1007. Begg AC, Janssen H, Sprong D, et al. Hypoxia and perfusion measurements in human tumors--initial experience with pimonidazole and IUdR. Acta Oncol. 2001;40(8):924-8.

1008. van Laarhoven HW, de Geus-Oei LF, Wiering B, et al. Gadopentetate dimeglumine and FDG uptake in liver metastases of colorectal carcinoma as determined with MR imaging and PET. Radiology. 2005;237(1):181-8.

1009. Carnell DM, Smith RE, Daley FM, et al. An immunohistochemical assessment of hypoxia in prostate carcinoma using pimonidazole: implications for radioresistance. Int J Radiat Oncol Biol Phys. 2006;65(1):91-9.

1010. Wijffels KI, Marres HA, Peters JP, et al. Tumour cell proliferation under hypoxic conditions in human head and neck squamous cell carcinomas. Oral Oncol. 2008;44(4):335-44.

1011. Evans SM, Jenkins KW, Jenkins WT, et al. Imaging and analytical methods as applied to the evaluation of vasculature and hypoxia in human brain tumors. Radiat Res. 2008;170(6):677-90.

1012. Ragnum HB, Vlatkovic L, Lie AK, et al. The tumour hypoxia marker pimonidazole reflects a transcriptional programme associated with aggressive prostate cancer. Br J Cancer. 2015;112(2):382-90.

1013. Evans SM, Jenkins KW, Chen HI, et al. The Relationship among Hypoxia, Proliferation, and Outcome in Patients with De Novo Glioblastoma: A Pilot Study. Transl Oncol. 2010;3(3):160-9.

1014. Olive PL, Banuelos CA, Durand RE, et al. Endogenous and radiation-induced expression of gammaH2AX in biopsies from patients treated for carcinoma of the uterine cervix. Radiother Oncol. 2010;94(1):82-9.

1015. Raleigh JA, Varia MA, Lee DYW. Hypoxia and Differentiation: Contrast Between Pimonidazole Binding and CK19 Expression in Tumors Derived From Stratified and Simple

Epithelia. International Journal of Radiation Oncology, Biology, Physics. 2013;87(2):S667-S8.

1016. Hoppin JA, Tolbert PE, Taylor JA, et al. Potential for selection bias with tumor tissue retrieval in molecular epidemiology studies. Ann Epidemiol. 2002;12(1):1-6.

1017. McShane LM, Altman DG, Sauerbrei W, et al. REporting recommendations for tumour MARKer prognostic studies (REMARK). Eur J Cancer. 2005;41(12):1690-6.

1018. Altman DG, McShane LM, Sauerbrei W, et al. Reporting Recommendations for Tumor Marker Prognostic Studies (REMARK): explanation and elaboration. PLoS Med. 2012;9(5):e1001216.

1019. Nordsmark M, Loncaster J, Chou SC, et al. Invasive oxygen measurements and pimonidazole labeling in human cervix carcinoma. Int J Radiat Oncol Biol Phys. 2001;49(2):581-6.

1020. Olive PL, Banath JP, Aquino-Parsons C. Measuring hypoxia in solid tumours--is there a gold standard? Acta Oncol. 2001;40(8):917-23.

1021. Nordsmark M, Loncaster J, Aquino-Parsons C, et al. Measurements of hypoxia using pimonidazole and polarographic oxygen-sensitive electrodes in human cervix carcinomas. Radiother Oncol. 2003;67(1):35-44.

1022. Nordsmark M, Loncaster J, Aquino-Parsons C, et al. The prognostic value of pimonidazole and tumour pO2 in human cervix carcinomas after radiation therapy: a prospective international multi-center study. Radiother Oncol. 2006;80(2):123-31.

1023. Evans SM, Judy KD, Dunphy I, et al. Comparative measurements of hypoxia in human brain tumors using needle electrodes and EF5 binding. Cancer Res. 2004;64(5):1886-92.

1024. Jenkins WT, Evans SM, Koch CJ. Hypoxia and necrosis in rat 9L glioma and Morris 7777 hepatoma tumors: comparative measurements using EF5 binding and the Eppendorf needle electrode. Int J Radiat Oncol Biol Phys. 2000;46(4):1005-17.

1025. Janssen HL, Hoebers FJ, Sprong D, et al. Differentiation-associated staining with anti-pimonidazole antibodies in head and neck tumors. Radiother Oncol. 2004;70(1):91-7.

1026. Dewhirst MW, Ong ET, Klitzman B, et al. Perivascular oxygen tensions in a transplantable mammary tumor growing in a dorsal flap window chamber. Radiat Res. 1992;130(2):171-82.

1027. Evans SM, Jenkins WT, Shapiro M, et al. Evaluation of the concept of "hypoxic fraction" as a descriptor of tumor oxygenation status. Adv Exp Med Biol. 1997;411:215-25.

1028. Evans SM, Koch CJ. Prognostic significance of tumor oxygenation in humans. Cancer Lett. 2003;195(1):1-16.

1029. Le QT, Kong C, Lavori PW, et al. Expression and prognostic significance of a panel of tissue hypoxia markers in head-and-neck squamous cell carcinomas. Int J Radiat Oncol Biol Phys. 2007;69(1):167-75.

1030. Shin KH, Diaz-Gonzalez JA, Russell J, et al. Detecting changes in tumor hypoxia with carbonic anhydrase IX and pimonidazole. Cancer Biol Ther. 2007;6(1):70-5.

1031. Russell J, Carlin S, Burke SA, et al. Immunohistochemical detection of changes in tumor hypoxia. Int J Radiat Oncol Biol Phys. 2009;73(4):1177-86.

1032. Wang F, Flanagan J, Su N, et al. RNAscope: a novel in situ RNA analysis platform for formalin-fixed, paraffin-embedded tissues. J Mol Diagn. 2012;14(1):22-9.

1033. Ljungkvist AS, Bussink J, Rijken PF, et al. Changes in tumor hypoxia measured with a double hypoxic marker technique. Int J Radiat Oncol Biol Phys. 2000;48(5):1529-38.

1034. Bennewith KL, Durand RE. Quantifying transient hypoxia in human tumor xenografts by flow cytometry. Cancer Res. 2004;64(17):6183-9.

1035. Ljungkvist AS, Bussink J, Kaanders JH, et al. Hypoxic cell turnover in different solid tumor lines. Int J Radiat Oncol Biol Phys. 2005;62(4):1157-68.

1036. Ljungkvist AS, Bussink J, Kaanders JH, et al. Dynamics of hypoxia, proliferation and apoptosis after irradiation in a murine tumor model. Radiat Res. 2006;165(3):326-36.

1037. Sun X, Li XF, Russell J, et al. Changes in tumor hypoxia induced by mild temperature hyperthermia as assessed by dual-tracer immunohistochemistry. Radiother Oncol. 2008;88(2):269-76.

1038. Rademakers SE, Rijken PF, Peeters WJ, et al. Parametric mapping of immunohistochemically stained tissue sections; a method to quantify the colocalization of tumor markers. Cell Oncol (Dordr). 2011;34(2):119-29.

1039. Achanta R, Shaji A, Smith K, et al. SLIC superpixels compared to state-of-the-art superpixel methods. IEEE Trans Pattern Anal Mach Intell. 2012;34(11):2274-82.

1040. Veta M, van Diest PJ, Kornegoor R, et al. Automatic nuclei segmentation in H&E stained breast cancer histopathology images. PLoS One. 2013;8(7):e70221.